Multi-isotopic study of the carbon and sulfur cycles in modern alkaline and stratified environments from Mexico and their microbialites

Robin Havas

Thèse de doctorat

Université de Bourgogne-Franche-Comté

Spécialité : **Géochimie isotopique**

Préparée au laboratoire Biogéosciences, UMR 6282 CNRS, à l'Université de Bourgogne
École doctorale Environnement Santé, UFR SVTE

Par

Robin Havas

Étude multi-isotopique des cycles du carbone et du soufre d'environnements modernes alcalins et stratifiés du Mexique et de leurs microbialites

Multi-isotopic study of the carbon and sulfur cycles in modern alkaline and stratified environments from Mexico and their microbialites

Composition du Jury :

Emmanuelle Vennin	Professeure des universités à l'Université de Bourgogne	Présidente
Magali Ader	Professeure des universités à l'Université de Paris Cité	Rapportrice
Yuichiro Ueno	Professeur à l'Institut technologique de Tokyo	Rapporteur
Nina Zeyen	Maîtresse de conférences à l'Université de Genève	Examinatrice
David A. Fike	Professeur à l'Université de Washington à Saint Louis	Examinateur
Christophe Thomazo	Maître de conférences à l'Université de Bourgogne	Directeur de thèse
Karim Benzerara	Directeur de recherche CNRS à Sorbonne Université	Invité

Laguna de Alchichica

Photograph. P. Boussagol

Remerciements

Je voudrais commencer par remercier les membres de mon jury, ayant toutes et tous spontanément et chaleureusement accepté de participer à l'évaluation de mon travail de thèse : Emmanuelle Vennin, pour le présider, Magali Ader et Yuichiro Ueno pour en être les rapporteurs, Nina Zeyen et David Fike, les examinateurs. Je vous remercie particulièrement pour les échanges précieux que nous avons pu avoir, et les portes que vous avez pu m'ouvrir. Je voudrais remercier Karim Benzerara qui m'a accompagné pendant cette thèse et apporté de précieux conseils, dès la fin de mon master, et que je tenais à inviter dans ce jury. Enfin, je ne pourrais jamais assez remercier Christophe Thomazo, qui n'a pas seulement dirigé cette thèse, mais m'a encadré dans le sens le plus complet du terme. Une disponibilité sans faille, une confiance et exigence qui m'ont toujours poussé vers l'avant, me permettant de m'accomplir en tant qu'apprenti chercheur, et surtout une philosophie du naturel au travail que je garderai pour exemple. De ma jeune carrière académique, venir travailler à Dijon avec toi est un des plus importants et meilleurs choix que j'ai fait.

J'aimerais également remercier les personnes qui m'ont amené jusqu'à cette thèse, à commencer par Vincent Busigny, qui m'a initié aux joies de la géochimie. Merci de toujours avoir été de bon conseil, et de bonne humeur ! Je pense également à Jérôme Gaillardet, Eric Gayer, Pascale Louvat, Mark van Zuilen et Joti Rouillard, qui m'ont aidé, encadré, aiguillé depuis ma L1. Merci à toutes les autres personnes qui m'ont permis de prêt ou de loin d'avoir ce parcours.

Merci à toutes celles et ceux qui rendent l'accomplissement de la thèse au sein du laboratoire possible, directement aux machines Ludo, Anne-Lise, Théophile, Ivan, Elodie, Justine sans qui le manuscrit ferait quelques pages de moins ! Merci évidemment à Tom et Hugo, que j'ai eu le plaisir d'avoir en stage, qui m'ont permis d'avancer plus vite et m'ont procuré une expérience très riche d'encadrement. Merci aussi, à Claire, Isabelle et Corine, qui ont gardé la patience malgré mon incapacité à remplir un OM ou une demande de devis correctement ^^ Merci également à Christelle Caillot et Thierry Rigaud à l'école doc qui ont toujours gardé leur porte ouverte et répondu à mes questions aussi vites qu'elles étaient posées.

Evidemment, j'ai eu de la chance de me retrouver dans cette bibliothèque, parce que c'est un bureau qu'a une sacrée classe (!), mais surtout j'ai pu être magnifiquement accompagné ! Erwan malgré tes passages entre deux avions, Ophélie, entre une petite fouine et une sauveuse de lapin ça aurait pu être compliqué mais faut croire qu'il y a des exceptions ;), Alice, my geochemist partner jusqu'au tréfonds du Pacifique ! Se faire faire face pendant 3 ans ça comporte des « risques », mais je suis chanceux de t'avoir eu ta petite tête dépasser au-dessus de mes écrans pendant tout ce temps ! Merci pour ta bonhomie et gentillesse de tous les jours. Jérôme enfin, notre grand druide multi-fonction, merci pour ton aide du début jusqu'à la (toute) fin de thèse, souvent collègue de travail *non-isolé* aux heures

un peu tardives, ça a été super de partager ce bureau avec toi et avec vous, on ne pouvait guère rêver mieux pour l'ambiance !

Le groupe des doctorants s'est bien étoffé avec le temps, et je tiens à vous remercier toutes et tous en n'oubliant personne autant que possible, pour cette vie entre doctorants de quasi-exclusivité parfois, au labo, comme en dehors ! Chris et Louis, mes inconditionnels du confinement, mais pas que, Pierre mon musicien tennisman préféré, Esteban merci de m'avoir rendu moins seul comme utilisateur inconditionnel du vélo (!); et toute cette belle bande du ski, Gaëtan, Mathilde, Maïwenn, Giovanni, Agathe, Lilla, et Alexandrine ! Plus deuxième édition, Luc, Camille, Myriam et Sarah ! Merci à Marlisa, notamment pour ces derniers jours et heures à finir de rédiger ensemble. Merci à Morgane, Julien, Clément, Quentin, Yann, Tessie, … la liste est longue mais je vous remercie tou(te)s sans exception. Pour l'aide dans les relectures et pour tout le reste, un grand merci également à Majd et Xu ! Ces petites dédicaces ne sont que trop courtes, mais l'essentiel est bien plus dans tous nos moments passés ensemble ! Pour finir, je crois qu'il faudra collectivement remercier le blues, l'american, la microbrasserie et les 2, 3 parcs aux alentours…

La liste serait encore plus (trop) longue, mais merci à tous mes amis de la plus tendre enfance jusqu'aux temps moins innocents du lycée et de la fac ! Merci à ceux qui ont pu me rendre visite et découvrir cette belle ville de Dijon, ou auraient aimé venir, ou que j'aurais dû inviter plus souvent. Je pense à vous toutes et tous, et ces moments passés m'ayant amenés jusqu'ici. J'ai hâte de vous revoir pour vous remercier de vive voix.

Merci enfin à ma famille, notamment mon frère, ma sœur, mon père et ma mère. Du début à la fin, je ne pourrais jamais assez exprimé toute la chance que j'ai de vous avoir, le bonheur et la force que vous me donnez, merci.

Preamble

As we go back in deep time, hundreds of million to billion years ago, the principle of actualism is challenged by a lack of comparability between the world today and in the past. Indeed, the complex biogeochemical cycles, and climatic, geologic, and biological processes that shaped the surface of the Earth million to billion years ago differed from those occurring today. “At issue” are the changes in key parameters that influence these processes such as the solar radiation, plate tectonic geodynamic, atmospheric and oceanic chemistry, or yet the extent of life development (Gargaud *et al.*, 2009). Nonetheless, the intrinsic physical and chemical reactions participating in these complex cycles will remain invariant regardless of the environmental context they occur in. Hence, retracing the past Earth’s surface conditions starts by understanding how bio-geo-chemical cycles function today, and how they are recorded, or transferred to the surficial geological record: sedimentary rocks. In order to reduce the “actualistic bias”, studying modern environments that resemble the ancient Earth is primordial to validate our models and interpretations about these past times. Motivated by this approach, the work I present in this PhD manuscript aims to improve our understanding of such modern environments, analogous to different periods of the past, and potentially future of the Earth.

Main table of content

Preliminary sections

Chapter 1: General Introduction

Chapter 2: Geological, climate, and limnological context

Chapter 3: Field work and analytical methods

Chapter 4: Carbon isotope signatures in redox-stratified alkaline lakes along an alkalinity gradient

Chapter 5: Carbon budget and sources in Alchichica: a modeling approach

Chapter 6: Sedimentary record of the carbon cycle in the Mexican lakes

Abstract

The study of modern environments that harbor conditions close to those we know existed in the primitive Earth represents a powerful approach to better understand ancient **biogeochemical cycles**, and is complementary to direct investigations of ancient geological deposits. For these reasons, my PhD work focused on characterizing four **volcanic crater lakes** from Mexico that can be used as **modern analogues** of ancient times. These lakes are **alkaline** and **stratified**, constituting extreme environments in terms of redox and water chemistry. They are also characterized by the presence of **microbialites**, that is, carbonated deposits formed from the interaction between microbial communities and abiological environmental factors, and whose first appearance is dated back to 3.5 Ga, making microbialites one of the most emblematic record of primitive life evolution on Earth. I characterized these Mexican ecosystems mainly using **isotope geochemistry**, a powerful tool that allows tracing back physico- and biogeo-chemical processes. **Carbon, oxygen,** and **sulfur** isotopes have been analyzed in multiple dissolved and particulate phases in the water column and sediments of the four lakes.

This study proposes a deep characterization of the biogeochemical processes involving C and S in the lakes today, and how they are recorded as chemical (isotopic) signatures in their sedimentary archives (gravitational and microbialite sediments). This approach brings to light the processes susceptible to be transferred to the geological repertoire, and those by contrast, which are not, or only partially. Thus, this work shows that carbonate deposits are weakly sensitive to biological and climatic processes in high alkalinity conditions over short time periods (hundred to thousand years). It is also shown that sedimentary organic matter only partially records the redox and chemical stratification of the water columns. However, key physiological processes carried out by microorganisms and having a strong influence on the C cycle of the lakes were evidenced after the original analysis of dissolved organic carbon (DOC) isotopic composition.

Lake-specific physico-chemical conditions generate differences in the degree of preservation and reorganization of the C and S geochemical sedimentary record. This thesis shows how key parameters such as the lakes hydrological dynamic, redox level, nutrients abundance, inorganic and organic supplies (*e.g.* in CO_2, SO_4^{2-}, DOC) directly influence the isotopic signatures recorded in carbonates, organic matter, and sedimentary pyrites.

Microbialites record is found to be altered by a number of biases (*e.g.*, meteoric waters, mineralogical variations), but brings a complementary message, more specific of local biological and environmental factors. For example, the precipitation of some of the microbialites under the influence of underground and runoff waters allows better understanding

the composition of fluids feeding the lakes. The formation of microbialites at fixed depths in the stratified water column also enables a more and punctual and specific record of the physico-chemical conditions in the water columns.

Coupling the geochemical approach to mineralogical, sedimentological, and microbiological, this study portrays the C and S cycles of the Mexican lakes studied, and in a broader way, describes some limits of geochemical signatures to reconstruct a geological biogeochemical story.

Nevertheless, the study of such modern systems – which allows both the identification of presently occurring biogeochemical processes (by measurements that cannot be applied to the fossil record) and the characterization of their expression as pristine geochemical signals in sediments – constitutes an important step in our understanding of transfer function to use in paleoenvironment reconstructions as well as the biogeochemical processes associated with microbialites formation.

Résumé synthétique

L'étude d'environnements modernes caractérisés par des conditions environnementales proches de ce que nous connaissons de la Terre ancienne (des **analogues**) constitue une approche puissante pour mieux comprendre les **cycles biogéochimiques** anciens, et complémentaire des études portant directement sur le répertoire géologique. Dans ce sens, mon travail de thèse s'est attaché à caractériser quatre **lacs de cratère** de volcans situés au Mexique. Ces lacs sont **alcalins** et **stratifiés** et constituent ainsi des environnements extrêmes notamment en termes de conditions redox et de chimie des eaux. De plus, ces lacs sont caractérisés par la présence de **microbialites**, des roches carbonatées dont la formation résulte de l'interaction de communautés microbiennes avec leur environnement, et dont les premières occurrences remontent à plus de 3.5 Ga, représentant un des enregistrements emblématiques de l'évolution précoce de la vie sur Terre. Durant ma thèse, j'ai caractérisé ces écosystèmes principalement par le biais de la **géochimie isotopique**, outil puissant permettant de retracer les processus physico- et biogéo-chimiques. Les isotopes du **C, de l'O et du S** ont ainsi été charterisés dans de multiples phases dissoutes (carbone inorganique et organique, sulfures, sulfates) et particulaires ou minérales (carbone organique en suspension, carbonates, pyrites) dans les colonnes d'eau et sédiments des quatre lacs.

Cette étude propose une caractérisation en profondeur à la fois des processus biogéochimiques du C et du S s'opérant actuellement dans ces écosystèmes, ainsi que des signatures biogéochimiques que ces derniers laissent dans l'enregistrement sédimentaire des lacs (sédiments gravitaires et microbialites). Cette approche met en lumière les processus susceptibles d'être transférés au répertoire géologique et au contraire ceux qui ne le sont pas, ou partiellement. Ainsi, ce travail montre que les réservoirs carbonatés, dans des conditions de forte alcalinité, sont peu sensibles aux processus biologiques ou climatiques pour de courtes échelles de temps (centaines à milliers d'années). Il est également montré que la matière organique sédimentaire n'enregistre que partiellement les conditions du milieu et ne permet pas toujours de reconstruire fidèlement la stratification redox et chimique des colonnes d'eaux. En revanche des processus physiologiques clés accomplis par les micro-organismes et ayant une forte influence sur le cycle du C de ces lacs ont été mise en évidence par l'analyse originale de la composition isotopique du carbone organique dissous.

De plus, les conditions physico-chimiques spécifiques à chacun des lacs engendrent des différences dans l'amplitude avec laquelle les registres sédimentaires du C et du S et leurs signatures géochimiques sont remaniés et préservés. Ainsi, cette étude montre comment des paramètres environnementaux clés tels que la dynamique hydrologique, le niveau d'oxydation, la teneur en nutriments et substrats organiques et inorganiques (*e.g.*, CO_2, SO_4^{2-}, carbone organique dissous) influencent directement la magnitude des compositions isotopiques enregistrées par les carbonates, la matière organique, et les pyrites sédimentaires.

L'enregistrement des microbialites est également altéré par un certain nombre de biais (*e.g.*, altération par les eaux météoriques, variations minéralogiques), mais apporte un message complémentaire, plus spécifique des processus biologiques et environnementaux locaux. Par exemple, la précipitation de certains microbialites directement au niveau des apports d'eaux souterraines et de ruissellement permet de mieux contraindre la composition des fluides alimentant les lacs. La formation des microbialites à une profondeur donnée de la colonne d'eau stratifiée permet également un enregistrement plus ponctuel et spécifiques des conditions physico-chimiques de la colonne d'eau.

En couplant l'approche géochimique, à des résultats de minéralogie, sédimentologie, et microbiologie, cette étude dresse le portrait des cycles du C et du S de ces lacs spécifiquement, et de manière plus générale, dans quelles limites l'enregistrement sédimentaire sous forme de signatures géochimiques peut nous permettre de reconstruire l'histoire géologique et biogéochimiques.

Toutefois, l'étude de ces milieux actuels permettant à la fois d'identifier les processus biogéochimiques présentement à l'œuvre (par des mesures qui ne peuvent être réalisées dans le répertoire fossile), ainsi que les signaux géochimiques isotopiques sédimentaires qui en résultent, constitue une étape importante dans notre compréhension des fonctions de transferts à utiliser pour reconstruire les paléoenvironnements anciens ainsi que les processus biogéochimiques associés à la formation des microbialites.

Résumé étendu

Préface

Le principe d'actualisme appliqué à des périodes vieilles de milliards ou de centaines de millions d'années peut être mis en défaut par les différences entre le monde d'aujourd'hui et celui d'un passé lointain. En effet, les cycles biogéochimiques et processus climatiques, géologiques et biologiques complexes ayant façonné la surface terrestre à ces périodes reculées diffèrent de ceux ayant cours aujourd'hui. En cause sont des changements des paramètres clés qui influencent ces processus tels que la radiation solaire, la tectonique des plaques, la chimie de l'océan et de l'atmosphère, ou encore l'étendue du développement du vivant. Néanmoins, les réactions physiques et chimiques participant aux processus surfaciques susmentionnés restent invariantes face aux différents environnements dans lesquels elles se produisent. Ainsi, le décryptage des conditions de surface de la Terre au cours de son histoire commence par l'appréhension de ces cycles bio-géo-chimiques aujourd'hui et de la manière dont ils sont enregistrés, *i.e.*, transférés dans le registre géologique *via* les roches sédimentaires. Afin de réduire le « biais actualiste » et de valider nos concepts et interprétations sur ces périodes passées, il est primordial d'étudier des environnements modernes qui ressemblent à la Terre ancienne. Motivé par ces considérations, le travail présenté dans ce manuscrit de thèse vise à améliorer notre compréhension de tels environnements actuels, analogues de différentes périodes de la Terre passées, et potentiellement futures.

Introduction

La faible teneur en dioxygène et la stratification redox des océans sont des caractéristiques majeures de la Terre Précambrienne (>500 Ma). L'étendue des eaux pauvres en dioxygène est également amenée à augmenter avec le réchauffement climatique actuel. La stratification redox d'un milieu (l'équilibre entre les espèces chimiques oxydées et réduites) exerce une influence critique sur la diversité des réactions biotiques et abiotiques qui peuvent s'y dérouler, et réciproquement (*e.g.*, Fig. 1.2). L'étude de tels bassins stratifiés modernes a montré la complexité de ces environnements et la nécessité de mieux contraindre leur

enregistrement sédimentaire. À ces fins, les *signatures isotopiques* des réservoirs naturels représentent un potentiel outil puissant.

Des isotopes peuvent être définis comme les différentes "versions" d'un même élément chimique, se distinguant par leur nombre de neutrons (N), mais gardant un même nombre de protons (Z). Ces différences de masses entre isotopes (≠ N), malgré des propriétés chimiques similaires (même Z), dictent les échanges et la répartition de ces isotopes entre réactants et produits lors des réactions bio-physico-chimiques. Ainsi, les signatures isotopiques (*e.g.* de l'O dans l'H_2O) et les *fractionnements isotopiques* (*e.g.* de l'O entre l'H_2O et le $CaCO_3$) peuvent être utilisés comme traceurs de sources de ces éléments et des réactions par lesquelles ils sont passés.

Dans mon travail de thèse, j'ai principalement étudié les isotopes du carbone (C), du soufre (S), ainsi que de l'oxygène (O). Le cycle de ces éléments joue un rôle clé dans l'évolution des conditions de la surface terrestre, à la fois aux échelles de temps et d'espace géologiques et à l'échelle beaucoup plus fine de la biologie. De plus, les cycles respectifs de ces éléments sont intimement liés à travers une multitude de phénomènes géologiques et biologiques (*e.g.*, Fig. 1.8).

Les microbialites sont des objets emblématiques des sciences de la Terre, comme traceurs de l'évolution de la vie sur Terre, et de la chimie des eaux continentales et océaniques, comme archives paléoclimatiques, mais aussi comme roches stockant le CO_2 et les hydrocarbures. Ces qualités résultent des différents mécanismes de leur formation, directement influencée par de multiples processus biotiques (*e.g.*, photosynthèse) et abiotiques (*e.g.*, dégazage volcanique). Cependant, ces mécanismes sont complexes et demandent à mieux être compris pour que les signatures chimiques et isotopiques de tels objets puissent être correctement interprétées.

Objectifs et stratégie

L'objectif principal de cette thèse était d'évaluer la fiabilité des archives sédimentaires comme enregistrements des cycles biogéochimiques d'environnements modernes stratifiés. À ces fins, la comparaison de quatre lacs stratifiés contenant des microbialites fut établie à travers les analyses isotopiques du C, du S, et de l'O, depuis la caractérisation des processus ayant lieu

actuellement dans leur colonne d'eau jusqu'aux enregistrements géochimiques sédimentaires (sédiments de fond des lacs et microbialites).

Un certain nombre d'études d'analogues modernes existent mais décrivent un site en particulier (et donc un contexte environnemental spécifique). Ici, l'étude de plusieurs localités aux caractéristiques chimiques distinctes, mais partageant un contexte similaire (lacs alcalins, stratifiés, volcaniques) permet de cibler les effets de paramètres spécifiques sur les enregistrements géochimiques de ces lacs. Notamment, j'ai comparé l'influence qu'avaient différentes concentrations d'alcalinité, de bionutriments et de sulfates sur les quatre environnements et leurs sédiments.

Un atout majeur de l'étude d'environnements actuels par rapport à celle du répertoire géologique réside dans la possibilité de mesurer à la fois les phases dissoutes et solides. J'ai donc commencé par caractériser les processus biogéochimiques qui opèrent aujourd'hui (requérant les phases dissoutes), avant d'évaluer ce qu'il en reste dans les phases pérennes, c'est à dire solides.

Pour la première fois, ce travail de thèse s'attache à comparer les deux types d'enregistrement sédimentaire (gravitaire et microbialites) au sein d'un même environnement, en parallèle des processus actifs opérant dans les eaux de lac et de porosité sédimentaire. La comparaison de systèmes microbialitiques distincts reste rare et est également un atout de cette étude. De plus, des microbialites se formant en conditions anoxiques furent analysés, ce qui ne fut jamais réalisé pour des environnements modernes malgré le caractère clé de ce paramètre dans les temps Précambriens.

Les questions principales auxquelles je tente de répondre dans ce manuscrit sont : (i) quels traits majeurs des processus et de la biodiversité de ces environnements stratifiés peuvent ne pas être préservés dans les archives sédimentaires ? (ii) Quels sont les paramètres biotiques et abiotiques les mieux préservés dans ces enregistrements ? (iii) Lequel des répertoires de sédiments de fond du lac ou des microbialites est le plus spécifique aux conditions physico-chimiques et biologiques ? (iv) Comment la diagénèse précoce peut-elle les altérer et brouiller le message initialement enregistré ? À partir des motivations et questions présentées plus haut, ce manuscrit de thèse est séparé en trois parties : (I) les signaux isotopiques du C et de l'O de la colonne d'eau aux sédiments gravitaires (Chapitres 4, 5, 6) ; (II) les signatures isotopiques du S des quatre lacs et leur enregistrement dans les sédiments gravitaires (Chapitres 7, 8) ; (III)

descriptions pétrographiques et systématiques isotopiques du C, O et S des archives microbialitiques (Chapitres 9, 10, 11).

Terrains d'étude

Quatre lacs furent étudiés et se répartissent sur deux zones géographiques distinctes de la ceinture de volcans trans-mexicaine (TMVB) : Alberca de los Espinos dans le bassin de Zacapu (19°54'24''N ; 101°46'08''W), La Preciosa, Atexcac et Alchichica dans le bassin du Serdan-Oriental (19°22'0''N ; 97°24'50''W) (Fig. 2.1). Les quatre lacs remplissent des cratères volcaniques d'éruptions phréatomagmatiques, datées de la fin du Pleistocène à l'Holocène (Tableau 2.1). Ce sont des lacs endoréiques, c'est-à-dire seulement alimentés par des eaux souterraines et non par des sources de surface, et ils se trouvent dans des bassins fermés où les eaux de pluie ne rejoignent pas la mer.

La colonne d'eau de ces lacs est stratifiée – en température et pour un certain nombre de paramètres chimiques incluant la teneur en oxygène – avec un régime de mélange monomictique (mélange une fois par an). Ces lacs présentent tous un pH alcalin (~9), mais leur composition chimique suit un gradient de salinité et d'alcalinité notamment. Enfin, ils sont soumis à un climat aride à tempéré, avec plus d'évaporation que de précipitation (en particulier dans le bassin du Serdan-Oriental).

Méthodes

La majorité des analyses isotopiques ont été faites selon les méthodes traditionnelles de spectrométrie de masse en phase gazeuse, c'est-à-dire par la transformation d'échantillons liquides ou solides en un gaz (*e.g.*, CO_2, SO_2), purifié, puis dont les molécules isotopologues ionisés sont accélérées et séparées dans un champ magnétique. Les compositions isotopiques sont exprimées dans la notation classique de δ tel que $\delta = 1000(R_{échantillon}/R_{standard} - 1)$ où R représente l'un des isotopes lourds sur l'isotope léger de référence. L'analyse des quadri-isotopes du S fut elle menée à Tokyo à travers une méthode plus récente incluant une fluorination par pyrolyse. L'ensemble des analyses réalisées est résumé dans le Tableau 3.1. De plus, cette thèse s'appuie en partie sur des données minéralogiques et microbiologiques de pointe menées par nos collaborateurs de l'Université de Paris-Saclay et de Sorbonne Université.

Résultats et conclusions principales

Plus bas sont résumées les conclusions principales décrites dans le corps du texte. Les numéros entre parenthèses indiquent les chapitres concernés par celles-ci.

Partie I

Les concentrations et compositions isotopiques des réservoirs de C inorganique (carbone inorganique dissous, DIC, et carbonates sédimentaires) des quatre lacs montrent que plus l'alcalinité d'un milieu est forte, moins ces réservoirs sont sensibles aux conditions environnementales qui les affectent (*e.g.*, influence d'une activité biologique, changements climatiques et hydrologiques) car le réservoir de DIC est trop grand et donc tamponné (4, 10). Néanmoins, les systèmes de forte alcalinité favorisent la sursaturation et la précipitation de carbonates dont les compositions isotopiques sont à équilibre avec les eaux de lac (4, 10). Sur des échelles de temps relativement longues (10^3 à 10^6 années), ces carbonates représentent donc de potentiels enregistrements fidèles des changements environnementaux majeurs affectant ces contextes. Plus précisément, les carbonates des sédiments gravitaires de trois des quatre lacs précipitent dans la partie haute des colonnes d'eau, et notamment au niveau de l'oxycline (4, 6). Une implication majeure de cela est que les processus ayant cours dans le bas des colonnes d'eau ne sont pas enregistrés dans les sédiments, comme la méthanogènèse à Alberca de los Espinos.

De plus, les systèmes alcalins représentent des environnements extrêmes, où, une baisse de pH de la colonne d'eau vers les sédiments (qui fut observée dans les quatre lacs Mexicains) peut provoquer une réorganisation significative des dépôts carbonatés (et des silicates de Mg). A Atexcac, cela entraîne la dissolution de l'aragonite provenant du lac et la reprécipitation de calcite dans le sédiment (6). Ce processus mène donc à un enregistrement géochimique qui est secondaire, préservant l'eau de porosité plus que celle du milieu surplombant. Il est également trouvé que la quantité de C enfoui dans les carbonates (de 20 à 70 $gC.m^{-2}.yr^{-1}$) est *in fine* cohérente avec la teneur en alcalinité de chaque lac, et ce même si les taux de

précipitation/déposition ne suivent pas le gradient d'alcalinité initialement. Ceci indique la nécessité de prendre la diagénèse en compte lors de l'estimation des flux de stockage de CO_2.

La modélisation des processus et flux de C sur les 60 dernières années à Alchichica a permis de caractériser de manière quantitative le cycle du C de ce lac, mettant en évidence une contribution significative de dégazage de CO_2 volcanique (5). Ce travail met aussi en lumière l'importance de la position d'aval d'Alchichica par rapport à La Preciosa et Atexcac dans l'aquifère qui les alimente, ce qui influence fortement la composition chimique d'Alchichica (5). Ce travail de modélisation fut possible grâce aux mesures des eaux d'aquifère et aux relevés hydrologiques (données extérieures au lac), soulignant encore une fois la faible sensibilité du réservoir de DIC dans un contexte de forte alcalinité, et l'importance de prendre du recul par rapport au site d'étude spécifique afin d'en capturer une image plus complète.

Le réservoir de carbone organique dissous (DOC) – qui n'est pas enregistré dans les sédiments – a été mis en lumière comme un élément central du cycle du C des lacs étudiés (4), démontrant qu'il est primordial de l'analyser en complément du DIC et POC (carbone organique particulaire). En effet, la concentration et composition isotopique du DOC démontrent plusieurs processus difficilement retraçables d'après les seuls DIC et POC. À partir d'enrichissements extrêmes en isotopes lourds (^{13}C), les données de DOC montrent qu'une combinaison de forte radiation UV et disponibilité en CO_2, et de faibles teneurs en nutriments mènent à une production autochtone de matière organique dissoute maximale. L'étude du DOC dans ses environnements permet a également permis de contraindre le rôle du DOC dans le cycle du C à l'ère Précambrienne (4).

Les données de DOC ont permis de clairement identifier les communautés bactériennes planctoniques les plus actives : bactéries phototrophes oxygéniques et anoxygéniques, et possiblement les bactéries hétérotrophes présentes au redoxcline et en dessous (4). L'activité de chacun de ces groupes est très variée dans chacun des lacs, ce qui contribue à l'hétérogénéité de la matière organique sédimentaire (SOM), qui ne provient pas toujours des mêmes couches de la stratification selon le lac. Différents degrés d'altération de la SOM furent trouvés dans les quatre systèmes, avec un changement maximum +4 ‰ du $\delta^{13}C_{SOM}$ trouvé à Atexcac (6). L'évaluation des sédiments de fond de lac montrent que les plus forts enrichissements isotopiques de la SOM lors de la diagénèse devraient résulter d'une faible production primaire (*i.e.*, en conditions oligotrophiques), de faibles taux de sédimentation et d'une forte disponibilité d'oxydants dans le système (6).

Partie II

Les facteurs principaux influençant l'enregistrement isotopique du S dans les séquences sédimentaires des quatre lacs diffèrent (7, 8). À Alchichica, un cycle « cryptique » de reoxydation du S fut mis en évidence à partir des multi-isotopes du S des pyrites et des sulfates de l'eau de porosité. Les sulfures produits de la sulfato-réduction microbienne (MSR) sont réoxydés en espèces soufrées intermédiaires (*e.g.*, S élémentaire) qui sont ensuite disproportionnées en sulfures et sulfates dissous (7). La répétition de cet enchainement de réactions déplace la composition isotopique finale des pyrites vers des $\delta^{34}S$ plus négatifs, des et des $\Delta^{33}S$ plus positifs que ce qui serait attendu si seulement un mécanisme de distillation des sulfures par MSR était à l'œuvre. Des reconstructions environnementales basées sur la pyrite sédimentaire seule interpréteraient, *a posteriori*, un système d'eaux porales ouvert avec des concentrations de sulfates importantes, alors qu'il s'agit en réalité d'un système fermé et d'une distillation de Rayleigh rapprochant le $\delta^{34}S$ des sulfures et celui des sulfates dans la colonne d'eau (7). En d'autres termes, l'occurrence d'un cycle réoxydatif du S fut identifié à partir des données d'eau de porosité mais aurait été difficilement détecté si seulement le réservoir pérenne du S (les pyrites) était disponible, constituant donc un biais de préservation important.

Dans les autres lacs, le taux de MSR normalisé au nombre de cellules (csSRR) et la concentration des sulfates sont identifiés comme les principaux déterminants du fractionnement $\Delta^{34}S_{SO4\text{-}py}$ induit par la MSR (8). Combinant l'enregistrement des quatre lacs, cependant, la cause sous-jacente principale de l'enregistrement isotopique final des pyrites est la taille du réservoir de sulfates de chaque lac. Suivant « l'effet réservoir », l'amplitude du $\Delta^{34}S_{SO4\text{-}py}$ finale est modulée, et plus ou moins exprimée selon le degré de consommation des sulfates (8).

Par ailleurs, la signature isotopique des sulfates a permis d'identifier une influence de soufre volcanique dans les quatre lacs. À Atexcac, elle illustre une signature mantellique qui suggère fortement une contribution active des sources volcaniques à ce lac (8).

Partie III

Les descriptions pétrographique et isotopique des microbialites Mexicains ont permis de mieux comprendre les différentes étapes de leur formation et de l'effet de la diagénèse précoce après émersion (9, 10). Les observations pétrographiques ont permis d'évaluer : l'hydrodynamique des lacs avec en général plusieurs cycles d'immersion-émersion, l'identification de précipitations successives des carbonates des phases primaires jusqu'aux phases de recristallisation complète, l'évaluation de la diversité géochimique latérale de ces objets au sein d'un même lac liée aux changements des sources de fluides et de l'influence biologique (9). Tandis que l'alcalinité favorise la croissance des microbialites, elle engendre également une perte de leurs biosignatures isotopiques primaires dans les carbonates à travers une précipitation spontanée (« abiotique »), et leur remplacement. Comme pour les sédiments gravitaires, les carbonates des microbialites dans des contextes de forte alcalinité comme à Alchichica représentent donc une bonne capture des changements climatiques, sur des échelles de temps relativement longues (10). Puisque ces remplacements secondaires commencent par le centre des microbialites plutôt que par leur surface où l'on trouve les tapis microbiens actifs, les biosignatures isotopiques des carbonates ont plus de chances d'être préservées proche des contours des microbialites. Par opposition, une plus faible alcalinité à La Preciosa permet de retrouver des biosignatures isotopiques typiques de la photosynthèse dans les carbonates des microbialites de ce lac (en analyses totales, et locales).

Après émersion, l'altération de certains microbialites par des eaux météoriques est clairement démontrée, à la fois par les analyses pétrographiques et isotopiques (9, 10). Cela entraine une perte des microfossiles primaires (diatomées, tapis microbiens filamenteux), des faciès carbonatés, et des signatures isotopiques (particulièrement de l'oxygène). Cette fois, le message initial enregistré par les microbialites est mieux préservé vers le centre des objets (10).

À l'instar des sédiments de fond de lac, la minéralogie des carbonates primaires et secondaires des microbialites est d'une importance première pour l'interprétation de leurs signatures isotopiques (10). Déterminer la bonne composition isotopique de la source de C formant les microbialites est également très important afin d'interpréter correctement la potentielle présence de biosignatures, les mécanismes de formation des microbialites, et les enregistrements climatiques par les microbialites (10).

Bien que la matière organique totale des microbialites hérite principalement des signatures géochimiques des producteurs primaires photosynthétiques, elle est sensible à la position relative des microbialites par rapport au gradient redox de la colonne d'eau, soulevant l'intérêt d'échantillonner les microbialites à travers de tels gradients, et ainsi capturer l'ensemble de la variabilité latérale, et verticale de l'environnement étudié (10). Pour la même raison, ces travaux montrent l'intérêt qu'il y a à échantillonner à la fois les microbialites et les sédiments pélagiques d'un bassin, qui intègrent une information moyennée sur la colonne d'eau et le bassin dans son ensemble.

Les données de multi-isotopie du S des microbialites d'Alchichica (11) corroborent les conclusions des chapitres 9 et 10 sur les microbialites, ainsi que sur le cycle du S dans les sédiments (7, 8). Ces données suggèrent une source distincte de S pour les « microbialites bruns » venant de l'oxydation de pyrites détritiques de roches du cratère ou du sous-bassement, cohérent avec leur origine issue des eaux souterraines ou de ruissellement (11). Par la même cela soutient que ces microbialites se sont formés sous l'influence d'un environnement local différent de la majorité des microbialites (« blancs ») d'Alchichica (7, 8). Alors que les compositions isotopiques en S des pyrites de « microbialites bruns » reflètent un enregistrement efficace des sulfures produits par MSR, les pyrites de « microbialites blancs » montrent des signatures semblables à celles des sédiments de fond du lac (7), suggérant des réactions de réoxydation et disproportionation (11). Un avantage des dépôts microbialitiques pour identifier ces processus est qu'ils précipitent des carbonates *in situ*, fournissant un enregistrement local des sulfates, qui n'est pas disponible pour les sédiments gravitaires. Enfin, les isotopes du S des microbialites semblent être notoirement impactés par la stratification redox du lac (et son régime de mélange), soulevant encore une fois l'intérêt d'échantillonner ces objets à travers de tels gradients pour caractériser les stratifications passées.

Conclusion

Comme résumé plus haut, un bilan des réactions géochimiques affectant les cycles du C et du S dans quatre lacs stratifiés et alcalins du Mexique et de leurs microbialites est présenté dans ce manuscrit de thèse. En s'attachant à décrire les processus et phénomènes actuellement en cours au sein de ces environnements, ce travail illustre les conclusions biaisées qui peuvent émerger de leurs enregistrements sédimentaires, et comment ces derniers sont altérés par la diagénèse précoce. Certains processus clés au sein de ces environnements sont mis en évidence

grâce à l'analyse des phases dissoutes (dans les eaux de lacs et de porosité), mais ne sont pas préservés dans les réservoirs géologiques pérennes (sédiments gravitaires et microbialites). Cette étude améliore notre compréhension du cycle du C dans des environnements alcalins stratifiés, notamment en attestant du rôle majeur du réservoir de DOC, en identifiant les facteurs qui mènent à différents niveaux d'alcalinité de ces lacs, et comment ces derniers favorisent ou inhibent l'enregistrement de signatures biologiques ou climatiques primaires. Ce manuscrit démontre également quels sont les facteurs principaux influençant les signatures isotopiques du S enregistrées *in fine* dans les pyrites sédimentaires.

Les conclusions principales illustrant les biais et processus cryptiques qui peuvent être décelés à partir de l'étude de milieux stratifiés actuels sont résumées dans le Tableau 12.1 en fin de document. Celui-ci montre clairement qu'un certain nombre de phénomènes et métabolismes actuellement à l'œuvre dans ces lacs ne sont pas préservés dans les archives sédimentaires, nous mettant en garde lorsque le répertoire géologique ancien est analysé. Ce travail renouvelle l'intérêt qu'il y a à contraindre les contextes géologiques, stratigraphiques et pétrographiques de concert avec les données géochimiques. Par ailleurs, cela ouvre des perspectives prometteuses aux approches interdisciplinaires mélangeant minéralogie, microbiologie, géologie et géochimie. Il semble donc important de poursuivre de telles études intégratives et comparatives d'environnements modernes comme ceux présentés ici.

Par la suite, le conséquent jeu de données isotopiques acquis lors de ce doctorat sur des environnements stratifiés et leurs microbialites devra être mis en perspective plus systématiquement avec les données de microbiologie (« omics ») disponibles. Cela représentera un travail pionnier de combiner les descriptions microbiennes, physico-chimiques, géologiques et géochimiques en vue d'obtenir un portrait complet de ces écosystèmes. Une caractérisation en profondeur de ces environnements par des outils géochimiques de pointe comme les isotopes mineurs du soufre (^{33}S, ^{36}S) devra également être plus systématiquement produite. Les analyses *in situ*, par exemple par (nano-)SIMS, ouvrent des voies complémentaires pour comprendre les signatures primaires qui peuvent être préservées localement, malgré l'altération des signatures en roche totale. Ces approches étendues aux échantillons Mexicains, et comparées à d'autres systèmes lacustres stratifiés de contextes géologiques variés (tels que le lac Dziani Dzaha dans l'océan Indien, ou Cadagno dans les Alpes). Pour finir, un effort plus conséquent devra être fournit pour évaluer comment les conclusions précédentes peuvent s'appliquer à des bassins de taille supérieure, comparable aux océans passés, potentiellement en commençant par les zones d'oxygène minimum ('OMZ') dans les marges continentales.

Chapter 1
General introduction

Table of content

1.1. Past and present stratified environments at the surface of the Earth

Liquid water and the ocean at the surface of our planet formed relatively rapidly in the history of Earth, as early as ~ 4.4 Ga ago, about 150 Ma after the Earth accretion (Gargaud *et al.*, 2009). At this time, the atmosphere mostly consisted of N_2, H_2O, and CO_2, and one of the main differences with the world today was the absence of dioxygen (O_2) in the atmosphere and in the ocean (Gargaud *et al.*, 2009). Widely studied *via* a myriad of geochemical proxies (Farquhar *et al.*, 2011 and ref. therein), the appearance of O_2 in significant quantities at the Earth's surface was undisputedly demonstrated to occur after ~2.45 Ga ago, through the use of sulfur (S) minor stable isotopes (*e.g.* Farquhar *et al.*, 2000). At this time, the so-called great oxidation event (GOE), triggered by a globalization of oxygen release from oxygenic photosynthesis to the atmosphere, increased the O_2 partial pressures from less than 10^{-7} to 10^{-2} bar, compared to $2.1*10^{-1}$ bar today (Fig. 1.1; Catling and Zahnle, 2020). However, other studies showed sporadic increases of the Earth's surface oxygenation much before the GOE as early as 3.2 Ga ago (*e.g.* Kendall *et al.*, 2010; Thomazo *et al.*, 2011; Planavsky *et al.*, 2014; Satkoski *et al.*, 2015; Ossa Ossa *et al.*, 2018). Further rising O levels took place from at least 700-600 Ma ago to reach near modern values in the deep ocean at the onset of the Phanerozoic eon 541 Ma ago (Fig. 1.1; Ader *et al.*, 2014; Lyons *et al.*, 2014; Catling and Zahnle, 2020).

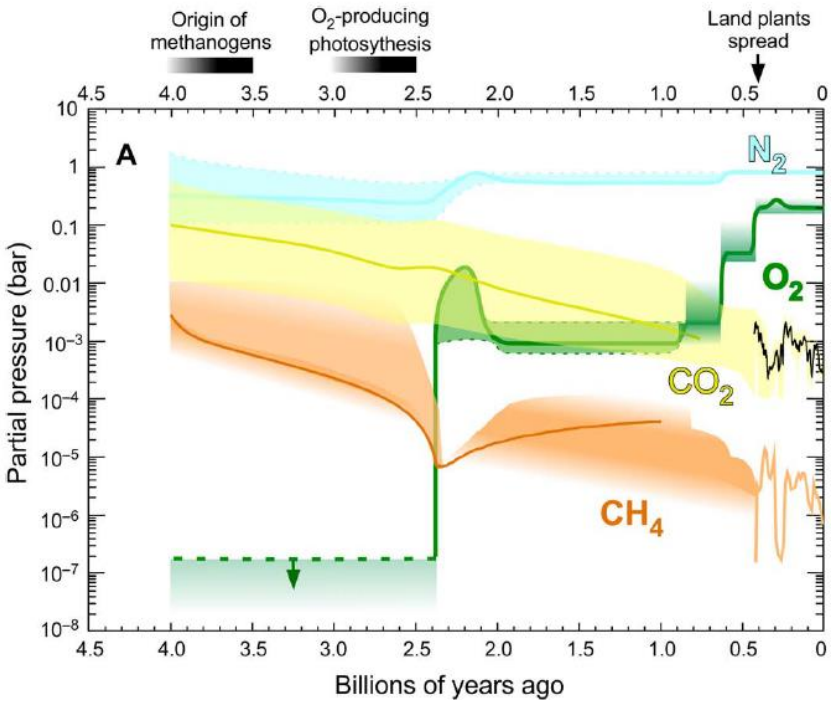

Figure 1.1: Overview of the Earth atmosphere evolution over the last 4 billion years in the context of biological evolution at the top (figure from Catling and Zahnle, 2020). The average pressure of the main atmospheric gases (dinitrogen, dioxygen, carbon dioxide, and methane), are represented with their uncertainty envelopes. The rise of oxygen *via* oxygenic photosynthesis is seen after 2.5 Ga, and would have oxidized methane. The secular decrease of CO_2 is a feedback effect in the geological carbon cycle induced by decreasing solar radiation (see more detail in section 1.3.1).

Within this extended period of time, from ~3200 to 541 Ma, redox and chemical stratification was thus a major trait of the ocean (*e.g.* Knoll *et al.*, 2016; Lyons *et al.*, 2014; Satkoski *et al.*, 2015). While in the Archean (4-2.5 Ga), the ocean would have been mostly ferruginous (Fe-rich; *e.g.* Knoll *et al.*, 2016), the exact chemistry of the deep ocean (the surface ocean being oxygenated) after the GOE remains debated. It would have mostly fluctuated between euxinic (sulfide-rich) and ferruginous conditions (*e.g.* Canfield, 1998; Poulton *et al.*, 2010; Planavsky *et al.*, 2011; Guilbaud *et al.*, 2015), but nitrogen (N) isotopes suggest that slightly oxygenic conditions could have reached the water-sediment interface already prior to 750 Ma ago, at the onset of the Neoproterozoic (*e.g.* Ader *et al.*, 2014, 2016).

Smaller and/or more isolated water basins (*e.g.* continental margins, inland seas, lakes) are intrinsically – by their size and dynamic – more prone to chemical changes and thence more likely to feature a chemical stratification. Hotspots of oxygen production in an anoxic world would generate strong redox gradients locally, and so would an efficient consumption of oxygen in a fully oxygenated environment. Accordingly, oxygen oases with significant redox reactions have been argued several hundred millions years before the GOE, on continental margins and inland waters (*e.g.* Ossa Ossa *et al.*, 2018). On the other hand of the geological clock, frequent ocean anoxic events ('OAE') occurred throughout the oxygen-rich Phanerozoic Eon (Jenkyns, 2010; Saitoh *et al.*, 2015; Raven *et al.*, 2018). In fact, the ongoing climate change participates in the resurgence of larger oxygen minimum zones (the OMZ; Stramma *et al.*, 2008).

The establishment of redox-stratification (*i.e.*, the depletion or enrichment of oxygen in water masses) results from numerous factors including the availability of reduced species for abiotic oxidation, basin physiography, water current circulations, and biology, which occupies a particularly central role in redox exchanges in surficial environments. First, because oxygenic photosynthesis is the only significant source of free oxygen at the Earth's surface (*e.g.* Lyons *et al.*, 2014). Then, because the oxidation of organic carbon (C) during microbial respiration processes is a major sink of O, especially in the more oxidized modern environments. These

respiration processes *sensu largo* will distribute vertically, following the order of electron acceptors providing the greatest free energy per mol of organic carbon oxidized (Fig. 1.2; Froelich *et al.*, 1979; Canfield and Thamdrup, 2009). Schematically, respiration reactions use an electron acceptor until depletion, before proceeding to the next one. Oxygen respiration yielding the greatest amount of energy for the organisms, O_2 is the first element to be consumed (Fig. 1.2). The state of a system can thus be positioned on a "redox-ladder", which describes the different chemical species used at a given depth in the sediments, or in the water column (Fig. 1.2). Therefore, redox-stratified environments represent hotspots of microbial diversity, where C is actively cycled (together with elements like S; sections 1.3 and 1.4).

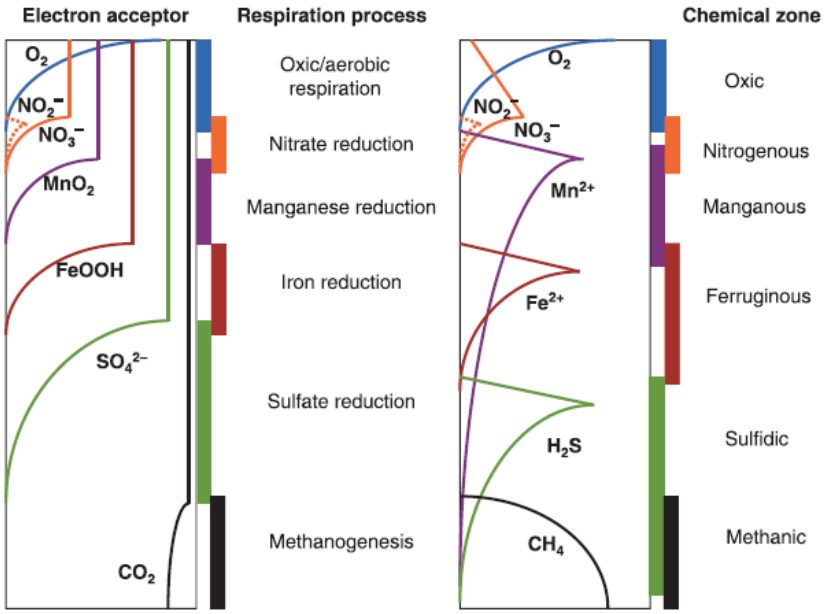

Figure 1.2: Idealized representation of the depth distribution of common electron acceptors in (modern) environments (from Canfield and Thamdrup, 2009). On the left, the decrease of each electron acceptor is associated to a respiration process. On the right, the reduced species resulting from these reactions are shown (except for oxygen and nitrogen) and give their names to the chemical, or redox zonation in such environments.

The study of modern redox-stratified water columns has shown the complexity of these environments, harboring very diverse ecological niches in relation with steep chemical gradients (*e.g.* Crowe *et al.*, 2011; Busigny *et al.*, 2014; Fulton *et al.*, 2018). Consistently, the export of particles from a preferential layer of a stratified basin will impact the composition of the sediments underneath (*e.g.* Posth *et al.*, 2017; Fulton *et al.*, 2018). Similarly, vertical or lateral displacement of the stratification would induce changes in the nature of (authigenic)

sediments as well. Complex sedimentary isotopic records from the geological records have been attributed to the deposition of sediments from different parts of stratified water columns (Calver, 2000; Ader *et al.*, 2009; Zhang *et al.*, 2018), highlighting that the dynamics within stratified water columns and how they are recorded in the sediments should be further investigated, especially in the context of resurging OMZ (Stramma *et al.*, 2008). Nonetheless, stable isotopes are sensitive to biological and physico-chemical processes, and thus represent powerful tracers of biogeochemical phenomena (section 1.2).

1.2. General definition, scientific principles, and notations about isotopes

Isotopes can be defined as the different "versions" of a single chemical element based on a number of neutrons which differs from each other – despite a same number of protons – conferring them each a distinct mass. Thus, any given isotope represents a proportion of the total amount of a given element. Initially fixed by nucleosynthesis in stellar processes, the overall proportion of each isotope within an isotopic system are, to a first order, similar throughout the diversity of natural reservoirs, for example: oxygen in the atmosphere or in the ocean is the total of approximately 99.8% ^{16}O, 0.04% ^{17}O and 0.20% ^{18}O (Grossman, 1998). However, the distinctive mass but similar chemical properties of isotopes, lead them to be partitioned differently between the products and reactants of bio-physico-chemical reactions affecting them, or during chemical changes of state. These *fractionations* can be due to different velocities of atoms and molecules, vibrational and rotational frequencies and thermodynamic energies (Dauphas and Schauble, 2016). In other words, these processes (slightly) modify the respective proportions of isotopes in natural reservoirs. Hence, isotopic signatures are characteristic of the source of these elements and the processes that they have been reacted through.

Because we want to compare the relative quantities of each isotope and it is much easier to measure the ratio of two isotopes than their absolute abundance, isotopic compositions are reported as ratios (R) of the heavier isotopes over the lighter one (*e.g.* $^{18}R = {}^{18}O/{}^{16}O$). Besides, in order to correct for an "isotopic bias" (a fractionation) occurring during isotope measurements and to facilitate inter-laboratory comparisons, these ratios are expressed as the

deviation from a chosen reference composition (a standard), in the 'δ' notation. These small deviations are expressed in permil (‰) such as 1.1:

$$\delta = \left(\frac{R_{sample} - R_{STD}}{R_{STD}}\right) * 1000 <=> \left(\frac{R_{sample}}{R_{STD}} - 1\right) * 1000 \qquad (1.1)$$

The different isotopes, their natural abundance and standards used for the isotopic systems studied in this PhD are summarized in Table 1.1. Notations specific to S isotopes (for which more than two isotopes were measured) will be presented in a toolbox specific to Chapter 7.

As mentioned, an isotopic fractionation can occur in a physico-chemical reaction due to a preferential incorporation of the heavy *vs.* light isotope (or *vice versa*) in one of the phases involved (Sharp, 2017 and references therein). The isotopic fractionations are usually divided in the two following categories: equilibrium (reversible) and kinetic (irreversible) fractionations, whereby the former relates to a difference in chemical bond energies and the latter to a difference in molecules velocity, both as the result of the different isotopes' mass.

An isotopic equilibrium fractionation occurring between two phases A (reactant) and B (product) can be expressed by the fractionation factor 'α' where:

$$\alpha_{A \rightarrow B} = \frac{R_A}{R_B} \qquad (1.2)$$

This fractionation can be approximated on the permil scale with the 'Δ' notation such as:

$$\Delta_{A\text{-}B} = \delta_A - \delta_B \approx 1000 * \ln(\alpha_{A \rightarrow B}) \qquad (1.3)$$

Also used, mostly for kinetic (*i.e.* unidirectional and non-equilibrium) processes and especially for biological reactions, is the 'ε' notation in permil as well, defined as:

$$\varepsilon_{A\text{-}B} = (\alpha_{A \rightarrow B} - 1) * 1000 \qquad (1.4)$$

The three notations 'Δ', 'ε' and $1000*\ln(\alpha_{A \rightarrow B})$ provide nearly identical values up to a 10 ‰ difference between the δ of A and B, and still very similar values (within 0.4 ‰) up to a 20 ‰ difference between A and B (Sharp, 2017).

Table 1.1. General information on C, O, N, and S analyses.

Elements	Stable isotopes (abundance in %)	Analyzed Gas	Measured δ	International standard
Carbon	^{12}C (98.89), ^{13}C (1.11)	CO_2	$\delta^{13}C$	Vienna Pee Dee Belemnite (VPDB)
Oxygen	^{16}O (99.76), ^{17}O (0.04), ^{18}O (0.2)	CO_2	$\delta^{18}O$	Vienna Standard Mean Water (VSMOW) and VPDB
Nitrogen	^{14}N (99.64) ^{15}N (0.35)	N_2	$\delta^{15}N$	AIR
Sulfur	^{32}S (95.02), ^{33}S (0.75), ^{34}S (4.21), ^{36}S (0.02)	SO_2, SF_6	$\delta^{33}S$, $\delta^{34}S$, $\delta^{36}S$	Vienna Canyon Diablo Troilite (VCDT)

Among important processes that can affect the isotopic composition of different reservoirs and whose equations were used during this PhD, I can notably mention mixing and Rayleigh-type distillation. Mixing of a reservoir A in a relative proportion *f* with a reservoir B in a complementary proportion (1-*f*) will combine the isotopic compositions of A and B such that:

$$\delta_{mix} = \delta_A * f + \delta_B * (1-f) \quad (‰) \qquad (1.5)$$

This can also be used to describe the dissociation of a "mix" reservoir into A and B reservoirs.

Rayleigh distillation generally describes a process by which a fixed fractionation, occurring during the formation of a product B and its separation from an initial reservoir A, is applied repeatedly on the reservoir A such that both δ_A and δ_B evolve in the same direction (because the fractionation affects δ_A and that δ_B results from δ_A). Mathematically, it can be described such as:

$$\delta_A = \delta_{A,0} + 1000\ (\alpha_{A/B} - 1) * \ln(F) \quad (‰) \qquad (1.6)$$

where $\delta_{A,0}$ is the initial isotopic composition of A, F is the fraction of A remaining and δ_B can be calculated from the fractionation $\alpha_{A/B}$. These processes will be graphically illustrated in Chapter 7.

These processes can largely shift reservoirs isotopic compositions. Combining all the aforementioned descriptors (δ, ε, *etc.*) is a powerful approach to distinguish between the sources of C, O, and S to a given environment, the organisms which metabolize them as well as the processes involved (*e.g.* mixing, distillation).

1.3. The carbon cycle

Carbon (C) in the Earth biogeochemical cycles is just as capital as the first letter of a sentence. It is central to the processes regulating the Earth's climate at geological timescales, and is the cornerstone of biological reactions at short timescales. Carbon has two stable isotopes (^{12}C, ^{13}C), and their abundances from the atmosphere to the mantle have been extensively analyzed to constrain the C geological and biological cycles.

1.3.1. Geological and biological carbon cycles

Throughout most the Earth history, CO_2 present in the atmosphere has constituted the main greenhouse gas, providing the Earth with an atmosphere sustaining a range of temperatures that makes the planet habitable (Catling and Zahnle, 2020). The CO_2 is mostly emitted by volcanic degassing to the atmosphere, where it accumulates and equilibrates within the hydrosphere. In parallel, the main sink of CO_2 is ensured by chemical weathering of the continental and oceanic crusts, and precipitation of carbonates (Fig. 1.3). When low atmospheric CO_2 partial pressures (pCO_2) prevail, lower weathering rates combined with sustained volcanic degassing elevate the atmosphere CO_2 content; conversely high pCO_2 lead to enhanced weathering and carbonates formation, acting as a negative feedback on atmospheric pCO_2. These feedback mechanisms have bound the Earth's climate to the C cycle throughout its history (*e.g.* Catling and Zahnle, 2020) and represent the long-term C cycle.

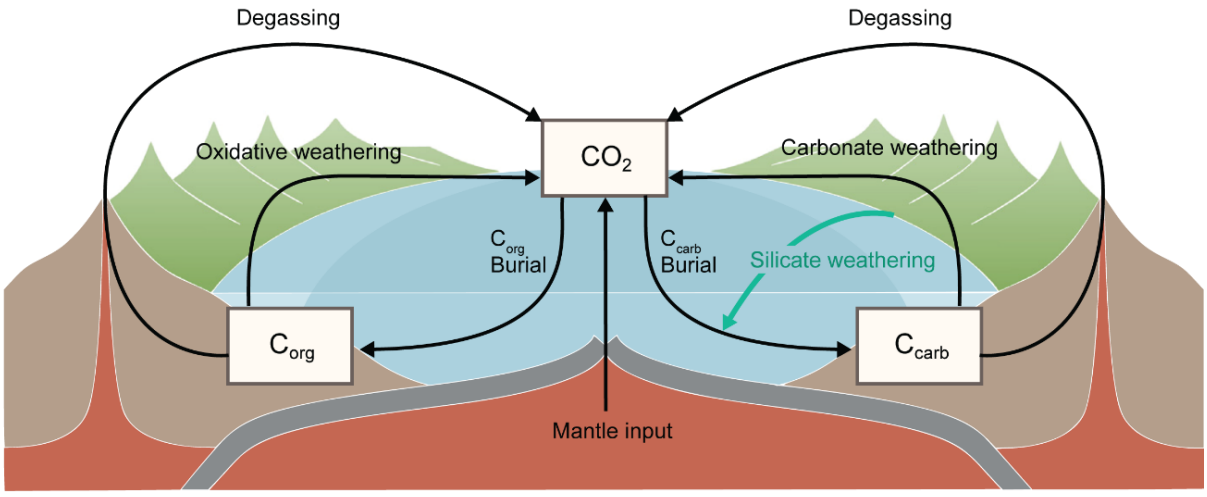

Figure 1.3: Representation of the long-term carbon cycle (modified from Mills *et al.*, 2019). The main C source to surficial reservoirs is *via* volcanic degassing, accumulating CO_2 in the atmosphere and hydrosphere. Atmospheric CO_2 can be pumped by silicate weathering combined to carbonate burial (C_{carb}), following the simplified equations: $CaSiO_3+H_2O+2CO_2 = SiO_2+Ca^{2+}+HCO_3^-$; and $Ca^{2+}+2HCO_3^- = CaCO_3+H_2O+CO_2$. The CO_2 is also captured as organic C by living organisms (C_{org}). Oxidation of C_{org}, and weathering of C_{carb} release CO_2 back to the atmosphere.

Another sink is the fixation of CO_2 as organic carbon by living organisms, participating in the short-term biological C cycle. Both aerobic and anaerobic autotrophic C fixation liberate some oxidant power, and are thus determinant in changing the redox state of surface environments. The most famous of these reactions, and likely the most impactful in changing the Earth's surface conditions, is that of oxygenic photosynthesis, stoichiometrically summarized as:

$$CO_2 + H_2O \rightarrow CH_2O + O_2 \qquad (1.7)$$

If organic matter is re-oxidized (*e.g.* microbially respired), the redox effect of photosynthesis is canceled out. Organic C burial, on the contrary, represents a net source of oxidant to the atmosphere by preventing OM reoxidation, hence directly connecting the C cycle to the atmosphere oxygenation (*e.g.* Lyons *et al.*, 2014; Krissansen-Totton *et al.*, 2015).

A steady-state assumption of the long-term C cycle is commonly made to constrain the redox and climate changes at the surface of the Earth. Considering relatively homogeneous C isotope signatures in the mantle (Cartigny, 2005), the mass balance of C isotope compositions in marine carbonates ($\delta^{13}C_{carb}$) and organic matter ($\delta^{13}C_{org}$) should reflect that of the input volcanic CO_2 ($\delta^{13}C_{in}$) (*e.g.* Schidlowski, 2001). This can be expressed as:

$$\delta^{13}C_{in} = f_{org} * \delta^{13}C_{org} + (1 - f_{org}) * \delta^{13}C_{carb} \qquad (1.8),$$

$$\text{or } f_{org} = (\delta^{13}C_{in} - \delta^{13}C_{carb}) / (\delta^{13}C_{org} - \delta^{13}C_{carb}) \qquad (1.9).$$

This illustrates how the redox state of the surficial Earth can be indirectly determined from f_{org} and the long term sedimentary C isotope record (Fig. 1.4). In more detail though, recent work showed that organic C burial may not have driven the C isotope record and Earth oxygenation alone (Krissansen-Totton *et al.*, 2015), and that other processes such as tectonic uplift may drive the above C isotope mass balance (Shields and Mills, 2017), showing that more work on the comprehension of C isotope records is still required.

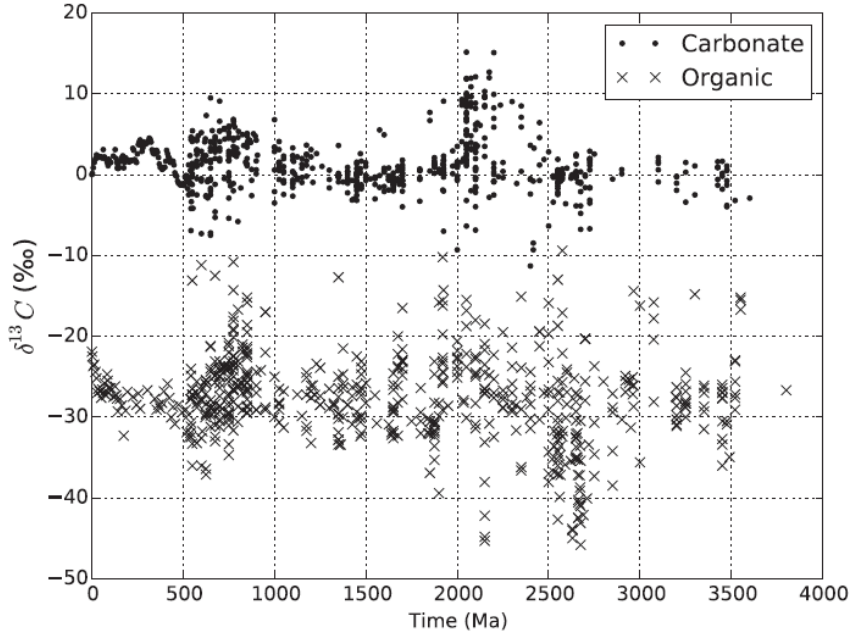

Figure 1.4: Compilation of carbon isotope compositions from sedimentary carbonates and organic matter over the last 3.5 Ga (from Krissansen-Totton *et al.*, 2015). Each data point represents the average per formation per author per lithology.

1.3.2. Carbon isotopes as biogenicity criteria

The record of ^{13}C-depleted isotopic signatures in organic matter can be seen as evidence for a significant biosphere since at least 3.5 Ga (Schidlowski, 2001; Thomazo *et al.*, 2009), although some secondary and/or abiotic processes can mimic this kind of signatures (*e.g.* van Zuilen *et al.*, 2002). Specific metabolic have been interpreted from organic C isotopes. For example, the existence of methanogenesis was inferred possibly as early as 3.48 Ga (Ueno *et al.*, 2006); oxygenic photosynthesis and anaerobic methane oxidation coupled to sulfate reduction were identified in the 2.73 lacustrine stromatolites from the Tumbiana formation (Coffey *et al.*, 2013; Lepot *et al.*, 2019). Nevertheless, many parameters influence the organic C isotope record (*e.g.* Hayes, 2001; Werne and Hollander, 2004), and there is a lot of overlap between metabolisms typical isotopic signatures (Fig. 1.5). Even for the widely studied oxygenic photosynthetic metabolisms the amplitude of isotopic fractionation are still not fully characterized (*e.g.* Thomas *et al.*, 2019). It suggests that organic C isotope signatures alone cannot be used as a definitive biosignatures of a given metabolism.

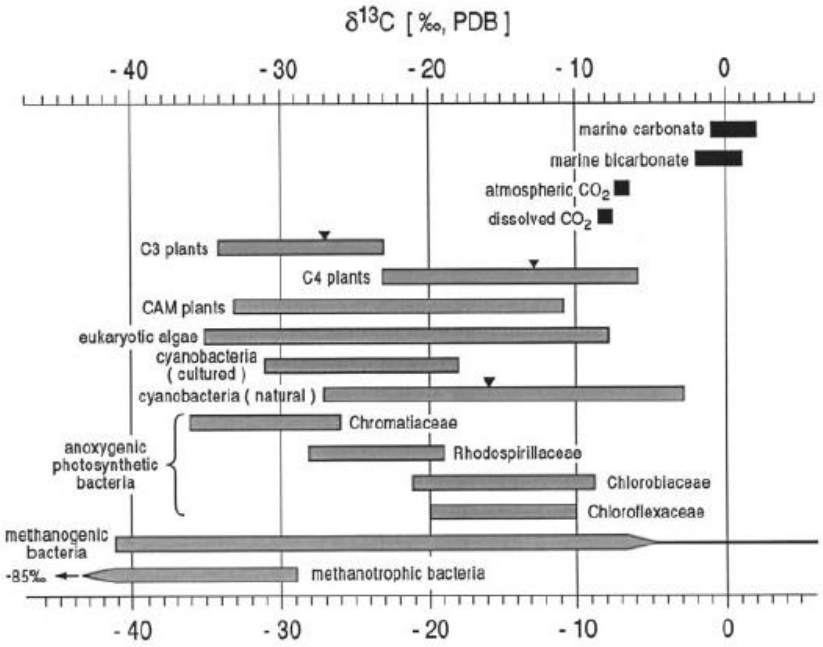

Figure 1.5: Typical carbon isotope signatures from different groups of living organisms and inorganic carbon species (from Schidlowski, 2001). The selectivity of biological processes in favor of the light C isotope (^{12}C) are evident from the more negative $\delta^{13}C$ of OM (gray) compare to inorganic reservoirs (black). However, these different groups of organic C show an important overlap.

1.3.3. Carbon fluxes in lacustrine basins

The C cycle in modern lakes is also widely studied to understand the significance of continental water bodies in the present global C cycle, notably in terms of C storing or emitting capacities. The burial rate of organic C in lakes worldwide amounts about 50% of the marine sediment rates (Sobek *et al.*, 2009; Mendonça *et al.*, 2017), despite representing ~35 times less surface than the ocean. However, organic C burial in lakes would represent only 20% of their net CO_2 evasion flux (*i.e.*, the net CO_2 degassing flux from lakes; Mendonça *et al.*, 2017). Indeed, the majority of lakes represent net CO_2 sources to the atmosphere because they inherit allochthonous organic C sources getting respired within the lakes. Lacustrine CO_2 emissions would range from 0.1 to 0.5 $PgC.yr^{-1}$, compared with the 1.4 $PgC.yr^{-1}$ for CO_2 dissolving in the ocean (Borges *et al.*, 2014 and ref. therein), and 10^{-5} $PgC.yr^{-1}$ for the anthropic CO_2 emissions (Friedlingstein *et al.*, 2019). It shows the importance lake C cycling for the global C cycle and climate. Borges *et al.* (2014) noted that most of these calculations used boreal and humic lakes as references, although they do not represent the largest area of lakes worldwide. Therefore, additional data from tropical and alkaline lakes such as those studied in this PhD are required.

1.4. The sulfur cycle

1.4.1. General trends in the S cycle

The sulfur (S) cycle is tightly bound to the C cycle, and with it, is a key element in investigations of the redox changes at the Earth's surface, and the emergence and evolution of life (Ueno *et al.*, 2008; Johnston, 2011; Fike *et al.*, 2015). Indeed, sulfur can be found in many oxidation states from -II in sulfides to +VI in sulfates (Fig. 1.6). It is thus highly reactive to redox changes and represents an advantageous specie to cycle for living organisms (Canfield, 2001; Zopfi *et al.*, 2004). Through a variety of metabolic pathways (primarily sulfate reduction, disproportionation, and sulfide oxidation), these microorganisms connect the S and C cycles *via* the remineralization of organic carbon in marine sediments (*e.g.* Fike *et al.*, 2015; Jørgensen, 2021). Today, sulfate anions represent the largest oxidant pool in the ocean with concentrations 150 times higher than O_2 (Hayes and Waldbauer, 2006). In consequence, microbial sulfate reduction (MSR) is the main pathway of organic matter remineralization in the subseafloor (Jørgensen, 2021), turning up to 65% of the organic carbon deposited back to inorganic carbon (Bradley *et al.*, 2020), and generating dissolved sulfides:

$$SO_4^{2-} + 2CH_2O \dashrightarrow H_2S + 2HCO_3^- \quad (1.10)$$

Sulfide can also be produced by the reduction of sulfate coupled to the anaerobic oxidation of methane (AOM), preventing CH_4 emissions from the subsurface (*e.g.* Treude *et al.*, 2005). Only a small portion of the MSR- and AOM-produced sulfides react with reactive iron to form pyrite (FeS_2), while the remaining diffuses up to the water column and is oxidized, thus further consuming oxidant power (Jørgensen, 2021). Hence, pyrite burial acts a net source of O_2 to the atmosphere while its exposure and weathering are a net sink of O_2. The microbial reactions presented above proceed, and impact the biological C cycle on short timescales and usually occur in restricted environments like sediment porewaters. However, on longer timescales, together with the deposition of mineral sulfate in evaporites, volcanic and hydrothermal emissions, they will affect the Earth redox state and C geological cycle (Fike *et al.*, 2015).

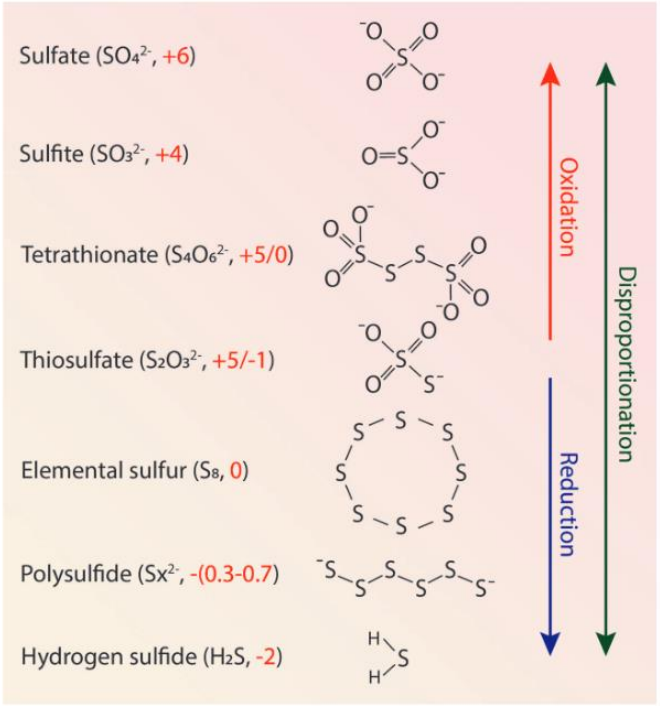

Figure 1.6: Inorganic sulfur species arranged according to the oxidation state (red numbers) of their sulfur atoms, together with their chemical and structural formula (from Jørgensen, 2021). The number of sulfur atoms in polysulfide chains mostly varies from 4 to 7.

1.4.2. The use of S isotopes to constrain the S cycle

The different processes metabolizing sulfur impart distinctive stable isotope fractionations (*e.g.* Farquhar *et al.*, 2003; Johnston, 2005a; 2007; Zerkle *et al.*, 2016). Sulfur stable isotopes (^{32}S, ^{33}S, ^{34}S, ^{36}S) can therefore be used to identify a variety of metabolisms in modern and ancient environments (*e.g.* Johnston *et al.*, 2005b, 2008; Ueno *et al.*, 2008; Fike *et al.*, 2009; Thomazo *et al.*, 2009; Crémière *et al.*, 2020; Guibourdenche, 2022). Further, major S isotopes in coeval sulfide and sulfate minerals (^{32}S and ^{34}S reported as $\delta^{34}S$) have frequently been used to reconstruct the past ocean chemistry and oxidation state (*e.g.* Canfield and Teske, 1996; Johnston *et al.*, 2005b; Fike *et al.*, 2006).

Similar as for the geological C cycle, the two main controls on the secular variation of $\delta^{34}S$ in sulfur species over geological time are (i) the variations in the net flux of sulfate reduced to sulfide eventually buried in the sediments, and (ii) the average fractionation associated with microbial activities producing this net sulfide burial flux (Fike *et al.*, 2015). Therefore, the secular fluctuations in sedimentary $\delta^{34}S$ can be described as in equation 1.11, by the pyrite

burial flux (f_{py}), the isotopic difference between sulfate and pyrite ($\Delta^{34}S_{SO4\text{-}py} = \delta^{34}S_{SO4} - \delta^{34}S_{py}$), and the isotopic composition of the S source (mainly riverine inputs; $\delta^{34}S_{in}$) such that:

$$\delta^{34}S_{in} = f_{py} * \delta^{34}S_{py} + (1 - f_{py}) * \delta^{34}S_{SO4} \quad (1.11),$$

$$<=> \delta^{34}S_{SO4} = \delta^{34}S_{in} + f_{py} * \Delta^{34}S_{SO4\text{-}py} \quad (1.12).$$

The MSR produces sulfide depleted in ^{34}S compared to the sulfate source (*e.g.* Chambers and Trudinger, 1979), resulting in $\delta^{34}S_{py} < \delta^{34}S_{SO4}$ and making the '$\Delta^{34}S_{SO4\text{-}py}$' term positive. Thus, when the pyrite burial flux (f_{py}) increases due to protracted marine anoxia, the residual sulfate isotopic composition evolves towards higher values (Eq. 1.12), together with the isotopic composition of sulfides produced subsequently. The isotopic difference between the sulfate and sulfide pools have also been used to reconstruct the sulfate concentration and riverine flux to the ocean (*e.g.* Canfield and Teske, 1996; Fike *et al.*, 2006; Halevy *et al.*, 2012).

Nonetheless, it has increasingly been demonstrated that local conditions of the depositional setting play a determinant role in the isotopic signatures recorded by pyrites and/or sulfate-bearing minerals (Pasquier *et al.*, 2017, 2021a, 2021b; Liu *et al.*, 2021; Houghton *et al.*, 2022; Marin-Carbonne *et al.*, 2022). Notably, pyrites tend to form within the sediments, where porewater sulfate may evolve independently of the overlying water column sulfate reservoir (*e.g.*, under conditions of high sedimentation rates and delivery of organic C and Fe; Pasquier *et al.*, 2021a). Similarly, the oxidation of MSR-produced sulfide, and its incorporation in sulfate-bearing minerals would bias the $\Delta^{34}S_{SO4\text{-}py}$ offset recorded in the sediments. In such cases, the isotopic signatures of pyrites relative to the marine sulfate do not represent a signal that can be interpreted globally, but reflect the local depositional dynamics. These aspects will be further discussed in the chapters 7 and 8.

1.5. Microbialites

1.5.1. General definitions

Microbialites are emblematic objects in Earth sciences, extensively characterized as paleoenvironmental archives, notably to retrace the emergence and evolution of life on Earth,

the chemistry of continental and marine waters through time, to trace back the paleoclimates, but also for their economic potential as oil reservoir rock.

Microbialites are most widely defined according to a "genetic" or "process" definition, introduced by Burne and Moore (1987), wherein microbialites are "organosedimentary deposits that have accreted as a result of a benthic microbial community trapping and binding detrital sediments, and/or forming the locus of mineral precipitation". In a more descriptive approach, the arrangement of sediment particles constituting the microbialites then usually classifies them in four broad subcategories: stromatolites, thrombolites, dendrolites, and leiolites (Fig. 1.7). From the above genetic definition of microbialites, another category of microbialites known as MISS (Microbially Induced Sedimentary Structures) can be considered (Fig. 1.7). The MISS do not grow vertically, but rather follow horizontal sediment surfaces, in a 2D space (*e.g.* Noffke and Awramik, 2013; Grey and Awramik, 2020). Besides, by contrast with the other microbialites subcategories, MISS are not constituted predominantly of carbonates but are rather typical of siliciclastic environments (Noffke and Awramik, 2013); they will not be discussed further.

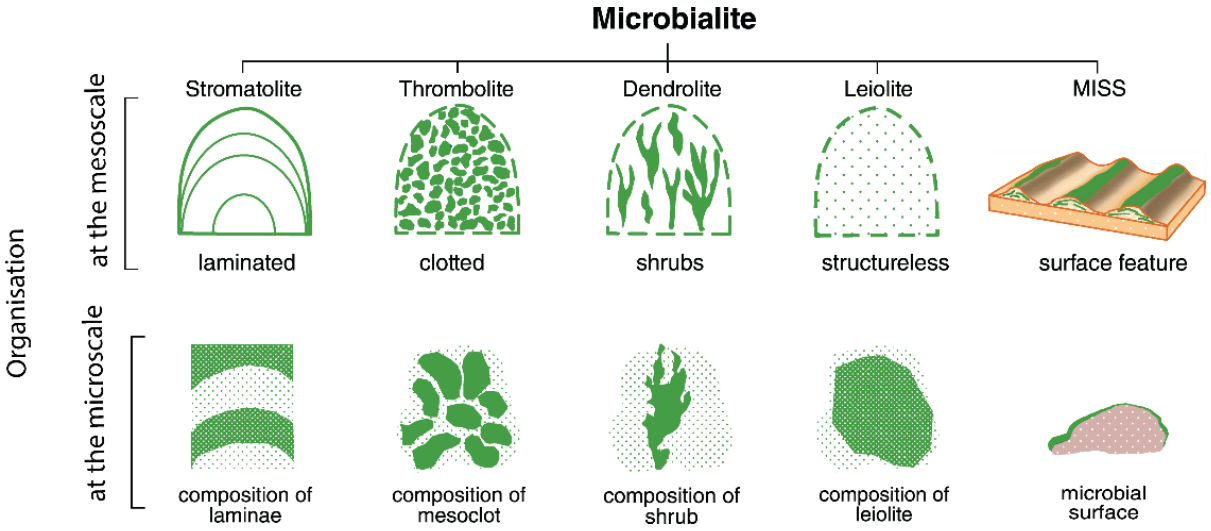

Figure 1.7: Schematic representation of the different microbialite types based on their mesoscale (1-10s cm) and microscale (<1 mm) organization (modified from Grey and Awramik, 2020).

At the interface with the aqueous medium, microbial mats form the external envelop of a microbialite, where its accretion takes place. They can be viewed as complex and thick biofilms (Gerdes, 2007), where a wide range of species carrying on a multitude of metabolic processes are organized as layers (Fig. 1.8), although, the actual spatial organization of the different

metabolisms is more heterogeneous and complex than this strict vertical distribution (Visscher and Stolz, 2005). The large diversity of metabolic processes in mats can be classified in a small number of functional groups including: oxygenic phototrophs, aerobic and anaerobic heterotrophs, sulfide oxidizing bacteria, fermenters, and methanogens (*e.g.* Visscher and Stolz, 2005; Dupraz *et al.*, 2009). Hence, microbial mats harbor steep redox gradients, and chemical micro-environments, where mineral precipitation may be directly triggered (section 1.5.2). Besides, Figure 1.8 highlights how the C and S cycles are strongly inter-related within the microbialites micro-environments.

These microorganism subgroups develop within a matrix of organic molecules referred to as expopolymeric substances (EPS). The EPS are produced and/or consumed by the different species within the mat (Dupraz *et al.*, 2009), and are thus important to its ecological and chemical stability (Decho, 2000). They represent a physical barrier protecting the cells and allowing the cohesiveness of the mat (Decho, 2000; Sutherland, 2001; Dupraz *et al.*, 2009). Besides, they play a major role in the microbialites formation (section 1.5.2).

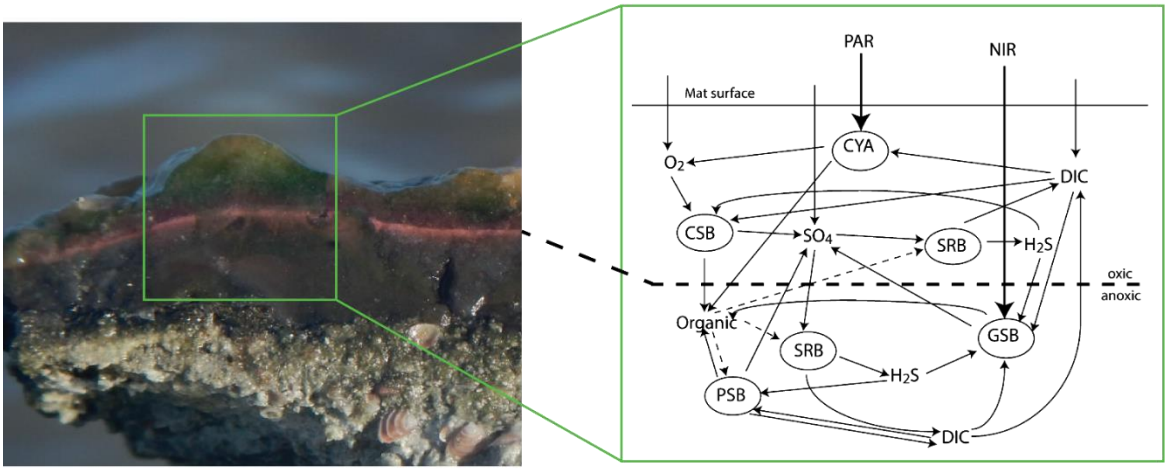

Figure 1.8: Photograph and schematic view of a microbial mat. On the left (from Bouton *et al.*, 2016a), the different layers of the mat are clearly visible from their respective colors, corresponding mainly to oxygenic phototrophs in green (cyanobacteria), anoxygenic phototrophs in pink, and mostly anaerobic heterotrophs in the darker layer (colored from pyrite precipitation). To the right (from Houghton *et al.*, 2014), the corresponding organisms and the organic and inorganic constituents they use are represented. It highlights the tight link between sulfur and carbon cycles, and the steep redox/chemical gradients existing in the mat. Abbreviations: PAR= photosynthetically active radiation; NIR=near infra-red; CYA=cyanobacteria; DIC=dissolved inorganic carbon; SRB=sulfate reducing bacteria; CSB=colorless sulfur bacteria; GSB=green sulfur bacteria; PSB=purple sulfur bacteria.

1.5.2. Processes involved in microbialites and carbonates formation

1.5.2.1. Formation processes and chemical equilibria in the inorganic C system

The process leading to microbialites accretion can be divided into two broad categories which fundamentally differ in terms of processes, the first one resulting from the trapping and binding of allochthonous grains, and the second from an autochthonous production of carbonates (*e.g.* Burne and Moore, 1987; Noffke and Awramik, 2013).

Trapping and binding corresponds to the agglutination of ambient detrital grains on the "sticky" microbial mats and EPS, and notably enhances the cohesiveness of the microbial construction (Burne and Moore, 1987; Riding, 1991; Sutherland, 2001; Corkeron *et al.*, 2012; Noffke and Awramik, 2013). Whereas this process is predominant in the formation of modern marine microbialites (*e.g.* Awramik and Riding, 1988; Reid *et al.*, 2003), authigenic precipitation of carbonate minerals in the microbial mats is the major process forming modern freshwater microbialites (*e.g.* Caumartin *et al.*, 2023), and would have dominated in ancient microbialites (Grotzinger, 1990; Corkeron *et al.*, 2012).

Authigenic minerals in microbialites mainly correspond to carbonates although microbially-mediated precipitation of other phases like Mg-silicates can also occur (Zeyen *et al.*, 2015). Carbonates may precipitate if the activity of its constituting ions in a solution are sufficiently high to exceed the solubility constant (K_s, specific to each carbonate specie). The likelihood for this to occur can be described by the saturation index (SI). For calcium carbonates ($CaCO_3$), the SI is expressed as:

$$SI = \log [(Ca^{2+})*(CO_3^{2-}) / K_s] \quad (1.13)$$

The solution is supersaturated with respect to $CaCO_3$ if SI > 0, leading to precipitation such that:

$$Ca^{2+} + CO_3^{2-} \leftrightarrow CaCO_3 \quad (1.14),$$

$$Ca^{2+} + 2HCO_3^{-} \leftrightarrow CaCO_3 + H_2O + CO_2 \quad (1.15).$$

Thus, any biotic or abiotic process favoring an increase of calcium or carbonate ions will favor the precipitation of $CaCO_3$; these processes being overall referred to as the "alkalinity engine" (Dupraz *et al.*, 2009). Accordingly, authigenic microbialite carbonates form within a continuum of biotic and abiotic influences (section 1.5.2.2 and 1.5.2.3; Burne and Moore, 1987; Riding, 2011).

A key, and intricate aspect of the relation in equation 1.13 with respect to CO_2, is that an increase of the total inorganic C available is favorable to the precipitation of carbonate, but the addition of significant CO_2 is detrimental to it (Eq. 1.15) because it shifts the solution to more acidic pH in virtue of the thermodynamic equilibria between the dissolved inorganic carbon (DIC) species; summarized as:

$$CO_{2(aq)} + H_2O \leftrightarrow H_2CO_3 \leftrightarrow HCO_3^- + H^+ \leftrightarrow CO_3^{2-} + H^+ \quad (1.16)$$

Whereas the addition of CO_2 adds DIC to the system, it also generates acidity, which tends to react with CO_3^{2-} and thus decrease its availability. On the contrary, CO_2 escape consumes protons, which react with bicarbonate, and favor the rise of CO_3^{2-} ions (*e.g.* Pentecost, 2005).

1.5.2.2. Abiotic factors favoring carbonate precipitation

Abiotic factors influencing CO_2 degassing will favor carbonate precipitation (see above). Degassing can be due to turbulent waters, resulting from strong winds or hydrodynamics (cascades, waves breaking on hard surfaces, *etc.*). These effects are dominant in the precipitation of travertine and tufa deposits (Riding, 2008; Fouke, 2011). Evaporation enhances the degassing of CO_2 by increasing its partial pressure (*e.g.* Li and Ku, 1997), and concentrates Ca ions as well. Higher temperatures favor a more efficient CO_2 degassing (by lowering its solubility according to Henry's law), and are associated with a lower solubility of carbonates (Pentecost, 2005).

Additionally, carbonate precipitation can be abiotically favored as a result of external sources of DIC and/or calcium. These can either be from groundwater connected to carbonate aquifers (*e.g.*, karsts), surface streams, or degassing sources (*e.g.*, from volcanic activity or gases rising along tectonic faults) (*e.g.* Boussagol *et al.*, 2023).

These factors thus directly connect the carbonate precipitates to climatic, limnologic, and geologic environmental constraints (*e.g.* Vennin *et al.*, 2021).

1.5.2.3. Biological factors favoring carbonate precipitation

The different degrees of biology's involvement in carbonate precipitation are usually divided and referred to as: biologically-influenced, -induced, and -controlled mineralizations.

In biologically-influenced mineralization, the chemical conditions of carbonate supersaturation are provided by external factors, but the organic microbial mat and EPS serve as a substrate and nucleation point for carbonate precipitation (Benzerara *et al.*, 2006; Dupraz *et al.*, 2009), notably by reducing the kinetic barriers to initial crystal precipitation (Kamennaya *et al.*, 2012).

In biologically-induced mineralization, micro-organisms directly modulate the chemistry of their surrounding environment *via* their respective metabolic activity, hence locally increasing the water SI and favoring carbonate precipitation (Arp *et al.*, 2001; Dupraz *et al.*, 2009). For example, photosynthetic organisms release alkaline power through the incorporation, and dissociation of HCO_3^- into CO_2 (fixed by the cell) and OH^- (released out of the cell) (Arp *et al.*, 2001; Visscher and Stolz, 2005). Anaerobic sulfate respiration directly releases alkalinity as bicarbonate ions (Eq. 1.10), resulting in an increase of the carbonate saturation state as well (Visscher and Stolz, 2005; Dupraz *et al.*, 2009).

At last, the biologically-controlled mineralization (less prevalent in microbialites formation) implies a stronger, possibly genetic control of the organism on precipitation (Dupraz *et al.*, 2009), *e.g.*, skeletons of eukaryotic microorganisms, or intracellular carbonates in some prokaryotes (Couradeau *et al.*, 2012; Benzerara *et al.*, 2014; Ollivier *et al.*, 2018).

In sum, microbialites are the result of complex and intertwined environmental constraints, reflecting differing degrees of biotic and abiotic influences. As such, an inherent quality of microbialites (especially those formed *via* authigenic carbonate precipitation) is to archive their environment of formation, and represent a door to the past. However, a great deal of diversity and complexity of morphological, mineralogical, microbiological, and geochemical signatures arises from the myriad of environmental parameters presented above (*e.g.* Riding, 2006, 2011; Della Porta, 2015; Saghaï *et al.*, 2015; Chagas *et al.*, 2016; Vennin *et al.*, 2019, 2021; Grey and Awramik, 2020; Iniesto *et al.*, 2021b; Zeyen *et al.*, 2021), leaving many questions open about their processes of formation.

The recent study by Caumartin *et al.* (2023) evidenced a minimum threshold of water saturation indexes required, at the basin-scale (*e.g.*, a lake, a sea), to form microbialites (Annex 3). Accordingly, biology may be a facilitator, but favorable physico-chemical conditions are a prerequisite to the formation of microbialites. To discern the respective influence of biotic and abiotic factors, isotope signatures may prove a powerful technique and will be explored in chapter 10.

1.5.3. Occurrence of microbialites through time and environments, and purpose of their study

Due to the crucial role of biological factors in the formation of microbialite, the preservation of these objects in the geological record as far back as 3.43 Ga (Allwood *et al.*, 2006; Wacey, 2010) puts them among the oldest traces of life on Earth (*e.g.* Lepot, 2020). Because the preservation of organic soft tissues in the geological record is difficult, mineral byproducts of biological activity, such as microbialites, are powerful objects to study the evolution of life through time; all the more since microbialites' occurrence cover most of the Earth history (Fig. 1.9; Riding, 2006).

Microbialites from lacustrine or isolated coastal basins have been reported as far back as ~2.7 and 2.8 Ga ago, respectively (Kamber *et al.*, 2004; Lepot *et al.*, 2009; Thomazo *et al.*, 2011), and are numerous since the Proterozoic (Fig. 1.9). Today, the majority of microbialite deposits are found in continental waters, including more than 50 lacustrine basins around the world (Ollivier *et al.*, 2018). Most of them correspond to alkaline basins, with pH often above 9, where microbialites form mostly *via* authigenic precipitation (*e.g.* Kempe *et al.*, 1991; Zeyen *et al.*, 2015). The oldest lacustrine microbialites reported, in the Tumbiana formation (Australia), also developed in an evaporative alkaline paleolake, suggesting that alkaline settings are and have been a predominant characteristic of inland microbialites throughout time.

Because of the geological and climatic influence on microbialite formation processes (section 1.5.2.2), these objects are widely used as paleoclimate proxies, notably in continental settings (Frantz *et al.*, 2014; Bouton *et al.*, 2016a; Roche *et al.*, 2018; Arenas *et al.*, 2019; Boussagol *et al.*, 2023). While the geochemical and isotopic signals of continental carbonates in gravitational sediments have been extensively constrained as paleoenvironmental proxies, such geochemical studies using microbialite carbonates are only emerging (*e.g.* Frantz *et al.*, 2014; Buongiorno *et al.*, 2018; Ingalls *et al.*, 2020). Thus, they deserve further investigations, especially because of the intertwined biotic/abiotic nature of these objects (section 1.5.2.1). A broader review of how these biological and environmental factors affect and are recorded in the isotopic signatures of microbialites will be presented in the introduction of chapter 10.

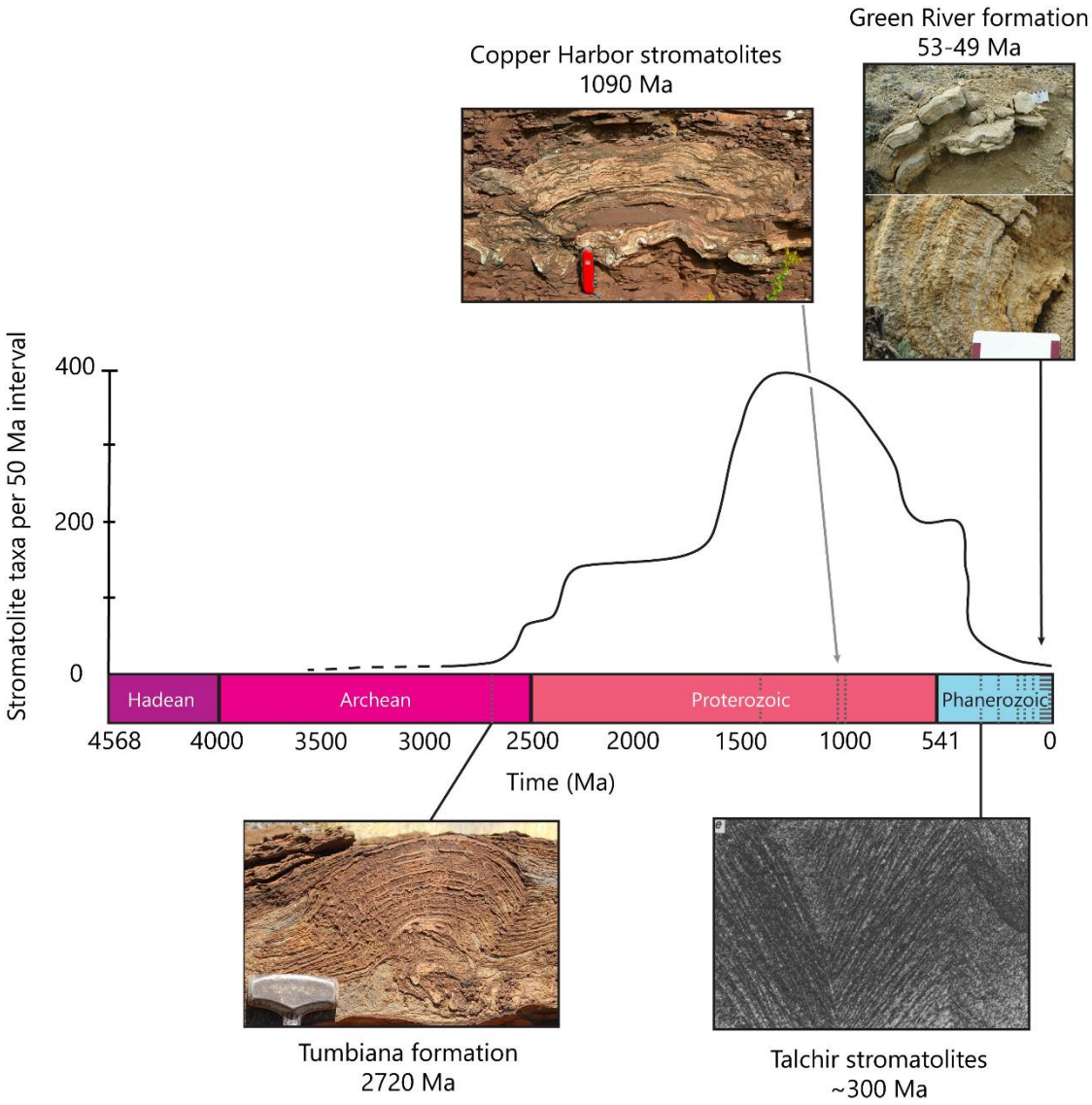

Figure 1.9: Variation of microbialites abundance, reported as taxa number, through Earth's history (modified from Riding, 2006). The 'stromatolite taxa' do not represent individual stromatolites, but categories of morphotypes. The four pictures show microbialites formed in lacustrine paleoenvironments: Tumbiana, Australia (Lepot *et al.*, 2009); Copper Harbor, USA (Fedorchuk *et al.*, 2016); Talchir, India (Ghosh *et al.*, 2001), and Green River, USA (Frantz *et al.*, 2014). Other lacustrine microbialites are reported with grey vertical bars within the Earth chronology, compiled from Ollivier *et al.* (2018), to which were added two locations from Sibley stromatolites, Canada (~1.4 Ga; Osterhout *et al.*, 2019) and Purbeck microbialites, UK (~150 Ma old; Bosence and Gallois, 2022).

1.6. Modern stratified analogues and the choice of the Mexican lakes

Modern redox-stratified analogues represent special environmental contexts within the modern Earth system, and notably relative to the modern ocean; however, a number of them can be found throughout the world. Some of the most studied and famous ones include the permanently stratified Black Sea (Eastern Europe), Cariaco Trench (Venezuela), and lakes Matano (Indonesia), Cadagno (Switzerland), Fayeteville (USA), or Pavin in France (*e.g.* Fry *et al.*, 1991; Crowe *et al.*, 2011; Busigny *et al.*, 2014; Posth *et al.*, 2017; Fulton *et al.*, 2018). But many – possibly millions – are increasingly studied (*e.g.* Schiff *et al.*, 2017; Cadeau *et al.*, 2020, 2022; Petrash *et al.*, 2022). Importantly, all of these analogues present specific characteristics, comparable to specific time periods of the past Earth, within the limits of our knowledge of ancient environments.

The characteristics of the lakes studied will be presented in more detail in Chapter 2; here I briefly present their main attributes and what makes their study purposeful. The four lakes are redox-stratified crater lakes with alkaline pH (~ 9) and monomictic mixing regimes (anoxic at depth, mixing once a year) (Zeyen *et al.*, 2021). The high pH and stratified water column specifically allow the target of continental and isolated basins from Precambrian times (section 1.1). Together with the presence of microbialites, this strongly connects the Mexican lakes with evaporative paleo-basins such as those containing the Tumbiana stromatolites (section 1.5.3) and their diversity of metabolic activities (*e.g.* Lepot *et al.*, 2009, 2019; Thomazo *et al.*, 2009; Stüeken *et al.*, 2017). Stüeken *et al.* (2017) highlighted the interest in studying these contexts by speculating that Archean microbial life could have diversified in such isolated continental environments. Besides, lacustrine redox-stratified conditions with neutral to alkaline pH were evidenced in the Gale crater on Mars (Hurowitz *et al.*, 2017), showing another potential application of the research focused on this kind of environments.

On Earth, an alkaline "soda ocean" with pH between 9 and 11 was initially suggested (*e.g.* Kempe and Degens, 1985). While the presence of large carbonate deposits already in the Early Archean argue against a very acidic ocean at the time, much higher pCO_2 than today have been used to discard the "soda ocean" hypothesis (Grotzinger and Kasting, 1993). Models estimated pH increasing from about 6.5 to 8 between 4 and 0.5 Ga ago, with possible maxima to 8.8 during Neoproterozoic glaciations (Halevy and Bachan, 2017; Krissansen-Totton *et al.*, 2018).

An important trait of the Mexican microbialites to serve as analogues of ancient microbialites is that they form *via* authigenic carbonate precipitation (section 1.5.2; Zeyen *et al.*, 2015; 2021). Indeed, whereas the widely studied modern marine Australian and Bahamian stromatolites form predominantly by a trapping and binding process (Awramik and Riding, 1988; Kempe *et al.*, 1991; Reid *et al.*, 2003), most modern and many ancient stromatolites formed by *in situ* carbonate precipitation (*e.g.* Grotzinger, 1990; Corkeron *et al.*, 2012; Caumartin *et al.*, 2023). Moreover, not all the modern environments containing microbialites feature anoxic waters, and to the best of my knowledge, none of these microbialites were reported in, or sampled from consistently anoxic water columns.

The ecological diversity in the four lakes (both in the plankton and microbialite benthic communities) is dominated by prokaryotic organisms (*e.g.* Saghaï *et al.*, 2015; Iniesto *et al.*, 2021a, 2021b, 2022), allowing comparisons with deep time microbial consortia (Gargaud *et al.*, 2009; Ollivier *et al.*, 2018).

While this work could build on extensive previous characterizations of the microbiology, limnology, physico-chemistry, and geology provided for these lakes (*e.g.* Macek *et al.*, 2020; Alcocer, 2021; Zeyen *et al.*, 2021; Iniesto *et al.*, 2022), the isotopic data were scant, and limited to a single lake (Briones *et al.*, 1998; Kaźmierczak *et al.*, 2011). Hence, this PhD work fills in a gap in our knowledge of these systems, and aims at integrating the isotopic approach in a multi-disciplinary understanding of these modern analogues.

Finally, a major advantage for studying these four lakes lies in that they could be characterized in parallel, *via* the same methodology, and thus extensively compared. Indeed, many studies of modern analogues focus on a single location, narrowing the scope of their observations to a single context. Here, while the four lakes share overall similar contexts (alkaline crater lakes, high altitude, closed basin, stratified, monomictic), their respective water chemical compositions vary, including different alkalinity and salinity contents (*e.g.* Zeyen, 2017; Zeyen *et al.*, 2021). This allowed to pinpoint environmental and chemical factors specific to each lake, and observe their differential influence in the four locations. For example, sulfate concentrations in the four water columns range from 12 µM to 12 mM, allowing a specific assessment of sulfate concentration effects on the sedimentary S isotope record (Chapter 8).

1.7. Objectives and outline of the PhD

The main objective of this PhD work was to assess the reliability of sedimentary archives in recording the biogeochemical functioning of modern stratified environments. The strategy implemented to tackle this issue was to draw a comparison of **multiple modern redox-stratified lacustrine environments containing microbialites** *via* the **simultaneous** use of **C, O, and S isotope systematics**, starting from their **current functioning** (*i.e.*, processes occurring within the water column and exchanges with external reservoirs), to end in their respective **sedimentary geochemical records** (both "gravitational sediments" and microbialite deposits).

A number of studies investigating modern analogues focus on the description of a single site, which therefore represents a singular context and analogy with a specific time in the past. Meanwhile, the chemical compositions of continental and marine waters have changed over the course the Earth's history, and their determination, tied to uncertainties, implies a certain variability of the specific conditions that have prevailed in the past. Here, the characterization of **several locations with distinct chemical water compositions**, but sharing a number of characteristics (section 1.6), enables **targeting the effects of specific parameters**. Notably, the impact of different alkalinity contents, nutrient and trophic levels, external fluid sources, and sulfate concentrations are compared among the four environments and their sedimentary records.

The C and S cycles, together with O, are intimately bound and central to the evolution of life and oxygenation at the Earth's surface (section 1.3, 1.4, and Fig. 1.8). Combining the interpretation of these cycles is thus a powerful approach, and was pursued in this PhD. A major asset of the study of modern analogues lies in the possibility to measure both the **dissolved and solid phases relevant to the C and S cycles.** Therefore, I focused on identifying the **biogeochemical processes that operate today**, before assessing how they are **transferred to a perennial record** in mineral phases.

Microbialites are emblematic geological objects, often tied to alkaline environments, and widely studied to reconstruct the emergence and evolution of life on Earth, as well as general environmental traits (*e.g.*, climate, hydrology, redox). Rarely, however, have microbialites been characterized and compared to concomitant gravitational sediment repositories. Here, for the first time, this PhD study proposes to **compare the two kinds of sedimentary records**, **within**

a specific study site, **in parallel to active processes** constrained in the water columns and sediments. The inter-comparison of distinct and diverse microbialite systems in a single study remains rare, and is, for the same reasons presented above, an important asset of this study. On top of environmental factors at the basin's scale, microbialites formation results from complex biotic and abiotic interactions at a millimetric scale. Therefore, **results from micro-sampling were integrated to this study** in order to connect these two approaches. Finally, some of the **microbialites form under anoxic conditions**, which has never been investigated before in modern environments, despite being a key parameter of many Precambrian microbialites.

Using stable isotope systematics, the strategy above should allow addressing the following major questions: *(i) what important processes and biological diversity may be omitted in the sedimentary records of these stratified environments? (ii) Which of the bottom lake sediments or microbialites repositories are more specific to physico-chemical and biological factors? (iii) What abiotic and biotic parameters are preserved in these records? (iv) How early diagenetic processes may alter these records and blur their initial messages?* Based on the above motivations and interrogations, the outline of this manuscript is divided into three parts: (I) the C and O isotope signals from the water columns to the bottom lake sediment records (Chapters 4, 5, 6); (II) the S isotope signatures in the four lakes and their record in the bottom lake sediments (Chapters 7, 8); (III) petrographic descriptions, C, O, and S isotope systematics from the microbialite archives (Chapters 9, 10, 11). All chapters begin with a detailed table of contents and are summarized below.

PhD Outline

Chapter 1 consists in this general introduction, providing the state of art about key aspects of this thesis: stratified environments throughout time, the isotopic tool, the C, and S cycles, the microbialite records, and the presently known modern analogues.

Chapter 2 will give a general presentation of the four lakes geological contexts, history of crater formation, climate, and limnological backgrounds.

Chapter 3 presents the field work and analytical methods performed during this PhD, including the tests that were carried out to validate some of the analytical techniques.

Part I

Chapter 4 comprises the characterization of the water column dissolved inorganic and organic carbon (DIC, DOC), and particulate organic carbon (POC) data, and connects with the isotopic compositions of sedimentary carbonate and organic matter reservoirs at the bottom of the four lakes. This chapter is made of two articles published as companion papers in the review "Biogeosciences" in 2023. The first paper investigates the sensitivity of DIC and POC reservoirs to physico-chemical and biological processes as a function of the respective lakes water chemistry (notably alkalinity). The second paper brings to light the key role of DOC in these stratified ecosystems, as being a diagnostic reservoir of microbial diversity and physiology. These results are then integrated to active debates about the role of DOC in past ocean chemistry.

Chapter 5 presents a box model of the C cycle in Lake Alchichica, constraining the most prominent sources and processes affecting the C reservoirs in this lake. It provides additional keys about the sensitivity of the DIC reservoir in alkaline environments, and explanations for the current and recent evolution of the lake's chemistry.

Chapter 6 characterizes the carbonate and organic C reservoirs in the sediment cores of the four lakes. First, I assess the strong role of diagenesis: how microbial respiration and dissolution/reprecipitation processes alter the organic C and carbonate C and O isotope signatures, respectively. Then, I show what primary climatic and hydrologic features may be preserved in these sediment carbonates.

Part II

Chapter 7 tackles the sedimentary S record in Lake Alchichica through multi-S isotopes. Lake Alchichica was the most characterized of the four lakes studied, which allowed a thorough description of microbial processes affecting the S isotope record during early diagenesis, including cryptic reoxidative S cycling. This chapter also contains a "toolbox" helping for the interpretation of multiple S isotope data.

Chapter 8 consists in a broader picture of the four lakes S cycle. First I present which biotic and abiotic factors are the most impactful for the pyrite isotopic record in the three lakes other than Alchichica (notably sulfate concentration, sulfate reduction rates). Then, I put in perspective how these sedimentary pyrite records would be interpreted *a posteriori*, in geological samples, and highlight the role of the "reservoir effect".

Part III

Opening the third and last part of this manuscript, **Chapter 9** presents a mineralogical and petrographic characterization of the Mexican microbialites. By contextualizing these features in the geology and geography of the respective lakes, and resuming the existing literature, I classify the studied microbialites into distinct facies. These facies reflect different histories of formation and post-deposition alteration. This classification is used as a base for interpreting isotopic messages in the next chapters, and assess how chemical and observational conclusions may or not overlap.

Chapter 10 investigates the microbialites C and O isotope signatures in carbonates and organic matter. I show how much these results are consistent and complement our understanding of microbialites formation processes introduced in Chapter 9. The effects of secondary carbonates replacement, and recrystallization are evidenced. By contrast, I subsequently show under what conditions can primary biosignatures, local sources, and climatic features be recorded in the carbonate archives. Doing so, I put constrain on the biotic *vs.* abiotic factors leading to these microbialites formation. Finally, I discuss the influence of the redox stratification on the microbialites OC isotope signatures.

Chapter 11 consists in the poster I presented at the 2023 Goldschmidt conference in Lyon. It represents a preliminary work about the multi-S isotope signatures in the pyrites and carbonate-associated sulfates (CAS) of Alchichica microbialites. Together with the analysis of the lake dissolved sulfate, these data suggest different sources of S to Alchichica microbialites, and a direct effect of the redox stratification on metabolisms of the microbialites and their S isotope signal.

Chapter 12 provides a general conclusion of this thesis, summarizing the main results, outcomes, and opening perspectives to this work.

Chapter 2

General presentation of the studied sites: geology, climate, and limnology

Table of content

2.1. Geological setting

The four crater lakes studied are located within a large Neogene to Holocene volcanic arc called the Trans-Mexican Volcanic Belt (TMVB), which crosses central Mexico oriented E-W, over a distance of ~1000 km, and a width of ~90-230 km (Fig. 2.1; Ferrari *et al.*, 2012). This arc is related to the subduction of the Cocos and Rivera plates under the North American Plate, and contains a few dozens of stratovolcanoes, large caldera complexes, hundreds of domes and shield volcanoes, and >3000 small monogenetic volcanoes such as scoria cones, tuff cones, and maars (Kshirsagar *et al.*, 2016 and references therein).

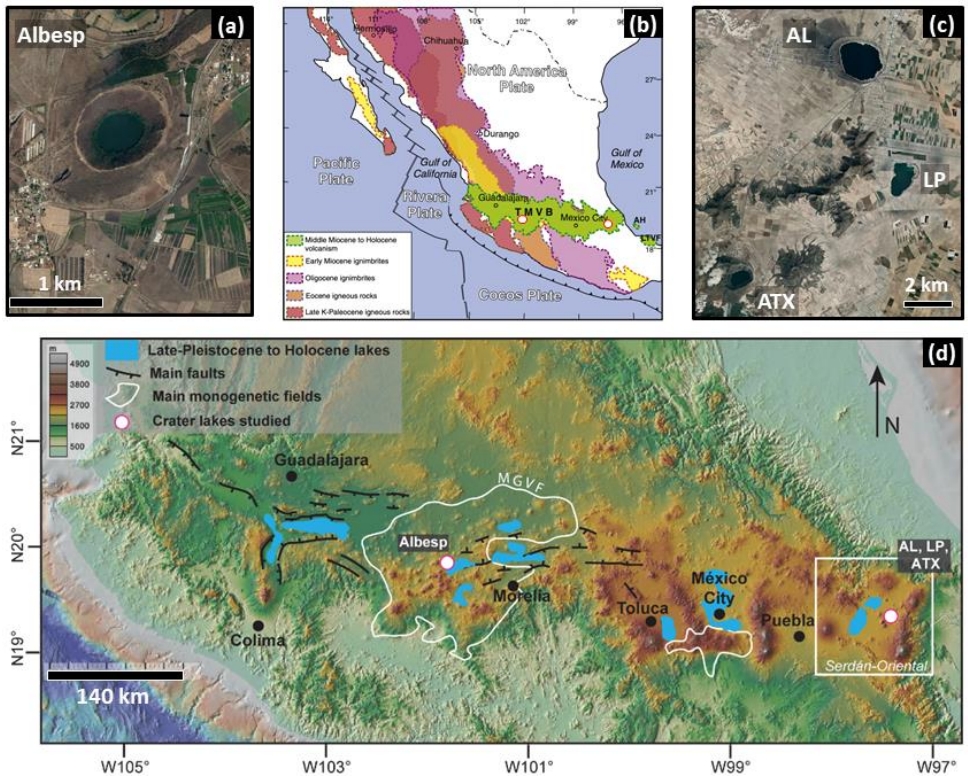

Figure 2.1 : Geographic and geological maps representing the trans-Mexican volcanic belt (TMVB) and the four lakes studied. (a) Google Earth view of Alberca de los Espinos. (b) Geological map of the TMVB from Ferrari *et al.* (2012). (c) Google Earth view of Alchichica, Atexcac, and La Preciosa lakes. (d) Topographic map of the TMVB, modified from Guilbaud *et al.* (2023). The lakes studied are located in two distinct regions of the TMVB: in the Serdán-Oriental basin for 'AL', 'ATX', and 'LP', and in the Michoacán-Guanajuato volcanic field (MGFV) for 'Albesp'.

The main general information about the four lakes are summarized at the end of this chapter in Table 2.1 and are presented in more detail in the following.

Alberca de los Espinos is located within the vast monogenetic Michoacán-Guanajuato volcanic field (MGVF), in the central-western part of the TMVB (Fig. 2.1). The lake infills a tuff cone volcano, formed in a highly faulted area at the margin of the Zacapu tectonic lacustrine basin (a paleolake; Siebe *et al.*, 2012). The crater itself lies on a normal fault, at a current altitude of ~1985 m above sea level (masl; Siebe *et al.*, 2012, 2014). The geological basement is composed of Pliocene and Quaternary basaltic andesite, andesite, and dacite rock types (Siebe *et al.*, 2012; Kshirsagar *et al.*, 2016), overlain by undifferentiated quaternary volcanic and alluvial sediments (Kshirsagar *et al.*, 2016).

In the easternmost part of the TMVB, Alchichica, Atexcac, and La Preciosa are three maar lakes found within a high plain closed basin called the Serdán-Oriental Basin (SOB), and are located less than 10 km away from each other (Figs. 2.1 and 2.2). At an average altitude of 2300 masl, the SOB is delimited by multiple volcanic edifices (Fig. 2.2), and notably to the east by the Citlaltépetl-Cofre de Perote volcanic range, which isolates the SOB from the Gulf of Mexico (Carrasco-Núñez and Chako-Tchamabé, 2022; Silva-Aguilera *et al.*, 2022a). The geological basement of this area is composed of folded and faulted Cretaceous limestone and shales, andesitic to basaltic lava flows from the Miocene to the Pleistocene epochs, further covered by undifferentiated Holocene pyroclastic and alluvial deposits (Fig. 2.2b; Carrasco-Núñez *et al.*, 2021).

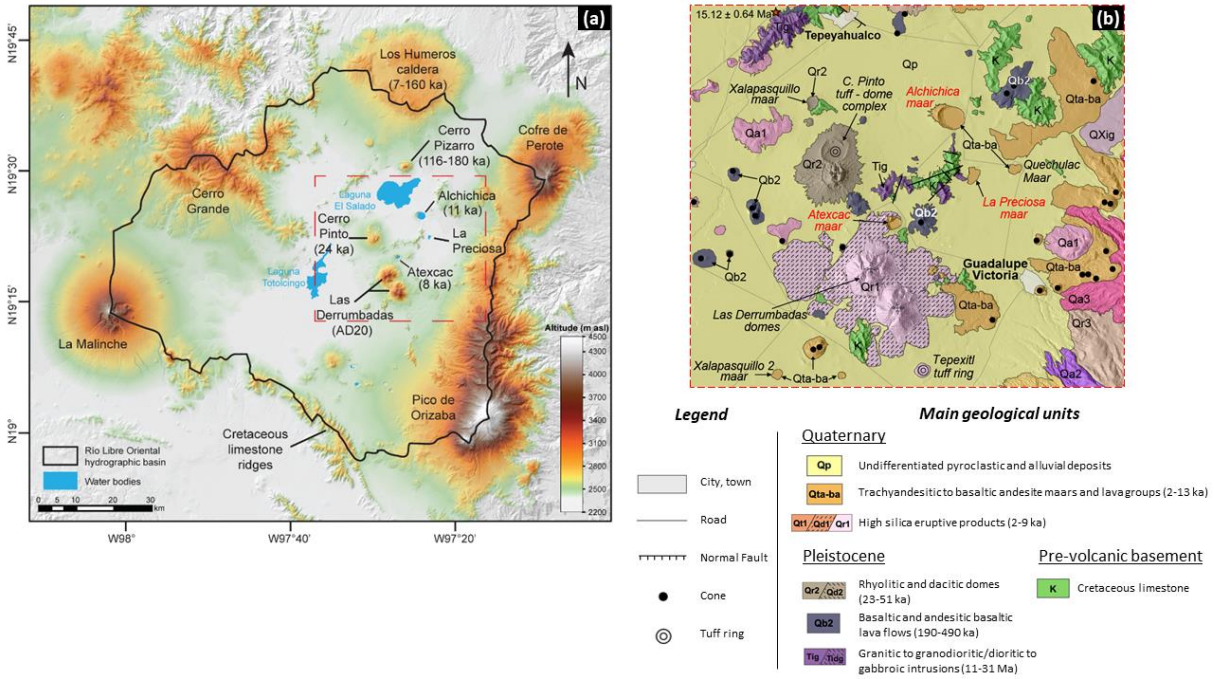

Figure 2.2 : Topographic and geological map of the Serdán-Oriental Basin (SOB). (a) Topographic map from Guilbaud *et al.* (2023), showing the location of the three studied lakes in the SOB, at minimum altitudes of about 2200 m above sea level, and the repartition of the volcanic edifices surrounding the basin. (b) Geological map from the red insert area in (a), modified from Carrasco-Núñez *et al.* (2021). The main geological units surrounding the studied maar lakes are shown in the legend. The other units correspond to different andesitic, dacitic, trachyandesitic, and rhyolitic lava flows, and Ignimbrite levels, all younger than 1.3 Ma (Carrasco-Núñez *et al.*, 2021). From all other maar craters indicated, Quechulac is the only one containing a lake.

2.2. Volcanic edifices

The four lakes are found in craters called *maar* volcanoes *sensu lato*, formed after phreatic, magmatic, and phreatomagmatic eruptions (Carrasco-Núñez *et al.*, 2007; Armienta *et al.*, 2008). Maars form by the interaction of ascending magmas with water, usually encountered at relatively shallow depths, for instance from an aquifer or a lake (*e.g.* Armienta *et al.*, 2008; Carrasco-Núñez and Chako-Tchamabé, 2022). Successive explosions cause the ejection of volcanic, and country-rock material, progressively deepening and widening the explosion loci (Fig. 2.3; Lorenz, 1986; Carrasco-Núñez and Chako-Tchamabé, 2022). *Sensu stricto*, maar volcanoes designate craters where the country-rock is exposed (Carrasco-Núñez and Chako-

Tchamabé, 2022), reflecting the fragmentation and excavation of older units (Fig. 2.3). Therefore, the maar crater walls are composed of pre-maar and maar sequences, as determined for Alchichica and Atexcac (Fig. 2.3b and c; Carrasco-Núñez *et al.*, 2007; Chako-Tchamabé *et al.*, 2020). By contrast, tuff rings and cones (like Alberca de los Espinos) usually consist of shallower craters, only exposing the pyroclastic products (Carrasco-Núñez and Chako-Tchamabé, 2022).

Figure 2.3a was taken from Carrasco-Núñez and Chako-Tachamabé (2022) to illustrate the processes and chronology of maar formation, through the example of Alchichica. The final craters' morphology can be very diverse, depending notably on the water/magma ratio, and on lateral and vertical variations of the explosion loci (Figs. 2.1, 2.3, and 2.4). In Alchichica, the crater is very asymmetrical with heights of 160 and 10-15 m for the western and eastern flanks, respectively (Fig. 2.4; Chako-Tchamabé *et al*., 2020). The shape of Atexcac crater is slightly elongated, resulting from the ENE displacement of the explosion loci (Carrasco-Núñez *et al.*, 2007), which corresponds to the orientation of some of the normal faults described just a few km away (Figs. 2.2b; in the outcropping limestone). The crater walls are asymmetrical as well, the northwestern wall reaching ~200 m above the current lake level, while the other sides are ~100 m above the lake. The crater in La Preciosa is shaped like a heart, with relatively "flat" flanks, less than 40 m in height relative to the lake water. By contrast, Alberca has a very regular rounded shape, and walls reaching about 100 m above the present lake surface (Figs. 2.1, 2.4).

The formation of Atexcac crater was dated between 8.3 and 5.1 ka (Chédeville *et al.*, 2020). In Alchichica, different dating techniques provided an age extending between 13 and 6 ka (Chako-Tchamabé *et al.*, 2020), centered around 11 ka (Chédeville *et al.*, 2020). La Preciosa was not dated but likely is Holocene in age (Carrasco-Núñez *et al.*, 2021). Alberca de los Espinos formed about 25 ka ago (Siebe *et al.*, 2012).

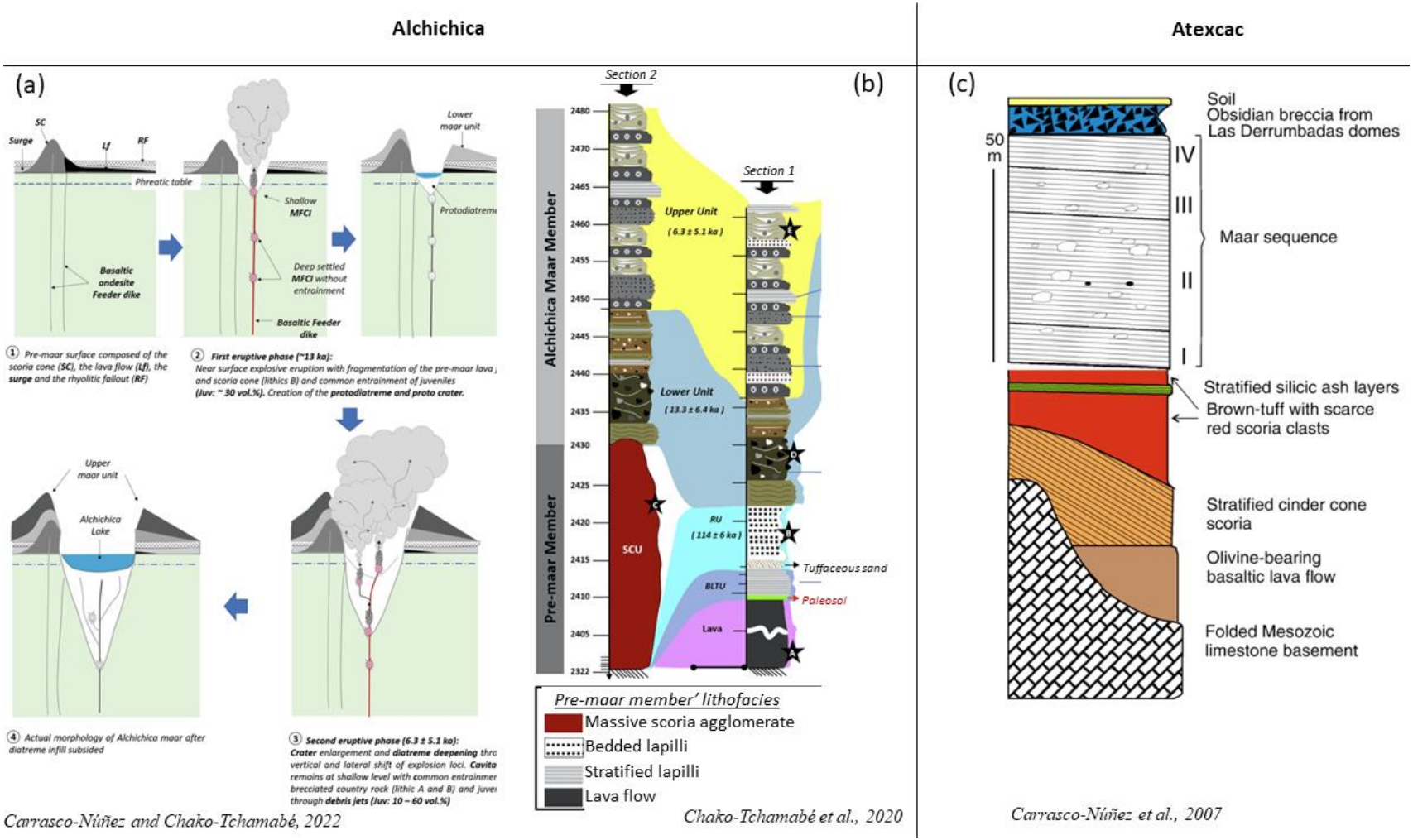

Figure 2.3 : Schematic view of the steps of Maar formation, and resulting stratigraphic sequences. (a) Scheme from Carrasco-Núñez and Chako-Tchamabé (2022) showing the chronologic steps in the process of Maar formation in Alchichica. Notably, one can see the progressive deepening and widening of crater *via* successive phreatomagmatic explosions, exposing older units, and covering them with maar deposits, seen in 'b'. (b) Correlation of two stratigraphic sections in Alchichica showing the pre-maar and maar deposits, from Chako-Tchamabé *et al.* (2020). The maar deposits are composed of diverse tuff, breccia, lapilli lithofacies. (c) Similar stratigraphic section for Atexcac maar, from Carrasco-Núñez *et al.* (2007).

Figure 2.4: Photographs of the four lakes studied. Courtesy of Pierre Boussagol for the picture of Atexcac. See figure 2.1 for an aerial view of the lakes.

2.3. Climate and limnology

The range of volcanoes east of the SOB, reaching altitudes of ~5600 masl, constitute a natural barrier to precipitations coming from the Atlantic Ocean (Silva-Aguilera *et al.*, 2022a). It provides the SOB with a specific local climate, ranging from temperate arid to temperate sub-humid in the area where the studied lakes are located (Silva-Aguilera *et al.*, 2022a). These conditions result in much higher evaporation than precipitation rates. In Alchichica, between 1981 and 2010 for example, these rates averaged 1686 *vs*. 392 $mm.yr^{-1}$, respectively (Silva-Aguilera *et al.*, 2022a). Higher altitudes and proximity with topographic tops, such as in Atexcac (Fig. 2.2), can locally increase the rain fall and decrease the temperatures (Silva-Aguilera *et al.*, 2022a). Nevertheless, this area remains drier than the region of Alberca de los Espinos, where precipitation rates over the same period averaged ~850 $mm.yr^{-1}$ (Kshirsagar *et al.*, 2015; though evaporation is also high, around 1850 $mm.yr^{-1}$; Servicio Meterológico Nacional).

The four lakes studied are located in endorheic basins, meaning that surface waters in these areas do not reach the sea. On a topographic map (Fig. 2.2), one can clearly see how rain water in the SOB will fall within the limits delimited by the surrounding volcanic ranges and limestone ridges, and then flow towards the center of the basin at lower altitudes (Fig. 2.2). The big "Lagunas" represented on the map are ephemeral lakes.

The four lakes are *closed lakes*, meaning that they have no surface inflow or outflow of water (*i.e.* rivers). Hence, these lakes are mainly groundwater fed (Armienta *et al.*, 2008; Kshirsagar *et al.*, 2015; Silva-Aguilera, 2019; Silva-Aguilera *et al.*, 2022b). The chemical composition of the groundwater (GW) thus greatly influences the lakes chemistry. As such, it was recognized from Sr isotopes that the SOB lakes are fed by GW altering both carbonates and basaltic/andesitic rocks, in contrast with Alberca de los Espinos where only volcanic rocks prevail (Zeyen *et al.*, 2021).

The petrology of the SOB basement should result in GW with lower $DIC/(Ca^{2+} + Mg^{2+})$ ratios than GW flowing through purely volcanic lithologies (Pecoraino *et al.*, 2015). Nonetheless, that ratio remains above unity in the water of the four lakes (Zeyen *et al.*, 2021). Under evaporative conditions, such waters evolve towards alkaline brine compositions (Pecoraino *et al.*, 2015; Zeyen *et al.*, 2021), explaining the high pH of these lakes, between 8.9 and 9.2 (from May 2019 measurements). The direction of the flow path also impacts the lakes

chemistry. As determined for the aquifer "de Libres Oriental" in the SOB (Silva-Aguilera, 2019; Lelli *et al.*, 2021), the chemical composition of GW evolves as it crosses different sediment strata and body of waters, like maar lakes (Fig. 2.5).

Due to intense anthropic use of groundwater in the SOB, the GW flux has diminished in the last decades, together with the lakes water level, and depth (*e.g.* Silva-Aguilera *et al.*, 2022b). Today, the maximum depths recorded in Alchichica, Atexcac, La Preciosa, and Alberca are 62, 39, 46, and 30 m, respectively (Siebe *et al.*, 2012; Zeyen *et al.*, 2021; Filonov *et al.*, 2022). The water level decrease is amplified by the much higher evaporation than precipitation rates prevailing in the region, and is perceptible year after year.

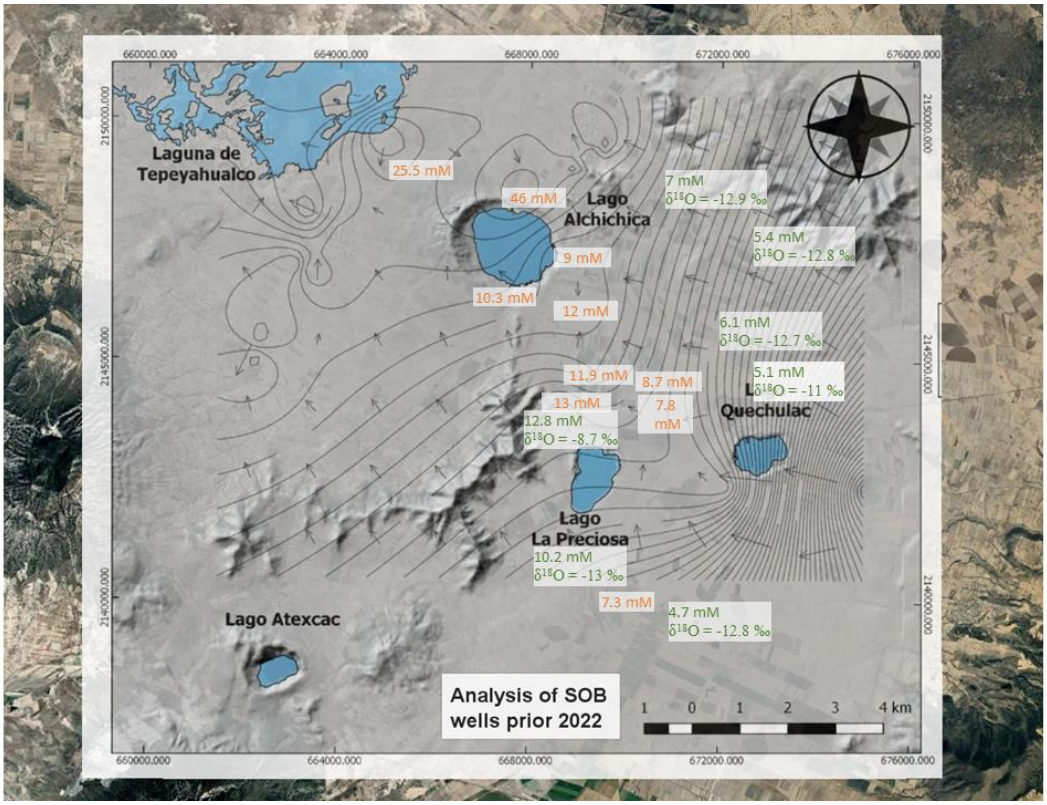

Figure 2.5 : Map of groundwater flow in the Serdán-Oriental Basin around Alchichica (Silva-Aguilera, 2019) superimposed to a Google Earth map. The lines correspond to equipotentials determined by extrapolating the wells water chemical compositions. Dissolved inorganic carbon (DIC) concentrations and water O isotope compositions measured in well-waters by Silva-Aguilera (2019) in orange, and by Lelli *et al.* (2021) in green, were added on the map. One can see the increase in both [DIC] and $\delta^{18}O_{H2O}$ (*vs.* VSMOW) after the GW has flown through Lake La Preciosa, and before it enters Alchichica. Similarly, the GW is even more concentrated as it exits this later lake.

The differences in geological basement, climate, and groundwater flow contribute to explain the distinct chemical compositions found in the four lake waters, despite their similar

alkaline pH (*e.g.* Vilaclara *et al.*, 1993; Armienta *et al.*, 2008; Zeyen *et al.*, 2021). Indeed, these lakes characteristically align on a gradient of water chemical compositions (along with six other Mexican crater lakes; Fig. 2.6; Zeyen *et al.*, 2021). Parameters including the Mg:Ca ratio, the sodium, sulfate, alkalinity, and DIC concentrations increase from Alberca de los Espinos, to La Preciosa, to Atexcac, and to Alchichica (Zeyen *et al.*, 2021). This variability results in salinity conditions ranging from freshwater (in Alberca) to hyposaline (in Atexcac and Alchichica), with salt concentrations increasing from approximately 0.7, to 1.4, to 7.4, and to 8.3 $g.L^{-1}$ (Zeyen *et al.*, 2021). The origin of this chemical gradient is further discussed in chapters 4 and 5.

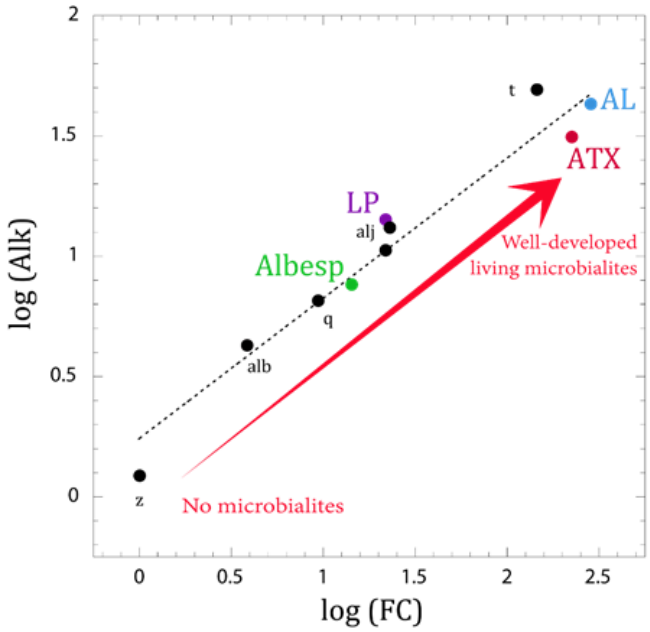

Figure 2.6 : Cross-plot of the logarithm of alkalinity *versus* the concentration factor for ten Mexican lakes, modified from Zeyen (2017). The concentration factor reflects an enrichment factor of dissolved ions, calibrated with sodium concentrations, normalized to that of Lake Zirahuén ('z'). The figure shows the relative abundance of microbial deposits increasing with the alkalinity. The lakes studied here are colored.

These differences, notably in alkalinity, lead to very different degrees of microbialites abundance in the four lakes (Fig. 2.6; Zeyen *et al.*, 2021), highlighting the determinant role of a water body's chemical context in microbialites formation (Caumartin *et al.*, 2023). The distribution and characteristics of microbialites will be further described in a subsequent dedicated chapter (Chapter 9). The planktonic diversity of the lakes, is dominated by prokaryotic organisms, and also changes along the gradient of salinity/alkalinity (Iniesto *et al.*, 2022). Overall, the main phyla correspond to Cyanobacteria, Bacteroidota, Planctomycetota, Actinobacteria, Alphaproteobacteria, Gammaproteobacteria, and Verrucomicrobiota (Iniesto *et al.*, 2022).

A final key aspect of these lakes is the physicochemical structure of their water column: the four of them are warm monomictic lakes (*e.g.* Rendon-Lopez, 2008; Sigala *et al.*, 2017; Zeyen *et al.*, 2021). It means that they are stratified most of the time but mix once a year (Fig. 2.7). The stratification is favored by the characteristic bowl-shape of crater lakes, and the mixing regime results from the seasonal climate (Alcocer *et al.*, 2000; Filonov *et al.*, 2022). A thermal stratification is well-established during the summer from May to October (*e.g.* Macek *et al.*, 2020), but can extend up to 9 months a year, starting when wind stress diminishes and temperatures increase (*e.g.* Alcocer *et al.*, 2000). During stratification, the water column is divided in three distinct layers: the epilimnion – at the top, in contact with the atmosphere – the metalimninon, or thermocline – where the temperature gradient is observed –, and the hypolimnion at the bottom, in contact with the lake sediments. After stratification is set, aerobic respiration at depths quickly drives the hypolimnion to anoxia (*e.g.* Macek *et al.*, 2020). Thence, the four lakes water column harbor strong chemical gradients during most of the year, with fully oxic conditions in the epilimnion, and anoxic conditions in the hypolimnon. In October, the decrease of surface temperatures towards those of the hypolimnion layer allows the circulation, and mixing of water masses from December to February (Alcocer *et al.*, 2000; Macek *et al.*, 2020).

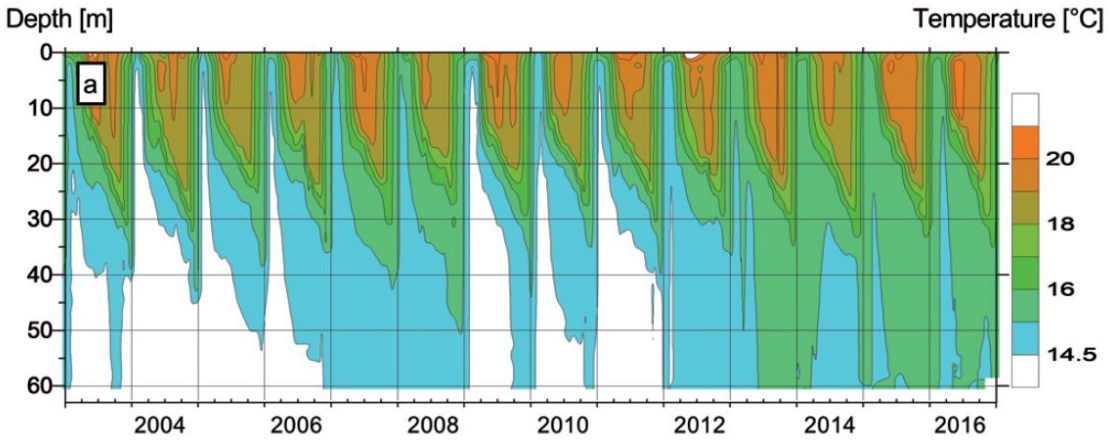

Figure 2.7: Thermal stratification record in Alchichica between 2003 and 2016, from Macek *et al.* (2020).

Table 2.1. General information of the studied lakes. Abbreviations: TMVB: Trans-Mexican volcanic belt; MGVF: Michoaćan-Guanajuato volcanic field; masl: meters above sea level. § values from May 2019.

Lake	General location	Sampling location	Elevation (masl)	Lake Basement	Age	Max Depth (m)	Area (km²)	Alkalinity (mM)§	Salinity (psu) §	pH §	Microbialites description
Alchichica	Serdán-Oriental Basin, eastern TMVB	19°24'51.5" N; 097°24'09.9" W	2320	limestone, andesites, basalts	6-13 ± 5-6 ka	62	~2.2	~35	7.9	9.22	Well-developed living microbialites, large fossil microbialite reefs
Atexcac	Serdán-Oriental Basin, eastern TMVB	19°20'2.2" N; 097°26'59.3" W	2360	limestone, andesites, basalts	8.3-5.1 ± 0.1-0.2 ka	39	~0.3	~26	7.4	8.85	Well-developed living microbialites, thick fossil microbialites covering the crater walls
La Preciosa	Serdán-Oriental Basin, eastern TMVB	19°22'18.1" N; 097°23'14.4" W	2330	limestone, andesites, basalts	Holocene	46	~0.8	~13.5	1.15	9.01	Living microbialites, sporadic fossil microbialites around the crater
Alberca de los Espinos	Zacapu Basin, MGVF, cental TMVB	19°54'23.9" N; 101°46'07.8" W	1985	andesites	25 ± 2 ka	30	~0.1	~7	0.6	9.14	Thin living microbialites, encrusting basalts

Chapter 3

Field work and analytical methods

Table of content

3.1. Introduction

Carbon (C), sulfur (S), and oxygen (O) are actively cycled through biological and abiological reactions between the atmosphere, hydrosphere and biosphere before precipitating and being fixed in the sedimentological/geological record. Understanding their cycle and how they are preserved in the rock record thus requires to analyze them in a number of gaseous, aqueous (or dissolved) and solid forms, in both organic and inorganic phases, and following a large number of techniques.

In this chapter, I present the protocols used to characterize the concentrations and isotopic compositions of these elements in the studied environments as well as validation tests performed during the course of this work. I also describe other methods used to complete the geochemical, mineralogical and physical characterization of the samples and for which I was not the first investigator, but whose results were directly used in the build-up of this PhD (summarized in Table 3.1). From the ANR project that funded my PhD, it was also possible to benefit from cutting-edge methods of microbial (*e.g.* metagenomics, metatranscriptomics) and mineralogical (*e.g.* FTIR, CLSM) characterization but they were performed by collaborators in the Université Paris-Saclay and Sorbonne Université, and I will not present them here.

Table 3.1 (below)

Summary of data that I collected during this PhD or in the preparation of which I was directly involved (in black) and/or outsourced but constituting major data for the PhD (in orange). IPGP: Institut de Physique du Globe de Paris; BGS: Biogéosciences (GISMO platform, Dijon); BetaAnalytic (Miami) ; TokyoTech : Tokyo Institute of Technology ; PSO :Pôle Spectrométrie Océan (Plouzané/Brest) ; SARM: Service d'Analyse des Roches et des Minéraux (Nancy) ; ERL : Environmental Radioactivity Laboratory (Liverpool) ; Sayens (Dijon).

Reservoir	Elements	Phase	Type of analyses	No. of analyzed samples	Laboratory of analysis
Lake water	C	DIC	[DIC], $\delta^{13}C$, (^{14}C)	31 (1)	IPGP (BetaAnalytic)
		DOC	[DOC], $\delta^{13}C$	26	BGS
		POC	[POC], $\delta^{13}C$, [PON], $\delta^{15}N$	23	BGS
	N	PON			
	O	H_2O	$\delta^{18}O$, δD	1	BetaAnalytic
	S	SO_4	[SO_4], $\delta^{34}S$, (^{33}S, ^{36}S)	18 (2)	BGS (TokyoTech)
	major and trace elements	Dissolved and particulate	concentrations	31	PSO
Bottom lake sediments	C	porewater DIC	[DIC], $\delta^{13}C$	34	IPGP
		bulk carbonates	[carbonates], $\delta^{13}C$	53	BGS
		plant debris	^{14}C, $\delta^{13}C$, ($\delta^{15}N$)	6	BetaAnalytic (BGS)
		bulk OM	[TOC], $\delta^{13}C$, [TON], $\delta^{15}N$	70	BGS
	N				
	O	bulk carbonates	$\delta^{18}O$	53	BGS
	S	porewater SO_4	[SO_4], $\delta^{34}S$, (^{33}S, ^{36}S)	20 (1)	BGS (TokyoTech)
		porewater H_2S	[H_2S] ($\delta^{34}S$)	19 (14)	BGS
		FeS_2	[FeS_2], $\delta^{34}S$, (^{33}S, ^{36}S)	68 (7)	BGS (TokyoTech)
	major and trace elements	Porewater and sediments	concentrations	39	SARM
	Pb	sediments	^{210}Pb	1 core	ERL
	physical characterization	sediments	XRD, dry density, color	50, 19, 56	BGS, Sayens
Mexican microbialites	C	bulk carbonates	[carbonates], $\delta^{13}C$, (^{14}C)	49 (2)	BGS (BetaAnalytic)
		micro-drill carbonates	$\delta^{13}C$	59	BGS
		bulk OM	[TOC], $\delta^{13}C$, [TON], $\delta^{15}N$	53	BGS
	N				
	O	carbonates	$\delta^{18}O$	49	BGS
	S	FeS_2	[FeS_2], $\delta^{34}S$, (^{33}S, ^{36}S)	37 (23)	BGS (TokyoTech)
		CAS	chem. extraction, $\delta^{34}S$, $\delta^{33}S$, $\delta^{36}S$	3	PSO + TokyoTech
	major and trace elements	bulk powder	concentrations	10	SARM
	other analyses	thin sections and powders	optical microscropy, µXRF-scanning, XRD	36	BGS
Archean samples	C	bulk OM	[TOC], $\delta^{13}C$, [TON], $\delta^{15}N$	15	BGS
	N				BGS
	S	FeS_2	[FeS_2], $\delta^{34}S$, (^{33}S, ^{36}S)	40 (19)	BGS (TokyoTech)

3.2. Field work, samples collection and preparation:

Virtually all samples from Mexico analyzed in the present study were sampled during a mission in May 2019, that is to say, before the start of my PhD thesis (in January 2020) and to which I could not participate. However, another filed trip was realized in October 2022, where a majority of sampling and sample preparation tasks were the same as in 2019, allowing me to cover this expertise, in addition to laboratory work and data treatment performed formerly. Both missions were supported by the ANR Microbialites and gathered colleagues from the laboratories Biogéosciences in Dijon, ESE in Paris-Saclay, IMPMC and IPGP in Paris.

The sampling seasons allowed to study the four lakes in their stratification period (Fig. 2 in Havas *et al.*, 2023a). Water columns were first characterized with a muti-parameter probe YSI Exo 2 (temperature, pH, ORP, conductivity, O_2, chlorophyll. a., phycocyanin, turbidity). Vertical profiles of these physico-chemical parameters were used notably to pinpoint the depths of special interest for more advanced laboratory analyses (that is, physico-chemical gradients and peculiarities like redox transitions, turbidity and chlorophyll a peaks). Water samples were collected at the chosen depths with a Niskin bottle preserving *in situ* conditions like oxygen levels (Fig. 3.1a). Indeed, this system allows the water to flow through the bottle and equilibrate before activation of the closing valves.

Total initial volumes of water collected at each depth (5 or 10 L) were divided into separate aliquots for the respective microbial, mineralogical and geochemical analyses in order to obtain this set of data from the exact same samples. These aliquots were then pre-treated directly on the field following procedures specific to each method.

For geochemical analyses, between 1.5 and 5 L of water were filtered with pre-combusted and weighted quartz fiber filters (Whatman GF/F, 0.7 µm) – and pre-rinsed with lake water – in order to collect particulate matter for particulate organic carbon and nitrogen (POC, PON), major and trace elements analysis (Fig. 3.1b, c). This processed water was then filtered at 0.22 µm with Filtropur S filters (also pre-rinsed with 0.7µm-lake water) and stored in exetenair tubes filled to overflowing for analysis of dissolved species.

In 2022, I also collected water samples from artesian wells surrounding Alchichica, Atexcac and La Preciosa lakes. About 500 mL of water were sampled in a plastic bottle directly

from pumping system pipes, made accessible by local inhabitants and farmers. All samples were filtered at 0.22 µm and pre-treated right after collection for DIC, DOC, sulfate, major and trace elements chemistry. For DOC, water aliquots were inoculated with 2N HCl (~0.5 mL per 20 mL of solution) and stored in borosilicate tubes covered with aluminum foil; for major/trace elements, they were inoculated with of a few drops of 15N HNO_3 and stored in Falcon® tubes; DIC and sulfate aliquots were stored in hermetic exetenair tubes and borosilicate tubes, respectively.

Sediment cores were collected using a 90mm Uwitec corer (Fig. 3.1d, e) at the bottom of each lake's center (Table 1 in Havas *et al.*, 2023a), where anoxic conditions prevail almost all year long. Cores measured 20, 41, 59.5 and 85.5 cm in length for lake La Preciosa, Atexcac, Alberca de los Espinos and Alchichica, respectively. Lake La Preciosa sediment core was collected in May 2016; Lake Alberca was not visited in 2022. The sediment cores from 2019 were cut into slices of 1 to 3 cm thickness mostly and were put into plastic bags or Falcon® tubes. Most of the porewater was drained out from the sediments using Rhizon samplers connected *via* tubing to syringes (filtration to 0.2 µm), connected to sediments stacked into the 50 mL Falcon® tubes (Fig. 3.1g). This whole 'core procedure' as well as pH measurement were performed under anoxia in a N_2 filled glove-bag, with oxygen levels monitored with an Oxi 340i WTW oxygen meter and were always below the detection limit of 0.1 $mg.L^{-1}$ (Fig. 3.1f). Sediments were then transported back to the laboratory within aluminized foils (Protpack, UK) and fully dried in a laboratory anoxic N_2-filled glove box.

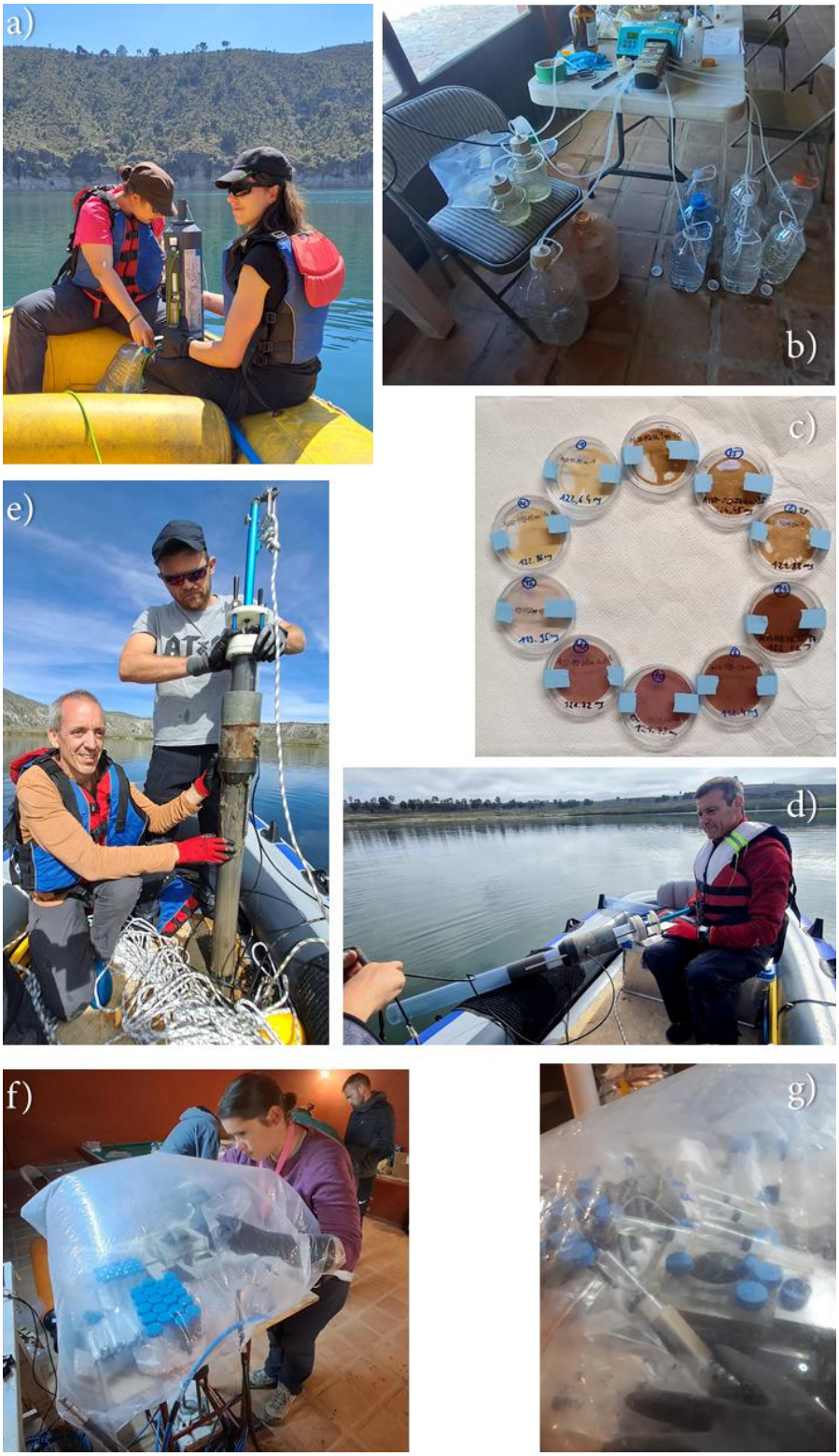

Figure 3.1: pictures of the field sample collection and preparation. a) C. Travert and J. Caumartin transferring water from Atexcac from the Niskin bottle to an intermediate plastic bottle. b) Multiple filtrations at 0.7 µm on quartz fiber filters and (c) resulting filters after clogging or after 5 L of water have been processed. d) D. Jézéquel holding the Uwitec corer before coring in La Preciosa. E) K. Benzerara (left) and C. Lefèvre (right) holding the corer tube containing the core sampled in La Preciosa (~100 cm). f) C. Travert proceeding to cutting and storing of a sediment core inside of the N2-filled glove bag. G) Zoom-in the globe bag at the moment of porewater sampling with syringes connected to the sediments *via* rhizons.

Microbialites were sampled both above the lake water surface as “subfossil” microbialites (on the lakes shores and crater rims) and below the lake water surface as “living” microbialites (Fig. 3.2). The latter were collected by professional divers at 5, 10, 20 (*2) and 40 m depths in Alchichica and at 5, 10, 15 (*2) and 20 m depths in Atexcac.

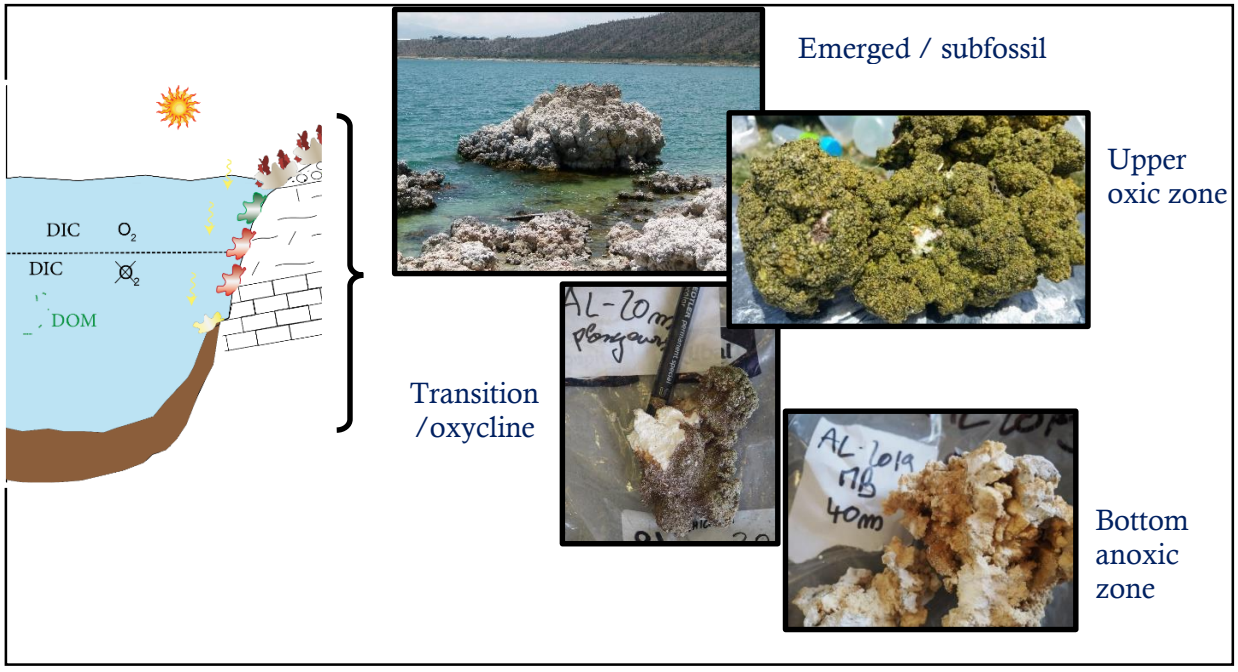

Figure 3.2: Example of the repartition of sampling in Alchichica with microbialites from above and below the water column

3.3. Analytical Methods

3.3.1. Mass-spectrometry and calibration of samples isotopic compositions to international references

The measurement of isotopic abundances is achieved with instruments called mass spectrometers[1]. They enable the separation and collection of elements and their isotopes according to differences of mass-to-charge ratio (m/z) of ionized samples. Thus, all mass spectrometers are built on three main components: the ion source, the analyzer, and the collectors which allow, broadly and respectively, to (i) ionize the sample, (ii) accelerate and separate the ions based on their *m/z* ratio and (iii) count the ions and amplify the generated electric signal. A fourth component can also be considered – as it is bound to the "mass-spec" itself in most cases – and consists of a sample preparation system.

Because of differences in the historical and analytical technique approaches, the "traditional" (H, C, N, O and S) and "non-traditional" (Li, Mg, Cl, Ca, Fe, among many others) isotopes are usually considered separately. This is in big part because technical difficulties restrained the determination of non-traditional isotopes until the 90s (Teng *et al.*, 2017) while analysis of traditional ones has existed and evolved since the first half of the 19th century (Sharp, 2017 and references therein). An important aspect of this difference is that traditional isotopes are measured through gas-source spectrometry while the others are mainly processed as solid or liquid particles, notably through thermal ionization mass spectrometry (TIMS) and multi-collector inductively coupled plasma-MS (MC-ICP-MS) (Johnson *et al.*, 2018). Accordingly, measurement of "traditional" isotopic systems in the frame of this PhD (C, O, N, S) were carried on by techniques referred to as isotope ratio mass spectrometry (IRMS).

The IRMS techniques compare the signal intensity obtained from repeated and alternated analyses of sample and standard materials (with a known composition relative to an international scale). Following the same preparation and analysis procedures for both allows to cancel out possible isotopic fractionations occurring during the measurements and the chemical pre-treatment. The analyzed substances are gases (*e.g.* CO_2 for $\delta^{13}C_{carb,\ org}$ and $\delta^{18}O_{carb}$, SO_2 or

[1] Here I do not include and discuss *spectroscopic* techniques which arose only recently in the last ~10 years, as opposed to more common *spectrometric* methods used since the late 40s.

SF_6 for $\delta^{34}S_{pyrite}$, *etc.*) transformed and purified from the initial solid or liquid material by the sample preparation system (Table 1.1). This first step is specific to each technique and is further described in the respective method subsections below.

The international scaling can be achieved based on a single standard or from several distinct ones forming a calibration curve (of 'true' *vs*. measured δ values). In that latter case, the linear regression equation for standards allows to associate each sample value to its "true" value. In the former case, determining the isotopic deviation of the standard (STD) relative to the working gas (WG) enables to correct back the sample's composition relative to the international scale (INT) such that:

$$\delta_{SAMPLE/INT} = \left[\left(\frac{\delta_{SAMPLE/WG}+1000}{\delta_{STD/WG}+1000}\right) * \left(\frac{\delta_{STD/INT}}{1000}+1000\right) - 1\right] * 1000 \qquad (11)$$

The choice of calibration method is specified below for each analytical technique.

3.3.2. Characterization of the water columns

3.3.2.1. Physico-chemical parameters of the water-columns

The depth profiles of several physico-chemical parameters were measured in the water columns of the four lakes using an YSI Exo 2 multi-parameter probe: temperature, pH, ORP (oxidation reduction potential), conductivity, O_2, chlorophyll a, phycocyanin, and turbidity. Precisions for these measurements were 0.01 °C, 0.1 pH unit, 20 mV, 0.001 $mS.cm^{-1}$, 0.1 $mg.L^{-1}$, 0.01 $\mu g.L^{-1}$, 0.01 $\mu g.L^{-1}$ and 2% FTU unit, respectively. The ORP signal was not calibrated before each profile and is thus used to discuss relative variations over a depth profile. Measurements of the aforementioned parameters allowed to pinpoint depths of interest for further chemical and isotopic analyses, notably around the redoxcline of the lakes.

3.3.2.2. Geochemical analyses of water samples

3.3.2.2.1. *Dissolved inorganic carbon (DIC) concentrations and isotopic compositions*

The DIC corresponds to the sum of $H_2CO_3/CO_{2(aq)}$, HCO_3^- and CO_3^{2-} species present in solution, whose proportions depend on the solution pH. Concentrations and isotopic

compositions of DIC were analyzed in 65 water samples from the four Mexican lakes in the water columns (n=31) and sediment porewaters (n=34). At the time of sampling, 12 mL of 0.22-µm-filtered solutions were placed in hermetic Exetainer® tubes in order to avoid exchange between DIC and atmospheric CO_2. DIC concentrations and isotopic compositions were then determined at the Institut de Physique du Globe de Paris (IPGP), using an Analytical Precision 2003 GC-IRMS, running under He-continuous flow, and following the protocol described by Assayag *et al.* (2006).

A given volume of water sample is taken out of the Exetainer® tube with a syringe, while the same volume of helium is introduced in order to maintain a stable pressure and atmospheric-CO_2 free conditions within the sample tubes (Fig. 3.3). The collected sample is introduced in another Exetainer® tube that was pre-filled with a few drops of 100% phosphoric acid (H_3PO_4) and pre-flushed with He gas (Fig. 3.3). Under acidic conditions, the DIC quantitatively converts to gaseous and aqueous CO_2, which equilibrates overnight within the He filled head space of the tube.

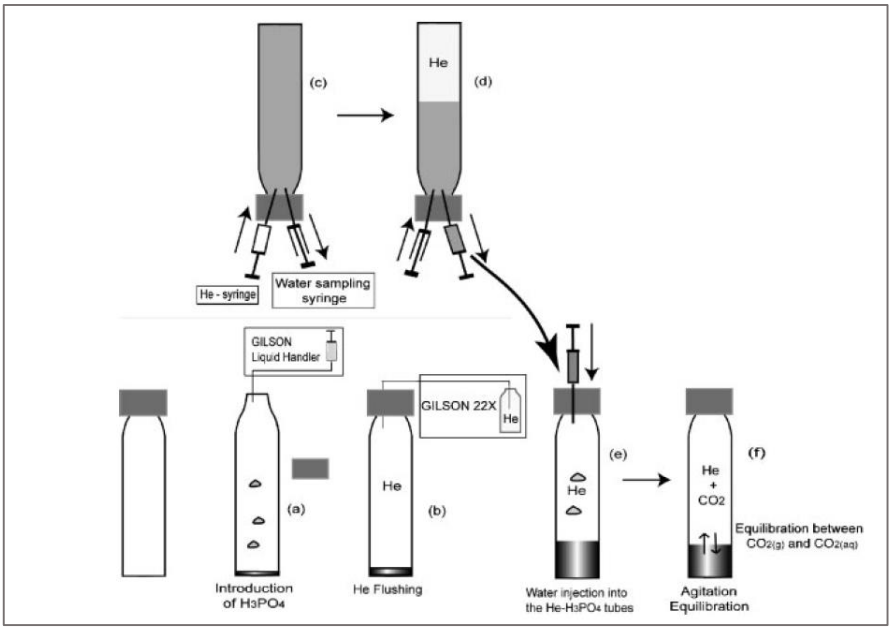

Figure 3.3: Sample preparation procedure for [DIC] and $\delta^{13}C_{DIC}$ measurement from Assayag *et al.* (2006).

Quantification and isotopic analyses of released gaseous CO_2 are then carried out by GC-IRMS. Equal volumes of CO_2+He gas mixture from the sample tubes are extracted and carried by an He flow through a Nafion® semi permeable membrane (to remove water) and a gas chromatography column (to separate CO_2 from other remaining gases). These steps reduce

possible isobaric interferences in the mass spectrometer. The AP2003 system is equipped with fixed collectors at masses 44, 45 and 46 primarily corresponding to molecules $^{12}C^{16}O^{16}O$, $^{13}C^{16}O^{16}O$ et $^{13}C^{16}O^{18}O$. These are the same analyzed molecules as in all CO_2-related techniques used throughout this PhD (*i.e.* for isotopic analysis of DOC, SOC and C/O in carbonates, see below).

Calibration of $\delta^{13}C_{DIC}$ values to the VPDB scale were determined by using a calibration curve based on the analysis of three different solutions of dissolved Ca-carbonate with known isotopic compositions (-9.77, 8.65 and 0.29 ‰ vs. VPDB, respectively). These "in-house" standards were prepared and analyzed throughout the sequences *via* the same protocol than the samples. Each measurement represents an average of four injections in the mass spectrometer. DIC concentrations were calibrated using two series of $NaHCO_3$ solutions – placed at the beginning and end of sequences – spanning a range of concentrations determined by dilutions of a $NaHCO_3$ mother solution. Chemical preparation and IRMS analysis were duplicated for all the samples. The $\delta^{13}C_{DIC}$ reproducibility calculated for the 65 samples was ± 0.2 ‰ on average, including internal and external reproducibility. Standard deviation for [DIC] was ± 0.6 mM on average.

Specific DIC speciation, *i.e.* $CO_{2(aq)}$, HCO_3^- and CO_3^{2-} activities was computed using the software Phreeqc 3 (Parkhurst and Appelo, 2013) and the thermodynamic database 'thermoddem.dat' (Blanc *et al.*, 2012) with the full water chemical compositions of each sample as an input. It should be noted that these results are provided by calculations of theoretical chemical equilibria and do not necessarily take into account local kinetic effects, which, for example, could lead to local exhaustion of $CO_{2(aq)}$ where intense photosynthesis occurs.

3.3.2.2.2. *Dissolved organic carbon (DOC) concentrations and isotopic compositions*

Dissolved organic carbon corresponds to aqueous organic C contained in molecules smaller than the filters pore's size (while organic C within larger molecules represent the particulate organic C). Thus, DOC is an operationally defined fraction within a continuum of organic molecules, here separated from particulate matter by filtration at 0.22 um before storage in glass tubes. Latter in the lab, these were acidified with 1N HCl to a pH of about 1-2 to gas out all the DIC and preserve the DOC only. Concentrations and isotopic compositions of DOC were analyzed in 29 water column samples from the four Mexican lakes.

DOC concentrations were measured with a Vario TOC at the GISMO Platform (Biogéosciences, Dijon, France) calibrated with a range of potassium hydrogen phthalate (Acros®) solutions. This technique is based on combustion of the samples at ~850 °C and conversion of organic carbon to CO_2. This gas is then carried by an N_2 flux and quantified by an infra-red detector. Before isotopic analyses, DOC concentration of the samples was adjusted to match the international standards at 5 ppm (USGS 40 glutamic acid and USGS 62 caffeine). Isotopic compositions were measured at the GISMO Platform (Dijon) using an IsoTOC (running under He-continuous flow) coupled with an IsoPrime stable isotope ratio mass spectrometer (IRMS; Isoprime, Manchester, UK). Samples were stirred with a magnetic bar and flushed with He before injection of 1 mL sample aliquots (repeated 3 times). DOC is then transformed into gaseous CO_2 by combustion at about 850 °C, quantitatively oxidized by copper oxides and separated from other combustion products in a reduction column and water condensers and finally transferred to the IRMS *via* an open split device. In order to avoid a significant memory effect between consecutive analyses, samples were separated by six aliquots of deionized water and their first aliquot was discarded from the isotopic calculations. Standard USGS 40 was used for isotopic calibration ($\delta^{13}C$ = -26.4 ‰ VPDB) and USGS 62 to verify the calibration ($\delta^{13}C$ = -14.8 ‰ VPDB). Average reproducibility on standard and samples for $\delta^{13}C_{DOC}$ was ± 1 and ± 0.5 ‰ (1SD), respectively. Average reproducibility for the 26 samples [DOC] measurements was ± 0.3 mM.

3.3.2.2.3. *Extraction of dissolved sulfates and H_2S for isotopic analysis*

Dissolved sulfates were precipitated to barium sulfate ($BaSO_4$) that can be analyzed then as SO_2 for classical $\delta^{34}S$ measurements (3.3.3.2.3) and as SO_2F_2 for multiple S and O isotopes (3.3.3.2.5). Here I detail the procedure followed and tested for sulfates extraction.

Barium sulfate is a very insoluble phase (~ $1.03x10^{-10}$ at 25 °C; Templeton, 1960), and can thus be precipitated very easily and quickly by adding a barium chloride salt to a solution containing sulfates. The applied protocol consisted in (i) acidifying from 10 to 30 mL of sample water to a pH of ~2 with 4N HCl (~ 200-300 µL), (ii) mixing it with a 1M $BaCl_2.2H_2O$ solution (set to a pH of 2) in centrifugation glass tubes, (iii) heating and agitating the mixture to react at 75 °C for 1 h and (iv) multiple cycles of centrifugation and rinsing with deionized water. The recovered $BaSO_4$ powder was then dried at 50 °C overnight, softly scratched from the tube and weighed. In order to verify the efficiency of the method and adjust some of the protocol's

parameter, I first applied it to a commercial water with known SO_4^{2-} concentrations (Hépar™, 1.53 $g.L^{-1}$, which is comparable to that of Lake Alchichica: 1.15 $g.L^{-1}$) before treating the samples. Tested parameters were: the reaction time (30 min or 1h), pH (1.5-1.9, 1.9-3.5), quantity of Ba added, the extraction method (filters or centrifugation) and pre-heating of the sample solution at 80 °C for 1 h or not (to see if dissolved organic compounds could inhibit $BaSO_4$ precipitation).

The results of these tests are summarized in Table 3.2 and showed an average yield (mass of precipitated over expected $BaSO_4$) of 93.5 ± 5.3 % (1σ, n=16). Average yield for 1 h reaction was slightly higher but not significantly different than for 30 min reaction (*p* value = 0.56). Average yield for pH below 1.9 was slightly higher but not significantly different than for pH between 1.9 and 3.5 (*p* value = 0.3). Average yield was significantly higher when retrieving the $BaSO_4$ precipitate *via* the filtration method (98.1 ± 4.1 %, n=7) than *via* centrifugation and scratching of the glass tubes (89.9 ± 2.7 %, n=9). This can be easily explained because the scratching method left a visible amount of precipitate sticking to the tube. However, the tests with filtration allowed me to ascertain that the conversion to $BaSO_4$ was virtually complete. Nonetheless, because the filtration method is more laborious and might facilitate SiO_2 contamination (detrimental for potential O isotope analyses) when scratching $BaSO_4$ from the quartz filter, the centrifugation method was chosen.

Dissolved H_2S in the sediment porewaters was initially fixed on the field by addition of zinc acetate. It was then extracted and analyzed *via* the same protocol as pyrite extraction described below.

The method and precision of S isotopes analysis for SO_4 and H_2S samples is presented in section 3.3.3.2.3.

Table 3.2. Results of tests for BaSO4 precipitation protocol. 'Hepou' correspond to a two-fold dilution of 'Hepar' solution.

	pH_{final}	V_{BaCL2}	Ratio Excess Ba	pre-heating at 80 °C	reaction time	extraction method	Yield
		mL			hour		%
Hep 1	1.88	1.6	10	0	1	centri	87.3
Hep 2	2.03	0.2	1.25	0	1	centri	88.6
Hep 3	1.99	1.6	10	0	0.5	centri	86.2
Hep 4	1.93	1.6	10	0	1	centri	90.3
Hep 5	2.02	0.48	3	0	1	centri	91.9
Hep 6	2.01	1.6	10	0	1	filter	97.8
Hep 7	2.03	1.6	10	0	1	centri	95.1
Hep 8		1.6	10	0	1	filter	95.6
Hep 9	1.99	1.6	10	0	0.5	centri	91.1
Hep 10	1.96	1.6	10	0	0.5	filter	69.6
Hep 11	3.51	1.6	10	0	1	centri	89.7
Hep 12	1.98	1.6	10	0	0.5	filter	98
Hep 13	1.53	1.6	10	0	1	filter	103.6
Hepou 1	1.84	1.6	10	1	1	centri	88.7
Hepou 2	1.85	1.6	10	0	1	filter	101.2
Hepou 3	1.81	1.6	10	1	1	filter	90.8
Hepou 4	1.83	1.6	10	0	1	filter	99.6

3.3.2.2.4. *Analyses of dissolved major and trace elements and cations/anions concentrations*

Dissolved elemental compositions were measured on acidified lake waters (2% HNO_3) at the Pôle Spectrométrie Océan (Plouzané, France) by inductively coupled plasma atomic-mass spectroscopy (ICP-AES, Horiba Jobin) by Céline Liorzou for major elements and by high resolution-ICP-mass spectrometry using an Element XR (HR-ICP-MS, Thermo Fisher Scientific) by Bleuenn Guéguen for trace elements. Major elements measurements reproducibility based on internal multi-elemental solution was better than 5%. Trace elements were analyzed by a standard-sample bracketing method and calibrated with a multi-elemental solution. Analytical precision for trace elements was generally better than 5%.

Dissolved sulfate (SO_4^{2-}) and chloride (Cl^-) concentrations were determined by ion-chromatography with conductivity detection (ICS-1100, Thermo Scientific Dionex) at the Institut de Physique du Globe de Paris (IPGP, France) by Laure Cordier. They were calibrated using a range of standard sulfate-chloride-fluoride solutions with concentrations overlapping those of the Mexican lakes. Nitrite (NO_2^-) and nitrate (NO_3^-) concentrations were determined

by ion-chromatography with UV detection, also at IPGP. Using this method, NO_2^- and NO_3^- peaks were overlapping with too high Cl^- peaks in Alchichica and Atexcac's waters and thus only gave reliable results for lakes La Preciosa and Alberca. Dissolved phosphate (PO_4^{3-}) and ammonium (NH_4^+) concentrations were determined by colorimetric analysis by Emmanuelle Raimbault at the IPGP. Analytical precision for cations and anions was generally better than 5%.

3.3.2.3. Geochemical analyses of particulate matter

Particulate matter was collected on pre-combusted (2 h at 490 °C) and weighted glass fiber filters (Whatman GF/F, 0.7 µm). Between 1.5 and 5 L of lake water were filtered before the GF/F filters got clogged. Filters were weighed again after drying at about 50 °C in order to determine the particulate matter concentrations using gravimetric mass balance.

3.3.2.3.1. *Particulate organic carbon and nitrogen (POC / PON)*

The loaded GF/F filters were ground in a ball mill before and after decarbonation. Decarbonation was performed with 12N HCl vapors in a desiccator for 48 h. Aliquots of dry decarbonated samples (25-70 mg) were weighed in tin capsules. POC and PON contents and their $\delta^{13}C$ and $\delta^{15}N$ were determined at the GISMO Platform (Biogéosciences, Dijon) using a Vario MICRO cube elemental analyzer (Elementar, Hanau, Germany) coupled in continuous flow mode with an IsoPrime IRMS (Isoprime, Manchester, UK). The Vario MICRO cube first combust the organic C and N compounds into CO_2 and NO_x gases at 950 °C. All the gases are then reduced in a furnace filled with copper and separated from each other by a temperature programmed desorption system. USGS 40 certified material ($\delta^{13}C$ = -26.24 ‰ VPDB and $\delta^{15}N$ = -4.52 ‰ AIR) was used for calibration and showed a reproducibility better than 0.15 ‰ for $\delta^{13}C$ and 0.4 ‰ for $\delta^{15}N$. Certified material IAEA 600 and internal standards were used to verify the calibration ($\delta^{13}C$ = -27.77 ‰ VPDB and $\delta^{15}N$ = +1 ‰ AIR). External reproducibility based on replicate analyses of samples (n=23; mostly analyzed 3 or 4 times) was 0.1 ‰ on average for $\delta^{13}C_{POC}$ and 0.5 ‰ for $\delta^{15}C_{PON}$ (1SD). External reproducibilities of POC and PON concentrations were on average 0.001 and 0.005 mM, respectively (*i.e.* 3 and 7 % of measured concentrations).

3.3.2.3.2. *Major and trace elements chemistry*

Glass fiber filters were drowned in a 1M HNO_3 solution to bleach the filters over a few days to dissolve particulate matter. The sample solution was then diluted with deionized water to a 2%-HNO_3 concentration (*i.e.* 0.3 M). Finally, elemental concentrations were determined by the same techniques and in the same place as dissolved elemental concentrations (see above).

3.3.2.4. Gas collection and analysis

Gas being emitted from the water columns of lakes Alchichica, Atexcac, and La Preciosa were collected in the 2022 field work. A floating chamber was placed at the water surface for 2 days in order to accumulate gases, after which the chamber was sampled by connecting a pre-vacuumed and hermetic stainless-steel tube (Fig. 3.4). The gas samples were delivered to the IFPEN laboratory (Rueil-Malmaison, France) where they are currently being analyzed for noble gases and CO_2 isotopic signatures.

Figure 3.4: pictures of the gas collection set-up on the field. a) pumping of the plastic tube part on the right side, before sampling. The stainless steel tube on the left part was pre-vacuumed in the laboratory in France. b) placement of the gas accumulation chamber on La Preciosa's surface with R. Tavera. c) collection of the gases after two days of accumulation by replacing the plugs on the lid and connecting the tubing system to the chamber instead.

3.3.3. Characterization of the sediments and microbialites

Microbialites were first ground by a mechanical grinder in an agate bowl (up to several hundred grams were ground). Each bowl was then poured into an agate mortar to ensure the thinness and homogeneity of the obtained powder and only then was placed into a plastic bag or tube for storing. Bottom sediments were directly ground in the agate mortar. When present and before complete grinding of the sediment, macroscopic remains of plants were picked up with a stainless-steel clamp for ^{14}C-dating. After the grinding step, both types of samples (microbialites and core sediments) were processed through the same preparation and analytical procedures (unless specified).

3.3.3.1. Mineralogical and physical characterization

3.3.3.1.1. *Mineralogy*

Mineralogical assemblages of bulk powders were determined by X-Ray diffraction (XRD) at the Laboratoire Biogéosciences (Dijon). Samples were ground in an agate mortar. Diffractograms were obtained with a Bruker D8 Endeavor diffractometer with CuKα radiation and LynxEye XE-T detector, under 40 kV and 25 mA intensity. Minerals identification were based on COD ("Crystallography Open Database") and BGMN databases. Estimation of their abundances was achieved using a Rietveld refinement analysis implemented in the Profex software (Döbelin and Kleeberg, 2015).

3.3.3.1.2. *Optical microscopy*

The lithology and sedimentary facies of the microbialites were examined by optical microscopy on a Nikon AZ100 microscope, on thin sections prepared by "Lithologie Bourgogne" (Dijon, France). The thin sections were observed under plane-polarized light and cross-polarized light coupled with a Tucsen TrueChrome 4K Pro camera (GISMO platform, Dijon). Additionally, UV-epifluorescence microscopy was carried out on the Nikon AZ100. Moreover, elemental mapping was carried out on entire thin sections and more specific zones using a micro X-Ray Fluorescence 2D scanner (Bruker M4 Tornado) composed of two SD

detectors and a Cr X-ray tube anode with polycapillary lens offering a 25 µm spot size (GISMO platform, Dijon).

3.3.3.1.3. *Density analyses*

The density of the bottom lake bulk dry sediments was determined on a selection of samples by a He gas pycnometer (AccuPyc II 1340, Micromeritics®) in the Institut Interdisciplinaire Carnot Bourgogne laboratory (Dijon, France) run by Thomas Tricone and Raminfar Al Rafrafin. A 1 cm^3 chamber filled with weighed sediments, was progressively purged with He gas at ~23 °C over 100 cycles in ~3 hours. At each cycle, the expansion of the gas in a second reference chamber makes it possible to measure the volume of the sample with help of the ideal gas law. The sample weight and the measured volume of sample are then used to automatically calculate the sediment's density. The standard deviation was usually equal or lower than 0.01 $g.cm^{-3}$.

3.3.3.1.4. *Color characterization*

A precise determination of color shades of the sediments from the three 2019 cores was achieved with the help of Jérôme Thomas. A few grams of dried and finely ground powder were put in tubes lid, forming a flat and regular surface (Fig. 3.5). They were then photographed with a Nikon D750 camera (AF-S VR Micro-Nikkor 105mm objective), under homogeneous white light along with a white/black color scale ("TrueColors Scuadra S") (Fig. 3.5). All pictures (n=56) were then treated on photoshop after black and white calibration. Red, green and blue endmembers of the average sediment color were then determined with the "eyedropper" tool of photoshop, and normalized by the sum of the three components to estimate the degree of whiteness of each sample.

Figure 3.5: Photographs of the sediment preparation for sediment color characterization before (left) and after (right) correction with the black and white color scale. On the right, the disk in the middle of the lid represents the sediment average color with RVB values on the right.

3.3.3.1.5. *Dating methods for the sediments*

Dating of samples from the sediment cores of lakes Alchichica, Atexcac and Alberca de los Espinos from the 2019 field campaign were achieved in order to determine sediment accumulation rates and to evaluate elemental depositional fluxes in these lakes. Furthermore, one DIC sample from Alchichica (at 36 m depth) and two microbialite carbonate samples from Alchichica (at 40 m depth in the lake) and Atexcac (at 20 m depth in the lake) were dated in order to constrain the sources and residence time of C as well as to estimate the microbialites "growing rates".

The DIC and microbialite carbonate dating were achieved *via* the ^{14}C-radiocarbon method. In the sediments, some remains of living organisms (plant debris or shells) could be found throughout the cores of lakes Atexcac and Alberca and thus be dated through the ^{14}C-method. All the radiocarbon dating (n_{total}=10) were performed in Beta Analytic® laboratories by accelerator mass spectrometry (AMS), which counts the number of ^{14}C-atoms per sample. Carbon is converted into CO_2 (by combustion for plant debris, and acidification for DIC samples) and further into graphite in a reducing H_2-atmosphere and in the presence of cobalt as a metal catalyst. Graphite ^{14}C is then ionized, highly accelerated and separated from other C atoms by a magnetic field in a several-step process before detection. Modern oxalic acid standards were analyzed in parallel to calibrate the ^{14}C count and resulting age. The results are given as an average age with an uncertainty of +/- 30 years. However, they are first reported as probability density functions, which are especially relevant to interpret the results since some of the dated material can correspond to multiple and distinct plant debris within a single sediment layer.

No macroscopic remains were found in the sediments of Lake Alchichica. Hence, and in order to have a higher resolution age model for the Lake Alchichica upper sediments, they were dated *via* a lead 210 (^{210}Pb) and cesium 137 (^{137}Cs) method. In more detail, sub-samples of Alchichica's sediments were analyzed for ^{210}Pb, ^{226}Ra and ^{137}Cs by direct gamma assay in the Liverpool University Environmental Radioactivity Laboratory, using Ortec HPGe GWL series well-type coaxial low background intrinsic germanium detectors (Appleby *et al.*, 1986). ^{210}Pb was determined *via* its gamma emissions at 46.5 keV, and ^{226}Ra by the 295 keV and 352 keV

γ-rays emitted by its daughter radionuclide ^{214}Pb following 3 weeks' storage in sealed containers to allow radioactive equilibration. ^{137}Cs was measured by its emissions at 662 keV. The absolute efficiencies of the detectors were determined using calibrated sources and sediment samples of known activity. Corrections were made for the effect of self-absorption of low energy γ-rays within the sample (Appleby *et al.*, 1992). For comparison, one bulk OC sample of Lake Alchichica's sediments was dated by the ^{14}C-method at the bottom of the core (it resulted in a much older age due to the DIC residence time in the lake).

3.3.3.2. Geochemical analyses of rock samples

3.3.3.2.1. *Carbonates analysis*

Sediments and microbialites total carbonate contents were initially determined by weighing samples before and after decarbonation with 1N HCl. Carbonates carbon and oxygen isotopic compositions ($\delta^{13}C_{carb}$, $\delta^{18}O_{carb}$) were carried out on bulk and micro-drilled powdered sediments at the GISMO platform (Dijon). Samples aliquots (70-140 µg) were loaded in glass vials and analyzed through a Kiel IV carbonate preparation device coupled in continuous flow mode to a ThermoScientific Delta V Plus IRMS. The preparation device transforms the carbonates into CO_2 by acidification with a few drops of H_3PO_4 at controlled temperature (~70 °C), purify the CO_2 with an adjustable temperature liquid nitrogen trap and concentrate it in a micro-volume before sending it to the mass-spectrometer.

Both $\delta^{13}C$ and $\delta^{18}O$ are reported relative to the international standard VPDB scale, unless specified for O. NBS-19 certified material was used for calibration ($\delta^{13}C$ = +1.95 ‰ VPDB, $\delta^{18}O$ = +2.20 ‰ VPDB) and had reproducibility better than 0.10 and 0.15 ‰ for $\delta^{13}C$ and $\delta^{18}O$, respectively. Out of the 102 samples measured for C and O isotopes of bulk carbonates, 93 were at least duplicated and showed average external reproducibility of ± 0.2 and ± 0.3 ‰, respectively.

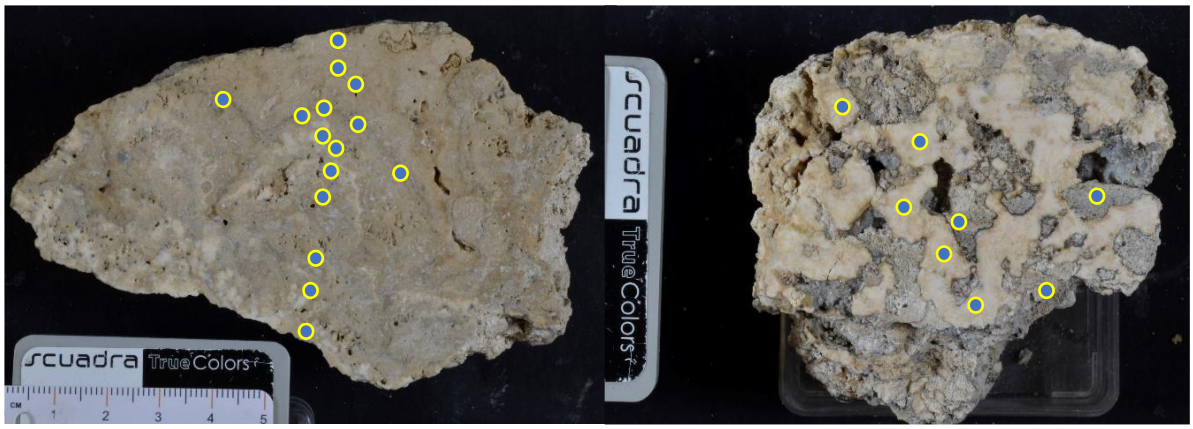

Figure 3.6: Examples of microbialites from Mexico (ATX-C21 on the left, PR-2 on the right) and spots where they were sampled with the microdrill. Spots are bigger than actual drilled holes.

Micro-drilling was performed on microbialites "macro-samples" (*i.e.* not ground) and allowed to pinpoint areas of microbialites flat surfaces (from saw cutting) that were first photographed and carefully examined. It allowed to identify and aim at different phases within the microbialites based on color and mineralogical differences (Fig. 3.6). The diameter of sampling was about 1 mm wide, allowing to obtain a few hundred micro-grams (of mostly carbonate material) which were then analyzed through the aforementioned protocol. Preparation work on microbialite carbonates was carried out or assisted by an intern under my direction, Hugo Bert from the ENS Lyon in his first year of Master's degree, and the analyses were then monitored by Théophile Cocquerez and Ivan Jovovic.

3.3.3.2.2. *Organic matter analyses*

Organic carbon and nitrogen (OC and ON) and their isotopic compositions were measured on carbonate-free residues of the sediment cores and microbialites produced after acid digestion. Protocols with 1N HCl digestion overnight and with 2N and 6N HCl digestion for 1 h were initially tested. All three methods allowed for a full dissolution of the carbonates (verified using XRD analyses after chemical treatment) and did not result in significantly different $\delta^{13}C$ and $\delta^{15}N$ results (Table 3.3). However, one can see a decrease in of the OC and ON contents in the microbialite samples (which were composed of >95 wt. % carbonates). Therefore, the least aggressive treatment was chosen for the rest of the samples (*i.e.* 1N HCl overnight). Aliquots of dried decarbonated samples (~ 2-70 mg) were weighed in tin capsules.

OC and ON contents and their δ values were determined at the GISMO platform (Dijon) using a Vario MICRO cube elemental analyzer (Elementar GmbH, Hanau, Germany) coupled in continuous flow mode with an IsoPrime IRMS (Isoprime, Manchester, UK). These instruments were run by Anne-Lise Santoni and the microbialite samples preparation were carried out or assisted by Hugo Bert. USGS 40 certified material was used for calibration and had a reproducibility that was mostly below 0.2 ‰ for both $\delta^{13}C_{OC}$ and $\delta^{15}N_{ON}$. Certified material IAEA 600 and internal standards were used to verify the calibration. Analyses from bottom sediments and microbialites samples were at least duplicated (except for 3 samples) and showed average external reproducibility of 0.1 and 0.2 ‰ for $\delta^{13}C$ and $\delta^{15}N$, respectively (1SD, n=123). External reproducibilities for OC and ON contents were 0.1 and 0.02 wt. % on average, respectively.

Plant debris in the sediments (mainly found in Alberca and Atexcac) were picked upon initial grinding were analyzed separately for C and N isotopic compositions (and for ^{14}C-dating).

Table 3.3. Results of the different decarbonation protocol tested. TOC and TON are given as the concentrations in the decarbonated powder and not in the bulk powder in order to avoid weighing biases.

		$\delta^{13}C_{moy}$ (‰, VPDB)			$\delta^{15}N_{moy}$ (‰, air)		
Concentration of HCl acid attack		1N	2N	6N	1N	2N	6N
Sediments	AL19_C2-11	-24.7	-24.7		5.4	5.9	
	Albesp19_C3-S12	-23.3	-23.3		4.3	4.5	
	ATX19_C1_10	-24.1	-24.0		3.6	3.8	
Microbialites	AL-T-9	-25.5	-25.7	-25.8	2.5	2.5	2.2
	PR-1	-24.9	-25.1	-24.8	4.3	4.4	4.5
	ATX-C12'	-26.1	-26.1	-26.1	3.1	2.9	3.4
	ATX-R4	-25.8	-25.7	-26.1	4.1	4.1	4.0
		TOC (wt. %)			TON (wt. %)		
Concentration of HCl acid attack		1N	2N	6N	1N	2N	6N
Sediments	AL19_C2-11	4.6	4.6		0.5	0.5	
	Albesp19_C3-S12	5.1	5.2		0.4	0.3	
	ATX19_C1_10	0.6	0.6		0.1	0.1	
Microbialites	AL-T-9	17.4	15.1	10.9	2.6	2.2	1.5
	PR-1	10.3	7.5	9.8	1.7	1.2	1.6
	ATX-C12'	9.0	7.1	6.2	0.8	0.7	0.6
	ATX-R4	10.4	8.2	7.2	1.1	1.0	0.9

3.3.3.2.3. *Chemical extractions of pyrite and carbonate-associated sulfate (CAS), and $\delta^{34}S$ analyses*

Pyrite extractions

Solid sulfides quantification and preparation for isotopic analyses were achieved in Dijon by Chromium-Reducible Sulfur (CRS) distillation following Gröger *et al.* (2009). In this method, the reduced sulfur compounds are quantitatively recovered by (i) dissolution into S^{2-} by reaction with a reducing Cr(II)-solution, (ii) reaction with H^+ brought by the addition of concentrated HCl and formation of H_2S, (iii) condensation of the H_2S gas carried in the cooling column by a N_2 gas flux and (iv) precipitation of solid Ag_2S in a 0.3 M $AgNO_3$ solution. In more detail, the 1M Cr(II)-solution was prepared on a weekly basis by mixing 266 g of $Cr(III)Cl_3.6H_2O$ with 20 mL of 12N HCl, and H_2O in a total volume of 500 mL; zinc metal chips were added and the solution was put within a reducing N_2-gas flux until the solution turned blue/turquoise. The 0.3M $AgNO_3$ capture solution was prepared by mixing ~51 g of $AgNO_3$ powder in a 1 L of deionized water.

Sample powder (~ 1.5 g for bottom sediments, up to 9 g for microbialites) or porewater (~2 mL) were mixed with 40 mL ethanol and 10 mL of 12 N HCl within a three-necked round bottom flask at room temperature first and under the N_2-flux, to extract potential acid volatile sulfides (AVS) during 2 h. If AVS were present, the capture solution was changed. Then, temperature was raised to ~80 °C and 20 mL of the Cr-solution were added to dissolve the CRS species for 2 h again. At the end of the procedure, Ag_2S precipitates were rinsed several times with deionized water and centrifuged and dried 50 °C for 24 h in an oven and weighted.

In total, 79, 37 and 41 samples from the bottom lake sediments, modern microbialites and Archean were treated for pyrite extraction, respectively, sometimes in duplicates. Modern microbialites were partly processed by a last year undergraduate student, Tom Grelet, under the direction of Christophe Thomazo and myself.

CAS extractions

Extractions of CAS were performed on a dozen modern microbialite samples from Mexico by Céline Liorzou at the Pôle Spectrométrie Océan (Plouzané, France) and following a protocol described by Wotte *et al.* (2012) and Killingsworth *et al.* (2019). Broadly, the soluble sulfate

compounds were first removed by rinsing multiple time with a 5% NaCl solution and rinsed with deionized water (DI). Then, CAS were extracted by dissolving carbonates with 32% HCl. The extractant solution was filtered at 0.45 µm on nitrocellulose filters. The filtered solution was acidified to pH<4 and dissolved sulfates were precipitated as $BaSO_4$ by adding a $BaCl_2.2H_2O$ solution with Ba being in excess of at least 500% relative to the expected $BaSO_4$ yield. The precipitate solution was let to settle overnight. The supernatant was removed by centrifugation and the extracts were rinsed with DI water three times. Finally, the samples were dried at 70 °C overnight.

Analysis of ^{32}S and ^{34}S isotopes

Isotopic analyses of ^{32}S and ^{34}S isotopes (*i.e.* $\delta^{34}S$) on Ag_2S and $BaSO_4$ powders (both from initially dissolved and solid phases) were performed at the Laboratoire Biogéosciences (Dijon) using a Vario PYRO cube (Elementar GmbH) connected online *via* an open split device to an IsoPrime IRMS system (Isoprime, Manchester, UK). Ag_2S and $BaSO_4$ powders were mixed with tungsten trioxide (W_2O_3) as a super-oxidant in 50-50 proportions (~300-300 µg) and combusted into SO_2 molecules in the PYRO cube at > 1100 °C. The SO_2 molecules are purified in a succession of adsorption/reduction columns at variable temperatures and analyzed on masses 64 and 66. International standard S1 was used for calibration of Ag_2S assuming $\delta^{34}S$ values of -0.3 ‰ on the Vienna Canon Diablo Troilite (VCDT) scale. International standards S2 and S3 (+22.7 and -32.3 ‰ VCDT) were always measured in the analysis sequences to verify the precision of measurements. Analytical reproducibility was better than ± 0.6 ‰ based on S1 replicates. For pyrites from bottom lake sediment samples, standard deviation based on duplicate or triplicate analyses (including all wet chemistry preparation) was 0.6 ‰ on average (1σ, n=52). Twelve samples were analyzed only once. Sample replicates impacted by an obvious "memoir effect" were discarded. $\delta^{34}S$ analysis of microbialite samples was not always duplicated due to their low pyrite content and low resulting Ag_2S extracts. They were calibrated to VCDT scale either based on S1 measurements, or from S1, S2 and S3 calibration curve depending on the sequence, and looking for optimal standard reproducibility. Standard deviation for duplicated samples was relatively high (1σ = 2.1 ‰ on average). It is most likely because their sequences of measurement often yielded low signal and were impacted by important memoir effect. Thus, when measured, microbialites $\delta^{34}S_{FeS2}$ from multi-S isotopes

analyses were used (see below). Analysis of Ag_2S from dissolved sulfides (porewater H_2S) were analyzed only once.

$BaSO_4$ powders from dissolved sulfates were calibrated with NBS 127 international standard assuming a $\delta^{34}S$ value of +20.3 ‰ on VCDT scale. Analytical reproducibility based on standard material replicates was ± 0.6 ‰ on average and ± 0.1 ‰ (1σ) for sample duplicates or triplicates (n=30 samples). The $\delta^{34}S$ analyses were monitored by Théophile Cocquerez and Ivan Jovovic.

Analysis of multiple sulfur isotopes

Multiple sulfur isotope analyzes were carried out in the Tokyo Institute of Technology in the frame of a collaborative work with Pr. Yuichiro Ueno and his team from July to September 2022. This project was made possible thanks to the Summer Program scholarship of the Japanese Society for the Promotion of Science (JSPS) partnering the Centre National de la Recherche Scientifique (CNRS).

During this period, a number of 52 samples were analyzed on a MAT 253 IRMS (Thermo Scientific™) after fluorination of Ag_2S powders to SF_6 gas through pyrolysis with CoF_3 (Ueno *et al.*, 2015); 49 samples corresponded to pyrites extracts as Ag_2S from CRS extraction (3.3.3.2.3) of microbialite and sediment powders from modern Mexican lakes and Archean South-African stromatolites; 3 samples initially corresponded to $BaSO_4$ powders from dissolved- (DS) and carbonate-associated-sulfates (CAS) from the Mexican lakes, transformed into Ag_2S through reaction with a "Kiba solution" (that is, a solution of $Sn(II)Cl_3.2H_2O$ and phosphoric acid under a N_2 atmosphere; Kiba *et al.*, 1955). Additionally, 4 samples were analyzed after fluorination of $BaSO_4$ powders to SO_2F_2 gas on a 'Ultra HR-IRMS' (Thermo Scientific™).

3.3.3.2.4. *Fluorination of Ag_2S to SF_6 by pyrolysis with CoF_3 and quadruple sulfur isotope analysis*

The procedure used for fluorination and purification is detailed in Ueno *et al.* (2015) and summarized here. Sulfur from the samples is converted to SF_6 *via* a "solid-solid" reaction between silver sulfide (Ag_2S, ~ 0.2-0.4 mg) and cobalt (III) fluoride (CoF_3, ~ 10-25 mg) occurring at 590 °C for 3 seconds following the simplified equation:

$$Ag_2S + 7CoF_3 = SF_6 + AgF + 7CoF_2 \quad (12)$$

Precise and rapid heating of the powder mixture is achieved by electromagnetic induction of an iron-nickel-cobalt alloy (pyrofoil) which is used to wrap the mixture and loses its ferromagnetic property at the Curie point temperature (*i.e.* 590 °C for the chosen pyrofoil). The pyrolysis reaction also generates several undesired gases including O_2, H_2O, HF and CO_2. In order to remove them, a series of purification steps is applied in a metal vacuumed line (Fig. 3.7). Trap 1 is cooled down at -196 °C by using liquid nitrogen which allows to separate and pump out the incondensable gases (*e.g.* O_2, H_2). Trap 2 was fixed at ~ -110 °C which let SF_6 go through to the injection loop but captured most of unwanted gases (~ 75 % of condensable gases at this temperature, mostly water, on average – estimated with manometer 1 during the purification procedure). Pre-purified SF_6 was then sent through two successive gas chromatography (GC) columns. The first one is a Prorapak-Q of 3 m length while the second one combines a Prorapak-Q of 1 m and a molecular sieve 5A of 2 m length to the collection loop where the purified SF_6 pressure was measured with manometer 2 in a calibrated volume (Fig. 3.7) which allowed to estimate the yield of Ag_2S to SF_6 conversion, after the whole procedure (about 40 ± 18 % on standard and sample material). The relatively low yields mostly result from Ag_2S partial conversion during flash-heating (and sometimes impure starting Ag_2S material). Importantly though, it should induce only negligible isotopic (mass-dependent) fractionation as it is an instantaneous solid–solid reaction. The sample is then concentrated in a micro-volume and before introduction into the mass spectrometer through dual inlet.

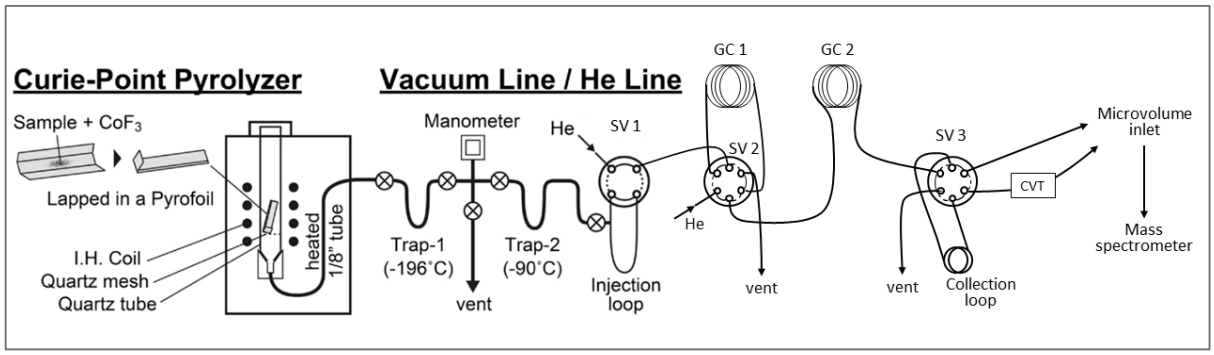

Figure 3.7: Scheme of the SF_6 purification line, modified after Ueno *et al.* (2015). 'GC' stands for gas chromatography; 'SV' for switching valve and 'CVT' for continuously variable transmission and refers to a manometer measuring both high and low pressures.

After ionization in the ion source of the mass-spec, the sample is separated by the magnetic field and collected as SF_5^+ ions. Since F is a monoisotopic element (only one stable isotope, mass ~19 amu), the measured signal of each mass 127, 128, 129 and 131 can be directly related to the signal of each sulfur isotope as $^{32}SF_5^+$, $^{33}SF_5^+$, $^{34}SF_5^+$ and $^{36}SF_5^+$, respectively. The isotopic composition of the samples was determined relative to an internal reference SF_6 gas in dual inlet mode; one measurement consisting of 8 cycles of reference and sample gas analysis, itself being repeated between 3 and 7 times for each sample depending on the amount of available SF_6 (for a total time of ~ 1 h). Reproducibility of the procedure and calibration of the isotopic compositions to the VCDT scale were obtained by repeating multiple analysis of international reference standard material S1. Most of my samples were analyzed during a "first session" of measurement before the first GC column had to be replaced. Over this period, 16 measurements of S1 were carried out with external reproducibilities of 0.25 ‰, 0.007 ‰ and 0.071 ‰ for $\delta^{34}S$, $\Delta^{33}S$' and $\Delta^{36}S$', respectively (2σ, n=16). Seven more samples were analyzed after GC-1 replacement and corrected according to S1 measured the same day (2.3 ‰, 0.001 ‰ and 0.17 ‰, 2σ, n=2). The fluorination procedure can cause small isotopic fractionations (*e.g.* due to differences in diffusion) which generate variability in the $\delta^{34}S_{S1}$ results. However, because all these processes are mass-dependent, they do not affect the reproducibility of $\Delta^{33}S$' and $\Delta^{36}S$'. Therefore, the samples error – calculated as $\sqrt{(\sigma_{samples}^2 + \sigma_{external\text{-}S1}^2)}$ – are dominated by S1 external reproducibility ('$\sigma_{external\text{-}S1}$', *i.e.* mostly ~0.25 ‰, 2σ) for $\delta^{34}S$, and rather by the IRMS internal error for $\Delta^{33}S$' and $\Delta^{36}S$' ('$\sigma_{samples}$', ~0.018 and 0.15 ‰, respectively, 2σ).

3.3.3.2.5. *Fluorination of $BaSO_4$ to SO_2F_2 and quadruple sulfur isotope analysis*

Fluorination of DS and CAS samples from $BaSO_4$ powders to SO_2F_2 gas using elemental fluorine (F_2) was preferred over the previously described method (pyrolysis with CoF_3) because this latter does not allow for the formation of sufficient SF_6 (Ueno *et al.*, 2015). Besides, SO_2F_2 can be used for measurement of sulfate isotopologues[2]. However, due to contaminations of the O signal around the time of my stay in Tokyo-Tech, I focused on measuring quadruple S rather than clumped isotopes.

[2] The term 'isotopologues' refers to different combinations of isotopes within a given type of molecule (*e.g.* see the different isotopologues of sulfate in Figure 6).

Optimally 5 mg (but as little as ~ 0.5 mg) of $BaSO_4$ powder were weighed, placed in a reaction tube, connected to a gas line and vacuumed overnight. In the morning, F_2 generator was heated to optimal temperature of ~ 290 °C to release sufficient amount of F_2 *via* the reaction: $K_3NiF_7 \leftrightarrows K_3NiF_6 + 0.5\ F_2$. Produced fluorine was then transferred to react with $BaSO_4$ for 3 h at 280 °C. The simplified reaction is: $BaSO_4 + 2*F_2 = SO_2F_2 + BaF_2 + O_2$, but generates undesired gases (O_2, CO_2, SiF_4, SF_6 and CF_4) which are removed through a series of cold traps and gas chromatography. Additionally, excess F_2 is pumped out (and trapped with a NaCl salt) after transferring the sample to the "calibrated trap" set at -196 °C with liquid N_2. Nitrogen is replaced by an ethanol slush (mixture of ethanol and liquid N_2) which stabilizes the temperature at ~ -110 °C, allowing the SO_2F_2 to be released and transferred to the "injection loop" frozen to liquid N_2 temperature while gases like water are immobilized at -110 °C and will later be pumped away. Remaining gases are then sent through the GC, and SO_2F_2 is isolated by freezing the "collection loop" and activating a switching valve in the appropriated timing following the arrival of the different gas peaks monitored and displayed by the GC software. Before capturing SO_2F_2 in a vessel tube for analysis, sample pressure is measured in the calibrated volume in order to estimate the conversion yield (usually between 80 and 100 %).

The SO_2F_2 gas was introduced in the bellow *via* the vessel tube for dual inlet analysis on the 'Ultra HR-IRMS' (Thermo Scientific™). One measurement consisted of 10 cycles of reference and sample gas analysis (about 1 hour 45 minutes), and was repeated 12 times or more, except for one sample (8 measurements). However, each measurement line combines the successive analyses of two close but distinct positions (Fig. 3.8). In other words, each line of measurements represents an average of 20 analyses and is repeated more than 12 times. The error for each sample is calculated as the 2σ reproducibility ($\frac{2\sigma}{\sqrt{n}}$) of the number of measurement and varied between: 0.01 and 0.54 ‰ for $\delta^{34}S$, 0.034 and 0.065 ‰ for $\Delta^{33}S$' and 0.114 and 0.604 ‰ (though mostly under 0.2 ‰) for $\Delta^{36}S$'. The highest errors correspond to a sample which was measured a smaller initial SO_2F_2 quantity and during a session when the mass-spectrometer was noticeably less stable than usual. Results for $\Delta^{36}S$' *via* the SO_2F_2 are not reported due to insufficient ^{36}S-characterization of the $BaSO_4$ standards on the international VCDT scale. The cups are (physically) moved and aligned to measure masses 102, 103, 104 and 106 corresponding to isotopologues $^{32}S^{16}O_2F_2^+$, $^{33}S^{16}O_2F_2^+$, $^{34}S^{16}O_2F_2^+$ and $^{36}S^{16}O_2F_2^+$, respectively (Fig. 3.8). Peaks alignment and setting of the measuring positions were adjusted between each measurement or every other measurement.

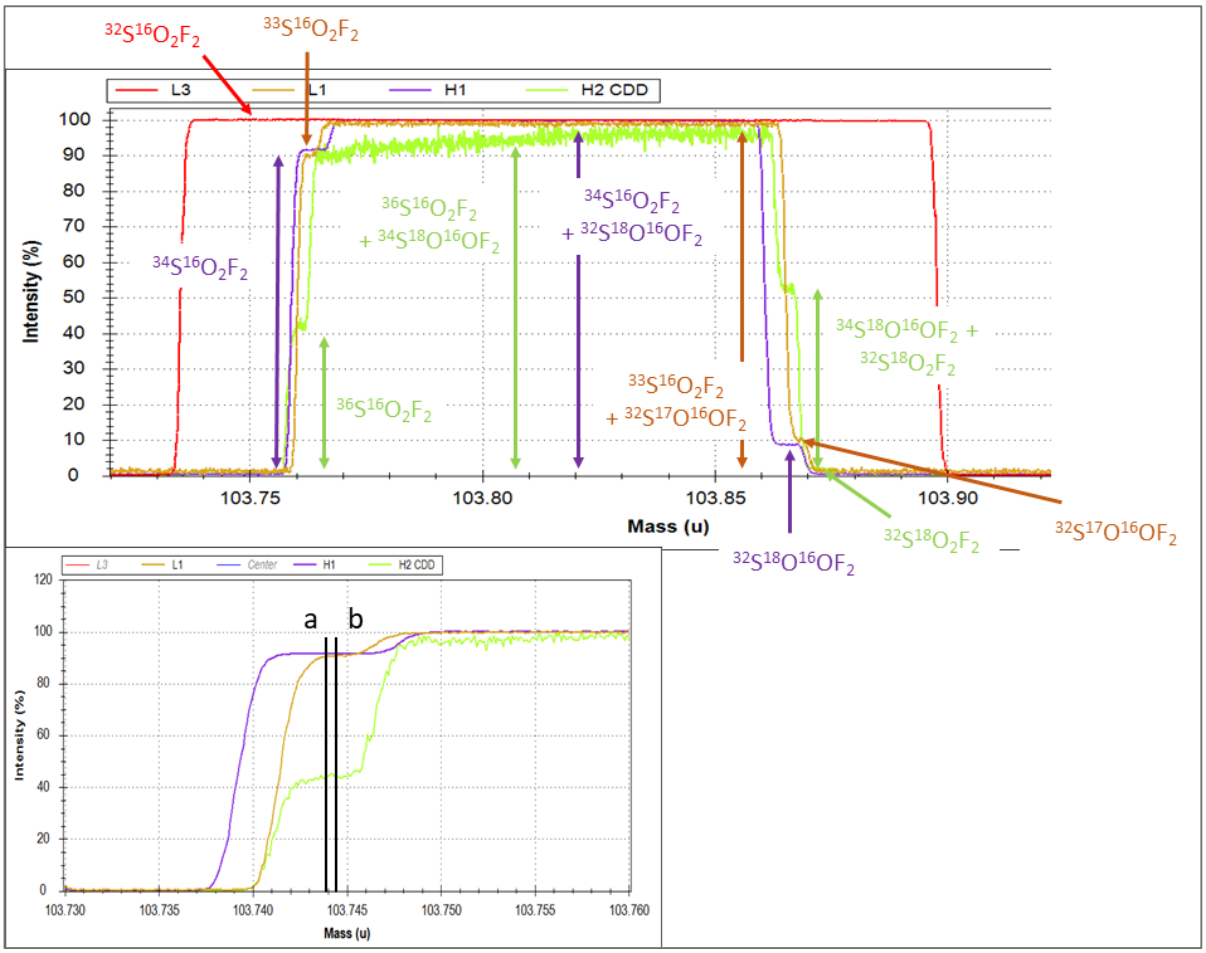

Figure 3.8: Mass-scan on the Ultra-HR-IRMS for analysis of the four S isotopes in SO_2F_2. Top panel: the peak shapes recorded by the four cups are described according to the different SO_2F_2 isotopologue they receive. Bottom panel: zoom on the left peak shoulder where the four S-masses are measured at the same time. Each analysis successively measures the "number of counts" on 'a' and 'b' positions (see text).

Part 1

The carbon cycle of modern stratified water-columns and their sediments

The first part of this dissertation aims at the characterization of the carbon (C) cycle in the four Mexican lakes studied. This includes: the identification and understanding of the biotic and abiotic processes that shape the C reservoirs and their geochemical signatures in the water column (Chapter 4); a time-integrated and quantitative model of the C fluxes in Lake Alchichica (Chapter 5); a description of the diagenetic reactions occurring in the four lake sediments allowing the identification of environmental (biological and climatic) processes that may be altered, or preserved in these sedimentary records (Chapter 6). This work can be used as a basis for future investigations of the biogeochemical processes occurring in these lakes, notably as presented in the second and third part of this manuscript.

Chapter 4 consists of two articles recently published as companion papers in the review "Biogeosciences". They were integrated in their published version below.

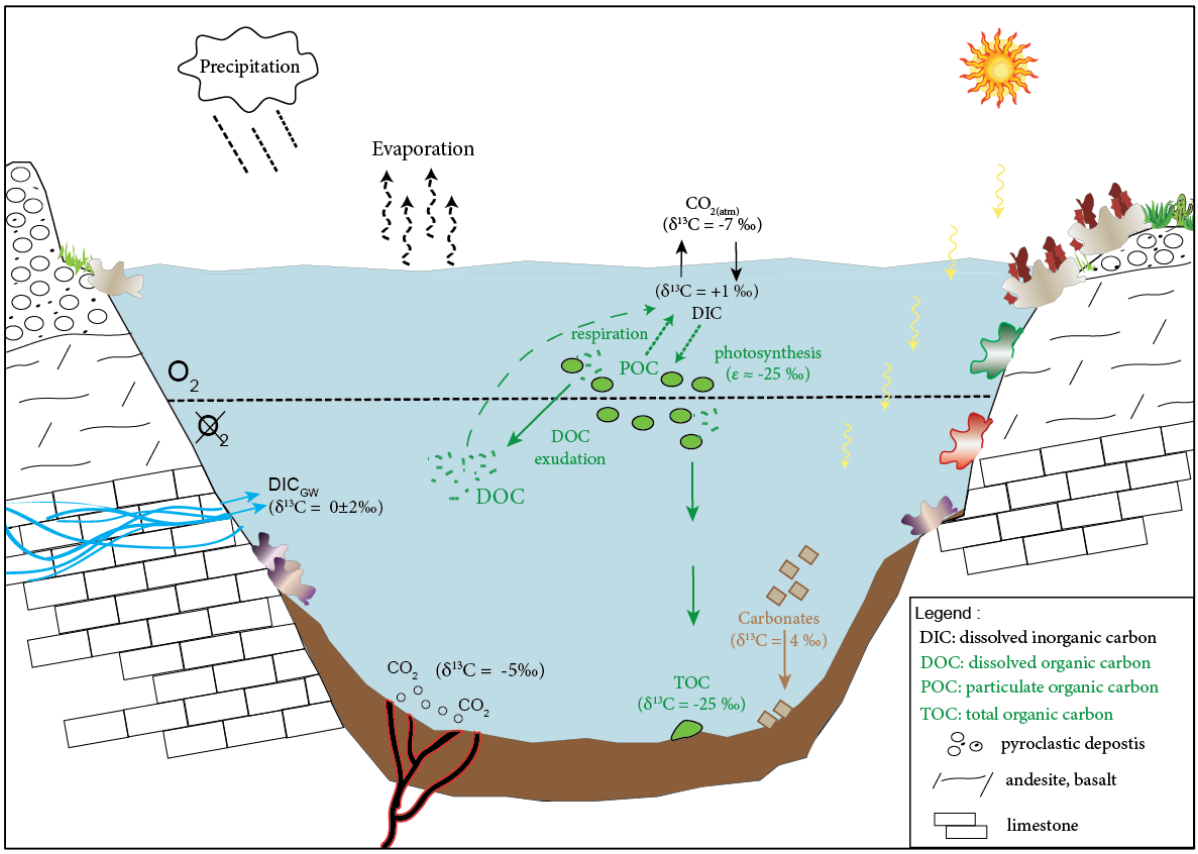

Schematic view of processes affecting the C cycle in a stratified crater lake. Isotopic compositions indicated are approximate.

Biogeosciences, 20, 2347–2367, 2023
https://doi.org/10.5194/bg-20-2347-2023

Biogeosciences Open Access EGU

Biogeochemical processes captured by carbon isotopes in redox-stratified water columns: a comparative study of four modern stratified lakes along an alkalinity gradient

Robin Havas[1], Christophe Thomazo[1,2], Miguel Iniesto[3], Didier Jézéquel[4,5], David Moreira[3], Rosaluz Tavera[6], Jeanne Caumartin[7], Elodie Muller[7], Purificación López-García[3], and Karim Benzerara[7]

[1]Biogéosciences, CNRS, Université Bourgogne Franche-Comté, 21000 Dijon, France
[2]Institut Universitaire de France, 75005 Paris, France
[3]Ecologie Systématique Evolution, CNRS, Université Paris-Saclay, AgroParisTech, 91190 Gif-sur-Yvette, France
[4]IPGP, CNRS, Université de Paris Cité, 75005 Paris, France
[5]UMR CARRTEL, INRAE and USMB, 74200 Thonon-les-Bains, France
[6]Departamento de Ecología y Recursos Naturales, Universidad Nacional Autónoma de México, Mexico City, México
[7]Institut de Minéralogie, de Physique des Matériaux et de Cosmochimie (IMPMC), CNRS, Muséum National d'Histoire Naturelle, Sorbonne Université, 75005 Paris, France

Correspondence: Robin Havas (robin.havas@gmail.com)

Received: 7 July 2022 – Discussion started: 14 July 2022
Revised: 25 April 2023 – Accepted: 4 May 2023 – Published: 21 June 2023

Abstract. Redox-stratified water columns are a prevalent feature of the Earth's history, and ongoing environmental changes tend to promote a resurgence of such settings. Studying modern redox-stratified environments has improved our understanding of biogeochemical processes and element cycling in such water columns. These settings are associated with peculiar carbon biogeochemical cycling, owing to a layered distribution of biological processes in relation to oxidant availability. Metabolisms from distinct biogeochemical layers are diverse and may differently imprint the sedimentological record. Paired carbon isotope compositions of organic matter and carbonates, which are commonly used to characterize these ecological dynamics, can thus vary from one stratified environment to another. Changes in the organic/inorganic carbon sources and mass balance can further complicate the isotopic message in stratified environments. Better understanding of these multifaceted carbon isotope signals requires further evaluation of how the processes occurring in redox-stratified water columns are transferred to the sediments. We therefore characterized and compared the isotopic signatures of dissolved inorganic carbon (DIC), carbonate, and organic matter reservoirs at different depths in the water column and upper sediments of four stratified Mexican lakes that follow a gradient of alkalinity and salinity. Comparing these systems shows strong diversity in the carbon isotope signals of the water column and sediments. Differences in inorganic carbon isotope signatures arise primarily from the size of the DIC reservoir, buffering the expression of redox-dependent biological processes as alkalinity increases. Combining this isotopic dataset with water column physicochemical parameters allows us to identify oxygenic photosynthesis and aerobic respiration in the four lakes studied, while anoxygenic photosynthesis is evidenced in only two of them. Sedimentary organic matter does not originate from the same water column layers in the four lakes, highlighting the ecological variability that can stem from different stratified water columns and how it is transferred or not to the sedimentary record. The least alkaline lake shows higher isotopic variability and signatures typical of methanogenesis in the sediment porewaters. This metabolism, however, does not leave diagnostic isotopic signatures in the sedimentary archives (organic matter and carbonates), underlining the fact that even when alkalinity does not strongly buffer the inorganic carbon reservoir, a comprehensive picture of the active biogeochemical carbon cycling is not necessarily transferred to the geological record.

Published by Copernicus Publications on behalf of the European Geosciences Union.

1 Introduction

The carbon cycle and biogeochemical conditions prevailing at the surface of the Earth are intimately bound through biological (e.g., photosynthesis) and geological processes (e.g., volcanic degassing and silicate weathering). The analysis of carbon isotopes in organic matter and carbonates ($\delta^{13}C_{org}$ and $\delta^{13}C_{carb}$) in the rock record has been used to reconstruct the evolution of the biosphere and the oxygenation of the Earth's surface (e.g., Hayes et al., 1989; Karhu and Holland, 1996; Schidlowski, 2001). Coupling $\delta^{13}C_{org}$-$\delta^{13}C_{carb}$ has frequently been used to infer the burial rate of organic C and thus the redox balance of the atmosphere and hydrosphere (e.g., Karhu and Holland, 1996; Aharon, 2005; Krissansen-Totton et al., 2015; Mason et al., 2017). It has also been used to deduce the presence of metabolisms like anoxygenic chemoautotrophic or methanotrophic bacteria (e.g., Hayes et al., 1999; Bekker et al., 2008; Krissansen-Totton et al., 2015). Coupling $\delta^{13}C_{org}$-$\delta^{13}C_{carb}$ has also been used to discuss ocean stratification and its effect on inorganic and organic C geochemical signatures in sediments (e.g., Logan et al., 1995; Aharon, 2005; Bekker et al., 2008; Ader et al., 2009). Stratification favors the expression and recording of different layers of the water column, with potentially very distinct isotopic signatures. As the oceans were redox stratified during most of the Earth's history (Lyons et al., 2014; Havig et al., 2015; Satkoski et al., 2015), processes affecting the C cycle were likely different from those occurring in most modern, well-oxygenated environments. This change of conditions could impact the $\delta^{13}C_{org}$ signal at various scales, from changes in diversity and relative abundance of microbial carbon and energy metabolism (e.g., Wang et al., 2016; Iñiguez et al., 2020; Hurley et al., 2021) to larger ecological interactions (e.g., Jiao et al., 2010; Close and Henderson, 2020; Klawonn et al., 2021) and global C dynamics (e.g., Ridgwell and Arndt, 2015; Ussiri and Lal, 2017).

Modern stratified lakes have been used as analogues of ancient redox-stratified systems to better understand the C cycle in the sedimentary isotopic record (e.g., Lehmann et al., 2004; Posth et al., 2017; Fulton et al., 2018). Several recent studies have investigated the C cycle in modern stratified water columns (e.g., Crowe et al., 2011; Kuntz et al., 2015; Posth et al., 2017; Schiff et al., 2017; Havig et al., 2018; Cadeau et al., 2020; Saini et al., 2021; Petrash et al., 2022), where many biogeochemical and physicochemical parameters can be directly measured, together with the main C reservoirs. However, investigations of such Precambrian analogues do not necessarily include sediment data and generally focus on a single environment without integrating views from several systems.

In this study, we measured the concentrations and isotopic compositions of dissolved inorganic carbon (DIC) and particulate organic carbon (POC) throughout the water column of four modern redox-stratified alkaline crater lakes, located in the Trans-Mexican Volcanic Belt (Ferrari et al., 2012).We also measured the concentrations and isotopic compositions of the sedimentary organic carbon and carbonates as well as porewater DIC from surficial sediments (~ 10 cm) at the bottom of the lakes. The four lakes share similar geological and climatic contexts but have distinct solution chemistries along a marked alkalinity–salinity gradient (Zeyen et al., 2021) – as well as distinct planktonic communities (Iniesto et al., 2022). We therefore seek to evaluate how these environmental and ecological differences are recorded in the C isotope signatures in the water columns (DIC–POC) and sedimentary archives (organic matter–carbonates). The four lakes are closed lakes in endorheic basins (Alcocer, 2021; Zeyen et al., 2021), which facilitates the identification of external environmental constraints (e.g., evaporation, C sources) and their influence on processes occurring within the water columns. Depth profiles of the main physicochemical parameters together with trace and major element concentrations were measured to pinpoint the dominant biogeochemical processes occurring in the water columns and link them to specific C isotopes signatures.

First, we constrain the main DIC sources and external controls on the lakes' alkalinities. Next, we describe the influence of the inter-lake alkalinity gradient on the inorganic C cycle and stratification of the lakes and how it is recorded in surficial sediments. Then, by combining POC and DIC data, we identify the sources of organic C to the lakes by describing the main autotrophic reactions occurring in the water columns (e.g., oxygenic and anoxygenic photosynthesis). Finally, we discuss the fate of POC, either recycled (e.g., via methanogenesis) or deposited in the sediments, and how all these processes are recorded (or not) in surficial sediments.

2 Setting and context

2.1 Geology

The four lakes studied here are volcanic tuff cones and maars formed after phreatic, magmatic, and phreatomagmatic explosions, related to volcanic activity in the Trans-Mexican Volcanic Belt (TMVB, Fig. 1). The TMVB originates from the subduction of the Rivera and Cocos plates beneath the North American plate, resulting in a long (~ 1000 km) and wide (90–230 km) Neogene volcanic arc spreading across central Mexico (Ferrari et al., 2012). The TMVB harbors a large variety of monogenetic scoria cones and phreatomagmatic vents (maars and tuff cones) as well as stratovolcanoes, calderas, and domes (Carrasco-Núñez et al., 2007; Ferrari et al., 2012; Siebe et al., 2014). Maar crater formation usually occurs when ascending magma meets water-saturated substrates, leading to successive explosions and the excavation of older units (Lorenz, 1986; Carrasco-Núñez et al., 2007; Siebe et al., 2012; Chako Tchamabé et al., 2020).

The first lake, Alberca de los Espinos (1985 m a.s.l.), is located at the margin of the Zacapu tectonic lacustrine basin

in the Michoacán–Guanajuato volcanic field (MGVF) in the central western part of the TMVB (Fig. 1). It lies on andesitic basement rocks and was dated at $\sim 25 \pm 2$ ka (Siebe et al., 2012, 2014). The other three lakes (La Preciosa, Atexcac, and Alchichica) are all in the same area ($\sim 50\,km^2$) of the Serdán-Oriental basin (SOB) in the easternmost part of the TMVB (Fig. 1). The SOB is a closed intra-montane basin at high altitude (~ 2300 m), surrounded by the Los Humeros caldera to the north and the Cofre de Perote–Citlatépetl volcanic range to the east. The basement is composed of folded and faulted Cretaceous limestones and shales, covered by andesitic-to-basaltic lava flows (Carrasco-Núñez et al., 2007; Armienta et al., 2008; Chako Tchamabé et al., 2020). The Alchichica and Atexcac craters was dated at ~ 6–13 ± 5–6 ka (Chako Tchamabé et al., 2020) and 330 ± 80 ka (Carrasco-Núñez et al., 2007), respectively (Table 1). The age of La Preciosa is not known.

2.2 Climate and limnology

Alberca is a freshwater lake (0.6 psu) with a temperate to semi-humid climate (Rendon-Lopez, 2008; Sigala et al., 2017). In contrast, lakes from the SOB experience a similar temperate to semi-arid climate (Armienta et al., 2008; Sigala et al., 2017). The current climate of the SOB is dominated by dry conditions, reflected by higher evaporation than precipitation fluxes in Lake Alchichica (~ 1686 vs. $392\,mm\,yr^{-1}$; Alcocer, 2021). In La Preciosa, Atexcac, and Alchichica, significant evaporation is reflected by a drop in water level, evidenced by the emersion of microbialite deposits (Fig. S1; Zeyen et al., 2021). This evaporation-dominated climate strongly contributes to the relatively high salinity values in these lakes (1.2–7.9 psu), ranging from sub- to hyposaline.

The four lakes are warm monomictic: they are stratified for about 9 months of the year, mixing only when thermal stratification breaks down in the cold of winter (Armienta et al., 2008). They are all closed lakes located in an "endorheic" basin (Alcocer, 2021; Zeyen et al., 2021), meaning that they have no inflow, outflow, or connection to other basins through surficial waters such as streams. The only water input is from precipitation and groundwater inflow (quantified for Lake Alchichica; Alcocer, 2021, and references therein).

The four lakes are alkaline (pH ~ 9) but cover a broad range of chemical compositions (including alkalinity, salinity, and Mg / Ca ratio), interpreted as reflecting different concentration stages of an initial alkaline dilute water (Table 1; Zeyen et al., 2021). Variations in concentration stages may be due to differences in climate and, more generally, different hydrological regimes. Microbialite deposits are found in all four lakes (Gérard et al., 2013; Saghaï et al., 2016; Iniesto et al., 2021a, b; Zeyen et al., 2021) and increase in abundance from lower to higher alkalinity conditions (Zeyen et al., 2021).

3 Method

3.1 Sample collection

The sediment core from Lake La Preciosa was collected in May 2016. All other samples were collected in May 2019. The depth profiles of several physicochemical parameters were measured in the water columns of the four lakes using an YSI EXO2 Multiparameter probe: temperature, pH, ORP (oxidation reduction potential), conductivity, O_2, chlorophyll *a*, phycocyanin, and turbidity. Precisions for these measurements were 0.01 °C, 0.1 pH unit, 20 mV, $0.001\,mS\,cm^{-1}$, $0.1\,mg\,L^{-1}$, $0.01\,\mu g\,L^{-1}$, $0.01\,\mu g\,L^{-1}$ and 2 % FTU (formazine turbidity unit), respectively. The ORP signal was not calibrated before each profile and is thus used to discuss relative variations over a depth profile. Measurements of the aforementioned parameters served to pinpoint depths of interest for further chemical and isotopic analyses, notably around the redoxcline of the lakes. Water samples were collected with a Niskin bottle. Particulate matter was collected on pre-combusted (2 h at 490 °C) and weighted glass fiber filters (Whatman GF/F, 0.7 µm) and analyzed for particulate organic carbon (POC), major elements, and trace elements. Between 1.5 and 5 L of lake water was filtered before the GF/F filters became clogged. The processed solution was filtered again at 0.22 µm with Filtropur S filters (pre-rinsed with lake water filtered at 0.7 µm) for analyses of dissolved inorganic carbon (DIC) and major, minor, and trace ions.

Sediment cores were collected using a 90 mm UWITEC corer close to the deepest point of each lake's water column (Table 1), where anoxic conditions prevail almost all year long. Cores measured between 20 and 85 cm in length. Slices of about 2–3 cm were cut under anoxic conditions, using a glove bag filled with N_2 (anoxia was monitored using a WTW3630 equipped with a FDO O_2 Optode). Interstitial porewater was drained out of the core slices using Rhizons in the glove bag. Sediments were transported back to the laboratory within aluminized foils (Protpack, UK). Sediments were then fully dried in a laboratory anoxic N_2-filled glove box.

3.2 Dissolved inorganic carbon (DIC) concentration and isotope measurements

Of the 0.7 µm filtered lake water, 12 mL was filtered at 0.22 µm directly into hermetic Exetainer® tubes to avoid exchange between DIC and atmospheric CO_2. The DIC concentrations and isotopic compositions were measured at the Institut de Physique du Globe de Paris (IPGP, France), using an Analytical Precision 2003 GC-IRMS (gas chromatography isotope-ratio mass spectrometry), running under He continuous flow, following the protocol described by Assayag et al. (2006). A given volume of the solution was extracted from the Exetainer® tube with a syringe, while the same volume of helium was introduced to maintain stable pressure and

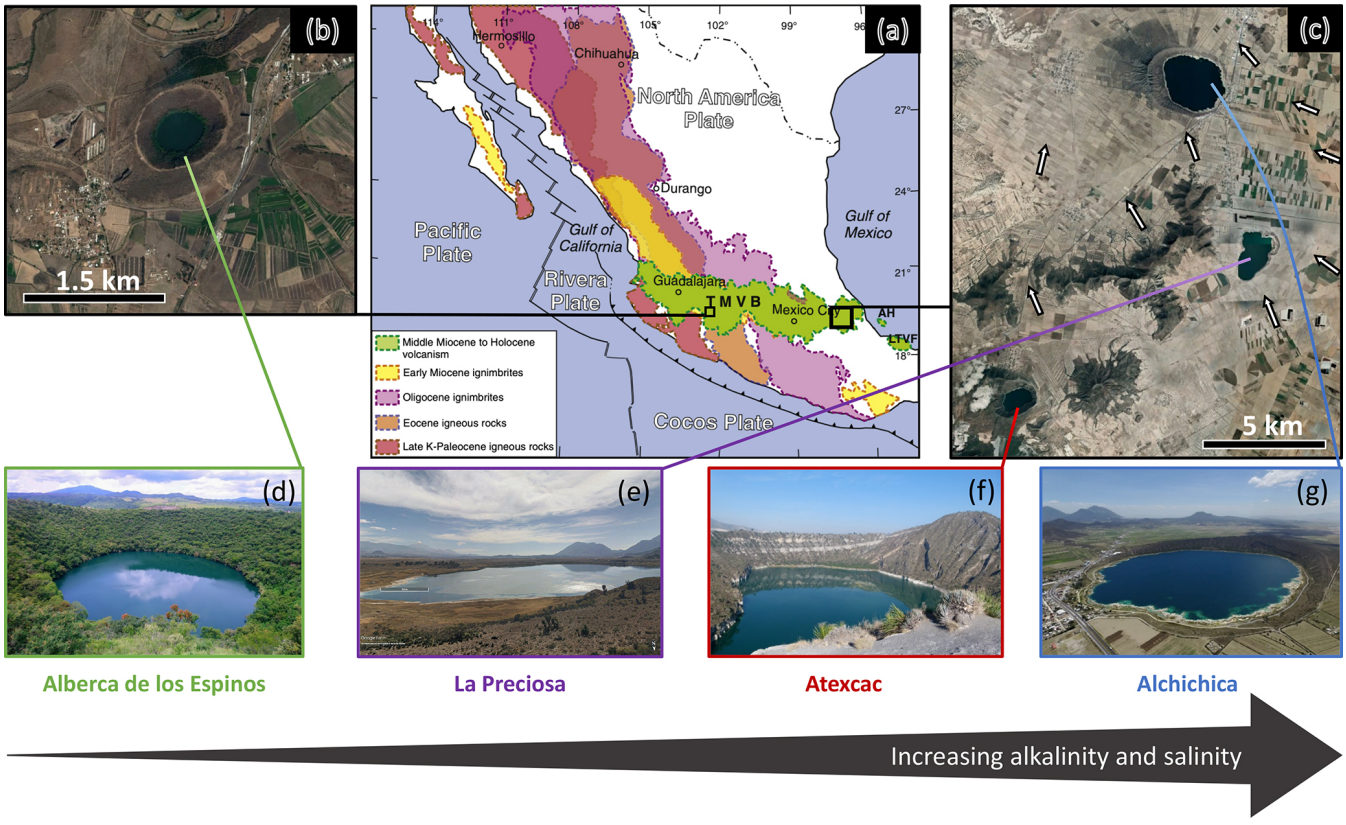

Figure 1. Geographical location and photographs of the four crater lakes. **(a)** Geological map from Ferrari et al. (2012), with black squares showing the location of the four studied lakes within the Trans-Mexican Volcanic Belt (TMVB). **(b, c)** Close up © Google Earth views of Alberca de los Espinos and the Serdán-Oriental basin (SOB). The white arrows represent the approximate groundwater flow path (based on Silva-Aguilera, 2019). **(d–g)** Photographs of the four lakes (panel **d** from © Google Image ["enamoratedemexicowebsite"], panel **e** from © Google Earth street view, and panel **g** from © "Agencia Es Imagen").

atmospheric-CO_2-free conditions within the sample tubes. The collected sample was inserted into another Exetainer® tube, pre-filled with a few drops of 100 % phosphoric acid (H_3PO_4), and pre-flushed with He gas. Under acidic conditions, DIC quantitatively converts to gaseous and aqueous CO_2, which equilibrates overnight within the He-filled head space of the tube. Quantification and isotopic analyses of released gaseous CO_2 were then carried out by GC-IRMS using internal standards of known composition that were prepared and analyzed via the same protocol. Each measurement represented an average of four injections in the mass spectrometer. Chemical preparation and IRMS analysis were duplicated for all the samples. The $\delta^{13}C_{DIC}$ reproducibility calculated for the 65 samples was better than ± 0.2 ‰, including internal and external reproducibility. Standard deviation for [DIC] was 0.6 ± 0.9 mmol L^{-1} on average.

Specific DIC speciation, i.e., $CO_{2(aq)}$, HCO_3^-, and CO_3^{2-} activities, was computed using PHREEQC with the full dissolved chemical composition of each sample as an input. It should be noted that these results are calculated from theoretical chemical equilibria and do not necessarily take into account local kinetic effects, which, for example, could lead to local exhaustion of $CO_{2(aq)}$ where intense photosynthesis occurs.

3.3 Particulate organic carbon and nitrogen (POC, PON)

Particulate organic matter from the lake water columns was collected on GF/F filters, dried at room temperature, and ground in a ball mill before and after decarbonation. Decarbonation was performed with 12N HCl vapors in a desiccator for 48 h. Aliquots of dry decarbonated samples (25–70 mg) were weighed in tin capsules. The POC and PON contents and $\delta^{13}C_{POC}$ were determined at the Laboratoire Biogéosciences (Dijon, France) using a Vario Micro Cube elemental analyzer (Elementar, Hanau, Germany) coupled with an IsoPrime IRMS (Isoprime, Manchester, UK) in continuous flow mode. The USGS40 and IAEA-600 certified materials used for calibration showed reproducibility better than 0.15 ‰ for $\delta^{13}C$. External reproducibility based on triplicate analyses of samples ($n = 23$) was 0.1 ‰ on average for $\delta^{13}C_{POC}$ (1SD). External reproducibility for POC and PON concentrations

Table 1. General information about the lakes studied. Abbreviations: TMVB, Trans-Mexican Volcanic Belt; MGVF, Michoacán–Guanajuato volcanic field; m a.s.l., meters above sea level. *NB*: Sampling took place in May 2019, except for the La Preciosa sediments sampled in May 2016.

Lake	General location	Sampling location	Elevation (m a.s.l.)	Lake basement	Age	Max depth (m)	Alkalinity ($mmol\,L^{-1}$)	Salinity (psu)	pH
Alchichica	Serdán-Oriental basin, eastern TMVB	19°24′51.5″ N; 97°24′09.9″ W	2320	Limestone, basalts	6–13 ± 5–6 ka	62	∼ 35	7.9	9.22
Atexcac	Serdán-Oriental basin, eastern TMVB	19°20′2.2″ N; 97°26′59.3″ W	2360	Limestone, andesites, basalts	8.3–5.1 ± 0.1–0.2 ka	39	∼ 26	7.4	8.85
La Preciosa	Serdán-Oriental basin, eastern TMVB	19°22′18.1″ N; 97°23′14.4″ W	2330	Limestone, basalts	Holocene	46	∼ 13.5	1.15	9.01
Alberca de los Espinos	Zacapu basin, MGVF, central TMVB	19°54′23.9″ N; 101°46′07.8″ W	1985	Andesite	25 ± 2 ka	30	∼ 7	0.6	9.14

was 0.001 and 0.005 $mmol\,L^{-1}$ on average, respectively (i.e., 3 % and 7 % of measured concentrations).

3.4 Geochemical characterizations of the sediments

Sedimentary organic carbon (SOC), sedimentary organic nitrogen (SON), and their isotopic compositions were measured on carbonate-free residues of the first 12 cm of the sediment cores, produced after overnight 1N HCl digestion. Plant debris (mainly found in Alberca and Atexcac) was identified upon initial sediment grinding in an agate mortar and analyzed separately. Aliquots of dried decarbonated samples (∼ 4–70 mg) were weighed in tin capsules. The SOC and SON contents and $\delta^{13}C$ were determined at the Laboratoire Biogéosciences (Dijon) using a Vario Micro Cube elemental analyzer (Elementar GmbH, Hanau, Germany) coupled with an IsoPrime IRMS (Isoprime, Manchester, UK) in continuous flow mode. The USGS40 and IAEA-600 certified materials used for calibration had a reproducibility better than 0.2 ‰ for $\delta^{13}C_{SOC}$. Sample analyses ($n = 67$) were at least duplicated and showed an average external reproducibility of 0.1 ‰ for $\delta^{13}C$ (1SD). External reproducibility for SOC and SON contents was 0.1 wt % and 0.03 wt %, respectively.

Carbon isotope compositions of sedimentary carbonates were analyzed at the Laboratoire Biogéosciences (Dijon) using a Thermo Scientific™ DELTA V Plus™ IRMS coupled with a Kiel IV carbonate device. External reproducibility was assessed by multiple measurements of NBS19 standard and was better than ± 0.1 ‰ (2σ). Total carbonate concentration was determined by mass balance after decarbonatation for SOC analysis.

Mineralogical assemblages of sediments were determined on bulk powders by X-ray diffraction (XRD) at the Laboratoire Biogéosciences (Dijon). Samples were ground in an agate mortar. Diffractograms were obtained with a Bruker D8 ENDEAVOR diffractometer, with CuKα radiation and LYNXEYE XE-T detector, under 40 kV and 25 mA intensity. Mineral identification was based on the COD ("Crystallography Open Database") and BGMN databases. Mineral abundances were estimated by Rietveld refinement analysis implemented in the Profex software.

Solid sulfide concentrations were determined on dry bulk sediments from Lake Alberca after a wet chemical extraction using a boiling acidic Cr(II) solution, as detailed in Gröger et al. (2009).

3.5 Major and trace element concentrations

Dissolved and particulate matter elemental compositions were measured at the Pôle Spectrométrie Océan (Plouzané, France) by inductively coupled plasma–atomic emission spectroscopy (ICP-AES, Horiba Jobin) for major elements and by high-resolution ICP–mass spectrometry using an Element XR (HR-ICP-MS, Thermo Fisher Scientific) for trace elements. Major element measurement reproducibility based

on internal multi-elemental solution was better than 5 %. Trace elements were analyzed by a standard sample bracketing method and calibrated with a multi-elemental solution. Analytical precision for trace elements was generally better than 5 %. Dissolved sulfate concentrations were analyzed by ion chromatography at the IPGP (Paris, France), with uncertainty lower than 5 %.

4 Results

4.1 Lake Alberca de los Espinos

Stratification of the water column was well defined in Alberca de los Espinos (Fig. 2). Temperature was higher than in the other lakes (decreasing from ∼ 23 °C at the surface to 16.5 °C at depth). Dissolved O_2 was oversaturated at the lake surface (118 %, i.e., 7.9 mg L^{-1}), rapidly decreasing to 0 between ∼ 5 and 12 m, while the oxidation reduction potential (ORP) only decreased below 17 m depth. The offset between O_2 exhaustion and ORP decrease can be explained by the presence of other oxidant species and/or extended chlorophyll *a* peaks (Supplement Text S1). Conductivity decreased from 1.20 to 1.17 mS cm^{-1} at 16 m before increasing to 1.27 mS cm^{-1} at 26 m (salinity between 0.58 and 0.64 psu). Chlorophyll *a* (Chl *a*) averaged 3.1 µg L^{-1}, and showed a profile with at least three distinctive peaks, (i) between 6 and 9.5 m, (ii) around 12.5 m, and (iii) between 16 and 19 m, all reaching ∼ 4 µg L^{-1}. The turbidity profile showed a pronounced increase from 16 to 19 m. The pH profile showed important variation from 9.15 at the lake surface to 8.75 between 6.5 and 10 m, further decreasing to 7.5 between 16 and 26 m. Based on the temperature profiles, epilimnion, metalimnion, and hypolimnion layers of Lake Alberca de los Espinos in May 2019 broadly extended from 0–5, 5–12, and 12–30 m, respectively (Fig. 2). The conductivity and pH profiles, however, show that different conditions prevail at the top and bottom of the hypolimnion.

Dissolved inorganic carbon (DIC) concentration progressively increased from 6.8 mM at 5 m to 8.7 mM at 26 m. The pCO_2 calculated for surface waters was near equilibrium with atmospheric $pCO_{2\,atm}$ but strongly increased with depth, up to ∼ 40 times the $pCO_{2\,atm}$ (Table S2). The $\delta^{13}C_{DIC}$ first decreased from about −2.5 ‰ to −4.1 ‰ between 5 and 10 m, before increasing again up to −2 ‰ at 25 m. Particulate organic carbon (POC) concentrations reached minimum values of 0.02 mM at 10 m but rose to maximum values in the hypolimnion (0.06 mM). The C : N molar ratio of particulate organic matter (POM) progressively decreased from 8.5 at the surface to less than 6.5 in the hypolimnion. The $\delta^{13}C_{POC}$ had minimum values at 10 and 17 m (−28.3 ‰ and −29 ‰, respectively). Above and below these depths, $\delta^{13}C_{POC}$ averaged −26.4 ± 0.5 ‰.

Dissolved sulfates as measured by chromatography were only detectable at 5 m, with a low concentration of 12 µM, while total dissolved S measured by ICP-AES showed values in the hypolimnion higher than in the upper layers (∼ 10.3 vs. 7.4 µM, Table S4). Dissolved Mn concentrations decreased from 1.5 to 0.5 µM between 5 and 10 m, then increased to 2 µM at 25 m. Aqueous Fe was only detectable at 25 m, with a concentration of 0.23 µM (Table S4). In parallel, particulate S concentrations increased with depth, with a marked increase from 0.1 to 0.6 µM between 20 and 25 m. Increase in particulate S was correlated with a 25-fold increase in particulate Fe (from 0.2 to 5.97 µM). Particulate Mn showed a peak between 17 and 20 m around 1 µM, contrasting with values lower than 0.15 µM in the rest of the water column (Fig. 2, Table S5).

In the first centimeters of sediments, DIC concentration in the porewater varied between ∼ 11 and 12 mM, and $\delta^{13}C_{DIC}$ varied between +8 ‰ and +10 ‰ (Figs. 3, 4). Surficial sedimentary carbonates corresponded to calcite and had a $\delta^{13}C$ around −1.5 ‰. Sedimentary organic matter had a $\delta^{13}C_{SOC}$ increasing from ∼ −29.4 ‰ to −25.5 ‰ and a C : N molar ratio varying between 11.6 and 14.3 (Figs. 3, 4; Table S3).

4.2 Lake La Preciosa

Lake La Preciosa was also stratified at the time of sample collection (Fig. 2). Temperature decreased from ∼ 20 °C at the surface to 16 °C at 15 m depth. Conductivity showed the same trend with values between 2.24 and 2.22 mS cm^{-1} (salinity around 1.15 psu). Dissolved O_2 was oversaturated at the lake surface (120 %, i.e., 8.4 mg L^{-1}), rapidly decreasing to 0 between ∼ 8 and 14 m, while the ORP decreased right below 16 m. Chl *a* concentration averaged 3 µg L^{-1} and recorded the highest peak compared to the other lakes (about 9 µg L^{-1} at 10 m) before decreasing to 0.7 µg L^{-1} below 15 m. Turbidity showed a large peak between 16 and 19 m. The pH showed a small decrease from 9 to 8.8 between the surface and 15 m depth. Based on the temperature profiles, epilimnion, metalimnion, and hypolimnion layers of La Preciosa in May 2019 broadly extended from 0–6, 6–15, and 15–46 m, respectively (Fig. 2).

The DIC concentration was constant throughout the water column at 13.3 mM, with an exception at 12.5 m, where it decreased to 11.5 mM (Fig. 3, Table S1). Calculated pCO_2 at the surface represented about 2 times the atmospheric $pCO_{2\,atm}$ (Table S2). The $\delta^{13}C_{DIC}$ decreased from about 0.5 ‰ to −0.36 ‰ between the surface and the hypolimnion. The POC concentration decreased from ∼ 0.06 mM in the epilimnion and metalimnion to 0.02 mM in the hypolimnion. Similarly, $(C : N)_{POM}$ decreased from ∼ 11.2 in the epilimnion and metalimnion to 7.6 in the hypolimnion. The $\delta^{13}C_{POC}$ increased downward from ∼ −27 ‰ to −25 ‰, with a peak of −23.5 ‰ at 15 m.

In the first 10 cm of sediments, $\delta^{13}C_{SOC}$ values increased downwards from ∼ −25.5 ‰ to −23.2 ‰ and the C : N molar ratio from 9.8 to 11 (Figs. 3, 4; Table S3). Carbonates corresponded to aragonite and calcite and had a bulk C isotope

composition averaging 2.6 ‰ (Table S3). Porewaters from the 2016 La Preciosa core were not retrieved.

4.3 Lake Atexcac

Stratification of the Lake Atexcac water column was also very well defined (Fig. 2). Temperature decreased from ∼ 20.6 °C at the surface to reach 16 °C below 20 m. Conductivity showed the same trend with values between 13 and 12.8 mS cm^{-1} near the surface (salinity around 7.4 psu). Dissolved O_2 was slightly oversaturated at the lake surface (115 % or 7.6 mg L^{-1}), rapidly decreasing to 0 mg L^{-1} between ∼ 10 and 20 m, while ORP signal decreased below a depth of 22 m. Chl *a* averaged 1 µg L^{-1} and showed a narrow peak centered at around 16 m, reaching ∼ 2 µg L^{-1}. Turbidity showed a pronounced increase below 20 m, peaking at 23.3 m and returning to surface values at 26 m. The pH remained around 8.85 throughout the water column. Based on the temperature profiles, the epilimnion, metalimnion, and hypolimnion of Atexcac in May 2019 broadly extended from 0–10, 10–20, and 20–39 m, respectively (Fig. 2).

The DIC concentration was around 26 mM throughout the water column, except at 23 m, where it decreased to 24.2 mM (Fig. 3, Table S1). Calculated pCO_2 was about 5 times higher than the atmospheric $pCO_{2\,atm}$ (Table S2). The $\delta^{13}C_{DIC}$ was stable around 0.4 ‰ in the epilimnion and metalimnion but increased to 0.9 ‰ at 23 m and reached 0.2 ‰ minimum values at the bottom of the lake. The POC concentration was ∼ 0.05 mM in the epilimnion and metalimnion, decreasing to 0.02 mM in the hypolimnion. The C : N molar ratio of POM showed the same depth profile, decreasing from ∼ 9.6 in the epilimnion and metalimnion to 6.6 in the hypolimnion (Fig. 3). The $\delta^{13}C_{POC}$ showed minimum values in the epilimnion and metalimnion (−29.3 ‰ at 16 m) and increased to −26.5 ‰ in the hypolimnion.

Dissolved sulfate concentration was relatively stable at ∼ 2.51 mM throughout the water column but increased to 2.64 mM at 23 m. Dissolved Mn concentration was constant at 1 µM down to 16 m, before dropping to 0 at 23 m and increasing again to 2.35 µM at 30 m (Fig. 2; Table S4). Similar depth profiles were found for other heavy elements as well, including Cu, Sr, Ba, or Pb among others.

In the first 12 cm of sediments, DIC concentration in the porewater varied between ∼ 21 and 26 mM, and $\delta^{13}C_{DIC}$ was around 0 ‰. Carbonates corresponded to aragonite and calcite and had a bulk C isotope composition between 2.1 ‰ and 2.6 ‰ (Table S3). Sedimentary organic matter had a $\delta^{13}C_{SOC}$ averaging −26.8 ± 0.1 ‰ and a C : N molar ratio increasing from 8 to 10 (Figs. 3, 4; Table S3).

4.4 Lake Alchichica

The water column of Lake Alchichica showed a pronounced stratification compared to previous years at the same period (Figs. 2, S2; Lugo et al., 2000; Adame et al., 2008; Macek et al., 2020). Temperature decreased from ∼ 20 °C at the surface to 15.5 °C at depths below 30 m. Conductivity showed the same trend with values between around 13.8 mS cm^{-1} (salinity decreasing from 7.9 to 7.8 psu). Dissolved O_2 was slightly oversaturated at the lake surface (112 % or 7.5 mg L^{-1}), rapidly decreasing to 0 mg L^{-1} between ∼ 10 and 20 m. The ORP followed a similar trend but decreasing below 30 m only. The offset between O_2 exhaustion and decrease of the ORP can be explained by the presence of other oxidant species and/or extended Chl *a* peaks (Supplement Text S1). Chl *a* averaged 2 µg L^{-1}, with a broad peak extending from ∼ 7 to 29 m (averaging 4 µg L^{-1}) and showing a narrow 6 µg L^{-1} maximum values at 23 m. Then, it decreased to minimum values of ∼ 0.5 µg L^{-1} in the lower water column. The pH remained constant at ∼ 9.2 over the whole water column. Based on the temperature profiles, the epilimnion, metalimnion and hypolimnion layers of Lake Alchichica in May 2019 extended from 0–10, 10–20, and 20–63 m, respectively (Fig. 2).

The DIC concentration was around 34.8 mM throughout the water column, except at 10 m where it decreased to 33 mM (Fig. 3; Table S1). Calculated pCO_2 was about 3 times higher than the atmospheric $pCO_{2\,atm}$ (Table S2). The $\delta^{13}C_{DIC}$ decreased from 2 ‰ to ∼ 1.5 ‰ between 5 and 60 m depth (Fig. 4; Table S1). The POC concentration was ∼ 0.09 mM in the epilimnion and metalimnion, decreasing to 0.02 mM in the hypolimnion. The $\delta^{13}C_{POC}$ increased from −26.5 ‰ in the top 30 m to −24.1 ‰ at 55 m. The C : N molar ratio of POM showed a similar profile with values around 10.5 down to 30 m, progressively decreasing towards 5.9 at 55 m (Fig. 3; Table S1).

In the first 12 cm of sediments, porewater DIC had a concentration of ∼ 35.5 mM, and $\delta^{13}C_{DIC}$ decreased from 0.4 ‰ to −0.5 ‰. Solid carbonates were contained within several phases (aragonite, hydromagnesite, huntite, and calcite) and had a bulk C isotope composition around 4.6 ‰ (Table S3). Sedimentary organic matter had a $\delta^{13}C_{SOC}$ increasing from −25.7 ‰ to −24.5 ‰ and a constant C : N molar ratio slightly higher than 10 (Figs. 3, 4; Table S3).

5 Discussion

5.1 Inorganic carbon: origins and implications of the alkalinity / DIC gradient

5.1.1 Sources of DIC and origin of the inter-lake alkalinity gradient

Salinity and DIC concentration gradually increase from Alberca de los Espinos (0.6 psu, 7 mM) to Alchichica (7.9 psu, 35 mM), while La Preciosa (1.15 psu, 13 mM) and Atexcac (7.44 psu, 26 mM) have intermediate values (Table 1 and S1). This trend matches the alkalinity gradient (with values of ∼ 8, 15, 32 and 47 meq L^{-1}, Fig. S3a) previously de-

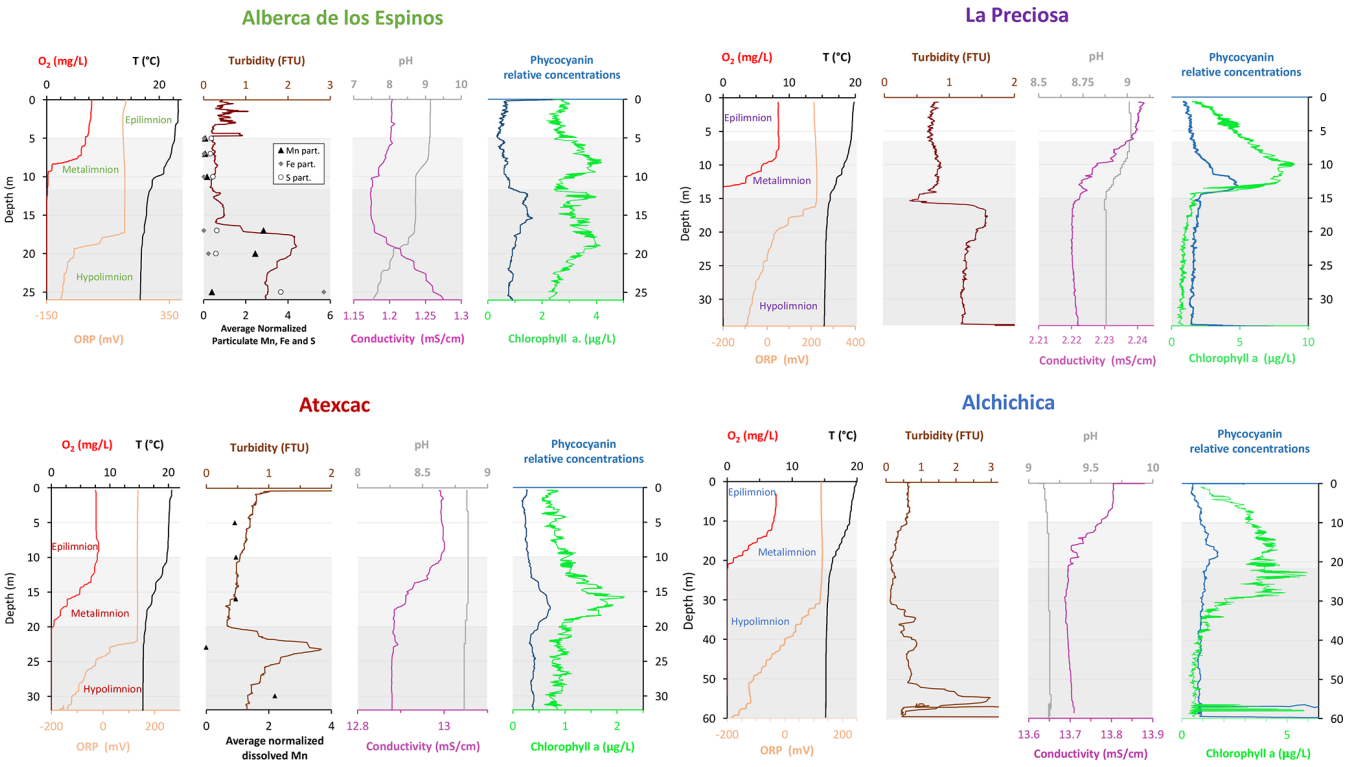

Figure 2. Physicochemical parameter depth profiles in Alberca de los Espinos, La Preciosa, Atexcac, and Alchichica in May 2019, including dissolved oxygen concentration (mg L^{-1}), water temperature (°C), oxidation-reduction potential (ORP, mV), turbidity (Formazin Turbidity Unit), pH, conductivity (mS cm^{-1}), phycocyanin, and chlorophyll *a* pigments (µg L^{-1}). Absolute values for phycocyanin concentrations were not determined, only relative variations are represented (with increasing concentrations to the right). Discrete concentration values of dissolved Mn in Atexcac and particulate Mn, Fe, and S in Alberca, normalized by their respective averages, are represented. Epilimnion, metalimnion, and hypolimnion layers are depicted for each lake according to temperature profiles. The three layers closely corresponded to oxygen-rich, oxygen-poor, and intermediate zones (except in La Preciosa where the oxycline was slightly thinner than the thermocline layer, ~5 vs. 8 m).

scribed for these lakes (Zeyen et al., 2021), consistent with the fact that alkalinity is mainly composed of HCO_3^- and CO_3^{2-} ions in most natural waters. This alkalinity gradient may result from different concentration stages of an initial dilute alkaline water (Zeyen et al., 2021), ultimately controlled by differences in hydrological regime between the four lakes. In the SOB, the weathering of basaltic and andesitic bedrock (Armienta et al., 2008; Carrasco-Núñez et al., 2007; Lelli et al., 2021) and Cretaceous limestone (with $\delta^{13}C \approx 0 \pm 1$ ‰; Gonzales-Partida et al., 1993; Armstrong-Altrin et al., 2011) favors the inflow of more alkaline and DIC-concentrated groundwater than in Alberca, which lies on an essentially basaltic basement (Rendon-Lopez, 2008; Siebe et al., 2014; Zeyen et al., 2021). The SOB is currently experiencing higher rates of evaporation than precipitation (Alcocer, 2021), which may play an important role in concentrating solutes and decreasing the water level in La Preciosa, Atexcac, and Alchichica (Anderson and Stedmon, 2007; Zeyen et al., 2021). Substantial "sub-fossil" microbialite deposits emerge well above the current water level in lakes Atexcac and Alchichica, confirming this fall in water level (~15 m for Atexcac and ~5 m for Alchichica). Scattered patches of microbialites emerge at La Preciosa (suggesting a water level decrease of ~6 m). By contrast, emerged microbialites are virtually absent in Lake Alberca de los Espinos (Fig. S1).

Additional local parameters such as variable groundwater paths and fluxes (Furian et al., 2013; Mercedes-Martín et al., 2019; Milesi et al., 2020; Zeyen et al., 2021) most likely play a role in explaining some of the variation in DIC concentration between lakes. La Preciosa's water composition significantly differs from that of Atexcac and Alchichica, despite a similar geological context and climate (all are located within 50 km^2, Fig. 1). Groundwater in the SOB area becomes more saline as it flows towards the center of the basin and through the crater lakes (Silva Aguilera, 2019; Alcocer, 2021). Since groundwater flows through La Preciosa first, its ionic strength (including DIC concentration) increases as it enters Alchichica (Silva Aguilera, 2019; Alcocer, 2021; Lelli et al., 2021). Different regimes of volcanic CO_2 degassing into these crater lakes may also contribute to variation in the C mass balance and $\delta^{13}C_{DIC}$ values between the four

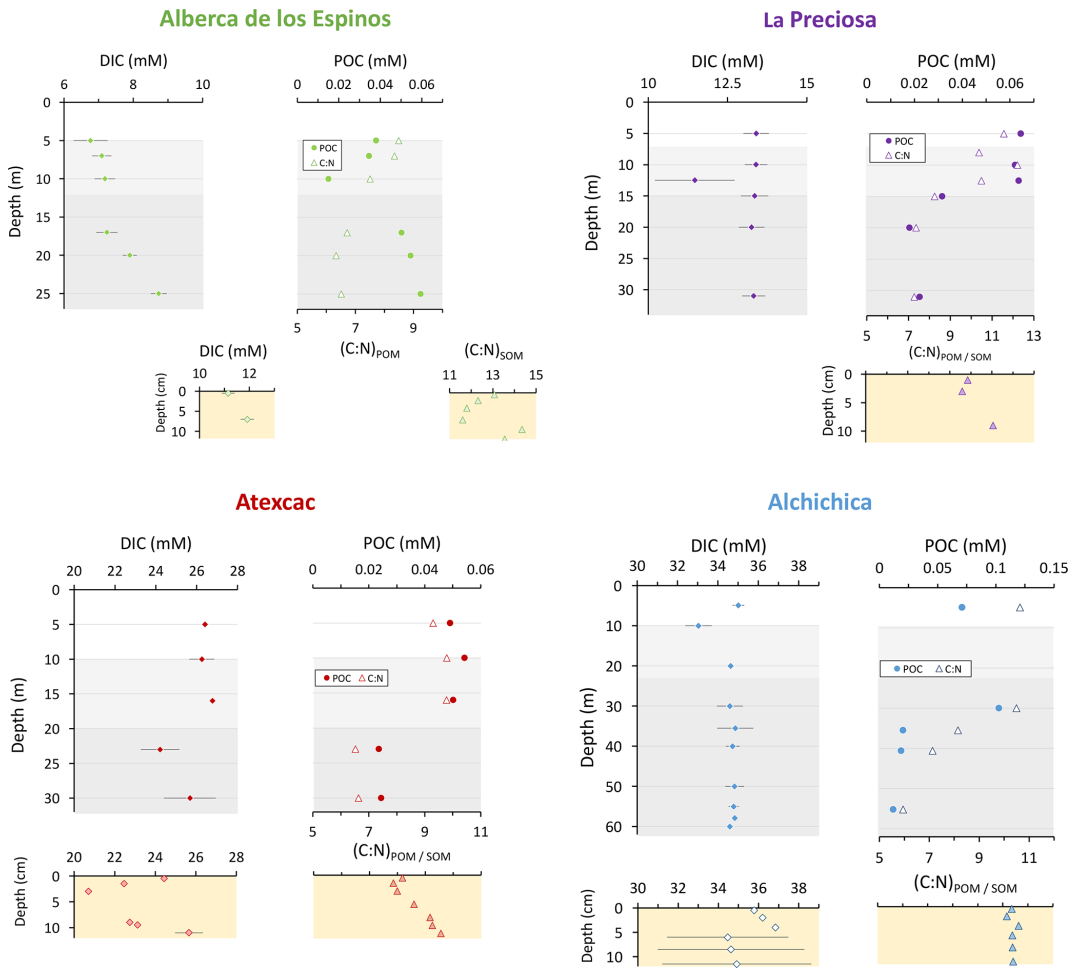

Figure 3. Concentrations in mmol L^{-1} (mM) of DIC, DOC, and POC and the sum of all three reservoirs; C : N molar ratios of POM as a function of depth in the water columns; and DIC concentrations in the surficial sediment porewaters and C : N molar ratios of sedimentary OM. Porewaters from La Preciosa's 2016 core were not retrieved.

lakes. Near the lakes from the SOB area, geothermal fluids derived from meteoric waters have been shown to interact with deep volcanic fluids as well as the calcareous basement rocks (Peiffer et al., 2018; Lelli et al., 2021). In the water column of Alberca, $\delta^{13}C_{total}$ averages −4.8 ‰ (Havas et al., 2023a). This isotopic composition is very similar to signatures of mantle CO_2 (Javoy et al., 1986; Mason et al., 2017), which could buffer the overall C isotope composition of this lake. Alberca is located on top of a likely active normal fault (Siebe et al., 2012), favoring the ascent of volcanic gases.

Differences in the remineralization rate of organic carbon (OC) could also contribute to the heterogeneous DIC content among the lakes. However, assuming that all OC from the lakes ultimately remineralized into DIC, it would still represent only a small proportion of the total carbon (9 % for Alberca, ∼ 5 % for La Preciosa and Alchichica, and 16 % for Atexcac; Havas et al., 2023). From an isotopic mass balance perspective, Lake Alberca exhibits more negative $\delta^{13}C_{DIC}$ (and $\delta^{13}C_{Carb}$), slightly closer to OC signatures, whereas the $\delta^{13}C_{DIC}$ of the three SOB lakes lies very far from OC isotopic signatures (Fig. 4). Dense vegetation surrounds Alberca (Fig. S1), making it the only lake in this study where OC respiration could be a significant source of inorganic C to the water column (potentially influencing the P_{CO_2}, [DIC], and pH profiles described above).

In summary, a combination of very local and external environmental factors generates the contrasting water chemistries of the lakes, notably a gradient in their alkalinity and [DIC]. This chemical variability stems from the exact nature of the basement rocks, the distinct groundwater flow paths feeding the lakes, differences in evaporation rates, and potentially different volcanic CO_2 degassing regimes.

5.1.2 Influence of alkalinity on physicochemical stratification in the four lakes

Stratified water columns can sustain strong physicochemical gradients, where a wide range of biogeochemical reactions

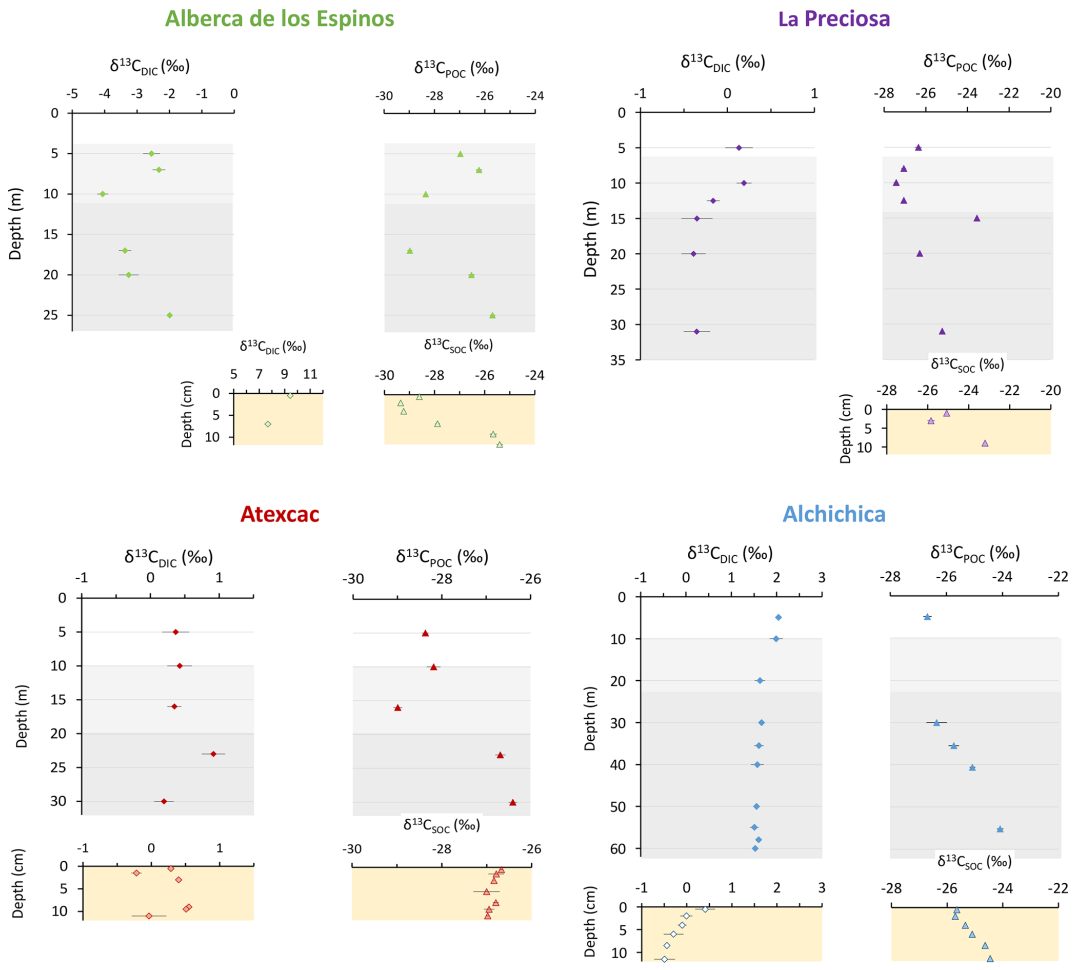

Figure 4. Isotopic compositions of DIC and POC reservoirs as a function of depth in the water columns, as well as isotopic compositions of the porewater DIC and total organic carbon from the surficial sediments.

impacting the C cycle can take place (e.g., Jézéquel et al., 2016). In the four lakes studied here, the evolution of pH with depth exemplifies the interplay between the alkalinity gradient, the physicochemical stratification of the lakes, and their respective C cycle. The pH shows a stratified profile in Alberca and La Preciosa but remains constant in Atexcac and Alchichica. The decline in pH at the oxycline of La Preciosa is associated with the decrease in POC and chlorophyll *a* concentrations and $\delta^{13}C_{DIC}$ values, reflecting the impact of oxygen respiration (i.e., carbon remineralization) at this depth (Figs. 2–4). In Alberca, the surface waters are markedly more alkaline than the bottom waters, with a two-step decrease in pH occurring at 8 and 17 m (with a total drop of 1.5 pH unit). As in La Preciosa, this pH decrease likely results from high OM respiration, although input of volcanic acidic gases (e.g., dissolved CO_2 with $\delta^{13}C \sim -5$ ‰) might also contribute to the pH decrease in the bottom waters, reflected by negative $\delta^{13}C_{DIC}$ signatures and an increase of [DIC] and conductivity in the hypolimnion (Figs. 2 and 4). By contrast, while the same evidence for oxygen respiration ([POC], chlorophyll *a*) can be detected in the other two lakes, it does not impact their pH profile in a similar way (Fig. 2). This result suggests that the acidity generated by OM respiration (and possibly volcanic CO_2 degassing) is buffered by the much higher alkalinity measured in these two lakes.

External forcings such as lake hydrology and fluid sources thus impact the alkalinity buffering capacity of these lakes and influence the vertical pH profile of the water columns, which is particularly important considering the critical interplay between pH and biogeochemical reactions affecting the C cycle (e.g., Soetaert et al., 2007).

5.1.3 Sinks of DIC along the alkalinity gradient

Interplay between pH and sources of alkalinity and DIC in the lakes also has a strong impact on their C storage capacity, as it can result in different fluxes of the C sinks (inorganic and organic C precipitation and sedimentation, CO_2 degassing).

Alkaline pH can store large quantities of DIC because it favors the presence of HCO_3^- and CO_3^{2-} species over $H_2CO_3^*$

(the intermediate species between gaseous $CO_{2(g)}$ and bicarbonate/carbonate ions, defined here as the sum of H_2CO_3 and $CO_{2(aq)}$). Carbonate and bicarbonate ions represent over 99 % of total DIC in the four lakes (Table S2). In Alberca de los Espinos, the lake with the lowest DIC, the surface water pCO_2 is slightly lower than atmospheric $pCO_{2\,atm}$ (Table S2). By contrast, large amounts of CO_2 degas at the surface of the SOB lakes, as indicated by their elevated surface water pCO_2, from 2 to 5 times higher than atmospheric $pCO_{2\,atm}$ (Table S2). These different CO_2 degassing potentials are consistent with the notion that higher DIC concentrations favor CO_2 degassing through higher pCO_2 (e.g., Duarte et al., 2008). Although Alberca and Alchichica (the two endmembers of the alkalinity gradient) have the same surface water pH, CO_2 degassing is 3 times higher at Alchichica for a given value of gas transfer velocity.

Another important C sink for these lakes is the precipitation of carbonate minerals, found in the microbialites and lake sediments. Lake alkalinity and the resulting mineral saturation index greatly influence the amount of C precipitated from the lake waters. Although the four lakes are supersaturated with aragonite, calcite, and the precursor-phase monohydrocalcite, they present highly contrasted amounts of carbonate deposits (Zeyen et al., 2021). The occurrence of microbialites increases along the alkalinity gradient, with limited presence at Alberca and more massive deposits at Atexcac and Alchichica (Zeyen et al., 2021; Fig. S1). Similarly, surficial sediments contain only 16 wt % for Alberca but from 40 wt % to 62 wt % carbonates for the SOB lakes (Table S3). Thus, the SOB lakes seem to bury more C than Alberca de los Espinos. Nonetheless, the data from May 2019 indicate that Alberca was the only one of the four lakes with a pCO_2 slightly lower than atmospheric $pCO_{2\,atm}$, thus representing a net sink of C. Classifying the three other lakes as net C sources or sinks – notably in order to see the influence of their respective position in the alkalinity gradient – will require a more detailed description of C in and out fluxes, since they all store and emit significant amounts of C (as organic and inorganic C deposits and via CO_2 degassing, respectively). However, such a C budget is out of the scope of the present study.

5.1.4 Isotopic signatures of inorganic C in the four lakes ($\delta^{13}C_{DIC}$ and $\delta^{13}C_{Carbonates}$)

The DIC isotopic composition of the lakes (between ~ -3 ‰ and $+2$ ‰ on average; Table S1) is consistent with the DIC sources described above. The lower $\delta^{13}C_{DIC}$ in Alberca is consistent with influence of remineralized OC and/or volcanic CO_2. The $\delta^{13}C_{DIC}$ in the SOB lakes suggests groundwater $\delta^{13}C_{DIC}$ values resulting from the dissolution of the Cretaceous limestone basement.

By controlling DIC speciation (H_2CO_3 / $CO_{2(aq)}$, HCO_3^-, CO_3^{2-}), pH also strongly influences $\delta^{13}C_{DIC}$. Indeed, there is a temperature-dependent fractionation of up to 10 ‰ between the different DIC species (Emrich et al., 1970; Mook et al., 1974; Bade et al., 2004; Table S6). The Mexican lakes present $\delta^{13}C_{DIC}$ values that are common for lakes with a pH around 9 (Bade et al., 2004), where DIC is dominated by HCO_3^-. However, the pH values of the four lakes studied here are too similar to explain the significant difference between their $\delta^{13}C_{DIC}$ (Fig. 4; $p = 4.2 \times 10^{-3}$ for La Preciosa and Atexcac, which have the closest $\delta^{13}C_{DIC}$). Part of the variability of $\delta^{13}C_{DIC}$ among the lakes may result from their distinct evaporation stages, as the mean $\delta^{13}C_{DIC}$ values of the lakes broadly correlate with their salinity and alkalinity (Fig. S3b). Evaporation generally increases the $\delta^{13}C_{DIC}$ of residual waters by increasing lake pCO_2 and primary productivity, which bolsters CO_2 degassing and organic C burial, both having low $\delta^{13}C$ compared to DIC (e.g., Li and Ku, 1997; Talbot, 1990). Accordingly, the pCO_2 of Alberca is lower than that of the other lakes (Table S2). The $\delta^{13}C_{DIC}$ in lakes with lower DIC concentrations is expected to be more easily influenced by exchanges with other carbon reservoirs, such as organic carbon (through photosynthesis and respiration), or other DIC sources (e.g., depleted volcanic CO_2 or groundwater DIC), compared to buffered, high DIC lakes (Li and Ku, 1997). As a result, the low DIC and alkalinity concentration in Alberca features the lowest $\delta^{13}C_{DIC}$ of the four lakes, likely reflecting organic and/or volcanic C influence and thus higher responsiveness to biogeochemical processes of the inorganic C reservoir. By contrast, the three SOB lakes exhibit $\delta^{13}C_{DIC}$ with less internal variability, with a maximum amplitude of 0.7 ‰ within a single water column.

Surficial sedimentary carbonates are in isotopic equilibrium with the $\delta^{13}C_{DIC}$ of the water columns, within the uncertainty of $\delta^{13}C_{DIC}$ measurement, and more specifically with the $\delta^{13}C_{DIC}$ values at the oxycline and thermocline of the lakes (Tables S6 and S7). The $\delta^{13}C_{DIC}$ at equilibrium with carbonates is estimated by correcting the carbonate C isotope composition ($\delta^{13}C_{Carb}$) by the fractionation value between DIC and the different carbonate mineralogies (Supplement Text S2). Therefore, the $\delta^{13}C_{Carb}$ also follows and reflects the alkalinity gradient, with the lowest $\delta^{13}C_{Carb}$ found in the surficial sediments of Alberca (~ -1.5 ‰), intermediate values in La Preciosa and Atexcac (~ 2.5 ‰), and the highest values in Alchichica ($\sim +4.6$ ‰) (Table S3).

In summary, although all four lakes present the same general structure and environmental conditions (i.e., tropical alkaline stratified crater lakes), external and local factors (e.g., hydrology, fluid sources, and stratification characteristics) result in contrasting water chemistry compositions, which have a critical impact on the physicochemical depth profiles of each lake and their biogeochemical carbon cycle functioning. These external factors represent a first-order control on the size, isotopic composition, and responsiveness to biogeochemical processes of the inorganic C reservoir. Lakes with the highest alkalinity and DIC content will poorly record internal biological processes. Interestingly, C storage in mineral carbonates seems to be significant in watersheds where

Table 2. Index for mathematical notations used in the text including C isotopic composition of a reservoir X ($\delta^{13}C_X$) and isotopic discrimination between the two carbon reservoirs X and Y ($\Delta^{13}C_{X-Y}$). In the main text, we report organic C isotope discrimination versus both bulk DIC ($\Delta^{13}C_{POC\text{-}DIC}$) – in a way to facilitate intercomparison studies and because it is the commonly reported raw measured data (Fry, 1996) – and calculated $CO_{2(aq)}$ ($\varepsilon_{POC\text{-}CO_2}$) in order to discuss the intrinsic isotopic fractionations associated with the lakes metabolic diversity. All C isotope values and fractionations are reported relative to the international standard VPDB (Vienna Pee Dee Belemnite).

Symbols	Mathematical expression	Signification
$\delta^{13}C_X$	$\left(\frac{\left(\frac{^{13}C}{^{12}C}\right)_X}{\left(\frac{^{13}C}{^{12}C}\right)_{VPDB}} - 1\right) \times 1000$	Relative difference in $^{13}C:{}^{12}C$ isotopic ratio between a sample of a given C reservoir and the international standard "Vienna Pee Dee Bee", expressed in permil (‰). $\delta^{13}C_{total}$ represents the weighted average of $\delta^{13}C$ for all DIC and POC.
$\Delta^{13}C_{X-Y}$	$=\delta^{13}C_X - \delta^{13}C_Y \approx 1000 \ln \alpha_{X-Y}$	Apparent isotopic fractionation between two reservoirs "X" and "Y". Difference between their measured C isotope compositions approximating the fractionation α in permil.
$\varepsilon_{X\text{-}CO_2}$	$=(\alpha_{X\text{-}CO_2} - 1)1000 \approx \delta^{13}C_X - \delta^{13}C_{CO_2}$	Calculated isotopic fractionation between a reservoir "X" and $CO_{2(aq)}$. $\alpha_{X\text{-}CO_2}$ is calculated as $(\delta^{13}C_X + 1000) / (\delta^{13}C_{CO_2} + 1000)$, where $\delta^{13}C_X$ is measured and $\delta^{13}C_{CO_2}$ is computed based on DIC isotopic composition and speciation (see Supplement text S3).

carbonate deposits pre-exist in the geological substratum (here, the Cretaceous limestone basement), providing more alkaline and C-rich sources.

5.2 Particulate organic carbon: from water column primary production to respiration recycling and sedimentary organic matter

5.2.1 Particulate organic C sources

Primary productivity by oxygenic photosynthesis in the upper water column

The C : N ratios of water column POM and bulk organic matter in the sediments of the four lakes ranged from 6 to 13 (Fig. 3), close to the phytoplankton Redfield ratio but much lower than land–plant ratios. Yet abundant vegetation covers the crater walls of Alberca and, to a lesser extent, of Atexcac, and some plant debris was found in the sediment cores of these two lakes. Its analysis resulted in high C : N ratios (between 24 and 68), typical of plant tissues and significantly higher than those of the bulk sediment and water column organic matter. Thus, the allochthonous organic carbon in these two lakes does not significantly contribute to their bulk organic signal. All four crater lakes are endorheic basins, with no surface water inflow or outflow, supporting the predominantly autochthonous origin of organic carbon sources (Alcocer et al., 2014), from planktonic autotrophic C fixation.

The importance of planktonic autotrophic C fixation as a major source of POC in the four lakes is further supported by the assessment of the isotopic discrimination between DIC and organic biomass, expressed as $\Delta^{13}C_{POC\text{-}DIC}$ and $\varepsilon_{POC\text{-}CO_2}$ (Table 2). The $\Delta^{13}C_{POC\text{-}DIC}$ varies between ~ -29 ‰ and -23 ‰ (corresponding to $\varepsilon_{POC\text{-}CO_2}$ between ~ -19 ‰ and -13 ‰) throughout the four water columns, within the typical range of planktonic oxygenic phototrophs (Pardue et al., 1976; Sirevag et al., 1977; Thomas et al., 2019). Yet these values exhibit variability – both within a single water column (up to 4.5 ‰) and among the four lakes (up to 6 ‰; Figs. 4 and 5). The $\Delta^{13}C_{POC\text{-}DIC}$ variability may reflect several abiotic and biotic factors.

Notably, lower DIC availability in Alberca and La Preciosa probably makes the carboxylation step less limiting during photosynthesis (e.g., O'Leary, 1988; Descolas-Gros and Fontungne, 1990; Fry, 1996), decreasing $|\varepsilon_{POC\text{-}CO_2}|$ in these lakes (between 14.5 ‰ and 17.7 ‰ at the peak of Chl *a*) compared to Atexcac and Alchichica (Fig. 5a; between 17.5 ‰ and 19.2 ‰). Lower $CO_{2(aq)}$ availability and/or higher reaction rates result in transport-limited rather than carboxylation-limited fixation, with smaller C isotope fractionation between POC and DIC (Pardue et al., 1976; Zohary et al., 1994; Fry, 1996; Close and Henderson, 2020). The isotopic fractionation associated with diffusion is much smaller than with carboxylation, and a higher proportion of the DIC entering the cells is converted into organic biomass (e.g., Fogel and Cifuentes, 1993). We consistently notice a correlation among the lakes between $a(CO_2)_{(aq)}$ (or [DIC]) and $|\varepsilon_{POC\text{-}CO_2}|$ at depths where oxygenic photosynthesis peaks (Fig. 6). Furthermore, Alberca and La Preciosa are considered less oligotrophic than the two other lakes (Lugo et al., 1993; Vilaclara et al., 1993; Havas et al., 2023), with higher chlorophyll *a* contents and thus smaller $|\varepsilon_{POC\text{-}CO_2}|$ (Fig. 5). Higher water temperatures in Alberca de los Espinos (by ~ 3 °C) could also partly contribute to a smaller $|\varepsilon_{POC\text{-}CO_2}|$ in this lake (Sackett et al., 1965; Pardue et al., 1976; Descolas-Gros and Fontungne, 1990).

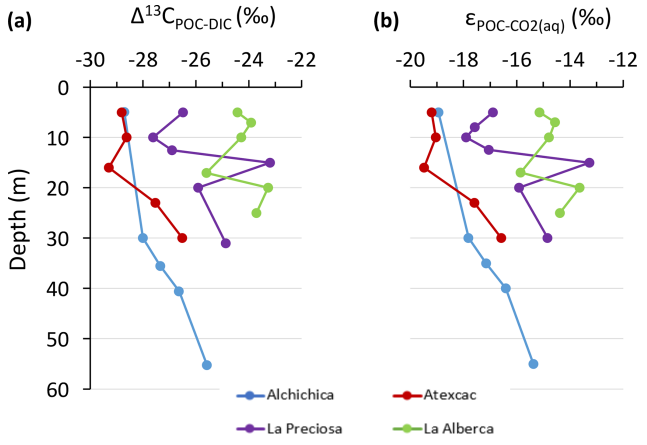

Figure 5. Isotopic fractionations between POC and DIC in the water columns of the four lakes, expressed as **(a)** $\Delta^{13}C_{x-y}$ and **(b)** $\varepsilon_{POC\text{-}CO_2}$. Refer to Table 2 for more detail about the Δ and ε notations.

Unlike $\delta^{13}C_{DIC}$, organic carbon isotope signatures do not evolve linearly with the alkalinity/salinity gradient, suggesting other lake- and microbial-specific controls on these signatures. These controls include diffusive or active uptake mechanisms, specific carbon fixation pathways, the fraction of intracellular inorganic carbon released out of the cells, cell size and geometry (Werne and Hollander, 2004, and references therein), and remineralization efficiency. Moreover, an increasing number of isotopic data have evidenced a significant variability of the isotopic fractionation achieved by different purified RuBisCO enzymes ($\varepsilon_{RuBisCO}$, Iñiguez et al., 2020) and even by a single RuBisCO form (Thomas et al., 2019). Thus, caution should be paid to the interpretation of the origin of small isotopic variations of the biomass in distinct environmental contexts because RuBisCO alone can be an important source of this variability (Thomas et al., 2019).

Primary production in the anoxic hypolimnion

Anoxygenic autotrophs commonly thrive in anoxic bottom waters of stratified water bodies (e.g., Pimenov et al., 2008; Zyakun et al., 2009; Posth et al., 2017; Fulton et al., 2018; Havig et al., 2018). They have been identified at different depths in the four Mexican lakes (Macek et al., 2020; Iniesto et al., 2022). In our samples collected during the stratification period, anoxygenic autotrophs appear to have a distinct impact on the C cycle of Alberca and Atexcac only. Lake Atexcac records a concomitant decrease in [DIC] and increase in $\delta^{13}C_{DIC}$ in the anoxic hypolimnion at 23 m, below the peak of Chl *a*, suggesting autotrophic C fixation by chemoautotrophy or anoxygenic photosynthesis. The calculated $\varepsilon_{POC\text{-}CO_2}$ at 23 m (-17.3 ‰) is consistent with C isotope fractionation by purple- and green-sulfur-anoxygenic bacteria (PSB and GSB), while $\varepsilon_{POC\text{-}CO_2}$ in Alberca's hypolimnion (~ -15 ‰) is closer to GSB canonical signatures (Posth et al., 2017 and references therein) (Fig. 5b). In Alberca, anoxygenic primary productivity is suggested by increasing POC concentrations below the oxycline, showing a distinct isotopic signature (Figs. 4 and 5). We also observe a Chl *a* peak in the anoxic hypolimnion of this lake (Fig. 2), which likely represents a bias of the probe towards some bacteriochlorophyll pigments typical of GSB (see Supplement text S4). In Atexcac, C fixation by anoxygenic autotrophs at 23 m causes a shift in the DIC reservoir, while oxygenic photosynthesis at 16 m does not, suggesting that anaerobic autotrophs are the main autotrophic metabolisms in this lake (in terms of DIC uptake). In Alberca, the increase in [POC] to maximum values below the oxycline also supports the predominance of anoxygenic versus oxygenic autotrophy (Fig. 3), similar to other stratified water bodies exhibiting primary production clearly dominated by anoxygenic metabolisms (Fulton et al., 2018).

Lastly, at 23 m in Atexcac and 17 m in Alberca, we find a striking turbidity peak precisely where the redox potential and the concentration of dissolved Mn drops (Fig. 2). In Atexcac, the concentration of dissolved metals such as Cu, Pb, or Co also drops at 23 m (Fig. S4). In Alberca, a peak of particulate Mn concentration is detected at 15 m (Fig. 2; data unavailable for Atexcac). This peak is most likely explained by the precipitation of Mn mineral particles, where reduced bottom waters meet oxidative conditions prevailing in the upper waters. These oxidized Mn phases can be used as electron acceptors during chemoautotrophy (Havig et al., 2015; Knossow et al., 2015; Henkel et al., 2019; van Vliet et al., 2021). Even at a low particle density, such phases can catalyze abiotic oxidation of sulfide to sulfur compounds, which in turn can be used and further oxidized to sulfate by phototrophic or chemoautotrophic sulfur-oxidizing bacteria (van Vliet et al., 2021). Autotrophic sulfur oxidation is also consistent with the small increase in $[SO_4^{2-}]$ observed at 23 m in Atexcac (Table S4).

In summary, combined POC and DIC data allowed us to recognize the most representative autotrophic metabolisms in the Mexican lakes. The upper water columns are all dominated by oxygenic photosynthesis. Lower in the water columns, anoxygenic photosynthesis and/or chemoautotrophy were found to have a noticeable impact on POC and DIC reservoirs in Alberca and Atexcac only. Their activity was associated with metal element cycling. More specifically in Alberca, the anoxygenic phototrophs correspond to GSB.

5.2.2 Sinks of particulate organic carbon: respiration and sedimentation

Aerobic respiration at the oxycline

At the oxycline of stratified water bodies, aerobic respiration of OM by heterotrophic organisms favors the transition from oxygenated upper layers to anoxic bottom waters. In the water column of the four lakes, $\Delta^{13}C_{POC\text{-}DIC}$ (and

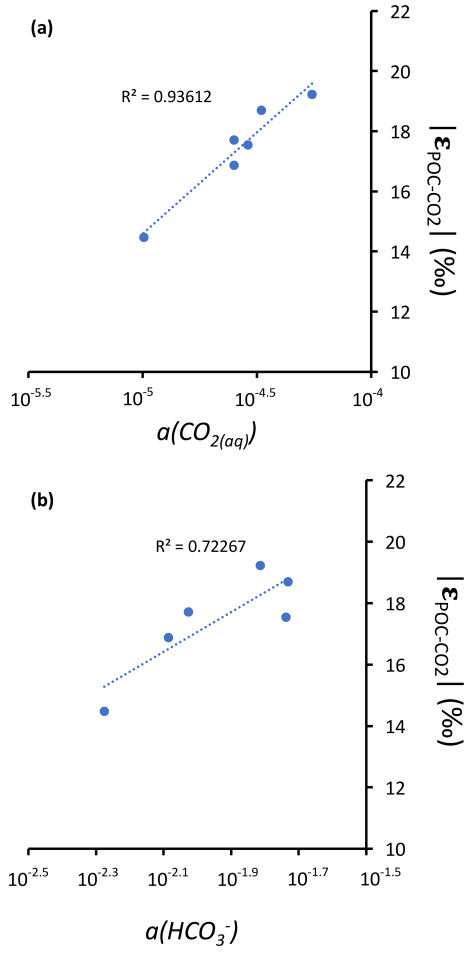

Figure 6. Cross plots of DIC species activities versus absolute values of calculated C isotopic fractionations between POC and CO_2 at depths of peak oxygenic photosynthesis where data were available (5 and 30 m for Alchichica, 16 m for Atexcac, 10 and 12.5 m for La Preciosa, and 7 m for Alberca). **(a)** Dissolved $CO_{2(aq)}$ activity and **(b)** bicarbonate activity as functions of $|\varepsilon_{POC\text{-}CO_2}|$ in permil plus linear correlation trends and corresponding R^2.

$\varepsilon_{POC\text{-}CO_2}$) show increasing values in the hypolimnion and especially below the chlorophyll *a* peaks (Figs. 2 and 5). The $\Delta^{13}C_{POC\text{-}DIC}$ trend correlates with increasing $\delta^{13}C_{POC}$, decreasing $(C:N)_{POM}$ ratios, and decreasing POC concentrations except in Alberca (Figs. 3 and 4). Decreasing POC concentrations near the oxycline and redoxcline are consistent with the fact that part of the upper primary production is degraded deeper in the water columns and/or that there is less primary production in the anoxic bottom waters. Increased $\delta^{13}C_{POC}$ in the hypolimnion of the lakes is consistent with heterotrophic activity and points out that POC at these depths could mainly record secondary production rather than being a residue of sinking degraded OM formed by primary production. Heterotrophic bacteria preferentially grow on available ^{13}C-enriched amino acids and sugars, thus becoming more enriched than their C source (Williams and Gordon, 1970; Hayes et al., 1989; Zohary et al., 1994; Briones et al., 1998; Lehmann et al., 2002; Jiao et al., 2010; Close and Henderson, 2020). The decrease in C : N ratios in the POM also reinforces this conclusion, since secondary heterotrophic bacteria biomass generally have C : N between 4 and 5 (Lehmann et al., 2002), whereas residual degraded OM from primary producers would carry higher C : N signatures (van Mooy et al., 2002; Buchan et al., 2014). These latter signatures are not recorded by POM in the lower water columns of the lakes (Fig. 3).

The $\delta^{13}C_{DIC}$ signatures in La Preciosa and Alchichica are consistent with the mineralization of OM, as they exhibit lower values below the oxycline than in surficial waters (Figs. 2 and 4). Similarly to what is observed in several other water bodies and notably stratified water columns such as the Black Sea (e.g., Fry et al., 1991), surface photosynthesis increases $\delta^{13}C_{DIC}$ by fixing light DIC, while respiration transfers light OC back to the DIC pool at depth. Such a decrease in $\delta^{13}C_{DIC}$ can also be seen in the oxycline of Lake Alberca between 7 and 10 m.

Influence of methanogenesis in Lake Alberca de los Espinos

Alberca shows the least saline and alkaline water column and most peculiar geochemical depth profiles among the four lakes. Notably, its [DIC] and $\delta^{13}C_{DIC}$ (the lowest of the studied lakes) increase from the lower metalimnion to the hypolimnion and further into the first cm of sediment porewaters, with $\delta^{13}C_{DIC}$ reaching almost 10 ‰ (Figs. 3, 4). The calculated CO_2 partial pressure (P_{CO_2}) increases downward from slightly less than $1\times$ $P_{CO_2\text{-}atm}$ near the lake surface up to almost $40\times$ at the bottom of the lake (Table S2).

While the increase of [POC] at depth may contribute to the observed $\delta^{13}C_{DIC}$ increase, by mass balance, it should also lower the [DIC] instead of increasing it. Similarly, the sinking of POC at depth followed by its remineralization into DIC cannot explain the $\delta^{13}C_{DIC}$ trend, since it would lower the $\delta^{13}C_{DIC}$ in the hypolimnion (Fig. 4). Overall, these observations require that a significant source of inorganic ^{13}C-rich carbon fuels the bottom waters of Alberca de los Espinos. The source of heavy carbon most likely results from methanogenesis, which consumes organic carbon in the sediments and produces ^{13}C-depleted methane and ^{13}C-rich carbon dioxide diffusing upward in the water column (i.e., acetoclastic methanogenesis, dominant in lacustrine contexts; Whiticar et al., 1986). Methanogenesis, as an "alternative" OM remineralization pathway, would be favored in Alberca because it is relatively rich in OM (notably with high [DOC], Havas et al., 2023) and depleted in SO_4^{2-} (Wittkop et al., 2014; Birgel et al., 2015; Cadeau et al., 2020) compared to the other three Mexican lakes. Based on the $\delta^{13}C_{SOC}$ and porewater $\delta^{13}C_{DIC}$, we can tentatively calculate the methane isotopic signature in Alberca (see Supplement Text S5). The resulting $\delta^{13}C_{CH_4}$ in the first 10 cm of sediments is between

−59 ‰ and −57 ‰, which is consistent with the range of isotopic composition of methane after biogenic methanogenesis (Whiticar et al., 1986).

Upward-diffusing methane may be either (i) partly lost from the lake's surface (i.e., escaping the system) by degassing or (ii) totally retained in the water column by complete oxidation (either abiotically by oxygenated surface waters or biologically by methanotrophic organisms). The oxidation of CH_4 in the water column should lead to the formation of ^{13}C-depleted carbon dioxide that would mix back with the lake DIC (and notably with heavy methanogenic CO_2 produced at depth) and/or ^{13}C-depleted biomass (as POC or SOC) if it occurs through methanotrophy. Thus, the net effect of combined methanogenesis and methane oxidation is expected to (i) generate a $\delta^{13}C_{DIC}$ gradient from high to low values between the sediment porewaters and the oxycline as proposed elsewhere (Assayag et al., 2008; Wittkop et al., 2014) and (ii) progressively lower sedimentary $\delta^{13}C_{SOC}$ in the case of methanotrophy. Abiotic oxidation of methane by dioxygen is consistent with the observation that $\delta^{13}C_{DIC}$ decreases from porewaters ($\sim +10$ ‰) to the oxycline (−4 ‰), reaching minimum values where dissolved O_2 starts to appear (Fig. 2). Microbial anaerobic oxidation of methane (AOM) could occur at the 17 m depth through Mn-oxide reduction (Cai et al., 2021; Cheng et al., 2021) and possibly bacterial sulfate reduction closer to the water-sediment interface, as inferred for the surficial sediments of meromictic Lake Cadagno (Posth et al., 2017). Indeed, we observe a net increase of particulate Fe and S concentrations at a depth of 25 m and a peak of solid sulfide minerals in the surficial sediments (Fig. S5). However, $\delta^{13}C_{SOC}$ and $\delta^{13}C_{POC}$ are far from calculated $\delta^{13}C_{CH_4}$, suggesting that AOM is not a major process in the bottom lake waters and surface sediments (Lehmann et al., 2004) and thus that methanotrophy is not the main CH_4 oxidation pathway in Lake Alberca.

Alternatively, if some portion of the methane escaped oxidation and degassed out of the lake, $\delta^{13}C_{DIC}$ would likely be driven to extreme positive values with time (Gu et al., 2004; Hassan, 2014; Birgel et al., 2015; Cadeau et al., 2020). Methane escape is not consistent with the average $\delta^{13}C_{DIC}$ in Alberca (~ -3 ‰; Fig. 4), unless an additional counterbalancing source of DIC to this lake exists. This source of DIC could be volcanic CO_2 degassing (see Sect. 5.1.1). Such a contribution may maintain the lake's average $\delta^{13}C_{total}$ close to a mantle isotopic signature and notably away from extreme positive values if CH_4 escape dominated. It is also possible that volcanic CO_2 degassing is coupled with methanogenesis by CO_2 reduction in addition to the acetoclastic type described above.

Although volcanic CO_2 could be an important source in the C mass balance of Lake Alberca, we note that it cannot explain the very positive $\delta^{13}C_{DIC}$ in the sediment porewaters alone, thus bolstering the identification of methanogenesis. Importantly, this methane cycle is cryptic to the sediment record, as it is evidenced in the dissolved inorganic C phase but not in the sedimentary organic matter or carbonates. This is a consequence of the lake's stratified nature, where the location of carbonate precipitation and methane production is decoupled.

Transfer of OM from the water column to the surficial sediments

The OC content in the first 12 cm of the sediment cores from the four lakes ranges from 1 wt % to 13 wt % (Table S3). These concentrations are relatively elevated considering the predominantly autochthonous nature of OC and the oligotrophic conditions in these lakes (Alcocer et al., 2014; Havas et al., 2023). In Lake Alchichica, the recent OC burial flux in the sediment was estimated to represent between 15 and 26 g yr^{-1} m^{-2} (Alcocer et al., 2014). These values are within the range observed for small lakes around the world (Mulholland and Elwood, 1982; Dean and Gorham, 1998; Mendonça et al., 2017), though most of them receive allochthonous OM inputs. Different factors can favor the preservation of OM, including lower respiration and oxidation rates due to anoxic bottom waters and scarce benthic biota and/or high sedimentation rates (Alcocer et al., 2014). Anaerobic respiration clearly occurs in the four lakes to some extent, as detailed for Alberca and as seen in the surficial sediment data of the other lakes as well (decreasing $\delta^{13}C_{DIC}$ in Alchichica, increasing C : N ratio in Atexcac and La Preciosa; Table S3). Nonetheless, the anoxic conditions prevailing in the hypolimnion most of the year are significantly more favorable to OM preservation than oxic conditions (Sobek et al., 2009; Kuntz et al., 2015). While the yearly mixing oxidizes most of the water column during the winter, it also generates a bloom of diatoms which fosters OM production (through shuttling up of bio-essential nutrients such as N and Si) and development of anoxia (e.g., Adame et al., 2008). In Alchichica, the large size of some of the phytoplankton was also suggested to favor OM preservation (Adame et al., 2008; Ardiles et al., 2011). Because bacterial sulfate reduction (BSR) is a major remineralization pathway in SO_4-rich environments (e.g., Jørgensen, 1982), the low sulfate content in Alberca probably favors the preservation of high TOC in the sediments, even though appreciable BSR rates may occur in this lake (see discussion above and Fig. S5), similarly to other sulfate-poor environments due to rapid S cycling (e.g., Vuillemin et al., 2016; Friese et al., 2021). Again, a complete mass balance of these lakes' C fluxes will be required to estimate their net C emission or sequestration behavior.

Although the nature and geochemical signatures of the OM that deposits in the sediments may vary throughout the year, it is interesting to infer from what part(s) of the water column surficial sedimentary OM comes during the stratified seasons. In the three lakes from the SOB, $\delta^{13}C_{SOC}$ and $(C:N)_{SOM}$ signatures of the surficial sedimentary OM lie somewhere between POM signatures from the upper wa-

ter column and from the hypolimnion (Figs. 3, 4). More precisely, in Alchichica, the most surficial $\delta^{13}C_{SOC}$ and $(C:N)_{SOM}$ signatures (-25.7 ‰ and 10.4 ‰, respectively) are much closer to values recorded in the upper water column (~ -26.5 ‰ and 10.5 ‰, respectively), implying that the upper oxygenic photosynthesis production is primarily recorded. It is consistent with previous studies, suggesting that most of the phytoplankton biomass being exported is composed of diatoms (Ardiles et al., 2011). In Lake Atexcac, however, $\delta^{13}C_{SOC}$ and $(C:N)_{SOM}$ signatures (~ -26.8 ‰ and 8, respectively) are closer to values recorded in the hypolimnion (~ -26.5 ‰ and 6.5 ‰, respectively), suggesting that SOM (sedimentary organic matter) records mostly the anaerobic primary production.

In Alberca, surficial $\delta^{13}C_{SOC}$ is markedly more negative (by ~ 2 ‰ to 3 ‰) than the deepest and shallowest water column values (Fig. 4) but close to what is recorded at the redoxcline depth of 17 m. However, the $(C:N)_{SOM}$ values are much higher than what is measured anywhere in the water column, which is consistent with OM remineralization by sulfate-reduction and methanogenesis in the sediments of this lake. Therefore, OM biogeochemical signatures in the surficial sediments of Alberca could be strongly influenced by early diagenesis occurring at the water-sediment interface – despite favorable conditions for OM preservation.

In summary, the OM depositing at the bottom of these stratified lakes does not always record geochemical signatures from the same layers of the water columns and can be modified by very early diagenesis. It does not necessarily record the signatures of primary production by oxygenic photosynthesis from the upper column. For example, in Lake Atexcac, sedimentary OM records primary production by anoxygenic photosynthesis, even though POC concentration is highest in the upper water column. This result highlights the diversity of geochemical signatures that can stem from continental environments despite their geographical, geological, and climatic proximity. A deeper understanding of the OM transfer process from water column to sediment will require more detailed analyses and comparison of the different OM pigments and molecules and could have strong implications for the interpretation of the fossil record in deep anoxic time.

6 Conclusions and summary

The carbon cycles of four stratified alkaline crater lakes were described and compared based on the concentration and isotopic compositions of DIC and POC in the water columns and surficial (~ 10 cm) sedimentary carbonates and organic carbon. Overall our study shows the wide diversity of geochemical signatures found in continental stratified environments despite similar geological and climatic contexts. We identify different regimes of C cycling in the four lakes due to different biogeochemical reactions related to slight environmental and ecological variations. In more detail, we show the following.

- External abiotic factors, such as the hydrological regime and the inorganic C sources in the lakes, control their alkalinity and, thus, the buffering capacity of their waters. In turn, these differences in buffering capacity constrain variations in pH along the stratified water columns, as well as the inorganic C isotope signatures recorded in the water columns and sediments of the lakes. The $\delta^{13}C_{carb}$ reflects the abiotic factors generating the alkalinity gradient, but it is poorly representative of biological processes in lakes with high alkalinity. The external environmental factors further impact the C mass balance of the lakes with probable consequences on their net C-emitting or C-sequestering status.
- Based on POC and DIC concentrations and isotopic compositions, combined with physicochemical parameters, we are able to identify the activity of oxygenic photosynthesis and aerobic respiration in the four lakes studied. Anoxygenic photosynthesis and/or chemoautotrophy are also evidenced in two of the lakes, but their POC and DIC signatures can be equivocal.
- Methanogenesis is evidenced in the surficial sediments of the OM-rich Lake Alberca de los Espinos and influences the geochemical signatures lower in the water column. However, it is recorded only in analyses of porewater dissolved species but not imprinted in the sedimentary archives (OM and carbonates).
- The SOM geochemical signatures of these stratified lakes do not all record the same "biogeochemical layers" of the water column (e.g., anaerobic vs. aerobic metabolisms) and, in some cases, can be greatly modified by early diagenesis.

Data availability. The data are publicly accessible at https://doi.org/10.26022/IEDA/112943 (Havas et al., 2023b).

Supplement. The supplement related to this article is available online at: https://doi.org/10.5194/bg-20-2347-2023-supplement.

Author contributions. RH and CT designed the study in a project directed by PLG, KB, and CT. CT, MI, DJ, DM, RT, PLG, and KB collected the samples in the field. RH carried out the measurements for the C data, DJ carried out the physicochemical parameter probe measurements, and EM provided data for trace and major elements. RH and CT analyzed the data. RH wrote the paper with important contributions from all co-authors.

Competing interests. The contact author has declared that none of the authors has any competing interests.

Acknowledgements. The authors thank Anne-Lise Santoni, Elodie Cognard, Théophile Cocquerez, and the GISMO platform (Biogéosciences, Université Bourgogne Franche-Comté, UMR CNRS 6282, France). We thank Céline Liorzou and Bleuenn Guéguen for the analyses at the Pôle Spectrométrie Océan (Laboratoire Géo-Océan, Brest, France) and Laure Cordier for ion chromatography analyses at IPGP (France). We thank Nelly Assayag and Pierre Cadeau for their help on the AP 2003 at IPGP. We warmly thank Carmela Chateau-Smith for improving the syntax and clarity of the manuscript.

Financial support. This research has been supported by the Agence Nationale de la Recherche (grant no. ANR-18-CE02-0013-02).

Review statement. This paper was edited by Tina Treude and reviewed by two anonymous referees.

References

Adame, M. F., Alcocer, J., and Escobar, E.: Size-fractionated phytoplankton biomass and its implications for the dynamics of an oligotrophic tropical lake, Freshw. Biol., 53, 22–31, https://doi.org/10.1111/j.1365-2427.2007.01864.x, 2008.

Ader, M., Macouin, M., Trindade, R. I. F., Hadrien, M.-H., Yang, Z., Sun, Z., and Besse, J.: A multilayered water column in the Ediacaran Yangtze platform? Insights from carbonate and organic matter paired δ^{13}C, Earth Planet. Sc. Lett., 288, 213–22, https://doi.org/10.1016/j.epsl.2009.09.024, 2009.

Aharon, P.: Redox stratification and anoxia of the early Precambrian oceans: Implications for carbon isotope excursions and oxidation events, Precambrian Res., 173, 207–222, https://doi.org/10.1016/j.precamres.2005.03.008, 2005.

Alcocer, J.: Lake Alchichica Limnology, Springer Nature, https://doi.org/10.1007/978-3-030-79096-7, 2021.

Alcocer, J., Ruiz-Fernández, A. C., Escobar, E., Pérez-Bernal, L. H., Oseguera, L. A., and Ardiles-Gloria, V.: Deposition, burial and sequestration of carbon in an oligotrophic, tropical lake, J. Limnol., 73, 223–235, https://doi.org/10.4081/jlimnol.2014.783, 2014.

Anderson, N. J. and Stedmon, C. A.: The effect of evapoconcentration on dissolved organic carbon concentration and quality in lakes of SW Greenland, Freshw. Biol., 52, 280–289, https://doi.org/10.1111/j.1365-2427.2006.01688.x, 2007.

Ardiles, V., Alcocer, J., Vilaclara, G., Oseguera, L. A., and Velasco, L.: Diatom fluxes in a tropical, oligotrophic lake dominated by large-sized phytoplankton, Hydrobiologia, 679, 77–90, https://doi.org/10.1007/s10750-011-0853-7, 2012.

Armienta, M. A., Vilaclara, G., De la Cruz-Reyna, S., Ramos, S., Ceniceros, N., Cruz, O., Aguayo, A., and Arcega-Cabrera, F.: Water chemistry of lakes related to active and inactive Mexican volcanoes, J. Volcanol. Geotherm. Res., 178, 249–258, https://doi.org/10.1016/j.jvolgeores.2008.06.019, 2008.

Armstrong-Altrin, J. S., Madhavaraju, J., Sial, A. N., Kasper-Zubillaga, J. J., Nagarajan, R., Flores-Castro, K., and Rodríguez, J. L.: Petrography and stable isotope geochemistry of the cretaceous El Abra Limestones (Actopan), Mexico: Implication on diagenesis, J. Geol. Soc. India, 77, 349–359, https://doi.org/10.1007/s12594-011-0042-3, 2011.

Assayag, N., Rivé, K., Ader, M., Jézéquel, D., and Agrinier, P.: Improved method for isotopic and quantitative analysis of dissolved inorganic carbon in natural water samples, Rapid Commun. Mass Spectrom., 20, 2243–2251, https://doi.org/10.1002/rcm.2585, 2006.

Assayag, N., Jézéquel, D., Ader, M., Viollier, E., Michard, G., Prévot, F., and Agrinier, P.: Hydrological budget, carbon sources and biogeochemical processes in Lac Pavin (France): Constraints from δ^{18}O of water and δ^{13}C of dissolved inorganic carbon, Appl. Geochem., 23, 2800–2816, https://doi.org/10.1016/j.apgeochem.2008.04.015, 2008.

Bade, D. L., Carpenter, S. R., Cole, J. J., Hanson, P. C., and Hesslein, R. H.: Controls of δ^{13}C-DIC in lakes: Geochemistry, lake metabolism, and morphometry, Limnol. Oceanogr., 49, 1160–1172, https://doi.org/10.4319/lo.2004.49.4.1160, 2004.

Bekker, A., Holmden, C., Beukes, N. J., Kenig, F., Eglinton, B., and Patterson, W. P.: Fractionation between inorganic and organic carbon during the Lomagundi (2.22–2.1 Ga) carbon isotope excursion, Earth Planet. Sc. Lett., 271, 278–291, https://doi.org/10.1016/j.epsl.2008.04.021, 2008.

Birgel, D., Meister, P., Lundberg, R., Horath, T. D., Bontognali, T. R. R., Bahniuk, A. M., de Rezende, C. E., Vasconcelos, C., and McKenzie, J. A.: Methanogenesis produces strong ^{13}C enrichment in stromatolites of Lagoa Salgada, Brazil: a modern analogue for Palaeo-/Neoproterozoic stromatolites?, Geobiology, 13, 245–266, https://doi.org/10.1111/gbi.12130, 2015.

Briones, E. E., Alcocer, J., Cienfuegos, E., and Morales, P.: Carbon stable isotopes ratios of pelagic and littoral communities in Alchichica crater-lake, Mexico, Int. J. Salt Lake Res., 7, 345–355, https://doi.org/10.1007/BF02442143, 1998.

Buchan, A., LeCleir, G. R., Gulvik, C. A., and González, J. M.: Master recyclers: features and functions of bacteria associated with phytoplankton blooms, Nat. Rev. Microbiol., 12, 686–698, https://doi.org/10.1038/nrmicro3326, 2014.

Cadeau, P., Jézéquel, D., Leboulanger, C., Fouilland, E., Le Floc'h, E., Chaduteau, C., Milesi, V., Guélard, J., Sarazin, G., Katz, A., d'Amore, S., Bernard, C., and Ader, M.: Carbon isotope evidence for large methane emissions to the Proterozoic atmosphere, Sci. Rep., 10, 18186, https://doi.org/10.1038/s41598-020-75100-x, 2020.

Cai, C., Li, K., Liu, D., John, C.M., Wang, D., Fu, B., Fakhraee, M., He, H., Feng, L., and Jiang, L.: Anaerobic oxidation of methane by Mn oxides in sulfate-poor environments, Geology, 49, 761–766, https://doi.org/10.1130/G48553.1, 2021.

Carrasco-Núñez, G., Ort, M. H., and Romero, C.: Evolution and hydrological conditions of a maar volcano (Atexcac crater, Eastern Mexico), J. Volcanol. Geotherm. Res., 159, 179–197, https://doi.org/10.1016/j.jvolgeores.2006.07.001, 2007.

Chako Tchamabé, B., Carrasco-Núñez, G., Miggins, D. P., and Németh, K.: Late Pleistocene to Holocene activity of Alchichica maar volcano, eastern Trans-Mexican

Volcanic Belt, J. South Am. Earth Sci., 97, 102404, https://doi.org/10.1016/j.jsames.2019.102404, 2020.

Cheng, C., Zhang, J., He, Q., Wu, H., Chen, Y., Xie, H., and Pavlostathis, S. G.: Exploring simultaneous nitrous oxide and methane sink in wetland sediments under anoxic conditions, Water Res., 194, 116958, https://doi.org/10.1016/j.watres.2021.116958, 2021.

Close, H. G. and Henderson, L. C.: Open-Ocean Minima in $\delta^{13}C$ Values of Particulate Organic Carbon in the Lower Euphotic Zone, Front. Mar. Sci., 7, 540165, https://doi.org/10.3389/fmars.2020.540165, 2020.

Crowe, S. A., Katsev, S., Leslie, K., Sturm, A., Magen, C., Nomosatryo, S., Pack, M. A., Kessler, J. D., Reeburgh, W. S., Roberts, J. A., González, L., Douglas Haffner, G., Mucci, A., Sundby, B., and Fowle, D. A.: The methane cycle in ferruginous Lake Matano: Methane cycle in ferruginous Lake Matano, Geobiology, 9, 61–78, https://doi.org/10.1111/j.1472-4669.2010.00257.x, 2011.

Dean, W. E. and Gorham, E.: Magnitude and significance of carbon burial in lakes, reservoirs, and peatlands, Geology, 26, 535–538, https://doi.org/10.1130/0091-7613(1998)026<0535:MASOCB>2.3.CO;2, 1998.

Descolas-Gros, C. and Fontungne, M.: Stable carbon isotope fractionation by marine phytoplankton during photosynthesis, Plant Cell Environ., 13, 207–218, https://doi.org/10.1111/j.1365-3040.1990.tb01305.x, 1990.

Duarte, C. M., Prairie, Y. T., Montes, C., Cole, J. J., Striegl, R., Melack, J., and Downing, J. A.: CO_2 emissions from saline lakes: A global estimate of a surprisingly large flux, J. Geophys. Res.-Biogeo., 113, G4, https://doi.org/10.1029/2007JG000637, 2008.

Emrich, K., Ehhalt, D. H., and Vogel, J. C.: Carbon isotope fractionation during the precipitation of calcium carbonate, Earth Planet. Sc. Lett., 8, 363–371, https://doi.org/10.1016/0012-821X(70)90109-3, 1970.

Ferrari, L., Orozco-Esquivel, T., Manea, V., and Manea, M.: The dynamic history of the Trans-Mexican Volcanic Belt and the Mexico subduction zone, Tectonophysics, 522/523, 122–149, https://doi.org/10.1016/j.tecto.2011.09.018, 2012.

Fogel, M. L. and Cifuentes, L. A.: Isotope Fractionation during Primary Production, in: Organic Geochemistry, Topics in Geobiology, edited by: Engel, M. H. and Macko, S. A., Springer US, Boston, MA, 73–98, https://doi.org/10.1007/978-1-4615-2890-6_3, 1993.

Friese, A., Bauer, K., Glombitza, C., Ordoñez, L., Ariztegui, D., Heuer, V.B., Vuillemin, A., Henny, C., Nomosatryo, S., Simister, R., Wagner, D., Bijaksana, S., Vogel, H., Melles, M., Russell, J. M., Crowe, S. A., and Kallmeyer, J.: Organic matter mineralization in modern and ancient ferruginous sediments, Nat. Commun., 12, 2216, https://doi.org/10.1038/s41467-021-22453-0, 2021.

Fry, B.: ^{13}C / ^{12}C fractionation by marine diatoms, Mar. Eco. Prog. Ser., 134, 283–294, https://doi.org/10.3354/meps134283, 1996.

Fry, B., Jannasch, H. W., Molyneaux, S. J., Wirsen, C. O., Muramoto, J. A., and King, S.: Stable isotope studies of the carbon, nitrogen and sulfur cycles in the Black Sea and the Cariaco Trench, Deep-Sea Res., 38, S1003–S1019, https://doi.org/10.1016/S0198-0149(10)80021-4, 1991.

Fulton, J. M., Arthur, M. A., Thomas, B., and Freeman, K. H.: Pigment carbon and nitrogen isotopic signatures in euxinic basins, Geobiology, 16, 429–445, https://doi.org/10.1111/gbi.12285, 2018.

Furian, S., Martins, E. R. C., Parizotto, T. M., Rezende-Filho, A. T., Victoria, R. L., and Barbiero, L.: Chemical diversity and spatial variability in myriad lakes in Nhecolândia in the Pantanal wetlands of Brazil, Limnol. Oceanogr., 58, 2249–2261, https://doi.org/10.4319/lo.2013.58.6.2249, 2013.

Gérard, E., Ménez, B., Couradeau, E., Moreira, D., Benzerara, K., Tavera, R., and López-García, P.: Specific carbonate–microbe interactions in the modern microbialites of Lake Alchichica (Mexico), ISME J., 7, 1997–2009. https://doi.org/10.1038/ismej.2013.81, 2013.

Gonzales-Partida, E., Barragan-R, R. M., and Nieva-G, D.: Analisis geoquimico-isotopico de las especies carbonicas del fluido geotermico de Los Humeros, Puebla, México, Geofis. Int., 32, 299–309, https://doi.org/10.22201/igeof.00167169p.1993.32.2.563, 1993.

Gröger, J., Franke, J., Hamer, K., and Schulz, H. D.: Quantitative Recovery of Elemental Sulfur and Improved Selectivity in a Chromium-Reducible Sulfur Distillation, Geostand. Geoanal. Res., 33, 17–27, https://doi.org/10.1111/j.1751-908X.2009.00922.x, 2009.

Gu, B., Schelske, C. L., and Hodell, D. A.: Extreme ^{13}C enrichments in a shallow hypereutrophic lake: Implications for carbon cycling, Limnol. Oceanogr., 49, 1152–1159, https://doi.org/10.4319/lo.2004.49.4.1152, 2004.

Hassan, K. M.: Isotope geochemistry of Swan Lake Basin in the Nebraska Sandhills, USA: Large ^{13}C enrichment in sediment-calcite records, Geochemistry, 74, 681–690, https://doi.org/10.1016/j.chemer.2014.03.004, 2014.

Havig, J. R., Hamilton, T. L., McCormick, M., McClure, B., Sowers, T., Wegter, B., and Kump, L. R.: Water column and sediment stable carbon isotope biogeochemistry of permanently redox-stratified Fayetteville Green Lake, New York, USA, Limnol. Oceanogr., 63, 570–587, https://doi.org/10.1002/lno.10649, 2018.

Havig, J. R., McCormick, M. L., Hamilton, T. L., and Kump, L. R.: The behavior of biologically important trace elements across the oxic/euxinic transition of meromictic Fayetteville Green Lake, New York, USA, Geochim. Cosmochim. Ac., 165, 389–406, https://doi.org/10.1016/j.gca.2015.06.024, 2015.

Havas, R., Thomazo, C., Iniesto, M., Jézéquel, D., Moreira, D., Tavera, R., Caumartin, J., Muller, E., López-García, P., and Benzerara, K.: The hidden role of dissolved organic carbon in the biogeochemical cycle of carbon in modern redox-stratified lakes, Biogeosciences, in press, 10.5194/egusphere-2023-23, 2023a.

Havas, R., Thomazo, C., Iniesto, M., Jezequel, D., Moreira, D., Tavera, R., Caumartin, J., Muller, E., Lopez Garcia, P., and Benzerara, K.: Carbon isotopes and alkalinity gradient for biogeochemical processes in modern stratified lakes v. 2, Version 1.0., Interdisciplinary Earth Data Alliance (IEDA) [data set], https://doi.org/10.26022/IEDA/112943, 2023b.

Hayes, J. M., Popp, B. N., Takigiku, R., and Johnson, M. W.: An isotopic study of biogeochemical relationships between carbonates and organic carbon in the Greenhorn Formation, Geochim. Cosmochim. Ac., 53, 2961–2972, https://doi.org/10.1016/0016-7037(89)90172-5, 1989.

Hayes, J. M., Strauss, H., and Kaufman, A. J.: The abundance of ^{13}C in marine organic matter and isotopic fractionation in the global biogeochemical cycle of carbon during the past 800 Ma, Chem. Geol., 161, 103–125, https://doi.org/10.1016/S0009-2541(99)00083-2, 1999.

Henkel, J. V., Dellwig, O., Pollehne, F., Herlemann, D. P. R., Leipe, T., and Schulz-Vogt, H. N.: A bacterial isolate from the Black Sea oxidizes sulfide with manganese(IV) oxide, P. Natl. Acad. Sci. USA, 116, 12153–12155, https://doi.org/10.1073/pnas.1906000116, 2019.

Hurley, S. J., Wing, B. A., Jasper, C. E., Hill, N. C., and Cameron, J. C.: Carbon isotope evidence for the global physiology of Proterozoic cyanobacteria, Sci. Adv., 7, eabc8998, https://doi.org/10.1126/sciadv.abc8998, 2021.

Iniesto, M., Moreira, D., Benzerara, K., Muller, E., Bertolino, P., Tavera, R., and López-García, P.: Rapid formation of mature microbialites in Lake Alchichica, Mexico, Environ. Microbiol. Rep., 13, 600–605, https://doi.org/10.1111/1758-2229.12957, 2021a.

Iniesto, M., Moreira, D., Reboul, G., Deschamps, P., Benzerara, K., Bertolino, P., Saghaï, A., Tavera, R., and López-García, P.: Core microbial communities of lacustrine microbialites sampled along an alkalinity gradient, Environ. Microbiol., 23, 51–68, https://doi.org/10.1111/1462-2920.15252, 2021b.

Iniesto, M., Moreira, D., Benzerara, K., Reboul, G., Bertolino, P., Tavera, R., and López-García, P.: Planktonic microbial communities from microbialite-bearing lakes sampled along a salinity-alkalinity gradient, Limnol. Oceanogr. lno., 67, 12233, https://doi.org/10.1002/lno.12233, 2022.

Iñiguez, C., Capó-Bauçà, S., Niinemets, Ü., Stoll, H., Aguiló-Nicolau, P., and Galmés, J.: Evolutionary trends in RuBisCO kinetics and their co-evolution with CO_2 concentrating mechanisms, Plant J., 101, 897–918, https://doi.org/10.1111/tpj.14643, 2020.

Javoy, M., Pineau, F., and Delorme, H.: Carbon and nitrogen isotopes in the mantle, Chem. Geol., 57, 41–62, https://doi.org/10.1016/0009-2541(86)90093-8, 1986.

Jézéquel, D., Michard, G., Viollier, E., Agrinier, P., Albéric, P., Lopes, F., Abril, G., and Bergonzini, L.: Carbon Cycle in a Meromictic Crater Lake: Lake Pavin, France, in: Lake Pavin: History, Geology, Biogeochemistry, and Sedimentology of a Deep Meromictic Maar Lake, edited by: Sime-Ngando, T., Boivin, P., Chapron, E., Jezequel, D., and Meybeck, M., Springer International Publishing, Cham, 185–203, https://doi.org/10.1007/978-3-319-39961-4_11, 2016.

Jiao, N., Herndl, G. J., Hansell, D. A., Benner, R., Kattner, G., Wilhelm, S. W., Kirchman, D. L., Weinbauer, M. G., Luo, T., Chen, F., and Azam, F.: Microbial production of recalcitrant dissolved organic matter: long-term carbon storage in the global ocean, Nat. Rev. Microbiol., 8, 593–599, https://doi.org/10.1038/nrmicro2386, 2010.

Jørgensen, B. B.: Mineralization of organic matter in the sea bed—the role of sulphate reduction, Nature, 296, 643–645, https://doi.org/10.1038/296643a0, 1982.

Karhu, J. A. and Holland, H. D.: Carbon isotopes and the rise of atmospheric oxygen, Geology, 24, 867, https://doi.org/10.1130/0091-7613(1996)024<0867:CIATRO>2.3.CO;2, 1996.

Klawonn, I., Van den Wyngaert, S., Parada, A. E., Arandia-Gorostidi, N., Whitehouse, M. J., Grossart, H.-P., and Dekas, A. E.: Characterizing the "fungal shunt": Parasitic fungi on diatoms affect carbon flow and bacterial communities in aquatic microbial food webs, P. Natl. Acad. Sci. USA, 118, e2102225118, https://doi.org/10.1073/pnas.2102225118, 2021.

Knossow, N., Blonder, B., Eckert, W., Turchyn, A. V., Antler, G., and Kamyshny, A.: Annual sulfur cycle in a warm monomictic lake with sub-millimolar sulfate concentrations, Geochem. Trans., 16, 7, https://doi.org/10.1186/s12932-015-0021-5, 2015.

Krissansen-Totton, J., Buick, R., and Catling, D. C.: A statistical analysis of the carbon isotope record from the Archean to Phanerozoic and implications for the rise of oxygen, Am. J. Sci., 315, 275–316. https://doi.org/10.2475/04.2015.01, 2015.

Kuntz, L. B., Laakso, T. A., Schrag, D. P., and Crowe, S. A.: Modeling the carbon cycle in Lake Matano, Geobiology, 13, 454–461, https://doi.org/10.1111/gbi.12141, 2015.

Lehmann, M. F., Bernasconi, S. M., Barbieri, A., and McKenzie, J. A.: Preservation of organic matter and alteration of its carbon and nitrogen isotope composition during simulated and in situ early sedimentary diagenesis, Geochim. Cosmochim. Ac., 66, 3573–3584, https://doi.org/10.1016/S0016-7037(02)00968-7, 2002.

Lehmann, M. F., Bernasconi, S. M., McKenzie, J. A., Barbieri, A., Simona, M., and Veronesi, M.: Seasonal variation of the δC and δN of particulate and dissolved carbon and nitrogen in Lake Lugano: Constraints on biogeochemical cycling in a eutrophic lake, Limnol. Oceanogr, 49, 415–429. https://doi.org/10.4319/lo.2004.49.2.0415, 2004.

Lelli, M., Kretzschmar, T. G., Cabassi, J., Doveri, M., Sanchez-Avila, J. I., Gherardi, F., Magro, G., and Norelli, F.: Fluid geochemistry of the Los Humeros geothermal field (LHGF – Puebla, Mexico): New constraints for the conceptual model, Geothermics, 90, 101983, https://doi.org/10.1016/j.geothermics.2020.101983, 2021.

Li, H.-C. and Ku, T.-L.: $\delta^{13}C$–$\delta^{18}C$ covariance as a paleohydrological indicator for closed-basin lakes, Palaeogeogr. Palaeocl., 133, 69–80, https://doi.org/10.1016/S0031-0182(96)00153-8, 1997.

Logan, G. A., Hayes, J. M., Hieshima, G. B., and Summons, R. E.: Terminal Proterozoic reorganization of biogeochemical cycles, Nature, 376, 53–56, https://doi.org/10.1038/376053a0, 1995.

Lorenz, V.: On the growth of maars and diatremes and its relevance to the formation of tuff rings, Bull. Volcanol., 48, 265–274. https://doi.org/10.1007/BF01081755, 1986.

Lugo, A., Alcocer, J., Sanchez, M. R., and Escobar, E.: Trophic status of tropical lakes indicated by littoral protozoan assemblages, Internationale Vereinigung für theoretische und angewandte Limnologie: Verhandlungen, 25, 4441–443, https://doi.org/10.1080/03680770.1992.11900159, 1993.

Lugo, A., Alcocer, J., Sánchez, M. del R., Escobar, E., and Macek, M.: Temporal and spatial variation of bacterioplankton abundance in a tropical, warm-monomictic, saline lake: Alchichica, Puebla, Mexico, Internationale Vereinigung für theoretische und angewandte Limnologie: Verhandlungen, 27, 2968–2971, https://doi.org/10.1080/03680770.1998.11898217, 2000.

Lyons, T. W., Reinhard, C. T., and Planavsky, N. J.: The rise of oxygen in Earth's early ocean and atmosphere, Nature, 506, 307–315, https://doi.org/10.1038/nature13068, 2014.

Macek, M., Medina, X. S., Picazo, A., Peštová, D., Reyes, F. B., Hernández, J. R. M., Alcocer, J., Ibarra, M. M.,

and Camacho, A.: Spirostomum teres: A Long Term Study of an Anoxic-Hypolimnion Population Feeding upon Photosynthesizing Microorganisms, Acta Protozool., 59, 13–38, https://doi.org/10.4467/16890027AP.20.002.12158, 2020.

Mason, E., Edmonds, M., and Turchyn, A. V.: Remobilization of crustal carbon may dominate volcanic arc emissions, Science, 357, 290–294, https://doi.org/10.1126/science.aan5049, 2017.

Mendonça, R., Müller, R. A., Clow, D., Verpoorter, C., Raymond, P., Tranvik, L. J., and Sobek, S.: Organic carbon burial in global lakes and reservoirs, Nat. Commun., 8, 1694, https://doi.org/10.1038/s41467-017-01789-6, 2017.

Mercedes-Martín, R., Ayora, C., Tritlla, J., and Sánchez-Román, M.: The hydrochemical evolution of alkaline volcanic lakes: a model to understand the South Atlantic Pre-salt mineral assemblages, Earth-Sci. Rev., 198, 102938, https://doi.org/10.1016/j.earscirev.2019.102938, 2019.

Milesi, V. P., Debure, M., Marty, N. C. M., Capano, M., Jézéquel, D., Steefel, C., Rouchon, V., Albéric, P., Bard, E., Sarazin, G., Guyot, F., Virgone, A., Gaucher, É. C., and Ader, M.: Early Diagenesis of Lacustrine Carbonates in Volcanic Settings: The Role of Magmatic CO_2 (Lake Dziani Dzaha, Mayotte, Indian Ocean), ACS Earth Space Chem., 4, 363–378, https://doi.org/10.1021/acsearthspacechem.9b00279, 2020.

Mook, W. G., Bommerson, J. C., and Staverman, W. H.: Carbon isotope fractionation between dissolved bicarbonate and gaseous carbon dioxide, Earth Planet. Sc. Lett., 22, 169–176, https://doi.org/10.1016/0012-821X(74)90078-8, 1974.

Mulholland, P. J. and Elwood, J. W.: The role of lake and reservoir sediments as sinks in the perturbed global carbon cycle, Tellus A, 34, 490–499, https://doi.org/10.1111/j.2153-3490.1982.tb01837.x, 1982.

O'Leary, M. H.: Carbon Isotopes in Photosynthesis, BioScience, 38, 328–336, https://doi.org/10.2307/1310735, 1988.

Pardue, J. W., Scalan, R. S., Van Baalen, C., and Parker, P. L.: Maximum carbon isotope fractionation in photosynthesis by blue-green algae and a green alga, Geochim. Cosmochim. Ac., 40, 309–312, https://doi.org/10.1016/0016-7037(76)90208-8, 1976.

Peiffer, L., Carrasco-Núñez, G., Mazot, A., Villanueva-Estrada, R. E., Inguaggiato, C., Bernard Romero, R., Rocha Miller, R., and Rojas, J. H.: Soil degassing at the Los Humeros geothermal field (Mexico), J. Volcanol. Geotherm. Res., 356, 163–174, https://doi.org/10.1016/j.jvolgeores.2018.03.001, 2018.

Petrash, D. A., Steenbergen, I. M., Valero, A., Meador, T. B., Paèes, T., and Thomazo, C.: Aqueous system-level processes and prokaryote assemblages in the ferruginous and sulfate-rich bottom waters of a post-mining lake, Biogeosciences, 19, 1723–1751, https://doi.org/10.5194/bg-19-1723-2022, 2022.

Pimenov, N. V., Lunina, O. N., Prusakova, T. S., Rusanov, I. I., and Ivanov, M. V.: Biological fractionation of stable carbon isotopes at the aerobic/anaerobic water interface of meromictic water bodies, Microbiology, 77, 751–759, https://doi.org/10.1134/S0026261708060131, 2008.

Posth, N. R., Bristow, L. A., Cox, R. P., Habicht, K. S., Danza, F., Tonolla, M., Frigaard, N.-U., and Canfield, D. E.: Carbon isotope fractionation by anoxygenic phototrophic bacteria in euxinic Lake Cadagno, Geobiology, 15, 798–816, https://doi.org/10.1111/gbi.12254, 2017.

Rendon-Lopez, M. J.: Limnologia fisica del lago crater los Espinos, Municipio de Jiménez Michoacan, Universidad Michoacana de San Nicolas de Hidalgo, INIRENA-UMSNH, 1–107, 2008.

Ridgwell, A. and Arndt, S.: Chap. 1 – Why Dissolved Organics Matter: DOC in Ancient Oceans and Past Climate Change, in: Biogeochemistry of Marine Dissolved Organic Matter, 2nd Edn., edited by: Hansell, D. A. and Carlson, C. A., Academic Press, Boston, 1–20, https://doi.org/10.1016/B978-0-12-405940-5.00001-7, 2015.

Sackett, W. M., Eckelmann, W. R., Bender, M. L., and Bé, A. W. H.: Temperature Dependence of Carbon Isotope Composition in Marine Plankton and Sediments, Science, 148, 235–237, https://doi.org/10.1126/science.148.3667.235, 1965.

Saghaï, A., Zivanovic, Y., Moreira, D., Benzerara, K., Bertolino, P., Ragon, M., Tavera, R., López-Archilla, A. I., and López-García, P.: Comparative metagenomics unveils functions and genome features of microbialite-associated communities along a depth gradient: Comparative metagenomics of microbialites from Lake Alchichica, Environ. Microbiol., 18, 4990–5004, https://doi.org/10.1111/1462-2920.13456, 2016.

Saini, J.S., Hassler, C., Cable, R., Fourquez, M., Danza, F., Roman, S., Tonolla, M., Storelli, N., Jacquet, S., Zdobnov, E. M., and Duhaime, M. B.: Microbial loop of a Proterozoic ocean analogue, bioRxiv, 2021-08, https://doi.org/10.1101/2021.08.17.456685, 2021.

Satkoski, A. M., Beukes, N. J., Li, W., Beard, B. L., and Johnson, C. M.: A redox-stratified ocean 3.2 billion years ago, Earth Planet. Sc. Lett., 430, 43–53, https://doi.org/10.1016/j.epsl.2015.08.007, 2015.

Schidlowski, M.: Carbon isotopes as biogeochemical recorders of life over 3.8 Ga of Earth history: evolution of a concept, Precambrian Res., 106, 117–134, https://doi.org/10.1016/S0301-9268(00)00128-5, 2001.

Schiff, S. L., Tsuji, J. M., Wu, L., Venkiteswaran, J. J., Molot, L. A., Elgood, R. J., Paterson, M. J., and Neufeld, J. D.: Millions of Boreal Shield Lakes can be used to Probe Archaean Ocean Biogeochemistry, Sci. Rep., 7, 46708, https://doi.org/10.1038/srep46708, 2017.

Siebe, C., Guilbaud, M.-N., Salinas, S., and Chédeville-Monzo, C.: Eruption of Alberca de los Espinos tuff cone causes transgression of Zacapu lake ca. 25,000 yr BP in Michoacán, México, Presented at the IAS 4IMC Conference, Auckland, New Zeland, 74–75, https://www.researchgate.net/publication/283927123 (last access: 8 June 2023), 2012.

Siebe, C., Guilbaud, M.-N., Salinas, S., Kshirsagar, P., Chevrel, M. O., Jiménez, A. H., and Godínez, L.: Monogenetic volcanism of the Michoacán-Guanajuato Volcanic Field: Maar craters of the Zacapu basin and domes, shields, and scoria cones of the Tarascan highlands (Paracho-Paricutin region), Presented at the Pre-meeting field guide for the 5th international Maar Conference, Querétaro, México, 1–37, https://www.researchgate.net/profile/Pooja_Kshirsagar/publication/275951848 (last access: 8 June 2023), 2014.

Sigala, I., Caballero, M., Correa-Metrio, A., Lozano-García, S., Vázquez, G., Pérez, L., and Zawisza, E.: Basic limnology of 30 continental waterbodies of the Transmexican Volcanic Belt across climatic and environmental gradients, Bol. Soc. Geológica Mex., 69, 313–370, https://doi.org/10.18268/BSGM2017v69n2a3, 2017.

Silva Aguilera, R. A.: Análisis del descenso del nivel de agua del Lago Alchichica, Puebla, México (Tesis de Maestría), Universidad Nacional Autónoma de México, Coordinación General de Estudios de Posgrado, UNAM, https://repositorio.unam.mx/contenidos/3534827 (last access: 6 June 2023), 2019.

Sirevag, R., Buchanan, B. B., Berry, J. A., and Troughton, J. H.: Mechanisms of $C0_2$ Fixation in Bacterial Photosynthesis Studied by the Carbon Isotope Fractionation Technique, Arch. Microbiol., 112, 35–38, https://doi.org/10.1007/BF00446651, 1977.

Sobek, S., Durisch-Kaiser, E., Zurbrügg, R., Wongfun, N., Wessels, M., Pasche, N., and Wehrli, B.: Organic carbon burial efficiency in lake sediments controlled by oxygen exposure time and sediment source, Limnol. Oceanogr., 54, 2243–2254, https://doi.org/10.4319/lo.2009.54.6.2243, 2009.

Soetaert, K., Hofmann, A. F., Middelburg, J. J., Meysman, F. J. R., and Greenwood, J.: The effect of biogeochemical processes on pH, Mar. Chem., 105, 30–51, https://doi.org/10.1016/j.marchem.2006.12.012, 2007.

Talbot, M. R.: A review of the palaeohydrological interpretation of carbon and oxygen isotopic ratios in primary lacustrine carbonates, Chem. Geol. Isot. Geosci., Sect. 80, 261–279, https://doi.org/10.1016/0168-9622(90)90009-2, 1990.

Thomas, P. J., Boller, A. J., Satagopan, S., Tabita, F. R., Cavanaugh, C. M., and Scott, K. M.: Isotope discrimination by form IC RubisCO from *Ralstonia eutropha* and *Rhodobacter sphaeroides*, metabolically versatile members of "*Proteobacteria*" from aquatic and soil habitats, Environ. Microbiol., 21, 72–80, https://doi.org/10.1111/1462-2920.14423, 2019.

Ussiri, D. A. N. and Lal, R.: Carbon Sequestration for Climate Change Mitigation and Adaptation, Springer International Publishing, Cham, https://doi.org/10.1007/978-3-319-53845-7, 2017.

Van Mooy, B. A. S., Keil, R. G., and Devol, A. H.: Impact of suboxia on sinking particulate organic carbon: Enhanced carbon flux and preferential degradation of amino acids via denitrification, Geochim. Cosmochim. Ac., 66, 457–465, https://doi.org/10.1016/S0016-7037(01)00787-6, 2002.

van Vliet, D. M., Meijenfeldt, F. A. B., Dutilh, B. E., Villanueva, L., Sinninghe Damsté, J. S., Stams, A. J. M., and Sánchez-Andrea, I.: The bacterial sulfur cycle in expanding dysoxic and euxinic marine waters, Environ. Microbiol., 23, 2834–2857, https://doi.org/10.1111/1462-2920.15265, 2021.

Vilaclara, G., Chávez, M., Lugo, A., González, H., and Gaytán, M.: Comparative description of crater-lakes basic chemistry in Puebla State, Mexico, Internationale Vereinigung für theoretische und angewandte Limnologie: Verhandlungen, 25, 435–440, https://doi.org/10.1080/03680770.1992.11900158, 1993.

Vuillemin, A., Friese, A., Alawi, M., Henny, C., Nomosatryo, S., Wagner, D., Crowe, S. A., and Kallmeyer, J.: Geomicrobiological features of ferruginous sediments from Lake Towuti, Indonesia, Front. Microbiol., 7, 1007, https://doi.org/10.3389/fmicb.2016.01007, 2016.

Wang, S., Yeager, K. M., and Lu, W.: Carbon isotope fractionation in phytoplankton as a potential proxy for pH rather than for $[CO_{2(aq)}]$: Observations from a carbonate lake, Limnol. Oceanogr., 61, 1259–1270, https://doi.org/10.1002/lno.10289, 2016.

Werne, J. P. and Hollander, D. J.: Balancing supply and demand: controls on carbon isotope fractionation in the Cariaco Basin (Venezuela) Younger Dryas to present, Mar. Chem., 92, 275–293, https://doi.org/10.1016/j.marchem.2004.06.031, 2004.

Whiticar, M. J., Faber, E., and Schoell, M.: Biogenic methane formation in marine and freshwater environments: CO_2 reduction vs. acetate fermentation – Isotope evidence, Geochim. Cosmochim. Ac., 50, 693–709, https://doi.org/10.1016/0016-7037(86)90346-7, 1986.

Williams, P. M. and Gordon, L. I.: Carbon-13: carbon-12 ratios in dissolved and particulate organic matter in the sea, Deep-Sea Res. Oceanogr., 17, 19–27, https://doi.org/10.1016/0011-7471(70)90085-9, 1970.

Wittkop, C., Teranes, J., Lubenow, B., and Dean, W. E.: Carbon- and oxygen-stable isotopic signatures of methanogenesis, temperature, and water column stratification in Holocene siderite varves, Chem. Geol., 389, 153–166, https://doi.org/10.1016/j.chemgeo.2014.09.016, 2014.

Zeyen, N., Benzerara, K., Beyssac, O., Daval, D., Muller, E., Thomazo, C., Tavera, R., López-García, P., Moreira, D., and Duprat, E.: Integrative analysis of the mineralogical and chemical composition of modern microbialites from ten Mexican lakes: What do we learn about their formation?, Geochim. Cosmochim. Ac., 305, 148–184, https://doi.org/10.1016/j.gca.2021.04.030, 2021.

Zohary, T., Erez, J., Gophen, M., Berman-Frank, I., and Stiller, M.: Seasonality of stable carbon isotopes within the pelagic food web of Lake Kinneret, Limnol. Oceanogr., 39, 1030–1043, https://doi.org/10.4319/lo.1994.39.5.1030, 1994.

Zyakun, A. M., Lunina, O. N., Prusakova, T. S., Pimenov, N. V., and Ivanov, M. V.: Fractionation of stable carbon isotopes by photoautotrophically growing anoxygenic purple and green sulfur bacteria, Microbiology, 78, 757–768, https://doi.org/10.1134/S0026261709060137, 2009.

Biogeosciences, 20, 2405–2424, 2023
https://doi.org/10.5194/bg-20-2405-2023

Biogeosciences
Open Access
EGU

The hidden role of dissolved organic carbon in the biogeochemical cycle of carbon in modern redox-stratified lakes

Robin Havas[1], Christophe Thomazo[1,2], Miguel Iniesto[3], Didier Jézéquel[4,5], David Moreira[3], Rosaluz Tavera[6], Jeanne Caumartin[7], Elodie Muller[7], Purificación López-García[3], and Karim Benzerara[7]

[1]Biogéosciences, CNRS, Université de Bourgogne Franche-Comté, 21 000 Dijon, France
[2]Institut Universitaire de France, 75005 Paris, France
[3]Ecologie Systématique Evolution, CNRS, Université Paris-Saclay, AgroParisTech, 91190 Gif-sur-Yvette, France
[4]IPGP, CNRS, Université de Paris Cité, 75005 Paris, France
[5]UMR CARRTEL, INRAE and USMB, 74200 Thonon-les-bains, France
[6]Departamento de Ecología y Recursos Naturales, Universidad Nacional Autónoma de México, México City, México
[7]Institut de Minéralogie, de Physique des Matériaux et de Cosmochimie (IMPMC), CNRS, Muséum National d'Histoire Naturelle, Sorbonne Université, 75005 Paris, France

Correspondence: Robin Havas (robin.havas@gmail.com)

Received: 6 January 2023 – Discussion started: 12 January 2023
Revised: 18 April 2023 – Accepted: 25 May 2023 – Published: 23 June 2023

Abstract. The dissolved organic carbon (DOC) reservoir plays a critical role in the C cycle of marine and freshwater environments because of its size and implication in many biogeochemical reactions. Although it is poorly constrained, its importance in ancient Earth's C cycles is also commonly invoked. Yet DOC is rarely quantified and characterized in modern stratified analogues. In this study, we investigated the DOC reservoirs of four redox-stratified alkaline crater lakes in Mexico. We analyzed the concentrations and isotopic compositions of DOC throughout the four water columns and compared them with existing data on dissolved inorganic and particulate organic C reservoirs (DIC and POC). The four lakes have high DOC concentrations with great variability between and within the lakes (averaging 2 ± 4 mM; 1 SD, $n = 28$; i.e., from ~ 15 to 160 times the amount of POC). The $\delta^{13}C_{DOC}$ signatures also span a broad range of values from -29.3 ‰ to -8.7 ‰ (with as much as 12.5 ‰ variation within a single lake). The prominent DOC peaks (up to 21 mM), together with their associated isotopic variability, are interpreted as reflecting oxygenic and/or anoxygenic primary productivity through the release of excess fixed carbon in three of the lakes (Alberca de los Espinos, La Preciosa, and Atexcac). By contrast, the variability of [DOC] and $\delta^{13}C_{DOC}$ in the case of Lake Alchichica is mainly explained by the partial degradation of organic matter and the accumulation of DOC in anoxic waters. The DOC records detailed metabolic functions such as active DIC-uptake and DIC-concentrating mechanisms, which cannot be inferred from DIC and POC analyses alone but which are critical to the understanding of carbon fluxes from the environment to the biomass. Extrapolating our results to the geological record, we suggest that anaerobic oxidation of DOC may have caused the very negative C isotope excursions in the Neoproterozoic. It is, however, unlikely that a large oceanic DOC reservoir could overweigh the entire oceanic DIC reservoir. This study demonstrates how the analysis of DOC in modern systems deepens our understanding of the C cycle in stratified environments and helps to set boundary conditions for the Earth's past oceans.

1 Introduction

Dissolved organic carbon (DOC) is a major constituent of today's marine and freshwater environments (e.g., Ridgwell and Arndt, 2015; Brailsford, 2019). It is an operationally defined fraction of aqueous organic carbon within a continuum of organic molecules spanning a broad range of sizes, compositions, degrees of reactivity, and bioavailability (Kaplan et al., 2008; Hansell, 2013; Beaupré, 2015; Carlson and

Hansell, 2015; Brailsford, 2019). Oceanic DOC is equivalent to the total amount of atmospheric carbon (Jiao et al., 2010; Thornton, 2014) and represents the majority of freshwater organic matter (Kaplan et al., 2008; Brailsford, 2019). The DOC reservoir (i) is at the base of many trophic chains (Bade et al., 2007; Hessen and Anderson, 2008; Jiao et al., 2010; Thornton, 2014), (ii) is key in physiological and ecological equilibria (Hessen and Anderson, 2008), and (iii) plays a critical role in climate change as a long-term C storage reservoir (Jiao et al., 2010; Hansell, 2013; Thornton, 2014; Ridgwell and Arndt, 2015). Although isotopic signatures are a powerful and widespread tool in biogeochemical studies, the use of DOC isotopes has been relatively limited owing to technical difficulties (Cawley et al., 2012; Barber et al., 2017). Radioisotopes or labeled stable isotopes of DOC have been used to date and retrace DOC compounds in diverse aquatic environments (e.g., Repeta and Aluwihare, 2006; Bade et al., 2007; Kaplan et al., 2008; Brailsford, 2019). Studies featuring natural abundances of DOC stable isotope data (i.e., $\delta^{13}C_{DOC}$) mainly used them to discriminate between different source endmembers (e.g., terrestrial vs. autochthonous) (e.g., Cawley et al., 2012; Santinelli et al., 2015; Barber et al., 2017). After a pioneer study by Williams and Gordon (1970), few studies have used natural DOC stable isotope compositions to explore processes intrinsically related to its production and recycling. Recently, Wagner et al. (2020) reaffirmed the utility of stable isotopes to investigate DOC biosynthesis, degradation pathways, and transfer within the food web.

Several studies have suggested a significant role for the DOC reservoir throughout geological time, when it would have been much larger in size and impacted various phenomena, including the regulation of climate and glaciations during the Neoproterozoic (e.g., Peltier et al., 2007), the paleoecology of Ediacaran biota and its early complex life forms (e.g., Sperling et al., 2011), the oxygenation of the ocean through innovations of eukaryotic life near the Neoproterozoic–Cambrian transition (e.g., Lenton and Daines, 2018), and the perturbation of the C cycle recorded in $\delta^{13}C$ sedimentary archives from the Neoproterozoic to the Phanerozoic (e.g., Rothman et al., 2003; Fike et al., 2006; Sexton et al., 2011; Ridgwell and Arndt, 2015).

The contribution of DOC reservoirs to the past and modern Earth's global climate and biogeochemical cycles remains poorly constrained (Jiao et al., 2010; Sperling et al., 2011; Dittmar, 2015; Fakhraee et al., 2021), and the existence and consequences of large ancient oceanic DOC are still debated (e.g., Jiang et al., 2010, 2012; Ridgwell and Arndt, 2015; Li et al., 2017; Fakhraee et al., 2021). Thus, in addition to modeling approaches (e.g., Shi et al., 2017; Fakhraee et al., 2021), the understanding of DOC-related processes in the past anoxic and redox-stratified oceans (Lyons et al., 2014; Havig et al., 2015; Satkoski et al., 2015) should rely on the characterization of DOC dynamics in comparable modern analogues (Sperling et al., 2011). Although many studies have explored the C cycle of modern redox-stratified environments (e.g., Crowe et al., 2011; Kuntz et al., 2015; Posth et al., 2017; Schiff et al., 2017; Havig et al., 2018; Cadeau et al., 2020; Saini et al., 2021; Petrash et al., 2022), very few have analyzed DOC, and even fewer have measured its stable isotope signature (Havig et al., 2018).

In this study, we characterize the DOC reservoir of four modern redox-stratified alkaline crater lakes from the Trans-Mexican Volcanic Belt (Ferrari et al., 2012) and its role within the C cycle of these environments. We report DOC concentration and isotopic composition at multiple depths in the four water columns and discuss these results in the context of physicochemical parameters (temperature, dissolved oxygen, chlorophyll *a*, and nutrient concentrations) and the isotopic composition of dissolved inorganic and particulate organic carbon (DIC, POC), all measured in the same lakes and from the same water samples as in Havas et al. (2023a). The four lakes show distinct water chemistries, along an alkalinity–salinity gradient (Zeyen et al., 2021), with diverse planktonic microbial communities (Iniesto et al., 2022; Havas et al., 2023a). These characteristics allow us to examine the effect of specific environmental and ecological constraints on the production and recycling of DOC in redox-stratified environments. We then present how the analysis of DOC deepens our understanding of the C cycle in these lakes compared to more classical DIC and POC analyses. Finally, the production and fate of the DOC reservoir in these modern analogues is used to discuss the potential role of DOC in past perturbations of the sedimentary C isotope record from the Neoproterozoic and Phanerozoic.

2 Site description

The main characteristics of the geological, climatic, and limnological context of the lakes under study are presented here, but a more detailed description is available in Havas et al. (2023a).

The four lakes are volcanic maars formed after phreatic, magmatic, and phreatomagmatic explosions and are located in the Trans-Mexican Volcanic Belt (TMVB, Fig. 1). The first lake, Alberca de los Espinos, is located at the margin of the Zacapu tectonic lacustrine basin in the Michoacán–Guanajuato Volcanic Field (MGVF) in the western-central part of the TMVB (Fig. 1). The other three (La Preciosa, Atexcac, and Alchichica) are located within the same zone ($\sim 50\,km^2$) of the Serdán-Oriental Basin (SOB) in the easternmost part of the TMVB (Fig. 1). Alberca, with a temperate semi-humid climate, is predominantly underlain by andesitic rocks (Siebe et al., 2012, 2014). By contrast, Alchichica shows much higher evaporation than precipitation rates, reflecting the temperate sub-humid to temperate arid climate experienced by the SOB lakes (Silva-Aguilera et al., 2022). These lakes overlie calcareous and basaltic or andesitic basement rocks (Carrasco-Núñez et al., 2007; Chako Tchamabé et al., 2020).

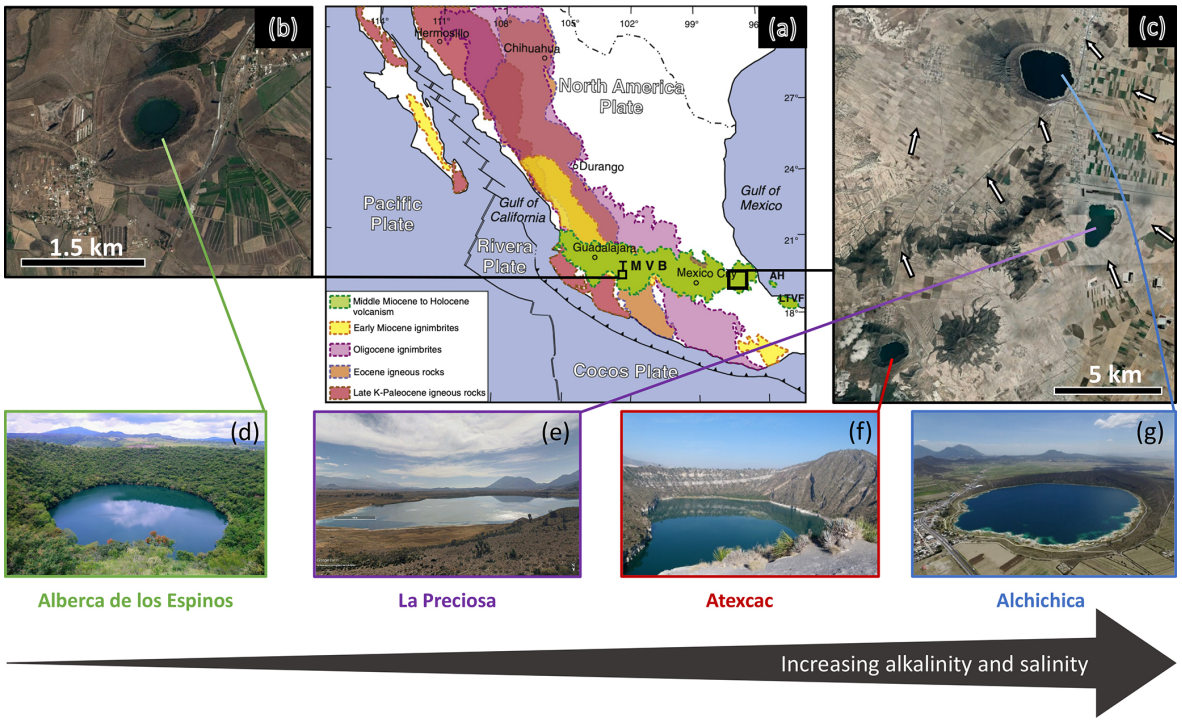

Figure 1. Geographical location and photographs of the four crater lakes. **(a)** Geological map from Ferrari et al. (2012) with black squares showing the location of the four studied lakes within the Trans-Mexican Volcanic Belt (TMVB). **(b, c)** Close-up ©Google Earth views of Alberca de los Espinos and the Serdán-Oriental Basin (SOB). The white arrows represent the approximate groundwater flow path (based on Silva-Aguilera, 2019). **(d–g)** Photographs of the four lakes (panel **d** from ©Google Image ["enamoratedemexicowebsite"] – panel **e** is from ©Google Earth street view, and panel **g** is from ©Agencia Es Imagen). Figure from Havas et al. (2023a).

These variations in geological context and hydrological processes generate a gradient of water chemical compositions, where salinity, alkalinity, and DIC increase in the following order: (i) Lake Alberca, (ii) La Preciosa, (iii) Atexcac, and (iv) Alchichica (Zeyen et al., 2021). The four lakes are alkaline with pH values around 9. Under these conditions, DIC is composed of HCO_3^-/CO_3^{2-} ions with minor amounts of $CO_{2(aq)}$ ($< 0.5\,\%$). This favors the precipitation of microbialite deposits, which are found in the four systems but more abundantly as alkalinity increases (Zeyen et al., 2021).

The four lakes are defined as warm monomictic with anoxic conditions prevailing in the bottom waters during most of the year (i.e., one mixing period per year, during winter; Armienta et al., 2008; Macek et al., 2020; Havas et al., 2023a). They are all closed lakes with no inflow or outflow of surficial waters and are thus fed by rain and groundwater only.

Atexcac is the most oligotrophic of the three SOB lakes (Lugo et al., 1993; Vilaclara et al., 1993; Sigala et al., 2017). Chlorophyll *a* data from May 2019 (Fig. 2), based on mean and maximum value categories (OECD et al., 1982), indicate ultra-oligotrophic conditions for Atexcac (≤ 1 and $2\,\mu g\,L^{-1}$, respectively), oligotrophic conditions for Alchichica (≤ 2 and $6\,\mu g\,L^{-1}$, respectively), intermediate conditions between oligo- and mesotrophic for Alberca (≤ 3 and $4.5\,\mu g\,L^{-1}$, respectively), and low-mesotrophic conditions for La Preciosa (≤ 3 and $9\,\mu g\,L^{-1}$, respectively). Total dissolved P concentrations from May 2019 show similar values for the three SOB lakes close to the surface (increasing in the anoxic zone of Alchichica) but much higher values for Alberca (Havas et al., 2023a). This pattern was observed during previous sampling campaigns (Zeyen et al., 2021). Alberca is surrounded by more vegetation, which could favor the input of nutrients to this lake. La Preciosa and Alberca are thus the least oligotrophic of the four lakes. Importantly, although differences in trophic status exist between the four lakes, they are more oligotrophic than eutrophic.

3 Method

3.1 Sample collection

All samples were collected in May 2019. Samples for DOC analyses were collected at different depths from the surface to the bottom of the water columns, particularly where the physicochemical parameters showed pronounced variation (e.g., at the chemocline and turbidity peaks; Fig. 2 and Table 1). Water samples were collected with a Niskin bottle. For comparison with DIC and POC data, the DOC was analyzed

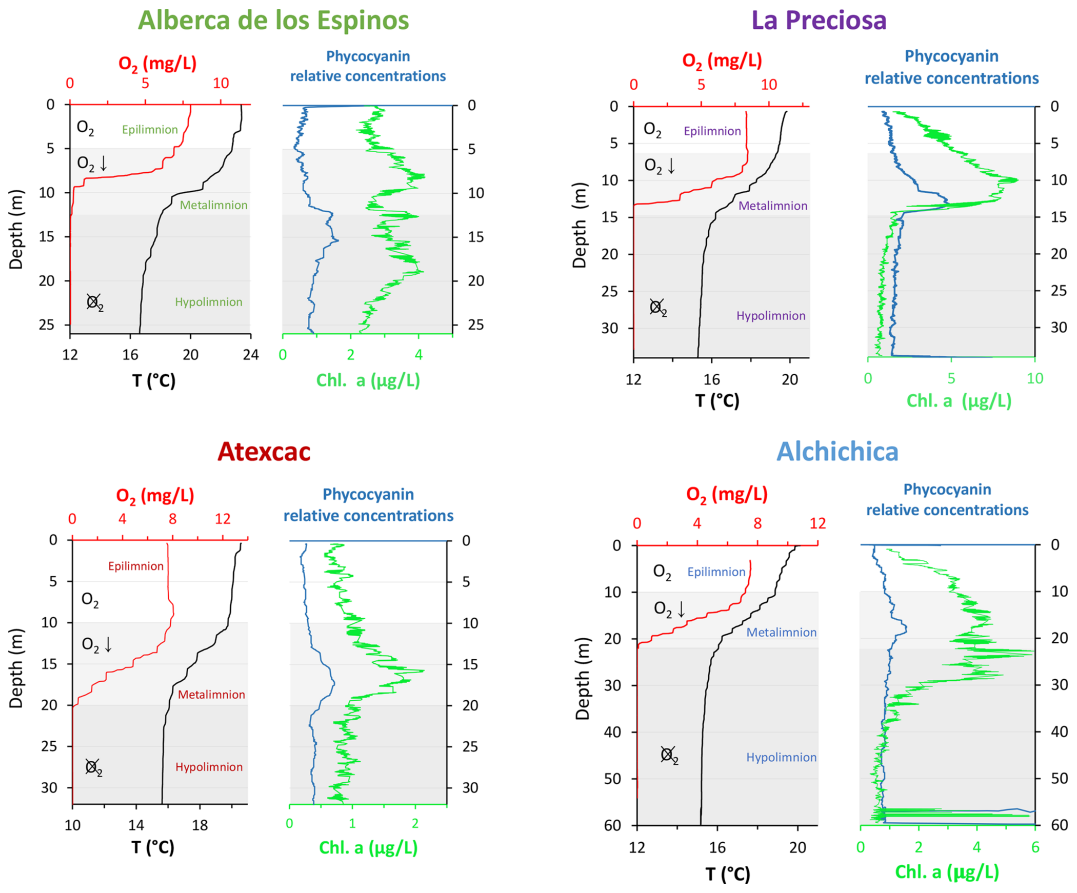

Figure 2. Physicochemical parameter depth profiles of Alberca de los Espinos, La Preciosa, Atexcac, and Alchichica: dissolved oxygen concentration (mg L^{-1}), water temperature (°C), and phycocyanin and chlorophyll *a* pigments (µg L^{-1}). Absolute values for phycocyanin concentrations were not determined; only relative variations are represented (with increasing concentrations to the right). Epi-, meta-, and hypolimnion layers are represented for each lake by the white, gray, and dark-gray areas based on temperature profiles with the metalimnion corresponding to the thermocline. The three layers match the oxygen-rich, intermediate, and oxygen-poor zones, except in La Preciosa). Original data from Havas et al. (2023a).

from the same Niskin sampling as in Havas et al. (2023a), except where indicated (Fig. 4; Tables 1 and 2). Analyses of DOC and major, minor, and trace ions were carried out after water filtration at 0.22 µm, directly in the field with Filtropur S filters pre-rinsed with lake water. Details about the sampling procedure and analysis of the physicochemical parameters, as well as DIC and POC measurements, are reported in Havas et al. (2023a).

3.2 Dissolved organic carbon (DOC) concentration and isotope measurements

Filtered solutions were acidified to a pH of ∼ 1–2 to degas all the DIC and leave DOC as the only C species in the solution. The bulk DOC was analyzed directly from the acidified waters (i.e., all organic C molecules smaller than 0.22 µm). The bulk concentration was measured with a Vario TOC at the Laboratoire Biogéosciences (Dijon), calibrated with a range of potassium hydrogen phthalate (Acros®) solutions. Before isotopic analysis, the DOC concentration of the samples was adjusted to match international standards at 5 ppm (USGS 40 glutamic acid and USGS 62 caffeine). Isotopic compositions were measured at the Laboratoire Biogéosciences using an IsoTOC (Elementar, Hanau, Germany), running under He-continuous flow and coupled with an IsoPrime stable isotope ratio mass spectrometer (IRMS; Isoprime, Manchester, UK). Samples were stirred with a magnetic bar and flushed with He before injection of 1 mL sample aliquots (repeated three times). The DOC was then converted into gaseous CO_2 by combustion at 850 °C, quantitatively oxidized by copper oxide, and separated from other combustion products in a reduction column and a water condenser. This CO_2 was transferred to the IRMS via an open-split device. To avoid a significant memory effect between consecutive analyses, each sample (injected and measured three times) was separated by six injections of deionized water, and the first sample measurement was discarded. Average $\delta^{13}C_{DOC}$ reproducibility was 1.0 ‰ for standards and 0.5 ‰ for sam-

ples (1 SD). The average reproducibility for sample [DOC] measurements was 0.3 mM, and blank tests were below the detection limit.

In addition to DOC measurements, we calculated the total carbon concentration as the sum of DOC, DIC, and POC concentrations, with DIC and POC data from Havas et al. (2023a). The corresponding isotopic composition ($\delta^{13}C_{Total}$) was calculated as the weighted average of the three $\delta^{13}C$. The DIC and POC isotope data were also used to calculate isotopic differences with $\delta^{13}C_{DOC}$, expressed in the $\Delta^{13}C$ notation. The values for $\delta^{13}C_{DIC}$ and $\delta^{13}C_{POC}$ are detailed in Havas et al. (2023a) and summarized in the results section.

4 Results

The water columns of the four lakes were clearly stratified in May 2019 (Fig. 2; Havas et al., 2023a). The epi-, meta-, and hypolimnion layers of each lake were identified based on the thermocline depths and correspond to the oxygen-rich, intermediate, and oxygen-poor layers in the four lakes, although the oxycline in La Preciosa is slightly thinner than the thermocline ($\sim$ 5 vs. 8 m). In the following, DIC, POC, O_2, chlorophyll *a* (Chl *a*), NH_4, P, and $CO_{2(aq)}$ data are also presented.

4.1 Lake Alberca de los Espinos

Bulk DOC had a concentration of $\sim$ 0.4 mM throughout the water column, except at 7 and 17 m, where it peaked at 1.0 and 1.7 mM, respectively (Fig. 3). Its isotopic composition ($\delta^{13}C_{DOC}$) was comprised between -27.2 ‰ and -25.1 ‰, except at 7 m, where it reached -14.7 ‰ (Fig. 3). It represented $\sim$ 8 % of total carbon on average and 93 % of the organic carbon present in the water column. Total C concentration increased downward from about 7 to 9 mM. The $\delta^{13}C_{total}$ decreased from -3.9 ‰ to -7.9 ‰ between 5 and 17 m and then increased to -3.2 ‰ at 25 m (Table 1). The isotopic difference between DOC and DIC ($\Delta^{13}C_{DOC\text{-}DIC}$) was between -21.2 ‰ and -25.2 ‰, except at 7 m depth, where it peaked to -12.4 ‰ (Fig. 4; Table 2). The $\Delta^{13}C_{DOC\text{-}POC}$ values were comprised between -1.5 ‰ and $+3.1$ ‰, except at 7 m depth, where DOC was enriched in ^{13}C by $\sim$ 11.5 ‰ (Fig. 4; Table 2). The DIC concentration and $\delta^{13}C_{DIC}$ averaged 7.5 ± 0.7 mM and -2.9 ± 0.8 ‰; the POC concentration and $\delta^{13}C_{POC}$ averaged 0.04 ± 0.02 mM and -27.1 ± 1.3 ‰. Dissolved oxygen showed a stratified profile with an oxycline layer transitioning from O_2-saturated to O_2-depleted conditions between 5 and 12 m depths (Fig. 2). Chl *a* concentration showed three distinct peaks at $\sim$ 7.5, 12.5, and 17.5 m depths, all reaching $\sim 4\,\mu g\,L^{-1}$ (Fig. 2). The average NH_4^+ and P concentrations were 3.9 and 11.3 µM, respectively. The activity of $CO_{2(aq)}$ was $10^{-5.00}$ at 7 m depth and increased to $10^{-3.40}$ at the bottom of the lake.

4.2 Lake La Preciosa

Bulk DOC had a concentration of $\sim$ 0.5 mM throughout the water column, except at 12.5 m, where it peaked at 1.6 mM. The $\delta^{13}C_{DOC}$ was -25.9 ± 0.4 ‰ throughout the water column, except between 12.5 and 15 m, where it reached -20.0 ‰ (Fig. 3). The DOC represented $\sim$ 3 % of the total carbon on average and 91 % of the organic carbon present in the water column. The total C concentration was relatively stable at $\sim$ 13.8 mM, while $\delta^{13}C_{total}$ was centered around -1 ‰ with a decrease to -2.8 ‰ at 12.5 m (Table 1). The $\Delta^{13}C_{DOC\text{-}DIC}$ values were very stable with depth around -26 ‰ but markedly increased at 12.5 m up to -19.8 ‰ (Fig. 4; Table 2). The $\Delta^{13}C_{DOC\text{-}POC}$ values decreased from ~ 1.3 ‰ in the upper waters to ~ -0.4 ‰ in the bottom waters but showed a peak at $+7.1$ ‰ at a depth of 12.5 m (Fig. 4; Table 2). The DIC concentration and $\delta^{13}C_{DIC}$ averaged 13.0 ± 0.8 mM and -0.2 ± 0.3 ‰; the POC concentration and $\delta^{13}C_{POC}$ averaged 0.05 ± 0.02 mM and -26.1 ± 1.4 ‰. Dissolved oxygen showed a stratified profile with an oxycline layer transitioning from O_2-saturated to O_2-depleted conditions between 8 and 14 m depths (Fig. 2). The Chl *a* concentration showed a large peak at $\sim$ 10 m, reaching $9\,\mu g\,L^{-1}$ (Fig. 2). The average NH_4^+ and P concentrations were 1.9 and 0.2 µM, respectively. The activity of $CO_{2(aq)}$ averaged $10^{-4.57}$.

4.3 Lake Atexcac

Bulk DOC had a concentration of $\sim$ 1.1 mM throughout the water column, except at 16 and 23 m, where it reached 7.7 and 20.8 mM, respectively. The $\delta^{13}C_{DOC}$ increased from -20.0 ‰ to -8.7 ‰ between 5 and 23 m and decreased to -11.2 ‰ at 30 m. It represented about 16 % of the total carbon on average and 98 % of the organic carbon present in the water column. Total C concentrations and $\delta^{13}C_{total}$ are centered around 27.7 mM and -0.6 ‰ with a clear increase to 38.9 mM and a decrease to -2.7 ‰ at 23 m, respectively. The $\Delta^{13}C_{DOC\text{-}DIC}$ values significantly increased from the surface (-20.4 ‰) to the hypolimnion (~ -11.4 ‰). The DOC isotope compositions were strictly and significantly less negative than POC (i.e., enriched in heavy ^{13}C), with $\Delta^{13}C_{DOC\text{-}POC}$ reaching as much as $+17.9$ ‰ at the depth of 23 m (Fig. 4; Table 2). The DIC concentration and $\delta^{13}C_{DIC}$ averaged 25.7 ± 0.9 mM and 0.5 ± 0.3 ‰; the POC concentration and $\delta^{13}C_{POC}$ averaged 0.04 ± 0.02 mM and -27.7 ± 1.1 ‰. Dissolved oxygen showed a stratified profile with an oxycline layer transitioning from O_2-saturated to O_2-depleted conditions between 10 and 20 m depths (Fig. 2). Chl *a* concentration showed a small peak at 16 m, reaching $2\,\mu g\,L^{-1}$ (Fig. 2). The average NH_4^+ and P concentrations were 2.5 and 0.3 µM, respectively. The activity of $CO_{2(aq)}$ averaged $10^{-4.27}$.

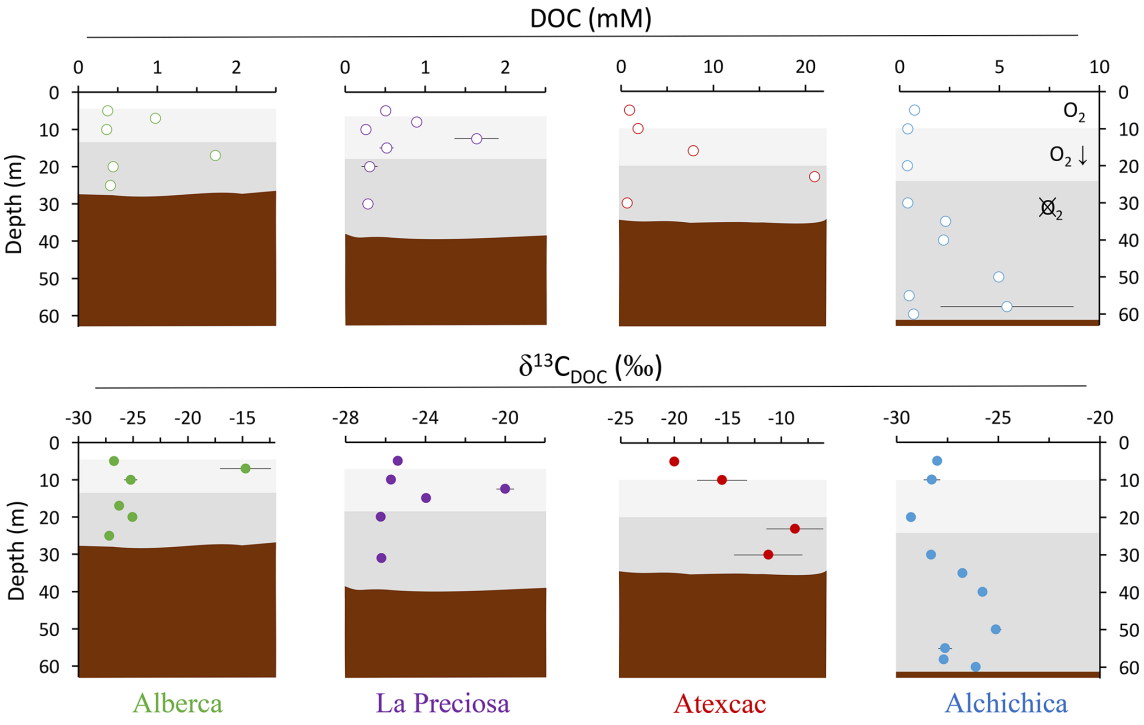

Figure 3. Vertical profiles of concentration and isotopic composition of dissolved organic carbon (DOC) throughout the water columns of the studied lakes: Alberca de los Espinos, La Preciosa, Atexcac, and Alchichica. Concentration is in mmol L^{-1} (mM), and isotopic composition is in ‰ vs. VPDB. The white, gray, and dark-gray shading are as in Fig. 2. The brown shading symbolizes the presence of sediment at the bottom of the water columns (showing the greater water depth in Lake Alchichica).

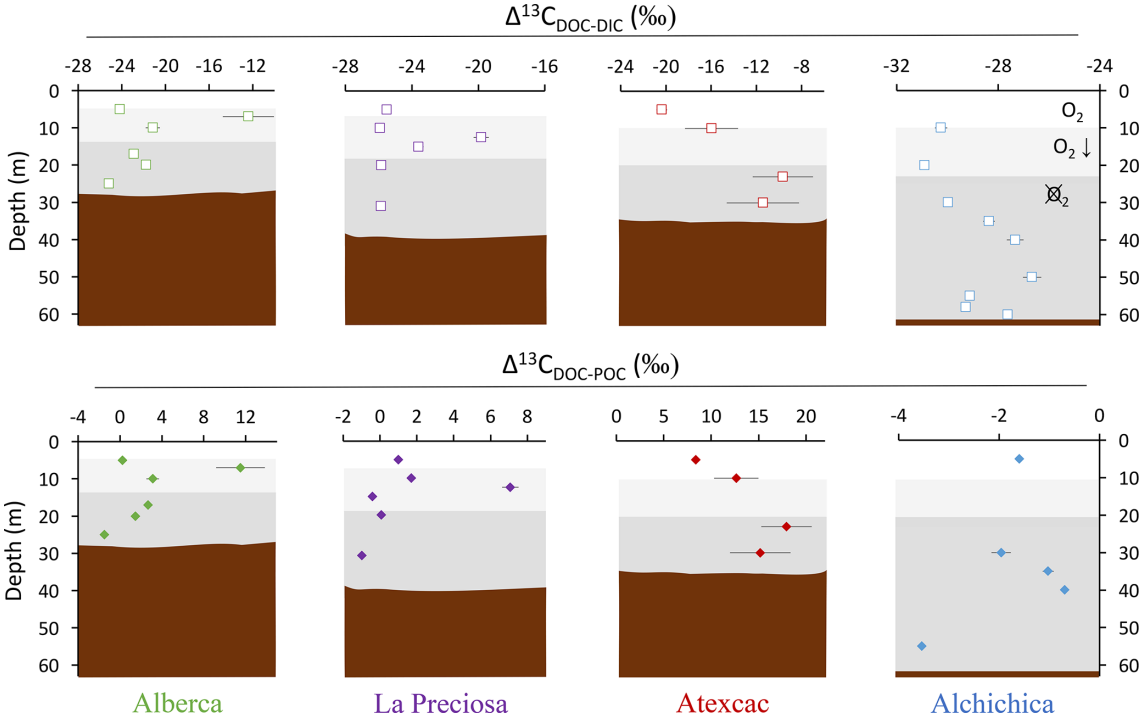

Figure 4. Vertical profiles of the difference in $\delta^{13}C$ values of DOC and DIC (top) and of DOC and POC (bottom) throughout the water columns of the four lakes (all expressed as $\Delta^{13}C$ in ‰ vs. VPDB). POC and DIC data used in these calculations are from Havas et al. (2023a). In Alchichica, $\delta^{13}C_{DOC}$ was not measured at 5 m, and its value at 10 m was used in this calculation of $\Delta^{13}C_{DOC\text{-}POC}$. The white, gray, and dark-gray shading are as in Fig. 2. The brown shading symbolizes the presence of sediment at the bottom of the water columns.

4.4 Lake Alchichica

Bulk DOC had a concentration of ~ 0.5 mM throughout the water column, except in the hypolimnion, where it reached up to 5.4 mM. The $\delta^{13}C_{DOC}$ varied from -29.3 ‰ to -25.1 ‰, with maximum values found in the hypolimnion (Fig. 3). The DOC represented about 5 % of the total carbon on average and 93 % of the organic carbon present in the water column. Total carbon concentration depth profile roughly followed that of DOC, while $\delta^{13}C_{total}$ was between -0.2 ‰ and 1.6 ‰ throughout the water column, except in the lower part of the hypolimnion, where it decreased to -2.3 ‰ (Table 1). The isotopic difference between DOC and DIC ($\Delta^{13}C_{DOC\text{-}DIC}$) was slightly smaller in the hypolimnion and was comprised between -26.7 ‰ and -30.9 ‰. The DOC isotope compositions were more negative than POC, with $\Delta^{13}C_{DOC\text{-}POC}$ values between -0.7 ‰ and -3.5 ‰ (Fig. 4; Table 2). The DIC concentration and $\delta^{13}C_{DIC}$ averaged 34.6 ± 0.6 mM and 1.7 ± 0.2 ‰; the POC concentration and $\delta^{13}C_{POC}$ averaged 0.01 ± 0.04 mM and -25.6 ± 1.0 ‰. Dissolved oxygen showed a stratified profile with an oxycline layer transitioning from O_2-saturated to O_2-depleted conditions between ~ 10 and 20 m depths (Fig. 2). Chl *a* showed a broad peak between ~ 10 and 30 m, averaging $4\,\mu g\,L^{-1}$ and with a narrow maximum of $6\,\mu g\,L^{-1}$ (Fig. 2). The average NH_4^+ and P concentrations were 4.3 and 1.5 µM, respectively. The activity of $CO_{2(aq)}$ averaged $10^{-4.53}$.

5 Discussion

The four Mexican lakes studied here have a high DOC content but very different profiles and signatures for [DOC] and $\delta^{13}C_{DOC}$ (Fig. 3). Evaporation may increase DOC concentration (Anderson and Stedmon, 2007; Zeyen et al., 2021) but would not explain the significant intra-lake DOC variability with depth. It is likely marginal because, in contrast with what was observed for DIC (Havas et al., 2023a), there is no correlation between the average DOC concentration in the Mexican lakes and their salinity ($R^2 = 0.47$, $p = 0.2$ for DOC and $R^2 = 0.93$, $p = 5.8 \times 10^{-5}$ for DIC). In the following discussion, we therefore explore the different patterns of DOC production and fate in relation to other environmental and biological variations and how this can provide information about past DOC-related perturbations of the C cycle.

5.1 Sources and fate of DOC

Due to their endorheic nature, the four lakes receive relatively little allochthonous OM (Alcocer et al., 2014b; Havas et al., 2023a). It is therefore possible to focus on DOC-related processes occurring within the water column, particularly on autochthonous DOC primary production. Autochthonous DOC can form through higher-rank OM degradation processes such as sloppy feeding by zooplankton, UV photolysis, or bacterial and viral cell lysis (Lampert, 1978; Hessen, 1992; Bade et al., 2007; Thornton, 2014; Brailsford, 2019), as well as passive (leakage) or active (exudation) release by healthy cells (e.g., Baines and Pace, 1991; Hessen and Anderson, 2008; Thornton, 2014; Ivanovsky et al., 2020). Generally, this C release (whether active or passive) tends to be enhanced in nutrient-limited conditions because recently fixed C is in excess compared with other essential nutrients such as N or P (Hessen and Anderson, 2008; Morana et al., 2014; Ivanovsky et al., 2020). For oxygenic phototrophs, this is particularly true under high photosynthesis rates because photorespiration bolsters the excretion of DOC (Renstrom-Kellner and Bergman, 1989). Oligotrophic conditions also tend to limit heterotrophic bacterial activity and thus preserve DOC stocks (Thornton, 2014; Dittmar, 2015). Both these production and preservation aspects are consistent with the trend of increasing DOC concentrations observed in the lakes, from the less oligotrophic Alberca and La Preciosa (0.7 mM on average) to the more oligotrophic Alchichica (1.8 mM) and Atexcac (6.5 mM).

5.1.1 DOC release by autotrophs

In the four Mexican lakes, DOC concentration profiles exhibit one or several peaks that occur in both oxic and anoxic waters (Fig. 3). These peaks correlate with Chl *a* peaks in Alberca and La Preciosa, but not in the other two lakes. However, in Atexcac, a remarkable DOC peak (Fig. 3) occurs at the same depth as a peak of anoxygenic photosynthesis (Havas et al., 2023a). These co-occurrences indicate that a large portion of DOC in these three lakes (at least at these depths) arises from the release of photosynthetic C fixed in excess. Phytoplankton in aerobic conditions generally release dissolved organic matter by (i) an active "overflow mechanism" (DOM exudation) or (ii) passive diffusion through the cell membranes, but this remains to be shown for anoxygenic organisms. In the first case, DOM is actively released from the cells as a result of C fixation rates higher than growth and molecular synthesis rates (e.g., Baines and Pace, 1991). Hence, DOM exudation depends not only on the nature of primary producers (different taxa may display very different growth rates, photosynthetic efficiency, and exudation mechanisms) but also on environmental factors such as irradiance and nutrient availability (e.g., Otero and Vincenzini, 2003; Morana et al., 2014; Rao et al., 2021). Exudation of DOM may also serve fitness-promoting purposes such as storage, defense, or mutualistic goals (Bateson and Ward, 1988; Hessen and Anderson, 2008). In the case of passive diffusion, DOM release also depends on cell permeability and the outward DOC gradient but is more directly related to the amount of phytoplankton biomass (e.g., Marañón et al., 2004). Thus, any new photosynthate production drives a steady DOM release rate, independent of environmental conditions to some extent (Marañón et al., 2004; Morana et al., 2014). The fact that Alberca and La Preciosa have lower DOC but Chl *a* concentrations higher than Atexcac and

Table 1. Concentration and isotopic composition of dissolved organic carbon (DOC). Total carbon concentration is the sum of DOC, DIC, and POC reservoirs. For LP 8 m, [DIC] was not measured, and the total carbon concentration was not calculated. The DIC and POC were determined by Havas et al. (2023a). The $\delta^{13}C_{Total}$ is the weighted average of the three $\delta^{13}C$. ND: non-determined.

Lake	Sample	DOC	Total carbon	$\delta^{13}C_{DOC}$	$\delta^{13}C_{Total}$
		mmol L^{-1}		‰	
Alberca de Los Espinos	Albesp 5 m	0.4	7.2	−26.7	−3.9
	Albesp 7 m	1.0	8.1	−14.7	−3.9
	Albesp 10 m	0.4	7.6	−25.2	−5.1
	Albesp 17 m	1.7	9.0	−26.3	−7.9
	Albesp 20 m	0.4	8.4	−25.1	−4.5
	Albesp 25 m	0.4	9.2	−27.2	−3.2
La Preciosa	LP 5 m	0.5	14.0	−25.4	−0.9
	LP 8 m	0.9		ND	ND
	LP 10 m	0.3	13.7	−25.7	−0.4
	LP 12.5 m	1.6	13.2	−20.0	−2.8
	LP 15 m	0.5	13.9	−24.0	−1.3
	LP 20 m	0.3	13.6	−26.2	−1.0
	LP 31 m	0.3	13.6	−26.2	−0.9
Atexcac	ATX 5 m	0.92	27.4	−20.0	−0.4
	ATX 10 m	1.8	28.1	−15.5	−0.7
	ATX 16 m	7.8	34.7	ND	ND
	ATX 23 m	21.0	45.2	−8.7	−3.6
	ATX 30 m	0.7	26.4	−11.2	−0.1
Alchichica	AL 5 m	0.7	35.8	ND	ND
	AL 10 m	0.4	33.5	−28.3	1.6
	AL 20 m	0.4	35.0	−29.3	1.3
	AL 30 m	0.4	35.1	−28.3	1.2
	AL 35 m	2.3	37.2	−26.8	−0.2
	AL 40 m	2.2	37.0	−25.8	−0.1
	AL 50 m	5.0	39.8	−25.1	−1.8
	AL 55 m	0.5	35.3	−27.6	1.1
	AL 58 m	5.4	40.2	−27.7	−2.3
	AL 60 m	0.7	35.3	−26.1	1.0

Alchichica overall suggests that DOC production does not directly relate to phytoplankton biomass and is not passively released. By contrast, active DOC release is supported by DOC isotope signatures. These tropical Mexican lakes correspond precisely to environmental contexts (high irradiance and oligotrophic freshwater bodies) where DOC exudation has been observed and is predicted (e.g., Baines and Pace, 1991; Morana et al., 2014; Thornton, 2014; Rao et al., 2021).

Release of DOC by primary producers can be characterized by the percentage of extracellular release (PER), which corresponds to the fraction of DOC over total (dissolved and particulate) OM primary production (e.g., Thornton, 2014). The PER is highly variable and averages about 13 % of C biomass over a wide range of environments (e.g., Baines and Pace, 1991; Thornton, 2014). Values as high as 99 % have been reported (see Bertilsson and Jones, 2003), showing that most of the fixed C can be released in the external aqueous media as DOC. At depths where oxygenic photosynthesis occurs, the DOC over total OC ratio averages approximately 95 %, 94 %, 99 %, and 85 % for Alberca, La Preciosa, Atexcac, and Alchichica, respectively. Thus, although the PER was not directly measured and some of the measured DOC may correspond to an older long-term DOC reservoir, the majority of DOC measured could represent a recent phytoplankton exudation.

The DOC peaks associated with primary production (mainly photosynthesis) are characterized by very positive $\Delta^{13}C_{DOC\text{-}POC}$ (from +3 ‰ to +18 ‰, Fig. 4). These signatures further support a primary origin of DOC as photosynthate release at these depths rather than a secondary origin by OM degradation. Bacterial heterotrophy would generate smaller and rather negative $\Delta^{13}C_{DOC\text{-}POC}$ (Sect. 5.1.2 and references therein), and cell lysis or zooplankton sloppy feeding would also produce $\delta^{13}C_{DOC}$ close to $\delta^{13}C_{POC}$ values. Photo-degradation is unlikely to proceed at these depths and would not generate such positive fractionations

(Chomicki, 2009). A switch from $CO_{2(aq)}$ to HCO_3^- as an inorganic C source (which differ by 10 ‰, e.g., Mook et al., 1974) would not adequately explain the deviation between $\delta^{13}C_{POC}$ and $\delta^{13}C_{DOC}$. The isotopic enrichment of DOC molecules relative to POC must therefore have a different origin.

The ^{13}C-enriched DOC could originate from photosynthetic organisms using a different C fixation pathway, inducing a smaller isotopic fractionation (provided that these organisms contributed predominantly to the DOC rather than to the POC fraction). In Alberca and Atexcac, anoxygenic phototrophic bacteria may release large amounts of DOC, especially under nutrient-limiting conditions (Ivanovsky et al., 2020). Unlike cyanobacteria or purple sulfur bacteria (PSB, anoxygenic phototrophs belonging to the Proteobacteria), which use the Calvin–Benson–Bassham pathway (CBB), green sulfur bacteria (GSB, another group of anoxygenic phototrophs belonging to the Chlorobi) use the reductive citric acid cycle or reverse tricarboxylic acid (TCA) cycle, which tends to induce smaller isotopic fractionations (between ∼ 3 ‰–13 ‰; Hayes, 2001). The DOC isotope signatures recorded in the hypolimnion of Alberca ($\varepsilon_{DOC\text{-}CO_2} \approx -13.5 \pm 2$ ‰) agree well with fractionations found for this type of organism in laboratory cultures and in stratified water bodies (Posth et al., 2017). By contrast, $\varepsilon_{DOC\text{-}CO_2}$ signatures in the hypolimnion of Atexcac are higher ($\varepsilon_{DOC\text{-}CO_2} \approx 0$ ‰) and thus cannot be explained by the use of the reductive citric acid cycle C fixation pathway. Consistently, GSB were identified in Alberca but not in Atexcac (Havas et al., 2023a).

Phytoplankton blooms may specifically release isotopically heavy organic molecules. Carbohydrates could be preferentially released under nutrient-limiting conditions as they are devoid of N and P (Bertilsson and Jones, 2003; Wetz and Wheeler, 2007; Thornton, 2014). Carbohydrates typically have a ^{13}C-enriched (heavy) isotopic composition (Blair et al., 1985; Jiao et al., 2010; Close and Henderson, 2020). Considering the isotopic mass balance of cell-specific organic compounds, this molecular hypothesis is insufficient to explain the full range of $\Delta^{13}C_{DOC\text{-}POC}$ variations measured in Alberca and Atexcac (Hayes, 2001).

Alternatively, such enrichments require that DOC and DIC first accumulate in the cells. If DOC molecules were released as soon as they were produced, their isotopic composition would tend towards that of the biomass (i.e., $\delta^{13}C_{POC}$, within the range of molecule-specific isotopic compositions), which is not the case. If DIC could freely exchange between inner- and outer-cell media, maximum carboxylation-limited fractionation (between ∼ 18 ‰ and 30 ‰ depending on RuBisCO form; Thomas et al., 2019) would be expressed in all synthesized organic molecules, as represented in Fig. 5a (e.g., O'Leary, 1988; Descolas-Gros and Fontungne, 1990; Fry, 1996). This is also inconsistent with the DOC isotopic signatures (see $\varepsilon_{DOC\text{-}CO_2}$ in Table 2).

Under the environmental conditions of the lakes studied (i.e., low CO_2 relative to HCO_3^-, local planktonic competition for CO_2, and low nutrient availability), the activation of an intracellular DIC-concentrating mechanism (DIC-CM) is expected (Beardall et al., 1982; Burns and Beardall, 1987; Fogel and Cifuentes, 1993; Badger et al., 1998; Iñiguez et al., 2020). This mechanism is particularly relevant in oligotrophic aqueous media (Beardall et al., 1982), where CO_2 diffusion is slower than in the air (O'Leary, 1988; Fogel and Cifuentes, 1993; Iñiguez et al., 2020). A DIC-CM has been proposed to reduce the efflux of DIC from the cells back to the extracellular solution. This internal DIC is eventually converted into organic biomass, thereby drawing the cell isotopic composition closer to that of $\delta^{13}C_{DIC}$ (Fig. 5; Beardall et al., 1982; Fogel and Cifuentes, 1993; Werne and Hollander, 2004). As a conceptual model, we suggest that the activation of a DIC-CM could preserve a large $\Delta^{13}C_{POC\text{-}DIC}$ while generating an apparent fractionation between the DOC and POC molecules. The initially fixed OC would be discriminated against the heavy C isotopes and incorporated into the cellular biomass (Fig. 5c, t_i). In turn, following the overflow mechanism scenario, high photosynthetic rates (due to high irradiance and temperature and high DIC despite low CO_2) coupled with low population growth rates and organic molecule synthesis (due to limited abundances of P, N, and Fe) would result in the exudation of excess organic molecules with heavy $\delta^{13}C_{DOC}$ as they are synthesized from residual internal DIC, which progressively becomes ^{13}C enriched (Fig. 5c, t_{ii}). This process could explain the formation of DOC with δ^{13}C very close to DICand/orCO_2 signatures as observed in Lake Atexcac. This suggests that oligotrophic conditions could be a determinant factor in the generation of significantly heavy $\delta^{13}C_{DOC}$, even more so if they are coupled to high irradiance. This also demonstrates that considerable isotopic variability can exist between these two organic C reservoirs.

In summary, the unusual [DOC] and $\delta^{13}C_{DOC}$ profiles in Alberca, La Preciosa, and Atexcac could be interpreted as mainly reflecting a prominent exudation of autochthonous C, fixed in excess by oxygenic and/or anoxygenic phototrophs in nutrient-poor and high-irradiance conditions. The striking ^{13}C-rich signatures of these exudates are interpreted as reflecting either the activation of a DIC-CM by oxygenic and/or anoxygenic phototrophs or the fixation of C via the reductive citric acid cycle. We propose a conceptual model involving the DIC-CM, whereby oligotrophic and high irradiance contexts can lead to high $\delta^{13}C_{DOC}$ compared to both $\delta^{13}C_{DIC}$ and $\delta^{13}C_{POC}$.

5.1.2 OM partial degradation and DOC accumulation: the case of Lake Alchichica

From the previous discussion, it appears that the environmental conditions of the Mexican lakes favor substantial phytoplankton production of DOC. Alcocer et al. (2014a) proposed that an early-spring cyanobacterial bloom in Lake Alchichica may favor the production of DOC in the epilimnion. How-

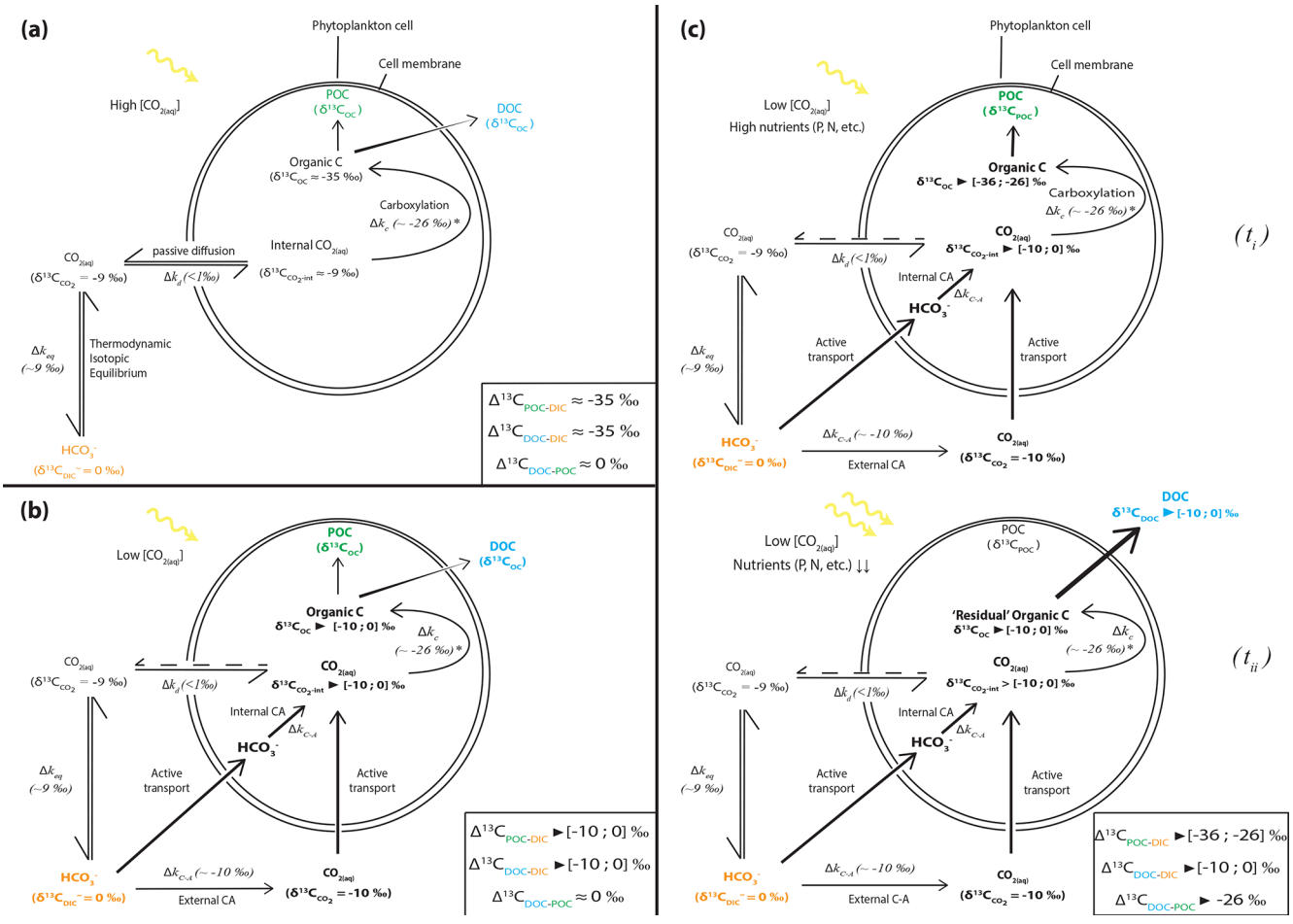

Figure 5. Schematic view of phytoplankton cells during autotrophic C fixation through different C supply strategies and associated apparent isotopic fractionation between DIC and POCorDOC and between DOC and POC. **(a)** Case where $[CO_{2(aq)}]$ is high enough to allow for a DIC supply by passive $CO_{2(aq)}$ diffusion through the cell membrane and where $CO_{2(aq)}$ is at equilibrium with other DIC species. Isotopic fractionation is maximum (minimum $\delta^{13}C_{OC}$) because C fixation is limited by the carboxylation step. DOC is released following an in- to outward cell concentration gradient and has a similar composition to POC. **(b)** Classic view of C isotopic cycling resulting from active DIC transport within the cell because of low ambient $[CO_{2(aq)}]$ (through a DIC-CM). Carbonic anhydrase (CA) catalyzes the conversion between HCO_3 and $CO_{2(aq)}$ inside or outside the cell with isotopic fractionation close to equilibrium fractionation ($\sim 10‰$). While inward passive $CO_{2(aq)}$ diffusion can still occur, the DIC-CM activation reduces the reverse diffusion, resulting in internal $CO_{2(aq)}$ isotopic composition approaching that of the incoming DIC (depending on the fraction of internal $CO_{2(aq)}$ leaving the cell). Acting as a "closed system", most of the internal DIC is fixed as OC, and minimum isotopic fractionation is expressed for both POC and DOC. **(c)** Proposed model for C isotopic fractionation with active DIC transport including isotopic discrimination between POC and DOC. (t_i) Initially fixed C is isotopically depleted and incorporates the cell's biomass as long as there are sufficient nutrients to enable the synthesis of complex organic molecules. (t_{ii}) In low nutrient conditions but with high photosynthetic activity – subsequently, fixed C is released out of the cell as DOC following the overflow hypothesis and inherits heavier isotopic compositions from the residual internal DIC. This leads to distinct POC and DOC isotopic signatures, with small fractionation between DOC and DIC, the amplitude of which will depend on the rate of CO_2 backward diffusion and the ratio of the biomass C (POC) to released C (DOC).

ever, at the time of sampling, the DOC reservoir in this lake was not correlated with any sizable autotrophic activity at any depth. The large epilimnetic Chl *a* peak did not correlate with any changes in [DOC] or $\delta^{13}C_{DOC}$ (Fig. 3). Compared with the other lakes, the geochemical conditions in which Chl *a* was produced in Alchichica may have been incompatible with the activation of a DIC-CM and significant DOC exudation. Alchichica had similar $[CO_{2(aq)}]$ to La Preciosa but higher P and NH_4^+ concentrations (Havas et al., 2023a); Alberca had higher P concentrations but similar $[NH_4^+]$ and lower $[CO_{2(aq)}]$. In contrast with measurements from 2013 (Alcocer et al., 2014a), we found a large increase in DOC in the middle of the anoxic hypolimnion of Alchichica, which did not correspond to any change in the DIC reservoir, unlike

that observed for La Preciosa at 12.5 m and for Atexcac at 23 m (Havas et al., 2023a). At these depths, photosynthetic active radiation (PAR) is below 0.1 % in Alchichica during the stratified season (Macek et al., 2020), which might not be sufficient to trigger major anoxygenic phytoplankton DOC release.

The DOC reservoir in Alchichica is characterized by a $\delta^{13}C_{DOC}$ (and $\Delta^{13}C_{DOC\text{-}DIC}$) lower than in the other lakes, systematically showing ^{13}C-depleted signatures relative to POC (i.e., $\delta^{13}C_{DOC} < \delta^{13}C_{POC}$; Fig. 4). Thus, if the DOC increase in the hypolimnion of Alchichica resulted from the release of photosynthetic OC, as in some of the other lakes, it was not associated with the same C isotope fractionation (e.g., if anoxygenic phototrophs did not concentrate intracellular DIC – cf. Fig. 5a). Some PSB have been identified, but they only become abundant toward the end of the stratification (from July–August to December–January; Alcántara-Hernández et al., 2022; Iniesto et al., 2022).

Alternatively, the hypolimnetic DOC increase in Lake Alchichica may reflect the preservation and accumulation of DOM over the years, consistent with the higher [DOC] measured in 2019 than in the previous years (Alcocer et al., 2014a). While alteration of the DOC reservoir by UV photolysis would induce positive isotopic fractionation (Chomicki, 2009), the slightly negative $\Delta^{13}C_{DOC\text{-}POC}$ signatures support the possibility of DOC being mainly a recalcitrant residue of primary OM degradation by heterotrophic organisms (Alcocer et al., 2014a). The preferential consumption of labile ^{13}C-enriched molecules by heterotrophic bacteria would leave the residual OM with more negative isotopic signatures (Williams and Gordon, 1970; Lehmann et al., 2002; Close and Henderson, 2020). The DIC and POM data were also consistent with heterotrophic activity from the surface to the hypolimnion of Alchichica by recording complementary decreasing and increasing δ^{13}C, respectively, and a decreasing C : N ratio (Havas et al., 2023a). Degradation by heterotrophic bacteria leaves more recalcitrant DOM in the water column, which tends to accumulate over longer periods of time (Ogawa et al., 2001; Jiao et al., 2010; Kawasaki et al., 2013). The DOM content is a balance between production by autotrophs and consumption by heterotrophs, especially in environments where both types of organism compete for low-concentration nutrients (Dittmar, 2015). If the DOC in Alchichica represents a long-term reservoir, its presence might favor the development of bacterial populations. A shift of the cyanobacterial DOC from the epilimnion toward the hypolimnion of Alchichica was described at the end of the spring (Alcocer et al., 2014a, 2022). Thus, part of the hypolimnetic DOC in Alchichica may originate from a phytoplankton release, as observed in the other lakes, but it was already partially degraded by heterotrophic bacteria at the time we sampled it. The deeper and darker anoxic waters of Alchichica could help to better preserve this DOC from intense microbial and light degradation, hence allowing its accumulation over time.

In conclusion, the DOC reservoir in Alchichica (notably in the hypolimnion) more likely represents an older, more evolved DOM pool. The time required for its accumulation and long-term stability has not yet been evaluated.

5.2 DOC analysis provides deeper insights into planktonic cell functioning and water column C cycle dynamics than POC or DIC analyses

The depth profiles of DOC concentration and isotope composition differ significantly from those of POC. Notably, in La Preciosa, the photosynthetic DOC production (+1.5 mM) at the Chl *a* peak depth matches the decrease in DIC (−2 mM), while there was no change in [POC] or $\delta^{13}C_{POC}$ (Havas et al., 2023a). Just below, at 15 m depth, $\delta^{13}C_{POC}$ exhibited a marked increase (+3.6 ‰), interpreted as reflecting heterotrophic activity (Havas et al., 2023a). It is likely explained by the production of DOC with heavier isotope compositions between 12.5 and 15 m depth and its consumption by heterotrophic organisms (as seen with $\Delta^{13}C_{DOC\text{-}POC} \approx 0$). In Alberca, the peaks of oxygenic and anoxygenic photosynthesis clearly stand out from DOC concentrations (+0.5/1.5 mM) but not from POC concentrations ($+ < 0.03$ mM), while the DIC geochemical signatures reflected the influence of OC respiration, sediment-associated methanogenesis, and possible volcanic degassing at the bottom of the lake (Havas et al., 2023a). In Atexcac, anoxygenic photosynthesis is clearly evidenced by [DOC] and $\delta^{13}C_{DOC}$ data (see Sect. 5.1.1) but is not recorded by the POC reservoir (a decrease of 0.03 mM at this depth) and not as distinctively by the DIC reservoir (a decrease of $\sim$ 2 mM; Havas et al., 2023a). It implies that recently fixed OC is quickly released out of the cells as DOC, transferring most C from DIC to DOC rather than POC, which is therefore an incomplete archive of the biogeochemical reactions occurring in water columns. The isotopic analysis of DIC, and by extension of authigenic carbonates, especially in alkaline-buffered waters, might not be sensitive enough to faithfully record all environmental and biological changes.

The $\delta^{13}C_{DOC}$ values recorded in Alberca, La Preciosa, and Atexcac present peculiar heavy signatures, which provide strong constraints on plankton intra-cellular functioning and their use of C. These signatures may arise from the activation of a DIC-CM or from a specific metabolism or C fixation pathway. By contrast, the use of a DIC-CM is poorly captured by $\delta^{13}C_{POC}$, although recognition of active DIC uptake has often been based on this signal (by reduced isotopic fractionation with DIC; e.g., Beardall et al., 1982; Erez et al., 1998; Riebesell et al., 2000). Most interestingly, intra-cellular amorphous Ca carbonates (iACC) are formed in some of the cyanobacteria from Alchichica microbialites, possibly due to supersaturated intra-cell media following active DIC uptake through a DIC-CM (Couradeau et al., 2012; Benzerara et al., 2014). While the link between DIC-CM and iACC still needs to be demonstrated (Benzerara et al., 2014),

Table 2. Isotopic fractionation between DOC and DIC and between DOC and POC, where $\Delta^{13}C_{x-y} = \delta^{13}C_x - \delta^{13}C_y$ is the apparent fractionation and ε is computed as the actual metabolic isotopic discrimination between CO_2 and DOC. In Alchichica, $\delta^{13}C_{DOC}$ was not measured at 5 m, and its value at 10 m was used in this calculation of $\Delta^{13}C_{DOC\text{-}POC}$. The full chemistry at depths 35 and 58 m was not determined; thus, the calculation of $\delta^{13}C_{CO_2}$ for these samples is based on the composition of samples above and below. Isotopic data for DIC, POC, and CO_2 are from Havas et al. (2023a).

Lake	Sample	$\Delta^{13}C_{DOC\text{-}DIC}$	$\Delta^{13}C_{DOC\text{-}POC}$	$\varepsilon_{DOC\text{-}CO_2}$
		‰		‰
Alberca de Los Espinos	Albesp 5 m	−24.2	0.2	−14.8
	Albesp 7 m	−12.4	11.5	−3.0
	Albesp 10 m	−21.2	3.1	−11.6
	Albesp 17 m	−22.9	2.7	−13.1
	Albesp 20 m	−21.8	1.5	−12.2
	Albesp 25 m	−25.2	−1.5	−15.9
La Preciosa	LP 5 m	−25.5	1.0	−15.7
	LP 10 m	−25.9	1.7	−16.0
	LP 12.5 m	−19.8	7.1	−9.8
	LP 15 m	−23.6	−0.4	−13.5
	LP 20 m	−25.8	0.1	−15.7
	LP 31 m	−25.8	−1.0	−15.7
Atexcac	ATX 5 m	−20.4	8.4	−10.6
	ATX 10 m	−16.0	12.6	−6.1
	ATX 23 m	−9.7	17.9	0.6
	ATX 30 m	−11.4	15.2	−1.2
Alchichica	AL 5 m	ND	−1.6	
	AL 10 m	−30.3		−20.1
	AL 20 m	−30.9		−20.5
	AL 30 m	−30.0	−2.0	−19.5
	AL 35 m	−28.4	−1.0	−17.9
	AL 40 m	−27.3	−0.7	−16.8
	AL 50 m	−26.7		−16.2
	AL 55 m	−29.1	−3.5	−18.7
	AL 58 m	−29.3		−18.8
	AL 60 m	−27.6		−17.1

the active use of DIC-CMs in Mexican lakes is independently supported by the DOC isotopic signature.

In summary, the analysis of DOC concentrations and isotope compositions showed that most of the autochthonous C fixation ends up in the DOC reservoir, thus highlighting important features of the lakes and their C cycle that were not evidenced by POC and DIC analyses alone, notably the activation of a DIC-CM and a better description of the planktonic diversity. In the future, it will be interesting to couple the present analyses with deeper molecular and compound-specific isotopic analyses of DOM (Wagner et al., 2020).

5.3 Implications for the hypothesis of a large DOC reservoir controlling past carbon cycling

In these Mexican lakes, the DOC concentrations (from 0.6 to 6.5 mM on average) are between 14 and 160 times higher than the POC concentrations. The DOC represents from 5 % to 16 % of the total C measured in the four lakes. In comparison, it remains under 0.3 mM in large-scale anoxic basins such as the Black Sea (Ducklow et al., 2007). In the modern ocean, DOC is also the main organic pool, but its concentration rarely exceeds 0.08 mM (Hansell, 2013). Thus, the DOC pools of these lakes are much larger than in the modern ocean and can be used to draw comparisons with studies invoking past occurrences of oceanic carbon cycles dominated by vast DOC reservoirs (e.g., Rothman et al., 2003; Sexton et al., 2011).

5.3.1 Eocene carbon isotope excursions (CIEs)

Ventilation and/or oxidation cycles of a large deep-ocean DOC reservoir have been inferred to explain carbonate isotopic records of successive warming events through the Eocene (Sexton et al., 2011). In this scenario, the release of carbon dioxide into the ocean–atmosphere system following

DOC oxidation would trigger both the precipitation of low $\delta^{13}C$ carbonates and an increase of the atmospheric greenhouse gas content. The size of this DOC reservoir should have been at least 1600 PgC (about twice the size of the modern ocean DOC reservoir) to account for a 2–4 °C increase in deep-ocean temperatures (Sexton et al., 2011). However, the main counter-argument to this hypothesis is that the buildup of such a DOC reservoir at modern DOC production rates implies sustained deep-ocean anoxia over several hundred thousand years, while independent geochemical proxies do not support the persistence of such anoxic conditions (Ridgwell and Arndt, 2015). Our study suggests, albeit at a different scale, that this kinetic argument may be weak. In these Mexican lakes, the lowest recorded [DOC] is 260 µM (Table 1), which is about 6 times the deep modern ocean concentration (∼ 45 µM; Hansell, 2013). Yet the entire water columns of these lakes down to the surficial sediments are seasonally mixed with di-oxygen, showing that high [DOC] (notably in Alchichica, which likely harbors a long-term DOC reservoir) can be achieved despite frequent oxidative conditions. The oxidation of only half of the DOC in the lakes would generate average $\delta^{13}C_{DIC}$ deviations between −0.6 ‰ and −1 ‰, corresponding to the C isotope excursion magnitudes described by Sexton et al. (2011).

Similarly, deep anoxic waters in the Black Sea hold about 3 times the amount of DOC found in the modern deep open ocean (Ducklow et al., 2007; Sexton et al., 2011; Dittmar, 2015). In the Black Sea and in the Mexican lakes, low nutrient availability may limit sulfate-reduction despite high sulfate and labile organic matter concentrations, thus favoring DOM preservation and accumulation (Dittmar, 2015, and references therein). Margolin et al. (2016) argued that substantial DOM is maintained in the Black Sea by large terrigenous inputs only. Our study attests to the possibility for "autochthonous systems" to reach DOC concentrations well above what is found in the Black Sea without requiring terrigenous inputs. Therefore, it supports the hypothesis that the buildup of a large DOC reservoir may have influenced the carbonate isotopic record of Eocene warming events. Nonetheless, it remains to be proven how this could apply to larger oceanic-type basins, with more variable environmental conditions (e.g., tropical vs. polar latitudes), greater diversity of eukaryotic heterotrophs (in Phanerozoic oceans), and more-active water currents and ventilation processes. A better characterization of the molecular composition of DOM in the Mexican lakes will help us understand how it can accumulate over time and refine the suggested analogy with Phanerozoic carbon isotope excursions (CIEs). Furthermore, investigating the paleo-ecology and paleo-geography of the CIE time period will also help to constrain the potential applicability of a large DOC hypothesis (Sexton et al., 2011).

5.3.2 Neoproterozoic carbon isotope excursions (CIEs)

The presence of a large oceanic DOC reservoir has also been used to account for the Neoproterozoic C isotope record, where carbonates show $\delta^{13}C$ negative excursions of more than 10 ‰ over tens of millions of years (Rothman et al., 2003; Fike et al., 2006; Swanson-Hysell et al., 2010; Tziperman et al., 2011). Once again, this hypothesis has been questioned because of (i) the oversized DOC reservoir (10 times the contemporaneous DIC, i.e., 10^2 to 10^3 times that of modern DOC) and (ii) the amount of oxidants required to generate such a sustained DOC oxidation process (see Ridgwell and Arndt, 2015). Recent studies offered potential explanations for this latter issue, showing that pulses of continental weathering and an associated increase of sulfate supply would have provided sufficient oxidants (Shields et al., 2019; Chen et al., 2022), while lateral heterogeneity of the carbonate geochemical signatures – with a restricted record of the CIEs on the continental shelves – would require lower amounts of oxidants (Li et al., 2017; Shi et al., 2017).

Critically though, direct evidence for the existence of such high oceanic DOC levels in the past remains scarce (Li et al., 2017), although multiple studies have built on the Neoproterozoic large-DOC scenario (e.g., Sperling et al., 2011; Cañadas et al., 2022). Purported high oceanic DOC concentrations during the Ediacaran period have been estimated from the Ge/Si ratio of diagenetic chert nodules (Xing et al., 2022), but they reflect the sediment porewater geochemistry and remain difficult to directly relate to the ocean water itself. Besides, some modeling approaches have suggested that DOC abundance in the past Earth's oceans could not have markedly differed from today's values (Fakhraee et al., 2021).

Modern analogous systems such as the Black Sea or Mexican lakes studied here support the possibility of greater DOC accumulation in anoxic waters (Ducklow et al., 2007) but only to levels substantially lower than those required to account for the Neoproterozoic CIEs (minimum concentrations estimated between 25 and 100 mM; Ridgwell and Arndt, 2015). One could argue that the development of larger DOC pools in the three Mexican lakes from the SOB is hindered by relatively large sulfate reservoirs (especially in Alchichica – ∼ 10 mM). However, we notice that Alberca does not show a larger DOC reservoir despite having the lowest oxidant availability (both oxygen- and sulfate-free at depth) and being the only one of the four lakes to present isotopic signatures associated with methanogenesis (Havas et al., 2023a). Furthermore, the Mexican lakes are seasonally oxidized, which could consume part of their DOC reservoir. However, the Black Sea is permanently stratified and shows even lower [DOC], suggesting that DOC production might be the primary control on DOC concentration over DOC oxidation. The processes of DOC production and accumulation in the Neoproterozoic ocean could have been less efficient than today (Fakhraee et al., 2021). Nonetheless, an important limit

to the analogy between modern analogues and the Precambrian oceans is the difference in the time over which DOC could have accumulated in both environments (Ridgwell and Arndt, 2015). One could expect the formation of such a large autochthonous DOC reservoir to increase the ocean inorganic C isotope composition by mass balance. However, from $\delta^{13}C_{Carb}$ data compilation (e.g., Fike et al., 2006; Saltzman and Thomas, 2012; Li et al., 2017), we see that there are no positive increases of $\delta^{13}C_{Carb}$ at the magnitude of the negative CIEs tens to hundreds of millions of years before the Neoproterozoic CIEs. Thus, even if the oxidant paradox may have found satisfactory explanations, the origin of the massive DOC reservoir required to generate these excursions still remains to be elucidated (Jiang et al., 2010; Lu et al., 2013; Li et al., 2017).

In the alkaline lakes studied, oxidation of the DOC reservoir would generate a maximum $\delta^{13}C_{DIC}$ deviation of -2 ‰ in Alberca de los Espinos, which has the lowest alkalinity. The other lakes' $\delta^{13}C_{DIC}$ values are less impacted, notably because they are largely buffered by high DIC content (Havas et al., 2023a). Bade et al. (2004) showed that modern low-alkalinity and/or low-pH lakes generally show more negative $\delta^{13}C_{DIC}$ (down to ~ -30 ‰), partly due to a higher responsiveness of the $\delta^{13}C_{DIC}$ to remineralization of OM and especially DOC. Compiling our data with that of Bade et al. (2004), we consistently show a clear negative trend of $\delta^{13}C_{DIC}$ with an increasing DOC : DIC ratio over a broad range of lacustrine DOC and DIC concentrations (Fig. 6). This trend also matches modern ocean values (Fig. 6). These observations are consistent with the inference that systems where DOC : DIC $\gg 1$ should drive $\delta^{13}C_{DIC}$ to very negative values (Rothman et al., 2003). However, in modern environments, the biomass is largely influenced by aerobic heterotrophs, and high DOC : DIC waters usually lean toward acidic pH values (Fig. 6; Bade et al., 2004), at which carbonate precipitation is prevented. Instead, in anoxic waters, remineralization of OM through sulfate or iron reduction generates alkalinity (e.g., Tziperman et al., 2011). Hence, environmental conditions where DOC : DIC $\gg 1$ might be inconsistent with large carbonate deposits unless they are associated with anaerobic remineralization. This further supports the hypothesis that negative $\delta^{13}C_{Carb}$ excursions of the Ediacaran were triggered by continental sulfate addition to the ocean (Li et al., 2017; Shields et al., 2019; Chen et al., 2022) but following the oxidation of DOC by anaerobic (e.g., sulfate reduction) rather than aerobic (e.g., by free oxygen) pathways. At the same time, additional DOC inputs (e.g., terrigenous) might be necessary to reach the required high DOC conditions allowing the Neoproterozoic CIEs. This echoes previous suggestions of "Neoproterozoic greening", referring to a phase of biological land colonization, although evidence for this phenomenon currently remains equivocal (Lenton and Daines, 2017). While a concomitant supply of sulfate and DOC via rivers may cause a partial oxidation of

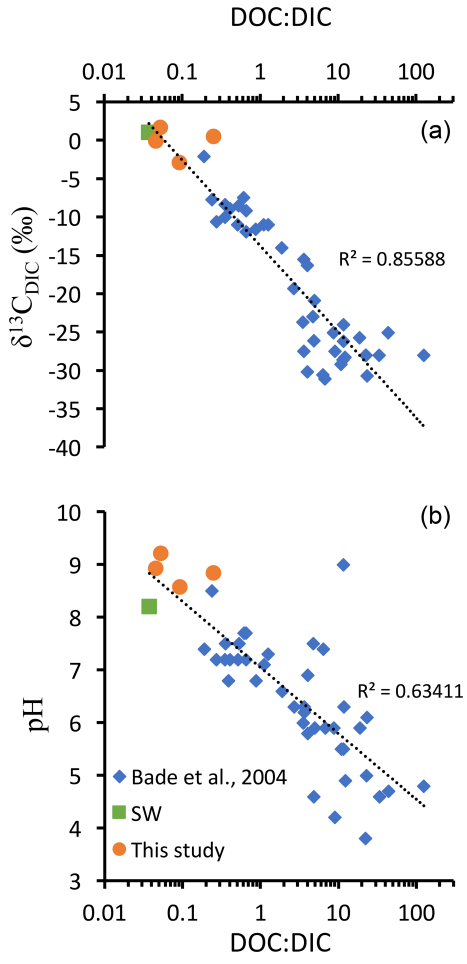

Figure 6. DOC : DIC ratios, pH, and $\delta^{13}C_{DIC}$ values from different lakes compiled from Bade et al. (2004) and the four Mexican lakes from Havas et al. (2023a), as well as modern surface ocean values (from Kroopnick, 1985; Zeebe and Wolf-Gladrow, 2009; and Hansell, 2013). **(a)** $\delta^{13}C_{DIC}$ as a function of DOC : DIC ratio represented with a logarithmic abscissa scale and logarithmic trend line which combines the three datasets. **(b)** pH as a function of DOC : DIC ratio, with a logarithmic abscissa scale and logarithmic trend line which combines the three datasets.

DOC at least, it would still result in a ^{13}C-depleted source of alkalinity to the coastal environments.

The inferences from Fig. 6 also foster the scenario proposed by Tziperman et al. (2011), where the anaerobic respiration of large DOM production leads to the sequestration of newly produced C in carbonates – with very negative $\delta^{13}C$ – and thereby to the drawdown of atmospheric pCO_2 and the initiation of Cryogenian glaciations. We therefore suggest that the climatic feedbacks associated with the negative Neoproterozoic CIEs have been controlled by the total amount and balance between different DOC sources (autochthonous vs. allochthonous) and different oxidation pathways (e.g., via O_2 vs. SO_4^{2-}).

In summary, Neoproterozoic carbonate carbon isotope excursions likely require DOC and DIC pools to be spatially decoupled (e.g., through terrestrial DOM inputs), which suggests that DOC was not necessarily larger than DIC in the entire ocean. The analogues studied here further support that the Neoproterozoic CIEs recorded in carbonates should have occurred following DOC oxidation through anaerobic rather than aerobic pathways.

6 Conclusions and summary

Based on its concentration and isotopic signatures, we characterized the nature and role of the DOC reservoir within the C cycle of four stratified alkaline crater lakes in comparison with previously described DIC and POC data. Despite similar contexts, the DOC reservoirs of the four lakes show considerable variability, driven by environmental and ecological differences, as summarized below.

The DOC is the largest OC reservoir in the water column of the studied lakes ($> 90\,\%$). Its concentration and isotopic composition provide novel information about the C cycle of these stratified water bodies. In each of the four lakes, diverse photosynthetic planktonic communities release greater or smaller amounts of DOC, depending strongly on environmental factors such as nutrient and DIC availability, and transfer most of the inorganic C to DOC rather than POC.

This process is marked by very heavy and distinct isotopic signatures of DOC compared with POC. They reflect different metabolism and C fixation pathways and/or the activity of a DIC-CM coupled with an overflow mechanism (i.e., DOM exudation), which could be active for both oxygenic and anoxygenic phototrophs and for which we propose a novel isotopic model of cell carbon cycling, integrating DOC molecules.

The DOC reservoir in one of the lakes was not characterized by this release process but rather by partial degradation and accumulation in anoxic waters, associated with more negative isotopic signatures.

Our results bring further constraints to the environmental conditions under which autochthonous DOM can accumulate in anoxic water bodies, providing boundary conditions to the large DOC reservoir scenarios. This study of modern redox-stratified analogues supports the idea that a large oceanic DOC reservoir may have generated the record of successive C isotope excursions during the Eocene. Our study suggests, however, that the Neoproterozoic large-DOC hypothesis and its record in carbonates as negative CIEs would only have been possible if external DOC sources largely contributed and if DOC oxidation occurred via anaerobic pathways.

Data availability. Data are publicly accessible at https://doi.org/10.26022/IEDA/112943 (Havas et al., 2023b).

Author contributions. RH and CT designed the study in a project directed by PLG, KB, and CT. CT, MI, DJ, DM, RT, PLG, and KB collected the samples in the field. RH carried out the measurements for C data, DJ carried out the physicochemical parameter probe measurements, and EM provided data for trace and major elements. RH and CT analyzed the data. RH wrote the paper with important contributions from all the co-authors.

Competing interests. The contact author has declared that none of the authors has any competing interests.

Disclaimer. Publisher's note: Copernicus Publications remains neutral with regard to jurisdictional claims in published maps and institutional affiliations.

Acknowledgements. The authors thank Anne-Lise Santoni, Elodie Cognard, Théophile Cocquerez, and the GISMO platform (Biogéosciences, University Bourgogne Franche-Comté, UMR CNRS 6282, France). We thank Céline Liorzou and Bleuenn Guéguen for the analyses at the Pôle Spectrométrie Océan (Laboratoire Géo-Océan, Brest, France) and Laure Cordier for the ion chromatography analyses at IPGP (France). We thank Nelly Assayag and Pierre Cadeau for their help on the AP 2003 at IPGP. We warmly thank Carmela Chateau-Smith for improving the syntax and clarity of the paper.

Financial support. This research has been supported by the Agence Nationale de la Recherche (grant no. ANR-18-CE02-0013-02).

Review statement. This paper was edited by Tina Treude and reviewed by three anonymous referees.

References

Alcántara-Hernández, R. J., Macek, M., Torres-Huesca, J., Arellano-Posadas, J., and Valdespino-Castillo, P. M.: Bacterioplankton, in: Lake Alchichica Limnology: The Uniqueness of a Tropical Maar Lake, edited by: Alcocer, J., Springer International Publishing, Cham, 183–196, https://doi.org/10.1007/978-3-030-79096-7_11, 2022.

Alcocer, J., Guzmán-Arias, A., Oseguera, L. A., and Escobar, E.: Dinámica del carbono orgánico disuelto y particulado asociados al florecimiento de Nodularia spumigena en un lago tropical oligotrófico, in: n Estado Actual del Conocimiento del Ciclo del Carbono y sus Interacciones en México: Sintesis a 2014, edited by: Paz, F. and Wong, J., Programma Mexicano del Carbono, 404–410, 2014a.

Alcocer, J., Ruiz-Fernández, A. C., Escobar, E., Pérez-Bernal, L. H., Oseguera, L. A., and Ardiles-Gloria, V.: Deposition, burial and sequestration of carbon in an oligotrophic, tropical lake, J. Limnol., 73, 223–235, https://doi.org/10.4081/jlimnol.2014.783, 2014b.

Alcocer, J., Merino-Ibarra, M., Ramírez-Zierold, J. A., Oseguera, L. A., Cortés-Guzmán, D., Castillo-Sandoval, F. S., Guzmán-Arias, A. P., and Pérez-Ramírez, M. G.: Physicochemical Characteristics, in: Lake Alchichica Limnology: The Uniqueness of a Tropical Maar Lake, 101–142, Cham, Springer International Publishing, https://doi.org/10.1007/978-3-030-79096-7_7, 2022.

Anderson, N. J. and Stedmon, C. A.: The effect of evapoconcentration on dissolved organic carbon concentration and quality in lakes of SW Greenland, Freshwater Biol., 52, 280–289, https://doi.org/10.1111/j.1365-2427.2006.01688.x, 2007.

Armienta, M. A., Vilaclara, G., De la Cruz-Reyna, S., Ramos, S., Ceniceros, N., Cruz, O., Aguayo, A., and Arcega-Cabrera, F.: Water chemistry of lakes related to active and inactive Mexican volcanoes, J. Volcanol. Geoth. Res., 178, 249–258, https://doi.org/10.1016/j.jvolgeores.2008.06.019, 2008.

Bade, D. L., Carpenter, S. R., Cole, J. J., Hanson, P. C., and Hesslein, R. H.: Controls of δ^{13}C-DIC in lakes: Geochemistry, lake metabolism, and morphometry, Limnol. Oceanogr., 49, 1160–1172, https://doi.org/10.4319/lo.2004.49.4.1160, 2004.

Bade, D. L., Carpenter, S. R., Cole, J. J., Pace, M. L., Kritzberg, E., Van de Bogert, M. C., Cory, R. M., and McKnight, D. M.: Sources and fates of dissolved organic carbon in lakes as determined by whole-lake carbon isotope additions, Biogeochemistry, 84, 115–129, https://doi.org/10.1007/s10533-006-9013-y, 2007.

Badger, M. R., Andrews, T. J., Whitney, S. M., Ludwig, M., Yellowlees, D. C., Leggat, W., and Price, G. D.: The diversity and coevolution of Rubisco, plastids, pyrenoids, and chloroplast-based CO_2-concentrating mechanisms in algae, Can. J. Botany, 76, 1052–1071, https://doi.org/10.1139/b98-074, 1998.

Baines, S. B. and Pace, M. L.: The production of dissolved organic matter by phytoplankton and its importance to bacteria: Patterns across marine and freshwater systems, Limnol. Oceanogr., 36, 1078–1090, https://doi.org/10.4319/lo.1991.36.6.1078, 1991.

Barber, A., Sirois, M., Chaillou, G., and Gélinas, Y.: Stable isotope analysis of dissolved organic carbon in Canada's eastern coastal waters: Stable isotope analysis of DOC, Limnol. Oceanogr., 62, S71–S84, https://doi.org/10.1002/lno.10666, 2017.

Bateson, M. M. and Ward, D. M.: Photoexcretion and Fate of Glycolate in a Hot Spring Cyanobacterial Mat, Appl. Environ. Microb., 54, 1738–1743, https://doi.org/10.1128/aem.54.7.1738-1743.1988, 1988.

Beardall, J., Griffiths, H., and Raven, J. A.: Carbon Isotope Discrimination and the CO_2 Accumulating Mechanism in Chlorella emersonii, J. Exp. Bot., 33, 729–737, https://doi.org/10.1093/jxb/33.4.729, 1982.

Beaupré, S. R.: The Carbon Isotopic Composition of Marine DOC, in: Biogeochemistry of Marine Dissolved Organic Matter, edited by: Hansell, D. A. and Carlson, C. A., Elsevier, 335–368, https://doi.org/10.1016/B978-0-12-405940-5.00006-6, 2015.

Benzerara, K., Skouri-Panet, F., Li, J., Férard, C., Gugger, M., Laurent, T., Couradeau, E., Ragon, M., Cosmidis, J., Menguy, N., Margaret-Oliver, I., Tavera, R., López-García, P., and Moreira, D.: Intracellular Ca-carbonate biomineralization is widespread in cyanobacteria, P. Natl. Acad. Sci. USA, 111, 10933–10938, https://doi.org/10.1073/pnas.1403510111, 2014.

Bertilsson, S. and Jones, J. B.: Supply of Dissolved Organic Matter to Aquatic Ecosystems: Autochthonous Sources, in: Aquatic Ecosystems, Aquatic Ecology, edited by: Findlay, S. E. G. and Sinsabaugh, R. L., Academic Press, Burlington, 3–24, https://doi.org/10.1016/B978-012256371-3/50002-0, 2003.

Blair, N., Leu, A., Muñoz, E., Olsen, J., Kwong, E., and Des Marais, D.: Carbon isotopic fractionation in heterotrophic microbial metabolism, Appl. Environ. Microb., 50, 996–1001, https://doi.org/10.1128/aem.50.4.996-1001.1985, 1985.

Brailsford, F. L.: Dissolved organic matter (DOM) in freshwater ecosystems, Bangor University, UK, https://research.bangor.ac.uk/portal/en/theses/dissolved-organic-matter-dom-in-freshwater-ecosystems(80ce7e34-f41a-43fb-b943-f24296419832).html (last access: 17 June 2023), 2019.

Burns, B. D. and Beardall, J.: Utilization of inorganic carbon by marine microalgae, J. Exp. Mar. Biol. Ecol., 107, 75–86, https://doi.org/10.1016/0022-0981(87)90125-0, 1987.

Cadeau, P., Jézéquel, D., Leboulanger, C., Fouilland, E., Le Floc'h, E., Chaduteau, C., Milesi, V., Guélard, J., Sarazin, G., Katz, A., d'Amore, S., Bernard, C., and Ader, M.: Carbon isotope evidence for large methane emissions to the Proterozoic atmosphere, Sci. Rep., 10, 18186, https://doi.org/10.1038/s41598-020-75100-x, 2020.

Cañadas, F., Papineau, D., Leng, M. J., and Li, C.: Extensive primary production promoted the recovery of the Ediacaran Shuram excursion, Nat. Commun., 13, 148, https://doi.org/10.1038/s41467-021-27812-5, 2022.

Carlson, C. A. and Hansell, D. A.: DOM Sources, Sinks, Reactivity, and Budgets, in: Biogeochemistry of Marine Dissolved Organic Matter, edited by: Hansell, D. A. and Carlson, C. A., Elsevier, 65–126, https://doi.org/10.1016/B978-0-12-405940-5.00003-0, 2015.

Carrasco-Núñez, G., Ort, M. H., and Romero, C.: Evolution and hydrological conditions of a maar volcano (Atexcac crater, Eastern Mexico), J. Volcanol. Geoth. Res., 159, 179–197, https://doi.org/10.1016/j.jvolgeores.2006.07.001, 2007.

Cawley, K. M., Ding, Y., Fourqurean, J., and Jaffé, R.: Characterising the sources and fate of dissolved organic matter in Shark Bay, Australia: a preliminary study using optical properties and stable carbon isotopes, Mar. Freshwater Res., 63, 1098, https://doi.org/10.1071/MF12028, 2012.

Chako Tchamabé, B., Carrasco-Núñez, G., Miggins, D. P., and Németh, K.: Late Pleistocene to Holocene activity of Alchichica maar volcano, eastern Trans-Mexican Volcanic Belt, J. South Am. Earth Sci., 97, 102404, https://doi.org/10.1016/j.jsames.2019.102404, 2020.

Chen, B., Hu, C., Mills, B. J. W., He, T., Andersen, M. B., Chen, X., Liu, P., Lu, M., Newton, R. J., Poulton, S. W., Shields, G. A., and Zhu, M.: A short-lived oxidation event during the early Ediacaran and delayed oxygenation of the Proterozoic ocean, Earth Planet. Sc. Lett., 577, 117274, https://doi.org/10.1016/j.epsl.2021.117274, 2022.

Chomicki, K.: The use of stable carbon and oxygen isotopes to examine the fate of dissolved organic matter in two small, oligotrophic Canadian Shield lakes, University of Waterloo, Canada, https://www.researchgate.net/publication/268368579 (last access: 17 June 2023), 2009.

Close, H. G. and Henderson, L. C.: Open-Ocean Minima in δ^{13}C Values of Particulate Organic Carbon in the Lower Euphotic Zone, Front. Mar. Sci., 7, 540165, https://doi.org/10.3389/fmars.2020.540165, 2020.

Couradeau, E., Benzerara, K., Gérard, E., Moreira, D., Bernard, S., Brown, G. E., and López-García, P.: An Early-Branching Microbialite Cyanobacterium Forms Intracellular Carbonates, Science, 336, 459–462, https://doi.org/10.1126/science.1216171, 2012.

Crowe, S. A., Katsev, S., Leslie, K., Sturm, A., Magen, C., Nomosatryo, S., Pack, M. A., Kessler, J. D., Reeburgh, W. S., Roberts, J. A., González, L., Douglas Haffner, G., Mucci, A., Sundby, B., and Fowle, D. A.: The methane cycle in ferruginous Lake Matano: Methane cycle in ferruginous Lake Matano, Geobiology, 9, 61–78, https://doi.org/10.1111/j.1472-4669.2010.00257.x, 2011.

Descolas-Gros, C. and Fontungne, M.: Stable carbon isotope fractionation by marine phytoplankton during photosynthesis, Plant Cell Environ., 13, 207–218, https://doi.org/10.1111/j.1365-3040.1990.tb01305.x, 1990.

Dittmar, T.: Reasons Behind the Long-Term Stability of Dissolved Organic Matter, in: Biogeochemistry of Marine Dissolved Organic Matter, Elsevier, 369–388, https://doi.org/10.1016/B978-0-12-405940-5.00007-8, 2015.

Ducklow, H. W., Hansell, D. A., and Morgan, J. A.: Dissolved organic carbon and nitrogen in the Western Black Sea, Mar. Chem., 105, 140–150, https://doi.org/10.1016/j.marchem.2007.01.015, 2007.

Erez, J., Bouevitch, A., and Kaplan, A.: Carbon isotope fractionation by photosynthetic aquatic microorganisms: experiments with *Synechococcus* PCC7942, and a simple carbon flux model, Can. J. Bot, 76, 1109–1118, https://doi.org/10.1139/b98-067, 1998.

Fakhraee, M., Tarhan, L. G., Planavsky, N. J., and Reinhard, C. T.: A largely invariant marine dissolved organic carbon reservoir across Earth's history, P. Natl. Acad. Sci. USA, 118, e2103511118, https://doi.org/10.1073/pnas.2103511118, 2021.

Ferrari, L., Orozco-Esquivel, T., Manea, V., and Manea, M.: The dynamic history of the Trans-Mexican Volcanic Belt and the Mexico subduction zone, Tectonophysics, 522–523, 122–149, https://doi.org/10.1016/j.tecto.2011.09.018, 2012.

Fike, D. A., Grotzinger, J. P., Pratt, L. M., and Summons, R. E.: Oxidation of the Ediacaran Ocean, Nature, 444, 744–747, https://doi.org/10.1038/nature05345, 2006.

Fogel, M. L. and Cifuentes, L. A.: Isotope Fractionation during Primary Production, in: Organic Geochemistry, Topics in Geobiology, edited by: Engel, M. H. and Macko, S. A., Springer US, Boston, MA, 73–98, https://doi.org/10.1007/978-1-4615-2890-6_3, 1993.

Fry, B.: $^{13}C/^{12}C$ fractionation by marine diatoms, Mar. Ecol.-Prog. Ser., 134, 283–294, https://doi.org/10.3354/meps134283, 1996.

Hansell, D. A.: Recalcitrant Dissolved Organic Carbon Fractions, Annu. Rev. Mar. Sci., 5, 421–445, https://doi.org/10.1146/annurev-marine-120710-100757, 2013.

Havas, R., Thomazo, C., Iniesto, M., Jézéquel, D., Moreira, D., Tavera, R., Caumartin, J., Muller, E., López-García, P., and Benzerara, K.: Biogeochemical processes captured by carbon isotopes in redox-stratified water columns: a comparative study of four modern stratified lakes along an alkalinity gradient, Biogeosciences, 20, 2347–2367, https://doi.org/10.5194/bg-20-2347-2023, 2023a.

Havas, R., Thomazo, C., Iniesto, M., Jezequel, D., Moreira, D., Tavera, R., Caumartin, J., Muller, E., Lopez Garcia, P., and Benzerara, K.: Carbon isotopes and alkalinity gradient for biogeochemical processes in modern stratified lakes v. 2, Version 1.0, Interdisciplinary Earth Data Alliance (IEDA) [data set], https://doi.org/10.26022/IEDA/112943, 2023b.

Havig, J. R., McCormick, M. L., Hamilton, T. L., and Kump, L. R.: The behavior of biologically important trace elements across the oxic/euxinic transition of meromictic Fayetteville Green Lake, New York, USA, Geochim. Cosmochim. Ac., 165, 389–406, https://doi.org/10.1016/j.gca.2015.06.024, 2015.

Havig, J. R., Hamilton, T. L., McCormick, M., McClure, B., Sowers, T., Wegter, B., and Kump, L. R.: Water column and sediment stable carbon isotope biogeochemistry of permanently redox-stratified Fayetteville Green Lake, New York, U.S.A., Limnol. Oceanogr., 63, 570–587, https://doi.org/10.1002/lno.10649, 2018.

Hayes, J. M.: Fractionation of Carbon and Hydrogen Isotopes in Biosynthetic Processes*, Rev. Mineral. Geochem., 43, 225–277, https://doi.org/10.2138/gsrmg.43.1.225, 2001.

Hessen, D. O.: Dissolved organic carbon in a humic lake: effects on bacterial production and respiration, in: Dissolved Organic Matter in Lacustrine Ecosystems: Energy Source and System Regulator, Developments in Hydrobiology, edited by: Salonen, K., Kairesalo, T., and Jones, R. I., Springer Netherlands, Dordrecht, 115–123, https://doi.org/10.1007/978-94-011-2474-4_9, 1992.

Hessen, D. O. and Anderson, T. R.: Excess carbon in aquatic organisms and ecosystems: Physiological, ecological, and evolutionary implications, Limnol. Oceanogr., 53, 1685–1696, https://doi.org/10.4319/lo.2008.53.4.1685, 2008.

Iniesto, M., Moreira, D., Benzerara, K., Reboul, G., Bertolino, P., Tavera, R., and López-García, P.: Planktonic microbial communities from microbialite-bearing lakes sampled along a salinity-alkalinity gradient, Limnol. Oceanogr., 67, 2718–2733, https://doi.org/10.1002/lno.12233, 2022.

Iñiguez, C., Capó-Bauçà, S., Niinemets, Ü., Stoll, H., Aguiló-Nicolau, P., and Galmés, J.: Evolutionary trends in RuBisCO kinetics and their co-evolution with CO_2 concentrating mechanisms, Plant J., 101, 897–918, https://doi.org/10.1111/tpj.14643, 2020.

Ivanovsky, R. N., Lebedeva, N. V., Keppen, O. I., and Chudnovskaya, A. V.: Release of Photosynthetically Fixed Carbon as Dissolved Organic Matter by Anoxygenic Phototrophic Bacteria, Microbiology, 89, 28–34, https://doi.org/10.1134/S0026261720010075, 2020.

Jiang, G., Wang, X., Shi, X., Zhang, S., Xiao, S., and Dong, J.: Organic carbon isotope constraints on the dissolved organic carbon (DOC) reservoir at the Cryogenian–Ediacaran transition, Earth Planet. Sc. Lett., 299, 159–168, https://doi.org/10.1016/j.epsl.2010.08.031, 2010.

Jiang, G., Wang, X., Shi, X., Xiao, S., Zhang, S., and Dong, J.: The origin of decoupled carbonate and organic carbon isotope signatures in the early Cambrian (ca. 542–520 Ma) Yangtze platform, Earth Planet. Sc. Lett., 317–318, 96–110, https://doi.org/10.1016/j.epsl.2011.11.018, 2012.

Jiao, N., Herndl, G. J., Hansell, D. A., Benner, R., Kattner, G., Wilhelm, S. W., Kirchman, D. L., Weinbauer, M. G., Luo, T., Chen, F., and Azam, F.: Microbial production of recalcitrant dissolved organic matter: long-term carbon storage in the global ocean, Nat. Rev. Microbiol., 8, 593–599, https://doi.org/10.1038/nrmicro2386, 2010.

Kaplan, L. A., Wiegner, T. N., Newbold, J. D., Ostrom, P. H., and Gandhi, H.: Untangling the complex issue of dissolved organic carbon uptake: a stable isotope approach, Freshwater Biol., 53, 855–864, https://doi.org/10.1111/j.1365-2427.2007.01941.x, 2008.

Kawasaki, N., Komatsu, K., Kohzu, A., Tomioka, N., Shinohara, R., Satou, T., Watanabe, F. N., Tada, Y., Hamasaki, K., Kushairi, M. R. M., and Imai, A.: Bacterial Contribution to Dissolved Organic Matter in Eutrophic Lake Kasumigaura, Japan, Appl. Environ. Microb., 79, 7160–7168, https://doi.org/10.1128/AEM.01504-13, 2013.

Kroopnick, P. M.: The distribution of ^{13}C of ΣCO_2 in the world oceans, Deep-Sea Res. Pt. A, 32, 57–84, https://doi.org/10.1016/0198-0149(85)90017-2, 1985.

Kuntz, L. B., Laakso, T. A., Schrag, D. P., and Crowe, S. A.: Modeling the carbon cycle in Lake Matano, Geobiology, 13, 454–461, https://doi.org/10.1111/gbi.12141, 2015.

Lampert, W.: Release of dissolved organic carbon by grazing zooplankton, Limnol. Oceanogr., 23, 831–834, https://doi.org/10.4319/lo.1978.23.4.0831, 1978.

Lehmann, M. F., Bernasconi, S. M., Barbieri, A., and McKenzie, J. A.: Preservation of organic matter and alteration of its carbon and nitrogen isotope composition during simulated and in situ early sedimentary diagenesis, Geochim. Cosmochim. Ac., 66, 3573–3584, https://doi.org/10.1016/S0016-7037(02)00968-7, 2002.

Lenton, T. M. and Daines, S. J.: Matworld – the biogeochemical effects of early life on land, New Phytol., 215, 531–537, https://doi.org/10.1111/nph.14338, 2017.

Lenton, T. M. and Daines, S. J.: The effects of marine eukaryote evolution on phosphorus, carbon and oxygen cycling across the Proterozoic–Phanerozoic transition, Emerg. Top. Life Sci., 2, 267–278, https://doi.org/10.1042/ETLS20170156, 2018.

Li, C., Hardisty, D. S., Luo, G., Huang, J., Algeo, T. J., Cheng, M., Shi, W., An, Z., Tong, J., Xie, S., Jiao, N., and Lyons, T. W.: Uncovering the spatial heterogeneity of Ediacaran carbon cycling, Geobiology, 15, 211–224, https://doi.org/10.1111/gbi.12222, 2017.

Lu, M., Zhu, M., Zhang, J., Shields-Zhou, G., Li, G., Zhao, F., Zhao, X., and Zhao, M.: The DOUNCE event at the top of the Ediacaran Doushantuo Formation, South China: Broad stratigraphic occurrence and non-diagenetic origin, Precambrian Res., 225, 86–109, https://doi.org/10.1016/j.precamres.2011.10.018, 2013.

Lugo, A., Alcocer, J., Sanchez, M. R., and Escobar, E.: Trophic status of tropical lakes indicated by littoral protozoan assemblages, Int. Ver. The., 25, 4441–443, https://doi.org/10.1080/03680770.1992.11900159, 1993.

Lyons, T. W., Reinhard, C. T., and Planavsky, N. J.: The rise of oxygen in Earth's early ocean and atmosphere, Nature, 506, 307–315, https://doi.org/10.1038/nature13068, 2014.

Macek, M., Medina, X. S., Picazo, A., Peštová, D., Reyes, F. B., Hernández, J. R. M., Alcocer, J., Ibarra, M. M., and Camacho, A.: Spirostomum teres: A Long Term Study of an Anoxic-Hypolimnion Population Feeding upon Photosynthesizing Microorganisms, Acta Protozool., 59, 13–38, https://doi.org/10.4467/16890027AP.20.002.12158, 2020.

Marañón, E., Cermeño, P., Fernández, E., Rodríguez, J., and Zabala, L.: Significance and mechanisms of photosynthetic production of dissolved organic carbonin a coastal eutrophic ecosystem, Limnol. Oceanogr., 49, 1652–1666, https://doi.org/10.4319/lo.2004.49.5.1652, 2004.

Margolin, A. R., Gerringa, L. J. A., Hansell, D. A., and Rijkenberg, M. J. A.: Net removal of dissolved organic carbon in the anoxic waters of the Black Sea, Mar. Chem., 183, 13–24, https://doi.org/10.1016/j.marchem.2016.05.003, 2016.

Mook, W. G., Bommerson, J. C., and Staverman, W. H.: Carbon isotope fractionation between dissolved bicarbonate and gaseous carbon dioxide, Earth Planet. Sc. Lett., 22, 169–176, https://doi.org/10.1016/0012-821X(74)90078-8, 1974.

Morana, C., Sarmento, H., Descy, J.-P., Gasol, J.M., Borges, A.V., Bouillon, S., and Darchambeau, F.: Production of dissolved organic matter by phytoplankton and its uptake by heterotrophic prokaryotes in large tropical lakes, Limnol. Oceanogr., 59, 1364–1375, https://doi.org/10.4319/lo.2014.59.4.1364, 2014.

OECD (Organization for Economic Cooperation and Development), Vollenweider, R. A., and Kerekes, J. (Eds.): Eutrophication of waters, Monitoring, assessment and control, OECD, Paris, 154 pp., http://lakes.chebucto.org/TPMODELS/OECD/OECD1982.pdf (last access: 17 June 2023), 1982.

Ogawa, H., Amagai, Y., Koike, I., Kaiser, K., and Benner, R.: Production of Refractory Dissolved Organic Matter by Bacteria, Science, 292, 917–920, https://doi.org/10.1126/science.1057627, 2001.

O'Leary, M. H.: Carbon Isotopes in Photosynthesis, BioScience, 38, 328–336, https://doi.org/10.2307/1310735, 1988.

Otero, A. and Vincenzini, M.: Extracellular polysaccharide synthesis by Nostoc strains as affected by N source and light intensity, J. Biotechnol., 102, 143–152, https://doi.org/10.1016/S0168-1656(03)00022-1, 2003.

Peltier, W. R., Liu, Y., and Crowley, J. W.: Snowball Earth prevention by dissolved organic carbon remineralization, Nature, 450, 813–818, https://doi.org/10.1038/nature06354, 2007.

Petrash, D. A., Steenbergen, I. M., Valero, A., Meador, T. B., Pačes, T., and Thomazo, C.: Aqueous system-level processes and prokaryote assemblages in the ferruginous and sulfate-rich bottom waters of a post-mining lake, Biogeosciences, 19, 1723–1751, https://doi.org/10.5194/bg-19-1723-2022, 2022.

Posth, N. R., Bristow, L. A., Cox, R. P., Habicht, K. S., Danza, F., Tonolla, M., Frigaard, N.-U., and Canfield, D.E.: Carbon isotope fractionation by anoxygenic phototrophic bacteria in euxinic Lake Cadagno, Geobiology, 15, 798–816, https://doi.org/10.1111/gbi.12254, 2017.

Rao, D. N., Chopra, M., Rajula, G. R., Durgadevi, D. S. L., and Sarma, V. V. S. S.: Release of significant fraction of primary production as dissolved organic carbon in the Bay of Bengal, Deep-Sea Res. Pt. I, 168, 103445, https://doi.org/10.1016/j.dsr.2020.103445, 2021.

Renstrom-Kellner, E. and Bergman, B.: Glycolate metabolism in cyanobacteria. III. Nitrogen controls excretion and metabolism of glycolate in Anabaena cylindrica, Physiol. Plant., 77, 46–51, https://doi.org/10.1111/j.1399-3054.1989.tb05976.x, 1989.

Repeta, D. J. and Aluwihare, L. I.: Radiocarbon analysis of neutral sugars in high-molecular-weight dissolved organic carbon: Implications for organic carbon cycling, Limnol. Oceanogr., 51, 1045–1053, https://doi.org/10.4319/lo.2006.51.2.1045, 2006.

Ridgwell, A. and Arndt, S.: Chapter 1 – Why Dissolved Organics Matter: DOC in Ancient Oceans and Past Climate Change, in: Biogeochemistry of Marine Dissolved Organic Matter, 2nd

Edn., edited by: Hansell, D. A. and Carlson, C. A., Academic Press, Boston, 1–20, https://doi.org/10.1016/B978-0-12-405940-5.00001-7, 2015.

Riebesell, U., Burkhardt, S., Dauelsberg, A., and Kroon, B.: Carbon isotope fractionation by a marine diatom: dependence on the growth-rate-limiting resource, Mar. Ecol.-Prog. Ser., 193, 295–303, https://doi.org/10.3354/meps193295, 2000.

Rothman, D. H., Hayes, J. M., and Summons, R. E.: Dynamics of the Neoproterozoic carbon cycle, P. Natl. Acad. Sci. USA, 100, 8124–8129, https://doi.org/10.1073/pnas.0832439100, 2003.

Saini, J. S., Hassler, C., Cable, R., Fourquez, M., Danza, F., Roman, S., Tonolla, M., Storelli, N., Jacquet, S., Zdobnov, E. M., and Duhaime, M. B.: Microbial loop of a Proterozoic ocean analogue, bioRxiv, 2021-08, https://doi.org/10.1101/2021.08.17.456685, 2021.

Saltzman, M. R. and Thomas, E.: Carbon Isotope Stratigraphy, in: The Geologic Time Scale, Elsevier, 207–232, https://doi.org/10.1016/B978-0-444-59425-9.00011-1, 2012.

Santinelli, C., Follett, C., Retelletti Brogi, S., Xu, L., and Repeta, D.: Carbon isotope measurements reveal unexpected cycling of dissolved organic matter in the deep Mediterranean Sea, Mar. Chem., 177, 267–277, https://doi.org/10.1016/j.marchem.2015.06.018, 2015.

Satkoski, A. M., Beukes, N. J., Li, W., Beard, B. L., and Johnson, C. M.: A redox-stratified ocean 3.2 billion years ago, Earth Planet. Sc. Lett., 430, 43–53, https://doi.org/10.1016/j.epsl.2015.08.007, 2015.

Schiff, S. L., Tsuji, J. M., Wu, L., Venkiteswaran, J. J., Molot, L. A., Elgood, R. J., Paterson, M. J., and Neufeld, J. D.: Millions of Boreal Shield Lakes can be used to Probe Archaean Ocean Biogeochemistry, Sci. Rep., 7, 46708, https://doi.org/10.1038/srep46708, 2017.

Sexton, P. F., Norris, R. D., Wilson, P. A., Pälike, H., Westerhold, T., Röhl, U., Bolton, C. T., and Gibbs, S.: Eocene global warming events driven by ventilation of oceanic dissolved organic carbon, Nature, 471, 349–352, https://doi.org/10.1038/nature09826, 2011.

Shi, W., Li, C., and Algeo, T. J.: Quantitative model evaluation of organic carbon oxidation hypotheses for the Ediacaran Shuram carbon isotopic excursion, Sci. China Earth Sci., 60, 2118–2127, https://doi.org/10.1007/s11430-017-9137-1, 2017.

Shields, G. A., Mills, B. J. W., Zhu, M., Raub, T. D., Daines, S. J., and Lenton, T. M.: Unique Neoproterozoic carbon isotope excursions sustained by coupled evaporite dissolution and pyrite burial, Nat. Geosci., 12, 823–827, https://doi.org/10.1038/s41561-019-0434-3, 2019.

Siebe, C., Guilbaud, M.-N., Salinas, S., and Chédeville-Monzo, C.: Eruption of Alberca de los Espinos tuff cone causes transgression of Zacapu lake ca. 25,000 yr BP in Michoacán, México, Presented at the IAS 4IMC Conference, Auckland, New Zeland, 74–75, https://www.researchgate.net/publication/283927123 (last access: 8 June 2023), 2012.

Siebe, C., Guilbaud, M.-N., Salinas, S., Kshirsagar, P., Chevrel, M. O., Jiménez, A. H., and Godínez, L.: Monogenetic volcanism of the Michoacán-Guanajuato Volcanic Field: Maar craters of the Zacapu basin and domes, shields, and scoria cones of the Tarascan highlands (Paracho-Paricutin region), Presented at the Premeeting field guide for the 5th international Maar Conference, Querétaro, México, 1–37, 2014.

Sigala, I., Caballero, M., Correa-Metrio, A., Lozano-García, S., Vázquez, G., Pérez, L., and Zawisza, E.: Basic limnology of 30 continental waterbodies of the Transmexican Volcanic Belt across climatic and environmental gradients, B. Soc. Geol. Mex., 69, 313–370, https://doi.org/10.18268/BSGM2017v69n2a3, 2017.

Silva Aguilera, R. A.: Análisis del descenso del nivel de agua del Lago Alchichica, Puebla, México (Tesis de Maestría), Universidad Nacional Autónoma de México, Coordinación General de Estudios de Posgrado, UNAM, https://repositorio.unam.mx/contenidos/3534827 (last access: 6 June 2023), 2019.

Silva-Aguilera, R. A., Vilaclara, G., Armienta, M. A., and Escolero, Ó.: Hydrogeology and Hydrochemistry of the Serdán-Oriental Basin and the Lake Alchichica, in: Lake Alchichica Limnology, edited by: Alcocer, J., Springer International Publishing, Cham, 63–74, https://doi.org/10.1007/978-3-030-79096-7_5, 2022.

Sperling, E. A., Peterson, K. J., and Laflamme, M.: Rangeomorphs, Thectardis (Porifera?) and dissolved organic carbon in the Ediacaran oceans: Rangeomorphs, Thectardis and DOC, Geobiology, 9, 24–33, https://doi.org/10.1111/j.1472-4669.2010.00259.x, 2011.

Swanson-Hysell, N. L., Rose, C. V., Calmet, C. C., Halverson, G. P., Hurtgen, M. T., and Maloof, A. C.: Cryogenian Glaciation and the Onset of Carbon-Isotope Decoupling, Science, 328, 608–611, https://doi.org/10.1126/science.1184508, 2010.

Thomas, P. J., Boller, A. J., Satagopan, S., Tabita, F. R., Cavanaugh, C. M., and Scott, K. M.: Isotope discrimination by form IC RubisCO from *Ralstonia eutropha* and *Rhodobacter sphaeroides*, metabolically versatile members of "*Proteobacteria*" from aquatic and soil habitats, Environ. Microbiol., 21, 72–80, https://doi.org/10.1111/1462-2920.14423, 2019.

Thornton, D. C. O.: Dissolved organic matter (DOM) release by phytoplankton in the contemporary and future ocean, Eur. J. Phycol., 49, 20–46, https://doi.org/10.1080/09670262.2013.875596, 2014.

Tziperman, E., Halevy, I., Johnston, D. T., Knoll, A. H., and Schrag, D. P.: Biologically induced initiation of Neoproterozoic snowball-Earth events, P. Natl. Acad. Sci. USA, 108, 15091–15096, https://doi.org/10.1073/pnas.1016361108, 2011.

Vilaclara, G., Chávez, M., Lugo, A., González, H., and Gaytán, M.: Comparative description of crater-lakes basic chemistry in Puebla State, Mexico, Int. Ver. The., 25, 435–440, https://doi.org/10.1080/03680770.1992.11900158, 1993.

Wagner, S., Schubotz, F., Kaiser, K., Hallmann, C., Waska, H., Rossel, P. E., Hansman, R., Elvert, M., Middelburg, J. J., Engel, A., Blattmann, T. M., Catalá, T. S., Lennartz, S. T., Gomez-Saez, G. V., Pantoja-Gutiérrez, S., Bao, R., and Galy, V.: Soothsaying DOM: A Current Perspective on the Future of Oceanic Dissolved Organic Carbon, Front. Mar. Sci., 7, 341, https://doi.org/10.3389/fmars.2020.00341, 2020.

Werne, J. P. and Hollander, D.J.: Balancing supply and demand: controls on carbon isotope fractionation in the Cariaco Basin (Venezuela) Younger Dryas to present, Mar. Chem., 92, 275–293, https://doi.org/10.1016/j.marchem.2004.06.031, 2004.

Wetz, M. S. and Wheeler, P. A.: Release of dissolved organic matter by coastal diatoms, Limnol. Oceanogr., 52, 798–807, https://doi.org/10.4319/lo.2007.52.2.0798, 2007.

Williams, P. M. and Gordon, L. I.: Carbon-13: carbon-12 ratios in dissolved and particulate organic matter in the sea, Deep-Sea

Res. Oceanogr. Abstr., 17, 19–27, https://doi.org/10.1016/0011-7471(70)90085-9, 1970.

Xing, C., Liu, P., Wang, R., Li, C., Li, J., and Shen, B.: Tracing the evolution of dissolved organic carbon (DOC) pool in the Ediacaran ocean by Germanium/silica (Ge/Si) ratios of diagenetic chert nodules from the Doushantuo Formation, South China, Precambrian Res., 374, 106639, https://doi.org/10.1016/j.precamres.2022.106639, 2022.

Zeebe, R. E. and Wolf-Gladrow, D. A.: Carbon Dioxide, Dissolved (Ocean), in: Encyclopedia of Paleoclimatology and Ancient Environments, Encyclopedia of Earth Sciences Series, edited by: Gornitz, V., Springer, Dordrecht, https://doi.org/10.1007/978-1-4020-4411-3_30, 2009.

Zeyen, N., Benzerara, K., Beyssac, O., Daval, D., Muller, E., Thomazo, C., Tavera, R., López-García, P., Moreira, D., and Duprat, E.: Integrative analysis of the mineralogical and chemical composition of modern microbialites from ten Mexican lakes: What do we learn about their formation?, Geochim. Cosmochim. Ac., 305, 148–184, https://doi.org/10.1016/j.gca.2021.04.030, 2021.

Chapter 5
Carbon sources and budget in Alchichica: a modeling approach

Table of Content

5.1. Introduction

We have seen previously how internal biological, and external physico-chemical processes influence the lakes C cycle at a given time today (see Chapter 4; Havas *et al.*, 2023a; 2023b). Notably, a gradient of alkalinity–salinity displayed by the water of these lakes has a tremendous impact on their biogeochemical functioning. It leads to different buffer capacity and sensitivity of the dissolved inorganic carbon (DIC) isotopes towards biological processes (Havas *et al.*, 2023a). Carbonate saturation indexes and microbialite formation also directly correlate with the alkalinity content of the lakes (Zeyen *et al.*, 2021). Microbial diversity of planktonic and benthic (from microbialites) communities were also interpreted to be influenced by the different alkalinity-salinity levels (Iniesto *et al.*, 2021, 2022).

To date, however, the exact environmental factors leading to this gradient of chemical compositions were not fully constrained. From a broader study about 10 Mexican lakes, Zeyen *et al.* (2021) explained this trend by differences in evaporation regimes and the nature of the weathered bedrock. They also suggested the influence of solutes concentration in groundwater, as well as of possible volcanic-CO_2 degassing from the lakes bottom. In the study presented in Chapter 4 (Havas *et al.*, 2023a), we qualitatively demonstrated that the groundwater flow path and its chemical composition do explain some of the variability in the water chemical compositions of the lakes studied. In La Preciosa, Atexcac, and Alchichica, volcanic degassing is supported by lake surface pCO_2 values higher than atmospheric pCO_{2atm} (Zeyen *et al.*, 2021; Havas *et al.*, 2023a), but an "inactive" status with no degassing was inferred by Armienta *et al.* (2008), based notably on pH, Cl and SO_4 data. The DIC stable isotope composition can in theory trace a putative volcanic-CO_2 influence (with typical signatures between -4 and -5 ‰; Mason *et al.*, 2017), but the $\delta^{13}C_{DIC}$ of the four lakes studied remain equivocal (between -3 and 2 ‰; Havas *et al.*, 2023a). This is partly because the size and isotopic composition of the DIC reservoir in a water body do not only represent a weighted average of its sources at a given time, but rather are the result of interactions between processes, sources, and sinks that may change over time (that is being out of steady state). A "dead" radioactive C signature (*i.e.* with no ^{14}C) cannot be used as evidence for a volcanic-CO_2 source either, since groundwater is loaded with "dead carbon" as well, from the dissolution of Cretaceous limestone.

To disentangle the C mass-balance and DIC isotope compositions of the lakes studied, and identify potential "hidden" C source, quantitative modeling of the C sources and C-related

processes taking place in the lakes is necessary. Such modeling approaches in modern stratified lakes have been used in Dziani Dzaha (Cadeau *et al.*, 2020), and Matano (Kuntz *et al.*, 2015), to constrain the effects of methane production/recycling and organic matter remineralization on their C cycle (and mass balance) over time.

In this chapter, I seek to model the isotopic composition of DIC and O in water through time, in order to reproduce the C and O isotope record of the lake sedimentary carbonates. Considering the processes and fluxes that can be clearly identified (evaporation, groundwater, carbonate precipitation, *etc*.), I tune the model to fit the sedimentary record, and evaluate if any hidden reservoir and fluxes (*e.g.* volcanic-CO_2) can be deduced from the evolution of the isotopic record through time. Specifically, the goal is to create a model that will reproduce the variations in lake volume, DIC concentration, and isotopic compositions of the sedimentary carbonates over time. Sediments from the four lakes have been characterized, but Alchichica remains the most studied, and the only one for which chronical hydrological and geochemical data are available. This chapter will thus focus on Lake Alchichica. Most of the necessary data is available for the last 60 years, allowing an evaluation of the results for this modeling approach over an appreciable time period. The first measurements of DIC concentration in Lake Alchichica even date back to 1940 (Taylor, 1943), while the carbonate record traces the lake $\delta^{13}C_{DIC}$ and $\delta^{18}O_{H2O}$ even further. Therefore, there is a relatively good constraint on the lake's chemistry, and potentially on the processes which drive it.

In the following, I will describe the model in detail, including: the hydrological and isotope mass-balance equations that were used for C and O, the determination of initial terms and fluxes over time, and their respective isotopic compositions. For C, the model was initially run under three distinct scenarios using three sets of input parameters. In the first "blank" scenario, I test the model with no volcanic-CO_2 degassing. In the second one, I add another source of C from OM remineralization, whereby OC fixation and respiration would be out of equilibrium, with more respiration than fixation. In the third scenario, I do not consider the respiration flux, but I add a volcanic-CO_2 flux degassing in the lake. A fourth, "satisfactory" scenario is finally discussed, and considers the volcanic-CO_2 flux, plus the fact that groundwater DIC represents a mix between C from OM respiration and from limestone dissolution. For O, the same set of parameters are chosen in each scenario.

5.2. Methods

5.2.1. Mathematical determination

5.2.1.1. Hydrological balance and DIC concentrations

The hydrological balance of the lake drives the changes of water volume through time and corresponds to the sum of water inflow and outflow such that:

$$\partial V/\partial t = Q_{GWi} + Q_P - Q_E - Q_{GWo} \quad (5.1)$$

and

$$V(t) = V_{t-1} + Q_{GWi} + Q_P - Q_E - Q_{GWo} \quad (5.2)$$

where V is lake volume (in liters) and Q_{GWi}, Q_{GWo}, Q_P and Q_E are the groundwater inflow, outflow, precipitation, and evaporation water fluxes (in liters per year), respectively. A meteorological station is located in Alchichica (recording precipitation and evaporation rates), and changes in the lake volume and groundwater fluxes have been estimated for the last decades (Alcalá, 2004; Silva-Aguilera, 2019; Silva-Aguilera *et al.*, 2022b).

The change in DIC concentration with time depends on the sum of these water fluxes weighted by their respective DIC content, and additional in- or out-fluxes of inorganic C to the lake such that:

$$\frac{\partial(V*[DIC]_{LW})}{\partial t} = Q_{GWi}[DIC]_{GWi} + Q_P[DIC]_P + F_{volc} + F_{respi} - Q_E[DIC]_E - Q_{GWo}[DIC]_{GWo} - F_{Net} - F_{\mu bialite} - F_{carb} - F_{OM} \quad (5.3)$$

where LW stands for lake water and F_{volc}, F_{respi}, $F_{\mu bialite}$, F_{carb} and F_{OM} represent the fluxes of volcanic-CO_2 degassing in the lake, CO_2 from organic C respiration, carbonate precipitating in the lakes microbialites, carbonate precipitation/deposition in the lake bottom sediments, and organic matter deposition in the bottom sediments (all expressed in megamoles of C per year). F_{Net} is the net flux of CO_2 degassing from the lake to the atmosphere, representing the difference between CO_2 evasion ($F_{evasion}$) and invasion ($F_{invasion}$). The lake DIC concentration for each year 't' is determined such that:

$$[DIC]_{LW,t} = [DIC]_{LW,t-1} * (1 - (\frac{\partial V}{\partial t})/ V_{t-1}) + (Q_{GWi}[DIC]_{GWi} + Q_P[DIC]_P + F_{volc} - Q_E[DIC]_E - Q_{GWo}[DIC]_{GWo} - F_{Net} - F_{\mu bialite} - F_{carb} - F_{OM}) / V_{t-1} \quad (5.4)$$

5.2.1.2. $\delta^{13}C(t)$

Similarly, the variation of oxygen and carbon isotope compositions through time can be expressed according to the isotopic compositions of the different fluxes affecting the lake O and C reservoirs (*e.g.* Herczeg *et al.*, 2003; Solari *et al.*, 2010). For carbon, Eq. 5.4 derives into:

$$\delta^{13}C_{LW,\,t} = \delta^{13}C_{t-1}*[1 - (\frac{\partial V}{\partial t})/V_{t-1} - (\frac{\partial DIC}{\partial t})/[DIC]_{LW,\,t-1}] + (Q_{GWi}[DIC]_{GWi}\delta^{13}C_{GWi} + Q_P[DIC]_P\delta^{13}C_P + F_{invasion}\delta^{13}C_{invasion} - Q_E[DIC]_E\delta^{13}C_E - Q_{GWo}[DIC]_{GWo}\delta^{13}C_{GWo} - F_{evasion}\delta^{13}C_{evasion} - F_{\mu bialite}\delta^{13}C_{\mu bialite} - F_{carb}\delta^{13}C_{carb} - F_{OM}\delta^{13}C_{OM}) / (V_{t-1} * [DIC]_{LW,\,t-1}) \quad (5.5)$$

where $\frac{\partial DIC}{\partial t} = [DIC]_{LW,\,t} - [DIC]_{LW,\,t-1}$, and $\delta^{13}C_{LW,\,t}$ designates the DIC isotope composition through time.

At pH ≈ 9, temperature ≈ 20 °C and salinity ≈ 8 psu, the lake DIC is composed of approximately 70% HCO_3^- and 30% CO_3^{2-}, but each flux can initially be added or removed from the lake's total DIC as CO_2 (*e.g.* atmospheric exchanges), HCO_3^- (*e.g.* groundwater influx) or CO_3^{2-} (*e.g.* carbonate precipitation). Because the three DIC species then exchange and equilibrate relatively fast, I consider that the isotopic fluxes described above apply to the bulk DIC reservoir. For example, each year, the lake's DIC loses ~6 megamoles of C into the biomass export with a ~-25 ‰ signatures, regardless of the initial C taken up by cells (*i.e.* HCO_3^- or CO_2).

5.2.1.2.1. *Correction for isotopic fractionation between DIC and solid carbonates*

In order to compare the sedimentary carbonate record with the modeled $\delta^{13}C_{LW,\,t}$ data, the isotopic difference between solid carbonate and DIC needs to be accounted for. Carbonate precipitation induces a temperature and mineralogy dependent isotopic fractionation such that bottom sediment carbonates only indirectly record the lake DIC isotope composition following:

$$\delta^{13}C_{carb} = \delta^{13}C_{DIC} + \Delta^{13}C_{carb\text{-}DIC}(Temp., R\text{-}CO_3) \quad (5.6)$$

where $\Delta^{13}C_{carb\text{-}DIC}$ is the isotopic fractionation between DIC and carbonate ('R-CO_3' designating the influence of different carbonate mineralogy). Considering the proportion of each carbonate mineralogy at all depths, a weighted average of this fractionation is calculated such as:

$$\Delta_{bulk\_carbonate\text{-}CO3} = \Sigma\, \Delta_{i\_carb\text{-}CO3} * f_i \quad (5.7)$$

where f_i is the proportion of each carbonate phase and $\Delta_{i\_carb\text{-}CO3}$ the isotopic fractionation between each of these and $CO_3^{2-}{}_{(aq)}$ (from which the carbonate phases actually precipitate). Since the respective proportions of each DIC specie and temperature remained similar over the studied period (Part 5.2.2.1, Table 5.1), I consider a constant isotopic difference between bulk DIC and CO_3^{2-} of 1.5 ‰. Therefore, $\Delta^{13}C_{carb\text{-}DIC}$ is computed as $\Delta^{13}C_{carb\text{-}CO3}$ + 1.5.

The morphology of the hydromagnesite grains in the sediments observed under SEM (Muller *et al.*, 2023) supports that this phase is detrital, coming from microbialites above in the lake, and thus formed ~3000 years before the period studied (Kaźmierczak *et al.*, 2011). Thus, I correct the measured $\delta^{13}C_{carb}$ and $\delta^{18}O_{carb}$ data from the hydromagnesite isotopic compositions (measured in this PhD and by Kaźmierczak *et al.*, 2011), and use this corrected value as a reference for the sedimentary record. Consistently, the sedimentary carbonate isotopic record is closer to isotopic equilibrium with $\delta^{13}C_{DIC}$ and $\delta^{18}O_{H2O}$ when this correction is applied than when it is not.

In Alchichica, water column temperatures at different depths and seasons vary between ~14 and 20 °C based on records from the last two decades (Macek *et al.*, 2020). From even older records, we see that these temperatures tend to increase with time (Lugo *et al.*, 2000; Adame *et al.*, 2008), in agreement with the increase of air temperatures since the 60s in Alchichica (Silva-Aguilera, 2019; Filonov *et al.*, 2022). Since the exact depths and season of carbonate precipitation are not known, I consider an average temperature of 16 °C over time and depth in the water column (Macek *et al.*, 2020). At this temperature, the $\Delta^{13}C_{carb\text{-}CO3}$ fractionation for aragonite and calcite would amount to ~ 1.0 and -0.8 ‰, respectively (Romanek *et al.*, 1992; Szaran, 1997), or $\Delta^{13}C_{carb\text{-}DIC}$ of +2.5 and +0.7 ‰. The final $\Delta^{13}C_{carb\text{-}DIC}$ considering the respective carbonate proportions at each depth (f_i) averages about 2.4 ‰.

5.2.1.3. $\delta^{18}O(t)$

Oxygen isotopes evolution with time is driven by the composition of the different fluids:

$$\partial(V*\delta^{18}O)/\partial t = Q_{GWi}\delta^{18}O_{GWi} + Q_P\delta^{18}O_P - Q_E\delta^{18}O_E - Q_{GWo}\delta^{18}O_{GWo}, \quad (5.8)$$

derives in:

$$\delta^{18}O_{LW,\,t} = \delta^{18}O_{t-1}*(1 - (\frac{\partial V}{\partial t})/\ V_{t-1}) + (Q_{GWi}\delta^{18}O_{GWi} + Q_P\delta^{18}O_P - Q_E\delta^{18}O_E - Q_{GWo}\delta^{18}O_{GWo})/V_{t-1} \quad (5.9)$$

5.2.1.3.1. *Correction for isotopic fractionation between H_2O and solid carbonates*

The precipitation of carbonates induces an O isotopic fractionation from water which is temperature and mineralogy dependent. At 16 °C this fractionation is equal to ~ 30.7, 30 and 33.6 ‰ on the VSMOW scale (Aharon, 1988; Kim and O'Neil, 1997; Kim *et al.*, 2007) for aragonite, calcite and hydromagnesite, respectively. Thus, $\delta^{18}O_{carb}$ from the model is calculated as:

$$\delta^{18}O_{carb} = \delta^{18}O_{LW} + \Delta^{18}O_{carb\text{-}H2O}(Temp., R\text{-}CO_3) \quad (5.10)$$

All O isotope compositions are expressed relative to the SMOW scale for water reservoirs and to VPDB for solid carbonate phases. The sediment $\delta^{18}O_{carb}$ are corrected from hydromagnesite compositions similarly as for C.

5.2.2. Determination of C and O initial values

5.2.2.1. DIC_{LW} concentration

Concentrations of DIC in Alchichica's water column have been measured since 1941 (Taylor, 1943) and then regularly since the 80s (Vilaclara *et al.*, 1993; Armienta *et al.*, 2008; Kaźmierczak *et al.*, 2011; Sigala *et al.*, 2017; Lelli *et al.*, 2021; Zeyen *et al.*, 2021; Silva-Aguilera *et al.*, 2022b; Havas *et al.*, 2023a). This provides a good constraint on this primary parameter throughout the 20th century. In this literature, DIC was sometimes calculated from measured total alkalinity (TA in $mg.L^{-1}$ as $CaCO_3$), or directly as DIC (in $mg.L^{-1}$ or $mmol.L^{-1}$). Considering the reported HCO_3^- and CO_3^{2-} or total DIC concentrations, it results in a non-linear DIC increase from 28 mM in 1941 to 43 mM in 2017, then decreasing to 32 ± 2 mM in 2019 (Fig. 5.1). However, there are some inconsistencies in these results and notably a mismatch when the two different methods were used (*i.e.* direct DIC measurement or calculation from TA), which led me to recalculate and homogenize this DIC dataset. In the calculation of [DIC] from [TA], it appeared that some authors used the theoretical pKa constant of pure freshwater (9.1; *e.g.* Villaclara *et al.*, 1993), while others used the one of pure seawater (10.35; Zeyen *et al.*, 2021). However, Alchichica has an intermediate salinity amounting ~8 psu (in 2019). Since all these publications featured the water's salinity/conductivity and temperature data, it was

possible to calculate the right pKa values for each sampled year (Millero *et al.*, 2006). This resulted in a pKa varying between 9.38 and 9.44 (Table 1). As pKa dictates the pH at which HCO_3^- and CO_3^{2-} ions are at equilibrium, this changes both the relative proportions of each ion, and the total amount of DIC calculated from TA since:

$$\text{Total alkalinity} \approx [HCO_3^-] + 2*[CO_3^{2-}] \text{ in meq.L}^{-1}. \quad (5.11)$$

After correction, the new DIC data form a more consistent time-profile (Fig. 5.1, Table 5.1), and most importantly, erase the inconsistencies related to the choice of measurement method. Besides, the new DIC matches the general evolution of Cl- and Na+ concentrations published in the same articles (Fig. 5.1b). I chose the initial [DIC] used in the model in order to fit the trend depicted by the data between 1941 and 2001. That is, [DIC]i is set to 31 mM in 1960 (Fig. 5.1, Table 5.1).

5.2.2.2. $\delta^{13}C_{LW,i}$ and $\delta^{18}O_{LW,i}$

From the 2019 data, it is found that the surficial sediment carbonates record the lake water composition at equilibrium (*i.e.* $\delta_{carb} = \delta_{LW} + \Delta_{carb\text{-}LW}$) (Havas *et al.*, 2023a). Therefore, the initial lake water DIC and O isotopic compositions from 1960 were determined based on the sedimentary carbonate signatures, such that $\delta^{13}C_{LW,i}$ = 2.4 ‰ (*vs.* VPDB), and $\delta^{18}O_{LW,i}$ = 1.5 ‰ (*vs.* VSMOW).

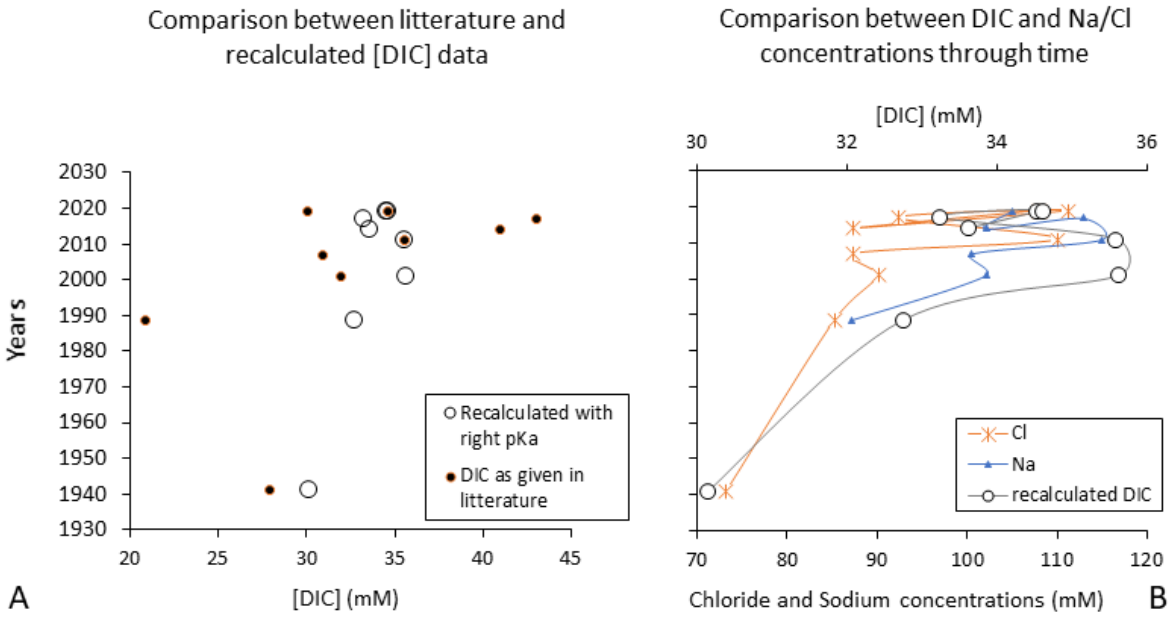

Figure 5.1: evolution of the dissolved inorganic carbon, chloride and sodium concentrations in mmol.yr^{-1} in Alchichica from 1941 to 2019. A) Comparison between the [DIC] as provided in the literature in solid dots (either directly measured as DIC or deduced from total alkalinity measurements, see main text), or recalculated from Alchichica-specific pKa, in empty dots. The two occurrences where both dataset match are when the DIC was not determined based on alkalinity, but from direct DIC measurements. B) Comparison between DIC, Cl and Na concentrations through time, when available. Very similar trends are observed for the three elements. Literature used: Taylor (1943); Villaclara *et al.* (1993); Armienta *et al.* (2008); Kaźmierzack *et al.* (2011); Sigala *et al.* (2017); Lelli *et al.* (2021); Zeyen *et al.* (2021) and Silva-Aguilera *et al.* (2022b).

Time of sampling	Reference	Measured quantity	Total Alkalinity	Literature [DIC]	pK_{a2} used in the literature	pH	Temp.	Salinity	pK_{a2}	HCO_3^-/CO_3^{2-}	'Recalculated' [DIC]	pCO_2/pCO_{2atm}
			$mg.L^{-1}$ as $CaCO_3$	mM			° K	$g.L^{-1}$		proportions	mM	
? **1941**	Taylor (1943)	Tot. Alk.	1915	27.9	?	9[#]	293	8.3	9.43	73 / 27	*30.2*	4.3
1988-1989 (every 3 months)	Vilaclara *et al.* (1993)	Tot. Alk.	2085	20.8	9.1	9.00	293	8.5	9.42	73 / 27	*32.7*	4.6
May **2001**	Armienta *et al.* (2008)	Tot. Alk.	2123	31.9	9.1	8.80	293	8.49[¤]	9.42	81 / 19	*35.6*	4.8
June **2007**	Kaźmierzack *et al.* (2011)	?	† 1545 (30.9 $meq.L^{-1}$)	X	X	8.88	293	8.7	9.42	X	†	X
June **2011**	Sigala *et al.* (2017)	DIC, Tot. Alk.	2225	35.6 (28.3)°	?	8.30	293	8.9	9.41	74 / 26	35.6	4.6
May **2014**	Zeyen *et al.* (2021)	Tot. Alk.	2150.5	41.0	10.35	9.02	293	8.3	9.43	72 / 28	*33.6*	4.3
June **2017**	Lelli *et al.* (2021)	Tot. Alk.	2150	43.0	?	9.06	293	8[¤]	9.44	71 / 29	*33.2*	
2019 (every month)	Silva-Aguilera *et al.* (2022b)	Tot. Alk.	2236	30.1	9.1	9[#]	293	10.1	9.38	70 / 30	*34.5*	
May **2019**	Havas *et al.* (2023a)	DIC	*§ 2358*	34.6	X	9.20	293	7.9	9.44	64 / 36	34.6	3.1

Table 5.1: Summary of literature allowing the recalculation of DIC concentration with time. † Alkalinity was not measured in this study, but calculated by cation-anion balance (as carbonate alkalinity). It is the only one being out of the alkalinity increasing trend with time. § Alkalinity concentration recalculated from the DIC measured during this PhD. Once all the [DIC] are corrected, they follow the same increasing trend as Total Alkalinity. ° 35.6 mM corresponds to the DIC concentration directly measured as bulk DIC; 28.3 mM is the DIC concentration as provided as HCO_3^- plus CO_3^{2-} concentrations. # A value of 9 was used in the calculation because pH was not provided in reference. ¤ Salinity values estimated from the measured conductivities in $mS.s^{-1}$. In the last column, values in *italic* correspond to the concentrations that were recalculated and used for reference in the model. The pK_{a2} is the acidity constant between HCO_3^- and CO_3^{2-} and is equal to ~9.1 for freshwater and ~10.4 for seawater at 293 K. The temperature is set to 293 rather than 289 K (*i.e.* 16 °C), because all reported measurements are from surface waters and were sampled during the summer time.

5.2.3. Determination of the fluxes and their isotopic signatures

5.2.3.1. Precipitation and evaporation fluxes

Precipitation and evaporation fluxes (Q_P, Q_E in $L.yr^{-1}$) were calculated based on the area of the lake and precipitation and evaporation rates (in $mm.yr^{-1}$) reported in Alcocer (2019) and Silva-Aguilera (2019). Initial data originate from the climatology station 21052 of the Mexican SMN (Servicio meteorológico nacional) located in Alchichica and I use a smoothing curve of this data set provided by Silva-Aguilera (2019) for the period 1966-2015. I linearly extrapolated the observed trends to encompass a total period from 1960 to 2020. The area of Lake Alchichica varied around 2.21 ± 0.02 km^2 in the last decades and this value was used in the calculation of Q_P and Q_E.

There are no direct measurements of the O isotope composition from precipitation in Alchichica ($\delta^{18}O_P$). Shallow groundwater assimilated to direct precipitation fluids, about 40 km east of Alchichica, had $\delta^{18}O$ values between -6 and -10 ‰ (Wassenaar *et al.*, 2009). An isoscape centered on Mexico predicted the same range of values for $\delta^{18}O_P$ (Kramer *et al.*, 2018). Thus, I choose an average $\delta^{18}O_P$ value of -8 ‰ (VSMOW).

Despite a net evaporation flux, oxygen from the lake water constantly exchanges with water vapor oxygen in the overlying atmosphere. This exchange is associated with an isotopic fractionation comprising both an equilibrium fractionation ($\alpha_{liq\text{-}vap}$) and a kinetic fractionation (also referred to as *enrichment factor*, ε_k) that directly relates to ambient humidity such as: $\varepsilon_k = 14.2*(1\text{-}h)$ (Gonfiantini, 1986). This relationship implies that a lower air humidity content produces higher isotopic fractionations, and *vice versa*. Overall, O isotope composition of water being evaporated and exchanged can be gathered and expressed such as:

$$\delta^{18}O_E = ((\delta^{18}O_{LW} - \varepsilon_{liq\text{-}vap})/\alpha_{liq\text{-}vap} - h*\delta^{18}O_{atm} - \varepsilon_k) / (1 - h + \varepsilon_k/1000) \qquad (5.12)$$

where $\varepsilon_{liq\text{-}vap} = (\alpha_{liq\text{-}vap} - 1)*1000$ and h is the ambient humidity content (Herczeg *et al.*, 2003; Gibson *et al.*, 2016). Humidity plays a major role in this calculation, but is poorly constrained over the period studied. It averaged about 54% in 2021 and 2022 (source meteoblue.com). For the period 2003-2005, Filonov *et al.* (2022) report values around 70%. Higher temperatures and evaporation rates through most of the studied period prior 2021 are consistent with the fact that ambient humidity would have been higher than today as well. Following this first order

assumption, I freely choose a constant (average) humidity value of 60% for the 1960-2020 period, which allow the model $\delta^{18}O$ to fit the $\delta^{18}O_{carb}$ data (see discussion 5.4.1).

The concentration of dissolved inorganic carbon within rain and evaporated water is negligible and was not considered.

5.2.3.2. Groundwater fluxes

Hydrological studies estimated groundwater fluxes entering the lake (Q_{GWi}) to be 10 times higher than outflowing groundwater (Q_{GWo}) with values of about 10^9 and 10^8 $L.yr^{-1}$, respectively (Alcalá, 2004; Silva-Aguilera, 2019; Silva-Aguilera *et al.*, 2022b). However, using these values for the studied period results in a much greater water level decrease (~ 22 m) than what the field surveys record (that is, ~ 2.6 m between 1960 and 1992 and ~ 2.4 m between 1992 and 2004; Alcalá, 2004; Silva-Aguilera *et al.*, 2022b). Thus, while the 10-fold ratio between Q_{GWi} and Q_{GWo} was kept, I recalculated the groundwater fluxes in order to match the lake water level decrease reported in the literature such that:

$$Q_{GWi} = (\partial V/\partial t - Q_P + Q_E) / (1 - 0.1) \quad (5.13)$$

with $Q_{GWo} = Q_{GWi}/10$

The lake volume variation with time ($\partial V/\partial t$) is fixed to a value allowing a match of the water level decrease record (-8 and -20 $cm.yr^{-1}$ for the periods 1960-1992 and 1992-2004, respectively; Silva-Aguilera *et al.*, 2022b). The $\partial V/\partial t$ parameter for the remaining period 2004-2022 is fixed such that lake level decrease has an intermediate value of 14 $cm.yr^{-1}$. This is justified by the fact that, anthropic GW exploitation kept increasing (Alcocer, 2019), but is balanced out by evaporation rates being the smallest of the studied time period. Starting from the current lake volume today (~$1.15*10^{11}$ L; Filonov *et al.*, 2022), one can estimate the lake volume since the 60s. Accordingly, the lake volume represented approximately $1.3*10^{11}$ L in 1960, corresponding to a volume decrease of $15*10^6$ L, and a water level decrease of slightly less than 7 m between 1960 and today.

Groundwater $\delta^{18}O$ isotopic composition was estimated from the local wells groundwater data from Lelli *et al.* (2021). The wells located before lakes Quechulac and La Preciosa harbor a composition close to ~ -12.5 ‰ (*vs.* VSMOW). The flux of GW flows through these lakes before it reaches Alchichica (Silva-Aguilera, 2019; Havas *et al.*, 2023a). This pattern generates

groundwater with $\delta^{18}O$ close to ~ - 9 ‰ as they reach Lake Alchichica (Lelli *et al.*, 2021; see figure 2.5 in Chapter 2).

In order to obtain the C flux from GW, $[DIC]_{GWi}$ needs to be considered. From the analysis of seepage water representing the GW inflowing Alchichica, $[DIC]_{GWi}$ averages ~10 mM (Kaźmierzack *et al.*, 2011; Silva-Aguilera, 2019). The isotopic composition of this DIC_{GWi} was considered to be equal to the calcareous basement C isotope composition, *i.e.* ~0 ‰ (Gonzales-Partida *et al.*, 1993). The concentration of DIC and isotopic compositions of GW out-flux were set to equal the lake [DIC] and $\delta^{13}C_{DIC}$.

5.2.3.3. Carbon precipitation in microbialites

The total flux of C being precipitated as microbialite carbonates ($F_{\mu bialite}$) was calculated as:

$$F_{\mu bialite} = (\sigma_{\mu bialite} * S_{crater\text{-}walls} *(1 - \emptyset_{\mu bialite}) * [carbonates] *\rho_{\mu bialite\text{-}carbonate})/ M_{C\text{-}\mu bialite} \quad (5.14)$$

where $\sigma_{\mu bialite}$ is the microbialites growth rate in $m.yr^{-1}$, $S_{crater\text{-}walls}$ is the surface of deposition (m^2), $\emptyset_{\mu bialite}$ is the porosity, [carbonates] is the microbialite carbonate content in wt. %, $\rho_{\mu bialite\text{-}carbonate}$ is the density of the carbonate phases composing the microbialites ($g.m^{-3}$) and $M_{C\text{-}\mu bialite}$ is the C molar mass of the microbialites ($gC.mol^{-1}$).

The $\sigma_{\mu bialite}$ was determined from ^{14}C-carbonate dating from a microbialite sample at 40 m depth. Considering the DIC reservoir effect (by dating water column $DI^{14}C$ at the same depth), I calculated the microbialite growth rate based on its size and age. This gave a growth rate of approximately 0.15 $mm.yr^{-1}$. Microbialite growth rate was also estimated from four *in situ* microbialite growth experiments run between 2012 and 2014, and 2014 and 2019 at shallow depths in Lake Alchichica and run by collaborators from the IMPMC (Paris). Resulting $\sigma_{\mu bialite}$ varied between 0.2 and 0.6 $mm.yr^{-1}$, which is slightly higher but close to the values determined from ^{14}C dating. Thus, a growth rate of 0.2 $mm.yr^{-1}$ was chosen. The surface of microbialite formation was considered to be the surface of the crater walls from 0 to 50m-depths (Fig. 5.2), and was calculated as the lateral area of truncated cone ($7.3*10^5$ m^2). This choice is motivated by previous field campaigns, which showed that microbialites can be found from the surface to at least 40 m in depth. $\emptyset_{\mu bialite}$ was chosen as 52 % following Bouton *et al.* (2020a). The carbonate content of Alchichica's microbialites was determined for 19 samples by acid

decarbonatation and gave an average concentration of 98 ± 0.7 wt. % (2σ). Alchichica's microbialites are composed predominantly of aragonite and hydromagnesite which have densities of 2930 and 2240 kg.m^{-3}, respectively. From field observations, I estimate aragonitic and hydromagnesitic microbialites to represent 25 and 75 % of total microbialites. This results in a $F_{\mu bialite}$ of 1.5*10^{6} molC.yr^{-1}. An isotopic fractionation of 4.5 ‰ was applied between the lake DIC and microbialites $\delta^{13}C$, based on $\delta^{13}C$ measurements of the current DIC and "living" (immerged) microbialites (Chapter 10 and Kaźmierzack *et al.*, 2011).

5.2.3.4. Carbon deposition in sediment organic matter and carbonates

The fluxes of C deposited in the bottom sediments as organic matter or carbonates (F_{OM} and F_{carb}) were computed as follows:

$$F_{OM} = SAR * A_{sed\text{-}deposit} * (1\text{-}\emptyset) * \rho_{bulk\_sediments} * [TOC] \quad (5.15)$$

$$F_{carb} = SAR * A_{sed\text{-}deposit} * (1\text{-}\emptyset) * \rho_{bulk\_sediments} * [carbonates] \quad (5.16)$$

where SAR is the sediment accumulation rate (m.yr^{-1}), $A_{sed\text{-}deposit}$ is the area of sediment deposition at the lake bottom (m²), ∅ is the sediment porosity, and $\rho_{bulk\_sediments}$ is the bulk sediments density (g.m^{-3}), all multiplied by the concentration of total organic carbon or carbonates in the sediments (in mol.g^{-1}).

The SAR is determined for each sediment horizon based on ^{210}Pb dating, and averaged 0.29 cm.yr^{-1} for the 25 cm studied here (see Chapter 6). In comparison, Alcocer *et al.* (2014b) reported an average SAR value of 0.3 cm.yr^{-1} for another core at the center of the lake (recording until 2002), whereas Caballero *et al.* (2003) reported a value of ~ 0.06 cm.yr^{-1} for sediments on the littoral area. Therefore, I only considered the area of the lake with depths below 50 m (~1.4 km²) for sediment deposition, based on the bathymetry and hypsographic-area determined by Filonov *et al.* (2022) (Fig. 5.2). In order to gauge its influence, A_{lake} is one of the parameters for which the sensibility of the model is tested. Porosity was initially determined from the volume of water extracted from each sediment horizon at the moment of sampling (*i.e.* the porewater volume divided by the volume of a sediment layer). However, this method yielded inconsistently low values (between 35 and 65%). Alcocer *et al.* (2014b) suggested a porosity of between 74 and 88 % for Alchichica's sediment type, based on Koegler (1967). In a sediment core with a very similar mineralogy (aragonite, hydromagnesite, amorphous-Si and albite), but

much higher OM content (which tends to increase the porosity volume), Milesi *et al.* (2020) determined porosities varying between ~95 % and 85 % in hydromagnesite-rich and hydromagnesite-poor layers, respectively. Considering all this, I fixed the porosity to a value of 85 % in the top layers, and 75 % in deeper layers. Bulk dry sediment density was measured with a pycnometer by He gas injection. Total carbonate content was determined by 1N-HCl decarbonatation. After this step, TOC concentrations were determined by EA-IRMS. The C isotope composition of TOC and carbonates exported to the sediments were measured for each sediment horizon.

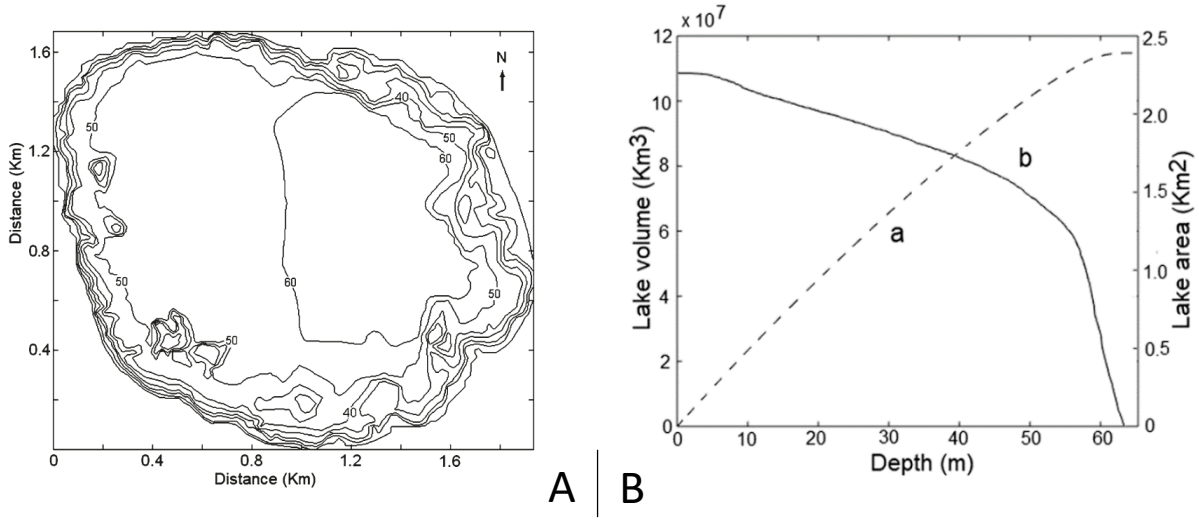

Figure 5.2: bathymetric map (A) and cumulative volume and area of Lake Alchichica (B). In 'B', the dashed line (a) represents the accumulative volume of the lake and the solid line (b) its hypsographic-area, versus depth in meters. Both figure are from Filonov *et al.* (2022).

5.2.3.5. Carbon exchanges with atmospheric CO_2

The atmosphere can either be a net source or sink of CO_2 to the lake, depending on the relative difference of their CO_2 partial pressures (pCO_{2w} and pCO_{2a}). Lake CO_2 degassing or "in-gassing" follow Fick's law equation:

$$F_{Net} = k.K_0.(pCO_{2w} - pCO_{2a}) \quad (5.17)$$

where the net CO_2 flux F_{Net} (mol.m^{-2}.s^{-1}) equals the product of gas transfer velocity (k in m.s^{-1}), gas solubility (K_0 in mol.m^{-3}.Pa^{-1}), and P_{CO2} difference between the water and the atmosphere (in Pa). The lake is degassing if this difference is positive. In Alchichica, pCO_{2w} calculated from 2019 water samples at all depths represented about 3 times atmospheric pCO_{2a} (Havas *et al.*,

2023a). Calculated with data from several preceding field campaigns (January 2012, May 2014 and 2016, and June 2017) from the "ANR group", and from published data (between 1941 and 2011), the lake's pCO_{2w} were even higher in the past. Logically, they reach maximum values (~4.8 pCO_{2a}) around the 2000, when [DIC] is the highest (Table 5.1). Thus, Lake Alchichica is and recently was a net source of C to the atmosphere. At an altitude of 2320 m, atmospheric pCO_{2a} was calculated to be about 308 ppm. Thus, the difference with lake pCO_{2w} in May 2019 was of about 600 ppm (or 60 Pa).

A K_0 of $3.9.10^{-4}$ $mol.m^{-3}.Pa^{-1}$ was determined based on the temperature and salinity of Lake Alchichica after Weiss (1974). In relatively large basins and above a threshold of about 3-5 $m.s^{-1}$, wind speed is generally the main factor influencing the gas transfer velocity '*k'* (Wanninkhof and Knox, 1996; Cole and Caraco, 1998; Wanninkhof *et al.*, 2009; Holgerson *et al.*, 2016, 2017). To take into account other parameters influencing *k* at low wind speeds (*e.g.* bubbles, rain events, buoyancy fluxes, or chemical enhancement), dedicated empirical laws usually include an asymptotical term that provides minimum *k* values. In Alchichica, wind speed averaged about 2.5 $m.s^{-1}$ in 2021 and 2022 (source: meteoblue.com), which is consistent with values during the spring 2002, lower than 1 $m.s^{-1}$ most of the day but averaging 5-6 $m.s^{-1}$ in the afternoon (Filonov *et al.*, 2006). Thus, I consider an average wind speed value of 2.5 $m.s^{-1}$ in the calculation of *k* for all the period studied. I used an equation empirically parametrized based on global wind and CO_2 flux data, as reviewed by Wanninkhof *et al.* (2009):

$$k = 3 + 0.1\langle U\rangle + 0.064\langle U^2\rangle + 0.011\langle U^3\rangle \quad (5.18)$$

with $\langle U\rangle$ as the average wind speed. At 2.5 $m.s^{-1}$, Eq. 5.18 gives a *k* value (3.8 $cm.h^{-1}$ or $1.1*10^{-5}$ $m.s^{-1}$) similar as from another equation determined from low-wind oligotrophic lake experiments (Cole and Caraco, 1998; $8.6*10^{-6}$ $m.s^{-1}$). Note that these values are well within the range found for lakes the same size as Alchichica (~ 2 km^2), where this parameter *k* was directly measured, worldwide (n=67; Holgerson *et al.*, 2017).

Following Eq. 5.17, the net evasion CO_2 flux calculated for 2019 equals ~7.6 $mol.m^{-2}.yr^{-1}$, *i.e.* ~17.10^6 $mol.yr^{-1}$ considering the area of Alchichica. In 2000, it goes up to ~15 $mol.m^{-2}.yr^{-1}$, or 33.10^6 $mol.yr^{-1}$. This estimation is slightly higher but close to the global average for freshwater lakes (5.8 $mmol.m^{-2}.yr^{-1}$; Cole *et al.*, 1994; Borges *et al.*, 2014), but lower than saline lakes worldwide (from 30 to 38 $mmol.m^{-2}.yr^{-1}$; Duarte *et al.*, 2008), and much lower than the measured flux from volcanic alkaline lakes worldwide (167 $mmol.m^{-2}.yr^{-1}$; Pérez *et al.*, 2011). Therefore, while this is consistent with previous characterization of Alchichica as being rather

an inactive maar lake, influenced by climate and groundwaters rather than volcanic degassing (Armienta *et al.*, 2008), the F_{Net} values calculated here are likely minimum estimates. Besides, high pH favors the hydration of CO_2 into and HCO_3^- and CO_3^{2-} (Wanninkhof and Knox, 1996), and this chemical enhancement factor is especially important in saline lakes with pH > 9 (Duarte *et al.*, 2008). Thus, I also considered the model with a minimum *k* value of ~7.5 ± 2.5 $cm.h^{-1}$ provided for alkaline lakes (Wanninkhof and Knox, 1996) and resulting in a F_{Net} of ~33.10^6 $mol.yr^{-1}$ in 2019 (as opposed to 17.10^6 above).

Despite a net flux of CO_2 from the lake to the atmosphere, isotopic exchange between the two reservoirs exists and implies that there is a degassing *and* a "in-gassing" flux, previously mentioned as the evasion and invasion fluxes. This exchange with atmospheric CO_2 is evidenced by the $DI^{14}C$ content of a water sample at a 40m-depth, showing 39% of modern C (*i.e.* atmospheric). Since the main source of DIC to Alchichica is the groundwater DIC (from basement carbonates dissolution), and potentially volcanic-CO_2 (both having dead C signatures, *i.e.* no ^{14}C), the presence of this "young" inorganic carbon requires the input of atmospheric CO_2. Because the lake DIC is not in isotopic equilibrium with atmospheric CO_2, evasion and invasion will carry different isotopic signatures and need to be considered separately. This can be done through the radiocarbon signature of the lake's DIC, which enables the determination of a ^{14}C-isotope mass balance (Turner *et al.*, 1983), such as:

$$\delta^{14}C_{LW}*[DIC]_{LW}*(\frac{\partial V}{\partial t}) + \delta^{14}C_{LW}*(\frac{\partial DIC}{\partial t})*V + (\frac{\partial \delta 14C}{\partial t})*[DIC]_{LW}*V = \Sigma F_i* \delta^{14}C_i*[DIC]_i$$

$$- \Sigma F_o* \delta^{14}C_o*[DIC]_o \qquad (5.19)$$

where F_i and F_o correspond to the in- and out-fluxes to the lake. From these, the invasion or evasion flux can be specifically isolated based on the net evasion flux calculated above, because $F_{Net} = F_{evasion} - F_{invasion}$. It follows that:

$$F_{invasion} = \{ \delta^{14}C_{LW} * ([DIC]_{LW} * (\frac{\partial V}{\partial t}) + (\frac{\partial DIC}{\partial t}) * V + F_{GWo} + F_{Net} * \alpha_{DIC\text{-}CO2} + F_{\mu bialite} * \alpha_{DIC\text{-}\mu bialite} + F_{TOC}*\alpha_{DIC\text{-}TOC} + F_{carb}*\alpha_{DIC\text{-}Carb} + \lambda*[DIC]_{LW}*V) - \delta^{14}C_{dead}*F_{GWi} + (\frac{\partial \delta 14C}{\partial t})*[DIC]_{LW}*V\} / \{ \delta^{14}C_{atm}*\alpha_{CO2\text{-}DIC} - \delta^{14}C_{LW*} \alpha_{DIC\text{-}CO2} \} \qquad (5.20)$$

where λ is the radioactive decay constant (1/8032 yr^{-1}) (Turner *et al.*, 1983) and α corresponds to the ^{14}C isotopic fractionation between the lake DIC and other C reservoirs when a fractionation occurs. It represents about twice the fractionation for ^{13}C. The $F_{invasion}$ stable isotope composition ($\delta^{13}C$) was set to global atmospheric values (-8.5 ‰; Graven *et al.*, 2020). That of $F_{evasion}$ was computed for each year such as:

$$\delta^{13}C_{evasion} = \delta^{13}C_{LW} - \Delta^{13}C_{DIC\text{-}CO2(g)}\ , \qquad (5.21)$$

with $\Delta^{13}C_{DIC\text{-}CO2(g)}$ set to -9 ‰ at an annual average surface temperature of 18 °C (Emrich *et al.*, 1970; Szaran, 1997; Macek *et al.*, 2020).

The previous model description includes all the parameters used in "scenario 1". Scenario 2 and 3 also include these parameters, but they are characterized by the addition of another one, corresponding to a DIC source from OC respiration, and volcanic-CO_2, respectively. These DIC sources are shortly presented below. All parameters used in the different scenarios are summarized in Table 5.2.

5.2.3.6. DIC from OC respiration (scenario 2)

In the second scenario, where CO_2 from OC respiration is added, F_{respi} was freely adjusted to best fit the lake $[DIC]_t$ data. The flux is chosen to be constant over time and is assigned a -25 ‰ isotopic composition (the average composition measured for OM in the water column and surficial sediments; Havas *et al.*, 2023a). It was added in both ^{13}C and ^{14}C mass-balance equations 5.5 and 5.19.

5.2.3.7. DIC source from Volcanic-CO_2 (scenario 3)

In the third scenario, volcanic-CO_2 is added as a source of C to the lake (but without respiration CO_2). F_{volc} was freely adjusted to best fit the lake $[DIC]_t$ and $\delta^{13}C_{model,\ t}$ data. I consider that on the timescale of this study, it should be constant over time. This flux was added in both ^{13}C and ^{14}C mass-balance equations 5.5 and 5.19. Canonical $\delta^{13}C$ composition of mantle CO_2 approaches -6 ± 2 ‰ while the global CO_2-release in volcanic arcs averages -4 ± 0.5 ‰ (Mason *et al.*, 2017 and references therein). In the geothermal field of Los Humeros in the north

of Alchichica, CO_2 degassing from fumaroles had a $\delta^{13}C$ between -3 and -6 ‰ (Lelli *et al.*, 2021), and soil CO_2 efflux isotopic signatures mostly spanned a range of values from ~ -3 to -8 ‰, but reaching down to -15 ‰ (Peiffer *et al.*, 2018). Additionally, $\delta^{13}C_{CO2}$ between -3.2 and -6.6 ‰ have been measured in fluids from geothermal wells in the same Los Humeros area (Truesdell and Quijano, 1988; Portugal *et al.*, 1994). Accordingly, three different values of $\delta^{13}C_{volc}$ (-3, -5 and -7 ‰) were tested in scenario 3.

			C inputs			C outputs		
			Process	Flux mole C.yr^{-1}	isotopic composition ‰ (VPDB)	Process	Flux mole C.yr^{-1}	isotopic composition ‰ (VPDB)
Scenario 1	Scenario 2	Scenario 3	Volcanic-CO_2	$2.5–3*10^7$	-3 – -7	Microbialite precipitation	$1.5*10^6$	$\delta^{13}C_{LW}$ + 4.5
			Groundwater in	$2–3*10^7$	0	Groundwater out	$[DIC]_{LW}$	$\delta^{13}C_{LW}$
			Atmospheric CO_2 ingassing	*$8–33*10^6$ #*	-8.5	Atmospheric CO_2 degassing	*$2.5–6.5*10^7$ #*	$\delta^{13}C_{LW}$ - 9
			OM respired-CO_2	$2.5–3*10^7$	-25	Sediment carbonate deposition	$4–9*10^6$	4.5–4.8
						Sediment organic C burial	$4–8*10^6$	-24.3 – -25.7

			O inputs			O outputs		
			Process	Flux L.yr^{-1}	isotopic composition ‰ (VSMOW)	Process	Flux L.yr^{-1}	isotopic composition ‰ (VSMOW)
Scenario 1	Scenario 2	Scenario 3	Precipitation	$8–10*10^8$	-8	Evaporation	$3–4*10^9$	-8 – -10
			Groundwater in	$2–3*10^9$	-9	Groundwater out	$2–3*10^8$	$\delta^{18}O_{LW}$

Table 5.2: fluxes and isotopic compositions of carbon and oxygen inputs and outputs in Alchichica for the three scenario presented in the method. All C outputs operate in the three scenarios, but volcanic-CO_2 input applies only to scenario 3, and respiration CO_2 input only to scenario 2. # Shows the fluxes that may vary from a scenario to the other.

5.3. Results

5.3.1. Description of the $[DIC]_{LW,(t)}$, $\delta^{13}C_{carb}$, $\delta^{18}O_{carb}$, and $V_{(t)}$ data used as reference

The DIC concentration in Lake Alchichica increased between 1940 and the early 2000s, from about 30 to 36 mM. After 2001, it fluctuated to reach 34.6 mM in 2019 (Fig. 5.3). After correcting for the presence of hydromagnesite (see above), $\delta^{13}C_{carb}$ shows a decrease from ~5 ‰ before 1956 to 4.1 ‰ in 2019 (Fig. 5.3). The corrected $\delta^{18}O_{carb}$ shows a slight increase from 1.1 to 1.3 ‰ between 1956 and 1980, before decreasing back to 0.9 ‰ in 2018. The lake volume was not precisely estimated throughout the studied period and its evolution is determined from estimation of the water level decrease on three distinct periods: 1960-1991; -2004; -2019 (Alcalá, 2004; Silva-Aguilera, 2019; Filonov *et al.*, 2022). Thus, from the estimation of $11.5.10^{10}$ L in recent years (Filonov *et al.*, 2022), its volume should have been about 12.0, 12.5 and $13.0*10^{10}$ L in 2002, 1992 and 1960, respectively (Fig. 5.3).

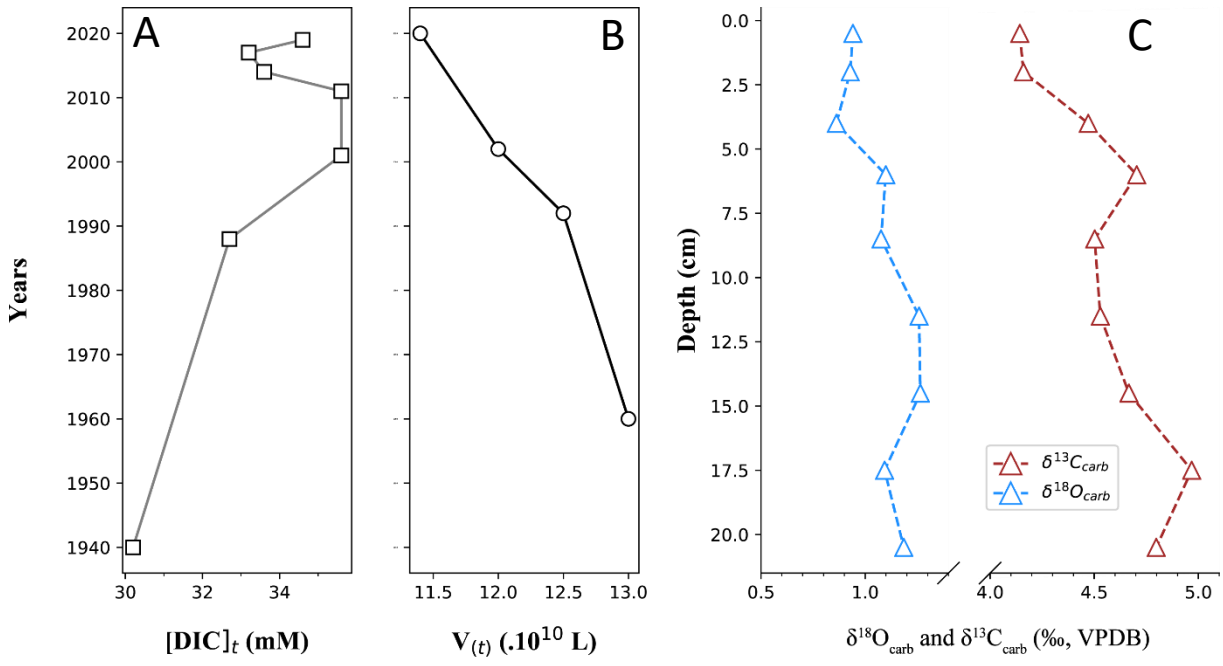

Figure 5.3: Evolution with time of the dissolved inorganic concentration in $mmol.L^{-1}$ (A), lake volume in liters (B), and carbon and oxygen isotopes compositions with depth (C). The isotopic compositions shown are the ones corrected from the contribution of detrital hydromagnesite (*i.e.* they slightly differ from bulk isotopic compositions).

5.3.2. Evolution of water and C fluxes with time

Evaporation and precipitation fluxes from meteorological data show broadly inversely correlated trends reaching maximum and minimum values, respectively, around 1990 (Fig. 5.4). Groundwater in- and out-fluxes, calculated to match the evolution of the lake volume, increase from 1960 to 1990, before decreasing until 2020 (Fig. 5.4). Note that the GW in-flux does not necessarily have to correlate with the precipitation flux since the former integrates the whole catchment area and is greatly impacted by anthropic activity.

The largest C flux to Alchichica is the GWi with an average of 26.10^6 mol.yr^{-1} (Fig. 5.4). In scenario 1, atmospheric invasion is the only other source of C, and represents 12.10^6 mol.yr^{-1} on average (Fig. 5.4). The net evasion flux of CO_2 to the atmosphere is equivalent to F_{GWi} with an average of 29.10^6 mol.yr^{-1} (Fig. 5.4). The GWo and sediment deposition sinks of C (carbonates and OC) represent between 6.8 and 8.10^6 mol.yr^{-1} , while C precipitation is the smallest flux with a value of $1.6.10^6$ mol.yr^{-1} (Fig. 5.4). In comparison, respired OC and volcanic-CO_2 fluxes added in scenario 2 and 3, respectively, represent 30.10^6 mol.yr^{-1} (Fig. 5.4).

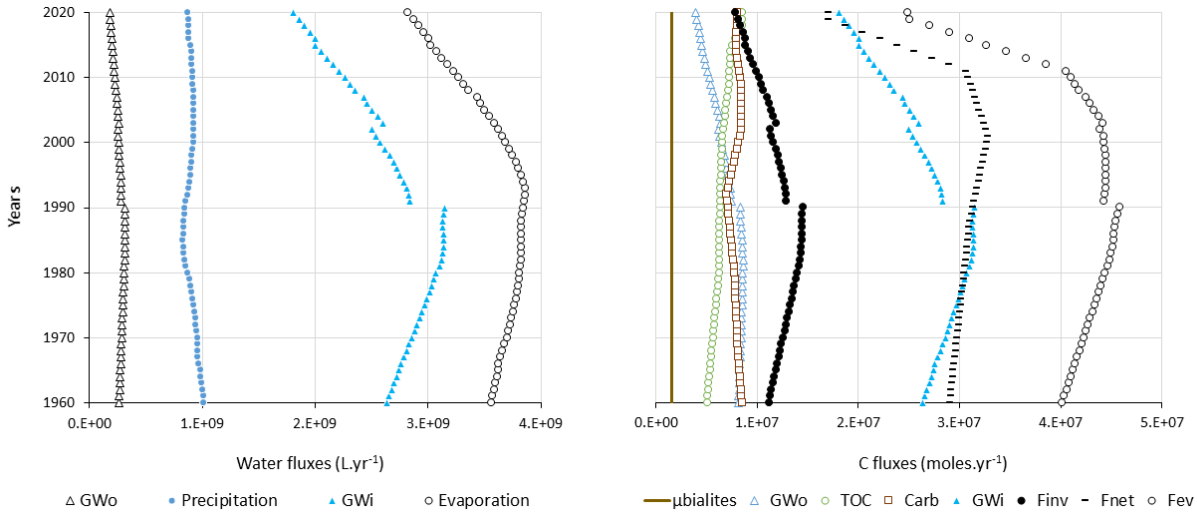

Figure 5.4: water and C fluxes in scenarios 1. In scenarios 2 and 3, a flux of $30*10^6$ mol.yr^{-1} of respired- or volcanic-CO_2 is added. It changes the ^{14}C balance of the lake such that calculated Fev and Finv are slightly different as well.

5.3.3. Modeled oxygen isotope compositions

Because water fluxes are kept constant among all scenarios, oxygen isotope modeling results does not change with the different scenarios. Modeled $\delta^{18}O$ has a nearly constant value of 1.1 ‰. In detail, it shows a decreasing trend from 1960 to 1990, then increase back between 1990 and 2000, and is then stable until 2020 (Fig. 5.5).

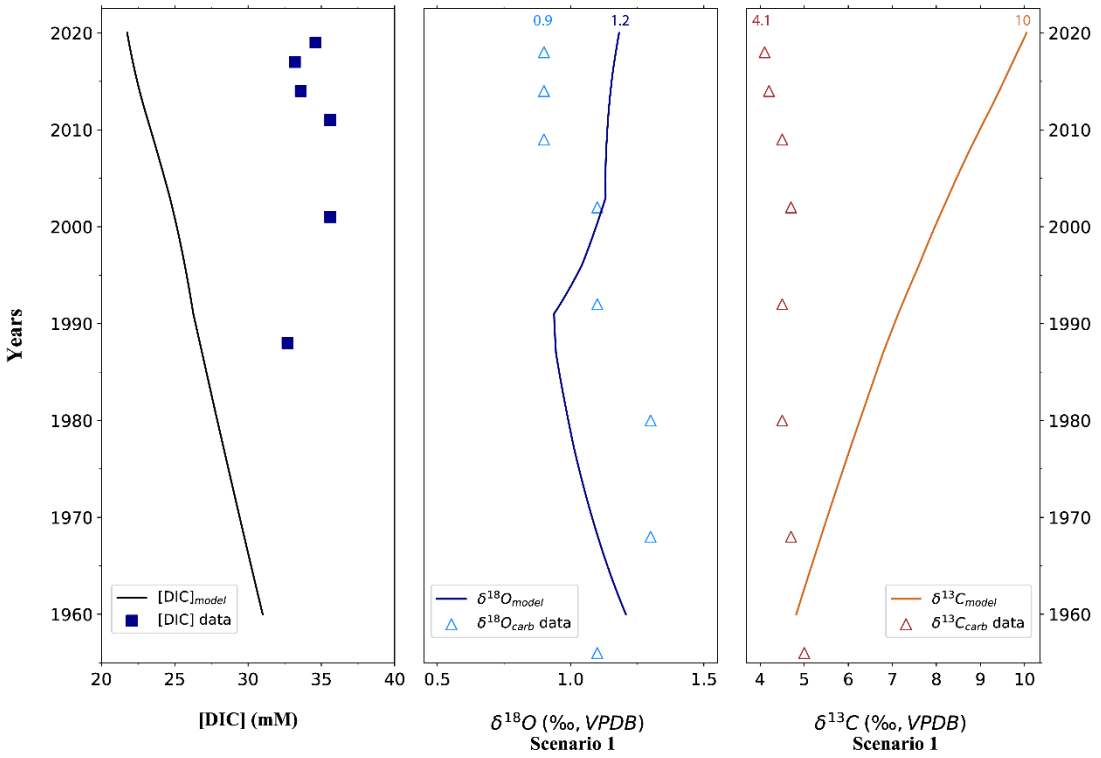

Figure 5.5: model results of the first scenario compared to the data for DIC concentration (left), oxygen isotopes (center) and carbon isotopes (right) *versus* time. Numbers in the top correspond to the different parameters value in 2020.

5.3.4. Modeled carbon isotope compositions

5.3.4.1. Scenario 1: no additional C source

The DIC concentration modeled without an external respiration or volcanic C source decreases from the initial 31 mM concentration in 1960 to 22 mM in 2020 (Fig. 5.5). In parallel, the modeled carbonate $\delta^{13}C$ uniformly increases from 4.8 to 10 ‰ between 1960 and 2020 (Fig. 5.5).

5.3.4.2. Scenario 2: addition of CO_2 from OC respiration

In order to follow the DIC concentration trend (Fig. 5.6), F_{respi} was set to vary between 25 and $30*10^6$ molC.yr^{-1}, resulting in a modeled [DIC] that increases linearly from 31 in 1960 to values between 34 and 36.4 mM in 2020, respectively (Fig. 5.6). The respired CO_2 is chosen to have a $\delta^{13}C$=-25 ‰. It results in a modeled $\delta^{13}C$ decreasing from the initial 4.8 ‰ to values 0.9 and -0.6 ‰ in 2020 (Fig. 5.6).

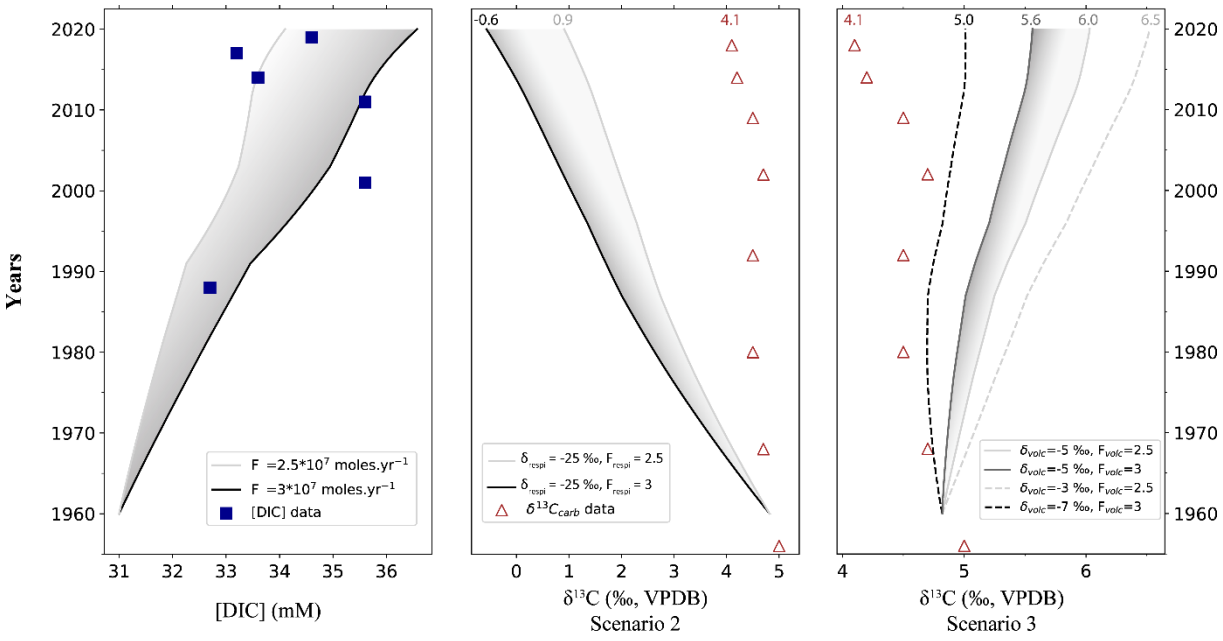

Figure 5.6: model results of the second and third scenarios compared to the data for DIC concentration and carbon isotopes *versus* time. The black line represents the case when F_{respi} or F_{volc} are set to $3*10^7$ mol.yr^{-1}; the light gray line represents the case for fluxes of $2.5*10^7$ mol.yr^{-1}. On the right for scenario 3, the black and gray dashed lines represent the model results in the most "extreme" scenarios, when adding $3*10^7$ mol.yr^{-1} of volcanic-CO_2 at -7 ‰, and $2.5*10^7$ mol.yr^{-1} at -3 ‰, respectively. In between, the dark and light gray lines are the results for a volcanic-CO_2 flux of $3*10^7$ mol.yr^{-1} and $2.5*10^7$ mol.yr^{-1}, respectively, both at -5 ‰. Numbers in the top of the frame of scenario 2 and 3 correspond to the different parameters value for the year 2020.

5.3.4.3. Scenario 3: addition of CO_2 from volcanic-CO_2

The F_{volc} is set to fit the DIC concentration trend as in scenario 2 (Fig. 5.6). Isotopic compositions of -3, -5 and -7 ‰ are tested for volcanic-CO_2. In the three cases the modeled $\delta^{13}C$ increases, but less than in model 1 (Fig. 5.6). It rises from the initial 4.8 ‰ in 1960 to values between 5 ‰ (F_{volc} = $30*10^6$ molC.yr^{-1} and $\delta^{13}C_{volc}$ = -7 ‰) and 6.5 ‰ (F_{volc} = $25*10^6$ molC.yr^{-1} and $\delta^{13}C_{volc}$ = -3 ‰).

5.4. Discussion

5.4.1. Fit of the $\delta^{18}O$ and validation of calculated water fluxes

Despite dominant evaporation over precipitation rates, the O isotope record of Lake Alchichica in the last 60 years does not show increasing values, but on the contrary, slightly decreasing ones, from 1.1 to 0.9 ‰ (Fig. 5.3). The modeled oxygen isotope composition fits the data well, as it remains stable overall (Fig. 5.5). This is notably because ambient humidity is high enough to prevent a highly fractionated evaporation flux ($\delta^{18}O_E \approx$ -8.7 ‰), which is thus balanced out by the precipitation and groundwater in-fluxes ($\delta^{18}O_P \approx$ -8 ‰ and $\delta^{18}O_{GWi} \approx$ -9 ‰).

The hydrological fluxes are relatively well constrained since P and E rates were obtained from on-site measurements (Alchichica meteorological station 21052), and GWi estimation directly follows field observations of the lake level decrease (Silva-Aguilera *et al.*, 2022b). The decline of GWi after 1990 is consistent with the intensification of farming activity in the area at that time (Silva-Aguilera *et al.*, 2022b). Setting the GWi flux to match a smaller lake level decrease (*e.g.* ~5 m instead of 7 m decrease in the last 60 years), is slightly better but does not critically change the modeled $\delta^{18}O$ (Fig. S5.1). Therefore, to a first order, the $\delta^{18}O_{model}$ confirms the good estimation of water fluxes, which is important for a good constraint on the lake DIC evolution.

Nonetheless, the modeled $\delta^{18}O$ curve does not fit the small $\delta^{18}O_{carb}$ temporal variations (Fig. 5.5). Two determinant parameters are under-constrained and could explain this observation. First, the isotopic composition of rain water is likely less buffered than that of groundwater and may have fluctuated over time. Changes in $\delta^{18}O_P$ between -6 and -10 ‰, for a given humidity value, would have a major impact on the lake's $\delta^{18}O_{model}$ (Fig. S5.2). Second, ambient humidity indirectly plays an even more significant role on $\delta^{18}O$ because it strongly influences the isotopic fractionation during evaporation. Humidity is related to temperature and evaporation rates such that higher values of these two parameters result in a higher humidity content. Humidity thus likely changed throughout the studied period. However, short time-scale variations of "h" and "$\delta^{18}O_P$" are largely under-constrained and only average values were considered (see 5.2.3.1).

Most importantly, these two factors will not affect the C mass balance of the lake. Only the water fluxes will, and these are independently well constrained. Therefore, I conclude that

the water- and O isotope-balance used are consistent, and adequate to further constraint the lake C balance.

5.4.2. Carbon mass balance

5.4.2.1. Scenario 1: without external volcanic or respiration DIC inputs

In the first scenario, the only considered in-fluxes of inorganic C are from GWi and atmospheric-CO_2 exchange. If DIC in the lake was at steady state (*i.e.* in- and out-fluxes equate to each other), the decrease in lake volume should automatically increase the concentration of remaining ions like HCO_3^-/CO_3^{2-}. In Alchichica, one can notice that the proportion of lake volume decrease more or less corresponds to that of the DIC increase, roughly 10 %. However, the question is whether the system is at steady state or not.

In the scenario 1 of the model, the GWi and atmospheric C sources are insufficient to explain the DIC and $\delta^{13}C_{carb}$ data variation (Fig. 5.5). Between 1960 and 2020, the modeled DIC concentration decreases of more than 9 mM while it should increase of ~4 mM, implying that the out-fluxes of DIC are greater than the in-fluxes. In parallel, $\delta^{13}C_{model}$ markedly increases by ~5 ‰, while it should decrease of ~ 0.5 ‰. A major driver for both [DIC] and $\delta^{13}C_{model}$ trends is the important net flux of CO_2 evasion (F_{Net}) resulting from the lake's high pCO_2 and carrying a highly negative isotopic signature. In the model, the estimated F_{Net} flux is high enough to push the system out of steady state, but even more so, to generate a decrease in the [DIC]. Therefore, either this flux is overestimated (possibly with other out-fluxes as well), or additional DIC sources to the lake exists. Importantly, from the current knowledge of CO_2 degassing, it is more likely that the F_{Net} flux was underestimated, than overestimated (see 5.2.3.5).

As a sensitivity test, the model still does not reproduce the increased DIC and decreased $\delta^{13}C_{carb}$ when F_{Net} is divided by half (Fig. S5.3a). Organic C fixation and deposition in the sediments can also be an important sink of isotopically light C. Yet again, dividing this flux, *and* F_{Net} by half still does not allow the model to reach the highest DIC concentration, and results in a final $\delta^{13}C$ of 6.3 instead of 4.1 ‰ (Fig. S5.3b).

These results show that the evaporative context of Lake Alchichica, and thus the decrease of the lake level, are not sufficient to concentrate DIC as observed since the 60s despite

evaporation being ~4 times higher than precipitation rates. A direct measurement of the net CO_2 degassing flux from Alchichica should definitely confirm (or rebut) this conclusion. For the time being, I conclude that an additional source of C is required to support and balance out the effect of CO_2 atmospheric degassing of the lake's [DIC] and $\delta^{13}C$. This source should hold a negative isotopic signature.

5.4.2.2. Scenario 2: additional CO_2 from respiration

Since a negative $\delta^{13}C$ source is required to match the data, one could argue that it comes from the remineralization of organic C (OC). Despite being oligotrophic, Lake Alchichica shows relatively high DOC concentrations, and sedimentary organic C export (Alcocer *et al.*, 2014b; Havas *et al.*, 2023b). Autotrophic C fixation followed by its respiration affect the lake's DIC and $\delta^{13}C_{DIC}$ in opposite ways such that they should not change the overall lake C mass balance. A net respired-CO_2 source thus requires that the 'lake + sediments' system is not in a steady state, but either (i) recently evolved to favor OC respiration over C fixation or (ii) receives external OC inputs that are being respired. In the water column, the total amount of OC would be exhausted in less than 10 years if it was respired at rates required to account for the [DIC] increase. In the sediments, OC content is higher at the top of the core than below, suggesting more important C fixation than respiration in the recent years. Besides, it was shown that the majority of particulate organic matter (POM) depositing and being processed in the sediments is *quickly* remineralized into DIC, which can diffuse back to the water column or accumulate in the sediments (as observed in the porewater of Alchichica's sediments), while a minor portion accumulates as refractory dissolved OM (Burdige *et al.*, 2016). It is therefore more likely that this putative source of respired-CO_2 comes from outside the lake itself. Organic matter in Alchichica is primarily autochthonous in origin (Havas *et al.*, 2023a; 2023b; Alcocer *et al.*, 2014b), but some DOC could be contained in GW (*e.g.* in relation with surrounding agriculture fields), and quickly remineralized in the lake.

To test this hypothesis in "scenario 2", an additional DIC source coming from respired allochthonous OC (F_{respi}) was added (see 5.2.3.6). The F_{respi} flux is set to values between 2.5 and $3*10^7$ $mol.yr^{-1}$, representing between 30 and 40% of the total inorganic C in-fluxes, and allowing to reproduce the general [DIC] trend (Fig. 5.6). It does not reproduce the peak of [DIC] around the 2000s, and its decrease afterwards (Fig. 5.3; 5.6), because F_{respi} is constant through time (this applies to both scenario 2, and 3, because F_{respi} and F_{volc} are set the same way).

Qualitatively, it is tempting to explain the decrease of [DIC] data by smaller evaporation rates after the 1990s (Fig. 5.3; 5.4). In the model however, [DIC] in the scenario 2 and 3 keeps increasing after 2000 mainly because GWi strongly diminishes. Thus, the calculation method for GWi might underestimate this flux after the 1990s. If I arbitrarily fix the GWi flux to its maximum values after 1990, it does reproduce the early 2000s [DIC] decrease in scenario 2 and 3, but does not compensate the lake DIC deficit at all in scenario 1. While it shows that GWi may indeed be slightly underestimated after 1990, but it does not contradict the requirement for an additional C source. Further, I thus consider the calculation of the GWi flux to be a reasonably good approximation of its true value, even if it is slightly underestimated between 1990 and 2020.

With this additional "respired-CO_2", the $\delta^{13}C_{model}$ drops to values between -0.6 and 0.9 ‰ in 2020 (Fig. 5.6). It clearly shows that CO_2 from OC respiration carries $\delta^{13}C$ signatures that are much too low to be the only additional C source. Indirectly, it supports that most of the OM in Alchichica is autochthonous (Havas *et al.*, 2023a, 2023b).

5.4.2.3. Scenario 3: additional volcanic-CO_2

In a third scenario, I test if the addition of a volcanic-CO_2 source (F_{volc}), degassing inside Lake Alchichica could fit the sediment carbonate data. Similarly to 'scenario 2', F_{volc} is set to range between 2.5 and $3*10^7$ $mol.yr^{-1}$ to reproduce the general [DIC] trend.

None of the tested $\delta^{13}C_{volc}$ values (-3, -5 and -7 ‰) allow a perfect match of the data, although they are closer to the reference dataset than in the first two scenarios (Fig. 5.6). A possibility explaining the offset between the $\delta^{13}C_{carb}$ data, and $\delta^{13}C_{model}$ modeled in scenario 3 is that the volcanic-CO_2 flux has an isotopic signature even more negative than -7 ‰. This could happen for example if volcanic-CO_2 mixed with biogenic CO_2. Other processes such as the interaction and isotopic exchange of ascending volcanic-CO_2 with groundwater DIC, or its precipitation as calcite in the crust could also lower the $\delta^{13}C_{volc}$ signature (Peiffer *et al.*, 2018). I found traces of such calcite in a volcanic conglomerate sampled from the crater's wall of Alchichica. The C isotope composition of this sample is -2.3 ‰, which differs from the basement limestone signatures (~0 ‰), but is consistent with a deep precipitation from volcanic CO_2 (Peiffer *et al.*, 2018), and with the signatures reported by Gonzales-Partida *et al.* (1993)

for similar materials. Calcite from this conglomerate thus likely corresponds to previously-formed deep calcite, excavated and mixed with volcanic pyroclasts during the crater's formation. Applying a -9 ‰ signature to $\delta^{13}C_{volc}$ in scenario 3 results in a good match with the DIC and $\delta^{13}C_{carb}$ data over time (Fig. S5.4). Nevertheless, it seems unlikely that the entire flux of volcanic-CO_2 reaching Alchichica carries these extremely negative values (*cf.* Mason *et al.*, 2017 and section 5.2.3.7). In summary, while scenario 3 provides closer fits to the data than scenario 2, it seems that neither the volcanic- or the respired-CO_2 source alone can fully explain the data.

5.4.2.4. Alternative satisfactory scenario, and summary of the modeling approach

In scenario 3, $\delta^{13}C_{model}$ departs from the data mostly after the mid-90s (Fig. 5.6). This can partly be explained by the decrease of GWi bearing $\delta^{13}C \approx 0$ ‰, together with increasing TOC burial ($\delta^{13}C \approx -25$ ‰). In a sensitivity test, if GWi is adjusted such that it decreases less rapidly after 1990, and F_{TOC} is set to a constant minimum value, the modeled $\delta^{13}C$ barely fits the data when $\delta^{13}C_{volc}$ is equal to -7 ‰, and does not fit the data when $\delta^{13}C_{volc}$ is equal to -5 ‰ (Fig. S5.5). It is also around the mid-90s that evaporation, and the resulting CO_2 evasion flux decline (Fig. 5.4). However, diminished CO_2 net evasion after 2000 should lead to a decrease of $\delta^{13}C$ as observed in the data, but not in the model (Fig. 5.6). Therefore, another parameter influencing the sediment signatures seems to be missing in the model.

Around the 1990s, the diminution of GWi flux to Alchichica has been associated to an intensification of anthropic activities in the area, notably of agriculture (Silva-Aguilera *et al.*, 2022b). It is possible that these farming activities influenced the nature of the GWi carbon flux, by adding more biogenic C to the groundwater DIC (*e.g. via* soil respiration). While the DIC concentration of GWi was measured (Kaźmierzak *et al.*, 2011; Silva-Aguilera, 2019; Lelli *et al.*, 2021), and is thus not a free-parameter, $\delta^{13}C_{GWi}$ is, and can be considered as the product of a mixing between calcareous-derived C (0 ‰) and organic-derived C (~-25 ‰). There is no constraint on the proportion of OC-derived DIC within groundwaters in recent or ancient years, so this parameter has to be set arbitrarily. In a fourth scenario, I consider that 15 % of DIC_{GWi} derive from OC before 1990 and 30 % after 1990 (following the increased anthropic influence). Hence, the $\delta^{13}C_{GWi}$ value used in the model becomes -3.75 and -7.5 ‰ for the periods before and after 1990, respectively. Because the DIC_{GWi} concentration is not changed, the input of volcanic CO_2 is still required to match the lake [DIC] increase ($F_{volc} = 3*10^7$ mol.yr^{-1}). In a way,

this fourth alternative scenario can be seen as intermediate between scenario 2 and 3. This time, the combination of this more negative $\delta^{13}C_{GWi}$ with the volcanic input allows to match the $\delta^{13}C_{carb}$ profile well (Fig. 5.7).

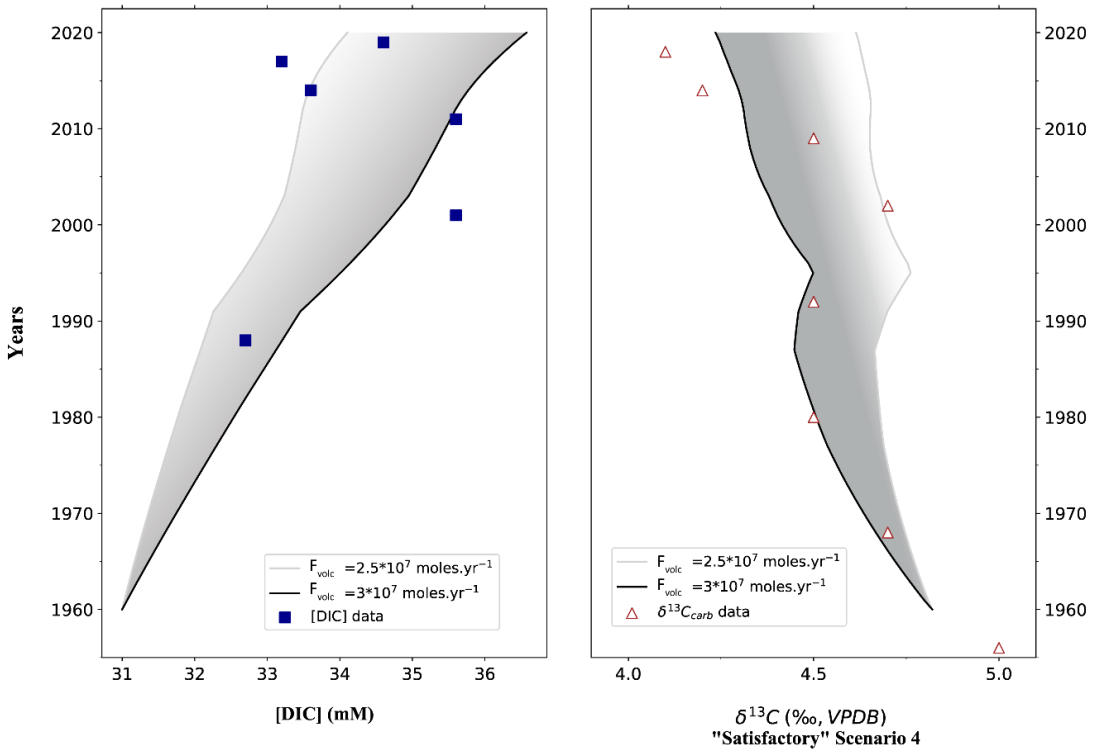

Figure 5.7: model results for the fourth "satisfactory" scenario. Here, a flux of volcanic-CO_2 from 2.5 to $3*10^7$ mol.yr^{-1} ($\delta^{13}C$=-5‰) is added but the isotopic composition of the GW-DIC represents a mix between the dissolution of the limestone basement and CO_2 from soil respiration, and is thus also negative. Due to an intensification of agriculture in the middle of the 1990s, I consider a larger contribution of respired CO_2 after 1995.

Clearly, a number of parameters are only estimated and their exact value could vary. Among these parameters, sediment porosity and area of deposition, $\delta^{13}C_{GWi}$, the groundwater and net evasion fluxes (GWi, F_{Net}) have a primary influence. Importantly, 'scenario 1' does not properly fit the data, even if (i) F_{Net} is reduced by 50%, (ii) maximum GWi values are kept after 1990 (which are inconsistent with the lake level decrease), (iii) $\delta^{13}C_{GWi}$ is adjusted to -4 ‰, and (iv) the porosity is adjusted to 90% or more to reduce the sediment C export (Fig. 5.8).

Considering these parameters, a small $0.5*10^7$ mol.yr^{-1} flux of volcanic-CO_2 is still required to fit the data. On the contrary, if the higher range of F_{Net} estimation (see discussion

on the *k* parameter in section 5.2.3.5) is considered in the alternative scenario 4, a F_{volc} of at least $5*10^7$ mol.yr^{-1} is required. The area of sediment deposition is chosen as 1.4 km² for depths above 50 m, which is likely a minimum estimation. Higher area of deposition would induce higher sediment C export, and thus require the input of even larger C influxes.

It is concluded that a scenario with no volcanic-CO_2 inputs is unlikely, and that the source of DIC from groundwater differs from that of the limestone due to mixing with biogenic C. A better evaluation of the parameters used in the model will allow narrowing the range of F_{volc} estimations.

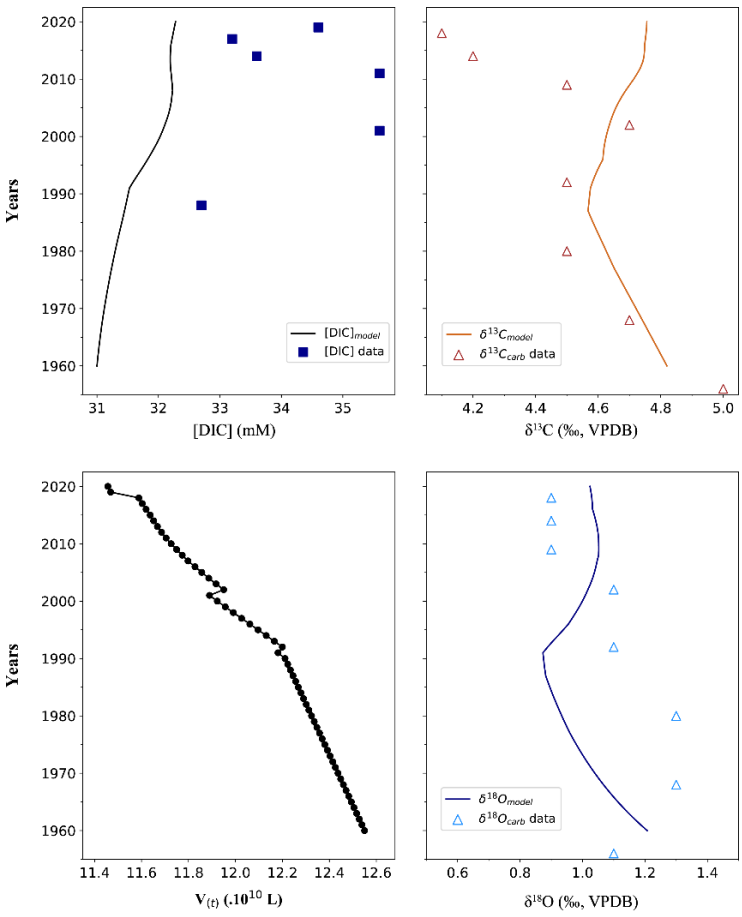

Figure 5.8: results of an alternative scenario where the different water and C fluxes are adapted to try to better fit the data without an additional volcanic C flux. Notably, the decrease of GW influx after 1990, the CO_2 evasion flux, and the sedimentary C deposition fluxes are reduced. One can see that even in this unrealistic extrapolation of the fluxes, the data is hardly reproduced, showing that an additional source of DIC such as volcanic-CO_2 is likely required.

5.4.3. Perspective on the geological context of Alchichica and similar environments

Some authors concluded that Alchichica and other Mexican maar lakes were not active, or even quiescent, based on punctual chemical analyses, and notably on their high pH (Armienta *et al.*, 2008). The time integrated view of Alchichica's C cycle presented in this chapter supports on the contrary, that volcanic degassing does influence the water chemistry of this lake. While it is obvious that degassing does not occur at the same rate than in highly active volcanic lakes, it is also obscured by processes taking place in the lake, notably due to its geological context. As an example, Lake Dziani-Dzaha (Mayotte, France) experiences significant magmatic degassing, but preserves a pH above 9 due to important evaporation and photosynthesis rates (Milesi *et al.*, 2020).

Lake Alchichica is a high pH, alkalinity-buffered lake (Havas *et al.*, 2023a), and the acidity generated by volcanic gases (HCl, SO_2/H_2S and CO_2) could have been either dissipated through time and followed by CO_2 degassing only, and/or buffered by the calcareous basement rocks and alkaline aquifer (Pecoraino *et al.*, 2015). Lake Alchichica would thus correspond to a *low activity volcanic lake*, as defined by Rouwet *et al.* (2014), where direct CO_2-degassing does not necessarily occur, but CO_2-enrichment is bolstered by regional CO_2-degassing in the groundwater. Mixing between magmatic and limestone C was inferred for the Los Humeros geothermal field (Peiffer *et al.*, 2018; Lelli *et al.*, 2021), which shares the same aquifer "de Libres Orientale" as Alchichica. On the contrary, volcanic-CO_2 degassing in Alberca de los Espinos – where there is only a basaltic basement (Zeyen *et al.*, 2021) – would have a more straightforward impact on the lake's chemistry. Consistently, a clear decrease of the lake's pH at depth, and average DIC isotope compositions close to volcanic signatures were found in Alberca (Havas *et al.*, 2023a).

In Alchichica, while volcanic degassing is not directly evidenced from $\delta^{13}C_{DIC}$ and pH values, it participates to obscure the influence on $\delta^{13}C_{DIC}$ of the evaporation process, which should favor an increase of the DIC isotope composition. Indeed, without the volcanic-CO_2 contribution, $\delta^{13}C_{DIC}$ would strongly increase (*cf.* scenario 1, Fig. 5.5). The lake $\delta^{13}C_{DIC}$ is also highly impacted by the flow path of groundwater – whose ion concentration increases when passing through La Preciosa before reaching Alchichica ($[DIC]_{GWi} \approx 7$ *vs.* 10 mM; Silva-Aguilera, 2019; Havas *et al.*, 2023a) – and by the anthropic use of groundwater (*cf.* scenario 4; section 5.4.2.4).

The O isotope composition of Alchichica's water is also influenced by the anthropic use of groundwater and the direction of their flow path in the aquifer ($\delta^{18}O_{GWi}$ equals -13 and -8.7 ‰ before and after La Preciosa, respectively; Lelli *et al.*, 2021). Together with small local climatic variations (*e.g.* changes in evaporation rate, humidity), this explains the decreasing $\delta^{18}O_{carb}$ record despite higher evaporation than precipitation rates. All these parameters (climate/evaporation, volcanic- and groundwater-fluids) counterbalance and mask each other, complicating the interpretation of the C and O isotope records.

Based on the same premises as for Alchichica, Lakes Atexcac and La Preciosa were described as inactive (*i.e.* with no volcanic degassing) by Armienta *et al.* (2008). However, they share the same aquifer than Alchichica and Los Humeros (García-Sánchez *et al.*, 2022) and are also CO_2 super-saturated with respect to the atmosphere (Zeyen *et al.*, 2021). In 2019, their pCO_2 represented ~5 and 2 times the $pCO_{2\text{-}ATM}$, respectively (Havas *et al.*, 2023a). It is thus tempting to assume that Atexcac and La Preciosa also receive some volcanic gas inputs, especially in Atexcac.

5.5. Conclusion

In this chapter, I modeled the C cycle of Lake Alchichica over the last 60 years. Integrating hydrological, physico-chemical, and geochemical parameters of the lake water and sediments, I tested different scenarios featuring different fluxes and C isotope compositions for a variety of sources. I showed that evaporation alone was not enough to explain the recent increase in alkalinity and DIC concentration. A large additional C source (equivalent to the other main source of C, *i.e.* from GW) is required to balance both the quantity and isotopic composition of inorganic C in Alchichica. This C source is most likely coming from volcanic-CO_2 degassing into the lake, or delivered *via* the underlying aquifer (from 0.5 to 5 $mol.yr^{-1}$), although a better quantification of water and C fluxes will be necessary to precisely determine how much C this flux actually represents.

To fit the data, it is found that the groundwater DIC needs to bear a negative isotopic composition, differing from the limestone basement signatures, due to the contribution of respired biogenic C. Moreover, intensification of anthropic activities may have influenced the

flux of groundwater to Alchichica, but also the nature of its DIC, by favoring the contribution of respired CO_2.

The combination of these processes produces the slight decrease in $\delta^{13}C$ and $\delta^{18}O$ observed in the lake carbonate record, and prevents a clear recognition of the evaporation prevailing at the studied site, and of volcanic-CO_2 contributions.

Overall, this work allows a better understanding of the environmental factors leading to the alkalinity-salinity gradient characteristic of the lakes studied (Zeyen *et al.*, 2021; Havas *et al.*, 2023a). Very local differences in the composition of ascending volcanic gases and groundwater feeding each lake, may participate in differentiating the chemical nature of Alchichica, Atexcac, and La Preciosa, which share otherwise very close climatic and geological contexts.

5.6. Supplementary figures

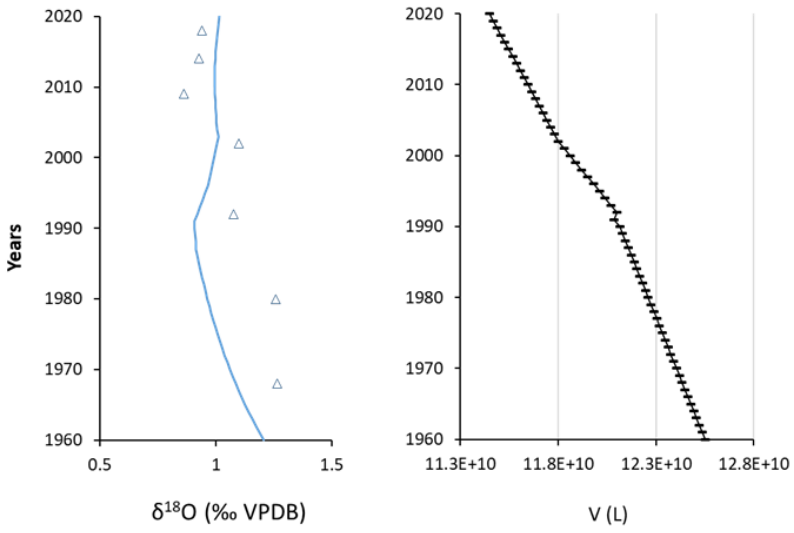

Results of the model for $\delta^{18}O$ if the lake volume is set to **fit a 5 m decrease of the water level** *vs*. nearly 7 m in the scenarios considered in the text (*cf.* Figure 5).

Figure S5.1: Model $\delta^{18}O$ results when the water level to set to decrease of 5 m between 1960 and 2022. On the left, the blue line (model) ends in 2020 with a value that is closer to the data than when a 7 m decrease is modeled. The evolution of the lake volume corresponding to this 5 m decrease is shown on the right.

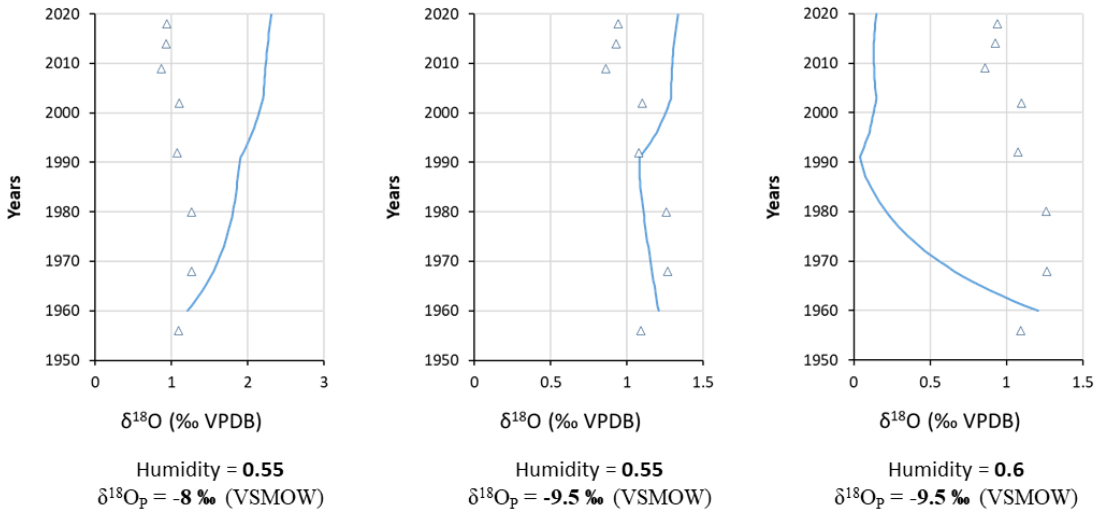

Figure S5.2: Graphs showing the very sensitive response of the modeled $\delta^{18}O$ to the values chosen for $\delta^{18}O_P$ for precipitation, and ambient humidity. Changed individually, these parameters have a huge impact, but other combination than the one selected in the model (-8 ‰ and 0.6, respectively) can fit the data. The selected values are consistent with available data for these parameters. Average values over the period studied were used because small temporal variations of these parameters are under-constrained.

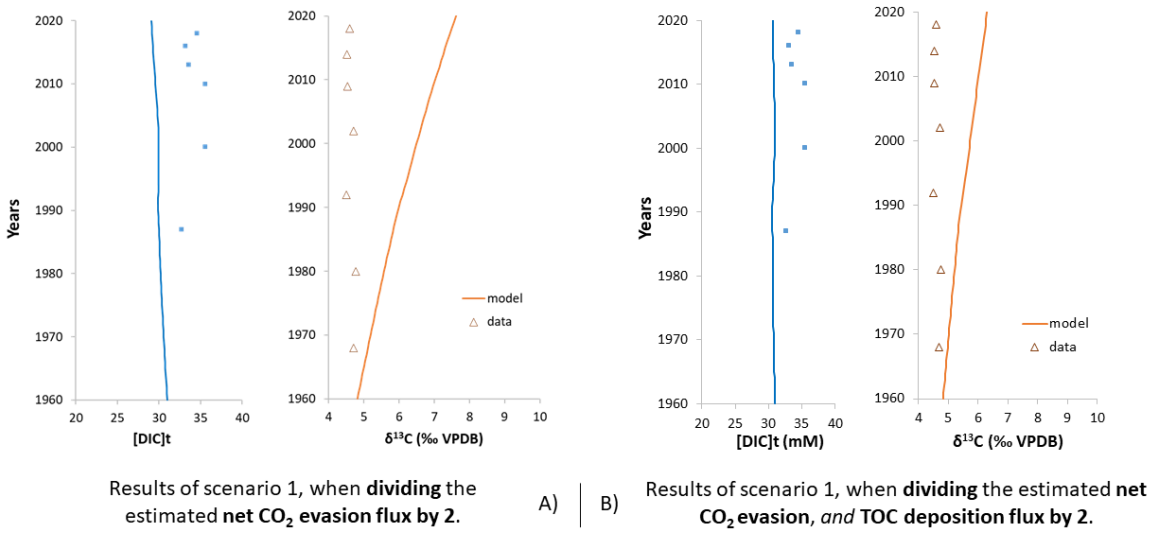

Figure S5.3: Sensitivity tests for the net CO_2 evasion flux (A) and net CO_2 evasion flux + TOC deposition flux (B). Neither the modeled DIC concentration and $\delta^{13}C_{DIC}$ match the data in scenario one even if the two mentioned fluxes are divided by two.

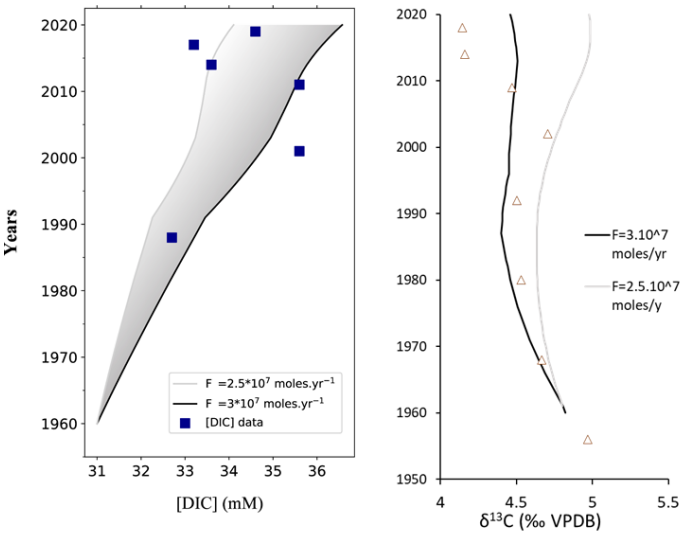

Results of scenario 3 when the **volcanic-CO_2** flux is set to $2.5*10^7$ (gray line) or $3*10^7$ (black line) moles.yr^{-1} with an **isotopic composition of -9‰.**

Figure S5.4: Sensitivity test for the isotopic composition of volcanic CO_2 in scenario 3. On the left is the [DIC] data together with [DIC] modeled in scenario with F_{volc} flux of 2.5 and $3*10^7$ mol.yr^{-1}. In the same conditions the modeled $\delta^{13}C_{DIC}$ is represented on the right for $\delta^{13}C_{volc}$ = -9 ‰.

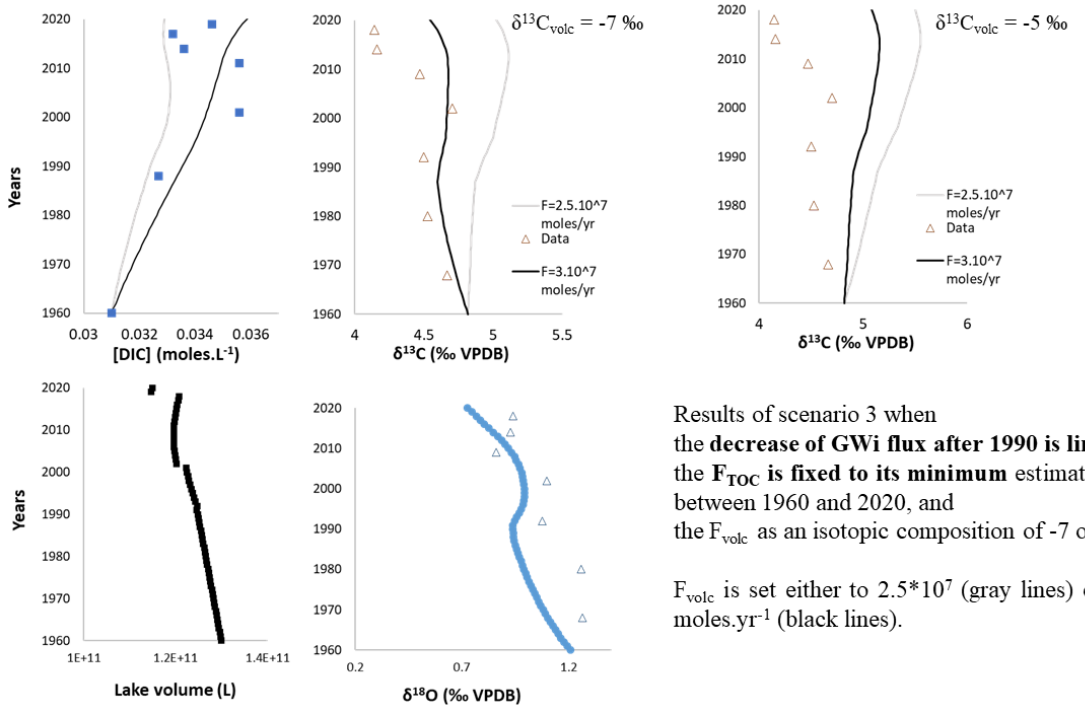

Results of scenario 3 when
the **decrease of GWi flux after 1990 is limited**,
the **F_{TOC} is fixed to its minimum** estimated value between 1960 and 2020, and
the F_{volc} as an isotopic composition of -7 or -5 ‰.

F_{volc} is set either to $2.5*10^7$ (gray lines) or $3*10^7$ moles.yr^{-1} (black lines).

Figure S5.5: Sensitivity test to scenario 3, changing the GWi and F_{TOC} fluxes compared to the initial model. After 1990, GWi is set in order to decrease less rapidly than initially considered, but still allowing a general decrease of the lake volume. F_{TOC} is set constant, to the minimum values estimated for the whole 1960-2020 period. The F_{volc} is set to values of $2.5*10^7$ (gray line) and $3*10^7$ (black line) mol.yr^{-1}. And the $\delta^{13}C_{volc}$ is given a composition of -7 or -5 ‰. At low F_{volc} fluxes ($2.5*10^7$ mol.yr^{-1}), the modeled [DIC] is slightly to low, and $\delta^{13}C_{carb}$ is too high., which is also true for F_{volc}=$3*10^7$ mol.yr^{-1} when $\delta^{13}C_{volc}$ = -5 ‰. It can be noticed that a smaller GWi decrease after 1990 results in a better modeling of the decreasing $\delta^{18}O$ after 1990.

Chapter 6

Sedimentary record of the carbon cycle in the Mexican lakes

Table of content

6.1. Introduction

The objective of this chapter is to describe how much the processes influencing the C cycle in the lakes' water column (Chapters 4 and 5) is recorded in the lakes' sediments, both in the inorganic and organic C reservoirs. For this purpose, I first assess the impact of early diagenesis on these sedimentary records, then discuss how much of their respective environment features can be recorded and how it compares among the four lakes. In the same fashion as for the water column processes, the study of four different sedimentary cores in parallel facilitates the understanding of specific chemical, biological, and climatic processes in play.

6.2. Results

6.2.1. Alchichica

The mineralogy as well as major elements in porewaters of Alchichica's sediments were described in detail before by Muller *et al.* (2023). Carbonates are composed mainly of aragonite, with traces of calcite throughout the core, and significant hydromagnesite and huntite in the very top and in the middle of the core (Fig. 6.1, Table S6.1). They represent about 40 wt. % of the total sediment, as determined by acid digestion (Fig. 6.2). Bulk carbonate C ($\delta^{13}C_{carb}$) isotope composition shows limited variability (between 4.3 and 5.1 ‰) with somewhat of a cyclic pattern along the core (Fig. 6.2). The $\delta^{18}O_{carb}$ varies between 0.7 and 2.6 ‰, mostly decreasing in the bottom core from 85 to 40 cm in depth and then being relatively stable until the top. The only exception are the layers where hydromagnesite is present, where $\delta^{18}O_{carb}$ noticeably increases (Fig. 6.2; layers containing green or yellow in Fig. 6.1).

Total organic carbon (TOC) content varies between 2 and 5 wt. % (average of 3.3 wt. %), with higher values at the very top and bottom of the core (Fig. 6.2). The C:N ratio of organic matter (OM) globally increases from values slightly above 10 in the first cm, to ~11.5 at 85 cm. The $\delta^{13}C_{TOC}$ sharply increases from -25.7 to -24.3 ‰ between the water-sediment interface and 10 cm in depth, and then slowly increases to ~-23.5 ‰ at 85 cm (Fig. 6.2).

Pore-water dissolved inorganic carbon (DIC) progressively increases from ~35 mM at the surface, to 43 mM at 45 cm in depth, and then remains constant (Fig. 6.3). The $\delta^{13}C_{DIC}$

progressively decreases from 0.4 ‰ in the first cm to -2.35 ‰ at the bottom of the core. In parallel, pH decreases from ~9 at the water-sediment interface to a stable value of ~8.5 below 20 cm in depth (Fig. 6.3).

The Alchichica sediments were dated using the ^{210}Pb method down to 25 cm. The results demonstrate sedimentation rates of 0.25 cm.yr^{-1}, except in the upper 4 cm of the core (up to 0.44 cm.yr^{-1}) (Table 6.1). Extrapolation of these results suggest that the lowest horizon (84-85.5 cm) was deposited about 340 years ago (*i.e.* 1680 yrs CE). Since no plant debris were found, the bulk organic C at a 65.5 cm was dated depth *via* ^{14}C dating. This gave an age of 4400 BCE (*vs.* 1760 CE by ^{210}Pb extrapolation), consistent with the fact that TOC inherited "dead" carbon from the limestone basement and volcanic CO_2 (Chapter 5).

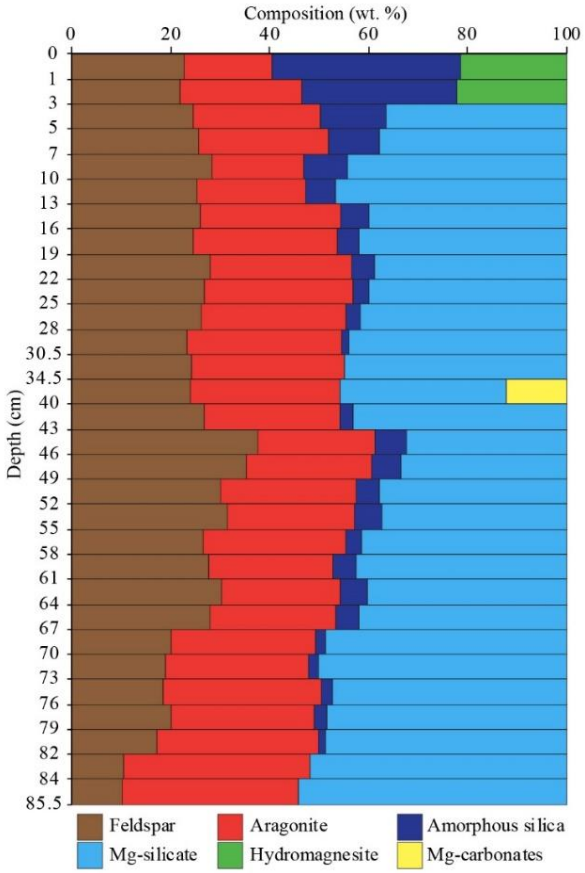

Figure 6.1 : Estimated mineral content of the Alchichica sediment (in wt. %) as function of depth, based on bulk chemical analyses using XRD and Fourrier Transform Infra-red (FTIR). From Muller *et al.* (2023; Annex 2).

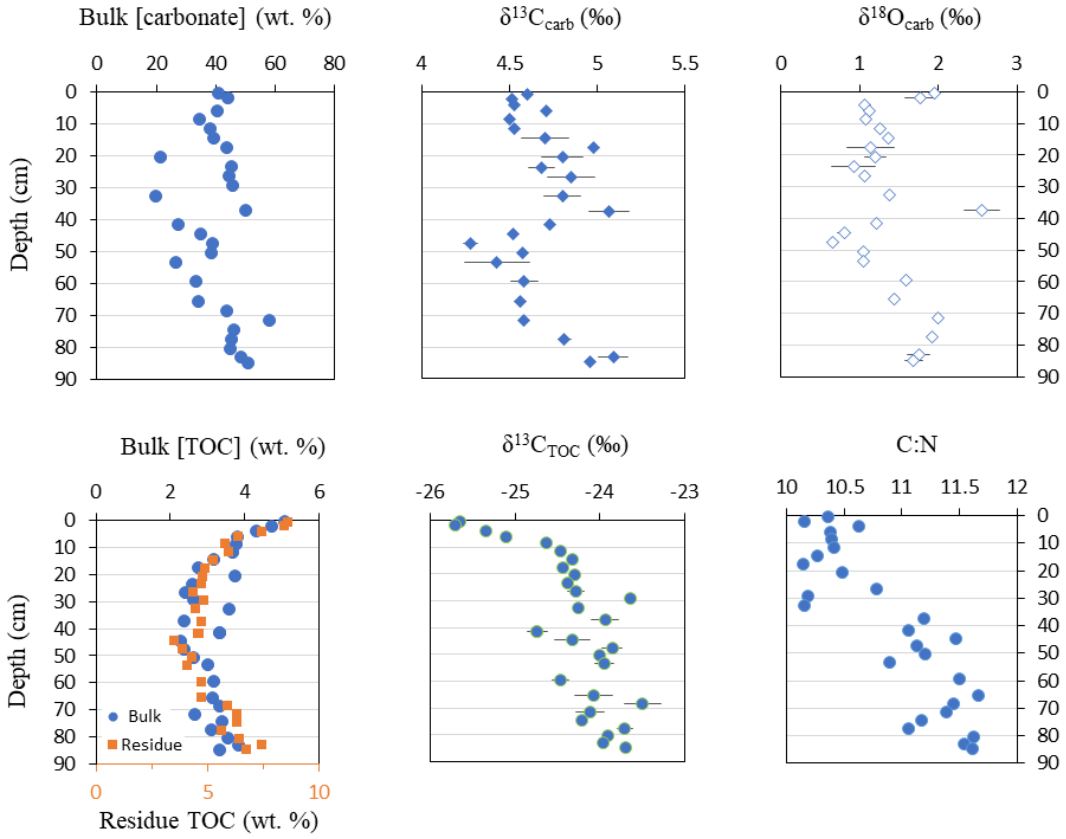

Figure 6.2 : Depth profiles of carbon-related chemical and isotopic parameters in Alchichica sediments. Concentrations are in weight percent, isotopic compositions in permil relative to VPDB, and 'C:N' is the molar ratio of carbon over nitrogen in the bulk organic matter. The bulk [TOC] is strongly influenced by the amount of carbonate determined by acid digestion, which may have been underestimated for a couple of samples (*e.g.* at 20 and 30 cm in depth). Thus, the TOC variations at these depths may be partly generated by the low carbonate content determined at these depths.

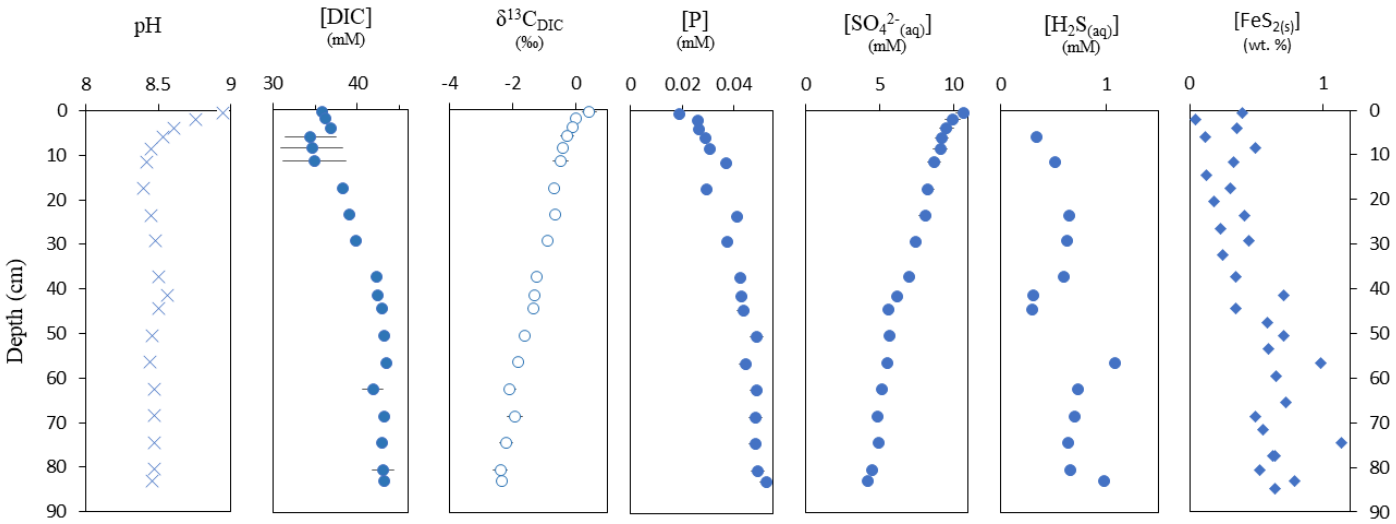

Figure 6.3: Depth profiles of chemical and isotopic parameters in Alchichica porewater, and sedimentary pyrite concentrations. Concentrations of dissolved species and pyrite are expressed in mmol.L^{-1} (mM) and weight percent, respectively.

6.2.2. Atexcac

Mineral phases in Atexcac sediments consist of plagioclase feldspar (mostly albite, andesine, and bytownite), carbonates (aragonite and calcite), quartz, and Mg-silicates. Using Rietveld refinement analyses (Table S6.1), the proportion of aragonite represents from 68 to 82 % of the crystalline phases in the first 17 cm (or ~90% of the carbonate assemblage). Below 17 cm, it decreases to ~15 % at 40 cm, reaching the same proportion as calcite at this depth (Fig. 6.4). Following the same trend, many geochemical proxies in the solid and water phases of Atexcac's sediments depict "step-like" profiles with relatively stable values between the 0-17 and 25-40 cm portions, and a steep gradient in between. The $\delta^{13}C_{carb}$ is stable (≈ 2.7 ‰) in the first 5 cm of the core, then decreases to 2 ‰ between 10 and 20 cm, and remains around 1 ‰ between 25 and 40 cm depths (Fig. 6.5). Following the same trend, $\delta^{18}O_{carb}$ decreases from 0 ‰ at the water-sediment interface to about -4 ‰ at the bottom of the core. The TOC content decreases downward from 1.3 to 0.4 wt.%, while C:N ratio increases from 8 to 14. The $\delta^{13}C_{TOC}$ decreases from stable -27 ‰ values in the upper 17 cm to -24 ‰ between 25 and 40 cm.

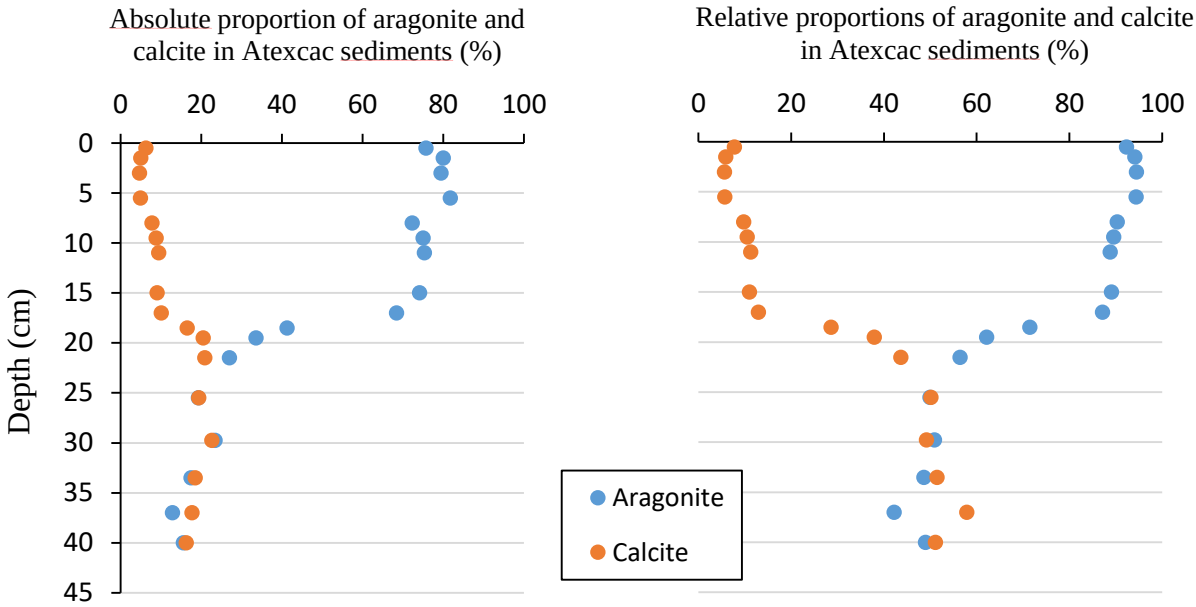

Figure 6.4 : Proportions of the carbonate phases in Atexcac sediments (aragonite in blue and calcite in orange). On the left, absolute proportions of carbonates relative to all crystalline phases determined by Rietveld refinement analysis. On the right, relative proportions of the two phases (*i.e.* completing to 100%).

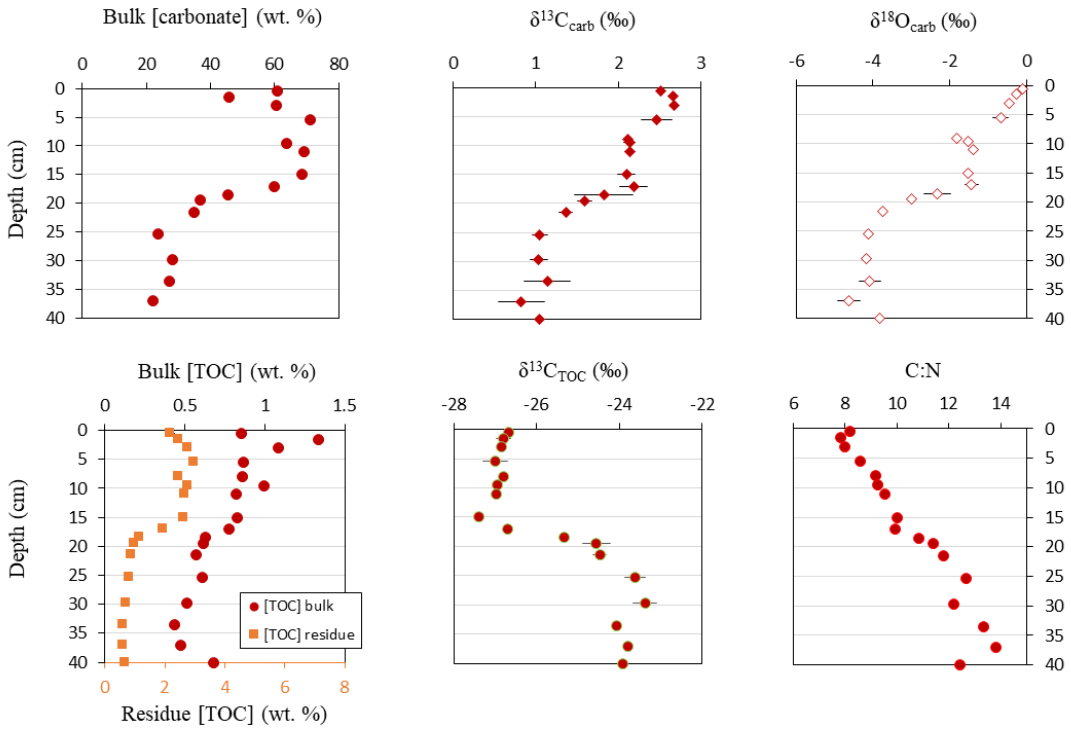

Figure 6.5 : Depth profiles of carbon-related chemical and isotopic parameters in Atexcac sediments. Concentration are in weight percent, isotopic compositions in permil relative to VPDB, and 'C:N' is the molar ratio of carbon over nitrogen in the bulk organic matter. Bulk [carbonate] shown here was determined by acid digestion. This carbonate concentration is smaller than the estimations by Rietveld analysis on crystalline phases due to the presence of amorphous OM and Mg-silicates in the bulk sediment. In the down left panel, '[TOC] residue' refers to the total organic carbon concentration within the decarbonated powder, while 'bulk [TOC]' is recalculated for the whole rock based on [carbonate] concentrations.

Pore-water DIC concentration increases from about 23 ± 2 mM near the water-sediment interface to a stable value of 26.2 ± 0.3 mM below 10 cm. The $\delta^{13}C_{DIC}$ decreases from about 0.5 ‰ near the surface to about -1 ‰ at 40cm in depth (Fig. 6.6). The pH remains mostly above 8.5 in the first 17 cm and decreases below 8.3 in the layer between 15 and 20 cm.

The age of two samples of detrital plant debris were determined by ^{14}C dating at 17 and 40 cm in depth (Table 6.1). They gave an age of 300 and 220 years (1720 and 1800 years CE), respectively. Because the samples represented a mixture of small plant debris, the one at 17 cm most likely contained older branches which deposited only a while after their formation. Thus, only the second age was considered. This results in a mean sedimentation rate of ~0.18 $cm.yr^{-1}$.

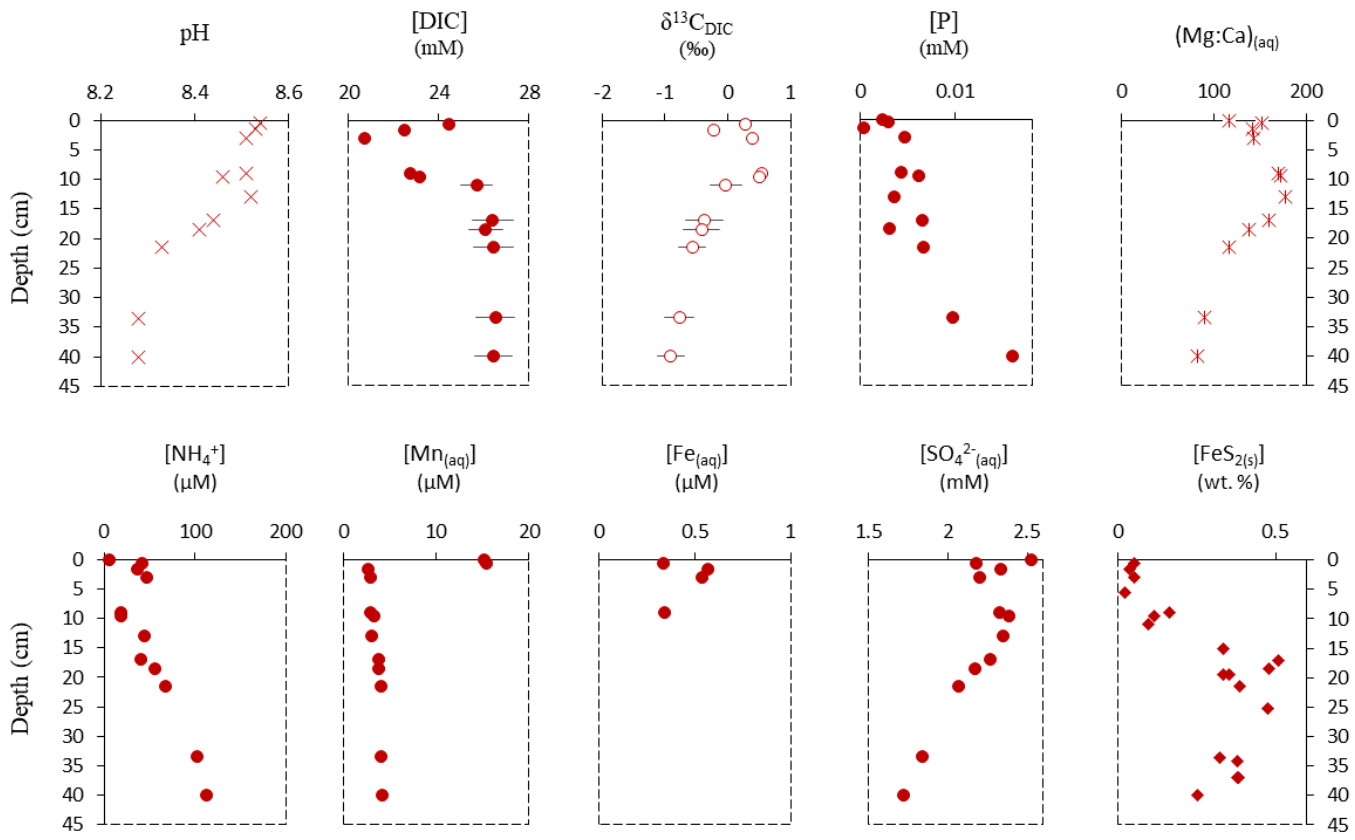

Figure 6.6: Depth profiles of chemical and isotopic parameters in Atexcac porewater, and sedimentary pyrite concentrations. Concentrations of dissolved species and pyrite are expressed in mmol.L^{-1} or µmol.L^{-1} and weight percent, respectively. $(Mg:Ca)_{(aq)}$ is the molar ratio of Mg over Ca dissolved in the porewater. "Missing" data points in the dissolved Fe profile correspond to depths where Fe was below detection limit.

6.2.3. La Preciosa

The core in La Preciosa was sampled in 2016, and previously analyzed by De Wever (2019), but porewaters were not retrieved at the time. Our mineralogical assemblage analyses are consistent with observations from De Wever (2019). The sediments consist mostly of aragonite, with small amounts of plagioclase feldspar, and minor amounts of calcite and quartz (Table S6.1). Mg-Silicates are barely identifiable from XRD analyses. Bulk carbonate content decreases with depth from about 60 to 50 wt. % (as determined by acid treatment), and is dominated by aragonite (95%) relative to calcite (5%) (based on XRD Rietveld refinement analyses). The $\delta^{13}C_{carb}$ and $\delta^{18}O_{carb}$ of bulk carbonate both show a small decrease with depth from around 2.6 to 2.3, and from -1.1 to -1.9 ‰, respectively (Fig. 6.7).

TOC content (2.3 ± 0.2 wt. %, 1 SD) decreases slightly downward. The $\delta^{13}C_{TOC}$ and C:N ratio increase downward from ~ -25.5 to -21.3 ‰, and from 10 to 12.5 at 19cm, respectively (Fig. 6.7).

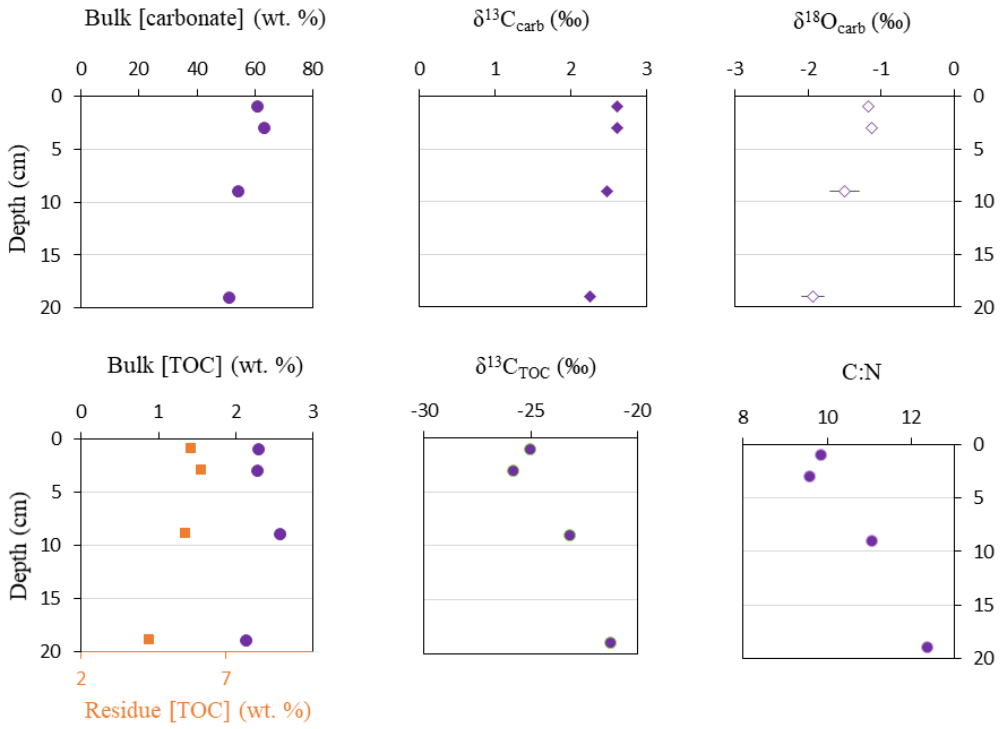

Figure 6.7: Depth profiles of carbon-related chemical and isotopic parameters in La Preciosa sediments. Concentration are in weight percent, isotopic compositions in permil relative to VPDB, and 'C:N' is the molar ratio of carbon over nitrogen in the bulk organic matter. In the down left panel, '[TOC] residue' refers to the total organic carbon concentration within the decarbonated powder, while 'bulk [TOC]' is recalculated for the whole rock based on [carbonate] concentrations.

6.2.4. Alberca de los Espinos

Calcite (and/or low Mg-calcite - LMC) are the only carbonate phases found in Alberca sediments. The rest of the mineralogical assemblage was not determined in detail but is mostly composed of plagioclase feldspar, potentially some metamorphic silicate minerals, and/or phosphate minerals (Table S6.1). Total carbonate content, as determined by acid treatment, averages 17 wt. %, and varies between 10 and 35 wt. % with the highest values at the bottom of the core (Fig. 6.8).

Carbon and oxygen isotopes from carbonates were not measured at all depths due to insufficient carbonate content. The $\delta^{13}C_{carb}$ value at the water-sediment interface is ~ -1.5 ‰,

and increase from -3 to +1.5 ‰ between 40 and 60 cm in depth. The $\delta^{18}O_{carb}$ values are less variable, varying between 0 and -1 ‰ throughout the core (Fig. 6.8).

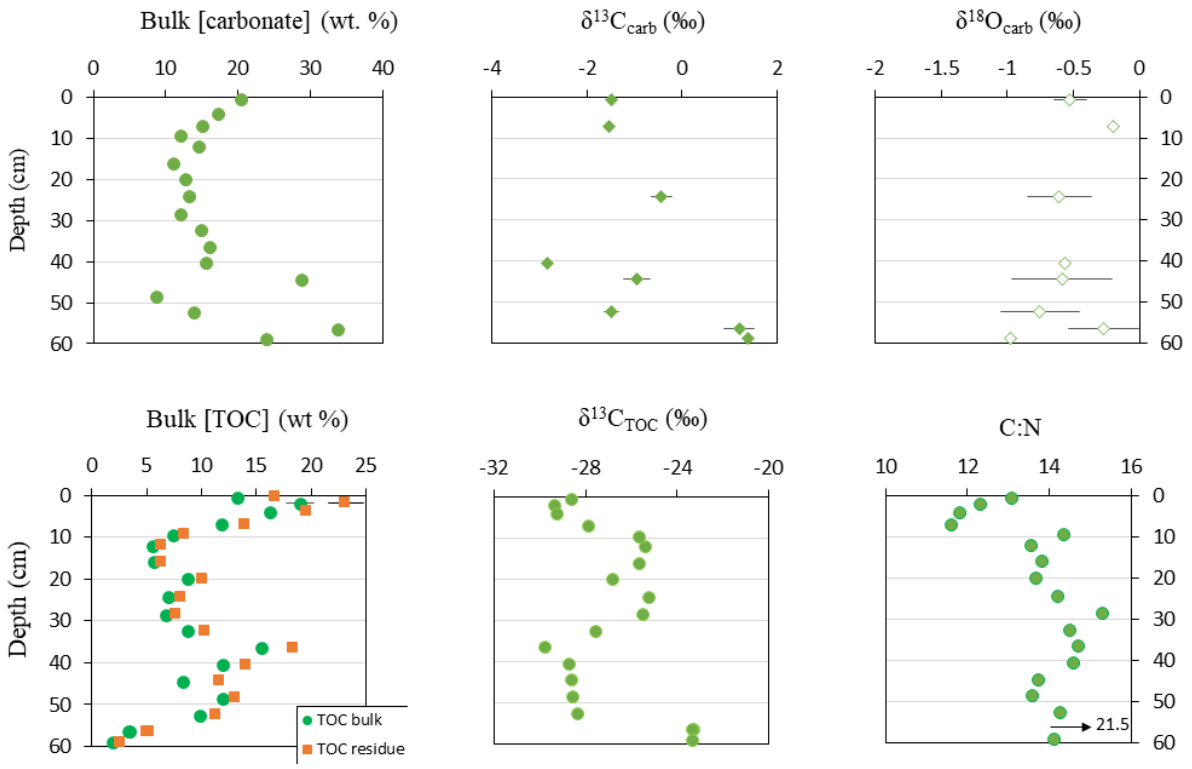

Figure 6.8: Depth profiles of carbon-related chemical and isotopic parameters in Alberca de los Espinos' sediments. Concentration are in weight percent, isotopic compositions in permil relative to VPDB, and 'C:N' is the molar ratio of carbon over nitrogen in the bulk organic matter. Most samples lacked sufficient carbonate content to obtain precise isotopic compositions. In the down left panel, '[TOC] residue' refers to the total organic carbon concentration within the decarbonated powder, while 'bulk [TOC]' is recalculated for the whole rock based on [carbonate] concentrations.

The TOC and $\delta^{13}C_{TOC}$ both have S-shaped profiles but are strongly anti-correlated (R^2=0.83, p=7*10^{-8}; Fig. 6.8). They vary between 2 and 19 wt. %, and -23 and -30 ‰, respectively. The C:N ratio increases irregularly with depth from about 12 to about 14-15 (except at 56.5 cm where it reaches 21.5, which might be linked to detrital contamination left in this specific sample). Indeed, organics of detrital origin were found and picked from multiple horizons (*e.g.* branch and leaf debris), and were characterized by high C:N ratios, typical of plants (between 24 and 68).

Pore-water DIC and $\delta^{13}C_{DIC}$ are both much higher than in the water column (~ 7.5 mM and -3 ‰) as they reach ~12 mM and 11 ‰, respectively (Fig. 6.9). The pH decreases with depth to 6.8 at 10 cm before increasing again to 7.2 at 16 cm.

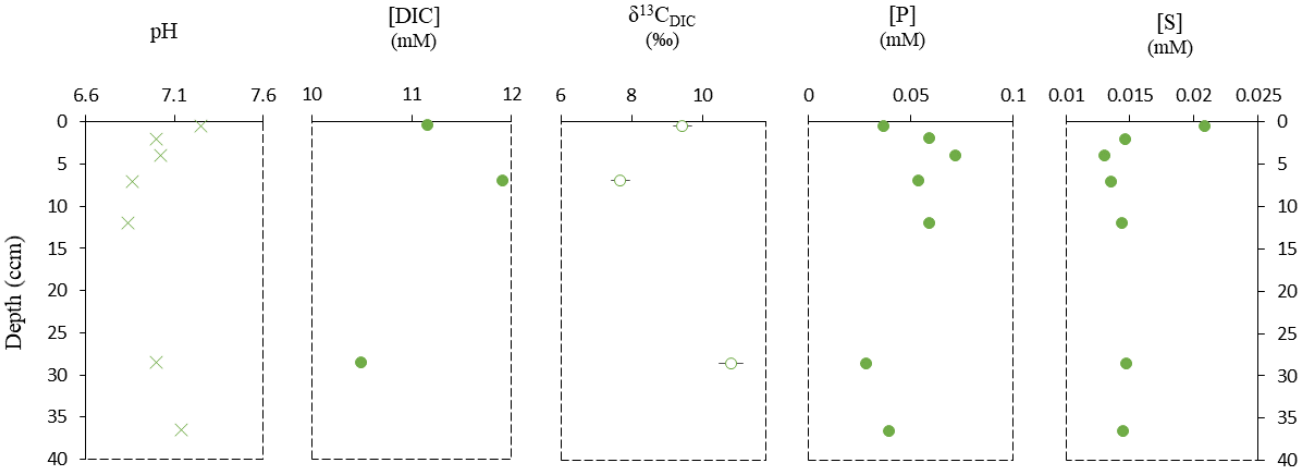

Figure 6.9: Depth profiles of chemical and isotopic parameters in the porewater of Alberca de los Espinos. Concentrations are expressed in mmol.L^{-1}. 'P' and 'S' were measured as total concentrations by ICP-AES. In the case of 'S', it mostly represents sulfide concentrations. Not enough porewater was retrieved for some of the depths (note that there is no data for the bottom of the core from 36.5 to 56.5 cm).

The age of two samples of plant debris at 0.5 and 12 cm, as well as a gastropod shell, and bulk carbonates at the 56.5 cm depth was determined by ^{14}C dating (Table 6.1). The plant debris have average ages of 20 and 250 years (2000 and 1770 yrs CE), respectively. The gastropod and carbonate samples date back to 2160 and 1400 years ago (140 yrs BCE and 620 yrs CE), respectively. Only the age of the carbonate sediment was considered for sedimentation rate calculation; because the deposition of the shell could have been delayed, while the carbonate grains would have deposited sooner after precipitation. Sedimentation rates at 0.5, 12, and 56.5 cm depths equal to 0.025, 0.050, and 0.039 cm.yr^{-1}, respectively. The last value represents a minimum estimation because the carbonate's age could have been lowered by the DIC residence time, or by the presence of "dead" volcanic CO_2 in the lake.

Table 6.1: Results of sediment dating in the three cores from 2019.

Lake (name of core)	Depth in the core	Object dated	Method	Age	Sedimentation rate	Average sedimentation rate
	cm			years common era (yrs CE)	$cm.yr^{-1}$	$cm.yr^{-1}$
Alchichica (AL19-C2)	0	Bulk sediments	^{210}Pb	2019		0.29 $cm.yr^{-1}$
	0.5	Bulk sediments	^{210}Pb	2018	0.44	
	2	Bulk sediments	^{210}Pb	2014	0.4	
	4	Bulk sediments	^{210}Pb	2009	0.32	
	6	Bulk sediments	^{210}Pb	2002	0.26	
	8.5	Bulk sediments	^{210}Pb	1992	0.25	
	11.5	Bulk sediments	^{210}Pb	1980	0.25	
	14.5	Bulk sediments	^{210}Pb	1968	0.25	
	17.5	Bulk sediments	^{210}Pb	1956	0.24	
	20.5	Bulk sediments	^{210}Pb	1943	0.24	
	23.5	Bulk sediments	^{210}Pb	1931	0.24	
	64.5	Bulk OC	^{14}C	-4400	0.010	
Atexcac (ATX19-C1)	17	detrital plant debris	^{14}C	1720	0.057	
	40	detrital plant debris	^{14}C	1800	0.182	0.18 $cm.yr^{-1}$
Alberca de los Espinos (ALBESP19-C3)	0.5	detrital plant debris	^{14}C	2000	0.025	0.04 $cm.yr^{-1}$
	12	detrital plant debris	^{14}C	1770	0.048	
	56.5	gastropod shell	^{14}C	-140	0.023	
	56.5	bulk carbonate sediment	^{14}C	620	0.039	

6.3. Primary and early diagenetic signatures of the Mexican lakes sedimentary organic matter

In a recently published study, we evidenced that the four lakes sediment cores received organic matter (OM) derived from different parts of the water columns (Havas *et al.*, 2023a): upper water-column oxygenic photosynthetic organisms in Alchichica; lower water-column anaerobic autotrophs in Atexcac; a mix of both upper and lower layers in La Preciosa. In

Alberca, OM is already influenced by respiration processes in the very first centimeters. These inferences were drawn from describing only the very surficial sediments (<12 cm) in the four locations studied. However, deeper in the cores (down to 86.5 cm in Alchichica), the effects of early diagenesis on OM can be evaluated. In the following section 6.3, I will question how do the primary OM signatures evolve through early diagenesis. Notably, I will focus on the metabolic processes involved in each core. Further, I will present the primary factors enhancing OM degradation/preservation and how they may generate variability on top of that inherited from the water column deposition.

6.3.1. Alchichica, a relatively well preserved OC record

The overall increase of porewater [DIC] and $(C:N)_{OM}$, along with the decrease in $\delta^{13}C_{DIC}$, are evidence for OM respiration occurring in Alchichica sediments (Fig. 6.2, 6.3). The respiration of OM transfers isotopically light organic C to the DIC reservoir, and preferentially removes organic N over C (*e.g.* Lehmann *et al.*, 2002; Bouton *et al.*, 2020b). The increase of dissolved P with depth, especially in the first 10 cm, also supports this conclusion since it is preferentially remineralized as well. Porewater SO_4^{2-} concentration decreases with depth while H_2S increases (Fig. 6.3), suggesting that OM respiration throughout the core is, at least partially, carried out by microbial sulfate reduction (MSR). Sulfate and DIC concentrations are inversely correlated with a DIC:SO_4 ratio of 1.7 (Fig. 6.10), which is close to values expected for MSR (between 1 and 2; Harerimana *et al.*, 2010), and thus supports that it is a major OM remineralization pathway in Alchichica sediments. The TOC content also shows a strong decrease of more than 2 wt. % in the first 20 cm. This trend could be explained by several parameters including: changes of OM deposition or preservation rates, as well as of respiration pathways, or sedimentation rates.

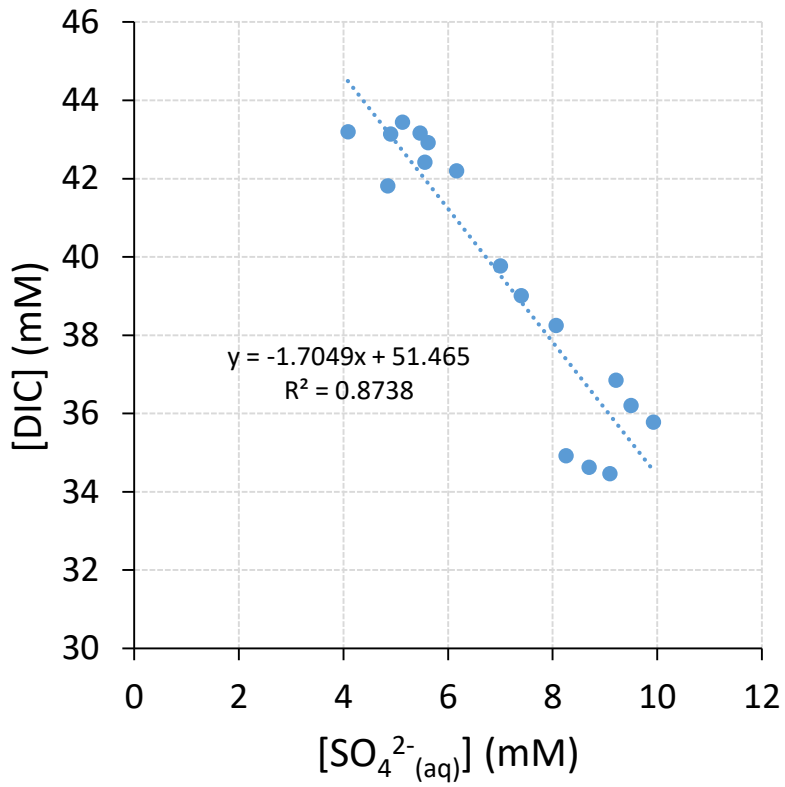

Figure 6.10 : Inverse correlation between dissolved inorganic carbon and sulfate concentrations in the porewaters of Alchichica. Both concentrations are expressed in $mmol.L^{-1}$.

Taking the sedimentation rates into account still results in decreasing TOC accumulation rates with depth (Chapter 5), implying that variable sedimentation does not primarily shape the TOC concentration profile. The [TOC] increases back below 50 cm, although respiration still affects the OM reservoir at these depths, as suggested by higher $(C:N)_{OM}$ and [P], and lower $\delta^{13}C_{DIC}$ and $[SO_4^{2-}]$ in the lower sediment layers (Fig. 6.2, 6.3). Thus, OM remineralization alone cannot explain the variations of TOC content with depth. Moreover, assuming the TOC decrease in the top 20 cm was due to remineralization alone, it implies an OC degradation rate of about 45% in the first 20 cm of sediments. Other lacustrine environments showed slightly lower rates (between 25 and 40%), although they were less consistently anoxic than Lake Alchichica (Teranes and Bernasconi, 2000; Lehmann *et al.*, 2002). Therefore, it supports that at least part of the TOC variations recorded in Alchichica sediments reflect primary changes in the lake's primary productivity. As such, OC production in Alchichica seems to have increased in the recent years (especially in the last 70 years).

The TOC isotope composition ($\delta^{13}C_{TOC}$) in the very first layer of the core matches the compositions that were recorded in the higher part of the water column in 2019 (-25.7 and -26.5 ‰, respectively). It is consistent with previous studies describing the occurrence of upper water column diatom and cyanobacterial blooms in the winter and spring, respectively, and

showing that most of the organic C that deposits in Alchichica sediments corresponds to large oxygenic phototrophs (*e.g.* Adame *et al.*, 2008; Ardiles *et al.*, 2012). Besides, the isotopic $\Delta^{13}C_{TOC\text{-}DICeq}$ shift recorded in this core is limited (≤ 1.5 ‰; Fig. 6.11), suggesting that (i) the effect of OM remineralization on $\delta^{13}C_{TOC}$ is limited, and (ii) primary productivity (PP) and heterotrophic activity in the lake cycle organic C are at near-steady state. From the previous paragraph, the decrease of $\delta^{13}C_{TOC}$ upward in the core more likely suggests a small change in PP isotopic fractionation, but further analyses on organic-compounds are required to fully differentiate this from an early diagenetic (microbial) effect (Blaser and Conrad, 2016).

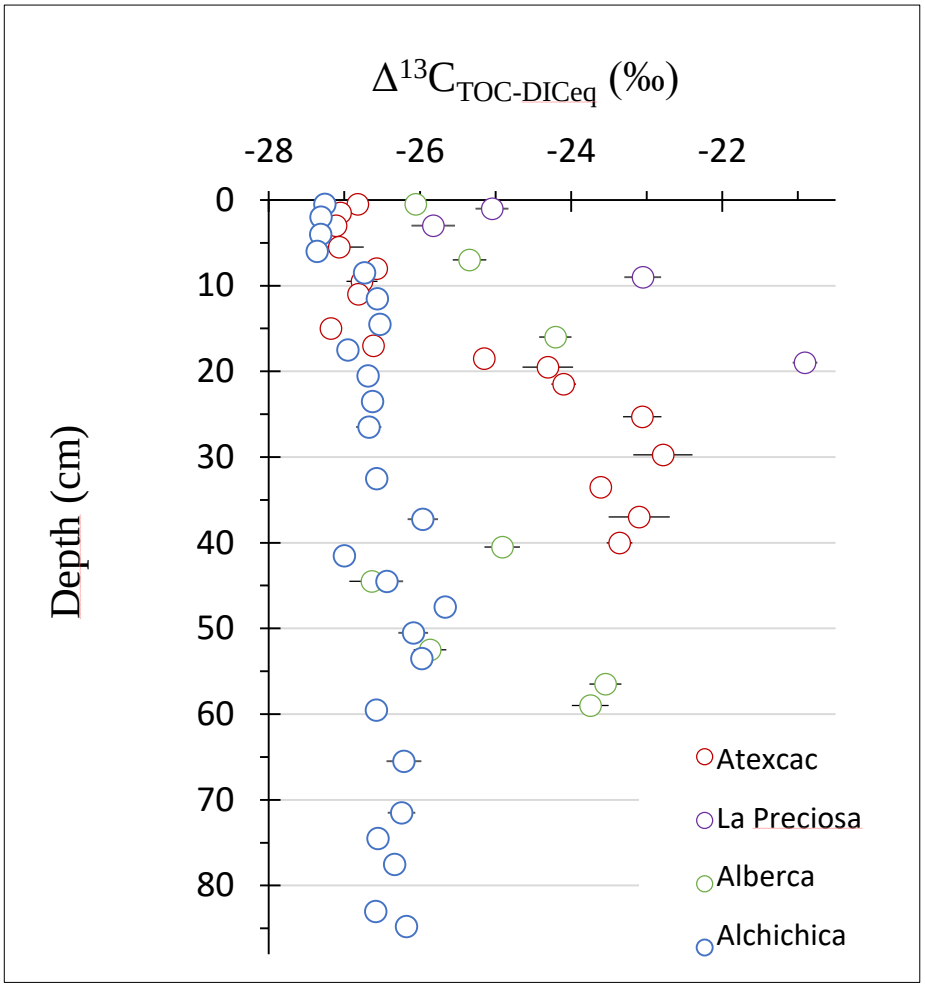

Figure 6.11 : Isotopic fractionation between organic and inorganic carbon in the sediments of the four lakes. Δ is expressed in permil relative to the VPDB. 'TOC' refers to total organic carbon and 'DICeq' refers to dissolved inorganic carbon that would have been in isotopic equilibrium with the carbonates C in each sediment layer. The regular DIC value is not chosen because it can be strongly shifted within the sediment porewater, and thus would not reflect the DIC composition from which OC was fixed.

6.3.2. Atexcac, a marked positive shift in $\delta^{13}C_{TOC}$ caused by MSR

The increase of the $(C:N)_{OM}$ ratio and dissolved P content with depth (Fig. 6.5, 6.6) suggest that OM is being respired throughout the core of Atexcac (*e.g.* Lehman *et al.*, 2002; Bouton *et al.*, 2020b). The TOC content, however, decreases, but mostly between 15 and 20 cm. This decrease suggests heterogeneous rates of organic matter remineralization. Depth profiles of redox sensitive elements support that OM respiration could be carried out by diverse metabolisms, following a "classical" distribution with depth. Indeed, the transition zones, and the succession of nitrogen, manganese, iron, and sulfur oxidation/reduction follow the order expected theoretically (Figs. 6.6 and 6.12; Canfield and Thamdrup, 2009).

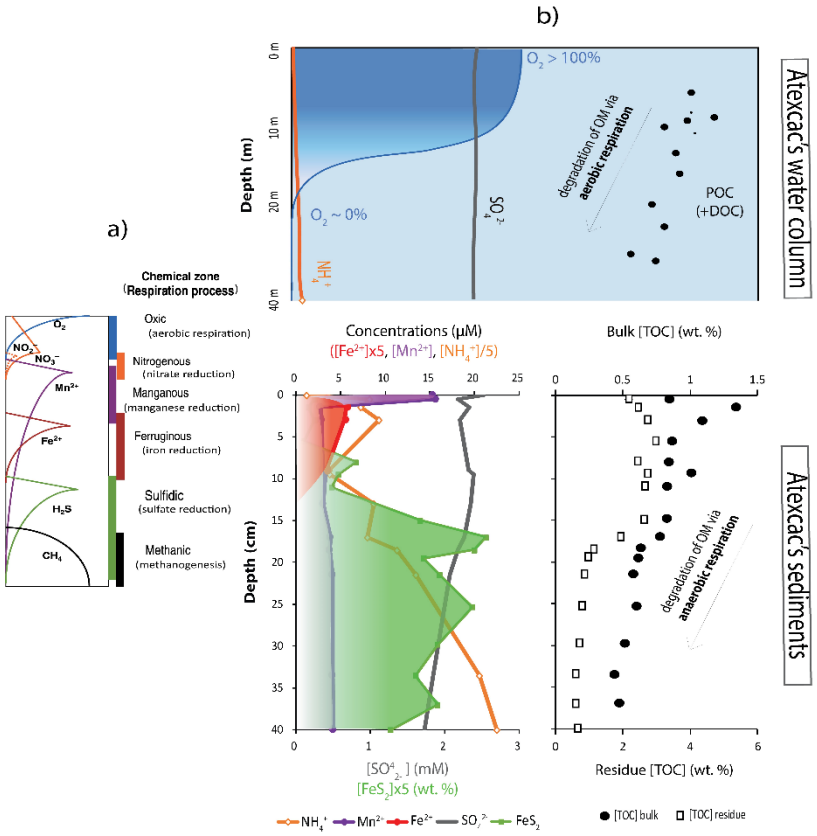

Figure 6.12: Schematic view of the redox zonation in Atexcac sediments. 'a' is the modified 'figure 1' from Canfield and Thamdrup (2009), showing the successive zones where oxygen, nitrate, manganese, iron, sulfate, and carbon dioxide are used as the main electron acceptors in respiration processes, influencing the chemical zonation in the porewater. The full figure can be found in Chapter 1. In 'b', the same succession if found, as represented with the blue, orange, purple, red, and green colored areas. Nitrate concentration was not measured but ammonium (in orange) is complementary and increases at the start of the manganous zone, as would be expected after nitrate reduction (and OM degradation). Dissolved H_2S was not measured but is reflected by the precipitation of pyrite (in green). The transitions are associated with decrease in OC content in the water column and sediments. Total organic carbon content measured in the decarbonated powders ("Residue [TOC]") shows a marked decrease where sulfate reduction starts (represented by the sulfidic zone in green and SO_4 decrease).

The main decrease of TOC concentration occurs below 15 cm where [SO_4^{2-}] also starts to decline (Fig. 6.5, 6.6, 6.12), corresponding to an abrupt increase of $\delta^{13}C_{TOC}$ by about 3.5 ‰. Concomitantly, [DIC] increases and $\delta^{13}C_{DIC}$ decreases, supporting the occurrence of OC remineralization. Just below 15 cm, dissolved Fe disappears and pyrite concentration peaks, suggesting that the available Fe is quantitatively precipitated at this depth due to MSR (Figs. 6.6 and 6.12). Thus, the [SO_4^{2-}] transition at these depths is rather related to microbial sulfate reduction downward, rather than to an abrupt sulfate enrichment in the lake water at the time the upper sediment horizons deposited. The 3.5 ‰ isotopic enrichment in $\delta^{13}C_{TOC}$ is consistent with the activity of heterotrophic sulfate reducing bacteria, which generally incorporate isotopically heavy organic C (*e.g.* Hayes *et al.*, 1989; Lehman *et al.*, 2002).

An alternative interpretation of increasing [TOC] upward is that it reflects higher primary productivity (PP) in more recent times. It is contradicted however, by the direction in which the $\delta^{13}C_{TOC}$ changes. First, if the TOC variation was primary, $\delta^{13}C_{TOC}$ should follow the increasing trend displayed by $\delta^{13}C_{DIC}$ (which is not the case), unless the isotopic fractionation induced by primary producers increased. However, the increased PP would tend, on the contrary, to reduce the isotopic fractionation induced, whereas an increase of $\Delta^{13}C_{TOC\text{-}DICeq}$ is recorded (Fig. 6.11). Besides, higher PP should decouple the carbonates C and O isotope records, which is also not observed in the C and O records in Atexcac (Figs. 6.5 and 6.21). Therefore, the $\delta^{13}C_{TOC}$ shift in Atexcac is rather diagenetic than primary in origin, in contrast to Alchichica.

This isotopic shift may be larger in Atexcac because the TOC reservoir's size is much smaller, and thus the proportion of newly formed bacterial OC is bigger. Under the condition that OC deposition and remineralization rates remain stable with time, it is possible that the surficial $\delta^{13}C_{TOC}$ also ends up being shifted by ~3.5 ‰. In other words, that this isotopic shift is constant over time and would not mask a primary evolution of $\delta^{13}C_{TOC}$. However, it is important to note that: (i) fluctuation of this shift would bias the sedimentary record, and (ii) the amplitude of this shift may vary, even among comparable geological settings (section 6.3.1, 6.3.3, 6.3.4).

6.3.3. La Preciosa, a shift in $\delta^{13}C_{TOC}$ despite conditions favorable to OM preservation

Similar to the first two lakes, a (slight) decrease of TOC with depth is observed, and an increase of $\delta^{13}C_{TOC}$ and $(C:N)_{OM}$ suggesting OM degradation (Fig. 6.7). The available porewater data from 2016 (De Wever, 2019) show increasing P and decreasing S contents (Fig. 6.13). These two proxies are well inversely-correlated (R^2=0.92), suggesting that OM (and phosphorus) remineralization is carried out by sulfate reducing organisms. Sulfate concentration evolves from being close to that of the overlying water column, and decreases to near 0 values at 19 cm in depth. In parallel, pyrite concentration increases mostly between 4 and 10 cm, and is rather stable below (Fig. 6.13). Thus, it should mark the end of OC respiration through MSR in the sediments of La Preciosa. Depletion of sulfate and negligible quantities of Fe in the sediment porewater likely result in a lack of electron acceptors for microbial respiration, and thus in a better preservation of sedimentary OM. Nonetheless, the shift in of $\Delta^{13}C_{TOC\text{-}DICeq}$ is relatively important (4 ‰), even if, again, it could also be partly due to an increase of the fractionation from primary producers. It is difficult to further interpret OM diagenetic reworking in La Preciosa's sediments without the porewater pH or DIC data, and because the core's depth is limited.

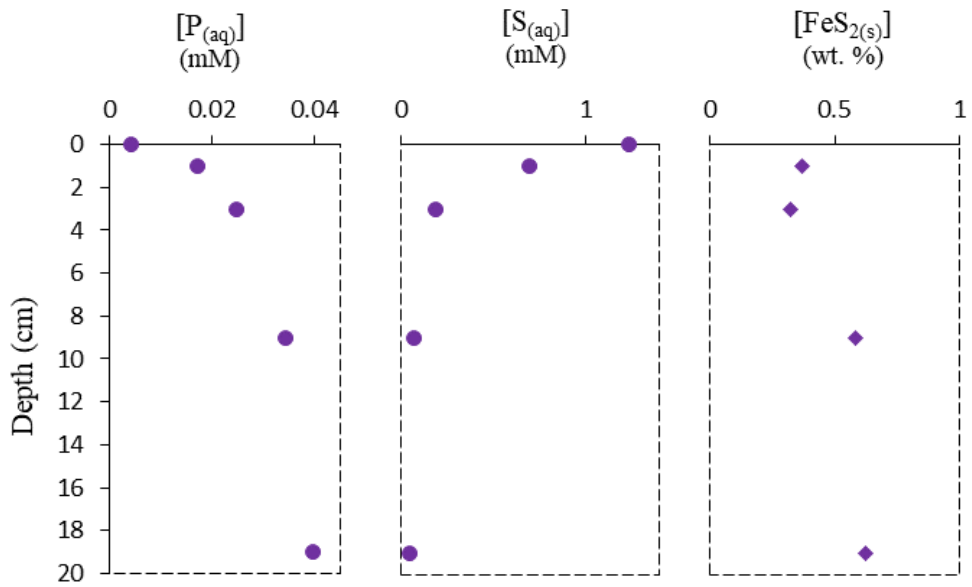

Figure 6.13 : Depth profiles of dissolved phosporus (P) and sulfur (S) in the porewater of La Preciosa and pyrite concentrations. Concentrations of dissolved species and pyrite are expressed in mmol.L^{-1} and weight percent, respectively. 'P' and 'S' were measured as total concentrations by ICP-AES (data from De Wever, 2019). In the case of 'S', it closely approximates the sulfate concentration.

6.3.4. Alberca de los Espinos, most reducing conditions leading to an optimal OM preservation

In Alberca, TOC concentrations exhibit very high values (average of 9.3 wt. %) with great variability, between 2 and 19 wt. %. This is consistent with weak sulfate concentrations, and methanogenesis being the main remineralization pathway in the sediments of Alberca (Havas *et al.*, 2023a), which constitute optimal conditions for preservation (Kuntz *et al.*, 2015). Again, the observed [TOC] variability could originate from (i) post-depositional processes (*e.g.* changes in the degradability of OM or in the nature of bacteria feeding on it), (ii) changes in sediment accumulation rates (SAR), or (iii) reflect a secular variation of the lake's productivity.

The [TOC] shows both increasing and decreasing trends throughout the core, while neither $(C:N)_{OM}$, $[NH_4^+]$, or dissolved P significantly increase below 10 cm (Fig. 6.8, 6.9). It suggests that OM remineralization is mostly active in the surficial sediments but is not driving the [TOC] variability throughout the entire core. Methanogenesis was identified in the most surficial sediment layers (Havas *et al.*, 2023a), suggesting that more reducing conditions are reached at shallower depths than in the sediments of the other lakes (Fig. 6.16). Accordingly, it is possible that a higher preservation of OM (and its geochemical signatures) below ~ 10 cm may be achieved due to a lack of electron acceptors other than H_2O (*e.g.* Fe(III), SO_4^{2-}; Fig. 6.12a), and a limitation of related respiration processes. Therefore, the variability in Alberca's sedimentary OM record is more likely driven by processes (ii) and (iii) than by post-depositional alteration.

At rates above 0.01 $cm.yr^{-1}$, sedimentation tends to have a diluent effect over a preservational effect (Tyson, 2001). Consistently, much higher SAR in Alchichica and Atexcac than in Alberca favor much lower [TOC] in the former lakes. Furthermore, lower TOC contents in Alberca are found at depths where there the SAR are higher. Indeed, the sedimentation rates are equal to 0.025 $cm.yr^{-1}$ near the water-sediment interface, and 0.05 $cm.yr^{-1}$ at a 12 cm depth where [TOC] equals 19 and 5.5 wt. %, respectively. An even lower TOC content at the bottom of the core (~3.5 wt. %) was associated to a rate of 0.039 $cm.yr^{-1}$ (as a minimum approximation; *cf.* result section 6.2.4). Thus, sedimentation rates seem to influence the overall TOC content among the four lakes, but also the specific TOC depth profile Alberca's sediments. Besides, very low SAR in this lake cause a longer exposition of OM to the water-sediment interface where it is exposed notably to methanogenesis (and potentially SO_4-reduction). This explains why much higher $(C:N)_{OM}$ ratios are found in the first cm of Alberca sediments than in the water column POM. In contrast, the surficial OM in the other lakes was deposited more recently

and its geochemical signatures closely resemble that of the present water column POM. Moreover, the low SAR (*i.e.* long exposure and accumulation of OM) in a restricted and physically-stratified basin like Lake Alberca, likely plays a role in depleting the lake of its oxidant species (*i.e.* favoring the establishment of the reducing conditions found in Alberca).

The TOC concentration is significantly and inversely correlated with $\delta^{13}C_{TOC}$ signatures (R^2=0.83). Part of the $\delta^{13}C_{TOC}$ variability is likely linked to fluctuations of the $\delta^{13}C_{DIC}$. Indeed, a depth profile of $\Delta^{13}C_{TOC\text{-}DICeq}$ (Fig. 6.14) shows a more limited range of variations (<3.1 ‰) compared to $\delta^{13}C_{TOC}$ (~6 ‰). However, the remaining $\delta^{13}C_{TOC}$ variability may be due to changes in the isotopic fractionation of primary producers. Therefore, [TOC] and $\delta^{13}C_{TOC}$ variability in Alberca is likely primarily driven by processes (ii) and (iii) stated above, as well as the isotopic composition of the source DIC.

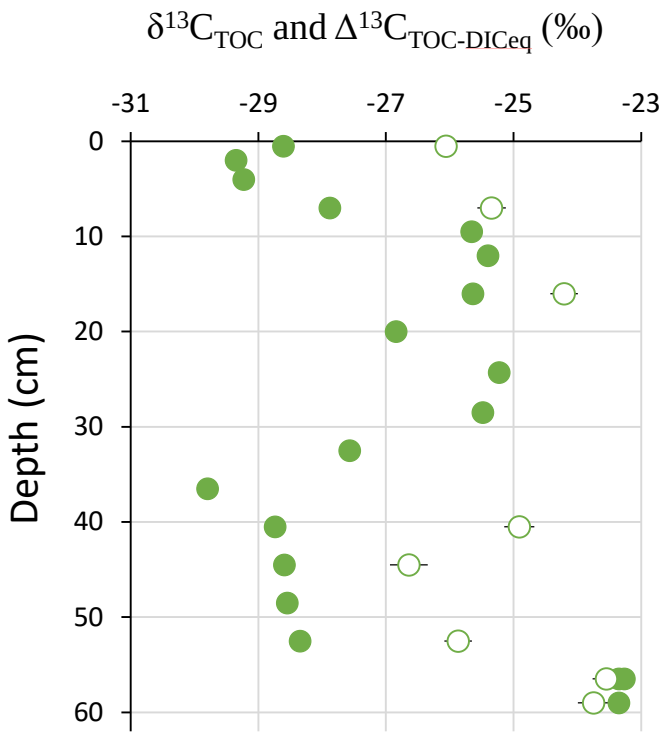

Figure 6.14 : Total organic carbon isotope composition ($\delta^{13}C_{TOC}$) and fractionation with equilibrium DIC ($\Delta^{13}C_{TOC\text{-}DICeq}$) in the sediments of Alberca. $\delta^{13}C_{TOC}$ is shown with the full dots, $\Delta^{13}C_{TOC\text{-}DICeq}$ with the empty dots ('DICeq' referring to dissolved inorganic carbon that would have been at isotopic equilibrium with the carbonates C in each sediment layer). The regular DIC value is not chosen because it is strongly shifted by methanogenesis here (Havas *et al.*, 2023a), and thus would not reflect the DIC composition from which OC was fixed.

6.3.5. Summary and comparison of the sedimentary organic matter record in the Mexican lakes

Overall, a generally high proportion of OC is deposited and preserved throughout the sediment cores of these redox-stratified lakes, notably compared with oxic marine settings where less than 1 % is preserved (Bralower and Thierstein, 1984; Jahnke, 1996). Here, considering as a maximum approximation, that the decrease of TOC concentrations in surficial sediments reflects its degradation, less than 50% of OC is remineralized *via* microbial degradation, underlining the high potential of anoxic environments for OM preservation.

Based on the sedimentation rates determined for Alchichica, Atexcac, and Alberca de los Espinos, I estimated the OC burial flux to be about 50, 12 and 40 $gC.m^{-2}.yr^{-1}$ respectively. This is very consistent with lacustrine OC burial fluxes worldwide (Fig. 6.15; Mendonça *et al.*, 2017), and specifically with small oligotrophic lakes (Fig. 6.15; Mulholland and Elwood, 1982). Besides, this is consistent with Atexcac being the most oligotrophic of the three lakes (*e.g.* Havas *et al.*, 2023b), and showing a potentially higher proportion of OM degradation in the sediments. Microbial respiration may strongly influence the burial flux in this lake, where that flux is estimated to 18 and 8 $gC.m^{-2}.yr^{-1}$, when considering either the first, or last 3 cm of the core. Alchichica and Alberca have a similar trophic status (Havas *et al.*, 2023b), but [TOC] are much higher in Alberca because its sediments have much smaller accumulation rates and are more reducing than in Alchichica.

In the four lakes, smaller [TOC] are associated with smaller $|\Delta^{13}C_{TOC\text{-}DICeq}|$ fractionations. In Alchichica and Alberca, this trend was rather primary than diagenetic and shows larger $|\Delta^{13}C_{TOC\text{-}DICeq}|$ in the more recent sediment layers (Fig. 6.11). Meanwhile, a consistent association between MSR and a positive $\delta^{13}C_{TOC}$ shift suggests a secondary origin for the changes in $|\Delta^{13}C_{TOC\text{-}DICeq}|$ in La Preciosa, and even more visibly in Atexcac. This small positive shift (between 3 and 4 ‰) is slightly larger than what is observed in modern environments (mostly around 1.5 ‰; Hayes *et al.*, 1999 and references therein). The extent of isotopic fractionation related to MSR may arise from: the initial TOC content (by mixing effect between primary and reworked OM), the microbial and enzymatic diversity of organisms performing MSR, and the nature and resistance of primary OM to microbial degradation (Londry and Des Marais, 2003; Goevert and Conrad, 2010; Blaser and Conrad, 2016). This isotopic shift remains small but not negligible, which calls attention for interpreting small isotopic variations in the

geological record, especially since its amplitude is not the same everywhere (*e.g.* between 0 and 1.5 ‰ in Alchichica *vs.* 3.5 ‰ in Atexcac).

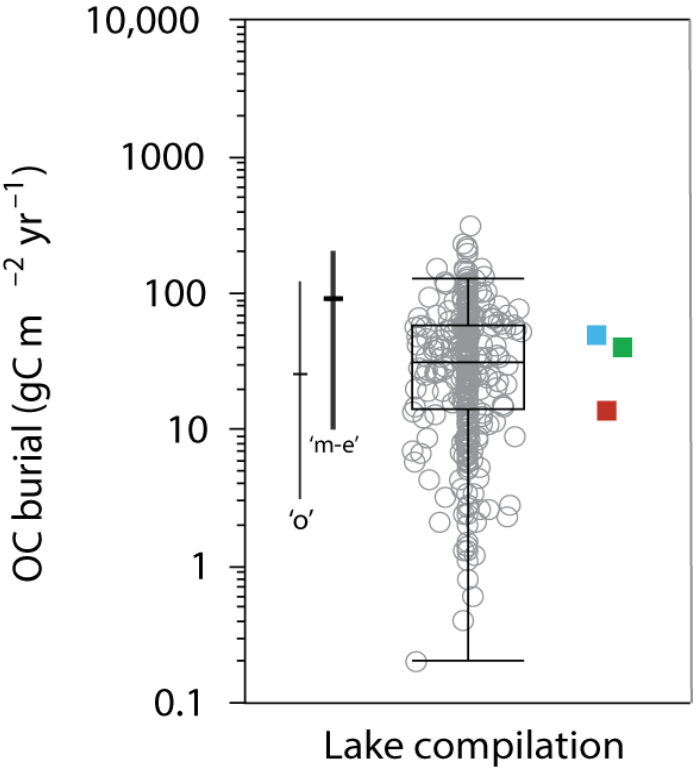

Figure 6.15 : compilation of organic carbon burial fluxes in lacustrine systems worldwide from Mendonça *et al.* (2017) and Mulholland and Elwood (1982). 'o' and 'm-e', ranges of burial fluxes for small (<100 km^2) oligotrophic (n=14) and meso-eutrophic (n=18) lakes worldwide, respectively, with the cross bar representing the average burial rate (Mulholland and Elwood (1982). Blue, green and red squares represent the fluxes estimated for lakes Alchichica, Alberca and Atexcac, respectively (this study). Figure with the grey dots and box plot (showing median, interquartile and 10th-90th percentile values) for 344 lakes worldwide modified from Mendonça *et al.*, (2017).

The nature of the organic substrate is also of great matter for the outcome of MSR on the porewater's pH. Indeed, MSR is generally considered to release alkalinity (and to favor carbonate precipitation) in microbial mats (*e.g.* Visscher and Stolz, 2005; Braissant *et al.*, 2007; Dupraz *et al.*, 2009; Tziperman *et al.*, 2011), and sediment porewaters (*e.g.* Berner *et al.*, 1970; van Lith *et al.*, 2002). However, the exact effect of MSR on pH will eventually depend on the composition of the organic substrate (Gallagher *et al.*, 2014; Meister, 2014). In Alchichica, and especially in Atexcac and La Preciosa, the activity of MSR is concomitant to the onset of more acidic porewater pHs and/or to carbonate dissolution (see section 6.4). This is consistent with some modeling studies showing that MSR in alkaline conditions would drive pH to lower values

(Meister, 2013), while others showed that sulfate reduction would favor calcification only when it is associated to pyrite precipitation (Soetaert *et al.*, 2007). In our dataset, the clear correlation in depth between sulfate reduction and the decrease of pH, albeit not representing a direct evidence, and despite pyrite precipitation occurring in the cores, could indicate that MSR in alkaline conditions does favor a pH decrease as suggested by Meister (2013). If true, this may be the first evidence of carbonate dissolution *via* MSR in a natural system.

The extent of OC alteration differs among the four lakes and depends upon three main parameters: primary productivity (PP), oxidant availability, and sediment accumulation rates (SAR). While the four lakes are redox-stratified with anoxic bottom waters, changes in these parameters lead to more or less reducing conditions in the sediments, and differential OC preservation and geochemical transformation (Fig. 6.16; Table 6.2). In Alberca, intermediate productivity, together with low SAR and oxidant availability, enable highly reducing conditions and a large OC accumulation, mostly degraded by ("inefficient") methanogenesis (Fig. 6.16). This enables the preservation of an isotopic compositions likely recording primary variations. In contrast, OC is the limiting factor in Atexcac, where PP is smaller, oxidant availability higher, and where higher SAR have a diluent effect. Thus, OC respiration in the sediments occurs through Mn-, Fe-, and SO_4-reduction before OC is almost depleted, but some SO_4 still remains. The redox balance is thus not as reducing in Atexcac (Fig. 6.16), and buried OC is more impacted by respiration and records a 4‰-increase (Table 6.2). In Alchichica, large oxidant availability (mostly SO_4^{2-}) prevents the onset of reducing conditions beyond sulfidic conditions (at least in the limits of the core's depth; Fig. 6.16), despite OC burial flux similar to Alberca. Higher SAR may help favoring the burial and preservation of OC in Alchichica. These conditions seem to generate a small and steady shift of $\delta^{13}C_{TOC}$. In La Preciosa, the core is a little short and SAR values are lacking. Despite a higher trophic status than Alberca and Alchichica (Havas *et al.*, 2023b), the TOC content in La Preciosa is lower, possibly due to higher SAR. However, TOC content should be well preserved due to limiting oxidant species. The $\delta^{13}C_{TOC}$ records a 4‰-increase but is difficult to be linked with primary or secondary variations.

Interestingly, the SAR seems to be a more or less direct consequence of the alkalinity gradient, since it is much faster in high-alkalinity lakes Alchichica and Atexcac compared to Alberca. Most likely, carbonate precipitation and deposition (with concentrations in the upper sediments of ~40, 65, and 17 wt. %, respectively) are determining in the observed SAR values. By extension of the discussion linking the SAR to redox levels in the environments studied,

another outcome of the alkalinity gradient (*cf.* Zeyen *et al.*, 2021; Havas *et al.*, 2023a) is its indirect control on the redox balance of the lakes.

Therefore, these observations reaffirm that early respiration processes can imprint a small positive isotopic shift to the primary $\delta^{13}C_{org}$ (here from 0 to 4‰), which should be the strongest where lower organic content and more oxic conditions prevail. It shows the complexity of constraining the variability in degradation potential in redox-stratified environments, which can show wide productivity and redox gradients. Besides, the isotopic shift recorded here extends previous estimations usually considered below 3 ‰, and averaging 1.8 ‰ (Hayes *et al.*, 1989; Ohkouchi *et al.*, 2008; Fulton *et al.*, 2018). It calls attention on interpreting such small isotopic variations in the geological record.

The use of compounds specific isotopic analyses is helpful in assessing the diagenetic biases discussed above (*e.g.* Hayes *et al.*, 1989; Fulton *et al.*, 2018). In the future, it would be interesting to apply this type of analysis to the studied Mexican lakes. Moreover, the placement of sediment traps at the bottom of lakes Alchichica, Atexcac, and La Preciosa during the fieldwork of 2022 should be of great help to further understand these processes.

Table 6.2: synthesis about diagenesis effects on organic matter in the Mexican cores. The organic C isotopic shift ($\Delta^{13}C_{TOC\text{-}DICeq}$) is calculated as the difference between total organic carbon and $\delta^{13}C_{DIC\text{-}eq}$ isotope compositions. This latter was calculated as the DIC isotope composition in equilibrium with $\delta^{13}C_{carb}$ at each depth. The 'repartition with depth' column presents the main trends with depth of geochemical proxies discussed in the text. The type of metabolisms identified can be used to illustrate the redox state of the sediments studied.

Lake (year of sampling)	Depth of the core (cm)	Average sedimentation rate ($cm.yr^{-1}$)	Shift $(C:N)_{OM}$	Shift of $\Delta^{13}C_{TOC\text{-}DICeq}$ (origin)	Repartition with depth	Type of metabolisms identified	Limiting factor for further OM degradation	Net burial of TOC ($g.m^{-2}.yr^{-1}$)
Alchichica (2019)	85	0.26	yes, ~ + 1/1.5	< + 1.5 ‰ (mostly primary)	$\delta^{13}C_{TOC}$ and $\Delta^{13}C_{TOC\text{-}DICeq}$ ↗ from surface towards 50 cm-depth, C:N progressive ↗	Sulfate reducers	none	~ 50
Atexcac (2019)	40	0.18	yes, ~ + 6	~ + 4 ‰ (mostly secondary)	$\delta^{13}C_{TOC}$ and $\Delta^{13}C_{TOC\text{-}DICeq}$ sharply ↗ below 15 cm, C:N progressive ↗	Sulfate reducers (Fe and Mn reducers? NH_4^+-oxidizers?)	organic matter	~ 12
La Preciosa (2016)	20	ND.	yes, ~ + 2.5	~ + 4 ‰ (primary or secondary)	progressive ↗ of $\delta^{13}C_{TOC}$, $\Delta^{13}C_{TOC\text{-}DICeq}$ and C:N	Sulfate reducers	oxidant species	ND.
Alberca de los Espinos (2019)	60	0.04	yes, ~ + 2.5	~ ± 3 ‰ (mostly primary)	variable trends for $\delta^{13}C_{TOC}$, $\Delta^{13}C_{TOC\text{-}DICeq}$ and C:N. Degradation mostly at the WSI	Methanogens, sulfate reducers	oxidant species	~ 40

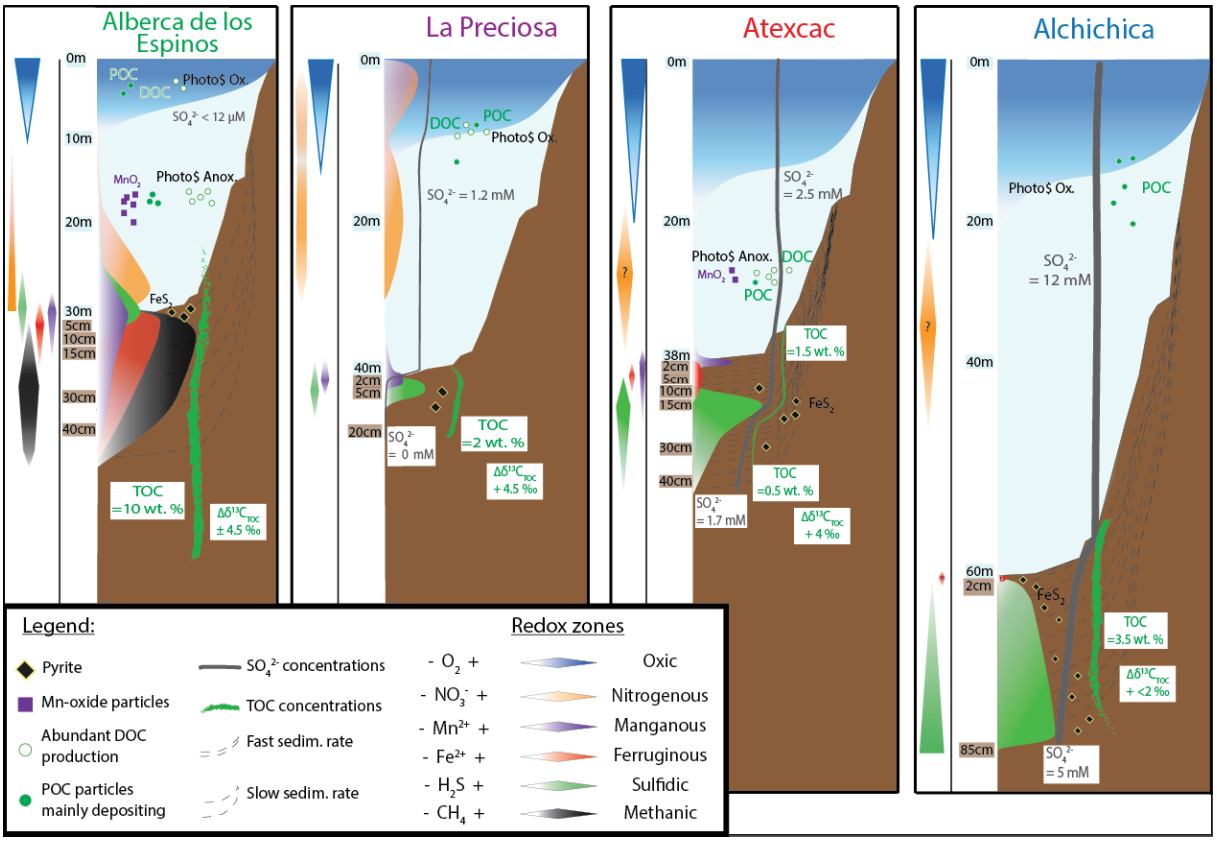

Figure 6.16: Synthetic scheme about diagenesis effect on organic matter in the Mexican cores. The width of the colored redox zones illustrates the relative abundance of O_2, NO_3^-, Mn^{2+}, Fe^{2+}, H_2S, and CH_4 species. Nitrate was not determined in Atexcac and Alchichica. The mention of oxygenic and anoxygenic photosynthesis indicates from which part of the water column (WC), organic matter (OM) in the sediments is mostly derived from (based on 2019 data). It does not mean these metabolisms are not active in the four WC. The $\Delta\delta^{13}C_{TOC}$ described the $\delta^{13}C_{TOC}$ variations with depth. The four lakes show oxygenated upper waters (in blue), become anoxic between 10 and 20m in the WC, but then have different distribution of their redox zonation. This relates to the amount of OC deposited, oxidant availability, and sediment accumulation rates (SAR). High TOC concentrations in Alberca are both a result and a reason for very reducing conditions in this system, and are partly due to slow SAR. The methanic zone is reached already at the water-sediment interface. Because of slow SAR, the OC accumulates in the sediments, and its exposition to the lake water is longer, however, because of the poor oxidant availability, its isotopic signal may be mostly primary. La Preciosa has a smaller TOC content, likely due to higher SAR because of a higher carbonate production/deposition in this lake. TOC is thus buried faster, while sulfate is low and quickly exhausted, which should favor TOC's preservation and a primary $\delta^{13}C_{TOC}$. Atexcac has the least productive waters and fastest SAR, which results in the lowest TOC content of the four lakes. Respired through a cascade of different redox reactions, TOC is almost consumed while sulfate is still available, suggesting that the degradation of TOC and its isotopic composition is maximum in this lake. The +4 ‰ increase in $\delta^{13}C_{TOC}$ likely reflects the contribution of heterotrophic secondary production. In Alchichica, slightly smaller SAR than in Atexcac favor slightly higher TOC. Sulfate is abundant but does not reach exhaustion. The $\delta^{13}C_{TOC}$ in Alchichica are interpreted as primary, with a possible constant offset from primary production due to bacterial sulfate reduction under steady state. Where organics and oxidant remains, it is possible that the sedimentary biogeochemical processes and their record keep evolving with depth in the core.

6.4. Early diagenesis effect on the Mexican lakes carbonates

Due to the alkaline nature of the studied lakes, their waters are oversaturated with respect to a lot of carbonate phases (Figs. 6.17 and 6.18), but to different degrees following a gradient of alkalinity (Zeyen, 2017; Zeyen et al., 2021). However, the chemistry and notably the pH of porewaters significantly evolve such that possible diagenetic dissolution and precipitation reactions occur and may affect the carbonate record of these Mexican lakes. Here I want to investigate what could this diagenetic effect be on the Mexican lakes sedimentary carbonates, in order then, to see what primary features of their environment they may preserve (Section 6.5).

6.4.1. Alberca and La Preciosa

In Lake Alberca, pH decreases strongly between the bottom of the water column and the upper sediments, which leads to an undersaturation of these waters with respect to calcite (Fig. 6.17). Consequently, the decrease of bulk carbonate concentration between the water-sediment interface and ~20 cm in depth in the sediments is likely due to the dissolution of calcite after deposition. However, then, pH stabilizes and the calcite saturation index slightly increases (from -0.35 to -0.30 between 7 and 28.5 cm, no data is available for lower depths; Fig. 6.17). It coincides with an increase of carbonate content between 20 and 60 cm. This could be explained by an initially higher content, and/or a weaker dissolution/alteration of carbonates at these depths (reprecipitation seems unlikely since the porewater remained undersaturated with calcite).

Diagenesis effect for the sediment core of Lake La Preciosa (20 cm deep) were already discussed in the PhD work of Alexis de Wever (2019). Diagenetic precipitation or dissolution was suggested to be sparse. Though one can notice an increase of dissolved Ca^{2+} and a small diminution of aragonite content which could be related to the dissolution of this phase. The 2016 data (De Wever, 2019), it can be seen that porewater sulfate concentration is quickly depleted while Fe is not present in detectable quantities. Because active anaerobic OM respiration (*via* sulfate reduction) is predominant within the core first 3 cm, whereas the carbonate dissolution occurs below that same 3 cm limit, it is possible that MSR buffers the porewater alkalinity until it stops and aragonite dissolves. Although pH was not measured for this core, one can imagine that it likely decreased with depth, similar to what is observed in

Alchichica and Atexcac. Virtually no calcite (or another carbonate phase) precipitates following aragonite dissolution in the first 20 cm (Table S6.1). Since no isotopic fractionation is expected from carbonates dissolution, the bulk carbonates may therefore preserve their primary isotopic signature despite diagenetic aragonite dissolution.

Sediment cores from 2016 in Atexcac (9.5 cm deep) and Alchichica (19 cm deep) were also discussed by De Wever (2019), but the cores from 2019 are significantly deeper (41 and 85.5 cm, respectively), and provide a more comprehensive view of diagenetic processes, as discussed below.

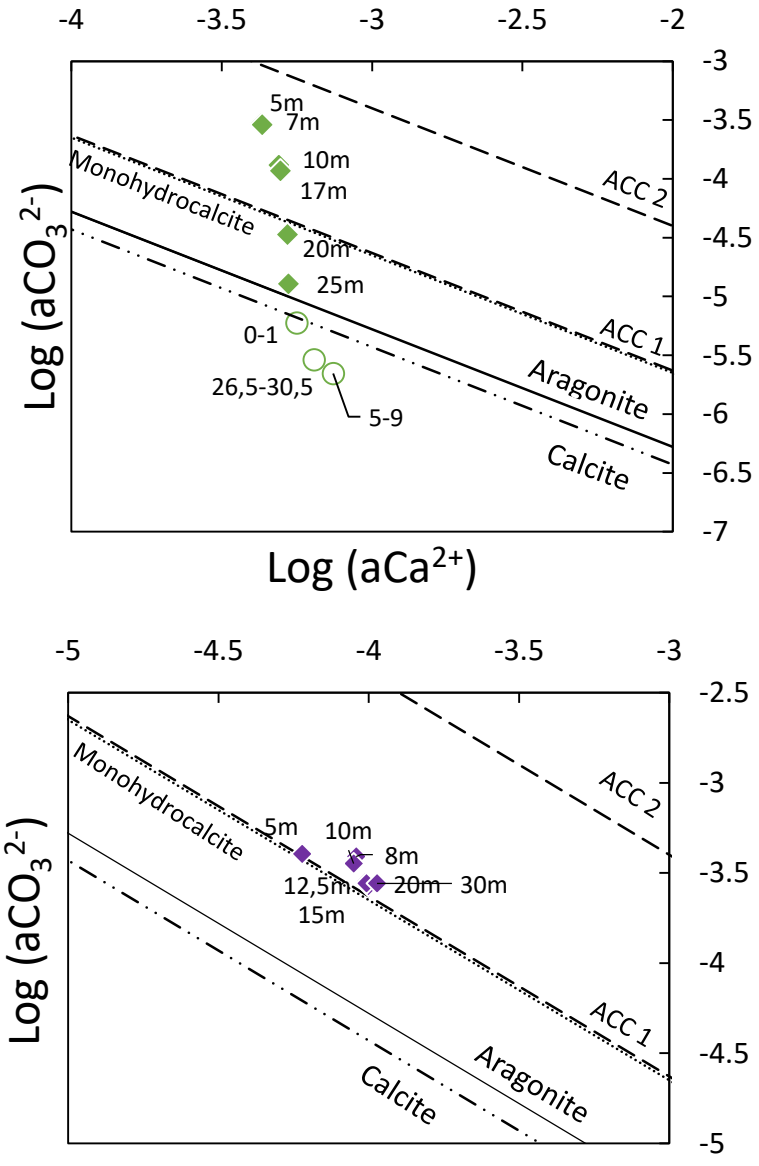

Figure 6.17: Solubility diagram in the log[a(CO_3^{2-})] – log[a(Ca^{2+})] space for Alberca (top) and La Preciosa (bottom) core samples. Diamonds correspond to aqueous solutions from the water column (with depth in meters) whereas circles correspond to porewaters (with depths in centimeters). The solubilities of calcite and aragonite at 15 °C from Muller *et al.* (2023) were used. The solubility of monohydrocalcite (MHC) was defined by Fukushi and Matsumiya (2018). The solubility lines of amorphous Ca carbonate 1 and 2 (ACC 1 and 2) were measured by Kellermeier *et al.* (2014) and (Brečević and Nielsen, 1989).

6.4.2. Alchichica

During the course of this PhD, I participated in the publication of an article directly related to the topic of Alchihica's sediments diagenesis (Muller *et al.*, 2023; Annex 2). I briefly summarize this work and its implication for the C cycle here. Muller *et al.* (2023) show how the hydromagnesite and amorphous diatom frustules depositing in Alchichica sediments are diagenetically replaced to form Mg-silicates phases (amorphous sepiolite) following the equations:

$$3Mg_5(CO_3)_4(OH)_2{\cdot}4H_2O + 20SiO_4 + 7H_2O \Rightarrow Mg_3Si_4O_{10}(OH)_2{\cdot}H_2O + 12HCO_3^- + 12H^+ \quad (6.1), \text{ or}$$

$$3Mg^{2+} + 4SiO_4 + 5H_2O \Rightarrow Mg_3Si_4O_{10}(OH)_2{\cdot}H_2O + 6H^+ \quad (6.2).$$

From these equations, a first obvious outcome is that the dissolution of hydromagnesite reduces the amount of carbonates, *i.e.* C, being captured in the sediments. The reaction mostly occurs in the surficial layers, such that the DIC generated would either accumulate in the porewater, or diffuse back to the water column. While hydromagnesite carries a heavy $\delta^{13}C$ signature, the DIC accumulating in porewaters becomes ^{13}C-depleted with depth as a result of OM remineralization *via* MSR (section 6.3). Thus, the DIC coming from hydromagnesite's dissolution more likely diffuses back to the water column (or is small compared to pore water DIC from OC remineralization). This is consistent with a surficial porosity still connected to the water column, and an upward DIC gradient from higher to lower concentrations.

Since the dissolution is quantitative, and only affects hydromagnesite, it should not alter the isotopic signal of remaining carbonates phases (mostly aragonite), which thus can be used to retrace processes occurring the in the lake (*e.g.* Chapter 5). Moreover, the very independent profile of $\delta^{13}C_{Carb}$ with depth, while $\delta^{13}C_{DIC}$ decreases, bolsters that the C isotope composition of aragonite is not affected by secondary exchanges or reprecipitation from the porewater DIC.

An important outcome of this work for the C cycle is that it evidences a mechanism called 'reverse weathering' (Mackenzie and Kump, 1995). This process refers to the sequestration of cations in authigenic silicates rather than in carbonates, eventually leading to the return of inorganic C to the hydrosphere-atmosphere system as CO_2. By constraining the solubility constant of these Mg-silicate phases to lower values, this study by Muller *et al.* (2023) suggests that reverse weathering may have been more important in the past. Lake Alchichica thus represents a great natural laboratory for the exploration of reverse weathering functioning.

6.4.3. Atexcac

6.4.3.1. Mineralogical reworking through diagenesis

The sediments of Atexcac give a clear-cut example of the tight link existing between biological, chemical, and mineralogical processes and how they can affect the sedimentary record quickly after its deposition. In the first 40 cm of Atexcac sediments, most geochemical proxies exhibit important variations with depth and a lot of them show a well-defined transition between the upper 15 cm and lower 20 cm of the core (both in the sediment solid- and dissolved-phases) (Fig. 6.5, 6.6). Notably, in this sediment horizon, bulk carbonate concentration decreases of about 40 wt. % while $\delta^{13}C_{carb}$ and $\delta^{18}O_{carb}$ increase of about 1 and 3 ‰, respectively (Fig. 6.5). These profiles raise the following questions about the carbonate record of the lake: (i) does it record a "dramatic" event affecting the lake's chemistry (*e.g.* a volcanic gas release event, a rapid drainage of the lake, or a shift to more productive waters)? (ii) does it record a progressive evolution of the lake's chemistry? or (iii) does it record a (clear) diagenetic overprint? I address these questions in the following.

From the stability diagrams of carbonate and silicate phases (Fig. 6.18), one can see a clear shift from (i) water column samples which are supersaturated with respect to crystalline and amorphous Ca-carbonate and Mg-silicate phases, to (ii) porewater samples which become undersaturated with the same phases (Fig. 6.18). pH also decreases from 8.9 in the water column to less than 8.6 in the surficial sediments. The source of this acidity could originate from volcanic CO_2 degassing in the lake through the sediments, similar as in Lake Dziani Dzaha in Mayotte (Milesi *et al.*, 2020), and as suggested for Alchichica which exhibits pCO_2 two times lower than Atexcac (Chapters 4 and 5). It could also result from the concomitant activity of MSR which is most active at the depths where pH drops (see section 6.3.5; Soetaert *et al.*, 2007; Meister, 2013). Whatever the source of acidity is, it results in important mineralogical and geochemical rearrangement of Atexcac sediments.

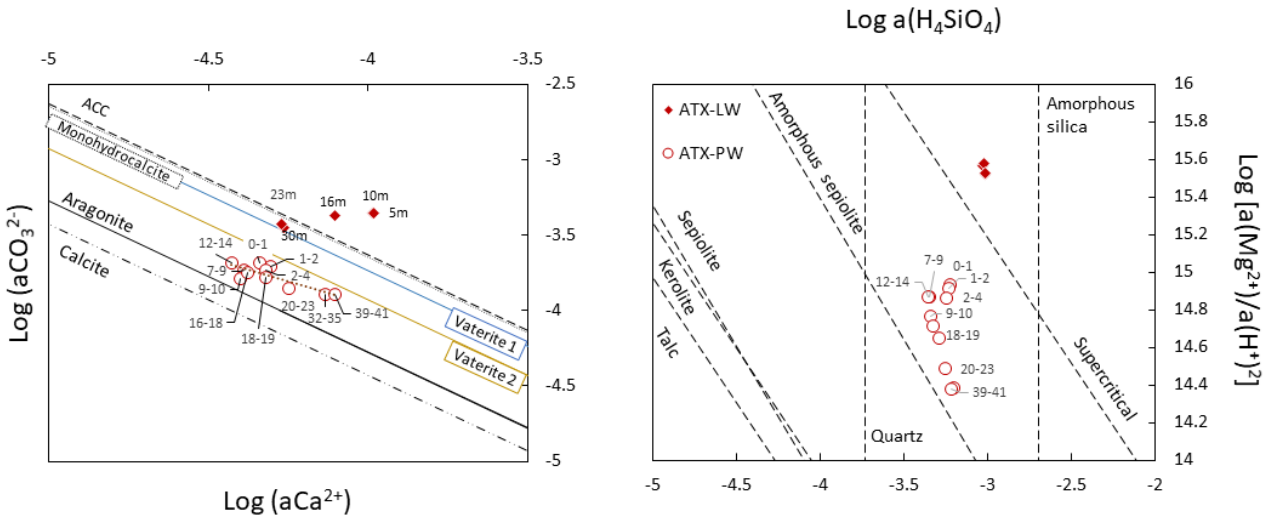

Figure 6.18: Solubility diagram in the log[a(CO_3^{2-})] – log[a(Ca^{2+})] and log[a(Mg^{2+})/a(H^+)^2] – log[a(H_4SiO_4)] spaces (left and right, respectively) in Atexcac. Diamonds correspond to aqueous solutions from the water column whereas circles correspond to porewaters (with numbers corresponding to depth horizons in the sediments in centimeters). The solubilities of calcite and aragonite at 15 °C from Muller *et al.* (2023) were used. The solubility of monohydrocalcite (MHC) was defined by Fukushi and Matsumiya (2018) and the solubility of amorphous Ca carbonate (ACC) was measured by Kellermeier *et al.* (2014). Solubilities of Vaterite 1 and 2 were determined at 25 °C by (De Visscher and Vanderdeelen, 2003). On the right panel, the solubility lines of talc (Jones and Galan, 1988), stevensite (Chahi *et al.*, 1997), kerolite and sepiolite (Stoessell, 1988), amorphous sepiolite (Wollast *et al.*, 1968), quartz and amorphous silica (Truesdell and Jones, 1974) were determined at 25 °C. The ''supercritical" line results from experiments conducted by Tosca *et al.* (2011) and Tosca and Masterson (2014) and relates to homogeneous nucleation of Mg-silicate phases from solution.

First, the progressive disappearance of a Si-Mg phase is observed between 0 and 9 cm, evidenced through the XRD profile of the five first samples of the core (Fig. 6.19), possibly *via* a reaction inverse to what is seen Alchichica:

$$Mg_3Si_4O_{10}(OH)_2{\cdot}H_2O + 6H^+ \Rightarrow 3Mg^{2+} + 4SiO_4 + 5H_2O \qquad (6.3)$$

Accordingly, the Mg:Ca ratio of the solid fraction decreases at these depths while Mg:Ca in porewater increases (Fig. 6.6). This is the opposite in Alchichica, or Dziani, where hydromagnesite is present at the top of the sediments, dissolves first, and favors Mg-silicate precipitation (Milesi *et al.*, 2020; Muller *et al.*, 2023). The difference with Alchichica, notably, is that the Atexcac's lake water is already supersaturated with respect to these Mg-Si phases (Fig. 6.18), which thus directly deposit in the upper sediments while they only become supersaturated in the porewater of Alchichica (Muller *et al.*, 2023). Thus, on the contrary to Alchichica where Si-depletion in the lake water ([H_4SiO_4] between 0 and 0.03 mM) is fostered by the precipitation of Mg-silicates, in Atexcac ([H_4SiO_4] ≈ 1 mM), the dissolution of these

phases likely favor the return of some Si to the water column in a "shuttle-type" process (*e.g.* Planavsky *et al.*, 2010). Compared to Alchichica sediments, a broad amorphous silica peak related to diatoms is not evident, suggesting a smaller deposition of diatoms in Atexcac. It is consistent with the previous inference that Atexcac SOM rather records the bottom water column organic matter, but is surprising considering that abundant diatoms are found in microbialites down to minimum 20 m depth (Chapter 4; Havas *et al.*, 2023a).

Despite initial dissolution in the most surficial sediments, another Mg-silicate phase precipitates in equilibrium with the porewaters below 15 cm, as seen on the stability diagram where all samples start to align on a straight line after 'ATX-5' (8-10 cm), that is, when the $(Mg:Ca)_{(aq)}$ ratio stops to increase (Fig. 6.18). In the XRD diffractograms, the typical bumps of Mg-Si silicates appear again at 17 cm ('ATX-7') and grow until 20 cm in depth, below which they are systematically found (Fig. 6.20). Thus, the final Mg-silicate phase in Atexcac sediments formed diagenetically, in equilibrium with the sediment porewater, but not with the lake water.

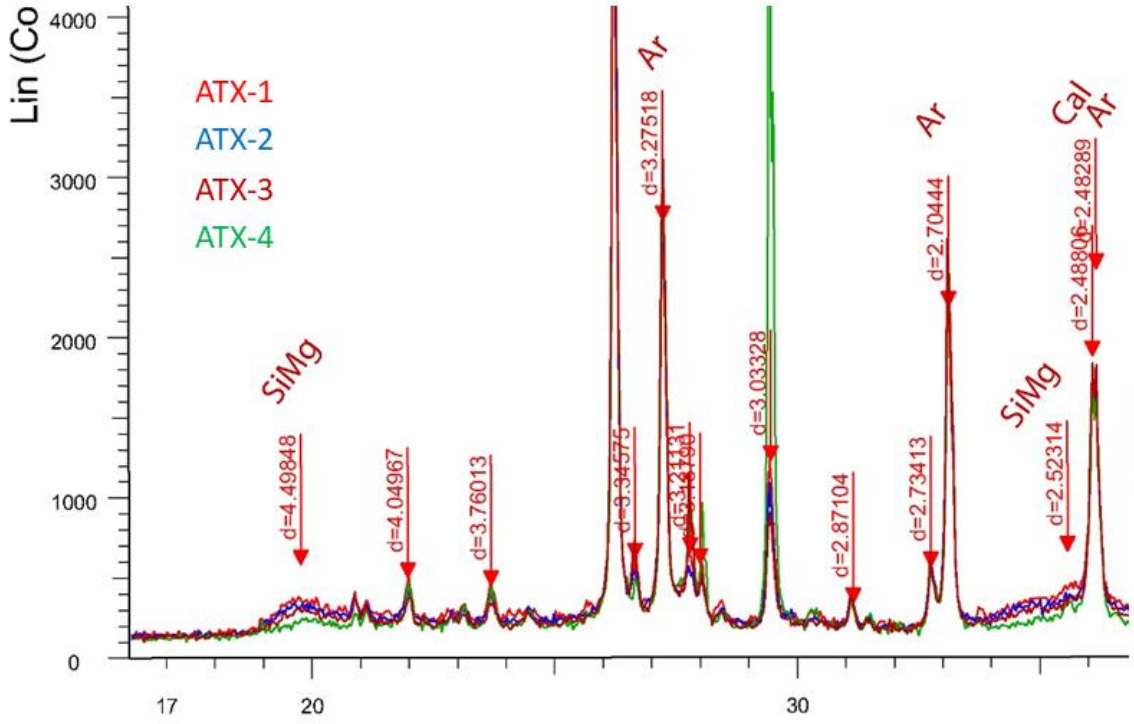

Figure 6.19: Zoom in diffractograms of sediment powders from Lake Atexcac (0-9 cm). The abscissa axis represents the 2θ angle of diffraction and the ordinate axis the number of counts. 'SiMg', 'Ar' and 'Cal' refer to authigenic Mg-silicate phases (see text), aragonite and calcite, respectively. There is a progressive disappearance of Mg-silicates between ATX-1 in light red (0-1 cm in depth) and ATX-4 in green (7-9 cm in depth).

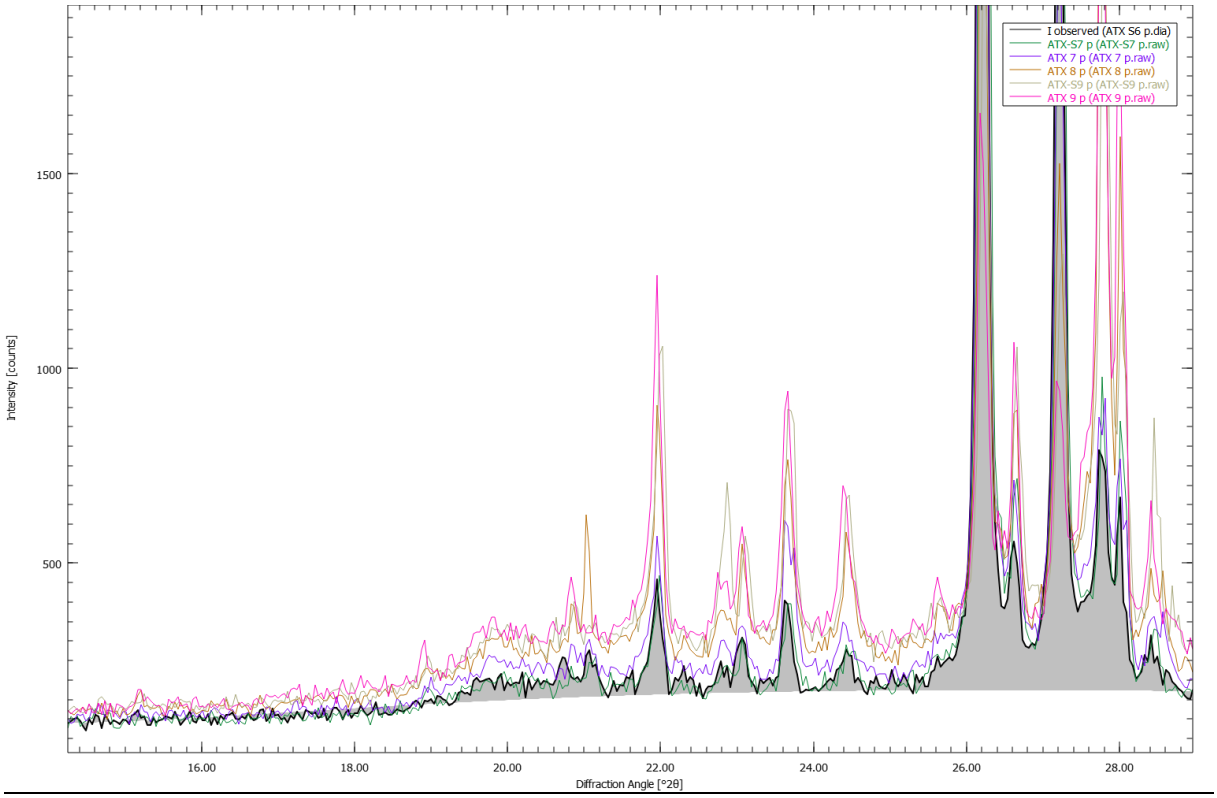

Figure 6.20: Zoom in diffractograms of sediment from Lake Atexcac (10-22 cm). The abscissa axis represents the 2θ angle of diffraction and the ordinate axis the number of counts. There is a progressive re-appearance of Mg-silicates (at ~20°) starting from ATX-7 in purple (16-18 cm in depth) to ATX-9 in dark green (18-20 cm in depth), after which the corresponding bump remains. On the left, where there are no peaks the background signal is similar for all samples.

Right after the initial exhaustion of the "primary" Mg-Si phase (around 8 cm in depth), there is a slight decrease of aragonite, and increase of calcite. Aragonite would start to dissolve when the pH-buffer effect of the Mg-Si phase stops, whereas calcite (which is less soluble) would precipitate following the increase in Ca^{2+} and CO_3^{2-} ion concentrations. After 15 cm, where pH also decreases, aragonite content drops. However, again, a small proportion of the dissolved aragonite is reprecipitated as calcite (or a similar hydrated carbonate or LMC phase).

There is little doubt that the increase of calcite with depth corresponds to a secondary precipitation within the porewaters and not to a primary phase from the water column. This notably because (i) there is virtually no calcite found in the emerged microbialites of the crater walls (except a few recrystallized ones; Chapter 9), and (ii) the Mg:Ca ratio of the porewater remains above 80 throughout the whole core, which is way above the limit where calcite and aragonite can precipitate from the same environment (Müller *et al.*, 1972; De Choudens-

Sanchez and Gonzalez, 2009). Based on a comparison between >10 Mexican lakes (including the ones studied here), Zeyen (2016) suggested that Mg:Ca ratios above 10-12 led to the formation of aragonite only. Thus, the porewater chemistry indicates that no primary calcite could have precipitated from the water column in recent years. However, it is surprising that dolomite is not precipitating as the secondary phase here. It could be specifically linked to microbial sulfate reduction, which was shown to favor Mg-calcite precipitation at similar SO_4 concentrations (Nöthen and Kasten, 2011). Alternatively, it may be a problem of kinetics, where low Mg-calcite precipitates first, and dolomite in a second time.

It also seems more consistent that the drop of aragonite below 15 cm rather describes a dissolution process than a secular change in aragonite content. Indeed, concentrations of dissolved Ca^{2+} and DIC are greater in the lower part of the core (Table S6.1), which is highly inconsistent with smaller aragonite concentrations/lesser precipitation occurring at the moment these layers deposited. On the contrary, it is well explained by a carbonate dissolution at these depths. Besides, secondary calcite precipitation is more likely if dissolution of another carbonate phase happened before (Sharp, 2017).

Microscope observations of these carbonated sediments (*e.g.* by SEM) would bring complementary and definitive evidences about their primary or secondary nature. Nonetheless, from the previous discussion it is possible to answer the initial questions and state that Atexcac sediments are not recording a "dramatic" event, but rather reflect a mix of diagenetic processes including carbonate dissolution and reprecipitation.

6.4.3.2. Effects of diagenesis on the carbonate isotope record

One question remains about whether these carbonates may still preserve a primary isotopic signature or not. Because calcite and aragonite precipitation induce different isotopic fractionations for O and C, the isotopic composition of the fluid they precipitated from has to be recalculated first (based on a "mineralogy-weighted" isotopic fractionation applied to $\delta^{13}C_{Carb}$ and $\delta^{18}O_{Carb}$). Then we can verify if these isotopic compositions also show the correlation found between $\delta^{13}C_{carb}$ and $\delta^{18}O_{carb}$ in the carbonate minerals. The results obtained for these '$\delta^{13}C_{DIC\text{-}eq}$' and '$\delta^{18}O_{H20\text{-}eq}$' are shown in Figure 6.21. They show a range of isotopic variation that is smaller than what is recorded by the minerals, especially for C. Moreover, there is a very good correlation between the $\delta^{13}C_{DIC}$ actually measured in the porewater and the

composition of the precipitation fluid ($\delta^{13}C_{DIC\text{-}eq}$) in the lower part of the core, but not in the top (Fig. 6.22). This strongly supports that carbonates from the lower part record a diagenetic signature while those from the top are closer to a primary (*i.e.* water column) signal. Unlike the other lakes, the $\delta^{13}C_{DIC\text{-}eq}$ in Atexcac's surficial sediments were found be slightly lower than $\delta^{13}C_{DIC}$ in the water column, while they contained more secondary calcite as well. Therefore, secondary calcite may slightly alter the bulk carbonate isotopic compositions already in the surficial layers. In the Ca^{2+}/CO_3^{2-} stability diagram (Fig. 6.18), porewaters start to align on a straight line only after 'ATX-6' (12-14 cm). This is consistent with the fact that the porewater chemistry is controlled by the precipitation of a Ca-carbonate phase below this depth, but not above (maybe calcite precursor phases like low-Mg calcite, a hydrated calcite phase, or vaterite; Fig. 6.18).

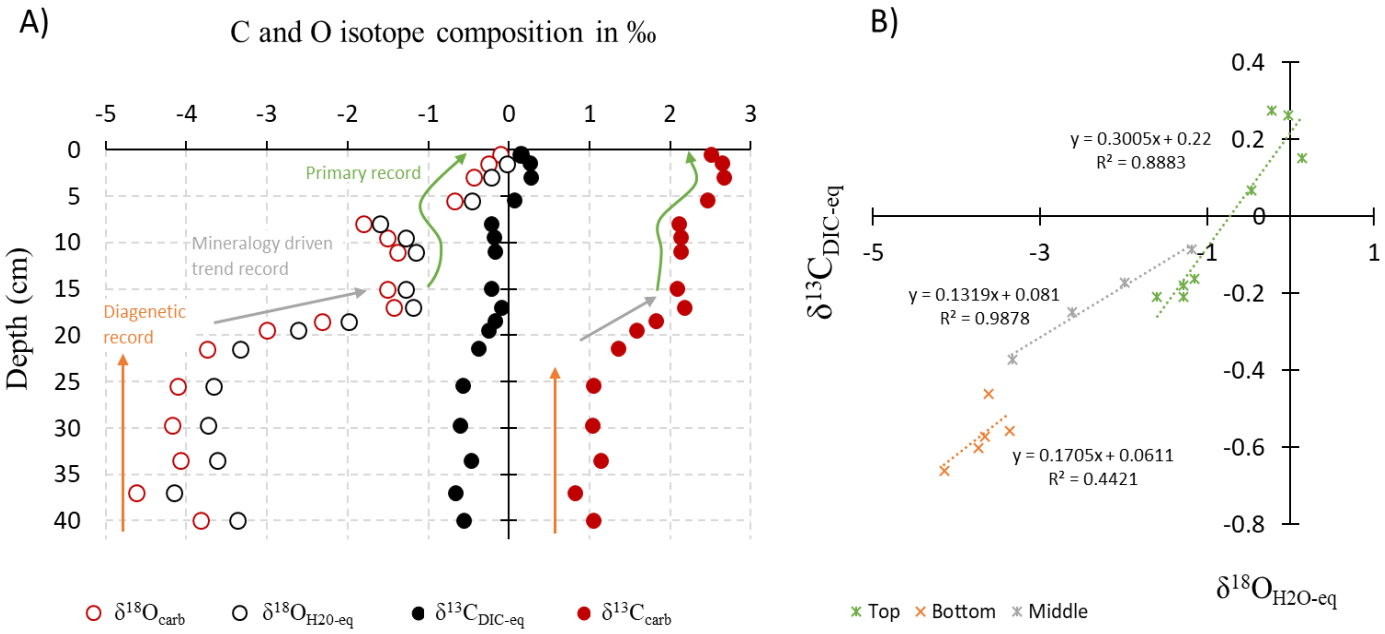

Figure 6.21: C and O isotope compositions in sedimentary carbonates of Atexcac and their fluid of precipitation. A) $\delta^{13}C_{carb}$ and $\delta^{18}O_{carb}$ correspond to the properly measured bulk carbonate C and O isotope compositions and are expressed on the VPDB scale. $\delta^{13}C_{DIC\text{-}eq}$ and $\delta^{18}O_{H2O\text{-}eq}$ correspond to the isotopic compositions of the fluid carbonates precipitated from, they are expressed on the VPDB and VSMOW scale, respectively. They were calculated as the difference between δ^{x}_{carb} and the isotopic fractionations associated with the different carbonate phases proportions. B) Cross-plot of $\delta^{13}C_{DIC\text{-}eq}$ and $\delta^{18}O_{H2O\text{-}eq}$ with slope and R^2 for the bottom (40-25.5 cm), middle (21.5-17 cm), and top (15-0 cm) of the core in Atexcac. The strongest correlation is found in the middle of the core where the C and O isotope trends are driven by the carbonates mineralogy.

The precipitation of this calcite within the sediments thus should record the composition of the porewater (Fig. 6.21). The influence of bacterial sulfate reduction (MSR) at these depths would tend to lower both C and O isotope compositions (Londry and Des Marais, 2003; Brunner *et al.*, 2005; Farquhar *et al.*, 2008), while possibly inducing calcite precipitation (Nöthen and Kasten, 2011). This is consistent with the observed $\delta^{13}C$ and $\delta^{18}O$ values, which start to harbor a stable and more negative value precisely where [TOC] and $\delta^{13}C_{TOC}$ shift as a result of MSR (Fig. 6.5). Thus, even if calcite precipitation is relatively early and inherits some of the ions from aragonite dissolution, it will primarily record the isotopic composition of the porewater (Fig. 6.21). In other words, a mix between initial porewaters, C from OM respiration, primary carbonates dissolution, and potentially later diagenetic fluids. Importantly, this is the isotopic composition of calcite that will be preserved in time, and not the primary aragonite.

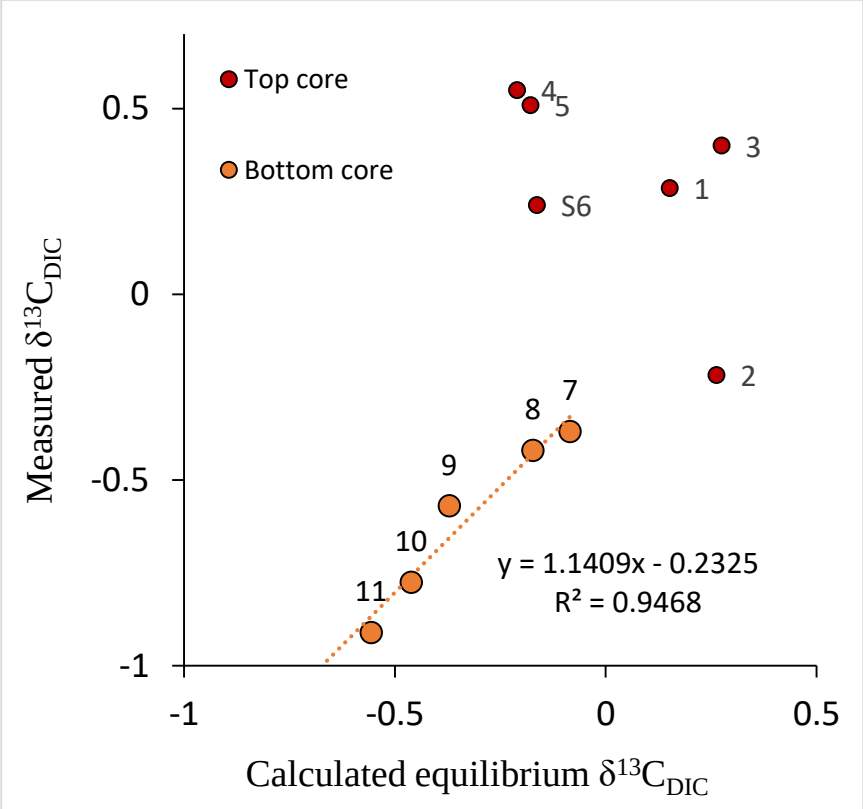

Figure 6.22: covariations between the isotopic composition of DIC measured in the porewater of Atexcac sediments and that of DIC in equilibrium with the carbonates (both in ‰ *vs.* VPDB). The two parameters are correlated with a slope close to 1 for samples from the lower part of the core (orange dots) but not for the upper part (red dots). Numbers next to the dots designate the sequential order of sediment horizons from top (1) to bottom (11).

Table 6.3: synthesis about diagenesis effects on carbonates in the Mexican cores.

Lake (year of sampling)	Total Depth of the core	Average sedimentation rate	Diagenetic dissolution ?	Cause of dissolution	Diagenetic precipitation ?	Preservation of primary isotopic signal	Deposition and/or burial rates of carbonates
Alchichica (2019)	85 cm	0.26 $cm.yr^{-1}$	yes, hydromagnesite, mostly in the first 5 cm (↘ ~12wt. %)	Local acidification by Mg-Si precipitation? By volcanic CO_2 degassing ?	maybe, tiny amounts of calcite ?	yes	~ 70 $g.m^{-2}.yr^{-1}$
Atexcac (2019)	40 cm	0.18 $cm.yr^{-1}$	yes, aragonite, mostly btw 15 and 20 cm (↘ ~55 wt. %)	Local acidification by sulfate reduction? By Mg-Si precipitation? By volcanic CO_2 degassing ?	yes, calcite, mostly btw 15 and 20 cm (↗ ~10-15 wt. %)	mostly before 15 cm in depth	~ 120 $g.m^{-2}.yr^{-1}$ (60)
La Preciosa (2016)	20 cm	ND.	maybe, aragonite, btw 4 and 20 cm (↘ ~15 wt. %)	lack of data	maybe, tiny amounts of calcite ?	probably yes	ND.
Alberca de los Espinos (2019)	60 cm	0.04 $cm.yr^{-1}$	yes, calcite, mostly in the first 20 cm (↘ ~10 wt. %), better preserved at depth	acidification at the bottom of the lake by methanogenesis (+ volcanic CO_2?)	no	yes	~ 10-20 $g.m^{-2}.yr^{-1}$

6.5. What primary environmental constraints are recorded in the sedimentary carbonates of the Mexican lakes?

It was demonstrated that the record of Alchichica, La Preciosa, and Alberca carbonates should preserve a primary isotopic signal while in Atexcac, it is the case only for the upper core (section 6.4). Hence, it is now possible to assess how these cores preserve the environmental factors influencing the lakes C cycle. These environmental constraints exert a strong control on the lakes DIC reservoir and generate a gradient of water chemical compositions from Alberca to Alchichica (Zeyen *et al.*, 2021; Havas *et al.*, 2023a). Notably, they give rise to an alkalinity gradient linked to specific evaporation rates, groundwater sources, and possible volcanic fluid inputs. The following section investigates how the carbonate deposits reflect these processes and sources.

6.5.1. Are the carbonates C burial fluxes consistent with the alkalinity gradient?

The average deposition flux of carbonates estimated for Alchichica, Atexcac, and Alberca is about 70, 120, and 20 $gC.m^{-2}.yr^{-1}$, respectively, only considering the layers without diagenetic dissolution. This number was not determined for La Preciosa because porosity and sedimentation rate data are missing. The comparison between Alberca and the other two lakes is consistent with the alkalinity gradient and lower [DIC] in Alberca (Havas *et al.*, 2023a). However, almost twice as much C from carbonates is deposited in the sediments of Atexcac compared to Alchichica, although it has a lower position in the alkalinity gradient (Zeyen *et al.*, 2021), with DIC and alkalinity concentrations representing only from about 70 to 75% the concentrations found in Alchichica (Zeyen *et al.*, 2021; Havas *et al.*, 2023a). However, only considering the bottom layers of Atexcac sediments (after dissolution has occurred), the burial flux becomes smaller than in Alchichica with ~60 $gC.m^{-2}.yr^{-1}$, which is consistent with the respective alkalinity reservoirs of the two lakes. Thus, while carbonate precipitation in the water column of Atexcac may proceed at higher rates than expected from its alkalinity levels, the overall system (water column + sediments) is requilibrated by diagenetic carbonate dissolution.

The enhanced carbonate precipitation and deposition in Atexcac is at least partly due to higher lake water Ca (and Mg) concentrations than in Alchichica (0.4 *vs.* 0.15 mM for Ca).

Differences in cations concentration between Alchichica and Atexcac depend on the sources and sinks of these elements. Cation sinks unlikely explain the difference between the two lakes because there is a higher carbonate deposition flux in Atexcac sediments, and both lakes form conspicuous amounts of microbial deposits (Zeyen *et al.*, 2021). Alternatively, they receive fluid sources with distinct chemical compositions. It was seen previously that Alchichica is fed by downstream groundwaters that tend to have a higher ionic strength, suggesting that Atexcac would not receive more cations from groundwaters. Otherwise, there may be a higher leaching degree of the volcanic basement by volcanic fluids under Atexcac compared to Alchichica. This would also explain the slightly lower pH and a much higher pCO_2 of Atexcac (Havas *et al.*, 2023a; Chapter 4). Because of this high pCO_2, the fluxes of inorganic C going through Lake Atexcac, and thus the potential size of the DIC and alkalinity reservoirs, are larger than in the other lakes studied. Combined with an alkaline pH in the water column, it results in larger carbonate precipitation and deposition fluxes. However, this carbonate factory is, in a way, "over-revving" relative to how much alkaline power is actually available in Atexcac, hence leading to an early diagenetic carbonate dissolution in the sediments. From that, two main conclusions can be drawn: (i) even if the C source to a given environment (*e.g.* volcanic CO_2) is unlimited, carbonate formation/preservation is eventually limited by the acid-base balance; (ii) alkaline environments may reside at boundary pH conditions for carbonate precipitation (whatever the size of the DIC reservoir), such that diagenetic processes may critically upset the record of these environments in the sediments.

6.5.2. Are the carbonates isotopic records consistent with the alkalinity gradient and related environmental forcing?

6.5.2.1. The importance of carbonates mineralogy

The alkalinity gradient defined by the four lakes (Zeyen *et al.*, 2021) is reflected by the lakes $\delta^{13}C_{DIC}$ which increases from about -3 to +2 ‰ on average (Havas *et al.*, 2023a). Bulk carbonate C isotope compositions at the water-sediment interfaces are in equilibrium with the upper water columns DIC (once possible detrital inputs and diagenetic effects have been accounted for) and thus also reflect this gradient. Nevertheless, the isotopic range recorded by the sediments is slightly amplified because carbonates in Alchichica are composed of hydromagnesite and aragonite, while those in Alberca are composed of calcite. Indeed, the

precipitation of the first two phases generate a higher isotopic fractionation than calcite (~2.5 and 5 ‰ *vs.* 1 ‰, respectively). Moreover, the sediment core in Atexcac illustrates how an isotopic trend can be modulated by the carbonates mineralogy on top of primary environmental factors (Fig 6.21). This shows and reinforces that mineralogy of carbonates has to be carefully examined before interpreting about paleo-environments, and that facies or texture specific analyses should be carried out if possible (McCormack and Kwiecien, 2021).

6.5.2.2. The record of evaporation by carbonates

One of the main factors proposed to explain the alkalinity gradient is evaporation (Zeyen *et al.*, 2021). Closed basin under evaporative regime usually present an isotopic enrichment of $H_2{}^{18}O$ and $DI^{13}C$, which transfers to and covaries within sedimentary carbonates (*e.g.* Talbot, 1990; Frantz *et al.*, 2014; Buongiorno *et al.*, 2018; Ingalls *et al.*, 2020). Indeed, evaporation favors the escape of light ^{16}O isotope over ^{18}O isotope (*e.g.* Li and Ku, 1997; Talbot, 1990). Evaporation also tends to increase the lake pCO_2 and primary productivity, which bolster CO_2 degassing and organic C burial, both having low $\delta^{13}C$ compared to DIC (*e.g.* Li and Ku, 1997; Talbot, 1990). Thereby, it also increases the $\delta^{13}C_{DIC}$ of residual waters and generates a covariation with the water $\delta^{18}O$. In Figure 6.23 are presented the covariations between $\delta^{13}C$ and $\delta^{18}O$ in the sediment carbonates of the four Mexican lakes. Do they reflect well the alkalinity gradient with typical evaporitic trends in the alkalinity-rich lakes?

Carbonates in Alberca do not show any correlation (R^2=0.04, n=8), consistently with a lower alkalinity and a less arid climate in this area. Instead, most of the variability is found for C isotopes, averaging -0.8 ± 1.5 ‰, while O isotopes average -0.6 ± 0.2 ‰ (Fig. 6.23). On one hand this is consistent with DIC signatures easily influenced by biological processes (*e.g.* aerobic respiration, methanogenesis) due a small buffer effect of the DIC reservoir (Havas *et al.*, 2023a), and on the other hand with a low evaporation to precipitation balance relative to the other lakes.

In the lakes from the SOB however, the message is not straightforward. An evaporation-like correlation is found in Atexcac and La Preciosa, but not in Alchichica, despite its geographical proximity with the other SOB lakes, and the fact Alchichica has the highest position on the alkalinity–salinity gradient. In La Preciosa and Atexcac, $\delta^{13}C_{carb}$ and $\delta^{18}O_{carb}$ show very strong correlations (R^2=0.99, p=4*10^{-3}, n=4, and R^2=0.98, p=10^{-14}, n=17,

respectively), whereas a weak correlation is found for Alchichica sediments (R^2=0.24, p=0.02, n=24) (Fig. 6.23a). When only considering the covariation between $\delta^{13}C$ and $\delta^{18}O$ of the fluid of precipitation (by correcting for the mineralogical bias in the respective carbonate isotopic signatures), the correlation in Alchichica becomes inexistent (R^2=0.08, p=0.17, n=24) (Fig. 6.23b) but is preserved for the other two lakes (R^2=0.995, p=2*10^{-3}, n=4, and R^2=0.92, p=10^{-9}, n=17, respectively). This shows, again, the potential influence of carbonates mineralogy on their isotopic signatures. Thereafter, only the $\delta^{13}C_{DIC\text{-}eq}$-$\delta^{18}O_{H2O\text{-}eq}$ covariation trends are discussed. In Atexcac, only considering the primary carbonates from surficial layers (not or less affected by early diagenesis, section 6.4.3), it still resulted in a significant correlation (R^2=0.89, p=5*10^{-6}, n=8).

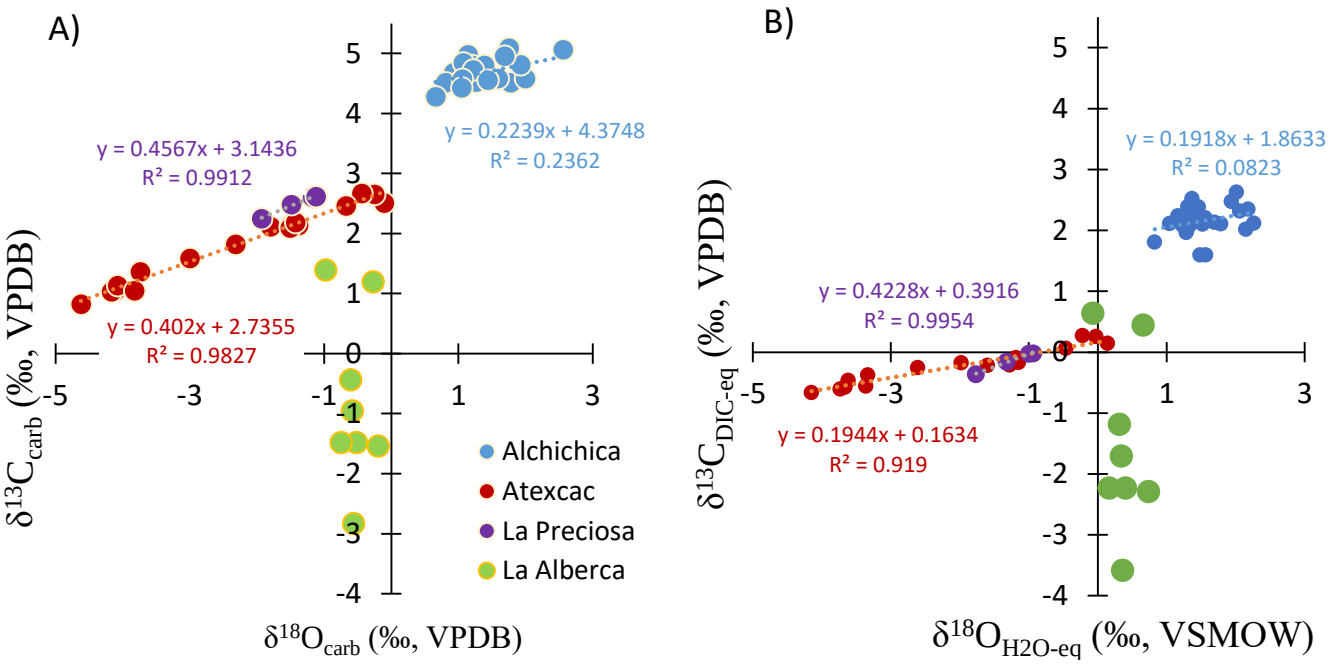

Figure 6.23: cross-plots of $\delta^{13}C_{carb}$ *vs.* $\delta^{18}O_{carb}$ (A), and $\delta^{13}C_{DIC\text{-}eq}$ *vs.* $\delta^{18}O_{H2O\text{-}eq}$ (B). For a better visualization, isotopic signal of O is expressed on the VPDB scale for carbonate and VSMOW for water reservoirs. It does not change the R^2 values, and mostly changes the intercept in the covariation equations. With a VPDB scale for O_{H2O}, the trend line equations become "y=0.1978x+7.7946"; "y=0.2004x+6.1739"; "y=0.4359x+13.464" for lake Alchichica, Atexcac and La Preciosa, respectively. Therefore, the only actual difference in slope equations between 'A' and 'B' is for Atexcac's sediments.

The specific covariation shape and $\delta^{13}C$-$\delta^{18}O$ slope of a given lake should reflect the proper hydrologic and geochemical state of that lake (Li and Ku, 1997). In Atexcac and La Preciosa, the $\delta^{13}C$-$\delta^{18}O$ correlation slopes (0.2 and 0.4, respectively, Fig. 6.23b) are in the lower range found for 41 lake carbonate sequences worldwide from 0.1 to 1.7 (Horton *et al.*, 2016). It is possible that the correlation slope recorded in Atexcac is flatter than in La Preciosa due to a higher DIC reservoir, and hence a higher buffer effect on C isotopes (Li and Ku, 1997). In parallel, more productive waters in La Preciosa (Havas *et al.*, 2023b) likely favor the steeper slope recorded in its carbonate minerals (Fig. 6.23). Yet, deductions that can be made from such slope numbers remain mostly qualitative (Talbot, 1990), and the records discussed here are relatively short-term and possibly influenced by a myriad of parameters (Li and Ku, 1997).

Why is this evaporitic trend not recorded by Alchichica sediments though, despite a clear drop of the water level in recent years (Alcocer, 2021; Havas *et al.*, 2023a) ? Other evaporitic basins were also shown to lack this correlation, but no clear explanation was provided (Horton *et al.*, 2016). In Alchichica, several factors may explain the stable $\delta^{13}C$ and $\delta^{18}O$ compositions despite an evaporation flux three times higher than the precipitation (Silva-Aguilera *et al.*, 2022). For O isotopes, the lake volume is larger in Alchichica than in Atexcac and La Preciosa, which may thus be harder to isotopically shift through evaporation. Meanwhile, C isotope composition is buffered by (i) a larger DIC lake reservoir, (ii) the DIC-rich GW influx, and (iii) a volcanic-CO_2 source (Chapter 5). These last two C sources have ^{13}C-depleted signatures which "go against" a $\delta^{13}C$ increase led by evaporation. This highlights how multiple and concomitant processes affecting a lake DIC/carbonate reservoir can counterbalance and mask each other (*i.e.* here mainly evaporation *vs.* volcanic C sources).

Nonetheless, the water of the three SOB lakes is isotopically enriched in comparison to their source water, most likely because they are closed basin, submitted to evaporation. Indeed, the GWi entering the three lakes have a $\delta^{18}O$ (around ~ -9 and -12 ‰ VSMOW; Lelli *et al.*, 2021) which is much lower than the lakes $\delta^{18}O_{LW}$ (between ~ -1 and +1.5 ‰ VSMOW). It was recognized from laboratory experiments that evaporation tends to generate a slope close to 1 (± 0.3, 1σ) between $\delta^{13}C$ and $\delta^{18}O$, while a compilation from 41 natural lacustrine carbonate systems showed significant correlations with an average slope of 0.62 (Horton and Oze, 2012; Horton *et al.*, 2016). From these slope values, it is possible to estimate the theoretical $\delta^{13}C_{GWi}$ feeding the Mexican lakes studied, and compare it with the lakes $\delta^{13}C_{DIC}$ (Fig. 6.24). Several conclusions arise from that graphic: (i) based on the available $\delta^{18}O_{GWi}$ data and slopes expected from evaporation processes, the $\delta^{13}C_{GWi}$ in the SOB should have negative values; (ii) the GWi

feeding Atexcac and La Preciosa have a similar isotopic composition whereas those feeding Alchichica are isotopically more enriched; (iii) the $\delta^{13}C_{GWi}$ estimated for Lake Alchichica corresponds well to the range of values used to fit the data in the previously described model (*i.e.* considering a volcanic CO_2 source to Alchichica); (iv) evaporation has driven the $\delta^{13}C_{DIC}$ and $\delta^{18}O_{LW}$ of the three lakes on timescales longer than that of the sediment cores (> 350 years); (v) the difference mentioned in 'ii' might explain the overall $\delta^{13}C_{DIC}$ and $\delta^{18}O_{LW}$ differences between the lakes (that is, $\delta^{13}C_{DIC}$ in Alchichica is heavier due to heavier $\delta^{13}C_{DIC}$-GW and not due to higher evaporation rates); and (vi) slopes recorded in Atexcac and La Preciosa carbonates reflect a lake specific covariation that deviates from a purely evaporitic process. This longer timescale evaporative trend is evidenced from the composition of groundwater measured today. However, it can be expected that it would not be preserved in the sedimentary record of Atexcac for example, due to the diagenetic carbonate dissolution and reprecipitation processes described above.

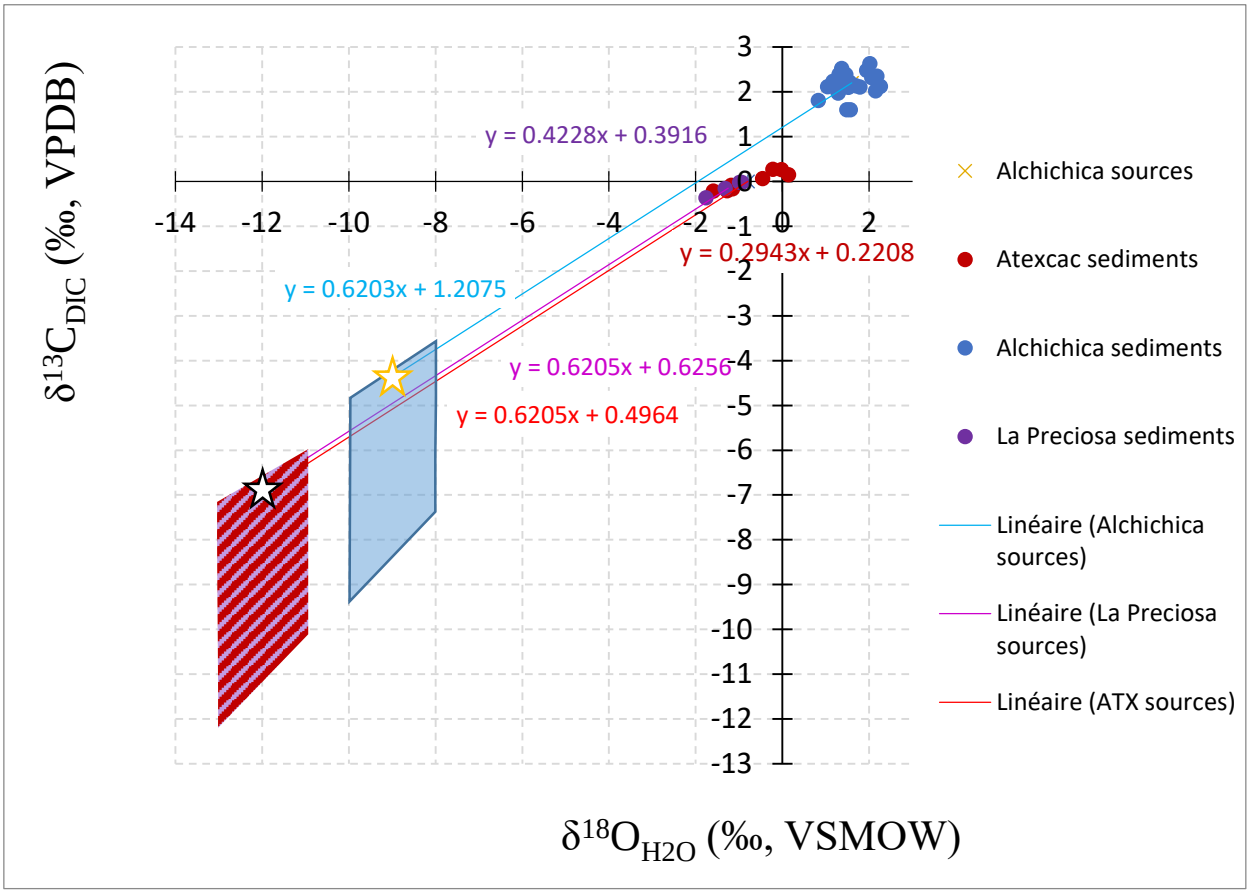

Figure 6.24: Cross plot of C and O isotope compositions in the waters of Alchichica, Atexcac, and La Preciosa lakes as well as groundwaters feeding them. The isotopic composition of lake waters was calculated from the sedimentary carbonate data - only the samples without a significant diagenetic effect were selected for Atexcac. The actual lake water compositions are in good agreement with the sediment-estimated values (in Alchichica, $\delta^{13}C_{DIC}$ ≈ 1.8 ‰ and $\delta^{18}O_{H2O}$ ≈ 1 ‰; in Atexcac $\delta^{13}C_{DIC}$ ≈ 0.4 ‰; in La Preciosa $\delta^{13}C_{DIC}$ ≈ 0.1 ‰; as determined by Lelli *et al.*, 2021 and Havas *et al.*, 2023a). The red and purple box represents the putative isotopic compositions of GW sources to Atexcac and La Preciosa, based on a $\delta^{18}O_{H2O}$ varying between -13 and -11 ‰ (following data from Lelli *et al.*, 2021), and a $\delta^{13}C_{DIC}$ calculated to match a slope between ~0.6 and 1. The blue box represents the same but for the GW sources to Alchichica, based on a $\delta^{18}O_{H2O}$ varying between -10 and -8 ‰, following data from Lelli *et al.*, 2021. The stars and associated trend lines represent the compositions of both sources chosen to match a slope of ~0.62 (*i.e.* the average value found for 41 lakes worldwide, Horton *et al.*, 2016). A slope of ~1 ±0.3 corresponds to what was found in evaporation laboratory experiments (Horton *et al.*, 2016). The trend line equations in dark purple and red are associated to La Preciosa and Atexcac sediments, respectively.

6.6. Conclusion and take-home messages

The C isotope signatures in the organic matter and carbonates were analyzed from the sediment cores of the four lakes studied. Together with mineralogy and element concentration data, I discussed how early diagenesis affects the two C reservoirs and what environmental signal they can preserve relatively early after their formation/deposition. The main conclusions can be summarized as:

- Besides receiving organic particles from different layers of the stratified water columns, each lake sedimentary organic matter (SOM) was prone to differential reworking. The degree of reworking (and OC burial rates) mainly is a function of SOM quantity (and thus primary production), oxidant availability, and sediment accumulation rates. These parameters may fluctuate in time and space, which further complicates the interpretation of organic C isotope signals as primary information in stratified water columns, and reaffirms the need to couple C isotopes to other proxies (molecular analysis, N isotopes, *etc*.). The C isotope shift associated with bacterial respiration varied from 0 to +4 ‰.

- The sediments in Atexcac may provide the first natural evidence of carbonate dissolution *via* the activity of microbial sulfate reduction (MSR). In Alchichica, a higher OM availability and prolonged MSR do not result in a pH decrease, which allows a better carbonate preservation. The effects of MSR on pH in natural environments thus need to be better understood.

- The alkalinity gradient among the four lakes influences the redox state of each lake, by generating large differences in carbonate production, sediment accumulation rates, and OC burial rates, leading to various degrees of oxidant consumption.

- Carbonate diagenetic dissolution occurred in the four lakes, but was only followed by significant carbonate reprecipitation in Lake Atexcac, for which I detail the geochemical and mineralogical transformation of the sediments. Diagenetic reprecipitation below a depth of ~15 cm in Atexcac sediments leads to the loss of a primary record in Atexcac carbonates, but the other lakes may preserve the primary chemical evolution of their respective water columns.

- Alkaline environments are prone to the precipitation of important carbonate deposits, but can also be severely impacted by pH changes. A systematic decrease of pH is found from the water column to the bottom sediments of the lakes studied. Consequences are two-fold: (i) sedimentary carbonates will only record the conditions in the upper part of the lakes rather than at the bottom (*e.g.* in Alberca, they keep no trace of methanogenesis occurring in the lower part of the lake); (ii) important dissolution may occur. In Atexcac for example, more than half of the carbonate content dissolves.

- From the above it results that the carbonate burial rates (from 20 to 70 $gC.m^{-2}.yr^{-1}$) are consistent with the alkalinity gradient between the four lakes, although carbonate deposition is initially much higher in Atexcac. It brings to light how the burial of carbonates in any alkaline environment is limited by its acid-base balance, on top of its DIC sources.

- Even without a strong diagenetic effect, the mineralogy of primary carbonates can shape the isotopic record, and should be considered before interpretations are made.

- In agreement with the conclusions about the lakes water column, higher alkalinity environments make the carbonate record less sensitive to environmental changes, at least on timescale of 100s years, as their DIC reservoirs are highly buffered. They may buffer the record of climatic/hydrologic phenomena as shown by the lack of $\delta^{13}C$–$\delta^{18}O$ covariation in Alchichica carbonates. While longer time series might help discerning such processes, they are also more favorable to diagenetic loss of information (*cf.* dissolution/reprecipitation Atexcac).

- The analysis of external groundwater sources was required to actually unravel the evaporative and closed-basin nature of Alchichica, highlighting the importance of considering a geochemical and isotopic frame to the interpretation of a given location.

Table S6.1. Sediment composition in wt. % estimated by Rietveld (proportion in the crystalline fraction). Phosphate compounds correspond to DCDP and HHP phases.

Sample ID	Depth (cm)	Albite	Bytownite	Aragonite	Calcite	Augite	Halite	Hmg	Huntite	Quartz	Hornblende	Hydrotalcite	Total
AL19-C2-1	0-1	17.2	8.8	39.4	2.4	4.0	10.3	11.4	1.3	5.2			100.0
AL19-C2-2	1-3	17.8	16.5	45.6	2.0	1.4	1.9	11.4	0	3.3			100.0
AL19-C2-3	3-5	18.3	11.9	53.7	1.7	4.6	2.4	1.3	1.4	4.8			100.0
AL19-C2-4	5-7	13.4	15.4	60.1	1.9	4.6	1.3	0.3	0	2.9			99.9
AL19-C2-5	7-10	22.6	25.3	39.4	2.1	5.8	1.2	0	0	3.7			100.0
AL19-C2-6	10-13	19.5	10.6	50.9	2.1	8.5	0.2	0	0	8.1			99.9
AL19-C2-S7	13-16	13.6	15.7	54.0	2.3	6.2	2.6	1.5	0	4.2			100.0
AL19-C2-7	16-19	14.8	13.2	56.8	2.4	6.5	1.0	0.0	0.7	4.6			99.9
AL19-C2-S8	19-22	16.4	15.0	53.7	2.9	5.5	1.4	0.2	0	4.9			100.0
AL19-C2-8	22-25	14.6	15.0	55.8	2.0	7.5	0.6	0.2	0	4.4			100.0
AL19-C2-S9	25-28	0	0	0	0	0	0	0	0	0			0.0
AL19-C2-9	28-30.5	15.0	10.0	61.8	2.1	5.5	0.6	0	0	5.0			100.0
AL19-C2-S10	30,5-34,5	8.1	16.7	58.9	2.0	5.3	2.1	0.6	1.9	4.4			100.0
AL19-C2-10	34,5-40	11.1	14.3	49.0	1.6	11.1	0.2	6.7	4.4	3.5			101.8
AL19-C2-11	40-43	0	0	0	0	0	0	0	0	0			0.0
AL19-C2-12	43-46	21.4	18.7	43.8	3.3	6.7	0.2	0.6	0	5.3			99.9
AL19-C2-S13	46-49	15.9	17.6	47.9	3.2	6.6	2.9	1.7	0	4.4			100.1
AL19-C2-13	49-52	15.7	16.1	48.2	2.4	4.9	0.1	1.4	0	2.9	8.4		100.0
AL19-C2-S14	52-55	18.3	17.3	43.3	2.8	7.0	3.0	0.3	0	4.0	4.1		100.0
AL19-C2-S15	58-61	14.5	15.2	45.8	2.9	8.5	1.6	1.6	0	6.8	3.2		100.1
AL19-C2-S16	64-67	14.4	19.7	46.7	2.5	6.5	2.2	0.3	0	4.4	3.3		100.0
AL19-C2-S17	70-73	16.4	10.0	57.0	1.1	4.7	5.3	0	0	3.3		2.2	100.0
AL19-C2-S18	76-79	14.5	6.9	61.4	1.7	6.4	3.8	0.4	0	5.1			100.0
AL19-C2-19	82-84	6.4	5.9	75.0	1.4	0	2.6	0	0	5.2	3.5		100.0
AL19-C2-S20	84-85,5	12.3	6.9	67.9	0.6	4.3	3.6	0	0	4.4			100.0

Sample ID	Depth (cm)	Albite	Bytownite	Aragonite	Calcite	Andesine	Halite	Hmg	Huntite	Quartz	Hornblende	Hydrotalcite	Total
ATX19-C1-1	0-1	4.3	1.7	75.7	6.3	7.9				4.2			100.0
ATX19-C1-2	1-2	6.8	1.5	80.1	5.1	3.1				3.5			100.0
ATX19-C1-3	2-4	4.7	4.7	79.4	4.7	1.9				4.7			100.0
ATX19-C1-S4	4-7	4.7	0.9	81.7	4.9	4.4				3.4			100.0
ATX19-C1-4	7-9	2.5	5.7	72.3	7.8	7.2				2.4	2.2		100.1
ATX19-C1-5	9-10	3.0	1.8	75.0	8.8	9.1				2.2	0.0		100.0
ATX19-C1-S6	10-12	2.0	4.7	75.3	9.5	6.1				2.4	0.0		100.0
ATX19-C1-S7	14-16	4.4	4.9	74.1	9.1	4.7				2.9	0.0		100.0
ATX19-C1-7	16-18	10.0	7.6	68.4	10.1	1.3				2.5	0.0		100.0
ATX19-C1-8	18-19	11.4	3.5	41.3	16.5	20.8				3.6	2.9		100.0
ATX19-C1-S9	19-20	7.6	13.4	33.6	20.5	17.5				3.9	3.5		100.0
ATX19-C1-9	20-23	12.9	7.2	27.0	20.8	24.6				3.3	4.2		100.0
ATX19-C1-S10A	23-27,5	6.2	26.7	19.3	19.4	23.3				3.2	2.0		100.1
ATX19-C1-S10B	27,5-32	7.0	7.2	23.4	22.6	33.3				3.6	3.0		100.0
ATX19-C1-10	32-35	16.0	6.7	17.5	18.5	31.6				3.5	6.3		100.0
ATX19-C1-S11	35-39	18.6	9.0	13.0	17.9	29.7				5.5	6.3		99.9
ATX19-C1-11	39-41	21.0	6.1	15.7	16.3	31.4				3.6	2.9		96.9

	Depth (cm)	Albite	Bytownite	Aragonite	Calcite	Sanidine	Quartz	Pyrrhotite	Total
LP16-C3-7	0-2	8.0	8.9	76.7	2.9		2.9	0.7	100.0
LP16-C3-8	2-4	14.3	2.4	79.6	2.8		1.0		100.0
LP16-C3-9	8-10	7.5	8.1	75.1	2.4	3.8	3.1		100.0
LP16-C3-10	18-20	11.0	13.3	63.9	3.2	4.5	4.1		100.0

	Depth (cm)	Albite	Bytownite	Calcite	Sanidine	Brookite (TiO_2)	Phosphate-compounds	Quartz	Hornblende	Mg-calcite	Total
Albesp19-C3-1	0-1	23.4	51.3	0.9	12	1.9				10.6	100.1
Albesp19-C3-3	2-4	36	43.4	10.3			10.4			0	100.1
Albesp19-C3-4	5-9	35.4	36.7	2.9			20.8	2.5		1.7	100.0
Albesp19-C3-S6	14-18	21.4	48.9	0.3			15.6	11.1	2.7	0	100.0
Albesp19-C3-S10	46.5-50.5	28.8	40.6	1.9	4.8		0	3.1	0	20.6	99.8
Albesp19-C3-S12	54.5-58.5	17.6	35.6	0.4	7.6		0	0.2	3.14	35.4	99.9

Part 1
Intermediate conclusion

Part 1 allowed a thorough description of the C cycle in the four Mexican redox-stratified lakes: Alchichica, Atexcac, La Preciosa, and Alberca de los Espinos.

The comparison of concentration and isotopic results in C reservoirs from each water column highlighted the poor sensitivity of DIC to climatic and biological processes in high alkalinity settings, and the partial record of POC as an ecological proxy. The DOC was evidenced as a powerful complementary C pool to analyze in redox-stratified environments. The DOC data evidenced the planktonic communities most actively cycling C, and recorded huge isotopic variability resulting from specific DIC uptake and DOM release mechanisms. These signatures reflect a specific combination of environmental parameters (high UV radiation and CO_2 availability but low nutrient levels). Importantly, however, they are not recorded in the POC which deposits in the sediments, constituting an important bias to the sediment-based interpretations of paleoecological studies. Besides, POM from different stratified layers of each water column are preferentially exported, further complexing these records.

Modeling the C processes and fluxes occurring in Lake Alchichica over the last 60 years suggests a significant contribution of volcanic-CO_2 to the lake. This source is not obvious from classical ^{13}C and ^{14}C analyses because the system is buffered by the carbonate basement and high pH/alkalinity of the lake. This result was demonstrated by combining hydrological and geochemical data of reservoirs external to the lake (groundwater, rain water), illustrating the necessity to zoom out in order to capture the full picture of a given water basin.

Carbonates mainly precipitate in isotopic equilibrium with the oxycline layer of the water columns. Thus processes occurring in the lower part of the lakes are not recorded in the bottom sediments. Important diagenetic reorganization (organic matter remineralization and carbonate dissolution/reprecipitation) may affect the sediment record. In Atexcac, most of the primary aragonite is dissolved and partly reprecipitated as calcite, thus recording the porewaters isotopic signatures, influenced by microbial respiration processes, rather than a primary signal. The carbonate burial flux after diagenetic dissolution seems consistent with the alkalinity levels in each lake. These diagenetic changes are strongly tied to the S cycle, in particular through microbial sulfate reduction. This will be the topic of the following ‘Part 2’.

Part 2

The sulfur sedimentary record: a biogeochemical imprint of diagenesis

The second part of this dissertation is dedicated to the study of sulfur (S) isotope compositions recorded in the bottom sediments of the four Mexican lakes studied. Its main objective is to assess what are the main factors influencing the S isotope record during diagenesis. Sulfur isotope compositions from the water column were measured; they are discussed to assert how they may transfer to, and evolve within the sediments (rather than to characterize the processes occurring in the water column). The opening chapter of 'Part 2' focuses on the sediments of Alchichica, where the extended dataset of major and minor S isotopes, from dissolved and solid S phases, allows untangling the complex diagenetic processes operating in this lake (Chapter 7). The imprint of diagenesis on the three other lake sedimentary records is discussed in Chapter 8. There, multiple S isotopes in the lake waters and sedimentary pyrites are used to trace the main sources of S in the four lakes, examine the impact of diagenetic processes on these records (*e.g.*, varying isotopic fractionations between the four lakes, within a single sediment core, distillation in the porewaters), and overall, assess the role of the sulfate reservoir's size ("reservoir effect") in pyrite isotopic compositions.

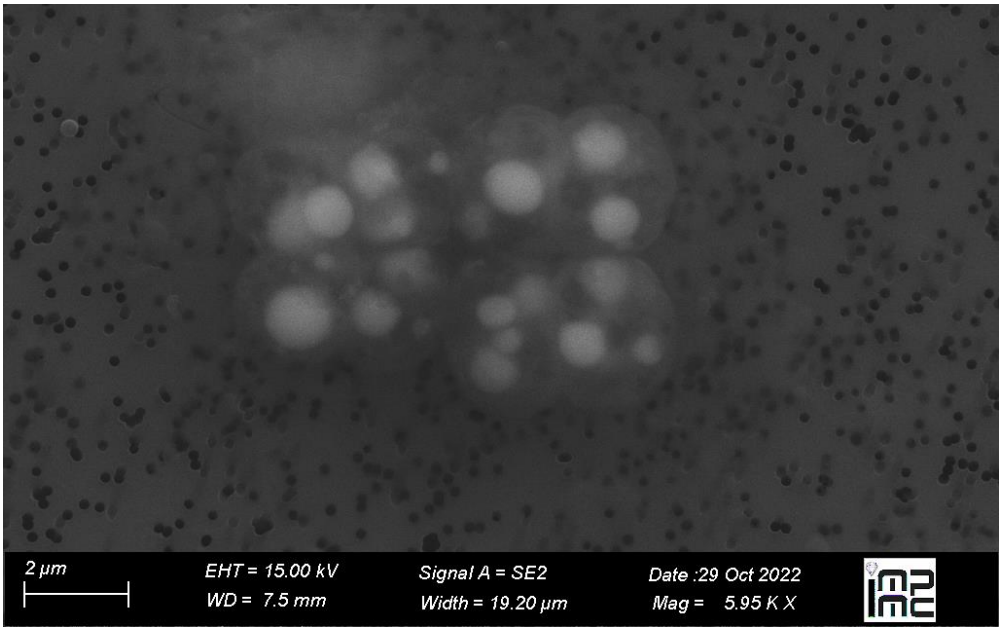

Fig. 2.0: scanning electron microscope image of elemental sulfur inclusions in prokaryotes from the water column. Courtesy: K. Benzerara.

Chapter 7

Characterization of a cryptic sedimentary reoxidative S cycle in Alchichica through the study of multiple sulfur isotopes

Table of content

7.1. Introduction

Much of the interpretations about the past sulfur cycle at the Earth's surface are based on its major isotope signatures (^{32}S, ^{34}S) reported as $\delta^{34}S$ from concurrent pyrite (FeS_2) and SO_4-bearing minerals (*e.g.* gypsum, barite) (Strauss, 1997; Canfield, 2004; Fike *et al.*, 2015). Notably, these data have been used to reconstruct the global ocean redox state (*e.g.* Canfield and Teske, 1996; Fike *et al.*, 2006; Halevy *et al.*, 2012; Wortmann and Paytan, 2012; Leavitt *et al.*, 2013), assuming, under steady state, that the $\delta^{34}S$ signature of the ocean reflects a balance between the isotopic composition of the source of S to the ocean, the burial flux of pyrite, and pyrite isotopic composition mediated by microbial sulfate reduction (MSR) (see general introduction).

Yet, a growing body of evidence points out the primary influence of local (post-) depositional conditions in shaping the S isotope record through early diagenesis processes, in particular since these conditions may fluctuate spatially and temporally (*e.g.* Liu *et al.*, 2021; Pasquier *et al.*, 2021a; Houghton *et al.*, 2022; Marin-Carbonne *et al.*, 2022). Trying to constrain these processes in modern and recent environments, different research groups have evidenced the impact of numerous factors including: sedimentation rates associated with climatic/eustatic variations (Pasquier *et al.*, 2017, 2021a; Houghton *et al.*, 2022), organic C deposition fluxes (Pasquier *et al.*, 2021b), sediments mineralogy and Fe-availability for pyrite precipitation (Liu *et al.*, 2020a, 2021; Masterson *et al.*, 2022), biological or physical sediment reworking (Fike *et al.*, 2015), diffusion/advection transport of dissolved chemical species (Jørgensen, 1979, 2021; Masterson *et al.*, 2022), sulfurization of OM (*e.g.* Raven *et al.*, 2016, 2018), and sulfate reservoir effects (Gomes and Hurtgen, 2013, 2015). The interpretation of S isotopes is further complicated by possible changes in the MSR fractionation itself (*e.g.* Sim *et al.*, 2011a; Leavitt *et al.*, 2013), and by biotic or abiotic reoxidation cycles of sulfides interfering with the primary isotopic signatures produced by MSR (*e.g.* Zerkle *et al.*, 2009, 2010; Strauss *et al.*, 2012; Pellerin *et al.*, 2015; Guibourdenche *et al.*, 2022).

The improvement of technical and conceptual expertise on S minor stable isotopes (^{33}S, ^{36}S) in the last decades has allowed a deeper understanding of these processes, and considerably improved our ability to discriminate the effects of different metabolisms on S isotopes (*e.g.* Farquhar *et al.*, 2003; Johnston *et al.*, 2005a, 2005b, 2007, 2008; Ono *et al.*, 2006; Leavitt *et al.*, 2013; Zerkle *et al.*, 2016). However, application of these systematics was only recently

extended to modern sedimentological contexts (Pellerin *et al.*, 2015; Masterson *et al.*, 2018), and only occasionally targeted geologically perennial S reservoirs (*e.g.* pyrite; Lin *et al.*, 2017; Liu *et al.*, 2020b, 2021, 2022; Masterson *et al.*, 2022). It is therefore crucial to further evaluate the isotopic imprint left by early diagenesis on the S sedimentary record (*e.g.* Liu *et al.*, 2020b).

To this end, the S isotope signatures of the stratified lakes studied here were determined in their water column and sediments. In this chapter, I present a thorough description of processes occurring in the sediments of Alchichica, whose multi-S isotope signatures were determined for both solid and dissolved phases (together with that of the lake sulfate).

In order to ease the readers' comprehension of S isotope data and their interpretation, a preliminary "toolbox subsection" on this matter is provided just below. It also contains the isotopic notations specific to S isotopes that were not presented in the general introduction.

Toolbox for reading sulfur isotope data

The representation and calculations of the four sulfur (S) isotopes slightly differ than for carbon (only two stable isotopes) and oxygen (three stable isotopes, but only two described here). This implies slightly different notations which are presented below.

Then, you may find a graphic visualization of how fractionating, mixing, and distillation processes affect S isotope compositions. The graphics are provided with the main equations needed to compute the effects of these processes, for sulfur major (^{32}S, ^{34}S) and minor (^{33}S, ^{36}S) isotopes. Regarding minor isotopes, the examples including numerical values are given for ^{33}S; the equations are valid for ^{36}S as well, but yield different visual representation. I use microbial sulfate reduction (MSR) as an example of fractionating process.

Basic notations for S isotopes

When isotopic systems have more than two stable isotopes, fractionating processes often follow *mass-dependent* laws. It means the different S isotopes, for example, will be fractionated proportionally to their mass difference, with $\delta^{33}S$ and $\delta^{36}S$ being roughly half and twice the $\delta^{34}S$, respectively. More precisely, these ratios correspond to and can be calculated as:

$$\lambda_{eq} = (1/m_1 - 1/m_2)/(1/m_1 - 1/m_3) , \qquad (7.1)$$

where m_1, m_2 and m_3 are the masses of ^{32}S, ^{33}S or ^{36}S and ^{34}S, respectively, and yield 0.515 and 1.9 for ^{33}S and ^{36}S, respectively (Young *et al.*, 2002). Thus, on a $\delta^{33}S$ *vs.* $\delta^{34}S$ diagram, data points following mass-dependent fractionations (MDF) should align on a slope of ~ 0.515 (as observed for the quaternary samples, Fig. 7.1) while samples influenced by *mass-independent* fractionations (MIF) will deviate from it, as seen in the analyzed Archean samples (Fig. 7.1). Therefore, isotopic signatures in ^{34}S are mostly expressed in the classical linear 'δ' notation, whereas ^{33}S and ^{36}S isotopes are more commonly expressed in the $\Delta^x S$ notation, which translates this deviation of $\delta^{33}S$ or $\delta^{36}S$ from values expected from theoretical equilibrium fractionation calculation (*e.g.* Johnston, 2011) such that:

$$\Delta^{33}S = \delta^{33}S - 1000*[(1+ /1000)^{0.515} - 1] \quad (7.2)$$

$$\Delta^{36}S = \delta^{36}S - 1000*[(1+ \delta^{34}S/1000)^{1.9} - 1] \quad (7.3)$$

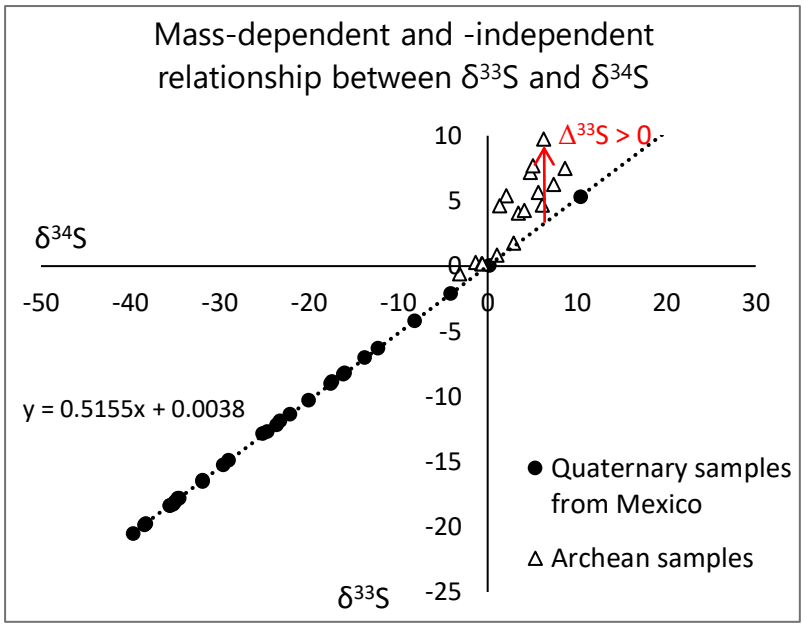

Figure 7.1. Example of relationship between $\delta^{33}S$ and $\delta^{34}S$ results measured in modern and Archean samples during the course of this study. The significantly positive $\Delta^{33}S$ mark mass-independent fractionations, only found in Archean samples.

High precision measurements of ^{33}S and ^{36}S developed for the last 30 years also allow to distinguish small non-zero $\Delta^{33}S$ and $\Delta^{36}S$ produced by MDF (through mixing, branching or distillation) and carrying precious insights into modern sulfur biogeochemical cycles (*e.g.* Ono *et al.*, 2006).

The $\Delta^{33}S$ and $\Delta^{36}S$ can also be expressed such as:

$$\Delta^{3x}S' = \delta^{3x}S' - \lambda_{eq}*\delta^{34}S' \quad (7.4)$$

where λ_{eq} is fixed to 0.515 and 1.9 for ^{33}S and ^{36}S, respectively, and the prime delta notation is defined as:

$$\delta^{3x}S' = \ln(^{3x}R_{sample} /^{3x}R_{reference}) * 1000 \text{ (‰)} \quad (7.5)$$

but also:

$$\delta^{3x}S' = \ln(\delta^{3x}S/1000 + 1)*1000 \text{ (‰)}. \quad (7.6)$$

While achieving virtually identical results to $\Delta^{33}S$ and $\Delta^{36}S$, the advantage of these prime notations is that they allow to normalize the isotopic compositions to the international VCDT scale by simple additions (Ono *et al.*, 2006) like for example:

$$\Delta^{33}S'_{sample/VCDT} = \Delta^{33}S'_{sample/working\ gas} + \Delta^{33}S'_{working\ gas/VCDT}. \qquad (7.7)$$

The isotopic compositions of SF_6 working gas (WG) relative to VCDT is assessed by repeated measurements of S1 standard (internationally calibrated to the VCDT scale) such that $\delta^{3x}S'_{WG/VCDT} = -\delta^{3x}S'_{S1/WG} + \delta^{3x}S'_{S1/VCDT}$. In this manuscript, I report ^{33}S and ^{36}S results in the $\Delta^{3x}S'$ notation but ^{34}S signatures as $\delta^{34}S$ to facilitate inter comparison with abundant literature regarding this parameter.

Effects of isotopic fractionation, mixing, and Rayleigh distillation on multi-S isotopes

Microbial sulfate reduction tends to deplete the residual sulfate reservoir in the light ^{32}S isotope, in favor of the produced sulfide (Fig. 7.2a) (*e.g.* Chambers and Trudinger, 1979 and references therein). The isotopic fractionation associated with that process can vary over a wide range, from near-equilibrium values ($^{34}\varepsilon$ = -70 ‰ and $^{33}\lambda = 0.515$), to values approaching $^{34}\varepsilon$ = -10 ‰ and $^{33}\lambda = 0.510$ (Sim *et al.*, 2011a, 2011b; Gomes and Hurtgen, 2013; Leavitt *et al.*, 2013; Bradley *et al.*, 2016).

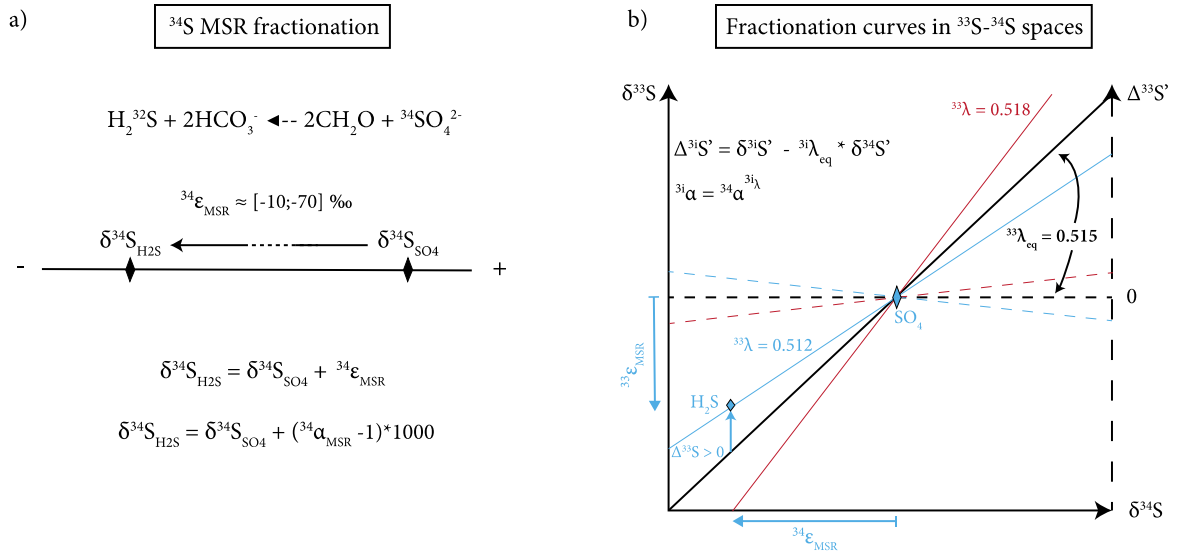

Figure 7.2: Fractionation curves for sulfur major (a) and minor (b) isotopes. In 'b' solid lines are plotted against the $\delta^{33}S$ axis and the dashed lines are plotted against the $\Delta^{33}S'$ axis. The black lines in b represent equilibrium processes that do not generate $\Delta^{33}S'$ changes.

Minor S isotopes are usually described with the $^{3i}\lambda$ and $\Delta^{3i}S'$ parameters, where '3i' designates the mass number '33' or '36'. On a $\delta^{33}S$-$\delta^{34}S$ diagram, products and reactants of a process occurring at thermodynamic equilibrium will spread on a $^{33}\lambda$ slope of 0.515 (solid black line in Fig. 7.2b). Thence, they will carry $\Delta^{33}S'$ signatures equal to 0 (dashed black line in Fig. 7.2b). By contrast, processes occurring out of equilibrium (like kinetic biological processes) will carry non-zero $^{33}\lambda$ and $\Delta^{33}S'$ signatures which can be process-specific (Fig. 7.2b). The products of reactions characterized by a $^{33}\lambda$ slope < 0.515 will inherit a $\Delta^{33}S' > 0$ when the isotopic fractionation is negative ($\varepsilon < 0$; *e.g.* MSR), but a $\Delta^{33}S' < 0$ when ε is positive. The opposite is true for slopes > 0.515 (*e.g.* most disproportionation reactions).

Mixing

Considering only the major S isotopes, mixing of two distinct reservoirs can intuitively be represented in a 1D space with the $\delta^{34}S$ notation where the mix composition reflects the proportion of each endmember (Fig. 7.3a).

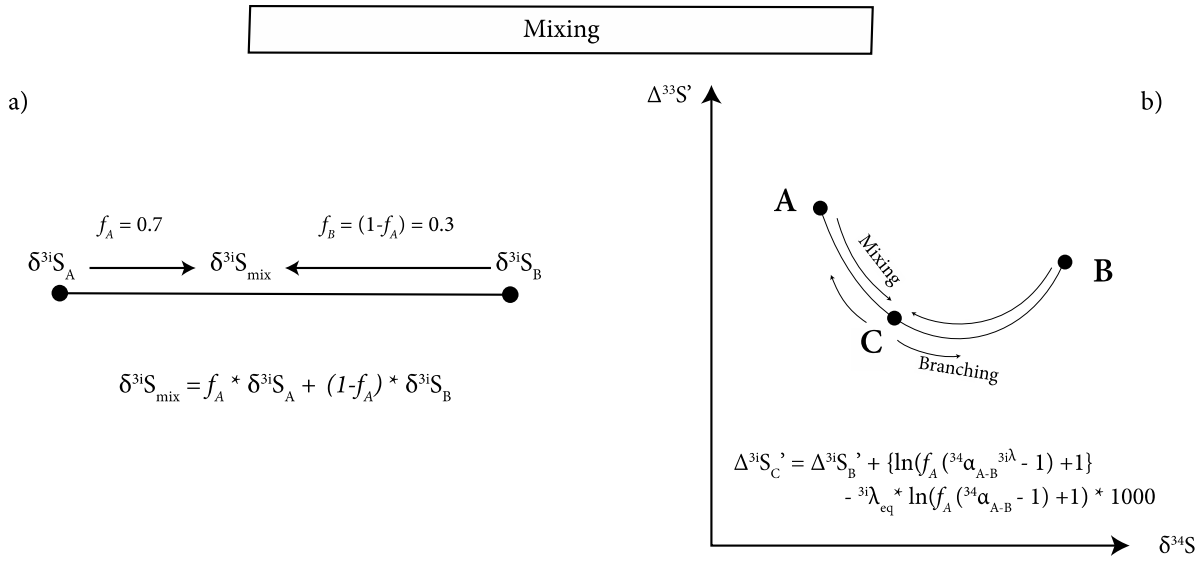

Figure 7.3: effect of mixing and branching processes on sulfur major (a) and minor (b) isotopes.

In $\Delta^{33}S'$-$\delta^{34}S$ spaces, mixing of 'A' and 'B' will produce a third reservoir 'C' with a lower $\Delta^{33}S'$ than both the initial reservoirs (Fig. 7.3b), provided that $^{33}\lambda$ is close to 0.515 (Ono *et al.*, 2006). The same principle applies to a branching process where 'C' is divided into 'A' and 'B' (Fig. 7.3b). *NB*: products of mixing will carry more positive $\Delta^{36}S'$ than the reactant reservoir, but branching will produce more negative $\Delta^{36}S'$ values (Ono *et al.*, 2006).

Rayleigh Distillation

In a closed-system, the progressive consumption of reservoir 'A' producing 'B' *via* a constant isotopic fractionation (ε) can be modeled by Rayleigh distillation equations (Fig. 7.4a). Applied to MSR, the depletion in ^{32}S-sulfate leads the residual sulfate reservoir (A) and the resulting "instantaneous" sulfide (B) (produced at any given time) to a theoretically infinite enrichment in ^{34}S isotopes (Fig. 7.4a).

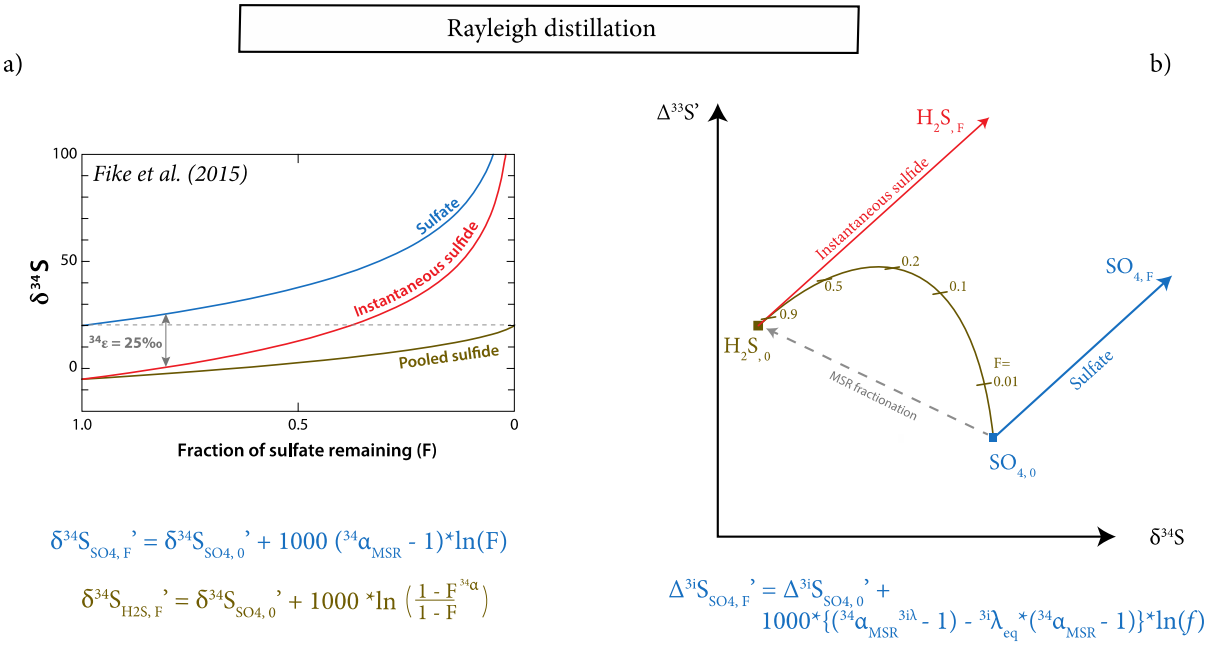

Figure 7.4 : effects of Rayleigh distillation by microbial sulfate reduction in a closed-system depicted for $\delta^{34}S$ (a) and $\Delta^{33}S'$-$\delta^{34}S$ (b) signatures (see text below for explanation).

The "pooled" or cumulated sulfide reservoir (B') will return to the initial source composition as it accumulates from all preceding reduction steps (Fig. 7.4a). This is because no fractionation is expressed if an entire reservoir is converted to another one. For simplicity, the calculations were made using $\delta^{34}S'$, but results are always represented with the more classical $\delta^{34}S$ notation ($\delta^{34}S' = \ln[\delta^{34}S/1000 + 1]*1000$). Equations were extracted from Ono *et al.* (2006) and Aoyama *et al.* (2014).

In a closed-system, MSR represents a series of branching reactions, thereby increasing the $\Delta^{33}S'$ of both sulfate and instantaneous sulfide, as well as their $\delta^{34}S$ (*cf.* Fig. 7.4b). Again, the sulfide pool will record that of the sulfate source if this latter is fully converted (Fig. 7.4b).

Processes' multi-S isotope signatures

Multiple S isotope data enable the discrimination and identification of processes producing overlapping $\delta^{34}S$ variations. Figure 7.5a, shows the diagnostic $^{33}\lambda$–$^{34}\varepsilon$ fields of different S redox changing reactions: microbial sulfate reduction (Johnston *et al.*, 2005a; Sim *et al.*, 2011a, 2011b; Leavitt *et al.*, 2013; Bertran *et al.*, 2018), intermediate S compound disproportionation (Johnston *et al.*, 2005a), and abiotic sulfide oxidation (Eldridge and Farquhar, 2018).

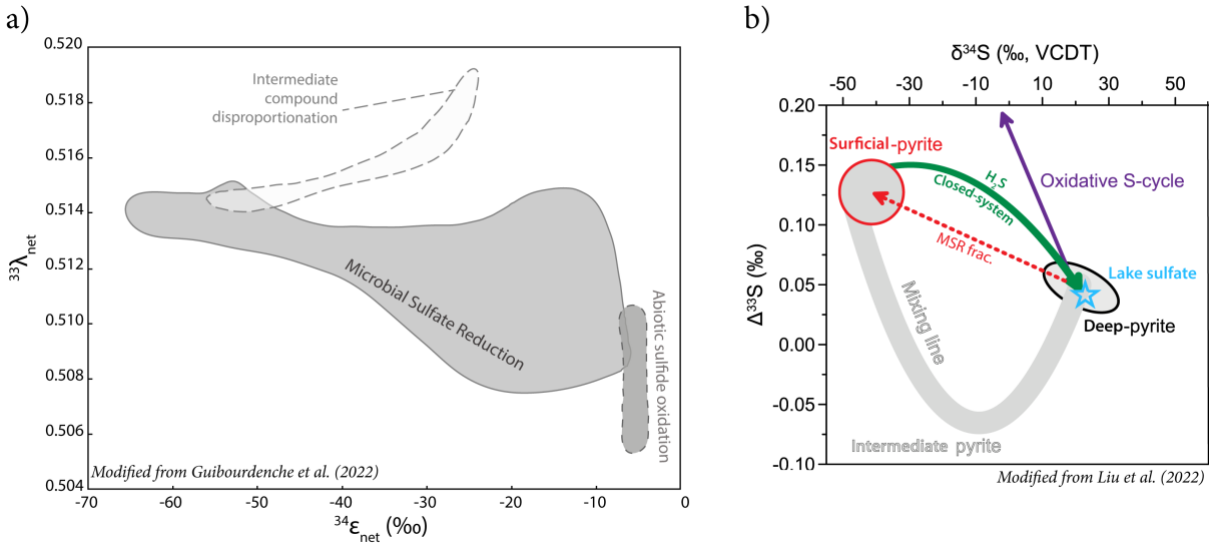

Figure 7.5 : classical diagnostic graphics using the $^{33}\lambda$-$^{34}\varepsilon$ parameters (a, modified from Guibourdenche *et al.*, 2022), and $\Delta^{33}S'$-$\delta^{34}S$ parameters (b, modified from Liu *et al.*, 2022).

Figure 7.5b, shows the possible reactions occurring in natural "closed-system" sediments and their respective $\Delta^{33}S$–$\delta^{34}S$ trends. These authors propose that early pyrite formed near the water-sediment interface will record MSR-derived signatures (in red), while those forming below the zone of sulfate depletion will record the sulfate source composition (in black), following the Rayleigh distillation trend depicted by pooled H_2S in a closed-system (in green; *cf.* Fig. 7.4b). Pyrite precipitating after the diffusion and mixing of surficial and deep H_2S would plot on a mixing line as shown in grey. Oxidative S-cycling (including oxidation + disproportionation) is suggested to harbor a negative $\Delta^{33}S$–$\delta^{34}S$ trend.

7.2. Results for Alchichica sediments

In Alchichica, the total porewater dissolved sulfide concentrations rapidly increase from 0.03 to 0.65 mM between the water-sediment interface and a depth of 17.5 cm (Fig. 7.6). They reach a local minimum from 30 to 45 cm, before reaching maximum values at 50 cm (1.08 mM). Near-maximum concentrations are met again at the bottom of the core (Fig. 7.6). During the extraction protocol, most of the dissolved sulfide was released after the addition of the reduced Cr-solution (chromium-reducible-sulfide; CRS), but a little amount was also released after addition of HCl-ethanol (acid-volatile-sulfide; AVS) throughout the core. The AVS concentration was too little to be quantified and separated from the CRS, except in three samples between 37 and 45 cm in depth and notably at 42 cm, where 94% of the dissolved sulfide extracted corresponded to AVS (Fig. 7.6). Sulfate concentrations gradually decrease from 9.9 to 4.1 mM from the water-sediment interface to the bottom core at 83 cm (Fig. 7.6). They show a faster decrease in the first 40 cm of sediments than below (1.1 *vs.* 0.4 mM/10cm).

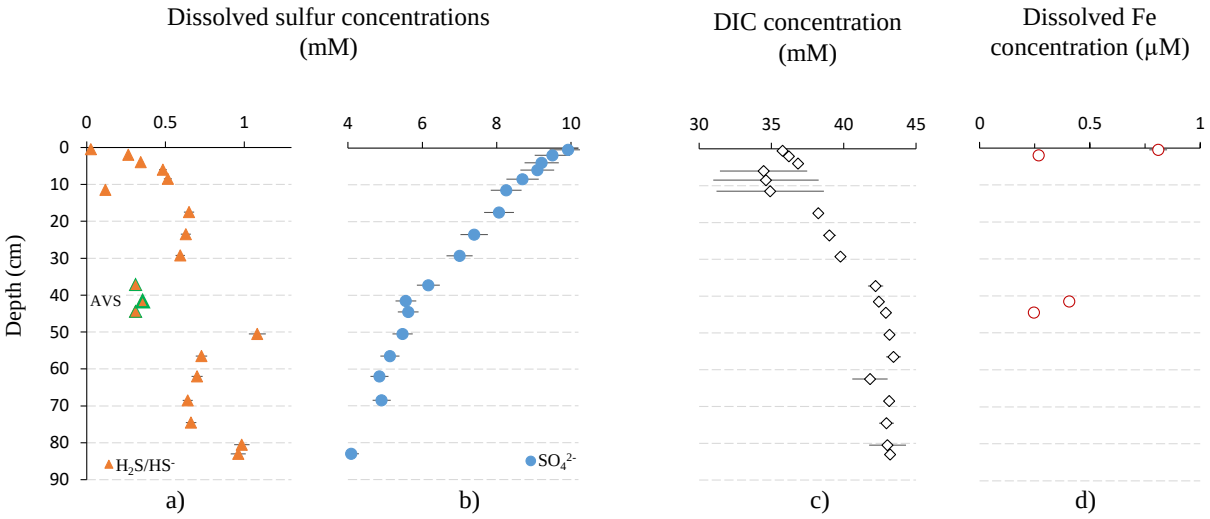

Figure 7.6: Concentration depth profile for dissolved sulfides (H_2S/HS^-), sulfates (SO_4^{2-}), inorganic carbon (DIC) and Fe in the porewater of Alchichica sediments in mmol.L^{-1}. 5% error bars are represented for each profile. Samples with enough acid volatile sulfides (AVS) for quantification are shown with the green triangles. Notably at 42 cm, 94% of the extracted dissolved sulfide corresponded to AVS (~10% for the other two samples).

Bulk pyrite concentrations, as determined by CRS extraction, show a clear increasing trend with depth in the sediment (Fig. 7.7), rising from near 0 values to ~0.8 wt. %. A shift to higher pyrite content can be observed between 40 and 50 cm in depth (maximum of 1.1 wt. % found at 75 cm) (Fig. 7.7). The ratio of CRS-extracted Fe to bulk total Fe content (from ICP-MS measurements) also increases with depth from ~ 0.05 to 0.50 (Fig. 7.7). The bulk Fe:Al molar ratio shows maximum values at the top and bottom of the core (between 0.25 and 0.30), and minimum values of 0.19 at 45 cm in depth, similar in shape to the TOC profile (Fig. 7.7).

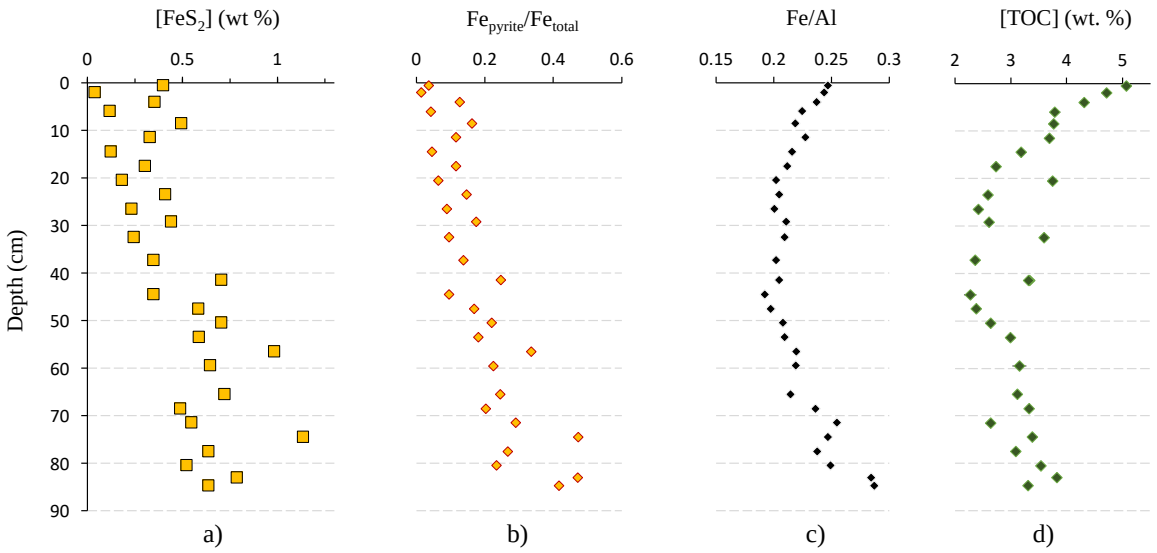

Figure 7.7: Depth profiles for solid sediment concentration of pyrite (a), total organic carbon (d), and ratio of pyrite Fe to total Fe (b) and total Al (c).

Dissolved sulfide $\delta^{34}S$ show a steady increase from ~ -23 to -19 ‰ between 0 and 37 cm in depth, stepping up to ~ -12 ‰ at 42 cm, and then steadily increasing again to reach -1 ‰ at 83 cm in depth (Fig. 7.8). The sulfate $\delta^{34}S_{SO4}$ steadily increases from ~ 22 to 56 ‰ between 0 and 83 cm in depth (Fig. 7.8). The bulk pyrite $\delta^{34}S_{py}$ show less variability, with values mostly comprised between ~ -26 and -22 ‰ except near the water-sediment interface where they reach values between -17 and -15 ‰, and at 50 cm in depth where it rises to -14 ‰ (Fig. 7.8).

Minor S isotope compositions were measured in two pyrite samples (at 4 and 83 cm in depth), one porewater sulfate (at 6 cm in depth), and one lake water sulfate sample (assumed to reflect the sulfate composition at the water-sediment interface). The $\delta^{34}S$, $\Delta^{33}S$ and $\Delta^{36}S$ for these samples are presented in Table 7.1.

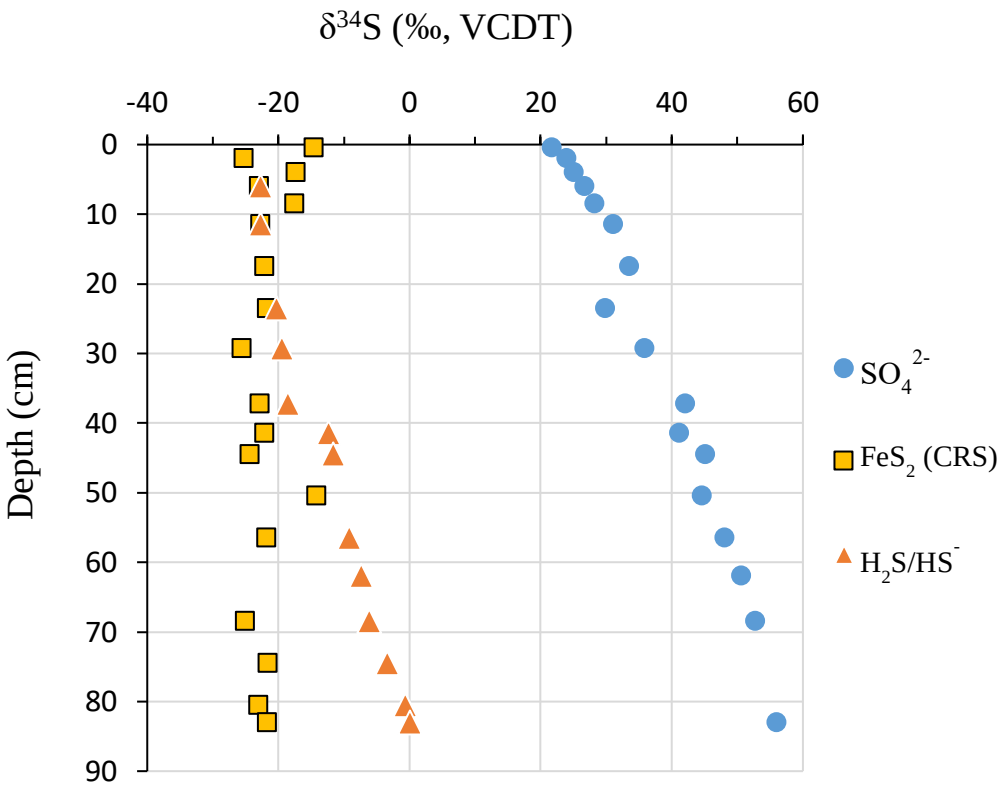

Figure 7.8: Sulfur $\delta^{34}S$ isotopic compositions for dissolved sulfide, sulfate and pyrite in the sediment core of Alchichica. All data were measured for bulk samples, by SO_2 method. 'CRS' stands for 'Chromium-Reducible-Sulfur' and corresponds to the bulk pyrite extraction (see Methods). Dissolved sulfides were fixed on the field with Zn-acetate, and then directly extracted from the solution *via* the CRS protocol. Errors bars from replicate measurements for sulfate and pyrite are smaller than the data points ($1\sigma < 0.4$ and 1.1 ‰, respectively). All dissolved sulfide samples but one were measured only once. The duplicated sample had an external reproducibility of 0.4 ‰; all other dissolved sulfide samples were represented with an error bar of 0.6 ‰ (*i.e.* the average reproducibility for pyrite samples analyzed within the same series).

The pyrite $\delta^{34}S$ determined from SF_6 and SO_2 methods differed on average from 2.2 ‰, whereas the sulfate $\delta^{34}S$ measurements (SF_6/SO_2F_2 *vs.* SO_2, see the method chapter 3) only differed from 0.1 ‰ on average (Table 7.1). The relatively poor reproducibility for $\delta^{34}S_{py}$ likely results from the poor stability of the mass-spectrometer during the series of SO_2 measurements that included these two samples; however, these differences are small compared to the range of variation discussed here (Fig. 7.8). In all plots and calculations featuring minor S isotope data, the $\delta^{34}S$ values from SF_6/SO_2F_2 methods were used.

Table 7.1: Multiple sulfur isotope compositions in the Alchichica water column and sediments.

Sample name	Type/Analysis method	Depth	$\delta^{34}S$	*2σ*	$\Delta^{33}S'$	*2σ*	$\Delta^{36}S'$	*2σ*
			‰ VCDT					
AL19-C2-03	Pyrite / SF_6	4 cm	-20.1	*0.3*	0.086	*0.011*	-0.76	*0.128*
	Pyrite / SO_2		-17.4	*0.1*				
AL19-C2-19	Pyrite / SF_6	83 cm	-23.3	*0.3*	0.18	*0.016*	-1.22	*0.104*
	Pyrite / SO_2		-21.7	*0.4*				
AL19-40m	Lake water / SF_6	40 m	18.90	*0.01*	0.013	*0.017*	-0.66	*0.18*
	Lake water / SO_2		18.95	*0.11*				
AL19-C2-04	Pore water / SO_2F_2	6 cm	26.8	*0.5*	0.030	*0.050*	*ND.*	
	Pore water / SO_2		26.7	*0.2*				

7.3. Discussion

7.3.1. An overall signature of microbial sulfate reduction

Several geochemical parameters evidence the action of microbial sulfate reduction (MSR) in the sediments of Lake Alchichica, starting with the decrease of dissolved sulfate (SO_4^{2-}), and the increase of dissolved sulfide (H_2S/HS^-) and inorganic carbon (DIC) concentrations with depth (Fig. 7.6 and 7.2a). The tight correlation between the decrease of $\delta^{13}C_{DIC}$ and the sulfate concentration (Fig. 7.9) shows that the remineralization of organic matter is strongly related to MSR (Chapter 6). Major sulfur isotopes (^{32}S, ^{34}S) also evidence this process with $\delta^{34}S_{H2S}$ being lower than $\delta^{34}S_{SO4}$ by approximately 55 ‰ (Fig. 7.8; and toolbox).

The near parallel increase of $\delta^{34}S_{H2S}$ and $\delta^{34}S_{SO4}$ suggest an evolution through a Rayleigh-type distillation in sediment porewaters approaching a closed-system. This "pooling" effect (*i.e.* distillation) is possible if the lake- and pore-water sulfate pools are disconnected, either physically (locked porosity), and/or because the rate of sulfate consumption (*e.g. via* MSR) overcomes the rate of sulfate replenishment by diffusion (*e.g.* Fike *et al.*, 2015; Pasquier *et al.*, 2017; Guibourdenche *et al.*, 2022). In the case of Lake Alchichica, pooling is favored by the

absence of bioturbation in anoxic bottom waters, and the absence of any strong currents that could physically rework the sedimentary pile. A closed-system distillation is further supported by the very good correlation observed between $\delta^{34}S_{SO4}$ and the fraction of residual sulfate in the porewater (Fig. 7.10b, $R^2 = 0.96$; Gomes and Hurtgen, 2013).

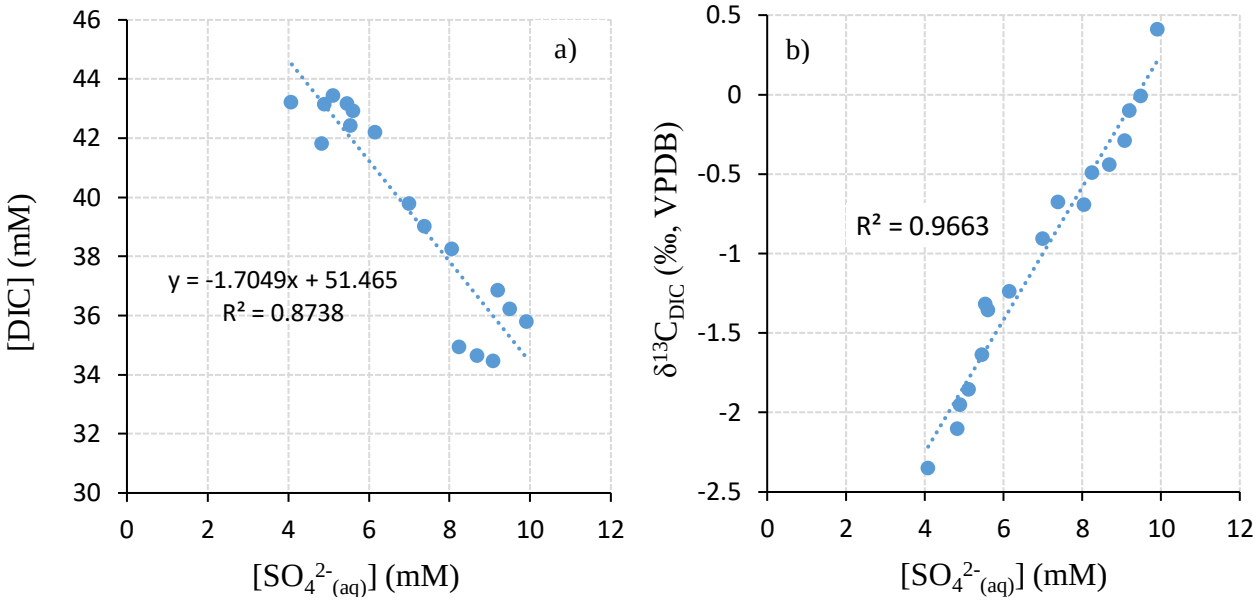

Figure 7.9 : Correlations between the sulfate concentration and DIC concentration (a) and DIC isotopic composition (b).

A Rayleigh distillation equation enables a very good fit of the $\delta^{34}S_{SO4}$ data, and estimates a $^{34}\varepsilon_{MSR}$ between -42 and -45 ‰ (Fig. 7.10a). These values are well within the range of MSR fractionations predicted theoretically (*e.g.* Brunner and Bernasconi, 2005; Johnston *et al.*, 2007), found experimentally (*e.g.* Sim *et al.*, 2011b; Leavitt *et al.*, 2013), and observed in natural environments (*e.g.* Canfield *et al.*, 2010; Zerkle *et al.*, 2010). The modeled $\delta^{34}S$ for pooled sulfides, however, largely deviates from the measured $\delta^{34}S_{H2S}$ after 40 cm in depth (Fig. 7.10). Furthermore, neither the modeled or measured $\delta^{34}S_{H2S}$ match the isotopic composition of pyrite minerals after a depth of ~30 cm (Fig. 7.10), although pyrite precipitation induces only a small fractionation (< 4 ‰; Eldridge *et al.*, 2021). Sampling-related biases, such as partial oxidation of dissolved sulfide to sulfates can be excluded here, as they would impart a depth-independent isotopic offset for dissolved sulfides, and would deviate the $\delta^{34}S_{SO4}$ in the sulfide-rich bottom porewaters, whereas the fit between measured- and modeled-$\delta^{34}S_{SO4}$ is consistent with depth.

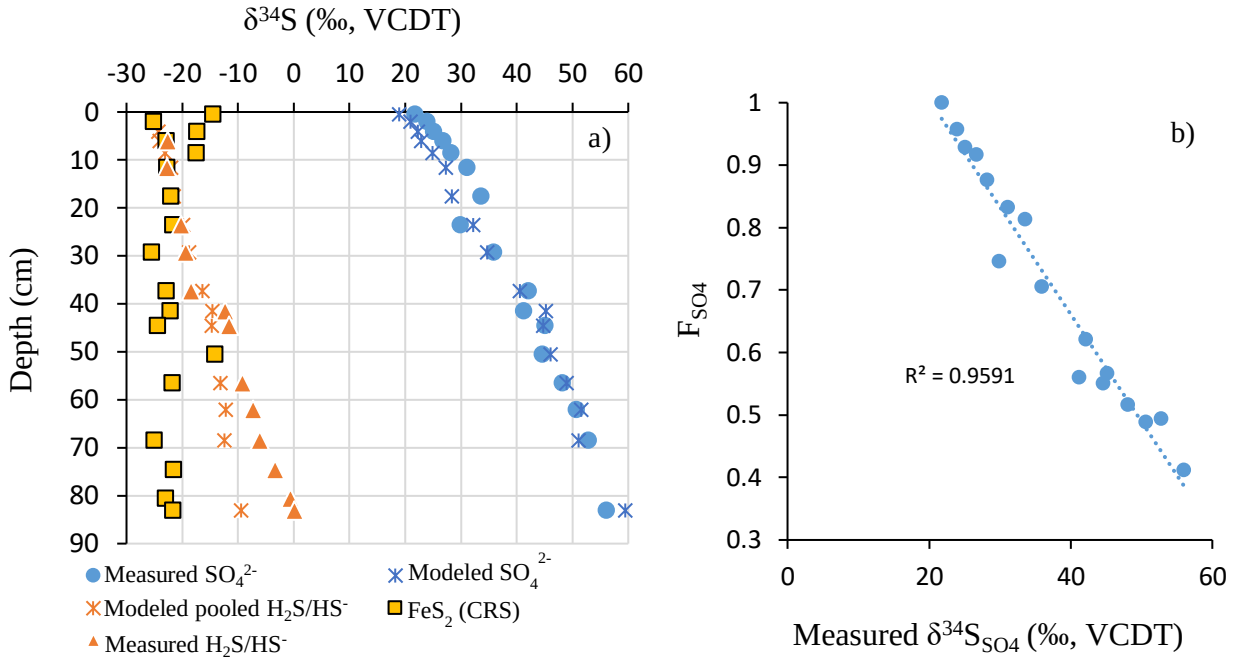

Figure 7.10 : Depth profiles of dissolved sulfide, sulfate and pyrite $\delta^{34}S$ isotopic compositions measured and modeled by Rayleigh distillation equation in the sediments of Alchichica. (a) Modeled sulfate and sulfide correspond to the residual reactant pool and cumulated/pooled sulfide product, respectively, and are computed here with a $^{34}\varepsilon$ set to -44 ‰. (b) Correlation between the residual fraction of sulfate in the porewater (F_{SO4}) and the measured $\delta^{34}S_{SO4}$. The F_{SO4} was calculated from the porewater data as $[SO_4]_i$ at each depth 'i' divided by the [SO4] at the water-sediment interface.

Similar ^{34}S-enrichment of H_2S/HS^- compared with coeval pyrite is a common feature in marine sediments (Raven *et al.*, 2016 and references therein), and was sometimes interpreted to reflect an early pyrite formation before further evolution of the dissolved sulfide pool with depth (*e.g.* Jørgensen, 1979; Liu *et al.*, 2020a; Masterson *et al.*, 2022). Here, the increase of total pyrite content with depth and Fe_{py}/Fe_{tot} ratio with depth suggest that pyrite formed throughout the core, and not only at the water-sediment interface (Fig. 7.7; Gomes and Hurtgen, 2013). The very distinct $\Delta^{33}S$' signatures recorded by pyrite at the top and bottom of the core also support that conclusion (Table 7.1; Fig. 7.7).

Offsets between $\delta^{34}S_{FeS2}$ and $\delta^{34}S_{H2S}$ have also been explained by S reoxidation/disproportionation cycling (discussed below), or by the influence of organic S (OS) (Raven *et al.*, 2016 and references therein). In this latter hypothesis, pyrite precipitates in biofilms near the production of ^{34}S-depleted MSR sulfide, whereas remaining sulfides diffusing away in the porewater can exchange with ^{34}S-enriched organic matter (Raven *et al.*, 2016). By

contrast with Raven *et al.* (2016), who observe different H_2S and pyrite compositions throughout their entire cores, some of the most surficial pyrites in Alchichica have a $\delta^{34}S$ equivalent to the H_2S/HS^- pool, showing that they precipitated at equilibrium with it at least in the surficial sediments. The deviation between the measured $\delta^{34}S_{FeS2}$ and $\delta^{34}S_{H2S}$, as well as their respective deviation from values predicted by Rayleigh distillation, start at depths where the TOC content is minimum (Figs. 7.7 and 7.10), which reduces the chances for possible isotopic exchange between organic S and dissolved sulfides. Thus, while it would be interesting to characterize the OS reservoir, especially for multi-S isotope signatures (Jovovic *et al.*, 2020), OS is not further considered as a primary driver of the trends reported in Alchichica.

The system may also be out of steady state, and dissolved H_2S/HS^- isotopic signatures do not reflect the long-term pyrite record (Masterson *et al.*, 2022). This possibility is hard to test. Nonetheless, it would not explain the offset measured between some of the very shallow pyrites and aqueous sulfides (*i.e.* those which formed very recently), nor the deviation between modeled and measured $\delta^{34}S_{H2S}$. Moreover, at the lake's time scale, the core's bottom age is relatively recent (< 350 years), which makes it unlikely that pyrite precipitation and H_2S production are significantly uncorrelated in time.

Therefore, the above observations about Alchichica sediments suggest either that: (i) the fractionations induced by MSR vary with depth, or (ii) other S-metabolisms and processes contribute in shaping the isotopic compositions of dissolved and mineral sulfides. Minor S isotopes can help differentiate these effects and I discuss these possibilities below. However, because previous studies have made a case for the relevance of diffusion in porewaters even when closed-system distillation seems to apply (*e.g.* Jørgensen, 1979), I first further discuss and invalidate this hypothesis.

7.3.2. Connected porosity and diffusion effects

Sediment porewaters are subject to mass exchanges, diffusion, and advection, even though their S isotope signatures usually mimic closed-system conditions. Therefore, the intrinsic MSR and other metabolic isotopic fractionations cannot be properly determined by a Rayleigh distillation model, nor by the direct measurement of $\delta^{34}S_{SO4}$ and $\delta^{34}S_{H2S}$ (Jørgensen, 1979; Canfield, 2001; Masterson *et al.*, 2018, 2022). Although the respective diffusion coefficients of H_2S and SO_4^{2-} isotopologues are nearly identical (Bourg, 2008; Donahue *et al.*, 2008a, 2008b),

it was proposed that open system and diffusion of H_2S (upward) and SO_4^{2-} (downward), act to increase the difference between $\delta^{34}S_{SO4}$ and $\delta^{34}S_{H2S}$ compared to a closed system (Jørgensen, 1979, 2021; Donahue *et al.*, 2008a, 2008b). Here, by contrast, a smaller isotopic difference is found between $\delta^{34}S_{SO4}$ and measured $\delta^{34}S_{H2S}$, than between $\delta^{34}S_{SO4}$ and modeled $\delta^{34}S_{H2S}$ (by closed-system equations; Fig. 7.10). Diffusion/advection would also not explain the difference found between solid and aqueous sulfide signatures (Fig. 7.10).

The $\Delta^{33}S$' isotopic signature of pyrite forming at depths between the water-sediment interface, and the depth of SO_4 depletion, should tend towards that of the lake water sulfate (*e.g.* Liu *et al.*, 2021; Fig. 7.5b), similarly to the progressive increase seen in porewater $\delta^{34}S_{H2S}$ (Fig. 7.10). If the system was open (connected porewaters), diffusion would mix surficial and deep aqueous sulfides (Pasquier *et al.*, 2021b; Guibourdenche, 2022), such that pyrites precipitating at intermediate depths would plot on a mixing line between early-formed pyrites and those formed near the SO_4-depletion depth (Fig. 7.5b; Liu *et al.*, 2020b, 2021, 2022). Such mixing lines for Alchichica are shown in Figure 7.11. In Alchichica, the pyrite sampled at 83 cm in depth clearly plots out of such a range (Fig. 7.11).

Therefore, while a quantitative assessment of open-system effects would require a dedicated reactive transport model (Pellerin *et al.*, 2015; Masterson *et al.*, 2018), it can already be assessed that diffusion/advection of S species are not governing the S isotopic profiles here. It should also be noted that such transport models would not be sufficient to detect cryptic sulfur cycling (Jørgensen, 2021). The fact that Alchichica sediment porewaters approach a closed-system, at least with respect to S, is likely favored by relatively fast sedimentation rates (~0.25 $cm.yr^{-1}$), the absence of bioturbation and strong water currents, and an efficient combined sulfate reduction−pyrite precipitation.

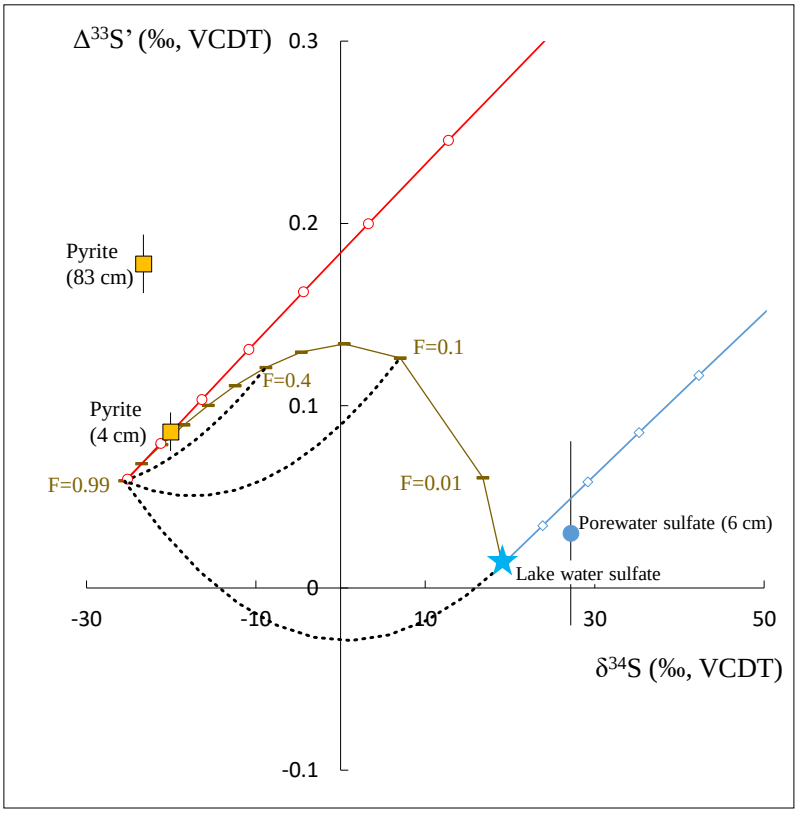

Figure 7.11 : Cross-plot of $\Delta^{33}S'$ *vs.* $\delta^{34}S$ for measured and modeled sulfate and sulfide reservoirs in Alchichica. The red, brown and blue lines represent, the instantaneous product, cumulated product, and residual sulfate reservoirs, respectively, modeled from MSR occurring in a closed-system. The 'F' numbers indicate the fraction of residual sulfate at each dot on these lines. The $^{34}\varepsilon_{H2S\text{-}SO4}$ and $^{33}\lambda_{MSR}$ parameters are set to -44 ‰ and 0.514, respectively. The black dotted lines represent mixing between the sulfide pool formed first (F=0.99), and that formed after different stages of sulfate consumption (F=0.4, F=0.1 and F=0). At 83 cm, 60% of the initial sulfate reservoir has been consumed, such that sulfide/pyrite forming at this depth should plot on the brown line at F=0.4, or on the corresponding mixing line if diffusion and mixing occurred. Errors bars correspond to 2σ uncertainties.

7.3.3. Changing MSR isotopic fractionation with depth

A second possibility for the discrepancy between measured and Rayleigh-modeled $\delta^{34}S_{H2S}$, is that ε_{MSR} changed with depth in the sediments. Indeed, fractionation of major and minor S isotopes by MSR can vary over a wide extent (*cf.* toolbox), and is strongly tied to the sulfate concentration and to the cell-specific sulfate reduction rate (csSRR) – high [SO_4^{2-}], and low csSRR favoring large fractionations (*e.g.* Fike *et al.*, 2015; Bradley *et al.*, 2016).

The csSRR strongly depends on the amount and bioavailability of electron donors (*i.e.* the organic C substrate) (*e.g.* Sim *et al.*, 2011b; Leavitt *et al.*, 2013). Thus it usually decreases (of

up to several orders of magnitude) in the first tens of cm of marine and lacustrine sediments (Holmer and Storkholm, 2001; Pellerin *et al.*, 2015; Raven *et al.*, 2016; Jørgensen, 2021; Treude *et al.*, 2021). Such a drawdown should lead to an increase of the isotopic fractionation (Sim *et al.*, 2011a, 2011b; Leavitt *et al.*, 2013), and thus to $\delta^{34}S_{H2S}$ values becoming lower than what is expected from Rayleigh distillation with fixed $^{34}\varepsilon$. The opposite is observed in Alchichica sediment porewaters with higher measured $\delta^{34}S_{H2S}$ than modeled (Fig. 7.10).

Lower [SO_4^{2-}] towards the bottom core of Alchichica (Fig. 7.6) could decrease the magnitude of $^{34}\varepsilon_{MSR}$ (Bradley *et al.*, 2016), and thus shift the $\delta^{34}S_{H2S}$ to higher values than expected. Similarly to C isotope fractionation generated during organic C fixation (Chapter 4), ε_{MSR} will tend towards zero if the inorganic substrate (*i.e.* sulfate) concentrations are so low that most of the sulfate imported by the cells is converted to sulfide (Bradley *et al.*, 2016; Fig. 8.8 in Chapter 8). Therefore, ε_{MSR} will depend on the porewater [SO_4^{2-}] and on the cells capacity to incorporate SO_4^{2-}, which is notably characterized by the cellular half saturation-constant for sulfate (Ks) (Tarpgaard *et al.*, 2011; Bradley *et al.*, 2016). This Ks parameter is strain-specific and could thus widely vary in the environment. However, the smallest SO_4^{2-} concentration measured in the core (4.1 mM at 83 cm) is higher than the threshold below which the isotopic fractionation expressed by most sulfate reducing strains would start decreasing (Tarpgaard *et al.*, 2011; Bradley *et al.*, 2016). As a comparison, in the four Mexican lakes, smaller S isotope fractionations start to be recorded in pyrites for sulfate concentrations between ~2.5 and 1.2 mM (*i.e.* between Atexcac and La Preciosa sulfate contents; Chapter 8). Finally, a change of ε_{MSR} due to sulfate concentration would, again, not explain why coexisting pyrite and H_2S/HS^- reservoirs differ from each other in Alchichica sediments. This rather suggests that additional biological processes affect the S isotope signatures on top of microbial sulfate reduction (*e.g.* oxidation/disproportionation).

7.3.4. Cryptic reoxidative S cycle

Sulfide oxidation in sediments is ubiquitous, and can represent a non-negligible faith for H_2S produced by MSR (Holmer and Storkholm, 2001; Jørgensen, 2021). Sulfide may be fully oxidized to sulfate, or to S intermediate species used for disproportionation such as sulfite or elemental sulfur (Pellerin *et al.*, 2015; Jørgensen, 2021). These oxidation/disproportionation reactions constitute a cryptic cycle for the major S isotopes record, but result in distinctive ^{33}S–^{32}S–^{34}S patterns (*e.g.* Johnston *et al.*, 2005a; Zerkle *et al.*, 2009, 2016; Eldridge and Farquhar,

2018). Accordingly, minor S isotope signatures have been used to unravel the effects of S reduction, oxidation, and disproportionation in the environment (Canfield *et al.*, 2010; Zerkle *et al.*, 2010; Pellerin *et al.*, 2015; Strauss *et al.*, 2012; Masterson *et al.*, 2018, 2022; Guibourdenche *et al.*, 2022). Yet, a limited number of studies analyzed minor S isotopes in both dissolved and mineral phases (Aoyama *et al.*, 2014; Zerkle *et al.*, 2016; Lin *et al.*, 2017; Liu *et al.*, 2022; Masterson *et al.*, 2022). Here, both pyrite and dissolved sulfates were analyzed for multi-S isotopes in the sediments of Alchichica.

Similarly to $\delta^{34}S$, the sulfate $\Delta^{33}S'$ is well characterized by a Rayleigh distillation (Fig. 7.11), confirming the first-order control of MSR-distillation on the porewater isotopic signatures. The best match to the sulfate sample at 6 cm in depth is found for $^{33}\lambda$ values around 0.512 (Fig. 7.12), which are typical of values reported for MSR fractionation (*cf.* toolbox Fig. 7.5a). However, such $^{33}\lambda$ do not capture the isotopic signatures of the pyrite sample precipitated at the same depth (FeS_2 isotopic composition is considered to equate that of H_2S/HS^- near the water-sediment interface since their $\delta^{34}S$ are close to each other at these depths, and pyrite precipitation induces small fractionations – Eldridge *et al.*, 2021).

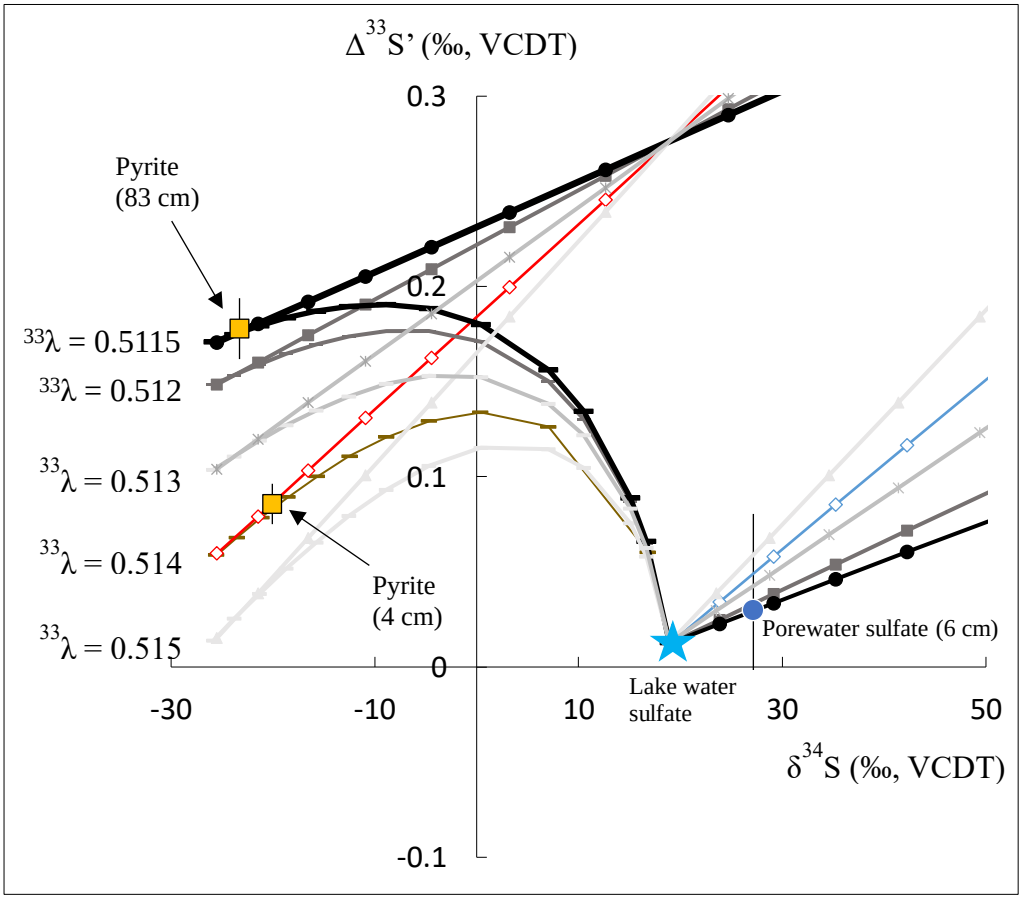

Figure 7.12 : Cross-plot of $\Delta^{33}S'$ *vs.* $\delta^{34}S$ for sulfate and sulfide reservoirs modeled by a Rayleigh distillation process caused by MSR. The trends are plotted using different $^{33}\lambda_{MSR}$ coefficients from 0.5115 to 0.515, and $^{34}\varepsilon_{H2S\text{-}SO4}$ fixed to -44‰. Curved lines model the cumulated sulfide production. Straight lines on the upper left side represent the instantaneous sulfide production, and those on the bottom right side the residual sulfate. $^{33}\lambda$ values between 0.5115 and 0.512 allow the best fit of surficial porewater sulfate compositions. A $^{33}\lambda$ value of 0.514 allows the match of both produced pyrite and residual sulfate compositions in the shallow sediments. A $^{33}\lambda$ value of 0.5115 allows the match of pyrite's isotopic composition at a depth of 83 cm, but only considering a sulfate consumption < 10%, while the sulfate reservoir at this depth is depleted by ~60%. Errors bars correspond to 2σ uncertainties.

In contrast, setting $^{33}\lambda$ to a value of 0.514 allows the 4 cm pyrite sample to plot on the Rayleigh distillation product line, while also being consistent with $\Delta^{33}S_{SO4}$' (within error; Fig. 7.12). Both $^{33}\lambda$ values were estimated using a $^{34}\varepsilon$ of -44 ‰, as determined by the $\delta^{34}S$ patterns (Fig. 7.10). Thus, on a $^{33}\lambda$–$^{34}\varepsilon$ space, the best match for the sulfate data plots near the field of MSR fractionation (Fig. 7.13), whereas the best match for sulfide + sulfate data plots closer to the disproportionation fractionation field (Fig. 7.13). This suggests that the sediments minor S isotope data are influenced by processes other than MSR, possibly involving other S metabolisms. When $^{33}\lambda$ is set to 0.5115, one can notice that the deep pyrite sample would match the MSR Rayleigh distillation if it had precipitated after a 15% depletion of the sulfate reservoir (*i.e.* F=0.85; Fig. 7.12). However, at a depth of 85 cm, the sulfate pool has already been depleted by about 60% (*i.e.* F=0.4; Fig. 7.6), further supporting the hypothesis that another process than MSR is influencing the sulfide pools deep in the core.

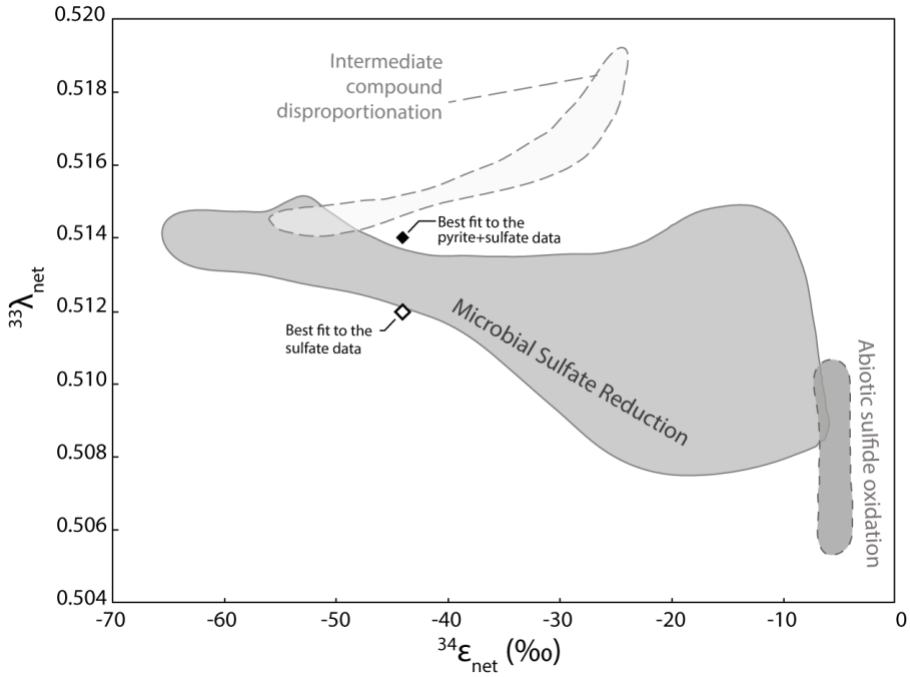

Figure 7.13 : Cross-plot of $^{33}\lambda$ *vs.* $^{34}\varepsilon$ factors showing the diagnostic fields of different S redox changing reactions, and featuring the data from Alchichica sediments. Figure modified from Guibourdenche *et al.* (2022) (see legend of Fig. 7.5 for references to original data). The best fit for the sulfate porewater data ($^{33}\lambda \approx 0.512$, $^{34}\varepsilon \approx -44$ ‰) is consistent with a primary origin from microbial sulfate reduction. The best fit for combined pyrite and sulfate data ($^{33}\lambda \approx 0.514$, $^{34}\varepsilon \approx -44$ ‰) lies in-between the MSR and disproportionation field, suggesting the implication of both processes.

Interestingly, similar negative $\Delta^{33}S–\delta^{34}S$ trends as observed between the shallowest and deepest pyrite in Alchichica (in terms of slope), have previously been interpreted to reflect an oxidative S cycle (Fig. 7.5b; Liu *et al.*, 2020b; 2022). More specifically, these trends were attributed to the oxidation of porewater sulfide to intermediate S species, such as elemental sulfur (S^0) and sulfite (SO_3^{2-}). In oxygen-depleted sediments, sulfide oxidation would be coupled to the reduction of metal oxides (Dos Santos Afonso and Stumm, 1992; Liu *et al.*, 2020b; Jørgensen, 2021) such that for example:

$$3H_2S + 2FeOOH \rightarrow S^0 + 2FeS + 4H_2O \quad (7.8),$$

$$H_2S + 3Fe_2O_3 + 10H^+ \rightarrow SO_3^{2-} + 6H_2O + 6Fe^{2+}_{(aq)} \quad (7.9).$$

The intermediate S species can then be used by disproportionating organisms:

$$4S^0 + 4H_2O \rightarrow 3H_2S + SO_4^{2-} + 2H^+ \quad (7.10), \text{ and}$$

$$4SO_3^{2-} + H^+ \rightarrow HS^- + 3SO_4^{2-} \quad (7.11).$$

At depths where dissolved sulfide and pyrite isotopic compositions start to deviate from each other, a marked decrease of the sulfide concentration can be noticed (between 30 and 50 cm; Fig. 7.6). This is consistent with a sulfide oxidation starting at these depths. It corresponds to the reappearance of measurable dissolved Fe in the porewater, consistently with a reduction and dissolution of Fe-(oxy)hydroxide phases (Fig. 7.6; equation 7.9). The same depth horizon is characterized by the slowdown of sulfate concentration decrease (Fig. 7.6), either evidencing a slower SRR, or the reoxidation of sulfide to sulfate. Just below, at 50 cm in depth, the highest H_2S/HS^- concentrations measured in the core match the maximum $\delta^{34}S_{py}$; at this depth, $\delta^{34}S_{py}$ approaches the value of $\delta^{34}S_{H2S}$ (Figs. 7.6 and 7.10). It implies that a significant sulfide production can trigger the precipitation of pyrite recording the porewater isotopic composition, while the oxidative sulfide-cycling above and below (as evidenced by lower H_2S/HS^- concentrations) shift the $\delta^{34}S_{py}$ to lower values (Fig. 7.10). The isotopic fractionations linked to the oxidation and disproportionation reactions are summarized in Table 7.2, and discussed below.

Table 7.2: sulfur fractionation factors considered in the conceptual model (at ambient temperatures).

Process	$^{34}\varepsilon$ (‰)	$^{33}\lambda$	Reference	Comments
Abiotic oxidation H_2S/HS^- to $S_2O_3^{2-}$, SO_3^{2-},SO_4^{2-}	- 5.8	0.508	Eldrige and Farquhar (2018)	Oxidation by metal oxides was not determined but is considered to have similar effects (Pellerin *et al.*, 2015; Guibourdenche, 2022). Inoculation with dissolved Fe provided similar results.
Chemolithotrophic oxidation H_2S to SO_4^{2-}	-4	0.513	Zerkle *et al.* (2016)	The λ value is associated to a large uncertainty
Disproportionation S^0 to H_2S	-6.2	0.517	Johnston *et al.* (2005a)	Original data are from Johnston *et al.*, but numerical values are adjusted to the respective reactions stoichiometry, as used by Pellerin *et al.* (2015).
Disproportionation S^0 to SO_4^{2-}	18.5	0.52		
Disproportionation SO_3^{2-} to H_2S	-45.2	0.512		
Disproportionation SO_3^{2-} to SO_4^{2-}	10	0.528		

To date, the most thoroughly characterized pathways for pyrite precipitation involve the reaction of Fe monosulfide with H_2S ("H_2S pathway") or polysulfide species ("polysulfide pathway") (Liu *et al.*, 2020a and references therein). It has been proposed that the polysulfide pathway produces a pyrite isotopic composition dominated by that of the polysulfide species (Liu *et al.*, 2020a). The co-occurrence of S^0 with free sulfide favors the formation of polysulfide species ($xS^0 + HS^- \rightarrow H^+ + S_x^{2-}$), leading to rapid pyrite formation *via* the polysulfide pathway (Yücel *et al.*, 2010; Liu *et al.*, 2020b), which is fostered at high pH such as in the sediments studied (Liu *et al.*, 2020a):

$$FeS + S_x^{2-} \rightarrow FeS_2 + S_{x-1}^{2-} \quad (7.12).$$

Therefore, the precipitation of pyrite at depths lower than ~30 cm in Alchichica sediments likely occurs after the S it incorporates has been cycled through multiple steps of oxidation, disproportionation, and possibly reduction, following equations like those from (7.8) to (7.12).

Although the presence of important AVS in the dissolved sulfide fraction is suggestive of S redox reaction taking place near the 40 cm sediment horizon more S speciation data in the porewater and sediments of Alchichica is yet required to confirm this scenario (notably targeting S^0 and polysulfide species and directly). Besides, the exact isotopic effects of disproportioning organisms have been characterized in limited amounts (Johnston *et al.*, 2005a), and a better quantification of these effects through reactive transport modeling remains to be completed (*e.g.* Pellerin *et al.*, 2015; Masterson *et al.*, 2018; 2022). Nevertheless, a conceptual model based on a cryptic S cycle can be proposed at first, to reconcile the H_2S/HS^- and pyrite isotopic records. This model is presented in the following section and in Figure 7.14.

7.3.5. Conceptual model for S isotopic signals in the sediments of Alchichica

Microbial sulfate reduction starts to proceed already in the shallowest sediment layers due to the anoxic bottom waters. The balance of sulfate reduction and sedimentation rates enables the disconnection of the porewater from the lake water (diffusion is not excluded but limited). Hence, both sulfate and dissolved sulfide pools become ^{34}S-enriched with depth, following a Rayleigh-type distillation process (*cf.* toolbox, and blue and red lines in Fig. 7.14). Down to ~25 cm in depth, pyrites record an isotopic composition close to that of the dissolved H_2S/HS^-, and therefore mainly record the MSR signature. At this depth, the sulfate reservoir has diminished by about 25% (*i.e.* F=0.75). Below, anoxic sulfide oxidation takes place (notably by reacting with Fe-oxides) and produces intermediate S species (*e.g.* S^0, SO_3^{2-}) with slightly more negative $\delta^{34}S$ and more positive $\Delta^{33}S$' signatures (Fig. 7.14; Table 7.2). Sulfides could also potentially be oxidized by chemolithotrophs, whose associated fractionations go in similar directions than the abiotic oxidation (*i.e.* small negative $^{34}\varepsilon$, and $^{33}\lambda < 0.515$; Table 7.2). However, the effects of these organisms are still poorly constrained, with large uncertainties for minor S isotopes (Zerkle *et al.*, 2016).

Disproportionation of elemental sulfur, with small negative $^{34}\varepsilon_{S0\text{-}H2S}$, and $^{33}\lambda_{S0\text{-}H2S} > 0.515$ (Table 7.2; Pellerin *et al.*, 2015), produces sulfide with slightly more negative $\Delta^{33}S$' and $\delta^{34}S$ values; in parallel, produced sulfate inherits much more positive $\Delta^{33}S$' and $\delta^{34}S$ signatures (Canfield and Thamdrup, 1994; Johnston *et al.*, 2005a). Repeated oxidation/disproportionation cycles would quickly reach more negative $\delta^{34}S$ for pyrite (Fike *et al.*, 2015), and more positive $\Delta^{33}S$' (Fig. 7.14). Disproportionation of sulfite with very negative $^{34}\varepsilon_{S0\text{-}SO3}$ and $^{33}\lambda_{S0\text{-}SO3} < 0.515$ (Table 7.2) would produce dissolved sulfide with high $\Delta^{33}S$' signatures in a more straightforward way. Most interestingly, a microbial family typically performing S oxidation (Comamonadaceae) was identified, although in small proportions, precisely at the depth where AVS phases were retrieved and reoxidative S cycling was suggested to start (37.5 cm; ANR-Microbialite, unpublished data). This microbial diversity should be further explored based on available metagenomic data in the future, and possibly combined with laboratory determination of the isotopic fractionation produced by these organisms.

In the end, the proposed scenario results in the production of pyrite with more negative $\delta^{34}S$ and more positive $\Delta^{33}S$' than what is produced by microbial sulfate reduction (Fig. 7.14). Importantly however, these isotopic compositions could also be produced by (and thus

interpreted as) MSR occurring in a sulfate-replete open-system, with a $^{33}\lambda$ of ~0.5115 (*cf.* Fig. 7.12). Previous modeling of $^{33}\lambda_{net}$–$^{34}\varepsilon_{net}$ fractionation parameters suggested that oxidation/disproportionation cycling would be difficult to distinguish from sole MSR fractionation in the case of net $^{34}\varepsilon$ values between -70 and -40 ‰ (Pellerin *et al.*, 2015). Accordingly, the net $^{33}\lambda$ determined for Alchichica sediments (*i.e.* 0.514, with $^{34}\varepsilon_{Net} \approx$ -44 ‰) is near the higher end of $^{33}\lambda_{MSR}$ values (Leavitt *et al.*, 2013; Fig. 7.15), and thus not easily distinguishable from a MSR process (*e.g.* Leavitt *et al.*, 2013). Here, the more likely scenario of cryptic oxidative S cycle is recognized by characterizing both the pyrite, *and* the porewater reservoirs. Thus, this kind of isotopic signatures constitute a potential challenge in interpreting geological samples.

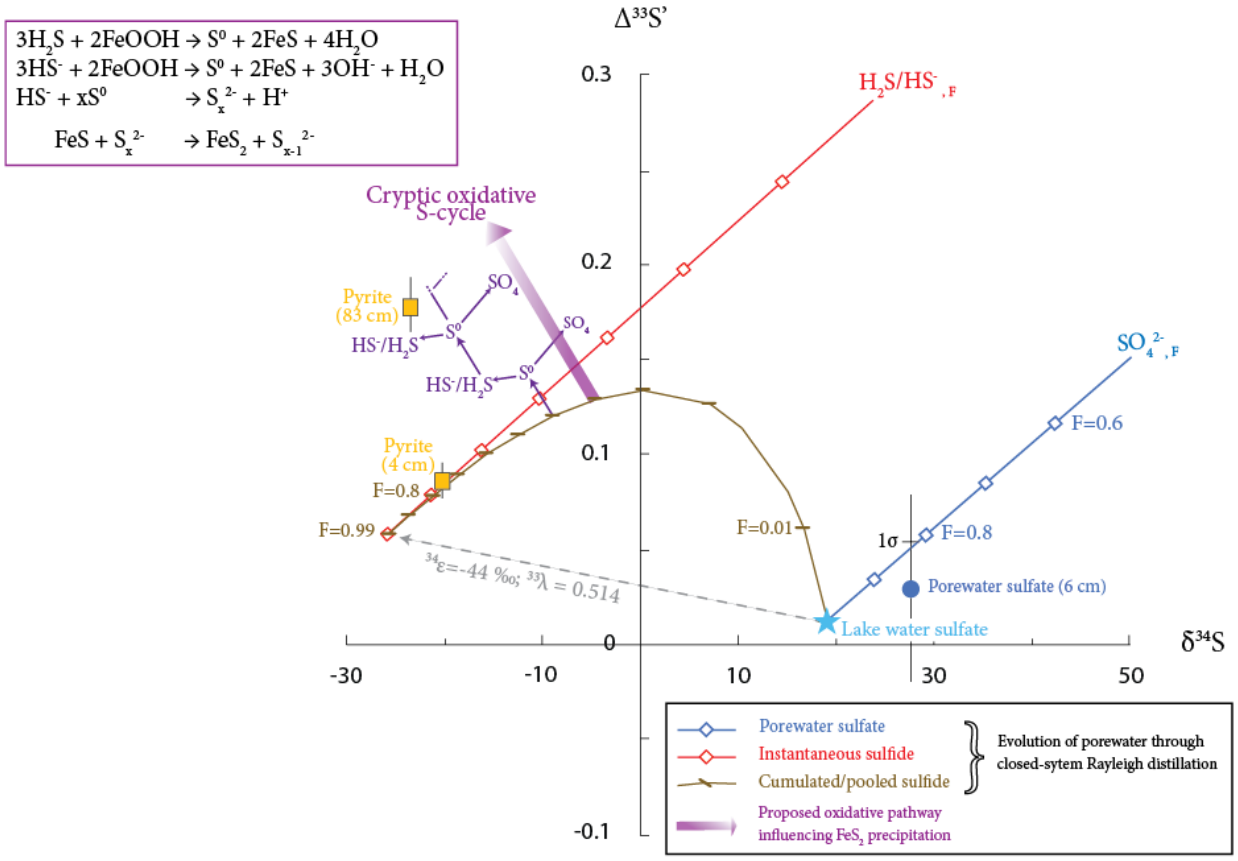

Figure 7.14 : Conceptual model proposing an explanation for the multi-S isotope signatures of dissolved and solid S species in Alchichica sediments. Equations of a Rayleigh distillation process in a closed system (red, blue, and, gold curve) allow to reproduce the porewater sulfate and pyrite isotope records well in the first 25cm of sediments. Below that, cycle of sulfide reoxidation followed by disproportionation (purple arrows) push the elemental S (S^0) and sulfides (HS^-/H_2S) towards lower $\delta^{34}S$ and higher $\Delta^{33}S'$ than if they were only driven by microbial sulfate reduction (MSR). As described in the purple frames, the isotopic effects of these cryptic reactions are eventually recorded in pyrites at depth below ~30 cm. Refer to section 7.3.5 for more details.

7.3.6. Exploring the ^{36}S signatures of Alchichica sediments

To substantiate the previous conclusions, ^{36}S data can also be used. It constitutes an exploratory approach, as ^{36}S data on both pyrite and sulfate from a same environment are even more fragmentary than ^{33}S (Johnston, 2011 and references therein). However, from laboratory experiments, their combination can give further insights in the identification of S based metabolisms (*e.g.* Johnston *et al.*, 2008; Johnston, 2011; Leavitt *et al.*, 2013 Fig. 7.15b).

Similar to the ^{33}S approach, one can fit the surficial pyrite isotopic composition using the Rayleigh distillation equations by adjusting the $^{36}\lambda$ parameter (with $^{33}\lambda$ and $^{34}\varepsilon$ fixed to values determined before). Represented in a $\Delta^{36}S'$–$\Delta^{33}S'$ space, the best fit of the pyrite data is found when $^{36}\lambda$ is set to 1.8995, *i.e.* very close to the equilibrium $^{36}\lambda_{eq}$ (1.9), and $^{33}\lambda$ is set to 0.5137 (Fig. 7.15a). These results perfectly corroborate the inference that disproportionation plays a role in the S cycle of Alchichica sediments (Fig. 7.15). Alike the ^{33}S results, the deep pyrite sample plots out of the range predicted by MSR Rayleigh distillation equations, implying again an active cryptic sulfur cycle at depth in the sediments. It remains to be investigated how the disproportionation-like signatures can imprint the pyrite samples already in the shallow sediments. The role of cryptic S cycling on ^{36}S isotope signal also will have to be further evaluated.

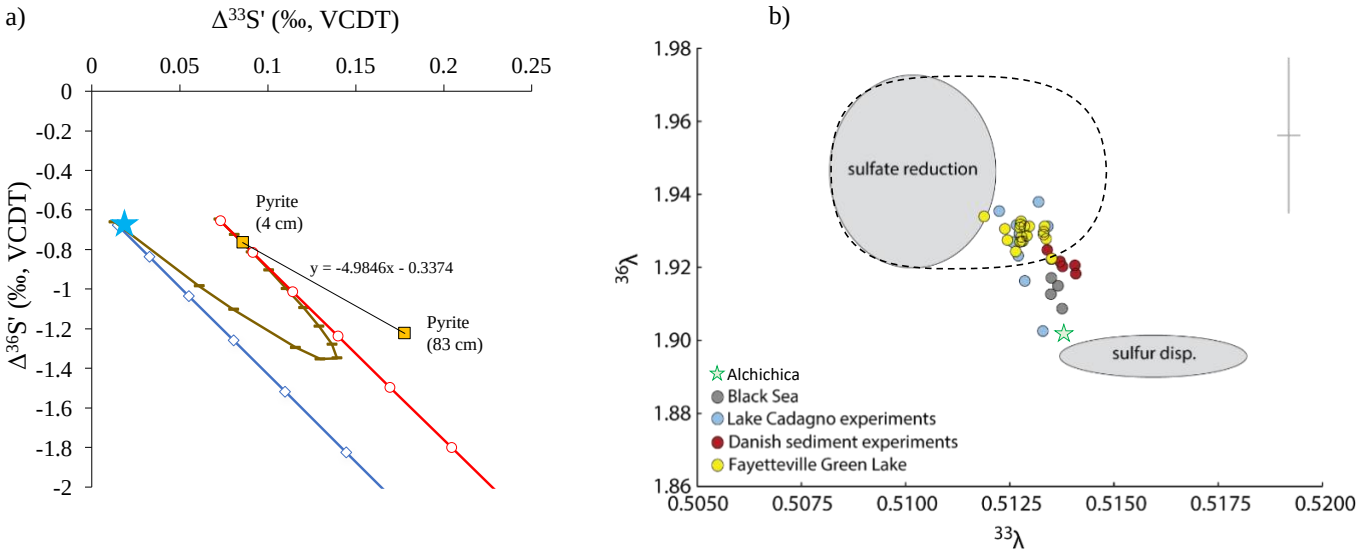

Figure 7.15 : diagnostic figures for the identification of disproportionation based on ^{33}S and ^{36}S data. a) Evolution of $\Delta^{33}S'$ and $\Delta^{36}S'$ signals through closed-system distillation modeled by Rayleigh equations. The blue line represents the residual sulfate pool and the red line represents the instantaneous sulfide produced by MSR (the fraction of residual sulfate decreases following the blue and red line towards the bottom right corner). The gold line represents the composition of the pooled/accumulated sulfide from MSR. The blue star represents the lake sulfate composition. In computing Rayleigh equations, $^{34}\varepsilon$, $^{33}\lambda$ and $^{36}\lambda$ were set to -44 ‰, 0.5137 and 1.8995, respectively, which allows to fit the surficial pyrite composition at 4 cm, but not that at 83 cm. b) The $^{33}\lambda$ and $^{36}\lambda$ used in the Rayleigh modeling are plotted in comparison with previous laboratory experiments and water column results (see Johnston, 2011 for references to the original data). The sulfate reduction field was extended with the dashed line area with $^{33}\lambda$ data from Leavitt *et al.* (2013). The $^{33}\lambda$ and $^{36}\lambda$ combination characteristic of Alchichica sediments is represented by the green star, close to the disproportionation field.

7.4. Conclusion and perspectives

A complex S isotope record has been untangled using multiple S isotope data in dissolved sulfate and solid pyrite reservoirs in Alchichica. This was done in concert with major S isotopes from the dissolved sulfide phases, as well as solid and dissolved major element concentrations. This dataset rules out physical transport (diffusion/advection), and changes in the nature of the MSR reaction as main drivers for the S isotopic variability observed. A clear pooling (or distillation) process is evidenced from porewater analyses. However, although pyrite precipitates throughout the core, it does not imprint the typical isotopic signatures of a distillation process yet evidenced in dissolved sulfides compositions. Besides, the Rayleigh distillation equation fits the dissolved sulfate, but not sulfide data. The best explanation for these inconsistencies involves cryptic oxidation and disproportionation reactions, leading to an increase of $\Delta^{33}S'$ pyrite signatures while driving their $\delta^{34}S$ signal to lower values, rather than increasing them following the distillation process. In the geological record, these low values compared to the sulfates (recorded from the water column), would be interpreted as reflecting an open-system setting with replete sulfate concentrations. Despite small intrinsic $^{34}\varepsilon$ fractionation of oxidation/disproportionation, these reactions have a large influence on both $\delta^{34}S_{py}$ and $\Delta^{33}S_{py}'$, as they both strongly differ from the initial MSR-produced H_2S isotopic compositions. Thus, without the porewater data, pyrite's major and minor S isotope signatures in Alchichica would be interpreted more simply as resulting from a MSR process with a specific set of $^{33}\lambda$ and $^{34}\varepsilon$ parameters. This result highlights the possible misleading conclusions drawn

in the geological record about (i) "closed-systems as open-systems", and (ii) MSR-related signals in lieu of cryptic S cycling in anoxic contexts (including biotic and abiotic reactions). These misleading conclusions are illustrated in Figure 7.16.

Undoubtedly, there would be much insights to gain from narrower analysis of pyrite and sulfate multi-S isotopes in the sediment core of Alchichica. Characterization of the available Ag_2S and $BaSO_4$ material would provide a detailed understanding of the transfer function of minor S isotopes from the porosity of a closed-system to the long-term pyrite record. Besides, it would constitute a pioneering work for ^{36}S isotopes. The comprehension of these processes would also benefit from coupling the existing dataset with sulfate $\delta^{18}O$ (*e.g.* Lin *et al.*, 2017), and organic multiple S isotopes signatures (*e.g.* Raven *et al.*, 2016; Jovovic *et al.*, 2020). Finally, it would be of great interest to further crosscheck these results and interpretations with microbial diversity data.

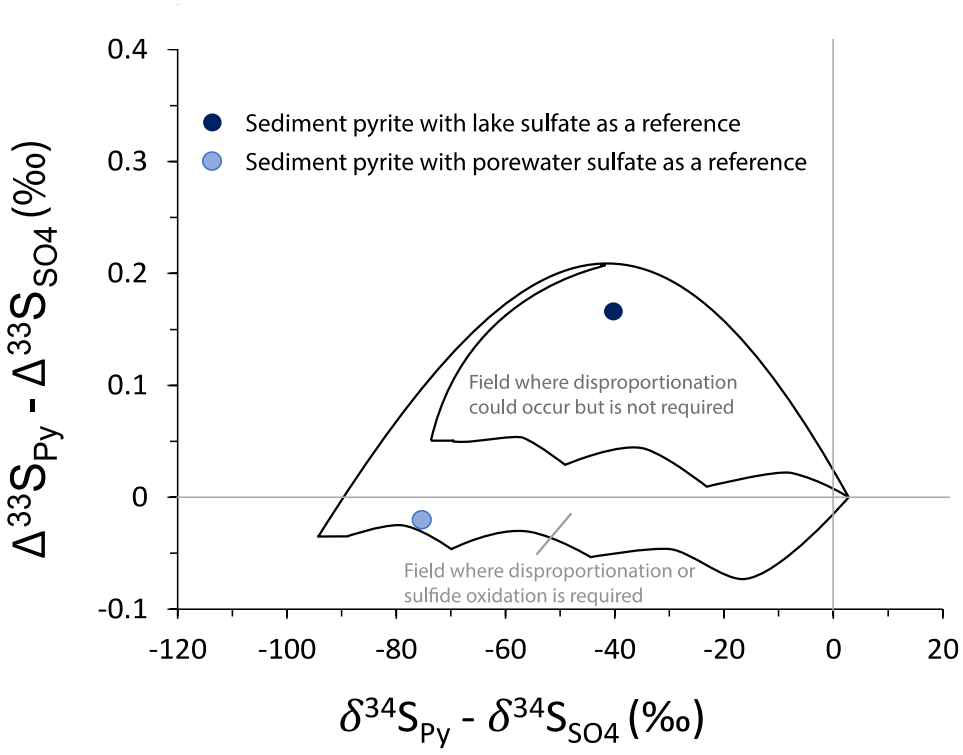

Figure 7.16 : $\Delta^{33}S$-$\delta^{34}S$ cross-plot modified from Lin *et al.* (2017), based on a model of Zhang *et al.* (2015) showing the distinct interpretations that can be drawn based on the choice of sulfate source composition (*i.e.* in a closed or open system). Based on pyrite negative $\delta^{34}S$, the deduction of an open-system setting would lead to use primary lake water sulfate as the source. Thus the pyrite at 83 cm depth would plot in the MSR field with no required disproportionation (dark blue dot). Considering the sulfate composition after 60% of the initial sulfate has been consumed in a closed-system, the 83cm-pyrite would plot in the field where oxidation/disproportionation is required (light blue dot).

Chapter 8

Comparison of the sulfur record in the four Mexican lakes and assessment of the reservoir effect

Table of content

8.1. Introduction

One of the main interests of the study of sedimentary S isotope record has been to reconstruct redox changes at the surface of the Earth. Notably, the offset between sulfate and pyrite S isotopes has frequently been used as a proxy for reconstructing past ocean sulfate concentrations (*e.g.* Algeo *et al.*, 2015), although as shown previously, sedimentary S isotope records can be influenced by a myriad of syn- and post-deposition factors related to environmental and/or biological constraints (Chapter 7). Yet, Gomes and Hurtgen (2013, 2015) suggested that pyrite S isotope signatures in euxinic settings with low sulfate content (< 5 mM) are controlled by a reservoir effect, because smaller sulfate reservoirs are more likely to be fully consumed during early diagenesis, such that the difference between $\delta^{34}S_{py}$ and the initial $\delta^{34}S_{SO4}$ shrinks along. By contrast, they propose that the pyrite isotopic records in high sulfate concentration conditions (> 10 mM) directly provide constraints on the biological and environmental parameters that influence $\delta^{34}S_{py}$.

The four lakes studied exhibit average SO_4^{2-} concentrations of 0.012, 1.2, 2.5, and 12 mM (Fig. 8.1). Considering previous reconstructions of the ocean sulfate content (Canfield and Farquhar, 2009; Algeo *et al.*, 2015), these concentrations are analogous to the ocean sulfate content during the Archean, Neoproterozoic, and early to middle Phanerozoic time periods (Fig. 8.2). They also cover the critical range described by Gomes and Hurtgen (2015) (*i.e.* from ~0 to >10 mM). Thus, studying the S isotope signatures in the sediments of these lakes allows testing the influence of reservoir *versus* local diagenetic effects, in a way integrated over the course of Earth's history (Fig. 8.2). Moreover, comparing records from different locations and contexts, and *via* different proxies, appears as a necessary step for assessing which environmental and biological constraints are the most recurrent and impactful throughout modern natural environments (*e.g.* Gomes and Hurtgen, 2015; Pasquier *et al.*, 2021b; Liu *et al.*, 2022; Marin-Carbonne *et al.*, 2022).

The four Mexican lakes thus provide ideal contexts to assess the effect of different sulfate reservoir sizes on pyrites isotopic signatures, and determine what are the dominant factors influencing the final pyrite record. In this chapter, I first briefly present what are the main S sources and processes that may explain the four lakes current sulfate concentration and isotopic composition. Then, I individually describe the diagenetic processes affecting the pyrites isotopic record in Alberca, La Preciosa, and Atexcac, before comparing the four lakes together

and concluding about the role of sulfate concentration on the pyrite isotopic record *i.e.*, the reservoir effect.

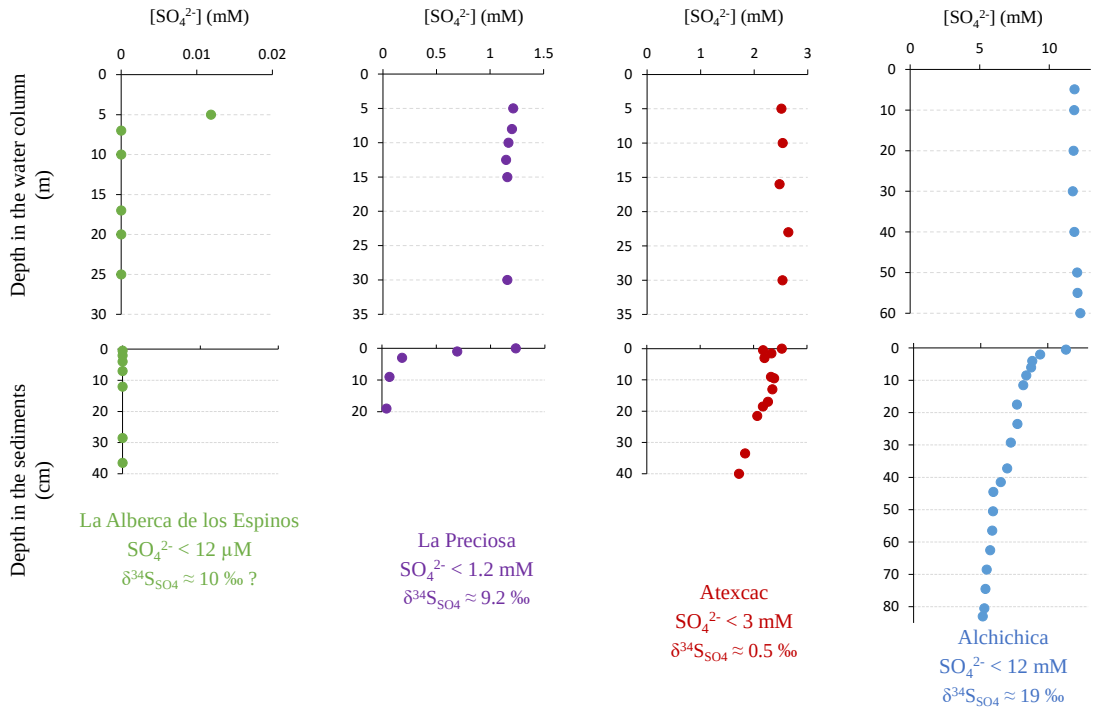

Figure 8.1 : Sulfate concentration with depth in the water column and sediment porewaters of the four lakes. Average values of the sulfate concentration and isotopic composition in each lake water column are indicated at the bottom (standard deviations around these average values are smaller 0.4 mM and 1.5 ‰).

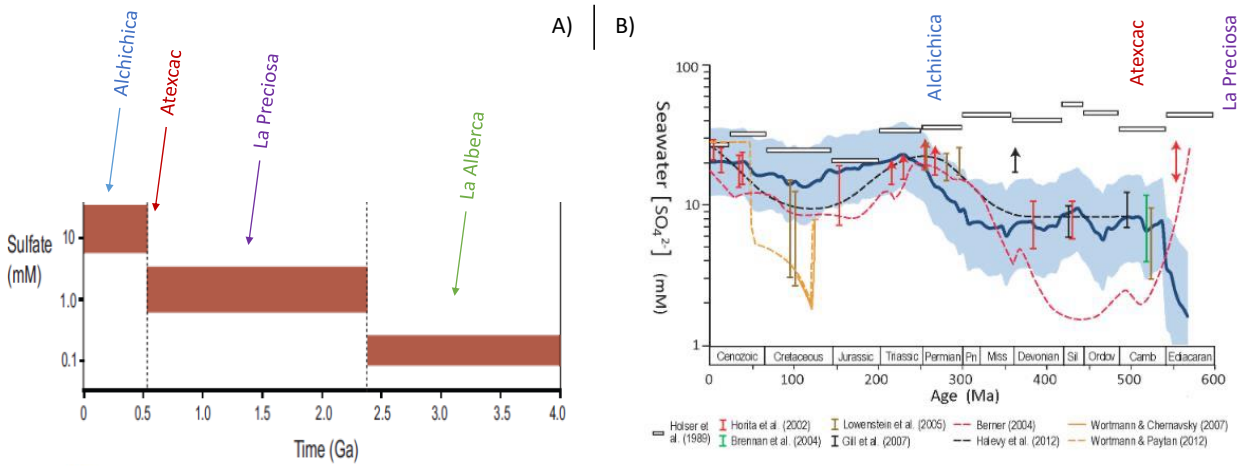

Figure 8.2 : Reconstruction of ocean sulfate concentration throughout time by Canfield and Farquhar (2009) in 'A' and by Algeo *et al.* (2015) for the Phanerozoic in 'B'. The figure in 'A' was built after culture experiments for the Archean, pyrite isotopic record for the Neoproterozoic, and fluid inclusions for the Phanerozoic. The blue line in 'B' is based on modern environments fractionation calibration (*cf.* Figure 8.10 in this chapter). This reconstruction is compared with results from fluid inclusions (Horita *et al., 2002*; Brennan *et al., 2004*; Lowenstrein *et al., 2005*) and modeling studies (references in Algeo *et al.,* 2015). The four Mexican lakes are positioned based on their water column average concentration.

8.2. Results

8.2.1. Alberca de los Espinos

Sulfate concentrations were below detection limit in the sediment porewater, and in the water column except at a 5m depth, where it amounts 12 µM (Fig. 8.3; Table 8.1). In the sediment porewater, total dissolved S – assumed to represent sulfides – varies between 21 and 13 µM (Fig. 8.3). Both dissolved sulfate and sulfide concentrations were too low to be extracted for isotopic analyses. The dissolved Fe concentration in the porewater increases from ~ 60 µM at the water-sediment interface to values between 90 and 150 µM below that (Fig. 8.3).

Bulk pyrite content, as determined by the CRS-extraction, is maximum in the first 7 cm of the sediment (from 0.23 to 0.83 wt. %), and does not exceed 0.07 wt. % below that (Fig. 8.3). It mirrors the ratio of Fe from pyrite over total Fe content (Fe_{py}:Fe_{tot}; Fig 8.3). The pyrite bulk $\delta^{34}S$ composition shows important variability, increasing from 10 ‰ at the water-sediment interface to a maximum of 25 ‰ at 53 cm in depth (Fig. 8.3).

Two pyrites samples were analyzed for multi-S isotopes. The $\delta^{34}S$ results for the SO_2 and SF_6 methods agree within 1 ‰ on average. The $\Delta^{33}S'$ is -0.055 ‰ at the top of the core, and -0.047 ‰ at a 20-cm depth, corresponding to a $\Delta^{36}S'$ of -0.15 and -0.42 ‰, respectively (Table 8.2).

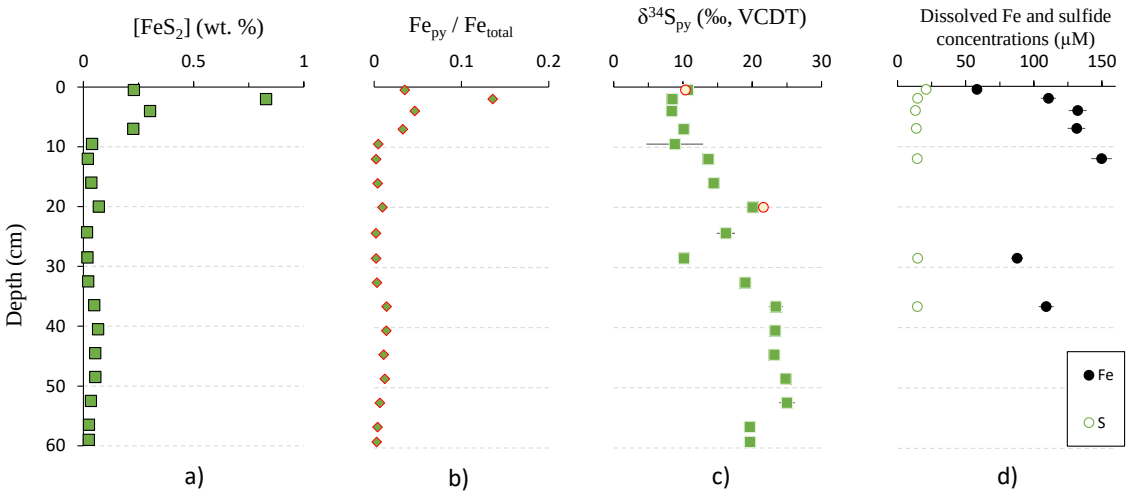

Figure 8.3 : Sulfur and iron characteristic depth profiles in the sediments of Alberca de los Espinos. (a) and (c) Pyrite concentration and isotopic composition determined after the CRS extraction. Error bars represent the external reproducibility, and red circles represent the results from SF_6 measurements. (b) Ratio of Fe from pyrite to total Fe. (d) Dissolved sulfide and iron concentrations in µmol.L^{-1}, at depths where enough porewater was available (5% error bars).

Table 8.1: Sulfate concentration and $\delta^{34}S$ composition in the water column and porewaters of Atexcac, La Preciosa, and Alberca de los Espinos.

Sample name	Type	Depth	$[SO_4^{2-}]$ mM	$\delta^{34}S_{SO4}$ ‰ VCDT	σ
Albesp19-5m	Lake water	5 m	0.012	ND.	
LP19-5m	Lake water	5 m	1.22	ND.	
LP19-8m	Lake water	8 m	1.20	9.2	0.1
LP19-10m	Lake water	10 m	1.17	9.3	0.1
LP19-12.5m	Lake water	12.5 m	1.15	9.2	0.0
LP19-15m	Lake water	15 m	1.16	8.7	0.5
LP19-20m	Lake water	20 m	1.16	9.2	0.1
LP19-30m	Lake water	30 m	1.16	9.0	0.3
ATX19-5m	Lake water	5 m	2.51	ND.	
ATX19-10m	Lake water	10 m	2.53	0.5	0.0
ATX19-16m	Lake water	16 m	2.48	0.6	0.1
ATX19-23m	Lake water	23 m	2.64	3.6	0.1
ATX19-30m	Lake water	30 m	2.53	ND.	
ATX19-C1-surnag	Core Supernatant	0 cm	2.53	0.9	0.2
ATX19-C1-1	Pore water	0.5 cm	2.18	17.4	ND.
ATX19-C1-2	Pore water	1.5 cm	2.33	ND.	
ATX19-C1-3	Pore water	3 cm	2.20	ND.	
ATX19-C1-4	Pore water	8 cm	2.32	ND.	
ATX19-C1-5	Pore water	9.5 cm	2.38	ND.	
ATX19-C1-6	Pore water	13 cm	2.35	ND.	
ATX19-C1-7	Pore water	17 cm	2.27	7.7	ND.
ATX19-C1-8	Pore water	18.5 cm	2.17	ND.	
ATX19-C1-9	Pore water	21.5 cm	2.07	ND.	
ATX19-C1-10	Pore water	33.5 cm	1.84	ND.	
ATX19-C1-11	Pore water	40 cm	1.72	ND.	

Table 8.2. Multiple sulfur isotope results for pyrite and lake water samples in lakes Atexcac, La Preciosa, and Alberca de los Espinos.

Sample name	Type/Analysis method	Depth	$\delta^{34}S$	*2σ*	$\Delta^{33}S'$	*2σ*	$\Delta^{36}S'$	*2σ*
			‰ VCDT					
ATX19-C1-01	Pyrite / SF_6	0.5 cm	-35.9	*0.3*	0.025	*0.017*	-0.25	*0.343*
ATX19-C1-07	Pyrite / SF_6	17 cm	-29.4	*0.3*	0.143	*0.013*	-0.63	*0.150*
ATX19-16m	Lake water / SO_2F_2	16 m	-0.4	*0.02*	0.007	*0.035*	*ND.*	
LP16-C3-7	Pyrite / SF_6	1 cm	-8.2	*0.3*	0.031	*0.015*	-0.62	*0.138*
Albesp19-C3-01	Pyrite / SF_6	0.5 cm	10.4	*0.01*	-0.055	*0.014*	-0.15	*0.202*
Albesp19-C3-S6b	Pyrite / SF_6	20 cm	21.6	*0.01*	-0.047	*0.007*	-0.42	*0.181*

8.2.2. La Preciosa

Sulfate concentrations in the water column average 1.18 ± 0.02 mM (Table 8.1). The small decrease between 8 and 12.5 m (from 1.22 to 1.15 mM) matches the 2019 oxycline depths (Fig. 8.1). The $\delta^{34}S_{SO4}$ averages +9.2 ± 0.2 ‰ throughout the water column (Table 8.1). Sediment results are from samples collected during 2016 field campaign. Only total dissolved S was measured in the porewater; it decreases from 1.2 to 0.04 mM in less than 20 cm (Figs. 8.1, 8.4). This profile likely reflects the sulfate concentration profile. Dissolved Fe was below detection limit throughout the core (Fig. 8.4).

Bulk pyrite content increases from ~ 0.35 wt. % in the first 3 cm to ~ 0.6 wt. % below 9 cm in depth (Fig. 8.4). It mirrors the Fe_{py}:Fe_{tot} ratio (Fig. 8.4). The pyrite $\delta^{34}S$ signatures broadly increase from ~ -8 ‰ to -3 ‰ at 20 cm in depth (Fig. 8.4). The pyrite sample at the water-sediment interface records a $\Delta^{33}S$' of 0.031 ‰ and $\Delta^{36}S$' of -0.62 ‰ (Table 8.2; SF_6 $\delta^{34}S$ agreed with the $\delta^{34}S$ by the SO_2 method within 0.5 ‰).

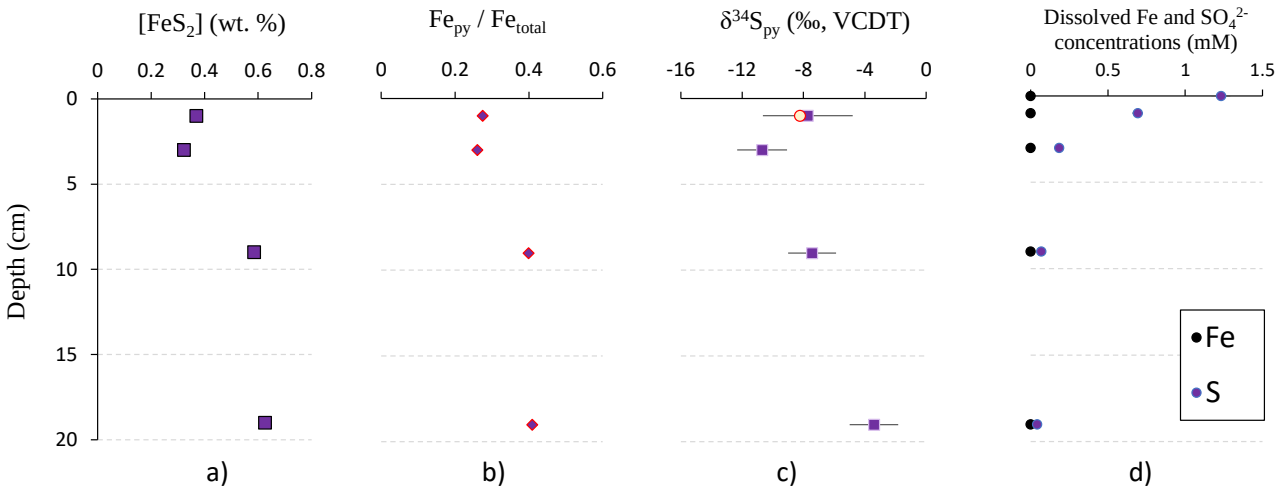

Figure 8.4 : Sulfur and iron characteristic depth profiles in the sediments of La Preciosa. (a) and (c) Pyrite concentration and isotopic composition determined after the CRS extraction. Error bars represent the external reproducibility, and red circles represent the results from SF_6 measurements. (b) Ratio of Fe from pyrite to total Fe. (d) Total dissolved sulfur and iron concentrations in $mmol.L^{-1}$ (5% error bars). Porewater data is from samples collected during the 2016 campaign. Fe was below detection limits. Total S corresponds to the sulfate reservoir.

8.2.3. Atexcac

Sulfate concentrations in the water column average 2.54 ± 0.06 mM. They show a small increase from 2.48 to 2.64 mM at 23m in depth, where anoxygenic autotrophs were described based on investigations of the active C cycle (Havas *et al.*, 2023a; 2023b), suggesting the presence of sulfide oxidizing bacteria. The $\delta^{34}S_{SO4}$ is ~0.5 ‰ above 16 m depth, and increases to 3.6 ‰ at 23 m depth (Table 8.1).

In the porewater, sulfate concentrations remain higher than 2.2 mM above 15 cm in depth, and then decrease to 1.7 mM at 40 cm (Fig. 8.5). Only the core's supernatant solution, and two porewater samples could be extracted for isotopic analyses. Small $BaSO_4$ quantities for these last two samples allowed a single $\delta^{34}S$ measurement, reaching relatively low signal. This signal was sufficient to obtain an approximate $\delta^{34}S$ composition, but there could be a few ‰ scatter with the "real" $\delta^{34}S$ value. The supernatant $\delta^{34}S_{SO4}$ matches the upper water column values (Table 8.2). At 1 and 17 cm depth in the porewater, $\delta^{34}S_{SO4}$ equaled 17.4 and 7.7 ‰, respectively. Dissolved sulfide was only retrievable in the upper 10 cm of the core by the CRS-protocol, which allowed an estimation of their concentrations to values lower than 0.01 mM on average. Dissolved Fe are above detection limit also in the upper 10 cm only (Fig. 8.5).

Bulk pyrite content increases from near 0 at the water-sediment interface to peak to 0.5 wt. % at 17 cm, before decreasing again to 0.3 wt. % at 40 cm (Fig. 8.5). The Fe_{py}:Fe_{tot} ratio is maximum between 15 and 18.5 cm, with values between 0.2 and 0.3 (Fig. 8.5). The pyrite $\delta^{34}S$ is very scattered in the first 3 cm (averaging -33 ± 9 ‰, n=3). It is more stable between 5 and 15 cm in depth (averaging -40 ± 2 ‰, n=5), after which it abruptly increases to -17 ‰ at 21.5 cm. It further increases below 30 cm, reaching -4 ‰ at 40 cm (Fig. 8.5). The TOC profile shows inverse trends, with quite scattered value at the top of the core, and two main decreases after 15 and 30 cm, reaching a low 0.4 wt. % concentration at 40 cm (Fig. 8.5). Two pyrite samples were analyzed for multi-S isotopes (at 0.5 and 17 cm). The $\delta^{34}S$ results for the SO_2 and SF_6 methods differ by 2.5 ‰ on average. The top and middle of the core are characterized by $\Delta^{33}S$' and $\Delta^{36}S$' of 0.025 and 0.143 ‰, and -0.25 and -0.63 ‰, respectively (Table 8.2).

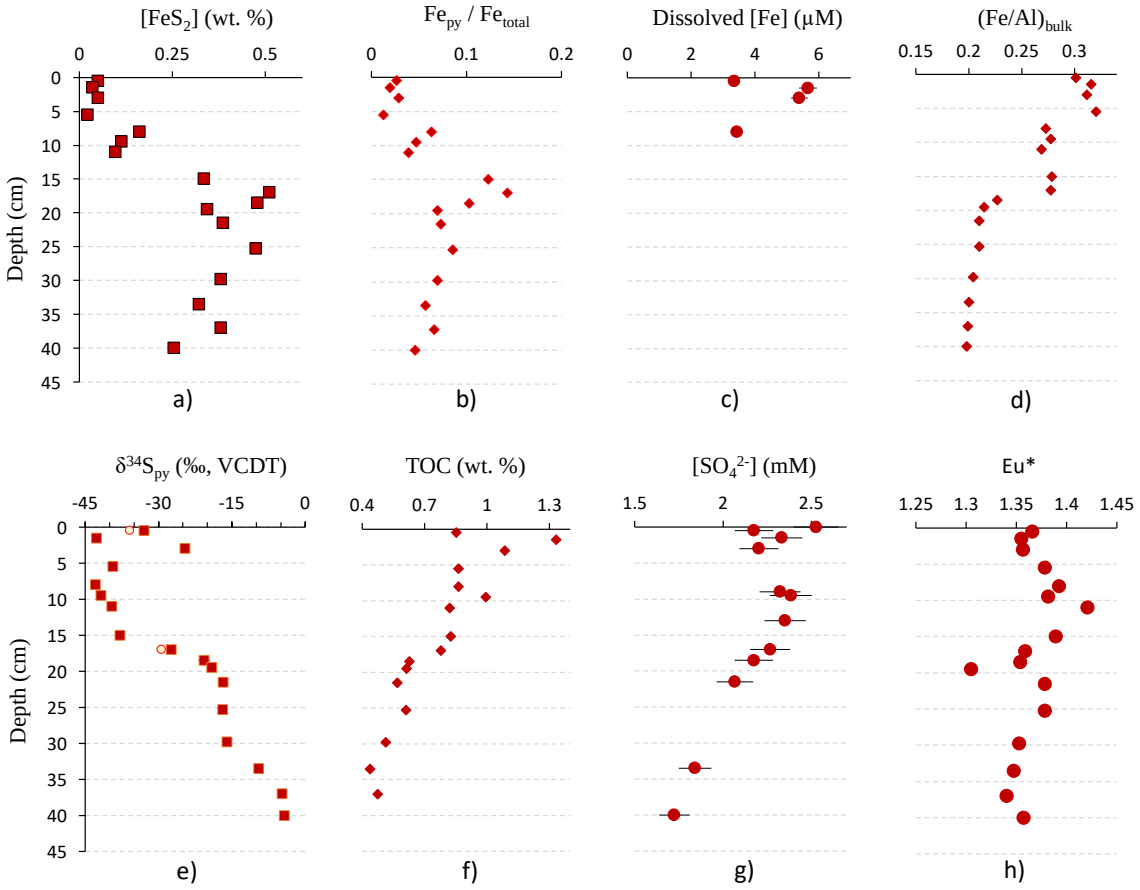

Figure 8.5 : Sulfur, iron, and organic carbon characteristic depth profiles in the sediments of Atexcac. (a) and (e) Pyrite concentration and isotopic composition determined after the CRS extraction. Error bars represent the external reproducibility, and red circles represent the results from SF_6 measurements. (b) Ratio of Fe from pyrite to total Fe. (c) Dissolved iron concentration in µmol.L^{-1} (5% error bars). (d) Bulk Fe to Al molar ratio. (f) Total organic carbon content in weight %. (g) Porewater sulfate concentration in mmol.L^{-1} (5% error bars). (h) Europium anomalies, calculated as Eu/(0.66*Sm+0.33*Tb), all normalized to their Post-Archean Australian shale abundance.

8.3. Discussion

8.3.1. Sulfur sources of the four lakes

8.3.1.1. Isotopic signatures of the potential main S sources

Isotopic signatures of the Cretaceous basement have not been measured in the proximity of the studied lakes. However, corresponding sulfate deposits from northern and southern parts of Mexico were analyzed (mainly gypsum, barite, and celestite), and carry $\delta^{34}S$ signatures

mostly around 16 ‰, although ranging from 6 to 40 ‰ (Kesler and Jones, 1980; Rye *et al.*, 1984). Cretaceous seawater sulfate was found to bear homogeneous $\Delta^{33}S'$ and $\Delta^{36}S'$ signatures of 0.043 ± 0.016, and -0.39 ± 0.15 ‰, respectively (Masterson *et al.*, 2016).

Volcanic S degassing can preserve mantle-like signatures, or depart from it. Mantle sulfur is considered to have $\delta^{34}S$, $\Delta^{33}S$, and $\Delta^{36}S$ close to 0 ‰ (*e.g.* Ueno *et al.*, 2008; Peters *et al.*, 2010; Labidi *et al.*, 2015). Consistently, the bulk isotopic signatures determined from pyrite contained in a volcanic conglomerate from the crater in Alchichica show $\delta^{34}S$ = 0.2 ± 0.25 ‰, $\Delta^{33}S'$ = -0.055 ± 0.016 ‰, and $\Delta^{36}S'$ = -0.01 ± 0.15 ‰.

Volcanic S departing from mantle signatures often reach positive values due to SO_2 disproportionation and precipitation of elemental S and sulfide deeper in the crust, as well as through the incorporation of heavy SO_4^{2-} from subducting material (value as high as +23 ‰; Kusakabe *et al.*, 2000; Varekamp and Kreulen, 2000). Near the studied area, $\delta^{34}S$ signatures between 0 and 8 ‰ were found for SO_2 degassing from Central American volcanoes, in relation with the Cocos plate subduction (de Moor *et al.*, 2022). There is a lack of data for multi-S isotopes in continental settings. I thus consider that the $\Delta^{33}S'$ of this source falls in between -0.05 and 0.05 ‰, *i.e.*, between the detrital pyrite analyzed from Alchichica, and marine-type sulfate compositions).

Oxidation and leaching of detrital pyrites constitute a possible source of S to the studied lakes. I use the conglomerate sample from Alchichica to approximate this source. It would carry the isotopic composition of the conglomerate in case of a full oxidation. If not, isotopic fractionations would be expressed and this detrital source would carry $\delta^{34}S \approx$ -5.6 ‰ and $\Delta^{33}S' \approx$ -0.015 ‰ (calculated from Eldridge and Farquhar, 2018; *cf.* Table 7.2, Chapter 7).

Isotopic signatures of modern atmospheric S compounds are centered around 0 ‰ (for the $\delta^{34}S$ and $\Delta^{3i}S'$ parameters), but can vary over a wide range of negative and positive values (*e.g.* Nielsen, 1974; Au Yang *et al.*, 2018). Thus, they are hardly diagnostic.

8.3.1.2. The origin of S in the four lakes

The four lakes exhibit very diverse sulfate concentrations and isotopic compositions (*e.g.* Fig. 8.1). Sulfate concentrations follow a gradient similar to that of alkalinity (Zeyen *et al.*, 2021; Havas *et al.*, 2023a), with micromolar sulfate levels in Alberca, and millimolar levels in the three lakes from the Serdán-Oriental Basin (SOB). Similarly as for alkalinity, this gradient

can be explained by (i) variable evaporation rates, (ii) differences in the basement rocks, (iii) changes in groundwaters' [SO_4^{2-}] along their flow path (*e.g.* $[SO_4^{2-}]_{GW}$ are higher preceding La Preciosa than Alchichica; Lelli *et al.*, 2021), (iv) different volcanic degassing rates, and (v) different degrees of biological sulfate consumption. In the SOB, the groundwater sulfate should correspond mainly to carbonate-associated sulfates (CAS) from the Cretaceous limestone basement. Evaporites interbedded with these limestone deposits are found throughout Mexico, notably in the basement of volcanoes less than 130 km away from the SOB (Armienta *et al.*, 2008). It is thus not excluded that such evaporites contribute to groundwater sulfate in the SOB (both CAS and evaporite sulfate should have a similar isotopic composition as described in 8.3.1.1). Because of the absence of such Cretaceous basement in the Zacapu basin (*e.g.* Zeyen *et al.*, 2021), the sulfur sources to Lake Alberca are likely restricted to atmospheric and/or volcanic sources, which is consistent with the very low SO_4^{2-} content in this lake.

In Alberca, assuming that sedimentary pyrites isotopic compositions approach that of the lake sulfates throughout the core (section 8.3.2.1), the negative $\Delta^{33}S'$ values confirm the absence of a calcareous/evaporitic basement (Fig. 8.6), and are consistent with a dominant volcanic S source with small negative $\Delta^{33}S'$.

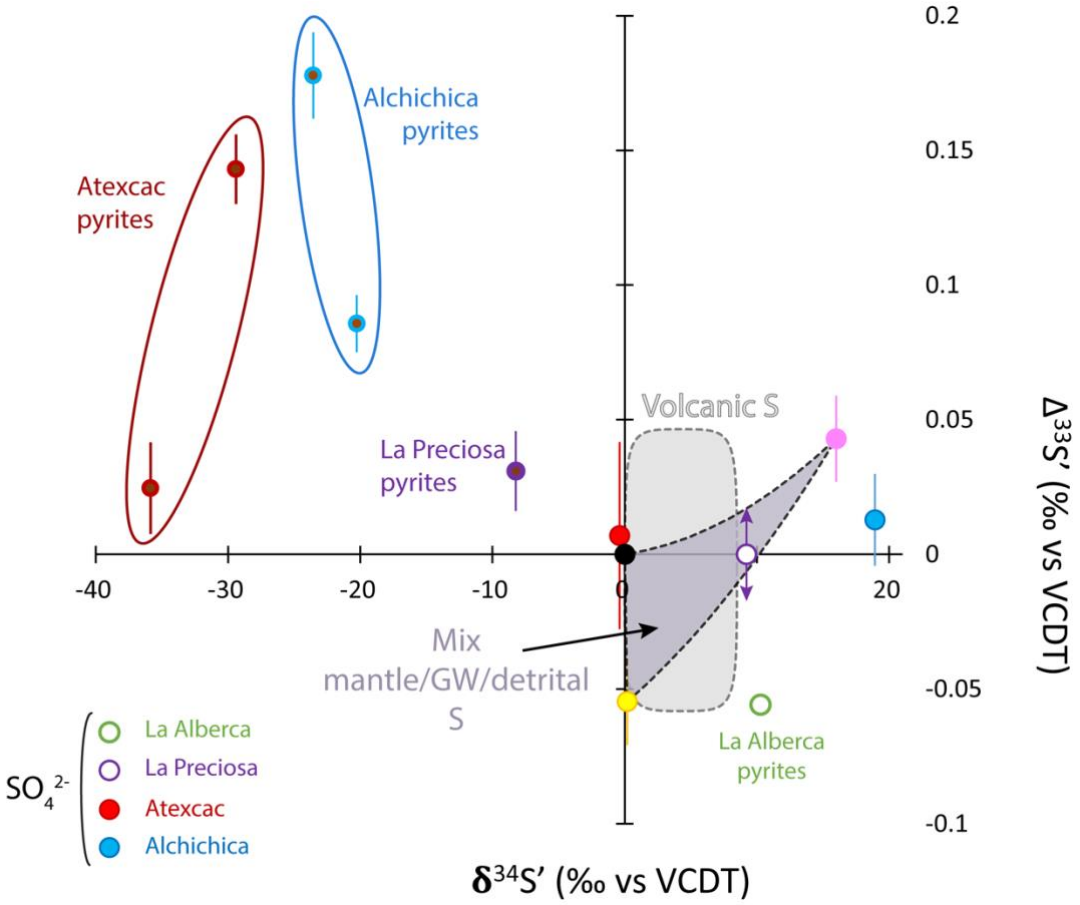

Figure 8.6 : Tracing the S sources to the lakes through $\delta^{34}S$ and $\Delta^{33}S'$ signatures. The main sources of S to the SOB lakes are represented with the "mix" purple area, delimited by mixing lines between a groundwater endmember (in pink, from Cretaceous deposits), a mantle endmember (in black), and a detrital pyrite oxidation endmember (in yellow). In red, the composition of Atexcac sulfate is dominated by a mantle S contribution. The $\Delta^{33}S'$ of La Preciosa sulfate (in white/purple) was not determined, but its $\delta^{34}S$ indicates that this sulfate reservoir could match a mixed source, between groundwater, detrital pyrite and mantle S signatures. In blue, the composition of Alchichica sulfate is out of the mixing trend suggesting additional sources or processes (*cf.* Figure 8.7). See the section 8.3.1.1 for the respective S source isotopic compositions. In white with green border, the composition of both sulfate and pyrite in Alberca, can reflect the contribution of volcanic S with an alternate and specific signature, and/or to the influence of AOM-SR (see 8.3.2.1).

In the SOB, whereas the quite positive $\delta^{34}S_{SO4}$ in Alchichica (+19 ‰) and La Preciosa (+9 ‰) sign the contribution of groundwater sulfate influenced by Cretaceous deposits, the near-0 ‰ $\delta^{34}S_{SO4}$ in Atexcac suggests volcanic degassing with a significant mantle contribution as the main S source (Fig. 8.6). Together with a lower pH, higher Cl^- concentrations, and very high pCO_2 (Havas *et al.*, 2023a), it provides strong evidence for the release of volcanic fluids into Lake Atexcac, and their predominant control on the lake's chemistry.

The sulfate compositions in Alchichica and La Preciosa differ from a pure groundwater source. In La Preciosa, it is well explained by a mixed-source between: (i) groundwater sulfate, (ii) mantle S degassing, and (iii) basement pyrite oxidation (Fig. 8.6).

In Alchichica, the current sulfate composition either requires an additional S source, or a process changing the sulfate sources signatures. Among the sources mentioned earlier, a plausible one is volcanic degassing with S bearing an even more positive $\delta^{34}S$ than the range found by de Moor *et al.* (2022) in central America (*i.e*. higher than 10 ‰; Fig. 8.6 and section 8.3.1.1). Although it seems at odds with the volcanic S signatures received in Atexcac, this scenario cannot be fully ruled out. An alternative hypothesis is that Alchichica initial sulfate reservoir corresponded to a similar mix as in La Preciosa, but its signatures subsequently evolved, in a relatively closed-system, for example under the effects of microbial sulfate reduction (Fig. 8.7). In other words, the current sulfate and pyrite reservoirs can be seen as the products of a branching process starting from an initial S reservoir: the $\Delta^{33}S'$ of both products would increase while their $\delta^{34}S$ evolve opposite ways (Fig. 8.7). This process requires that sulfate consumption in the lake is faster than its replenishment. A first few hypotheses, inspired from the C cycle model in Alchichica (Chapter 5), can be suggested to explain such a phenomenon: (i) the recent decrease in groundwater fluxes to the lake should reduce the inputs

of sulfate; (ii) higher recent TOC burial fluxes may favor a more efficient microbial sulfate reduction (MSR) and consumption of sulfate; (iii) on the contrary to DIC or Cl^-, sulfate concentrations in Alchichica have not increased as much on average since 1941 (Silva-Aguilera *et al.*, 2022b), suggesting an efficient mechanism of sulfate removal in the last decades. The closed-system view is at odds with the inferences drawn from modelling the C cycle in Alchichica which suggested volcanic CO_2 inputs into this lake (Chapter 5), unless these volcanic sources are enriched in C but not in S. This latter alternative is plausible, since CO_2 is the main gas component released in quiescent/recently extinct volcanoes and more acidic gases (SO_2, HCl and HF) may not reach the surface of some alkaline lake systems (Pecoraino *et al.*, 2015). A similar branching process as discussed for Alchichica could have affected the sulfate reservoir in La Preciosa, but is not mandatory (Fig. 8.6), depending on what is its exact $\Delta^{33}S$'. This latter remains to be measured.

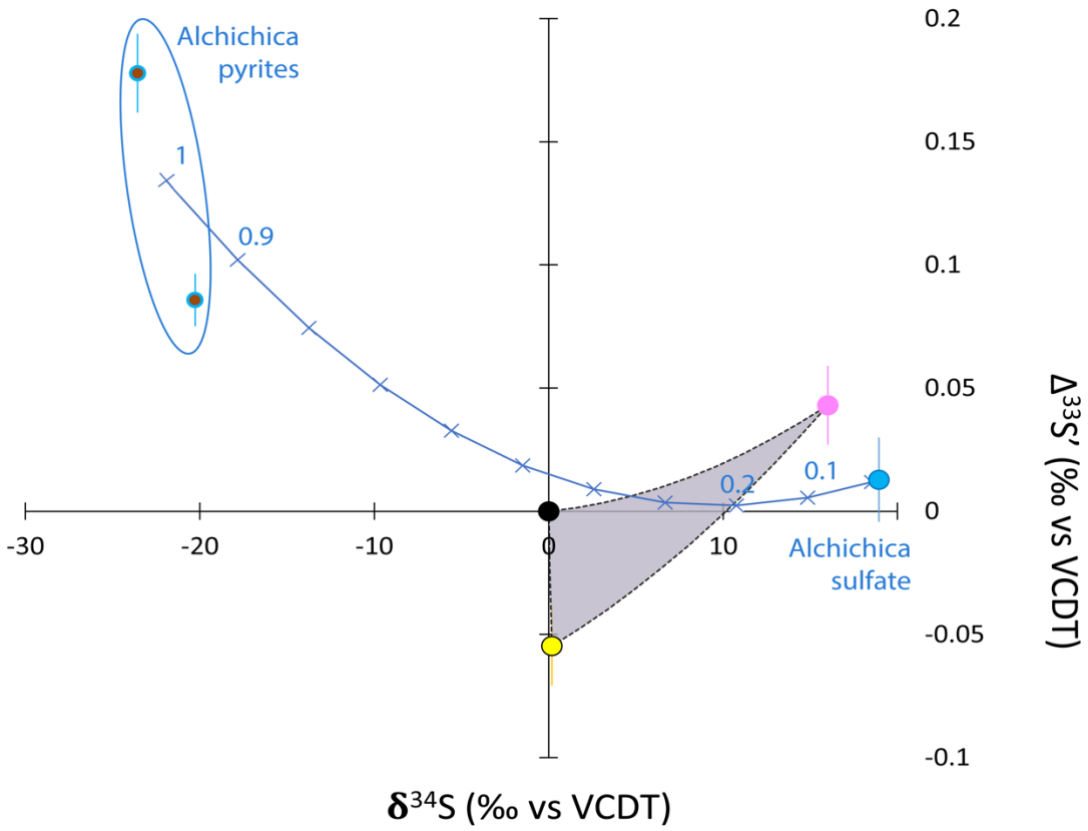

Figure 8.7 : Modeled evolution of $\delta^{34}S$ and $\Delta^{33}S'$ signatures for sulfur sources to Lake Alchichica. The crossed-line is a mixing line between the average bottom lake sediment pyrite and lake sulfate composition. It illustrates the connection between a starting S reservoir, and the two S pools produced from a fractionating branching process (namely, sulfide and residual sulfate after MSR) in a closed-system. Both products of this branching evolve towards higher $\Delta^{33}S'$ and opposite $\boldsymbol{\delta}^{34}S'$ (*cf.* Toolbox in Chapter 7). Consistently, this mixing line intersects the area that should contain the initial lake S reservoir composition (*cf.* Figure 8.6). The crosses indicate the proportion of the two endmembers (sulfide/residual sulfate); it points out that approximately 20 to 35% of the initial S reservoir has been buried as pyrite.

8.3.2. Diagenetic processes operating in the sediments of Alberca, La Preciosa, and Atexcac

8.3.2.1. Alberca de los Espinos

Micromolar level sulfate concentrations in Alberca prevented the measurement of its isotopic compositions. Nonetheless, since the quantity of C substrates in this lake is abundant (organic C and CH_4), these sulfate concentrations should allow a conservative transfer of their isotope signatures to reduced S pools (*e.g.* Gomes and Hurtgen, 2013; Crowe *et al.*, 2014). Dissolved Fe is low in the water column (<0.25 µM), but abundant in the sediment porewater (125 µM on average), allowing an effective capture of dissolved sulfides (Fig. 8.3). Peaks of particulate Fe and S are found in the deepest part of the lake and the upper sediments (Havas *et al.*, 2023a), evidencing the location where pyrite mainly precipitates and MSR takes place (Desulfobacterota mainly appear at the bottom water column and are significant in the core; Microbialite-ANR-project, unpublished data).

Pyrite $\delta^{34}S$ varies between +10 and 25 ‰ throughout the core (Fig. 8.3), a composition that is unexpected from MSR which usually generates negative fractionations, but explainable if the entire SO_4^{2-} reservoir is transferred to pyrite. The same applies to S minor isotopes. Measured $\Delta^{33}S'$ of ~ -0.055 ‰ does not reflect a sulfate pool that was processed *via* organoclastic-MSR (*cf.* toolbox, Chapter 7), but is consistent with a mantle S source and volcanic degassing (Fig. 8.6). Volcanic degassing was suggested as an explanation to the high bottom waters pCO_2 and low pH (Havas *et al.*, 2023a). These sources could partly explain the generally positive $\delta^{34}S_{py}$ found in Alberca, but it is unsure whether they would be sufficient on their own to reach values as high as those measured here (+25 ‰) and generate the variability observed over the timescale of this sediment core (~1330 yrs). If the trend of positive $\delta^{34}S_{py}$ does not reflect a change in the source isotopic composition, one can wonder if the origin of thtat trend is rather diagenetic. Sulfate reduction coupled to anaerobic oxidation of methane (AOM-SR) has been shown to increase the residual sulfate $\delta^{34}S$ while decreasing their $\Delta^{33}S'$ (*e.g.* Crémière *et al.*, 2020; Liu *et al.*, 2022). Methanogenesis was evidenced in the sediment core of Alberca (Havas *et al.*, 2023a). The porewater $\delta^{13}C_{DIC}$ showed high signatures up to +11 ‰, consistent with methanogenesis, but not with a significant methane oxidation (at least in the sediment porewater). The role of organic S would be worth investigating since organic matter is abundant in the sediments of Alberca (~9 wt. % TOC on average), even though,

previous studies suggested that pyrites would have ^{34}S-depleted signatures compared with coeval H_2S and organic S compounds (Raven *et al.*, 2016), which would imply the production of $\delta^{34}S_{H2S}$ and $\delta^{34}S_{org}$ even higher than +25 ‰. Alternatively, the pyrite content decreases concomitantly to the increase of porewater Fe concentrations (Fig. 8.3). This could reflect the reduction and dissolution of Fe particles, linked to pyrite oxidation. Yet, no change in the dissolved S is observed conversely to what would be expected under these circumstances.

If the variations observed are not diagenetic, a potential explanation for the $\delta^{34}S$ trend in Alberca is that it records the lake's $\delta^{34}S_{SO4}$ evolution through time. For example, starting from an isotopically more evolved SO_4^{2-} reservoir in the past (*e.g.* ^{34}S-enriched due to MSR), progressively returning back to smaller $\delta^{34}S$ as the contribution of volcanic S with low $\delta^{34}S$ values increases. Yet here again, the negative $\Delta^{33}S$' signatures at the bottom of the core are not consistent with a significant role of organoclastic-MSR in the past as that process shifts $\Delta^{33}S$' to higher values (*cf.* toolbox, Chapter 7). More data in this core will be required to know which of the above hypotheses are the most propable.

The exact $\delta^{34}S$ and $\Delta^{3i}S$ compositions of sulfate remain to be measured, and a variety of processes may affect the S cycle in Alberca. However, a $\delta^{34}S_{SO4}$ much higher than 25 ‰, and a $\Delta^{33}S_{SO4}$ lower than -0.06 ‰ are most unlikely considering the typical isotopic signatures of usual S sources (Fig. 8.6). Therefore, the small sulfate reservoir isotopic signatures should efficiently transfer to sulfides, and the net $\Delta^{34}S_{py\text{-}SO4}$ and $\Delta\Delta^{33}S_{py\text{-}SO4}$' likely approach 0. The final pyrite thus mostly records the composition, and small size of the SO_4^{2-} reservoir.

8.3.2.2. La Preciosa

Sulfate concentrations are nearly constant in the La Preciosa water column, but drop to ~0 mM in less than 10 cm in the sediments, suggesting a complete consumption by MSR (Fig. 8.4). Pyrite content and the Fe_{py}:Fe_{tot} ratio also reach maximum values at a depth of 10 cm (Fig. 8.4). Sulfide minerals forming after a complete reduction of sulfates should inherit the sulfate source isotopic composition that is ~ 9 ‰ (Fig. 8.4). However, the deepest pyrite sample still records a negative signature of -3.4 ‰ (Fig. 8.4). The composition of pyrite precipitated in deep layers, on top of surficial ones, can be calculated using the pyrites' relative abundance with depth (as Fe_{py}:Fe_{tot}), and their $\delta^{34}S_{py}$ (Liu *et al.*, 2020a), such that:

$$(Fe_{py}:Fe_{tot})_{deep} * \delta^{34}S_{py,\,deep} = (Fe_{py}:Fe_{tot})_0 * \delta^{34}S_{py,\,0} + (Fe_{py}:Fe_{tot})_{added} * \delta^{34}S_{py,\,added} \quad (8.1).$$

When applied to pyrites formed between 1 and 19 cm depths in La Preciosa (Fig. 8.4):

$$\delta^{34}S_{py,\ added} = (-3.4*0.41 + 7.7*0.27) / (0.41-0.27) = 4.9\ ‰,$$

this simple calculation confirms that the last H_2S produced by MSR has an isotopic composition (4.9 ‰) close to the lake sulfate (+ 9.2 ‰). Then, why is there still a large difference between this value and the -3.4 ‰ signature of bulk pyrite? Dissolved Fe concentrations are below detection limits throughout the water column and sediment porewaters, and are most likely limiting for pyrite precipitation. Thus, MSR-produced H_2S/HS^- would diffuse away in the porewater, explaining why $\delta^{34}S_{py}$ remains more negative than $\delta^{34}S_{SO4}$ (by ~ 12 ‰). This scenario could have been recurrent at times during the Neoproterozoic when Fe levels were low compared to sulfides (Guilbaud *et al.*, 2015 and ref. therein).

The net $\Delta^{34}S_{py\text{-}SO4}$ fractionation at the top of the core is about -20 ‰. This is much smaller than the thermodynamic equilibrium $^{34}\varepsilon_{msr}$ fractionation of ~ -70 ‰ (*e.g.* Brunner and Bernasconi, 2005; Johnston *et al.*, 2007). This 50 ‰ difference is too large to be explained by sulfide pooling and diffusion (Bourg, 2008; Donahue *et al.*, 2008b). High cell-specific sulfate reduction rates (csSRR) can significantly lessen the MSR fractionation (Sim *et al.*, 2011b; Leavitt *et al.*, 2013; Wing and Halevy, 2014). In comparison, however, a $^{34}\varepsilon_{msr}$ of about -45 ‰ was determined for Alchichica sediments, whose TOC and SO_4^{2-} contents are more than 2 and 5 times higher than those in La Preciosa, respectively. Thus, low csSRR likely proceed in La Preciosa compared with Alchichica, and cannot explain a small -20 ‰ fractionation. Rather, low [SO_4^{2-}] in La Preciosa are consistent with a smaller fractionation induced by microbial sulfate reducers ('I' in Fig. 8.8, and discussion in Chapter 7; Bradley *et al.*, 2016). On top of this small fractionation, sulfide pooling towards the bottom of the core can further narrow the apparent $\Delta^{34}S_{py\text{-}SO4}$ to -12 ‰ as described before.

Therefore, the impact of the small sulfate reservoir's size on la Preciosa pyrite isotopic record is 2-fold: (i) it induces smaller isotopic fractionations during MSR, and (ii) it facilitates a full SO_4^{2-} consumption which result in heavy sulfide production.

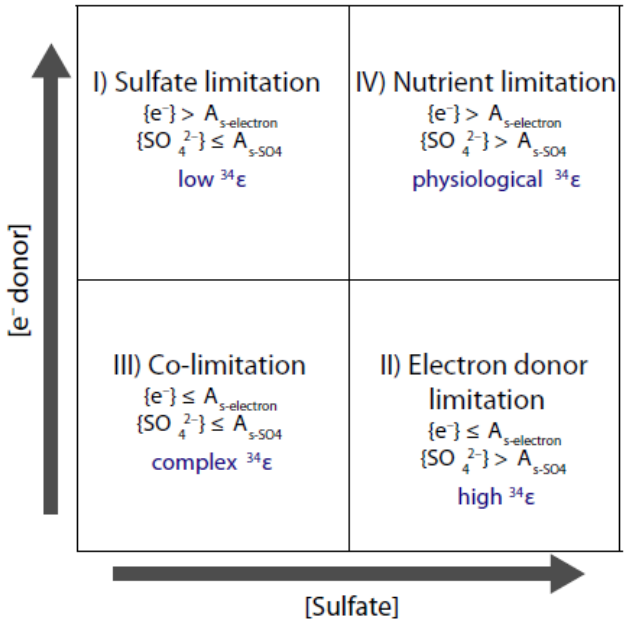

Figure 8.8 : schematic view of the sulfate $^{34}\varepsilon$ fractionation during MSR according to sulfate and electron donors (*e.g.* organic C) availability, figure from Bradley *et al.* (2016). A_s is the 'affinity' parameter, reflecting the capacity of a cell to transport electron donor or sulfate intracellularly. I) Under sulfate limitation, the cell-specific sulfate reduction rate (csSRR) exceeds the capacity for the organisms to "refill" with sulfate, thus the majority of sulfate entering the cell is reduced and low fractionation ($^{34}\varepsilon$) is expressed. II) Under e^- donor limitation, low csSRR relative to the availability of sulfate allows a higher reversibility of sulfate reduction steps, including sulfate uptake. Exchange with extracellular sulfate allows enables the preservation of high $^{34}\varepsilon$. III) A co-limitation of both electron donors and sulfate can result in a large range of fractionations, mixing complex environmental and physiological forcing (Bradley *et al.*, 2016). IV) When sulfate and e^- donors are abundant a physiological $^{34}\varepsilon$ is expressed.

8.3.2.3. Atexcac

In the first 10 cm of the core, lower sulfate concentrations than in the lake water, and a small increase in pyrite content suggest the activity of MSR. The main sulfate decrease occurs after a depth of 15 cm, where pyrite content peaks (Fig. 8.5). Disappearance of dissolved sulfide and Fe below 10 cm suggest that the product of MSR is quantitatively precipitated as pyrite at the bottom of the core. The importance of MSR in the 15/20-cm depth horizon is further demonstrated by the drop in TOC content below these depths.

A striking feature of Atexcac's sediments is the pronounced increase in $\delta^{34}S_{py}$ from -43 to -4 ‰ over a depth of 40 cm (Fig. 8.5). This profile could reflect a progressive ^{34}S-enrichement of the sulfide pool produced by MSR towards the lake $\delta^{34}S_{SO4}$ composition (0.5‰) *via* a distillation process as described before. At 40 cm, the -4 ‰ pyrite signature would therefore

suggest a near complete consumption of the sulfate pool. Yet, [SO_4^{2-}] has only decreased by ~30% at this depth (Fig. 8.5). The porewater $\delta^{34}S_{SO4}$ at 17 cm confirms that the sulfate reservoir is not that evolved compared with the lake water, as it reaches no more than 7.7 ‰ (Table 8.1).

A first possibility to explain the ^{34}S-enrichement of Atexcac sedimentary pyrites below 15 cm is that the porewater chemical composition today is different than that at the time pyrite precipitated. That is to say, the initial SO_4^{2-} pool was first nearly fully consumed, producing heavy SO_4-like $\delta^{34}S_{py}$, before the lake sulfate concentration rose again, and sulfate diffused back down through the porewater. This scenario cannot be ruled out, although it seems an unlikely coincidence that the present porewater [SO_4^{2-}] (putatively of "second generation") decreases precisely where the pyrite content and $\delta^{34}S_{py}$ increase (Fig. 8.5).

Another possible explanation is that pyrites at the bottom of the core precipitated from a volcanic mantle-like S source, which usually carry $\delta^{34}S$ (and $\Delta^{3i}S$) close to 0 (*e.g.* Ueno *et al.*, 2008; Peters *et al.*, 2010; Labidi *et al.*, 2015). However, the analysis of multi-S isotopes in the pyrite at 17 cm shows a very positive $\Delta^{33}S$' value (+0.14 ‰). This result is most consistent with a MSR signature (*cf.* toolbox), and evidences that Atexcac's pyrite did not form from a pristine abiotic sulfide source, at least down the 17cm-depth horizon.

The main increase in $\delta^{34}S_{py}$ occurs between ~15 and 20 cm, where the Fe_{py}:Fe_{tot} ratio peaks, and TOC content drops, that is, suggestively where MSR is the most active (Fig. 8.5). A second marked $\delta^{34}S_{py}$ increase occurs at 30 cm, where TOC decreases again (Fig. 8.5). These depth profiles suggest that the abundance of organic C and pyrites isotopic signatures are inversely correlated, which is confirmed by the cross-plot in Figure 8.9. This implies that the $\delta^{34}S_{py}$ is related to the dynamics of TOC consumption, which could have an impact on the fractionation factors. This inverse correlation between TOC and $\delta^{34}S_{py}$ is surprising though, because the opposite would be expected and has been found before (*e.g.* Pasquier *et al.*, 2021b). It was interpreted to reflect a change in pooling intensity due to changing sulfate-reduction rates at the community level, itself influenced by the flux of TOC deposition (Pasquier *et al.*, 2021b). The higher the TOC deposition flux, the more efficient MSR is, enhancing the effect of pooling, thence increasing $\delta^{34}S_{SO4}/\delta^{34}S_{py}$ values. In contrast, the present data suggests that lower TOC concentrations are a consequence of localized and intense MSR, leading to smaller fractionation and less ^{34}S-depleted pyrite signatures. Considering the well-layered redox-zonation described in Atexcac (Chapter 6), the sediment horizon at ~ 15-20 cm could represent a hotspot of MSR, harboring high csSRR, and thus low $^{34}\varepsilon_{msr}$ (Sim *et al.*, 2011a, 2011b; Leavitt *et al.*, 2013). This is supported by relatively constant, or even smaller proportions of the Desulfobacterota phylum

in this sediment horizon (Microbialite-ANR-project, unpublished data). Indeed, if more sulfate is reduced by the same number of organisms, the 'cell-specific reduction rate' (csSRR) automatically increases. Small isotopic fractionations would be all the more fostered by the combined effect of high csSRR with small [SO_4^{2-}] (frame 'I' in Fig. 8.8; Bradley *et al.*, 2016), as shown also by the correlation between $\delta^{34}S_{py}$ and [SO_4^{2-}] (Fig. 8.9).

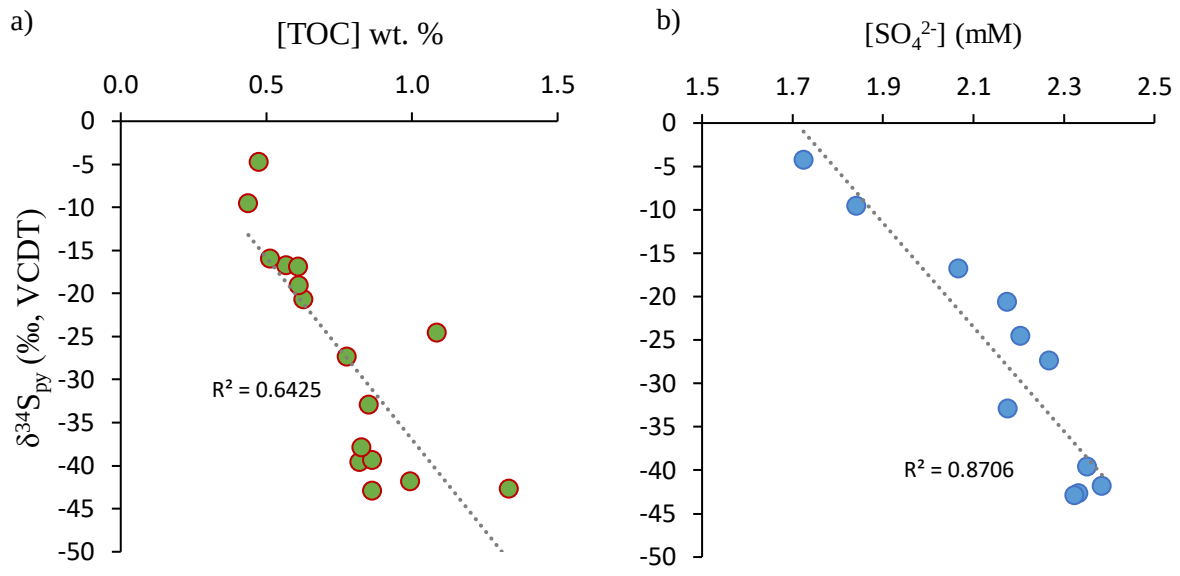

Figure 8.9 : Correlation between the $\delta^{34}S$ recorded in Atexcac sedimentary pyrites and the total organic C concentration (a), and dissolved sulfate concentration (b).

On top of its quantity, the organic carbon (OC) lability can impact the MSR fractionation (higher bioavailability resulting smaller $^{34}\varepsilon_{msr}$; Sim *et al.*, 2011b). In addition to diagenetic processes occurring between 10 and 20 cm in the sediments of Atexcac (Chapter 6), primary changes in the lake's chemistry may also have occurred. For example, bulk sediment europium anomaly (Eu*) wobbles at these depths, showing some perturbation in the lake's chemistry (Fig. 8.5). Thus, a change in the water column chemistry could have occurred, leading to a different kind and possibly higher primary productivity, in turn inducing smaller $^{34}\varepsilon_{msr}$. However, the possibility that these changes controlled the $\delta^{34}S_{py}$ profile is discarded here because high $\delta^{34}S_{py}$ values (implying smaller $^{34}\varepsilon_{msr}$) occur even below the main geochemical perturbations from 20 to 10 cm, *i.e.*, before the putative increase of primary production.

Applying the same method as for La Preciosa with equation 8.1, the isotopic composition of pyrite being added at depths between 0 and 10 cm, and between 10 and 17 cm can be compared. It results that pyrite forming at 10 cm has a $\delta^{34}S$ of ~-51 ‰, while pyrite forming at

the FeS_2 peak has a $\delta^{34}S$ of ~ -19 ‰. Together with the available porewater $\delta^{34}S_{SO4}$ data (Table 8.1), it shows that the isotopic fractionation in Atexcac evolves from near equilibrium values in the surficial layers (*i.e.* approaching -70 ‰), to about -27 ‰ at the peak of pyrite production. The high $\Delta^{33}S$' recorded at 17 cm (+0.14 ‰) also supports changing fractionations with depth (Table 8.2). Indeed, $^{34}\varepsilon_{msr}$ has been found to correlate with $^{33}\lambda_{msr}$ such that smaller fractionations are characterized by shallower $^{33}\lambda_{msr}$ slopes (Sim *et al.*, 2011a, 2011b; Leavitt *et al.*, 2013; Bradley *et al.*, 2016). The shallower the $^{33}\lambda$ slope, the higher the $\Delta^{33}S$' produced (*cf.* toolbox). Thus, a shift to lower $^{34}\varepsilon_{msr}$ should match lower $^{33}\lambda_{msr}$, resulting in a faster $\Delta^{33}S'_{py}$ increase down the core. The pyrite isotopic profiles in Atexcac would therefore be shaped by changes in the magnitude of MSR fractionations.

In conclusion, the apparent $\Delta^{34}S_{py\text{-}SO4}$ eventually recorded in Atexcac is extremely low – less than 5 ‰ –, although the intrinsic fractionation determined in the surficial sediment layers is much closer to the -70 ‰ equilibrium value. Smaller intrinsic $^{34}\varepsilon$ deeper in the sediments likely results from intense MSR activity, featuring high csSRR, potentially accentuated by the small sulfate concentration (< 2.5 mM). Alternatively, it cannot be fully excluded that pyrite precipitated from a SO_4^{2-} reservoir older than the current one, which would have produced the ^{34}S-enriched signatures through Rayleigh distillation in the porewater. In both scenario, the low lake sulfate concentration results in (and favors) the record of small $\Delta^{34}S_{py\text{-}SO4}$ values.

8.4. Synthesis of the four lakes S sources, isotopic record, and concluding remarks about the reservoir effect

The four lakes sulfate isotopic signatures are consistent with their geological context, but slightly differ from each other. The small sulfur reservoir in Alberca originates mostly from volcanic degassing, but is possibly also influenced by a secular change in the lake's isotopic signatures and/or the influence of diagenetic processes occurring in the sediments. In the SOB, Atexcac is strongly influenced by juvenile S, whereas Alchichica and La Preciosa receive mixed-signature inputs reflecting different proportions of: detrital pyrite leaching, grounwater "marine-like" sulfate, and mantle S. Additionally, the current sulfate composition in Alchichica evidences a subsequent evolution likely due to MSR and pyrite burial. Recent changes in the sulfate sources and sinks would have driven this lake sulfate reservoir out of steady state,

explaining that its current composition does not directly reflects the weighted average of its sources.

In Alberca, pyrites with very positive $\delta^{34}S$ signatures (*i.e.* opposite to MSR biosignatures) are formed although pyrites result from MSR activity occurring in the sediments and water column (*via* both OC and methane oxidation, section 8.3.2.1). Alike what is proposed for the Archean period (*e.g.* Crowe *et al.*, 2014) and as a result of the small SO_4^{2-} reservoir's size (< 12 µM), no net fractionation is deduced despite active biological S cycling.

Pyrites in La Preciosa record a final $\Delta^{34}S_{py\text{-}SO4}$ of 12 ‰, which would further approach 0 ‰ if the lake was not limited in Fe. This small apparent fractionation results, here again, from a complete diagenetic SO_4^{2-} consumption *via* MSR, but also from the effects of small sulfate concentrations (< 1.2 mM) on the intrinsic MSR fractionation.

The case of Atexcac is more complex, as the $^{34}\varepsilon$ diminishes with depth. Smaller fractionations likely result from intense MSR activity, combined with low porewater [SO_4^{2-}] (< 2.5 mM). The apparent $\Delta^{34}S_{py\text{-}SO4}$ varies between ~5 and 45 ‰.

In Alchichica an apparent $\Delta^{34}S_{py\text{-}SO4}$ of ~ 40 ‰ is preserved throughout the core despite the distillation affecting the porewater sulfur species in a closed-system. This high $\Delta^{34}S_{py\text{-}SO4}$ is maintained due to complex oxidative reactions, but also because the initial lake sulfate reservoir is large enough (> 10 mM) to prevent its full exhaustion in the sediments (Chapter 7). There is not enough data in the three other lakes (notably from the porewaters) to properly assess S reoxidative cycling. It is unlikely influential in Atexcac and Alberca because dissolved sulfides are efficiently sequestrated in pyrite minerals, but it could play a role in La Preciosa where H_2S/HS^- diffuses in the porewater.

When plotted on previous compilations of other modern systems, the $\Delta^{34}S_{py\text{-}SO4}$ of the four Mexican lakes are in good agreement with the observed trends of higher apparent $\Delta^{34}S_{py\text{-}SO4}$ at higher sulfate concentrations (Fig. 8.10). The exact fractionation value depends on a number of complex and intertwined factors (*e.g.* Fe limitation, changing $^{34}\varepsilon$, cryptic cycling). Nonetheless, pyrites forming from small sulfate reservoirs will inevitably tend towards the sulfate isotopic composition. Below certain sulfate concentrations, it will thus be difficult to discuss the environmental and biological factors driving the intrinsic S isotope fractionations (*cf.* Gomes and Hurtgen, 2015). The diagenetic history of pyrites in Alchichica, albeit complex, has more chances to unveil information about the environment that lead to their formation.

Therefore, the reservoir effect is a first order control on the final $\Delta^{34}S_{py\text{-}SO4}$ recorded in sediments as demonstrated by accumulating empirical evidences (Fig. 8.10). A thorough characterization of the geochemistry and geological context of a given sedimentary sequence is required before describing how and why the amplitude of this fractionation may vary (*e.g.* through closed-system distillation). Nevertheless, the reservoir effect sets the conditions for other factors to be expressed or not in the pyrites isotopic record. In addition to bulk analyses, small scale *in situ* measurements are a promising tool to complete our understanding of a given system, even when the bulk $\Delta^{34}S_{py\text{-}SO4}$ approaches 0 (*e.g.* Fike *et al.*, 2009; Fischer *et al.*, 2014). For instance, from NanoSIMS analyses in a microbialite sample from Lake Atexcac, we could differentiate primary S isotope signatures from MSR in micropyrite grains, and signatures related to a Rayleigh distillation process and/or sulfide oxidation in framboidal pyrites (Marin-Carbonne *et al.*, 2022; Annex 1). Therefore, combining both bulk and *in situ* analyses may allow the identification of both intrinsic fractionations and reservoir effects.

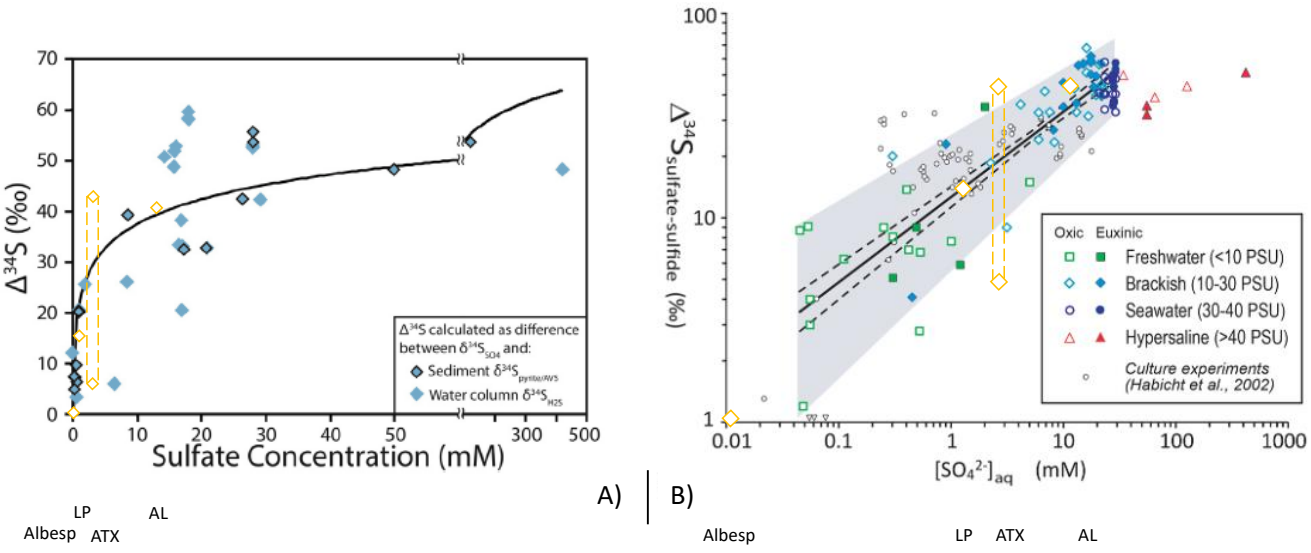

Figure 8.10 : Compilation of isotopic offsets between sulfate and sulfides ($\Delta^{34}S$) *versus* sulfate concentrations in modern environments. The figure in 'A' is from Gomes and Hurtgen (2015), the one in 'B' from Algeo *et al.* (2015). The data discussed in the text for the Mexican lakes is represented in yellow, for the four lakes Alberca ('Albesp'), La Preciosa ('LP'), Atexcac ('ATX'), and Alchichica ('AL'). The depicted $\Delta^{34}S$ fractionation is calculated based on the isotopic compositions of sulfate in the water columns, and solid sulfide recorded in the sediments (pyrite). In Alchichica sediments, this apparent $\Delta^{34}S$ is relatively constant with depths ~40 ‰; in Atexcac it varies between about 5 and 43 ‰ depending on which pyrite depth is preserved; in La Preciosa, it is ~13 ‰ in the final pyrite record; in Alberca, 0 net fractionation should be observed.

Part 2
Intermediate conclusion

This second part highlights a significant variability in the isotopic record of sedimentary pyrites in the four Mexican lakes, impacted by different diagenetic processes.

In Alchichica, the analysis of multiple S isotope signatures in sedimentary pyrites and porewater sulfates evidences a complex S cycle combining the effects of: (i) sulfide pooling – resulting from efficient MSR – leading to a concomitant increase in sulfate and sulfide $\delta^{34}S$, (ii) sulfide reoxidation – biologically and/or by oxidation with reactive Fe minerals – which produces intermediate S species available for disproportionation, (iii) disproportionation producing sulfide and sulfate. Repeated cycles of these reactions would favor the production of pyrites having a $\delta^{34}S$ lower, and $\Delta^{33}S'$ higher than the sulfide produced by pooling effect only. Importantly, if the final range of isotopic signatures recorded by pyrites had been measured in ancient samples – *i.e.*, with no characterization of the porewater – it would likely be interpreted as a result of MSR in an open system, instead of the scenario described above, highlighting the cryptic nature of this sedimentary record.

Multiple S isotope signatures enables the characterization of the dominant S sources to the lakes, notably showing a clear mantle contribution for Lake Atexcac.

In the three other lakes than Alchichica, the factors constraining the pyrites isotopic composition are also diverse. In Atexcac, the fractionation induced by MSR changes with depth, forming ^{34}S-enriched pyrites in the layer where high cell-specific reduction rates occur, possibly favored by the relatively small sulfate concentration. In La Preciosa, a small fractionation is recorded by pyrites as a result of low sulfate concentrations and distillation in the porewater. More data are required from Alberca to conclude about the exact mechanisms operating in this lake (possibly AOM-SR, exchange with organic S, pyrite reoxidation or a secular change in the lake sulfate composition). However, micromolar sulfate concentrations in the lake are likely fully consumed, transferring a strongly positive $\delta^{34}S$ to pyrites.

Comparing the four lakes, the first order control on final pyrite isotopic compositions is sulfate concentration: first, it can directly modify the amplitude of the MSR fractionation, but mostly, it modulates the effects of porewater sulfate distillation, allowing or obstructing the record of biogeochemical processes occurring within the sediments porewaters.

Part 3

The microbialite record in the Serdán-Oriental Basin

"Laguna Alchichica"

After characterizing some of the processes affecting the C, O, and S cycles in the water column and sediments of the four Mexican lakes, I now put in parallel the results of 'Part 1 and 2' with the geochemical records of microbialites present in the lakes from the Serdán-Oriental Basin (SOB): Alchichica, Atexcac, and La Preciosa. The fourth lake presented in 'Part 1': Alberca de los Espinos, contains very limited microbial deposits (Zeyen *et al.*, 2021) and no samples from there were studied in this PhD.

In the literature, microbialites from the three SOB lakes received different degrees of attention, with a higher focus on Alchichica. In this latter, genetic and meta-genomic/transcriptomic characterization of microbial communities (Couradeau *et al.*, 2011; Saghaï *et al.*, 2015, 2016; Valdespino-Castillo *et al.*, 2014, 2018; Alcántara-Hernández *et al.*, 2017; Águila *et al.*, 2021), as well as morphological, textural, and mineralogical descriptions of the microbialites were carried out (Kaźmierczak *et al.*, 2011; Couradeau *et al.*, 2013; Gérard *et al.*, 2013; Valdespino-Castillo *et al.*, 2018). In Atexcac and La Preciosa, on the other hand, a

single specific study about the petrography and mineralogy of microbialites was achieved (Zeyen *et al.*, 2015). More broadly, integrated studies of the phylogenetic/metabolic diversity and mineralogical and chemical compositions of microbialites throughout 9 Mexican lakes (including the ones studied here) have also been carried out (Iniesto *et al.*, 2021; Zeyen *et al.*, 2021). However, the isotopic signatures of these objects remain largely understudied. So far, only a few measurements of carbonate C and O isotopes in microbialites from Alchichica (Kaźmierczak *et al.*, 2011), and *in situ* S isotope analyses in microbialite pyrites from Atexcac were performed in a study that I co-authored (Marin-Carbonne *et al.*, 2022; Annex 1).

Therefore, in this third and last part of the dissertation, I will use the isotopic framework to discuss the formation mechanisms of the Mexican microbialites studied, how they record their environment (*e.g.*, oxic *vs*. anoxic conditions) as well as possible biosignatures, and what are the potential effects of early diagenesis on their petrographic and geochemical signatures.

This last part is subdivided in three chapters. Chapter 9 provides a general presentation and classification of the microbialites into different petrographic facies based on microscopic imagery techniques and mineralogical analyses. This chapter gives a first constrain on the microbialites history of formation, and a basis to better interpret the isotopic results. Chapter 10 investigates the carbonates and organic matter signatures in C and O isotopes from bulk and micro-drilled analyses. Chapter 11 consists of a poster that was presented at the Goldschmidt conference in 2023 in Lyon. It shows the multi-S isotope signatures from Alchichica microbialites, and notably how they change according to the water column stratification.

Chapter 9

Mineralogical and petrographic descriptions of the microbialite samples: initial constraints on their history of formation

Table of content

9.1. Introduction

The primary objective of this chapter is to draw a first order description of the microbialite samples, from macro- to microscale, in order to grasp what are the main traits in their formation history. Namely: what is the influence of biotic *vs.* abiotic factors in their precipitation? What is the timing of their precipitation within the lakes and within the microbialites (primary *vs.* secondary phases)? Which primary features can be preserved in subfossil microbialites (*e.g.* microfossils)?

To answer these questions, "living" and "subfossil' microbialites from the three SOB lakes (collected under- and above-water, respectively) were characterized mineralogically by XRD, texturally by optical and fluorescence microscopy, and chemically by XRF mapping (unfortunately bulk elemental concentrations were measured only for "living" microbialites). Together with field observations, this lab work initiated during the internship of Hugo Bert allowed classifying the microbialites into different groups based on their mineralogy, petrographic facies, and diagenetic overprint. I describe the results of this classification below.

The list and basic pieces of information about the microbialite samples studied in this PhD can be found in Table 9.1.

Table 9.1: main sampling and classification information about the microbialites studied. 'AL', 'LP/PR' and 'ATX' code names correspond to microbialites from lakes Alchichica, La Preciosa and Atexcac, respectively. The detailed characteristic of the facies groups are presented in the main text. 'Hmg', 'Hu', 'Ara' and 'Cal' stand for hydromagnesite, huntite, aragonite and calcite, respectively ('ND' for not determined).

Sample Name	Latitude	Longitude	Sampling date	Underwater // Subfossil (oxygen conditions)	Depth/height relative to current water level	Facies group	Carbonate content	Main carbonate mineralogy
					m		wt. %	
AL19-5m	19° 25' 10" N	97° 24' 22" W	05/21/2019	Underwater (oxic)	- 5	White	98.8	Hmg, Ara
AL19-10m	19° 25' 10" N	97° 24' 22" W	05/21/2019	Underwater (oxic)	- 10	White	99.5	Hmg, Ara
AL19-20ma	19° 25' 10" N	97° 24' 22" W	05/21/2019	Underwater (oxic, hypoxic)	- 20	White	94.1	Hmg, Ara, Hu
AL19-20mb	19° 25' 10" N	97° 24' 22" W	05/21/2019		- 20	White	99.3	Hmg, Ara, Hu
AL19-40m	19° 25' 10" N	97° 24' 22" W	05/21/2019	Underwater (mostly anoxic)	- 40	White	99.7	Hmg, Ara, Hu
AL-T-1	19° 25' 5.2" N	97° 24' 41.1" W	05/24/2019	Subfossil	≈ +2	White	96.1	Hmg, Ara
AL-T-3	19° 25' 0.4" N	97° 24' 49.3" W	05/24/2019	Volcanic conglomerate	≈ +50	Volcanic conglo	~30	Cal
AL-T-5	19° 24' 59.1" N	97° 24' 40.9" W	05/24/2019	Subfossil	≈ +2	Brown	96.5	Hmg, Ara
AL-T-6	//	//	05/24/2019	Subfossil	≈ +2	White	98.6	Hmg, Ara
AL-T-7	19° 24' 58.3" N	97° 24' 40.7" W	05/24/2019	Subfossil	≈ +2	White	98.4	Ara
AL-T-8	//	//	05/24/2019	Subfossil	≈ +2	Brown	96.5	Ara
AL-T-9	19° 24' 56.9" N	97° 24' 40.5" W	05/24/2019	Subfossil	≈ +2	Brown	96.5	Ara
AL-T-10	19° 24' 55.1" N	97° 24' 40.1" W	05/24/2019	Subfossil	≈ +2	Brown	95.6	Hmg, Ara
AL-T-11	//	//	05/24/2019	Subfossil	≈ +2	White	98.1	Hmg, Ara
AL-R-1	19° 25' 14.0" N	97° 24' 12.9" W	05/21/2019	Subfossil	+ 0	White	97.9	Hmg, Ara
AL-R-2	//	//	05/21/2019	Underwater (oxic)	- 0	White	97.1	Hmg, Ara
AL-R-3	//	//	05/21/2019	Subfossil	≈ +0.5	White	98.4	Hmg, Ara
AL-R-4	19° 25' 14.0" N	97° 24' 14.5" W	05/21/2019	Subfossil	≈ +1	White	98.7	Hmg, Ara
AL-R-5	19° 25' 15.1" N	97° 24' 14.7" W	05/21/2019	Subfossil	≈ +4	White	99.5	Ara
Al-Fe-W	?	?	05/24/2019	Subfossil	≈ +2	Brown	96.1	Ara
LP-50cm	19° 22' 12.7" N	97° 23' 1.3" W	05/24/2019	Underwater (oxic)	- 0.5	LP	84.6	Ara
PR-1	19° 22' 20.9" N	97° 22' 57.4" W	05/24/2019	Subfossil	≈ +1	LP	85.7	Ara
PR-2	19° 22' 12.7" N	97° 23' 1.3" W	05/24/2019	Subfossil	+ 0.5	LP	82.3	Ara
PR-3	19° 22' 18.7" N	97° 22' 56.6" W	05/24/2019	Subfossil	≈ +2	LP	76.4	Ara
ATX-C1	19° 20' 12.5" N	97° 26' 55.9" W	05/23/2019	Underwater (oxic)	- 0	Intermediate	92.9	Cal & Ara
ATX-C2	19° 20' 12.5" N	97° 26' 55.9" W	05/23/2019	Subfossil	≈ +1.2	Aquatic	74.7	Ara
ATX-C3	19° 20' 12.5" N	97° 26' 55.9" W	05/23/2019	Subfossil	≈ +2.2	Aquatic	90.3	Ara
ATX-C4	19° 20' 12.5" N	97° 26' 55.9" W	05/23/2019	Volcanic conglomerate	≈ +1.5	Volcanic conglo	~20-25	Cal, Ara
ATX-C5	19° 20' 12.5" N	97° 26' 55.9" W	05/23/2019	Subfossil	≈ +3.7	Aquatic	90.5	Ara
ATX-C6	19° 20' 12.5" N	97° 26' 55.9" W	05/23/2019	Subfossil	≈ +4.7	Aquatic	87.3	Ara
ATX-C7	19° 20' 12.5" N	97° 26' 55.9" W	05/23/2019	Subfossil	≈ +4.9	Aquatic	94.0	Ara
ATX-C8	19° 20' 12.5" N	97° 26' 55.9" W	05/23/2019	Subfossil	≈ +5.2	Aquatic	98.0	Ara
ATX-C9	19° 20' 12.5" N	97° 26' 55.9" W	05/23/2019	Subfossil	≈ +6	Aquatic	91.3	Ara

ATX-C10	19° 20' 12.5" N	97° 26' 55.9" W	05/23/2019	Subfossil	≈ +8	ND.	ND.	ND.
ATX-C11	19° 20' 12.5" N	97° 26' 55.9" W	05/23/2019	Subfossil	≈ +8	Recrystalized	96.3	Cal, Ara
ATX-C12'	19° 20' 12.5" N	97° 26' 55.9" W	05/23/2019	Subfossil	≈ +7.7	Recrystalized	98.8	Ara
ATX-C12	19° 20' 12.5" N	97° 26' 55.9" W	05/23/2019	Subfossil	≈ +8.3	Recrystalized	99.2	Ara
ATX-C13	19° 20' 12.5" N	97° 26' 55.9" W	05/23/2019	Subfossil	≈ +7.4	Recrystalized	99.7	Ara
ATX-C14	19° 20' 12.5" N	97° 26' 55.9" W	05/23/2019	Subfossil	≈ +10	Recrystalized	ND.	ND.
ATX-C15	19° 20' 12.5" N	97° 26' 55.9" W	05/23/2019	Subfossil	≈ +10	Recrystalized	99.9	Calcite
ATX-C16	19° 20' 12.5" N	97° 26' 55.9" W	05/23/2019	Subfossil	≈ +10.5	Recrystalized	99.3	Cal, Ara
ATX-C17	19° 20' 12.5" N	97° 26' 55.9" W	05/23/2019	Subfossil	≈ +10.7	Recrystalized	99.0	Ara
ATX-C18	19° 20' 12.5" N	97° 26' 55.9" W	05/23/2019	Subfossil	≈ +11	Recrystalized	98.1	Ara
ATX-C21	19° 20' 12.5" N	97° 26' 55.9" W	05/23/2019	Subfossil	≈ +10.7	Recrystalized	ND.	Ara
ATX19-5m	19° 19' 55" N	97° 27' 05" W	05/23/2019	Underwater (oxic)	- 5	Aquatic	85.7	Ara
ATX19-10m	19° 19' 55" N	97° 27' 05" W	05/23/2019	Underwater (oxic)	- 10	Aquatic	90.8	Ara
ATX19-15ma	19° 19' 55" N	97° 27' 05" W	05/23/2019	Underwater (mostly oxic?)	- 15	Aquatic	92.4	Ara
ATX19-15mb	19° 19' 55" N	97° 27' 05" W	05/23/2019		- 15	Aquatic	74.4	Ara
ATX19-20m	19° 19' 55" N	97° 27' 05" W	05/23/2019	Underwater (oxic to anoxic)	- 20	Aquatic	78.6	Ara
ATX-R4	19° 19' 52.7" N	97° 27' 13.2" W	05/22/2019	Subfossil	≈ +4	Intermediate	98.6	Cal, Ara
ATX-R6	19° 19' 52" N	97° 27' 12.7" W	05/22/2019	Subfossil	≈ +7	Intermediate	95.0	Ara

9.2. Alchichica microbialites

Two main groups are generally reported in Alchichica: (i) white cauliflower-shaped microbialites composed mainly of hydromagnesite with a thin layer of aragonite at their surface and located all around the lake, and (ii) red/brownish columnar microbialites composed mostly of aragonite and only located on the western shore of the lake (*e.g.* Kaźmierczak *et al.*, 2011; Valdespino-Castillo *et al.*, 2014). However, within that second group, Zeyen (2016) also reports microbialites that are mostly grey, or black and green inside and brown at their surface, and finally some that are red and white inside. Besides, they differentiate fully white hydromagnesite samples from those with a reddish surface.

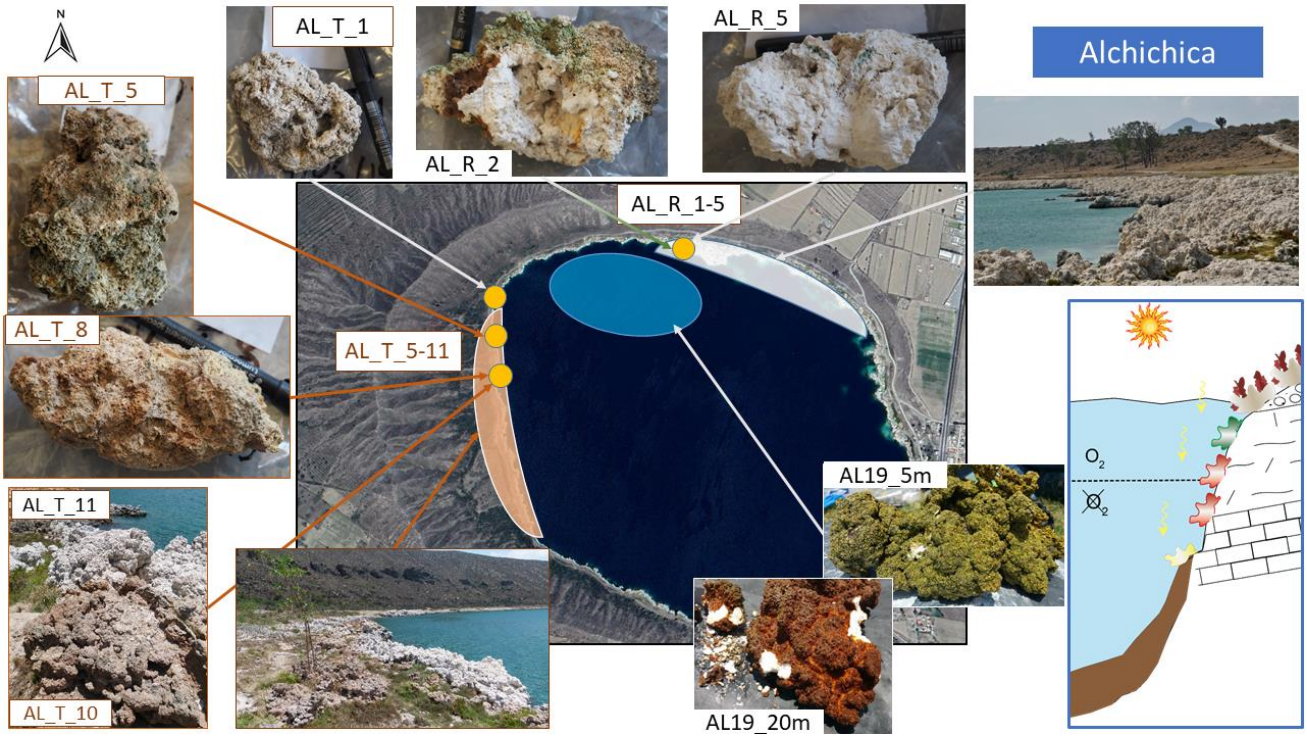

Figure 9.1: Satellite photograph of Lake Alchichica (~1.6 km wide) and representative pictures of the different microbialite macro- and megastructures. 'White' hydromagnesian microbialites are located all around the lake and in the water column while 'brown' aragonitic microbialites are restricted to the western shore.

Our observations converge with those of Zeyen (2016). The location and macro- to microscale characteristics of our samples in Alchichica can be found in Fig. 9.1 and Tables 9.1 and 9.2. The samples were composed almost exclusively of carbonates (from 95 to ~100 wt. %). Among the "cauliflower" hydromagnesite-dominated samples (n=14), some were "homogeneously" white inside as well as at their surface (AL-R-3 to -5) while others were white inside but had colored surfaces (AL-R-1, -2, AL-T-1, -6, -7). One of the samples combined a mix of grey, white, and orange parts (AL-T-11; Fig. 9.2). Overall, these differences in colors were also noticed in the respective proportions of aragonite and hydromagnesite determined by XRD, as well as in thin sections XRF-mapping, where a higher proportion of hydromagnesite and thinner Ca-rich layers corresponded to samples with a more homogeneous white color (see for example AL-R-3 and -R-5 *vs.* AL-T-11 and -R-2; Figs. 9.1, 9.2 and 9.3). On some of these samples, mesoclots typical of thrombolites (Grey and Awramik, 2020) could be found but quickly disappeared into a structure-less matrix below the microbialites' surface.

Figure 9.2: Picture of AL-T-11 microbialite slab.

Among the "columnar" aragonite-dominated samples (n=5), some were orange to green on the inside and surface (AL-T-5, -9, -10), while AL-T-8 was mostly orange, and AL-W-Fe was red-orange at the surface but white inside. These microbialites were mainly structure-less at the mesoscale. For the sake of clarity in the following text, I will still refer to the two main categories as "white" and "brown" microbialites, since they present the most remarkable differences (Table 9.2). Besides, it is important to note that all sampled "living" microbialites (AL-R-2 and samples from 5 to 40 m depths in the water column) belong to the "white" facies (Table 9.1).

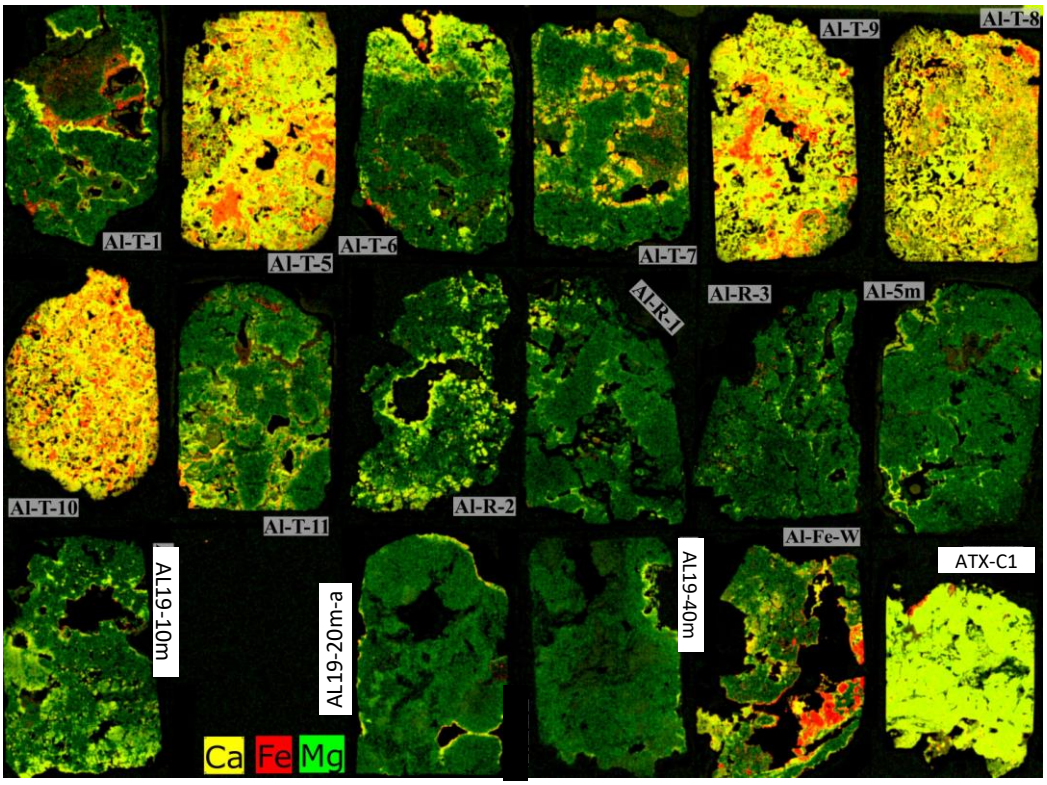

Figure 9.3: X-Ray fluorescence (XRF) maps of the thin sections from microbialites from Alchichica. Yellow, red and green colors reflect the abundance of Ca, Fe and Mg, respectively.

9.2.1. "White microbialites" petrographic facies

At a microscopic scale, "white microbialites" appear to be less porous than brown ones. The porosity of white samples is related to fractures or cavities, which are filled with muds and detrital grains via successive emersion/immersion cycles (Fig. 9.4). In these samples, the organic-rich layers concentrate near the edges of cavities and fractures, and are mostly associated with aragonite (Fig. 9.4b and 9.5; Kazmierzack *et al.*, 2011).

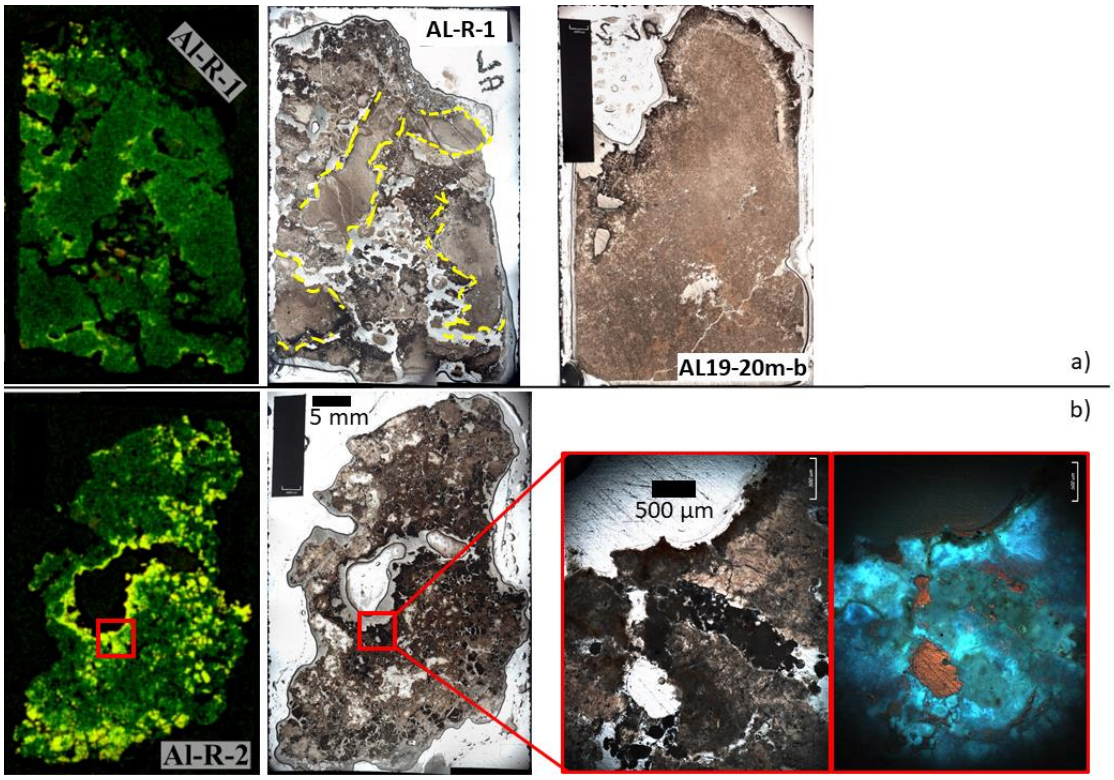

Figure 9.4: Thin sections of AL-R-1, AL19-20m-b (a) and AL-R-2 (b) microbialites seen in X-Ray fluorescence (XRF), visible light and UV-epifluorescence. In 'a', hydromagnesite is present as a homogeneous matrix, except where the microbialite is fractured (outlined in yellow dashed lines for AL-R-1). In 'b' the organic-rich layers in hydromagnesite-dominated microbialites concentrate near the edges of cavities and in the fractures, together with detrital clasts. This corresponds to surfaces where aragonite dominates (see left panel where yellow is linked to Ca expression and green to Mg).

This is consistent with observations from Gérard *et al.* (2013) and Couradeau *et al.* (2013), who concluded on the association between specific cyanobacterial species and aragonite precipitation in these microbialites, and suggested that hydromagnesite could precipitate (at least partly) abiotically. It was also suggested that hydromagnesite progressively replaced aragonite in an early-diagenetic process (Kazmierzack *et al.*, 2011). Accordingly, the inner,

non-porous parts of white microbialites correspond to a more homogeneous carbonate matrix (Fig. 9.4a).

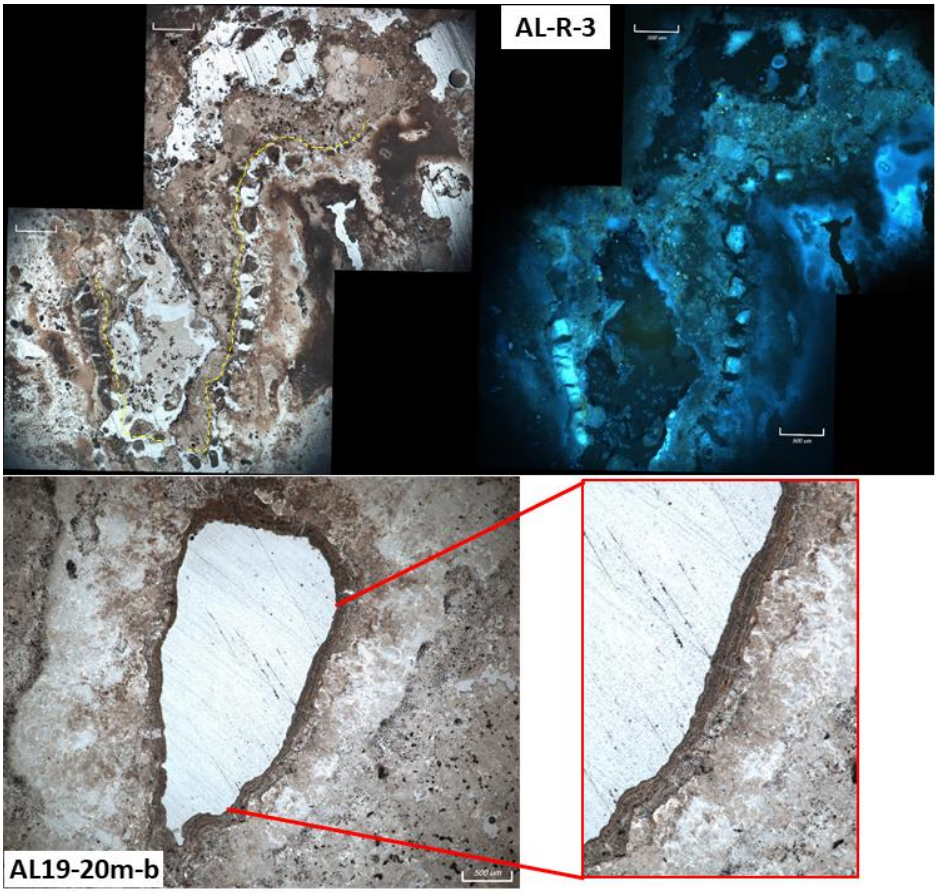

Figure 9.5 : AL-R-3 thin section under plane-polarized light (PPL) and by UV-epifluoresence (top) and AL19-20m-b under PPL (bottom). In AL-R-3, a secondary dark phase following an « S-shape » fills in the fracture and may correspond to a former fracture-filling microbial mat (highlighted in yellow on the left image), as noticed in epifluorescence by the organic-rich nature of this phase. In AL19-20m-b, one can see the superposition of layers, likely microbial mats, covering the surface of a cavity in an otherwise quite homogeneous matrix of hydromagnesite.

Moreover, peloidal hydromagnesian particles are agglutinated and incorporated within the hydromagnesite matrix by a cementation process which fosters the interpretation of a "spontaneous" and abiotic hydromagnesite precipitation in Alchichica (Fig. 9.6). Possibly as a result of the replacement of aragonite by hydromagnesite, biological remnants are very rare in the white microbialites. It can be noted that they were even scarcer in the fully white ones, but slightly more abundant in the samples closer to brown microbialites, *i.e.*, on the western shore. Finally, a replacement of hydromagnesite ($Mg_5(CO_3)_4(OH)_2.4H_2O$) and aragonite ($CaCO_3$) into huntite ($Mg_3Ca(CO_3)_4$) was found in the "living" microbialites at or 20 m below the current

water level. This was evidenced by the PhD work of Jeanne Caumartin and by XRF mapping in Dijon (Fig. 9.7), but the exact origin of this reaction remains to be determined.

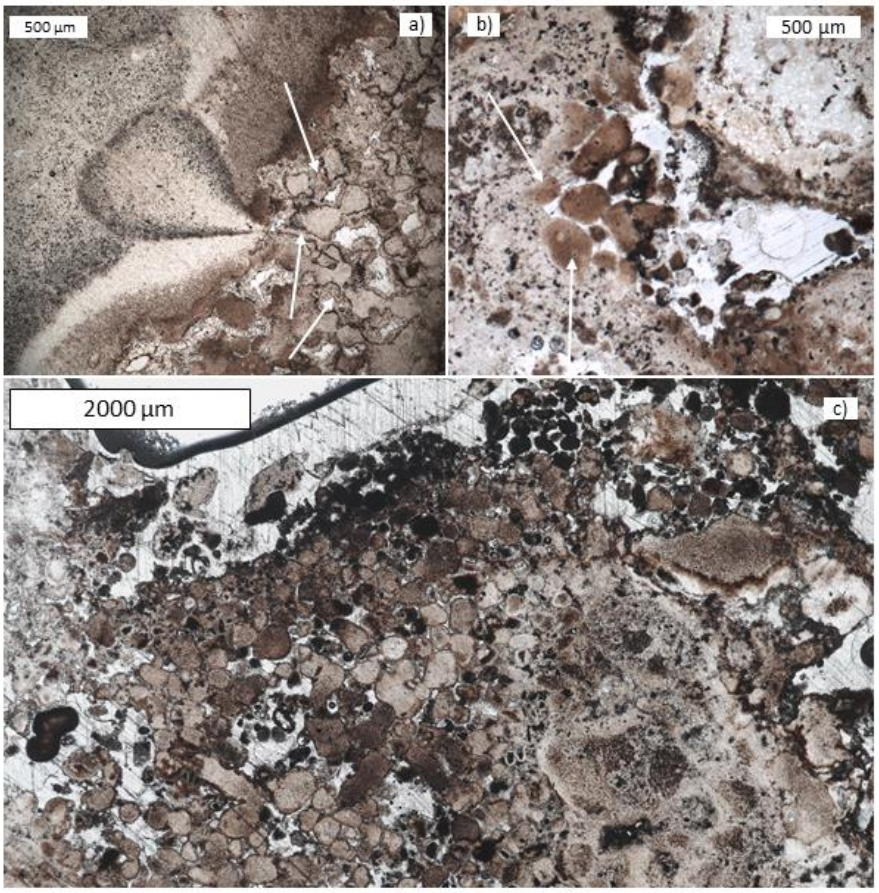

Figure 9.6: Photographs of agglutinating hydromagnesian peloids at the edge of white microbialites in Alchichica, seen under plane-polarized light. a) View of AL-R-1 with evidence of past fluid circulation and cementation around hydromagnesite grains (white arrows). b) View of AL-R-5 with incorporation of hydromagnesian peloids within the microbialites surface (white arrows). c) Similar processes seen in AL-R-3.

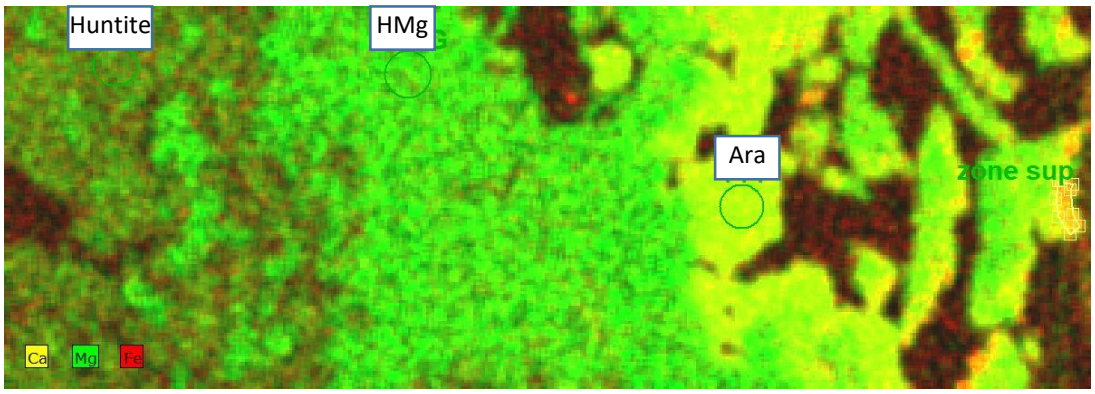

Figure 9.7: X-Ray fluorescence on zoomed area of AL19-40m microbialite. Yellow, green, and red colors reflect the respective abundances of Ca, Mg, and Fe. Note the three distinctive zones in the samples with huntite, hydromagnesite ('HMg'), and aragonite ('Ara') from left to right. Huntite was notably recognized by a characteristic Mg:Ca ratio of ~3.

9.2.2. "Brown microbialites" petrographic facies

"Brown microbialites" harbor smaller areas of mineralized material. This latter consists of detrital grains trapped and bound by microbial mats and/or of cohesive microbial mats themselves, which, on the contrary to "white microbialites", were ubiquitous (Figs. 9.8, 9.9). Part of the porosity consists of holes left by the former presence of insect nests and/or small plant roots or algae (Fig. 9.9d, e, f), which were also visible at a macroscopic scale sometimes.

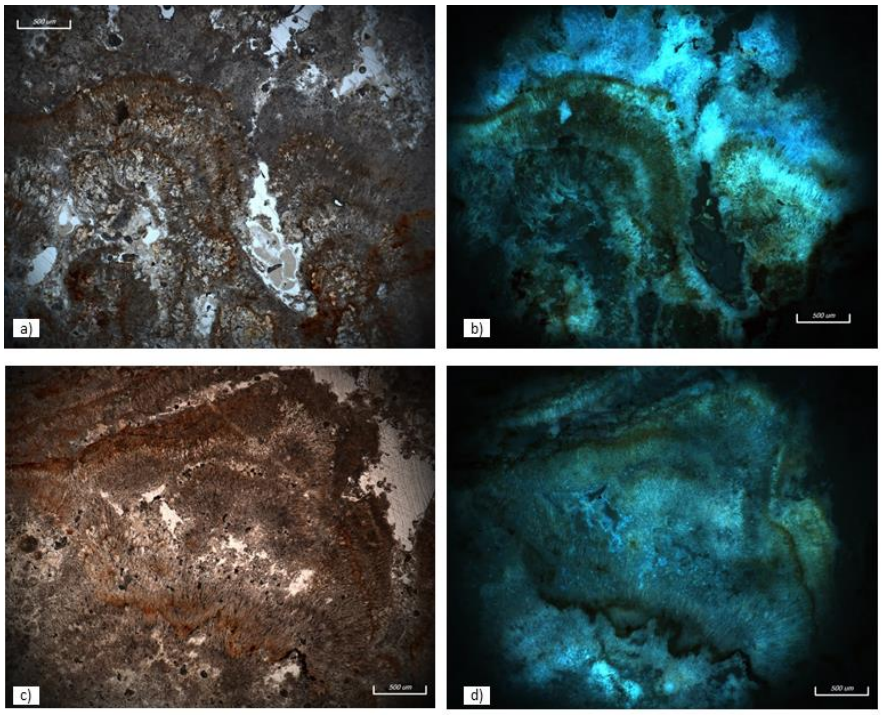

Figure 9.8: Plane-polarized light and UV-epifluorescence photographs of AL-T-9 thin section. They show laminae of filamentous microbial mats forming thick layers and bushes. The fluorescence of the mats is slightly diminished due to post-deposition oxidation of the mats. The white scale bars represent 500 µm.

Additionally, the porosity may be generated by grazing organisms and heterotrophic bacteria, whose traces are pervasive in the brown microbialites. Indeed, numerous remains of ostracod and gastropod shells were found, as well as pyrite framboids contiguous to microbial mats (Fig. 9.9). Therefore, on top of different mineralogical and chemical compositions than the white microbialites, brown microbialites seem to have formed at a different time and/or where local environmental conditions differed from that where white microbialites formed, even though both types can be found next to each other (Figs. 9.9, 9.10). The abundance of these biological remains suggests an ecologically-more dynamic environment, consistent with

a higher number of operationally defined unit (OTUs) found in Alchichica's western compared to northern microbialites (Iniesto *et al*., 2021), although most microbial studies in Alchichica focused on the white microbialite facies. Moreover, the preservation of these biological remains suggests that early diagenetic and/or syn-depositional recrystallization had a smaller effect than in white microbialites.

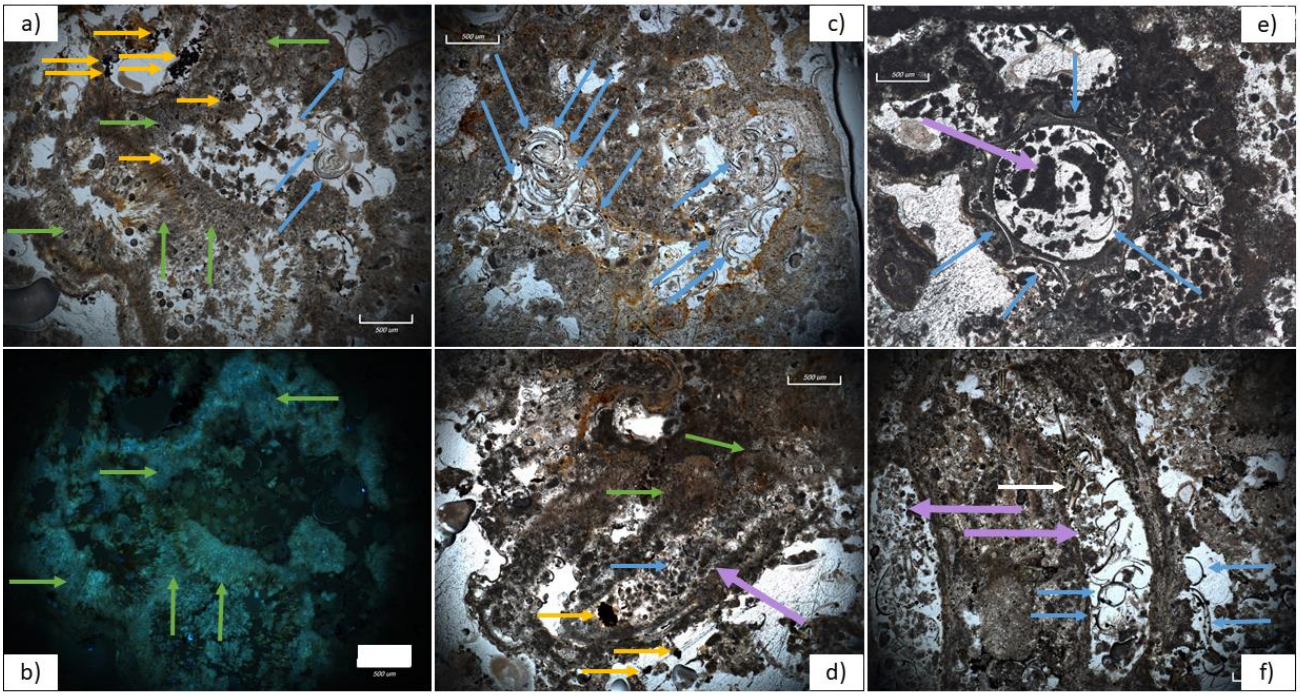

Figure 9.9: Faunic associations and pyrite grains in brown microbialites AL-T-10 (a, b and c) and AL-T-5 (d, e and f). All pictures are seen under plane-polarized light, except in 'b' which was taken under UV-epifluorescence. Blue arrows indicate some of the ostracod shells (and one gasteropod in 'a'). White arrow in 'f' points out a diatom frustule. Yellow arrows indicate the main pyrite framboids (or clusters) but other pyrite grains may be disseminated throughout the thin sections. Purple arrows indicate putative cavities left empty by insect sheaths or plant roots. Microbial filaments are highlighted with the green arrows and can be more or less organized as cohesive mats. Picture in 'b' highlights some of these mats (green arrows); it is noticed that grazers and pyrite grains (yellow arrows in a) are found in between the mats. The white scale bars represent 500 µm.

9.2.3. Relation between the two facies, summary and perspectives

Kaźmierczak *et al.* (2011) argued that the two main microbialite groups reflected different times of formation. They argued that white microbialites bioherms are older (~2.8 ka), and always overlain by younger brown microbialite structures (~1.1 ka) that would have formed during a period of high-water level in the lake. However, while an age difference is not to be

excluded, it would not explain the localization of brown microbialites only on the western shore of Alchichica. Besides, the distribution of both microbialite structures is more complicated – even without considering the subgroups within the white and brown microbialites – and rather seems to follow a pattern where white ones grew around but not necessarily underneath brown ones (Fig. 9.10e, f). The western side of the crater is the highest and steepest, and large areas of red scories and pyroclastic deposits are outcropping (Figs. 9.1; 9.10a, b, c; Chako-Tchamabé *et al*., 2020). Thus, alteration of these volcanic deposits by meteoric fluids followed by their infiltration and/or runoff could have locally influenced the water chemistry where brown microbialites formed. Additionally, on the southern side of the crater, bubbles were emerging from brown columnar microbialites and are indicative of out-flowing groundwaters and/or degassing volcanic gases (Fig. 9.10g, h). Thus, this facie may also be influenced by this type of local fluids circulation.

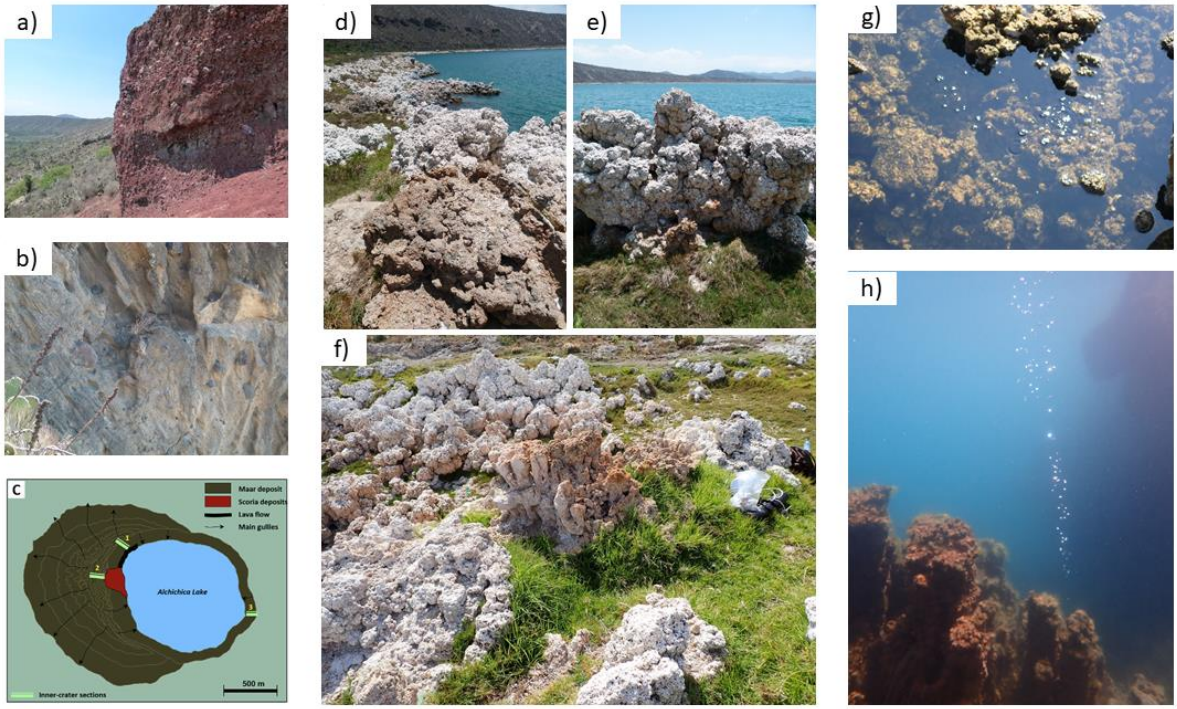

Figure 9.10: Pictures of the volcanic deposits (a-c), emerged white and brown microbialites (d-f) and immerged brown microbialites on the western/south-western shore of Lake Alchichica. a) Red scoria deposits, b) pyroclastic deposits (with ashes, lapilli and volcanic bombs). c) schematic map from Chako Tchamabé *et al*. (2020) showing the main location of the red scoria outcrop. d-f) Contiguous subfossil white and brown microbialites from the western shore showing white microbialites overlying or surrounding brown ones. g and h) Dense bubble emissions from brown microbialites. a, b, d and e photographs from C. Thomazo (2019), f from E. Vennin (2022), g and h from P. Boussagol (2022).

In summary, the two microbialite types seem to reflect temporally and/or spatially distinct environmental conditions of formation, where the "brown facies" would have grown in more productive waters, favorable to a more important biological activity, with notably a lot of heterotrophic organisms thriving in the microbialite structures. Additionally, a more important effect of diagenesis and/or syn-formation secondary precipitation in white microbialites seems to further differentiate them from the brown ones. This classification is summarized in Tables 9.1 and 9.2. In chapters 10 and 11, I will try to assess how much these observations are backed up and the interpretations deepened based on isotopic data. Besides, a further sedimentological and petrographic description effort initiated after the field work of 2022 should also improve our understanding of these complex objects.

ALCHICHICA microbialites	
'White' located all around the lake (and actively forming in the water column). ~ 85 and 14 wt. % hydromagnesite and aragonite. low porosity: mainly from fractures and macro-cavities. large areas of isopachous, structure-less hydromagnesite, possibly as syn-formation secondary recrystalization. aragonite precipitates as crusts on the edges. epifluorescence and organic remains mainly limited to the edges (where aragonite is). samples close to brown microbialites (western-shore) have slightly more biogenic remnants. further recrystalization of 'Ara' and 'HMg' into huntite below 20m in depth.	**'Brown'** only located on the western shore of the lake. ~ 96 wt. % aragonite. high porosity: loosely aggregated mat fragments and peloids + holes from plants/insects. some early isopachous cements between peloids. ubiquitous remains of living organisms (ostracods ++; filamentous microbial mats). pyrite grains and framboids frequently found. not sampled under-water.
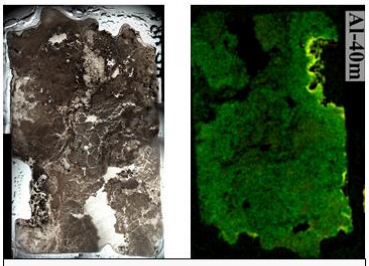 AL_R-1 to -5 AL_T-1, T-6, -7 and AL_T-11 AL-5m, -10m, -20ma, -20mb, -40m	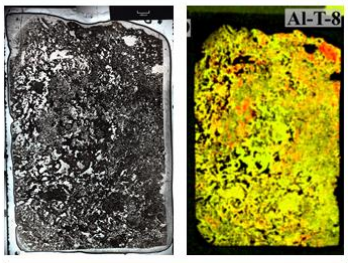 AL_T-5, AL_T-8 to -9 AL_W_Fe

Table 9.2: Summary of the microbialites classification in Alchichica with their main characteristics. Refer to Figure 9.1 for samples location. In XRF-scans, yellow, red and green reflect Ca, Fe and Mg abundances, respectively.

9.3. Atexcac microbialites

The sampling of a 11 m-tall log-section of subfossil microbialites (*i.e.* already emerged) on the N-NE crater wall of Atexcac (ATX-C1 to -C-21), together with immerged samples (from 5 to 20 m in depth), enables a first order description of the different formation stages, early diagenetic processes, and recrystallization history in Atexcac microbialites (Fig. 9.11; Table 9.3). The crater in Atexcac is much steeper than in Alchichica or La Preciosa, and microbialites develop mostly as large encrustations and mounds capping the crater walls (Fig. 9.11).

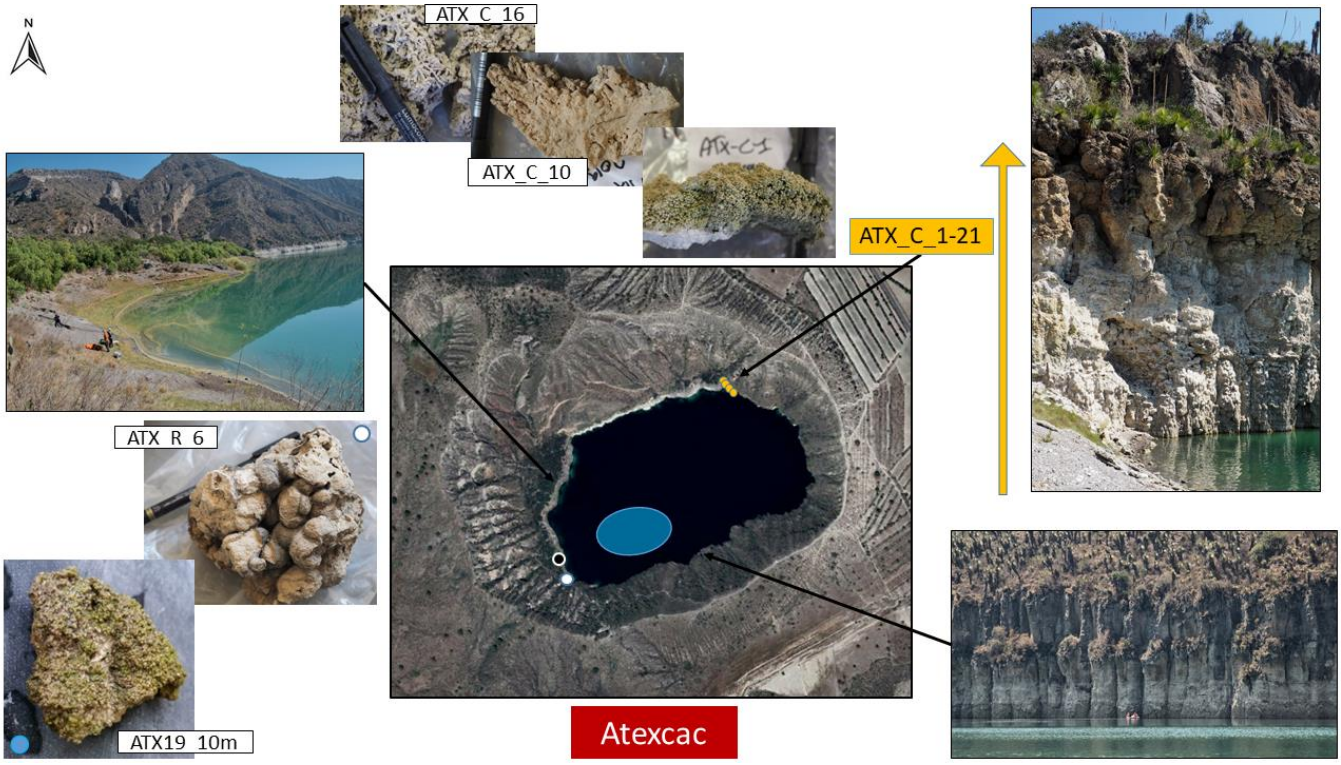

Figure 9.11. Satellite photograph of Lake Atexcac (~0.8 km wide) and representative pictures of the different microbialite macro- and megastructures. Microbialites forming crusts and mounds cover the crater walls on a height of ~11m. A microbialite log-section from within 50 cm in the water to up to 11 m above the water was sampled on the north-eastern side (ATX_C_1-21). Microbialites from 5 to 20 m down the water column were sampled near the south-western area (blue area). A few other emerged samples were collected from this side in two main locations (ATX-R-1-6).

At the macro-/mesoscale, samples underwater or emerged from less than 6 m above the current water level (cwl) were covered by more or less eroded mesoclots typical of thrombolites (Grey and Awramik, 2020), but quickly appeared structure-less below the crust. On the other hand, samples 6 m above cwl (*i.e.* above ATX-C9) lost their thrombolytic structure and appeared more eroded and altered. In the following, I will show that this broad distinction also corresponds to two main petrographic facies at a microscopic scale, hereafter referred to as the "Aquatic facies", and "Recrystallized facies" (Tables 9.1, 9.3). The former includes microbialites that were either in the water column or emerged up to ~6 m above cwl (ATX-C9), and the latter corresponds to microbialites emerged of more than 6 m above cwl (ATX-C9).

9.3.1. "Aquatic" petrographic facies

In this facies, the carbonate content was mostly between ~75 and 94 wt. % and consisted almost exclusively of aragonite (Table 9.1). But these microbialites also contained detectable Mg-silicate phases evidenced by XRD and XRF up to ~6 m above cwl (Fig. 9.12, 9.13).

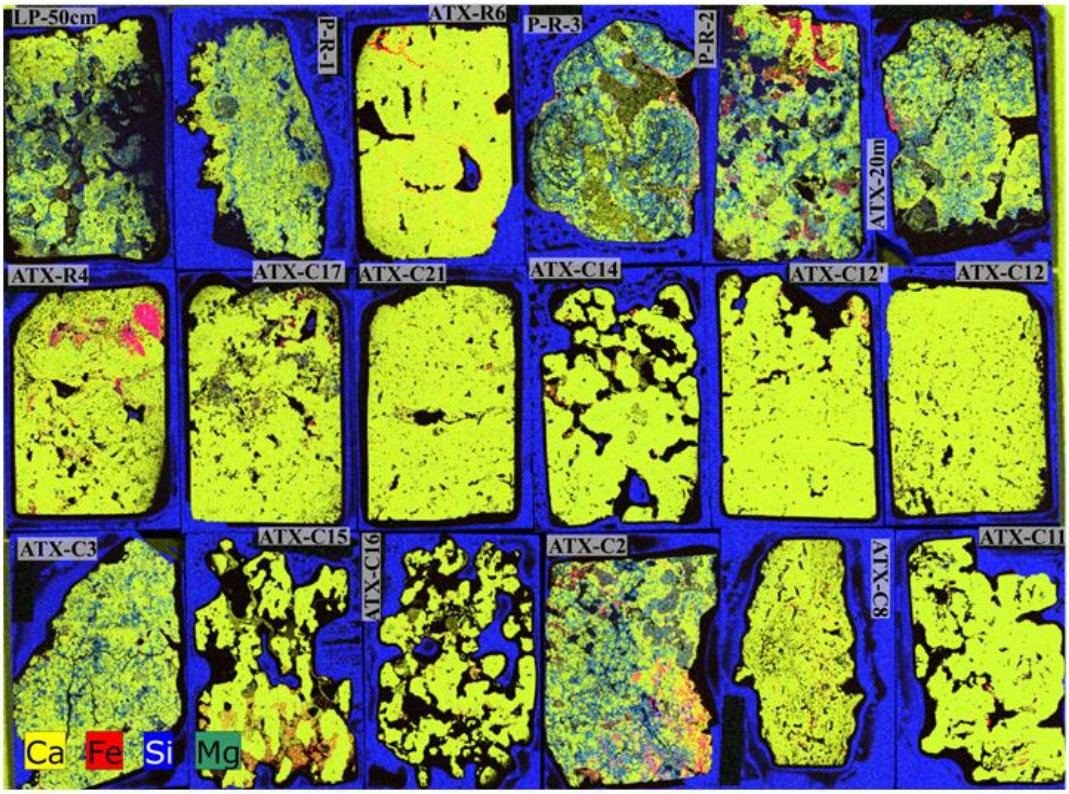

Figure 9.12: X-Ray fluorescence scans of the thin sections from Atexcac and La Preciosa microbialites. Yellow, red, blue and green colors reflect the abundance of Ca, Fe, Si and Mg, respectively.

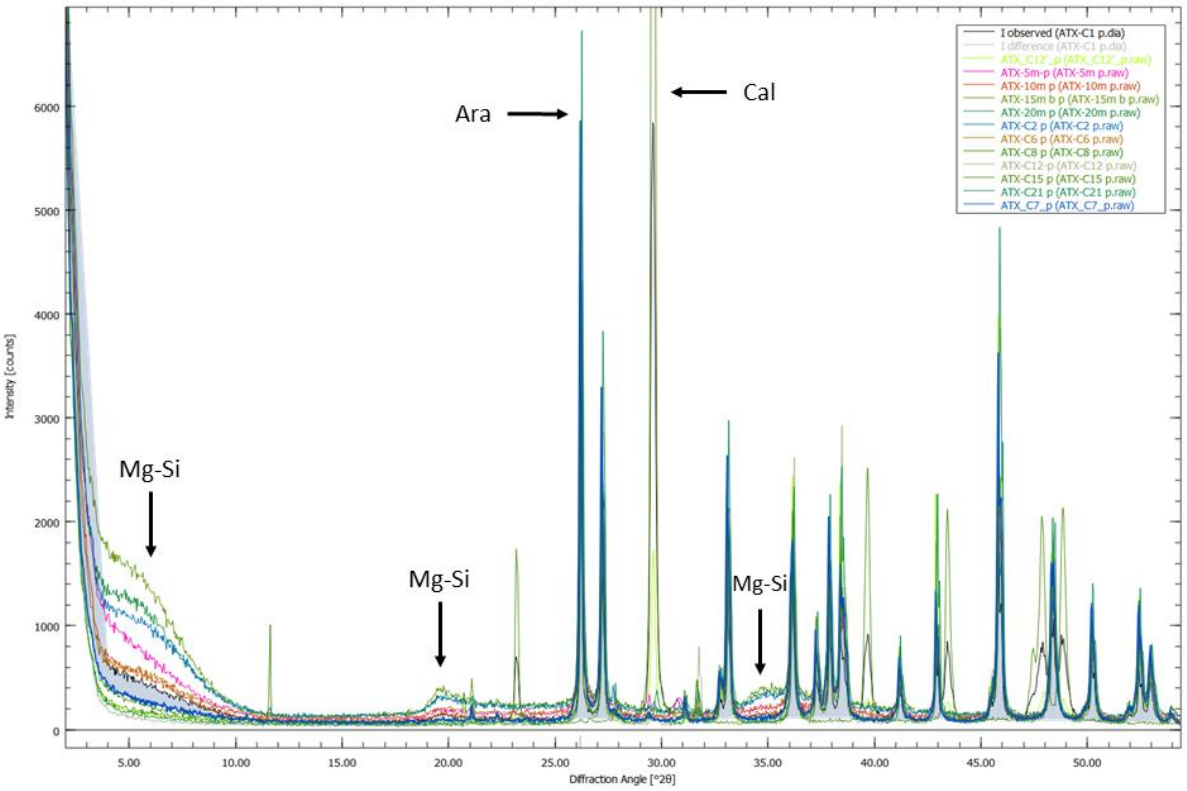

Figure 9.13: Selection of X-Ray diffraction profiles for the microbialite log section from the N-E side of Atexcac. The principle phases are aragonite ('Ara'), kerolite ('Mg-Si'), and calcite ('Cal'), and their main peaks are shown with the black arrows. In these diffractograms, calcite is significant only for ATX-C15, -C12' and C1. In blue, ATX-C7 is highlighted because it is the first sample where Mg-silicates significantly decreased but definitely disappeared below ATX-C9. The peak at ~11.5° 2θ corresponds to brushite ($CaHPO_4.2H_2O$) present in ATX-C8.

The Mg-silicate phases likely correspond to authigenic kerolite ($Mg_3Si_4(OH)_{10}$) which was previously described in Atexcac microbialites, sometimes in replacement of abundant diatom frustules or biofilms, thereby favoring the preservation of microfossils (Zeyen *et al.*, 2015). Diatom frustules were indeed found in abundance in samples immerged from 20 m below cwl, up to samples emerged by at least 8 m above cwl (Fig. 9.14), as well as remains of coccoidal and filamentous bacteria (Fig. 9.15). However, Mg-silicates are mostly replaced by ~4.7 m above cwl, and virtually absent ~6 m above cwl. This is evidenced by the progressive disappearance of corresponding XRD peaks (Fig. 9.13) and of the blue and green colors characterizing Si and Mg elements in XRF scans (Fig. 9.12). From XRF scans, it can also be noticed that this transition leads to a decrease of the porosity (see the difference between ATX-C3 and ATX-C8; the special case of ATX-C14, C15 and C16 is discussed below). It was suggested that Mg-silicates could act as precursor phases before abiotic replacement by aragonite and loss of the biogenic signature (Burne *et al.*, 2014). However, here, in agreement

with Zeyen *et al.* (2015), well-preserved remnants of diatoms and microbial cells in aragonite replacement material are found (Fig. 9.14c, d and Fig. 9.16). While organic matter is closely associated with Mg-silicates (Zeyen *et al.*, 2015), microscopic observations show that an important organic content, and biogenic structures are also preserved into the aragonite matrix up to 5.2 m above cwl (ATX-C8, where Mg-silicates are mostly gone) (Fig. 9.15c, d). These observations imply that organic remnants are first used as templates and incorporated in the preliminary Mg-silicates (Zeyen *et al.*, 2015; Jaramillo-Vogel *et al.*, 2019), and then are replaced by aragonite. This latter seems to precipitate mostly following the preexisting microbial textures (and Mg-silicates) (Fig. 9.15b-d), although this aragonite matrix sometimes appears as isophachous and structure-less (Figs. 9.15e; 9.17a, b, e).

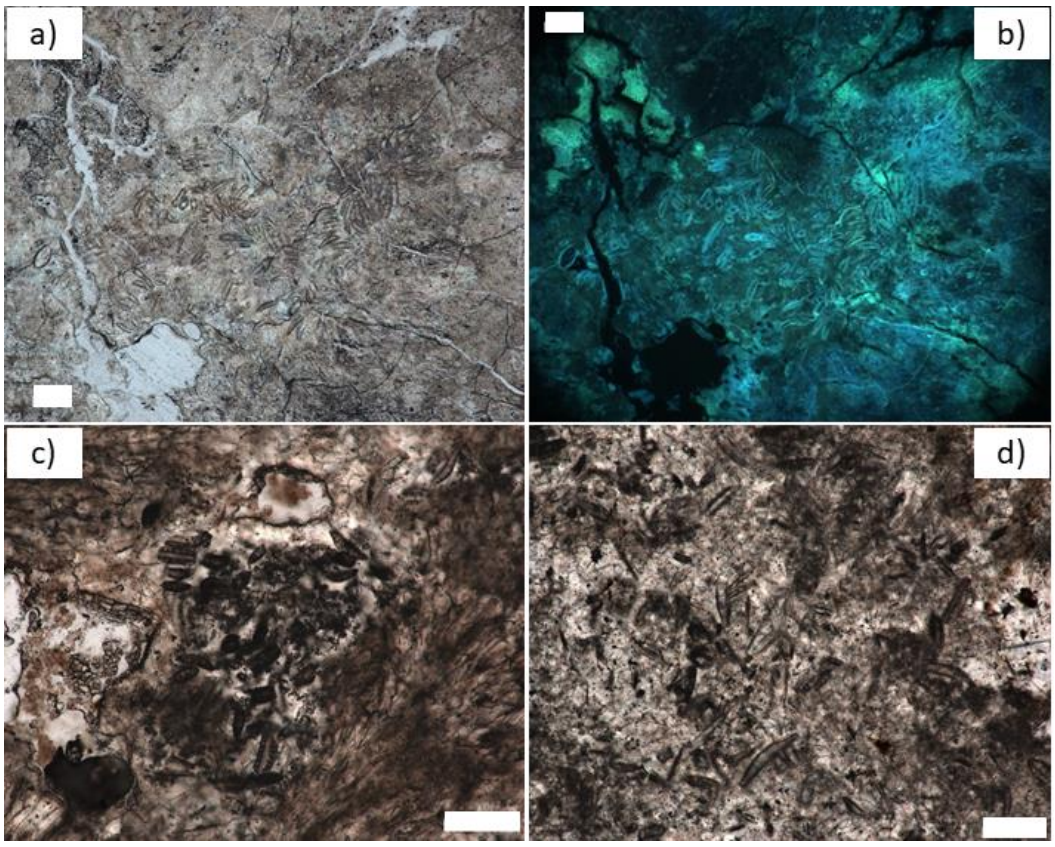

Figure 9.14. Photographs of encrusted diatoms in ATX-20m, ATX-C11, and -C1. A) and b) represent ATX-20m thin section under plane-polarized light (PPL) and UV-epifluorescence; c) and d) represent the thin sections of ATX-C11 (+8 m) and ATX-C1 (-0 m), respectively, under PPL. In 'c', the remnants of filamentous bacteria in the bottom right corner of the picture are also noticed. White scale bars represent 100 µm.

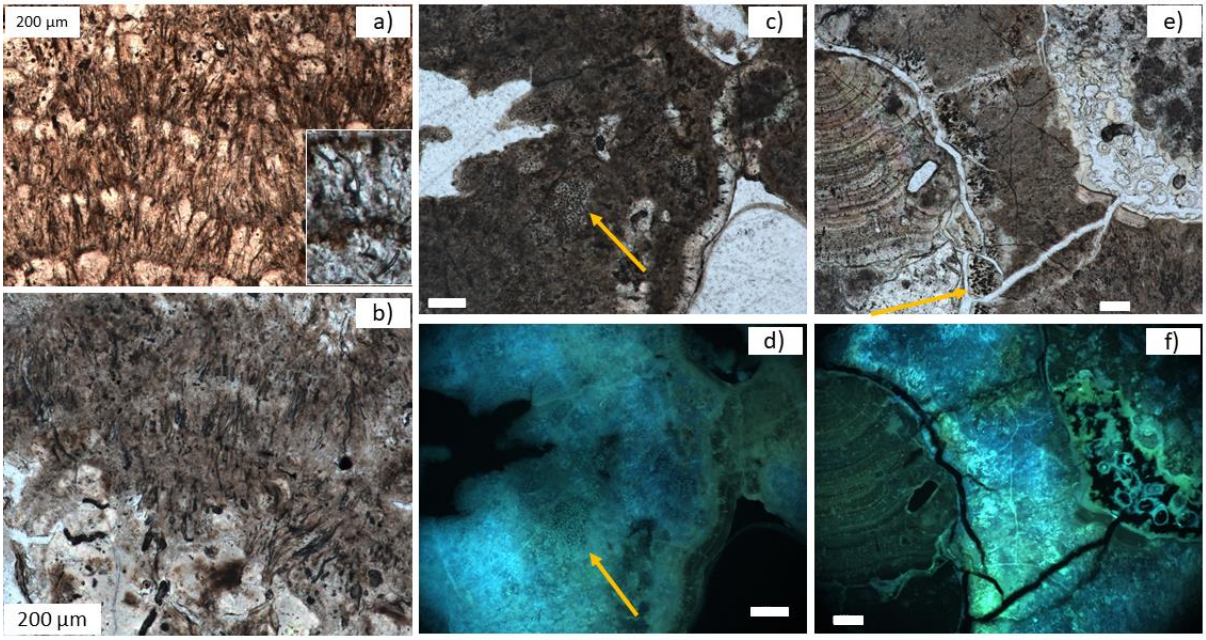

Figure 9.15: Photographs of encrusted filaments and putative coccoids in ATX-R6, ATX-C8 and ATX-20m. a) Filaments in ATX-R6, possibly the stacking of successive mats. The white frame is a zoom in a similar structure of the same sample (frame's width is ~140 µm). b) Filaments in ATX-C8. C) and d) Putative coccoids in ATX-C8 pointed out with the yellow arrows under plane-polarized light (PPL) and UV-epifluorescence; e) and f) Putative coccoids in ATX-20m pointed out with the yellow arrows, next to a botryoidal fabric suggesting emersion and secondary precipitation. White scale bars represent 100 µm unless specified.

Figure 9.16: Preservation of biogenic structures in aragonite microbialites from ATX-C17 (a-d) and ATX-R6 (e-g). a) Photograph under plane-polarized light (PPL), and b) UV-epifluorescence showing the absence of organic remains. C) Zoom in from the red frame in 'a' showing mineralized diatoms frustules. D) XRF map of the full ATX-C17 thin section. E) Zoom in ATX-R6 thin section under PPL and f) UV-epifluorescence showing a weak preservation of organic matter despite the preservation of microbial filament sheaths (except a remaining small bright portion of a mat). G) XRF map of the full ATX-R6 thin section (yellow=Ca, red=Fe, green=Mg, blue=Si). White scale bars represent 150 and 300 µm in top and bottom panels, respectively.

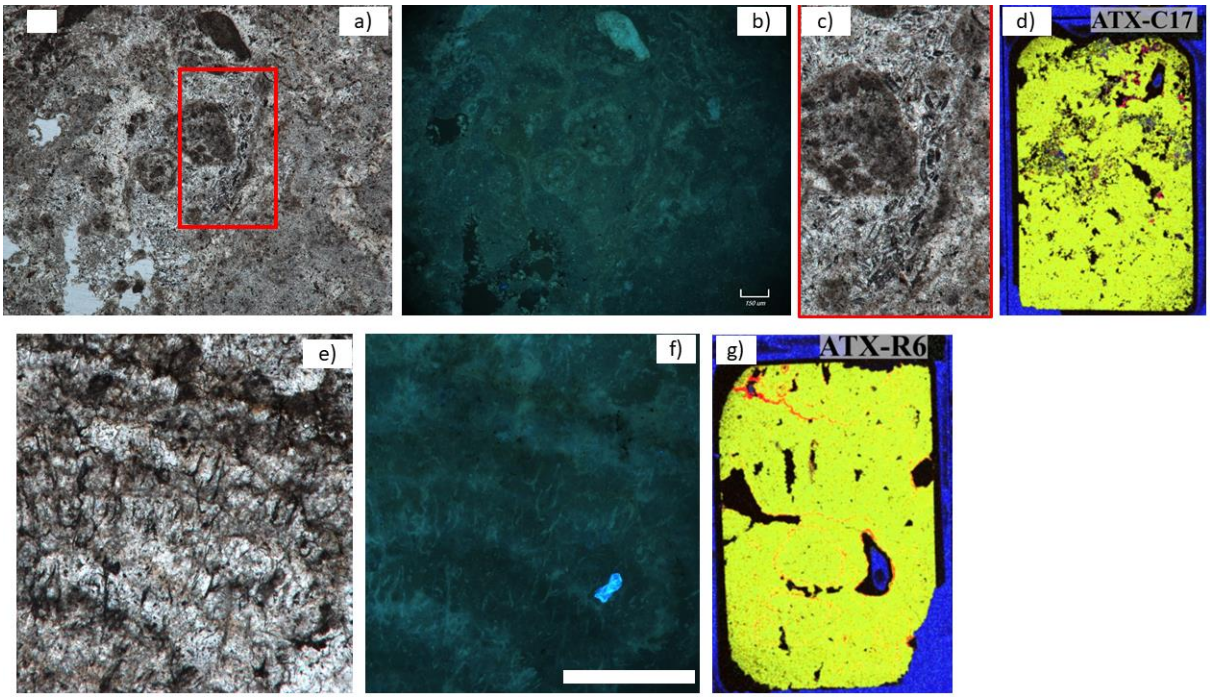

In ATX-20m, ATX-C1, -C2 and -C3, an additional and different fabric, typical of emersion periods is found (Fig. 9.17). This fabric is mostly circular-shaped or botryoidal-like, but can be found as flat laminae. It appears as pending and in-filling cavities, usually growing on past microbial mats. It can be covered by detrital muds and particles, or by a subsequent microbial mat, and sometimes is delimitated by oxidized layers (Fig. 9.17). Altogether, these features are characteristic of cyclic emersion/immersion patterns, and thus of the lake level fluctuations. For ATX-C1 to -C3, this is consistent with the fact they are located close to the current water level. In the case of ATX-20m, microscopic evidences suggest that the microbialite actually originates from a position closer to the lake's water surface, and recently fell to its current depth. This is evidenced by the occurrence of the "emersion botryoids", subsequently overlapped by muds, detrital particles and diatoms. No thin section was made from the other immerged microbialites. Thus, they cannot be described and characterized as ATX-20m. However, their mineralogy – containing both aragonite and Mg-silicates – and location in the water column are consistent with them belonging to the "aquatic facies".

In summary, the “aquatic facies” (up to ~6 m above cwl) is mainly characterized by the preservation of numerous traces of biological activity and a relatively important porosity. However, it already records several phases of mineral precipitation, and the biological remains can be highly mineralized.

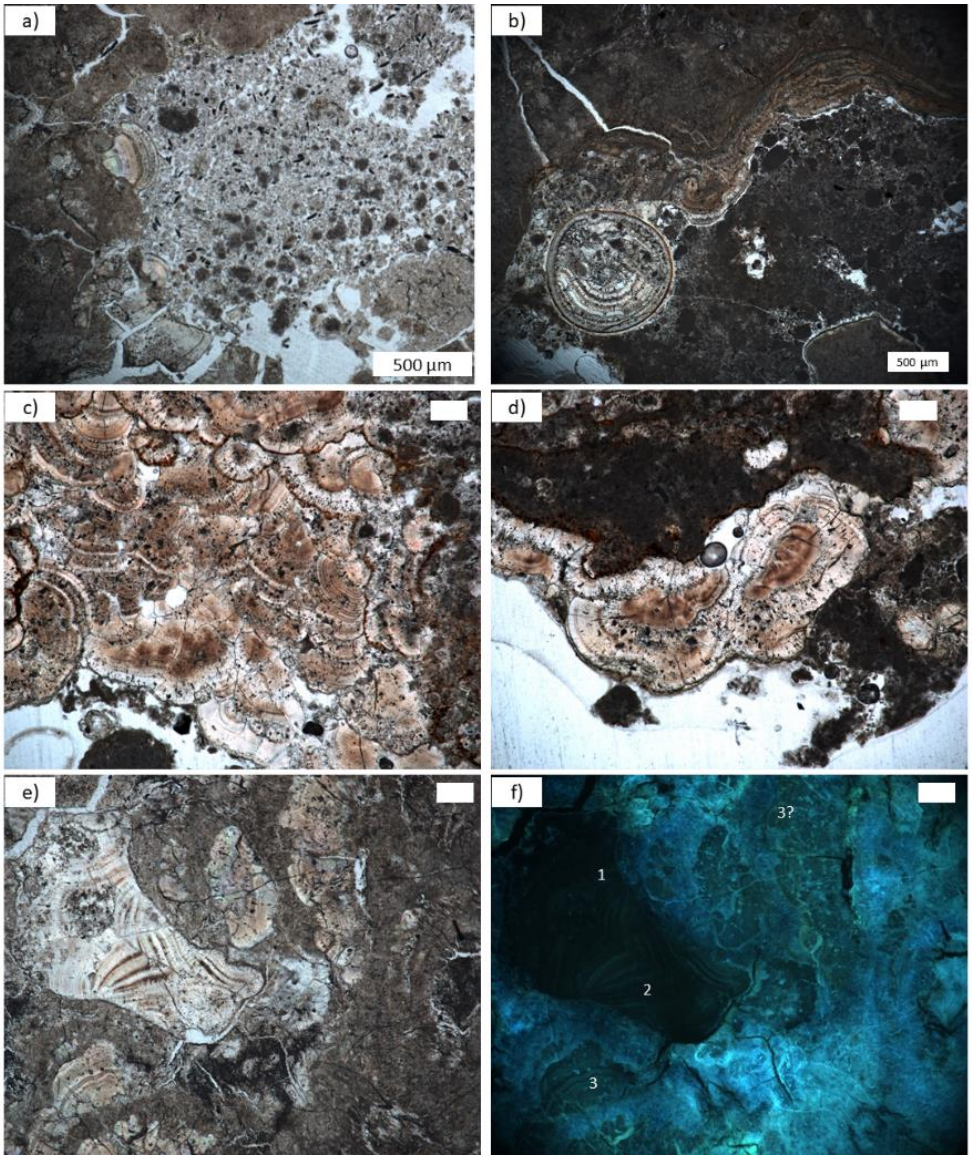

Figure 9.17: Photographs of « emersion botryoids » in ATX-20m (a), ATX-C2 (b), ATX-C1 (c and d) and ATX-C3 (e and f) under plane-polarized light and UV-epifluorescence. In ‘a’ are shown pending botryoids that were recovered by mud, diatoms and other particles after re-immersion. White scale bars represent 15 µm unless specified. In ‘b’, it can be seen that this secondary aragonite material may form laminae at the microbialites surface and replace the interior of a gastropod. The laminae were recovered by detrital particles following re-immersion. In ‘c’ and ‘d’, circular botryoids stack on top of each other and can be delimitated by oxidized surface and/or the recovery of a microbial mat. In ‘e’ and ‘f’ these botryoids in-filling cavities, and potentially being dissolved by and/or replacing the microbial mats. Under UV-light, at least three generations of these botryoids can be seen, once again showing the cyclicity of emersion/immersion cycles.

9.3.2. "Recrystalized" petrographic facies

Above ATX-C9, microbialites consist almost exclusively of aragonite or calcite, with total carbonate content mostly ≥ 99 wt. %. At a microscopic scale, new petrological fabrics consisting of a variety of crystal fans and botryoidal structures appear. In some samples, they cover almost the entire thin section (*e.g.,* ATX-C12'), while in other samples they are contiguous and interspersed with remaining organic-rich patches/layers (*e.g.,* ATX-C21).

The botryoids are made of euhedral elongated aragonite crystals, sometimes shaped like needles (B1 in Fig. 9.18). They contain abundant mineral inclusions and can size to > 1mm. Occasionally, these fibrous botryoids coalesce and form a continuous proto-lamination (A2 in Fig. 9.18). In that case, they can record growth lines (A1 in Fig. 9.18), which are possibly linked to cyclic environmental changes during "abiotic" precipitation stages (Jaramillo-Vogel *et al*., 2019). More often, they form irregular contacts between each other, and stack on top of each other. Thus, at a very local scale, they are randomly organized, but at the scale of the full thin section, they follow a similar general orientation and form an "irregular lamination" (*cf*. Jaramillo-Vogel *et al*., 2019; B2 and B3 in Fig. 9.18 and 9.19). This proto-lamination contrasts with the structure observed in stratigraphically lower samples pointing out the recrystallized nature of the carbonate fabric in microbialites above 6 m.

The botryoids and crystal fans are usually delimitated by a darker layer (Figs. 9.18 and 9.19) which likely corresponds to a degraded biofilm inherited from previous microbial mats. This underlines the role of microbial mats as nucleation points (*e.g.* B1, B2 and B5 in Fig. 9.18), although the precipitation mechanism of these euhedral crystals is bolstered by physico-chemical saturation of the medium water (Jaramillo-Vogel *et al*., 2019). Moreover, this process of massive aragonite precipitation tends to erase the traces of a former biological presence (Kremer *et al*., 2012; Jaramillo-Vogel *et al*., 2019). Consistently, a predominant loss of microbial textures is observed above ATX-C8, and only a few pristine traces of biogenic remnants can be found (Fig. 9.16 and 9.18) and are mostly associated with the more preserved organic-rich aragonite matrix. Previous studies described a micritization process of carbonated microbial mats, by which the disintegration of preliminary carbonate material produces fine grains down to a nanocrystal size (Pratt, 1982; Ge *et al*., 2021). Ge *et al*. (2021) further suggested that these nanocrystals can then be aggregated again to form aragonite botryoids and spherulites in microbial mats from Abu Dabi. From that, it is tempting to assume that micritization of the "aquatic" facies occurs first, and is then followed by a recrystallization as

botryoids or spherulites. Therefore, it is not primarily replacement of Mg-silicates by aragonite that erases the microbialites primary biogenic features (*cf.* Burne *et al.*, 2014), but the subsequent reprecipitation of aragonite (potentially by the combination of micritization and then recrystallization).

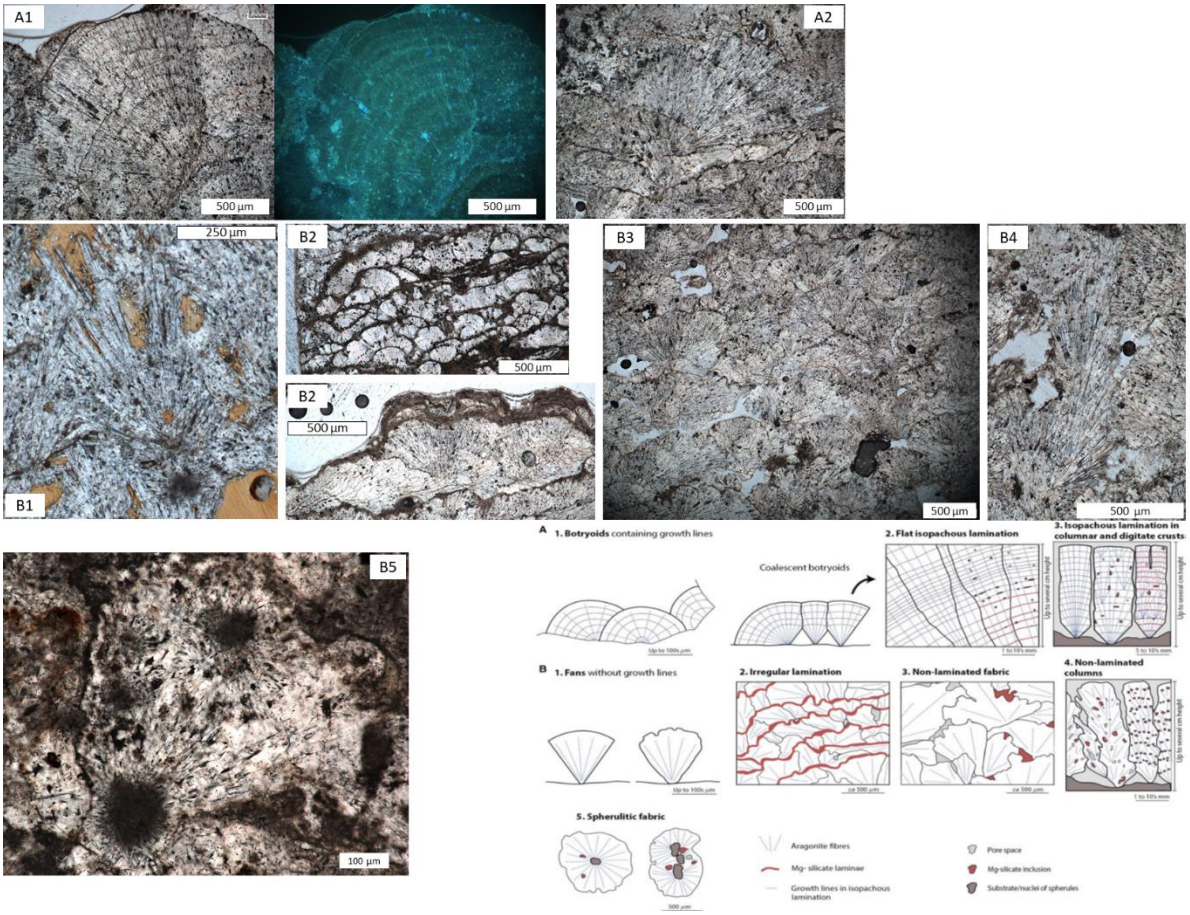

Figure 9.18 : Different botryoidal and spherulitic aragonite fabrics of the « recrystalized » and « intermediate » facies in Atexcac. The nomenclature refers to the classification sketched in the bottom right corner. This nomenclature and the sketches were taken from Jaramillo-Vogel *et al.* (2019). An important difference between our samples and the sketches from Jaramillo-Vogel *et al.* (2019) is that the darker/organic-rich layers and patches in our samples (*e.g.* in B2 and B3) are mostly devoid of Mg-silicates, which have already been replaced at this stage. Moreover, the flat isopachous lamination (A2) is at a preliminary stage in Atexcac. A1 from ATX-C12' ; A2 from ATX-C21 ; A1 from ATX-R4 ; B2 from ATX-C1 & ATX-C12 ; B3 from ATX-C12 ; B3 from ATX-C12 ; B5 from ATX-C1.

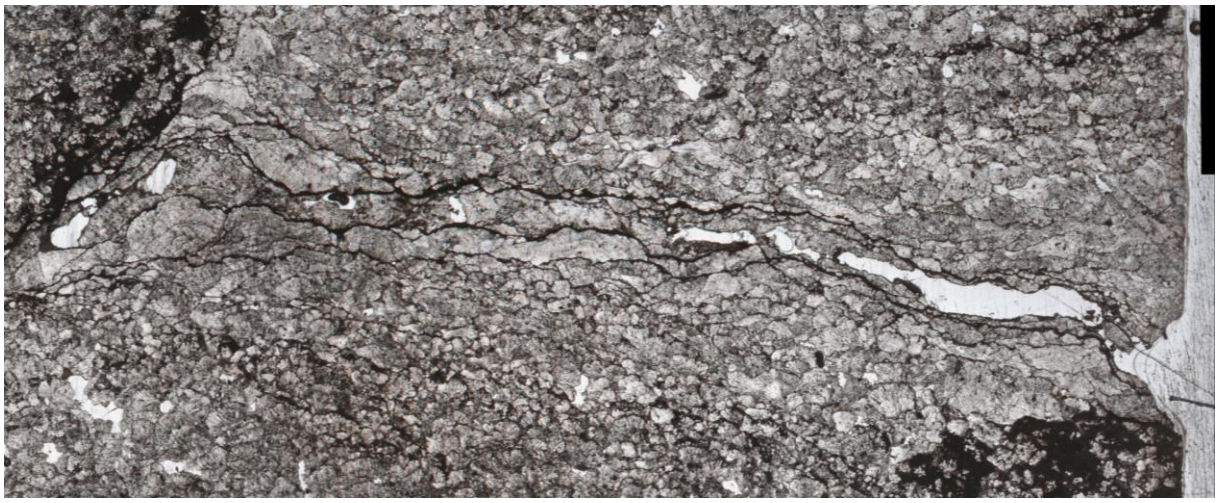

Figure 9.19: Zoom in the full ATX-C12′ thin section scan. Note the general orientation of the botryoids in the bottom part going upward, and those from the upper part going downward.

Very similar fibrous botryoidal structures have been seen in Pleistocene formations at a microscopic scale (*e.g.* Jaramillo-Vogel *et al*., 2019; Vennin *et al*., 2019; Fig. 9.18), and are common in Precambrian microbialites at a macroscopic scale (*e.g.* Sumner, 2002; Sumner and Grotzinger, 2004; Riding, 2008). These radiating crystal fan structures are generally seen as primary precipitates in origin, but have also been suggested to be secondary replacement material in some occurrences (*e.g.* Ge *et al*., 2021). In Atexcac, some of these precipitates clearly replace and overprint the initial microbial structures (Fig. 9.20 and discussion above), while some others are found to grow within the microbialites cavities (in agreement with the observed diminution of porosity above ATX-C8; Figs. 9.12, 9.20). Therefore, although the pervasive distribution of these botryoids, and the contrast with stratigraphically lower samples foster a secondary origin, a clear distinction from a primary formation cannot be fully resolved here. It is possible that both primary and secondary botryoids co-exist.

Some samples (ATX-C11, -C14, -C15 and -C16) were impacted by physical and chemical erosion linked notably to plant roots, and potentially insect nests like caddisflies (Fig. 9.21a). This is not surprising considering the proximity of abundant vegetation near the samples log section (Fig. 9.11). These samples also contain beautiful coprolites (Fig. 9.21d). Interestingly, these samples were also distinguished by the fact they were composed of more than ~90 % calcite, as evidenced by XRD analyses. This strongly suggests that the initial aragonite dissolved and reprecipitated as calcite. Moreover, it would also explain the reshaping of the microbialites macrostructure into thin shruby/chimney-like structures (Fig. 9.21c).

In summary, the “recrystallized facies” are mainly characterized by a more eroded macro-/meso-scopic structure (loss of the clotted fabric), and a change in the thin sections general aspect (less fractured and brighter than the “aquatic thin sections”). Moreover, at the microscopic scale, recrystallization fabrics become prominent, and biogenic structures are predominantly lost.

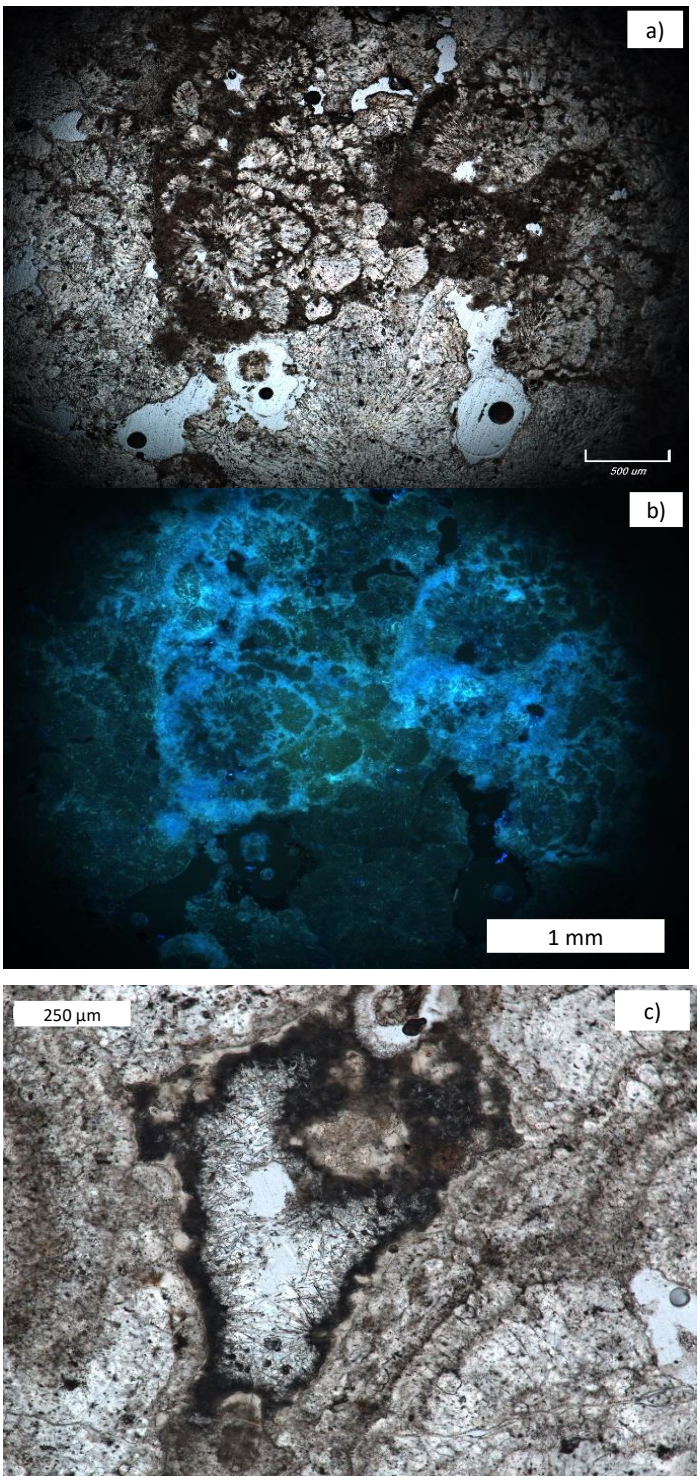

Figure 9.20: Photographs of ATX-C12 (top) and ATX-C1 (bottom) thin sections under plane-polarized light and UV-epifluorescence. a) Some remains of microbial mat are progressively replaced by the aragonite botryoid matrix. b) Same image as in ‘a’ under the UV-light, carbonates harbor different degrees of « extinction » whereas the mats harbor a bright blue color. c) In ATX-C1, aragonite needles precipitating towards the center of a cavity and nucleating on the microbial mat that recovers the cavity. From the outside isopachous matrix, it suggests that the cavity used to be larger than it currently is.

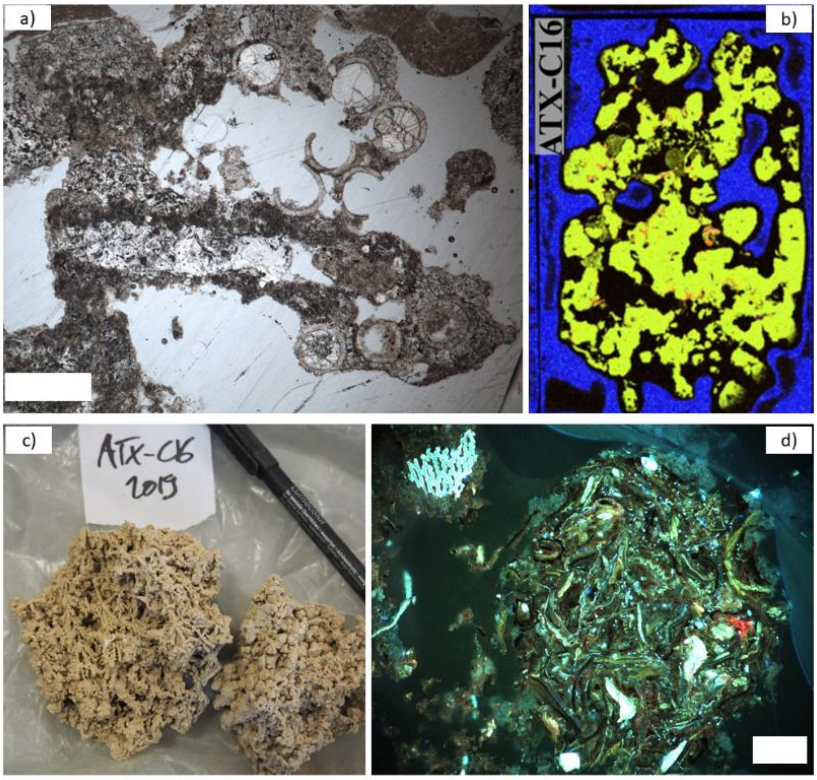

Figure 9.21. Pedogenetization, dissolution and reprecipitation in ATX-C16. a) Plane-polarized light photographs, with a caddisfly remain and former roots filled with calcite replacement material. b) X-Ray fluorescence map of ATX-C16 thin section, depicting a very significant porosity and a mineral matrix composed of $CaCO_3$. c) Photograph of ATX-C16 macroscopic sample. One can see the formation of small calcite « filaments» or "threads" (left) and « shrubs » (right) with a sandy/dusty aspect. d) Coprolite from ATX-C15 seen by UV-epifluorescence, showing filaments, coccoids, copepods and many other objects with multiple bright colors. White scale bars represent 250 µm.

9.3.3. "Intermediate" petrographic facies

Finally, three samples (ATX-C1, ATX-R4, and -R6) fall into a somewhat intermediate category, in the way that they share several of the textures described above. For ATX-C1, it likely reflects that the microbialite was initially at a higher position on the crater wall before falling (similarly to ATX-20m). For the other two, it likely relates to the fact that they were sampled on the other side of the crater and their syn-/post-depositional formation history integrates multiple steps of the previously described processes. In ATX-R6 (and to a lesser extent ATX-C1 and ATX-R4), we also observe the precipitation of thick and isopachous layers of aragonite, with relatively extinct UV-fluorescence but well-preserved microbial filaments. These laminae are alternated with thinner, darker, oxidized layers possibly richer in organic remains (Figs. 9.15, 9.22). This lamination marks the periodical turnover between carbonate-

precipitation-dominated and biology-dominated periods, possibly associated with cyclic environmental changes such oxic/anoxic conditions. This lamination develops into centimetric domes and branching columns (Fig. 9.22).

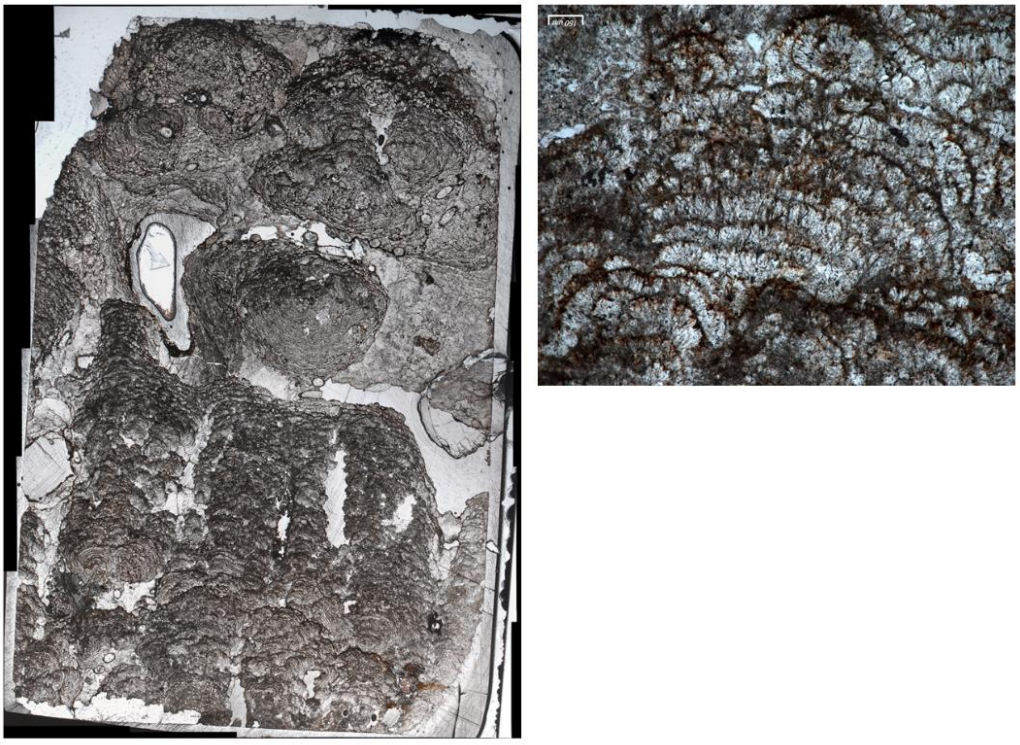

Figure 9.22: Scan of the full thin section and zoom in on the lamination of ATX-R6 microbialite. See figure 9 for a picture of the macroscopic samples. Scale bar on the right is 15 µm.

9.3.4. Summary about Atexcac microbialites

The different features and stages of mineral precipitation and replacement/recrystallization in Atexcac microbialites can be summarized as: (i) an initial precipitation of primary aragonite (carbonate phase 1: 'CP1') in parallel with the replacement/encrustation of primary biogenic matter by Mg-silicates (*cf.* Zeyen *et al.*, 2015); (ii) then, a secondary replacement of Mg-silicates in favor of aragonite ('CP2'), which is near-complete above 4.7 m (ATX-C6), but likely start already underwater (this replacement still preserves most of the biogenic structures); (iii) above 6 m (ATX-C9), a further recrystallization of aragonite into large crystal fans and botryoids ('CP3'), leading to the disappearance of most biogenic structures and organic compounds, though some filaments and/or diatoms may be preserved; (iv) a potential "pedogenetization" and physical erosion by plants and/or chemical dissolution and reprecipitation into calcite ('CP4'). Additionally, some other botryoidal fabrics ('CP5') – characteristic of emersion – reflect the fluctuation cycles of the lake level and the possible fall

of microbialites along the crater walls (*cf.* ATX-20m). In consequence, microbialite samples from Atexcac are thereafter referred to as three different facies named: "aquatic", "recrystallized" and "intermediate" as summarized in Tables 9.1 and 9.3. An important precision about the "recrystallized" facies is that the terminal fabric (the fibrous botryoids), appears massively above ~8 m but not progressively with height.

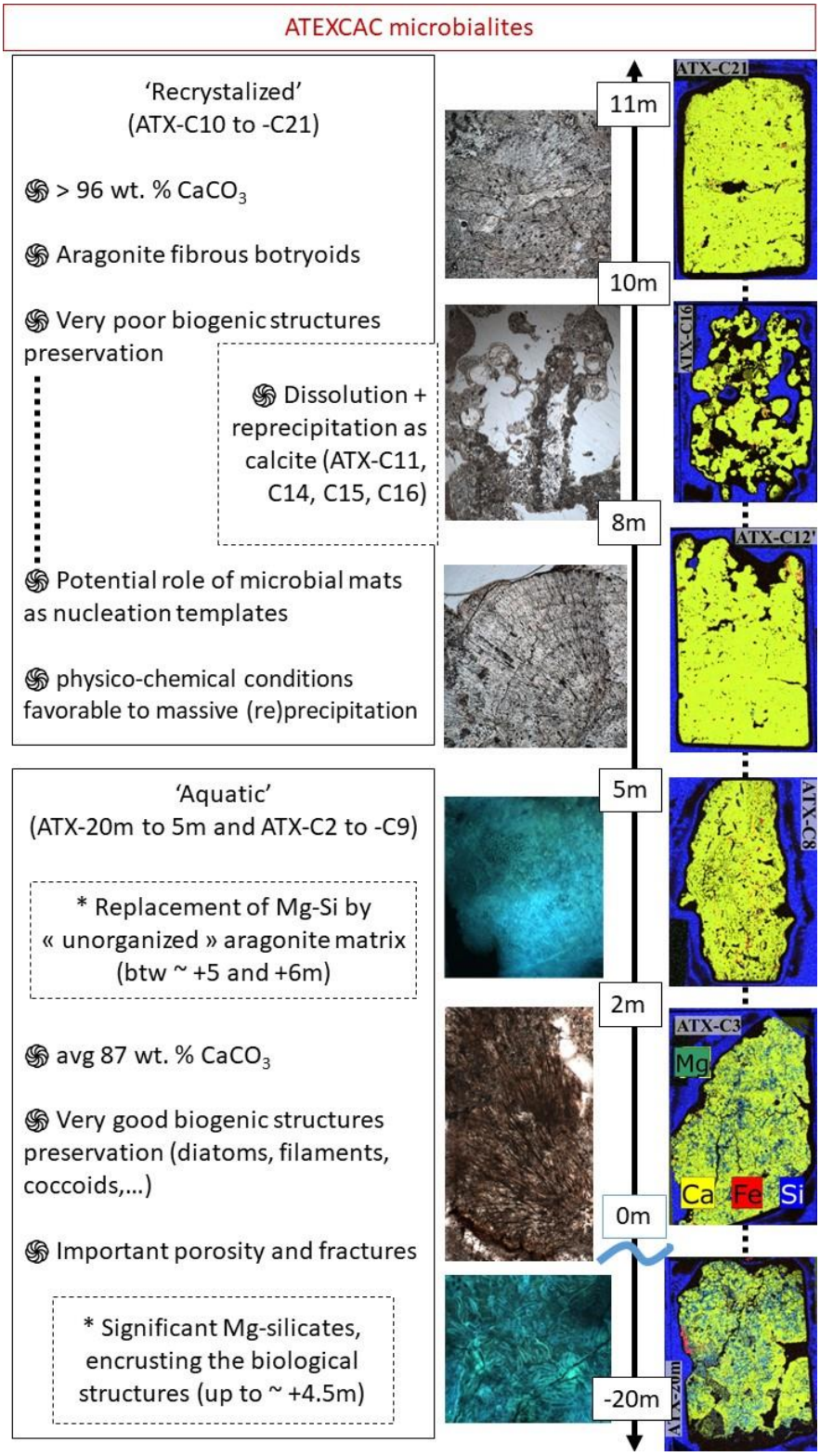

Table 9.3: Summary of the microbialites classification in Atexcac with their main characteristics. In addition to "recrystallized" and "aquatic" facies, a third "intermediate" facies is described in the text. This latter cumulates features from the other two and comprises sample ATX-C1 and 2 samples from the South shore of the lake (ATX-R4 and -R6, refer to Fig. 9.11 for locations).

Figure 9.23: Satellite photograph of Lake La Preciosa (~1.3 km from SW to NE) and representative pictures of the different microbialite macro- and megastructures. On the left, the gentle slopes surrounding the lake towards the south of the crater can be noticed. The yellow dots indicate where the four samples were collected. Microbialites usually harbor a mesoclotted fabric (*e.g.* PR_1) but can also be formed of shrubs typical of dendrolites, and voids filled detrital particles (see PR_2).

9.4. La Preciosa microbialites

Microbialites are less abundant in Lake La Preciosa (Zeyen *et al.*, 2021). In large part, this can be explained by a less saturated water-chemistry (Zeyen *et al.*, 2021), but also by the presence of more gentle crater slopes and soft surfaces compared to Alchichica and Atexcac. Indeed, previous studies suggested the preferential development of microbial deposits on hard/lithified substrates (*e.g.* Della Porta, 2015; Bouton *et al.*, 2016b, 2016a; Jaramillo-Vogel *et al.*, 2019). Accordingly, microbialites at the surface of Lake La Preciosa were mostly spreading around the few prominent hard surfaces of the crater (Fig. 9.23). On the northern shore, at the contact with the crater's wall, microbialites can also form steep bioherms (Zeyen, 2017). Microbialites could be found up to 6-7m above the current water level. They harbored more or less eroded clotted surfaces typical of thrombolites, and sometimes shrubs typical of dendrolites, with detrital particles infilling the voids (Fig. 9.23; Grey and Awramik, 2020).

La Preciosa microbialites contained between 76 and 86 wt. % of carbonates, almost exclusively aragonite. Aragonite was virtually the only crystalline phase as determined by

XRD, but poorly crystalline Mg-silicate phases were present as well (Fig. 9.24; Zeyen *et al.*, 2015). This is also clearly visibly in the whole thin section XRF scans (Fig. 9.12).

Alike some of the facies in Atexcac and Alchichica, filamentous microbial mats could be found in association with some ostracod shells and gastropods (mostly). La Preciosa microbialites were characterized by important pedogenetization, fracturing and refilling the cavities with detrital grains and muds (Fig. 9.25). The holes left by pedogenetization (*e.g.* by plants like reed) are filled in with muds or carbonated cements (Fig. 9.25), and detrital peloids start to be recovered by carbonated needle-shaped cements (Fig. 9.25). Therefore, similar to Atexcac, these samples experienced multiple emersion/immersion cycles. The sample collected a few meters above the water level (PR-3) exhibited higher and lower proportions of Mg-silicate and $CaCO_3$, respectively, than the "living" microbialite (LP-50cm) or the other subfossil samples closer to the current water level (PR-1 and -2). Thus, either PR-3 was not in the water long enough for the replacement of Mg-silicates by aragonite to occur, or it was immerged at a time when the lake's chemistry was not as saturated with carbonates as it is now.

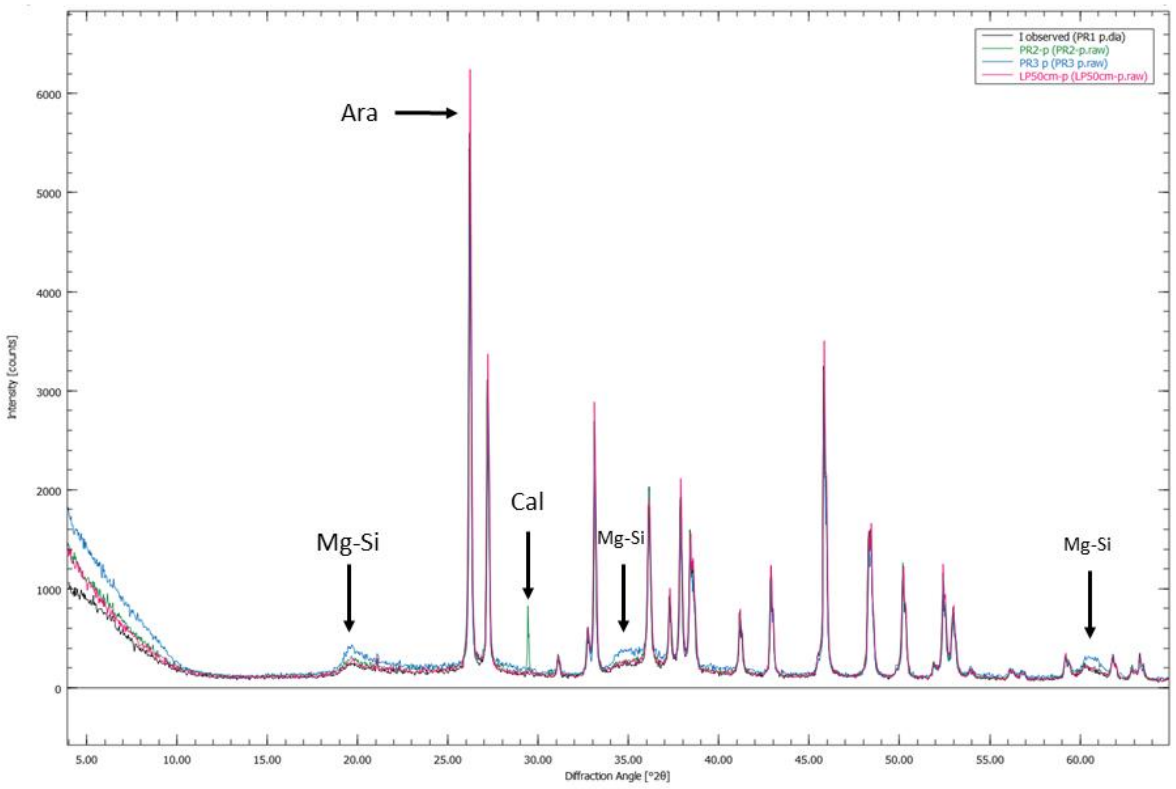

Figure 9.24: X-Ray diffraction profiles for the microbialites in La Preciosa. Except for PR-2 (where a little amount of calcite is found, <2%), aragonite is almost the only crystalline phase. Some Mg-silicate phases are evidenced as well (from ~15 to 25 wt. % as determined by mass-balance after decarbonation). This phase is most abundant in PR_3.

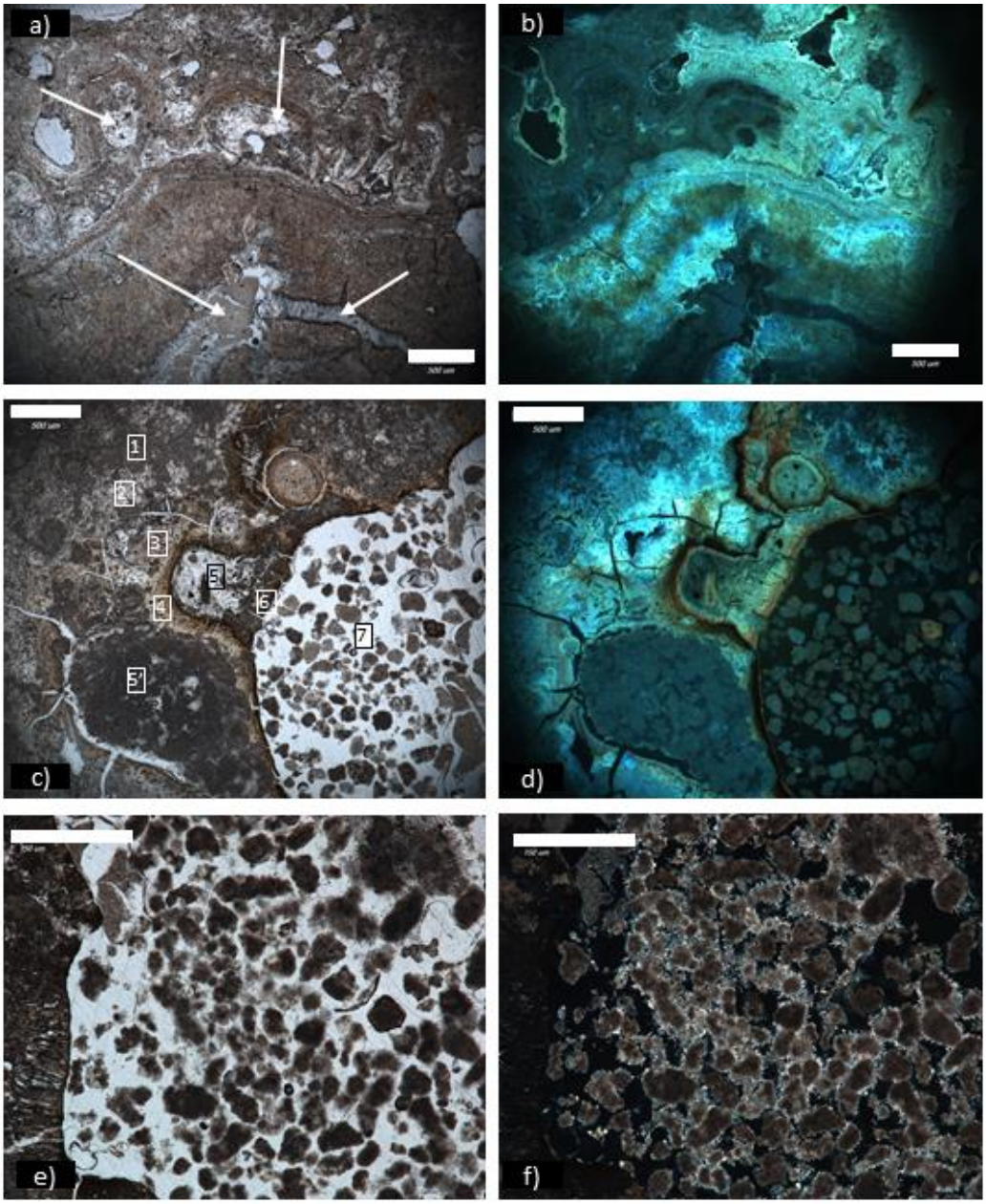

Figure 9.25: Photographs of La Preciosa thin sections under plane-polarized light (PPL) in cross-polarized light (CPL) and UV-epifluorescence. a) and b) filamentous microbial mats from LP-50cm. These mats are fractured, and filled with mud and secondary cements (white arrows). c) and d) Cavities in PR-3 filled and covered by multiple generations of detrital particles and microbial mats (shown with the numbers; to be compared with the image under UV-epi.). At the top, the interior of an ancient root (possibly of reed) is mineralized. e) and f) peloidal carbonate particles filling another cavity in PR-3, in PPL (left) and CPL (right), possibly coming from the desegregation of the microbialite itself. It can be seen on the CPL picture that the peloids start to be cementated and agglutinated by a different secondary phase, likely calcite, forming sharp needles. White scale bars represent 500 µm.

9.5. Conclusion

The different petrographic, mineralogical, and chemical observations presented in this chapter, together with existing literature, provide a strong basis for understanding the history of formation of the Mexican microbialites. They all result from multiple stages and processes of formation, at times of immersion and/or emersion which confer them a great diversity of macroscopic aspects, micro-petrographic textures, and mineral and biological preservation degrees. In Alchichica, the "brown microbialites" (composed exclusively of aragonite) feature a lot of biogenic remains ("micro-fossils"), suggesting a formation in more productive waters and a better preservation of the microbialites primary features, than "white microbialites". In these latter, aragonite at the rim of the microbialites is also associated with the microbial mats and bio-remnants, but the bulk matrix composed of hydromagnesite (and/or huntite) seems to occur as a replacing material, inducing the loss of most micro-fossils. In Atexcac, several steps of carbonate precipitation were evidenced, with a near-complete recrystallization of some of the emerged microbialites. In the underwater microbialites, and in the more recently emerged ones, the replacement of Mg-silicates by aragonite allowed the preservation of micro-fossils. Compared with the observations in Alchichica "white microbialites", it suggests that an initial fossilization by a silicate phase might be a prerequisite for the final preservation of microfossils in carbonates. A similar replacement of Mg-silicates by aragonite is also suggested in La Preciosa.

Overall, this work represents a solid frame for subsequent interpretations of these microbialites isotopic signatures. Further in this manuscript, bulk and local isotopic results from these objects will allow testing whether the isotopic and petrographic approaches converge, and how they can complement each other.

Chapter 10

The microbialites C and O isotope signatures

Table of content

10.1. Introduction

Microbialites are organo-sedimentary structures resulting from the interaction of biotic and abiotic factors (Burne and Moore, 1987). They can form through a process of particle trapping and binding (evidenced in modern marine microbialites; Awramik and Riding, 1988), but most modern freshwater and ancient marine microbialites are thought to form and to have formed through authigenic chemical precipitation, with a more or less direct biological influence (*e.g.* Grotzinger, 1990; Corkeron *et al.*., 2012; Caumartin *et al.*., 2023). Two main questions about microbialites and their geochemical signatures are explored in this chapter: (i) how much of their surrounding environment they can archive, and (ii), the biogenic traces they may preserve.

Microbialites are constituted of a mineral frame or structure, often composed of carbonates, and interspersed with remains of organic material from the microbial mats. It follows that, microbialite carbonates and organic matter represent the primary target reservoirs for investigating the formation processes of these objects. Isotopes, and especially that of carbon, are affected by both biological and abiotic environmental constraints, providing them with a strong potential to record these processes (Chagas *et al.*., 2016).

The isotopic record of microbialite-hosting carbonate sequences has been used to reconstruct basin-wide to global C cycle changes back to the Late Archean (*e.g.* Fischer *et al.*., 2009; Chakrabarti *et al.*., 2011). At a smaller scale, microbialite carbonate isotopes have been used to discuss the specific influence of autotrophic or heterotrophic organisms, and of evaporative conditions on microbialites formation throughout geological times, from the Paleogene (Frantz *et al.*., 2014), Cretaceous (Bahniuk *et al.*., 2015) or Permian (*e.g.* Friesenbichler *et al.*., 2018; Zhang *et al.*., 2021; Antunes *et al.*., 2022) periods, to the Proterozoic (Khelen *et al.*., 2017; Zhu *et al.*., 2021) and Archean (Xu, 2011) Eons. Yet, a proper understanding of the isotope transfer functions from the environment to the microbialites in modern analogous systems is mandatory in order to meaningfully interpret the ancient record, especially since relatively small variations are usually discussed in the literature (Houghton *et al.*., 2014; Della Porta, 2015).

Carbonates isotopic signatures from modern to Eocene microbialites have been increasingly analyzed to retrace continental climate and hydrological changes (*e.g.* Solari *et al.*., 2010; Frantz *et al.*., 2014; Newell *et al.*., 2017; Ingalls *et al.*., 2020; Bougeault *et al.*., 2020), but remain to be fully constrained (Buongiorno *et al.*., 2018; Arenas *et al.*., 2019). These

signatures, together with organic C isotopes, have also been used to decipher the respective influence of autotrophic *vs.* heterotrophic metabolisms (Fig. 10.1; Andres *et al.*., 2006; Breitbart *et al.*., 2009; Nitti *et al.*., 2012; Louyakis *et al.*., 2017; White III *et al.*., 2020), and abiotic environmental constraints (*e.g.* Muller *et al.*., 2022) on carbonatogenesis in modern environments.

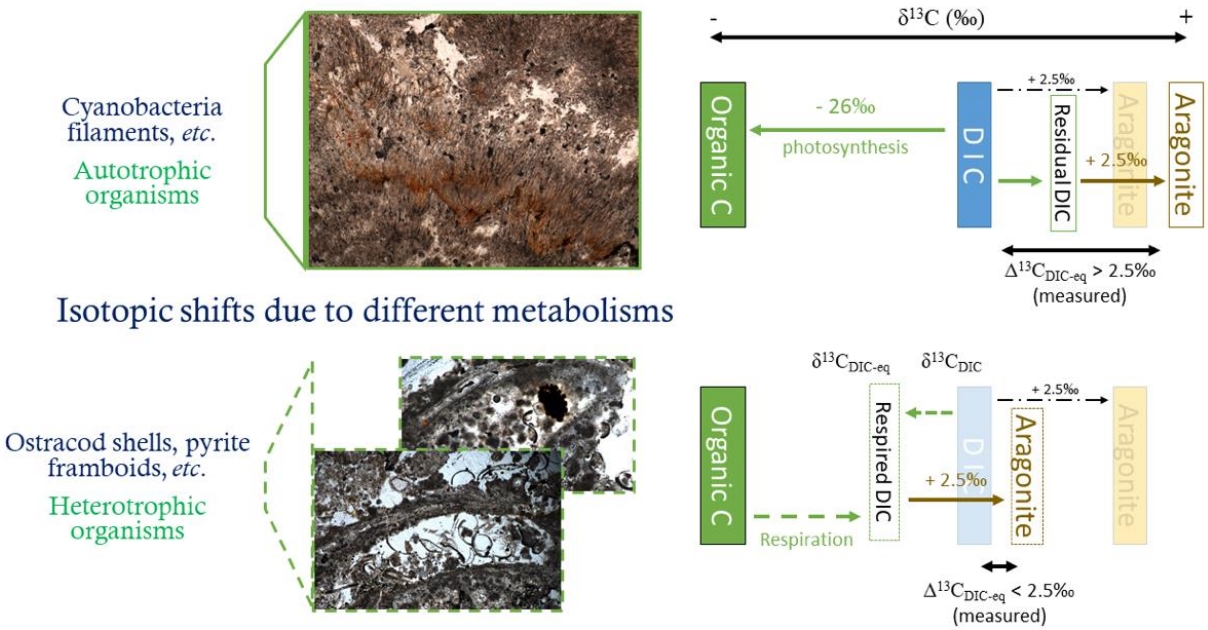

Figure 10.1: Schematic description of the production of "autotrophic" or "heterotrophic" biosignatures in carbonates. The initial DIC reservoir in blue, sees its isotopic composition increased or decreased by auto- and heterotrophic organisms, respectively. The precipitated aragonite (white and brown) thus records an isotopic composition which is isotopically more, or less enriched, respectively, than if it had precipitated from the unaffected DIC reservoir (transparent yellow and brown). The example of aragonite (which precipitates from DIC with a ~2.5 ‰ difference at 20 °C) is given here, but the same applies to any carbonate phase.

However, most studies of modern analogues focus on how environmental and biological factors may influence the primary signature of microbialite carbonates, but few consider its preservation potential, that is, how long the primary signatures may persist (Belan *et al.*., 2019). The determination of the DIC-source composition, and assessment of alternative secondary processes are also critical (Sumner, 2001), but not always properly addressed. The multiplicity and complexity of parameters influencing the carbonates isotopic signatures is summarized in Figure 10.1 and 10.2.

Organic carbon isotope data in microbialites from modern analogues have also been reported, but are fewer (*e.g.* Breitbart *et al.*, 2009; Nitti *et al.*, 2012; Louyakis *et al.*, 2017; White III *et al.*, 2020). Importantly, examples of study interested in microbialites forming in anoxic natural environments are even scarcer, although the oceans were anoxic at depth for most of the Earth's history (*e.g.* Lyons *et al.*, 2014; Satkoski *et al.*, 2015).

In this chapter, I discuss the isotopic data for carbonates C and O, from bulk and micro-drilled analyses and bulk organic C from the Mexican microbialites. The recognition of dissolution/recrystallization features, and of secondary precipitation in the samples studied (*cf.* "recrystallized facies" in Atexcac, and "white facies" in Alchichica, Chapter 9) allows a direct assessment of early post-depositional effect on carbonates C and O isotopes (subsection 10.3.1). After distinguishing between the different microbialites recrystallization history, I investigate the primary biological and environmental features recorded by the microbialite C and O isotope records (subsection 10.3.2 and 10.3.3). The C cycle of the Mexican lakes studied has been thoroughly characterized, and it was shown that its peculiarities were not all necessarily recorded in the lakes sediments (Part 1). Thus, the objective of these two subsections is to investigate if microbialites can be more specific archives than the sediments of the microbial diversity, the different C sources (*e.g.* volcanic-CO_2), processes (*e.g.* evaporation), and basin characteristics (*e.g.* redox-stratification) for these stratified environments. Finally, I present how the organic carbon isotope signatures evolve through the depth redox gradient of Alchichica and Atexcac, and how it compares to the outcropping subfossil microbialites (subsection 10.3.4).

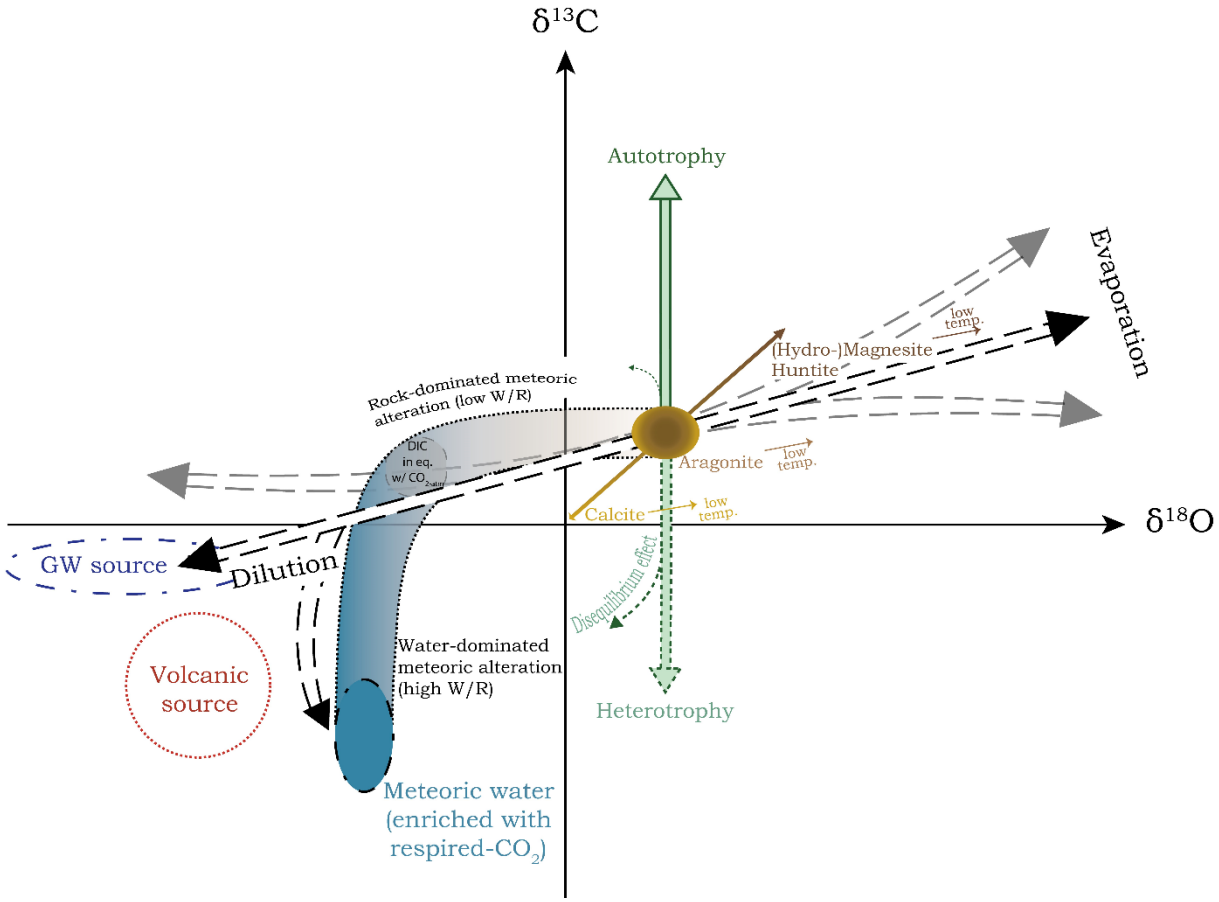

Figure 10.2: Effects of biotic and abiotic factors on carbonates C and O isotopes within the studied lakes context. Biological factors will mostly affect C isotopes, moving the carbonates vertically in a 2D $\delta^{13}C$–$\delta^{18}O$ space. Biological activity can lead to rapid precipitation rates which can generate disequilibrium effects, represented with the dashed and curved green arrows. Disequilibrium effect will favor a decrease of both $\delta^{13}C$ and $\delta^{18}O$. It is thus enhanced by heterotrophy, and would mostly affect $\delta^{18}O$ in case of autotrophy. Hydrological changes (evaporation or dilution with groundwater (GW) or meteoric water sources) will generate $\delta^{13}C$–$\delta^{18}O$ covariations, which can vary in slope. Similarly, the precipitation of various carbonate phases will tend to create a $\delta^{13}C$–$\delta^{18}O$ correlation; lower temperature of precipitation ("low temp." arrows) will induce higher isotopic fractionations, especially for O. Alteration of the precipitated carbonates by meteoric fluids tends to shift the O isotopes first, at low water:rock ratio, but the effect of time (*i.e.* increasing W:R ratio), or the addition of a C-rich source to the alteration fluid then shifts C isotopes as well. Carbon in meteoric water can correspond to atmospheric CO_2 but the incorporation of oxidized organic C may also drive the altered carbonates to lower values. The same applies to GW, which contains a mix of $CO_{2\text{-atm}}$, limestone DIC, and respired DIC. The GW space represented here applies to the context studied here, but could widely vary in other environments. Volcanic CO_2 sources would generate carbonates with a slightly negative $\delta^{13}C$, and a $\delta^{18}O$ between meteoric and GW values. One should note all the processes indicated except the meteoric alteration would affect the fluid from which carbonates precipitate, and not the carbonates directly.

10.2. Results

The main petrographic and mineralogical characteristics of the microbialite samples were described in Chapter 9. This allowed the classification of "white" and "brown" microbialite facie in Alchichica, "recrystallized", "intermediate", and "aquatic" facie in Atexcac, and a "La Preciosa" facies in the lake of the same name. In the following subsection are presented the main results associated with these microbialites carbonates and organic matter content.

In the result and discussion sections, $\delta^{13}C_{DIC\text{-}eq}$ and $\delta^{18}O_{H2O\text{-}eq}$ will refer to the calculated C and O isotope compositions of the DIC and H_2O in the precipitation fluid at equilibrium with the microbialite carbonates isotopic signal (Fig. 10.1). The shift between these isotopic compositions and the current lakes' $\delta^{13}C_{DIC}$ and $\delta^{18}O_{H2O}$ will be referred to in the 'Δ' notation such that for example: $\Delta^{13}C_{DIC\text{-}eq} = \delta^{13}C_{DIC\text{-}eq} - \delta^{13}C_{DIC}$.

10.2.1. Alchichica

"White microbialites" (n=14) have a bulk carbonate concentration of 98.2 ± 1.5 wt. %, including about 80 ± 12 wt. % of hydromagnesite, 14 ± 7 wt. % of aragonite, and negligible amounts of calcite (Table 10.1). Samples located at 20 and 40 m depths also contain huntite, ~20 and 37 wt. %, respectively. Bulk carbonate C and O isotope compositions ($\delta^{13}C_{carb}$ and $\delta^{18}O_{carb}$) average 6.2 ± 0.2 and 5.4 ± 0.7 ‰ VPDB, respectively (Fig. 10.3). Corresponding $\delta^{13}C_{DIC\text{-}eq}$ and $\delta^{18}O_{H2O\text{-}ea}$ average 1.7 ± 0.2 ‰ VPDB and 3.7 ± 0.6 ‰ VSMOW, respectively (Fig. 10.3). "White microbialites" have a small TOC content (0.3 ± 0.3 wt. %) with an average isotopic composition of -24.7 ± 1.2 ‰ VPDB.

"Brown microbialites" (n=5) have a bulk carbonate concentration of 96.2 ± 0.4 wt. %, including about 0.8 ± 1.1 wt. % of hydromagnesite, 97.4 ± 1.4 wt. % of aragonite, and 0.7 ± 0.3 wt. % of calcite (Table 10.1). The $\delta^{13}C_{carb}$ and $\delta^{18}O_{carb}$ average 2.1 ± 0.4 and -2.1 ± 0.3 ‰ VPDB, respectively (Fig. 10.3). The $\delta^{13}C_{DIC\text{-}eq}$ and $\delta^{18}O_{H2O\text{-}ea}$ average -0.4 ± 0.4 ‰ VPDB and -1.6 ± 0.3 ‰ VSMOW, respectively. "Brown microbialites" show slightly higher TOC content (0.6 ± 0.2 wt. %) with an average isotopic composition of -25.2 ± 1.0 ‰ VPDB.

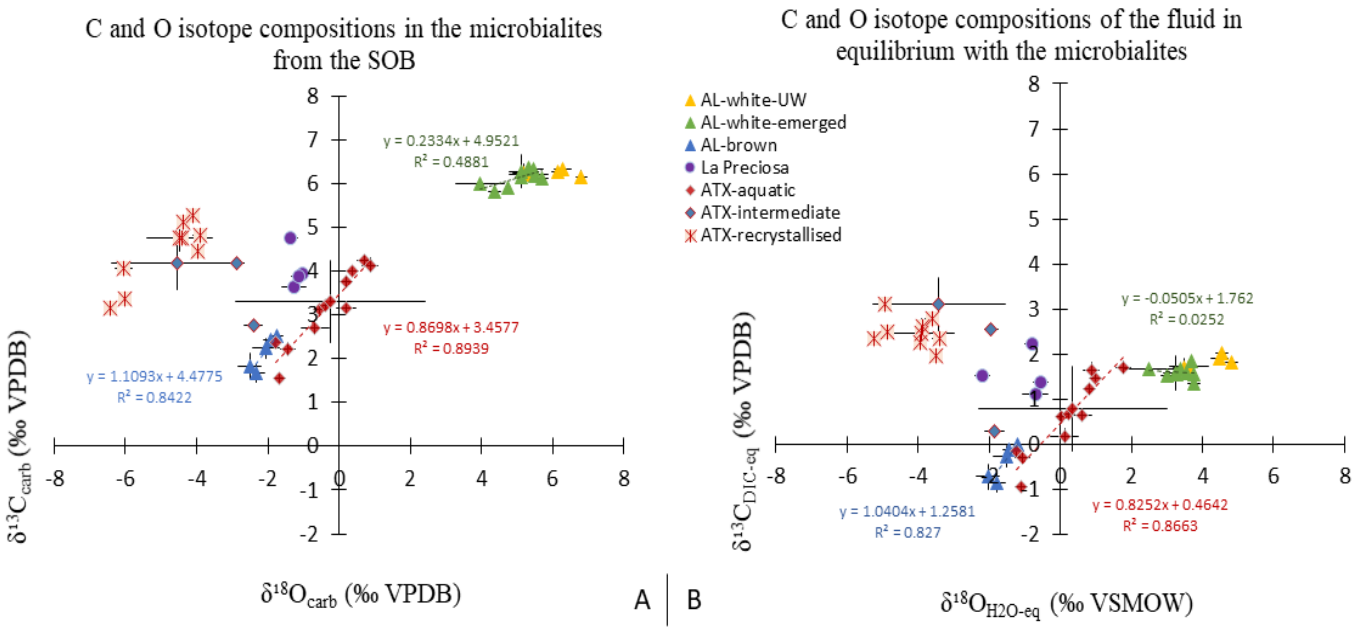

Figure 10.3: Cross-plot of carbonates carbon and oxygen isotope compositions in microbialites from Alchichica, Atexcac and La Preciosa lakes. A) Measured carbonates C and O isotopic compositions, both *vs.* VPDB. B) Calculated isotopic compositions of the precipitation fluid in equilibrium with the solid carbonates. Water oxygen isotopes are expressed on the VSMOW scale (a more common scale for O in fluids; on the VPDB scale, $\delta^{18}O_{H2O\text{-}eq}$ would range from about -25 to -35 ‰). 'AL-white-UW' designates Alchichica "white" underwater microbialites.

Four samples were micro-drilled and analyzed for carbonates C and O isotopes. "AL19-20m" and "AL19-40m" (immerged "white microbialites") showed limited isotopic variability over 5 analyses with maximum variations of 0.8 and 1.1 ‰ for C and O isotopes, respectively (Fig. 10.4). "AL-T-11" (subfossil "white microbialite"; but 24 wt. % of aragonite) was micro-drilled in orange aragonitic, white hydromagnesian, and gray nodules in at least three different nodules for each phase (Fig. 10.5). The gray and orange phases had similar isotopic compositions as the bulk sample ($\delta^{13}C$ = 6.0 and $\delta^{18}O$ = 4.0 ‰; VPDB), but the hydromagnesite nodules (white diamonds in Fig. 10.5) correlated from the bulk composition towards a heavy endmember with $\delta^{13}C$ = 9.0 and $\delta^{18}O$ = 13.2 ‰ (R^2= 0.99, n=5). Last, "AL-T-9" (subfossil "brown microbialite") had $\delta^{13}C$ varying from 1.5 to 3.3 ‰, and $\delta^{18}O$ from -3.0 to -1.2 ‰ (Fig. 10.5), both being correlated (R^2=0.82, n=6).

Table 10.1: Carbonate content and mineralogy of the Mexican microbialites. The bulk carbonate content was determined by mass balance after a bulk acid digestion. The different carbonate mineralogies abundance ('Ara' = aragonite, 'Cal' = calcite, 'HMg' = hydromagnesite, 'Hun' = huntite) relative to the total crystalline phases were estimated by Rietveld refinement analysis after XRD analysis using the Profex software, with the total shown on the right. The estimations of total carbonate content *via* the two methods agree well but may differ because amorphous phases (*e.g.* organic matter, amorphous Mg-silicate phases) are not detected by XRD analyses.

Sample Name	Facies group	Bulk carbonate content	Position to current water level	Main carbonate mineralogy	Ara.	Cal.	HMg.	Hun.	Total
		wt. %	m		Carbonate abundance in %				
AL19-5m	White	98.8	-5	Hmg, Ara	13.9	0.1	84.2	1.9	100.0
AL19-10m	White	99.5	-10	Hmg, Ara	18.0	0.0	82.0	0.0	100.0
AL19-20ma	White	94.1	-20	Hmg, Ara, Hu	9.1	0.0	66.7	24.2	100.0
AL19-20mb	White	99.3	-20	Hmg, Ara, Hu	19.4	0.1	62.1	18.4	100.0
AL19-40m	White	99.7	-40	Hmg, Ara, Hu	7.2	0.0	55.8	37.1	100.1
AL-T-1	White	96.1	≈ +2	Hmg, Ara	12.7	0.3	86.9	0.0	99.9
AL-T-5	Brown	96.5	≈ +2	Hmg, Ara	98.7	0.5	0.0	0.0	100.0
AL-T-6	White	98.6	≈ +2	Hmg, Ara	22.8	0.1	77.1	0.0	100.0
AL-T-7	White	98.4	≈ +2	Ara	26.5	0.1	73.4	0.1	100.0
AL-T-8	Brown	96.5	≈ +2	Ara	96.2	0.9	1.9	0.0	99.0
AL-T-9	Brown	96.5	≈ +2	Ara	95.9	0.9	2.1	0.0	98.9
AL-T-10	Brown	95.6	≈ +2	Hmg, Ara	96.5	0.7	0.2	0.0	97.4
AL-T-11	White	98.1	≈ +2	Hmg, Ara	23.9	0.1	75.2	0.0	99.2
AL-R-1	White	97.9	0	Hmg, Ara	8.5	0.0	91.4	0.0	99.9
AL-R-2	White	97.1	0	Hmg, Ara	15.8	0.1	84.1	0.0	100.0
AL-R-3	White	98.4	≈ +0.5	Hmg, Ara	5.9	0.1	93.6	0.4	100.0
AL-R-4	White	98.7	≈ +1	Hmg, Ara	11.9	0.1	87.9	0.2	100.1
AL-R-5	White	99.5	≈ +4	Ara	5.7	0.1	93.6	0.0	99.4
Al-Fe-W	Brown	96.1	≈ +2	Ara	99.7	0.3	0.0	0.0	100.0
LP-50cm	LP	84.6	-0.5	Ara	100	0			100.0
PR-1	LP	85.7	≈ +1	Ara	100	0			100.0
PR-2	LP	82.3	0.5	Ara	98.2	1.8			100.0
PR-3	LP	76.4	≈ +2	Ara	99.9	0.1			100.0
ATX-C1	Intermediate	92.9	0	Cal & Ara	46.7	49.5			96.2
ATX-C2	Aquatic	74.7	≈ +1.2	Ara	92.2	0.0			92.2
ATX-C3	Aquatic	90.3	≈ +2.2	Ara	97.6	0.0			97.6
ATX-C5	Aquatic	90.5	≈ +3.7	Ara	97.2	0.1			97.3
ATX-C6	Aquatic	87.3	≈ +4.7	Ara	99.3	0.0			99.3
ATX-C7	Aquatic	94	≈ +4.9	Ara	97.7	0.7			98.4
ATX-C8	Aquatic	98	≈ +5.2	Ara	97.2	0.1			97.3
ATX-C9	Aquatic	91.3	≈ +6	Ara	93.2	1.3			94.5
ATX-C11	Recrystalized	96.3	≈ +8	Cal, Ara	7.5	88.9			96.4
ATX-C12'	Recrystalized	98.8	≈ +7.7	Ara	96.4	1.4			97.9
ATX-C12	Recrystalized	99.2	≈ +8.3	Ara	84.4	12.1			96.5
ATX-C13	Recrystalized	99.7	≈ +7.4	Ara	98.8	0.7			99.5
ATX-C15	Recrystalized	99.9	≈ +10	Cal	0.0	97.5			97.5
ATX-C16	Recrystalized	99.3	≈ +10.5	Cal, Ara	4.6	94.0			98.6
ATX-C17	Recrystalized	99	≈ +10.7	Ara	97.9	2.0			99.9
ATX-C18	Recrystalized	98.1	≈ +11	Ara	97.9	2.0			99.9
ATX-C21	Recrystalized	ND.	≈ +10.7	Ara	93.6	3.2			96.8
ATX19-5m	Aquatic	85.7	-5	Ara	92.3	1.0			93.3
ATX19-10m	Aquatic	90.8	-10	Ara	99.9	0.2			100.0
ATX19-15ma	Aquatic	92.4	-15	Ara	98.6	0.5			99.1
ATX19-15mb	Aquatic	74.4	-15	Ara	99.8	0.2			100.0
ATX19-20m	Aquatic	78.6	-20	Ara	100.0	0.0			100.0
ATX-R4	Intermediate	98.6	≈ +4	Cal, Ara	15.3	84.7			100.0
ATX-R6	Intermediate	95	≈ +7	Ara	90.8	3.3			94.1

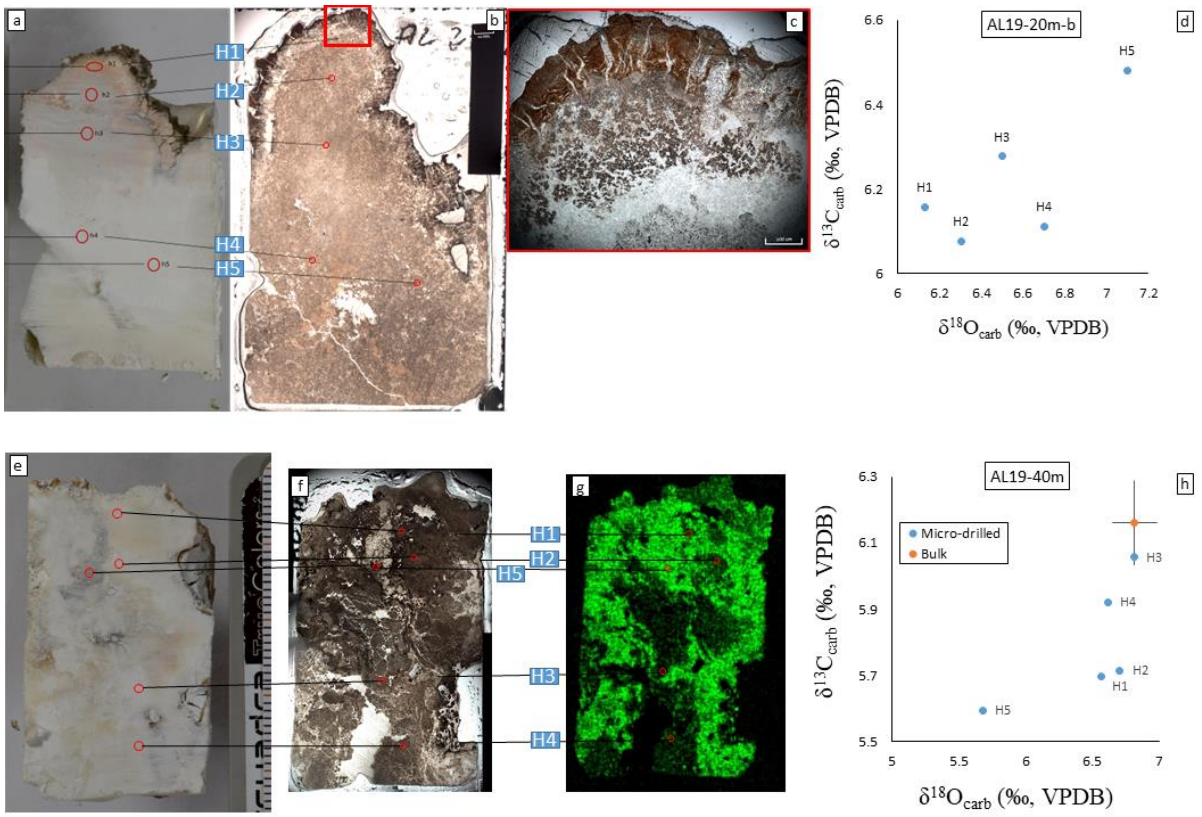

Figure 10.4: Micro-drill results for microbialites sampled at 20 and 40m depths in the water column of Lake Alchichica. a) Photograph of AL19-20m-b macro-sample with micro-drills location. b) Thin section seen under optical light microscope. c) Zoom in on the microbialite's edge, with aragonite-encrusted microbial layers transitioning to the more homogeneous hydromagnesite in the middle. d) C and O isotope compositions of the micro-drilled powders. e) Photograph of AL19-40m macro-sample with micro-drills location. f) Thin section seen under optical light microscope. g) Magnesium XRF-scan of the thin section. Bright green correspond to areas of hydromagnesite (lighter parts in 'f'), sampled in 'H5'; darker attenuated green correspond to areas of huntite (sampled in all other micro-drill sampling). h) C and O isotope compositions of the micro-drilled powders.

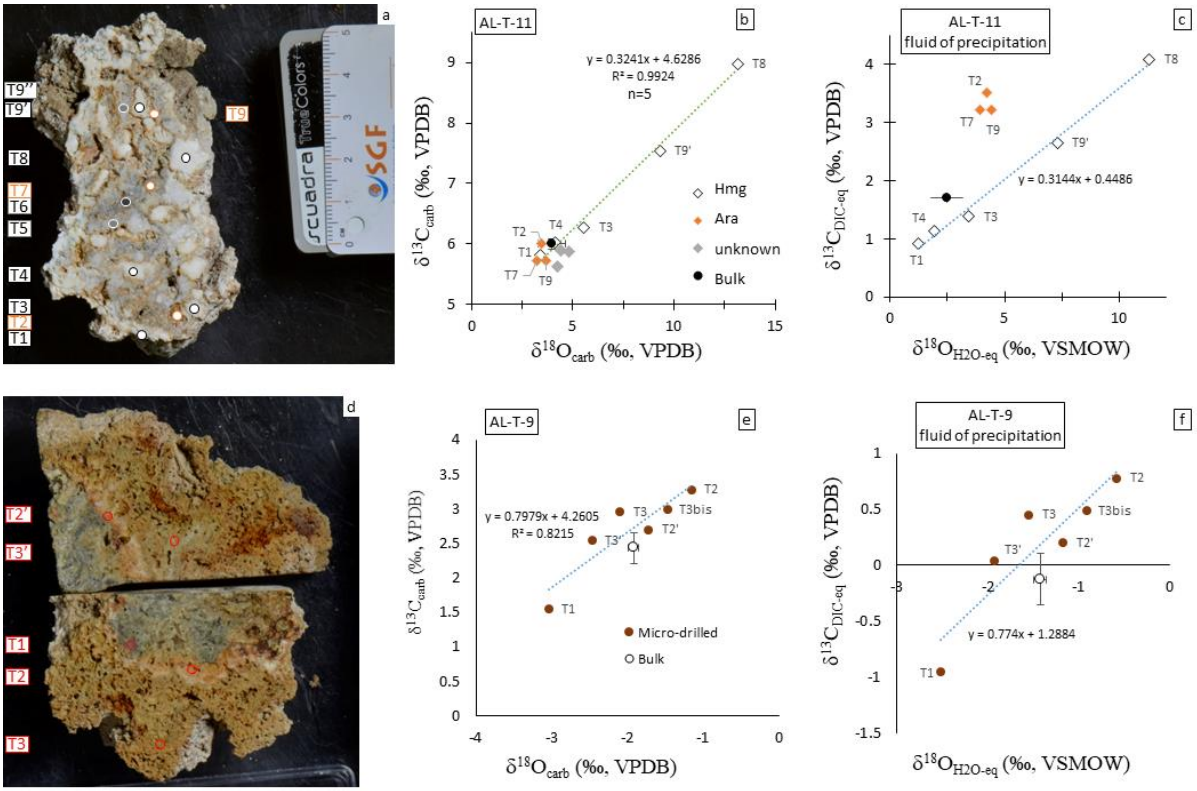

Figure 10.5: Micro-drill results for subfossil emerged microbialites from Lake Alchichica. (a) photograph of "AL-T-11" microbialite, which belongs to the "white" facies. White (HMg=hydromagnesite), gray (unknown) and orange (Ara=aragonite) nodules were sampled. The colors of micro-drilled powders were clearly distinguishable for the three groups. Isotopic compositions were measured from the carbonate powders (b, e), and recalculated for the equilibrium fluid of precipitation (c, f). The isotopic signatures of aragonite aliquots in "AL-T-11" (in b and c) should not be confounded with bulk aragonite measurements from the "brown microbialites". (d) Photograph of "AL-T-9" microbialite, which belongs to the "brown" facies. Layers of different colors were sampled, from two mirror faces of a single microbialite. The $\delta^{13}C$– $\delta^{18}O$ slope for this sample (e, f) is higher than what is recorded by hydromagnesite nodules in "AL-T-11" (b, c).

10.2.2. Atexcac

Microbialites from the "recrystallized facies" (n=9) have a bulk carbonate concentration of 99 ± 1 wt. %, containing almost exclusively either aragonite or calcite (Table 10.1). The $\delta^{13}C_{carb}$ and $\delta^{18}O_{carb}$ average 4.4 ± 0.8 and -4.9 ± 1 ‰ VPDB, respectively, with calcite and aragonite samples grouping separately (Fig. 10.3; calcite samples having lower isotopic compositions). In comparison to the bulk carbonate data, the isotopic compositions of the fluid DIC and H_2O in equilibrium with carbonates showed a narrower range of variations, with $\delta^{13}C_{DIC\text{-}eq}$ = -2.5 ± 0.3 ‰ VPDB, and $\delta^{18}O_{H2O\text{-}eq}$ = -4.1 ± 0.7 ‰ VSMOW (Fig. 10.3). The "recrystallized facies" has a very low TOC content (0.1 ± 0.1 wt. %) with an average $\delta^{13}C_{org}$ of -25.2 ± 1.2 ‰ VPDB.

Microbialites from the "aquatic facies" (n=12) have a bulk carbonate concentration of 97 ± 3 wt. %, almost exclusively composed of aragonite (Table 10.1). The $\delta^{13}C_{carb}$ and $\delta^{18}O_{carb}$ average 3.2 ± 0.7 and -0.4 ± 0.8 ‰ VPDB, respectively, both parameters correlating well (R^2=0.89; Fig. 10.3). The trend recorded by $\delta^{13}C_{DIC\text{-}eq}$ and $\delta^{18}O_{H2O\text{-}ea}$ is almost identical to that between $\delta^{13}C_{carb}$ and $\delta^{18}O_{carb}$. The $\delta^{13}C_{DIC\text{-}eq}$ averages 0.6 ± 0.7 ‰ VPDB, and $\delta^{18}O_{H2O\text{-}eq}$ averages 0.2 ± 0.9 ‰ VSMOW. The "aquatic facies" shows much higher TOC content than the recrystallized facies (1.1 ± 0.5 wt. %) with an average $\delta^{13}C_{org}$ of -27.2 ± 1.0 ‰ VPDB.

Microbialites from the "intermediate facies" (n=3) have bulk carbonate C and O isotope compositions in between the two preceding facies, with "ATX-C1" and "ATX-R4" closer to the recrystallized, and "ATX-R6" closer to the aquatic facies (Fig. 10.3).

"ATX-C21" from the "recrystallized facies" preserved a laminated macro-structure despite being mostly recrystallized and was micro-drilled across a 6cm-long transect, and along one of the laminae (Fig. 10.6). The lamina shows very homogeneous isotopic compositions ($\delta^{13}C$ = 4.7 ± 0.1 ‰, $\delta^{18}O$ = -4.1 ± 0.1 ‰, n=5). The $\delta^{13}C$ and $\delta^{18}O$ across the lamination are correlated with a small decreasing trend towards the top of the microbialite, but a sharp increase in the middle (+5.7 and -2.5 ‰, respectively). The different sampled layers correspond to different aragonite fabrics (laminated, peloidal, botryoidal), and contain more or less organic matter (Fig. 10.6).

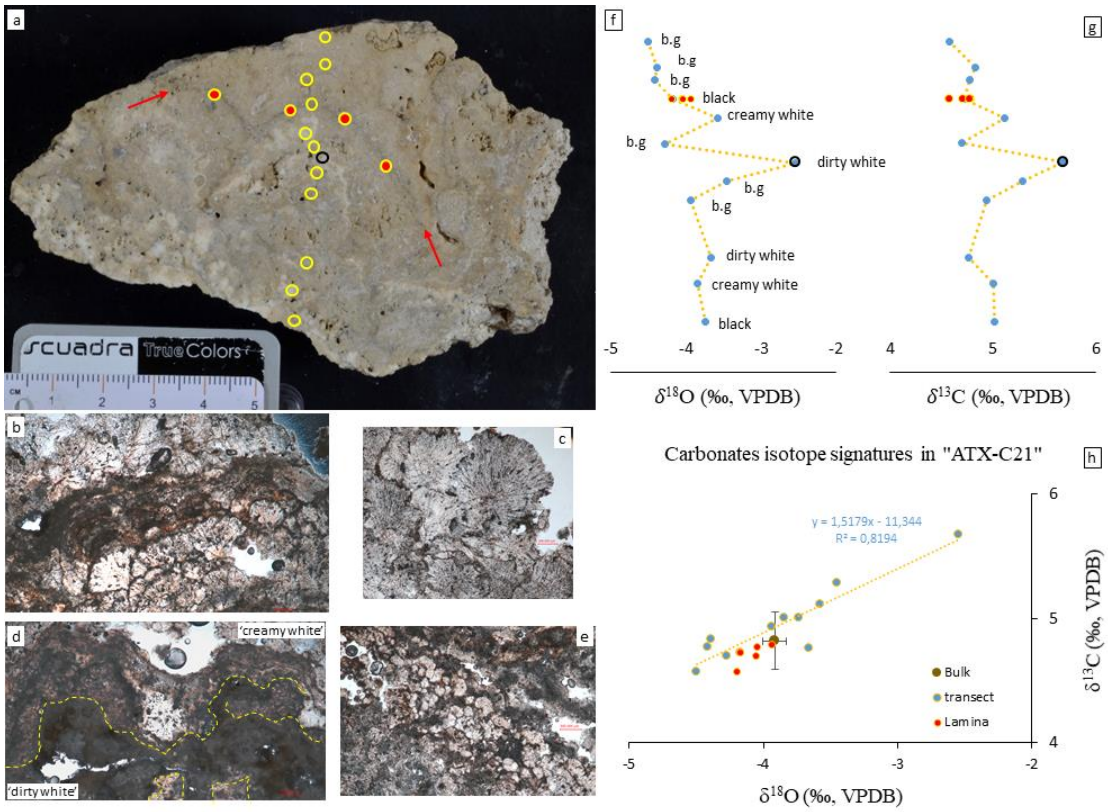

Figure 10.6: Micro-drill results for "ATX-C21" microbialite, from the "recrystallized facies" in Atexcac. a) Photograph of the sample and location of micro-drilling along a lamina (red) and across a vertical transect (yellow). b to e) Optical microscope photographs of the different carbonate fabrics sampled: the black lamina in 'b'; the different botryoidal-like fabrics corresponding to the beige-gray ('b.g') color in 'a'; the 'dirty white' layers correspond to areas with dense organic remains in 'd' and the 'creamy white' color in 'a' correspond to brown peloidal layers under the microscope and are brighter than the 'dirty white'. f to h) Carbon and oxygen isotope compositions of bulk and micro-drilled carbonates.

Micro-drilling in distinct secondary and more pristine fabrics of an "intermediate" microbialite was carried out (ATX-C1). The different secondary botryoidal textures showed isotopic signatures similar to the "recrystallized endmember" (*i.e.* closer to the bulk composition); the aliquot sampled in the lower, more pristine part of the microbialite showed isotopic signatures closer to the "aquatic" endmember (Fig. 10.7).

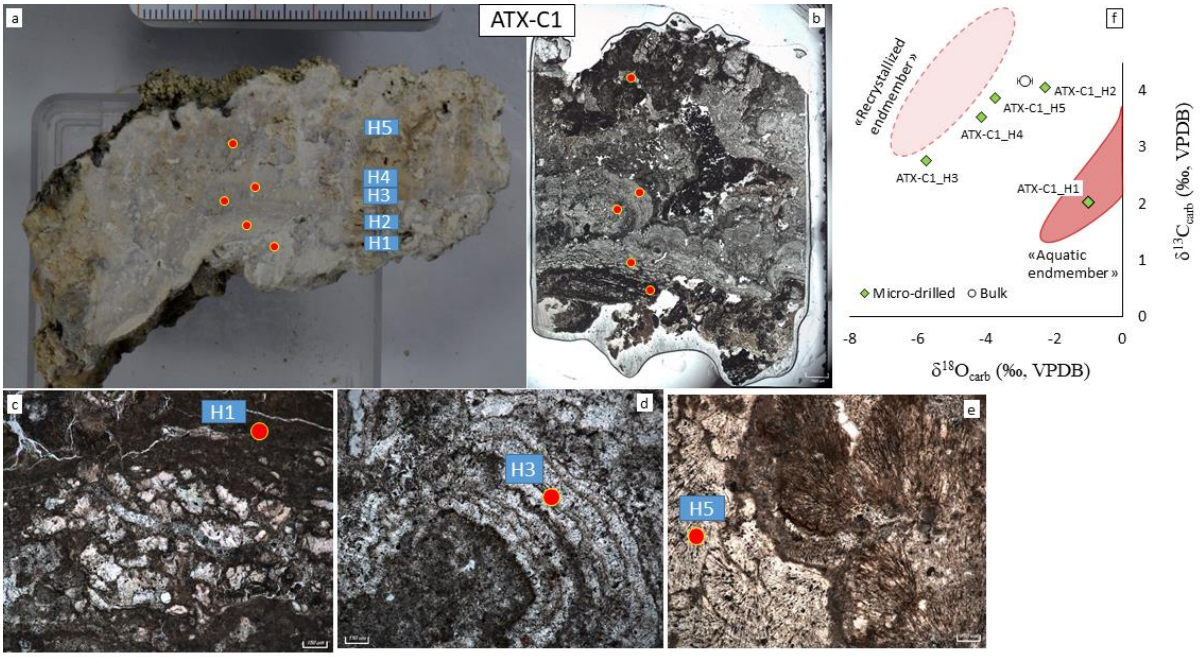

Figure 10.7: Micro-drill results for "ATX-C1" microbialite, from the "intermediate facies" in Atexcac. a-b) Photographs of the sample and corresponding thin section. c-e) Main carbonate fabrics sampled. f) Carbon and oxygen isotope compositions of the micro-drilled and bulk carbonates, with the fields characterizing the "aquatic" and "recrystallized" facie samples.

10.2.3. La Preciosa

Microbialites sampled in Lake La Preciosa (n=4) have homogeneous carbonate mineralogical and isotopic characteristics. Carbonates represent on average 82 ± 4 wt. % of the sample, almost entirely aragonite, with minor amounts of calcite (~ 0.4 wt. % of the bulk sample) (Table 10.1). The $\delta^{13}C_{carb}$ and $\delta^{18}O_{carb}$ average 4.1 ± 0.5 and -1.2 ± 0.2 ‰ VPDB, respectively, corresponding to $\delta^{13}C_{DIC\text{-}eq}$ of 1.5 ± 0.5 VPDB and $\delta^{18}O_{H2O\text{-}eq}$ of -0.6 ± 0.2 ‰ VSMOW (Fig. 10.3). Total organic carbon content is the highest of all analyzed samples, averaging 1.7 ± 0.2 wt. %, and $\delta^{13}C_{org}$ average -23.5 ± 1.4 ‰ VPDB.

The sample "PR-2" was micro-drilled in several primary dendrolitic shrubs together with the adjacent in-filling detrital matrix (Fig. 10.8). Aliquots from the primary shrubs all plot together and depict the most positive $\delta^{13}C$ values (4.5 ± 0.4‰, n=5). The detrital aliquots (consisting of cavity infilling grains) have lower $\delta^{13}C_{carb}$ values (2.9 ± 1.2‰, n=3) and interestingly encompass the isotopic composition of carbonates from the bottom lake sediments (Fig. 10.8).

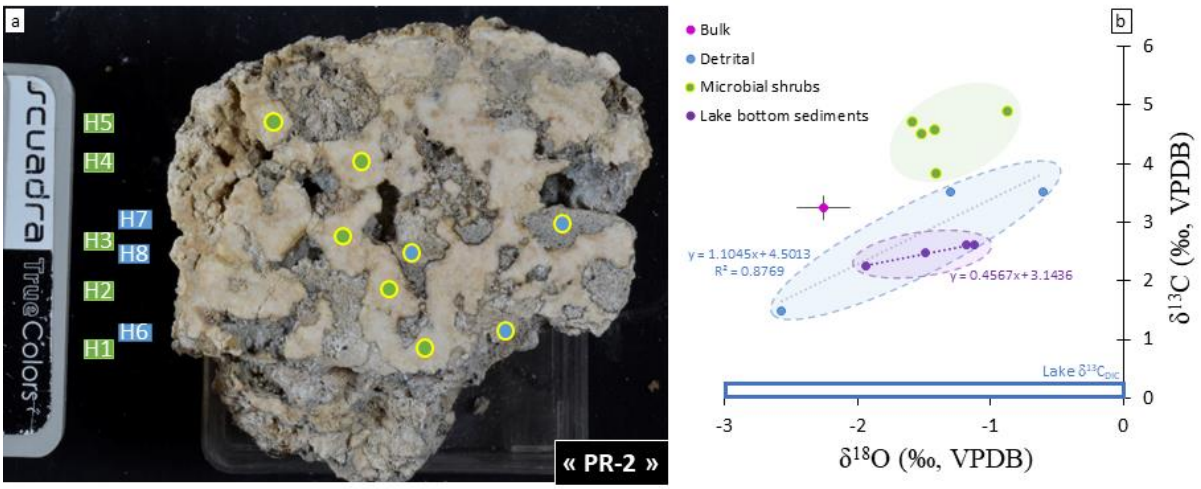

Figure 10.8: Micro-drill results for "PR-2" microbialite from Lake La Preciosa. a) Photograph of the sample and location of micro-drilling in the microbial shrubs (in green) and detrital void-filling sediments (in blue). b) Carbon and oxygen isotope compositions of the micro-drilled and bulk microbialites carbonates, as well as of the bottom lake sediments (purple). The lake DIC isotope composition is represented with the blue rectangle; the isotopic fractionation between DIC and aragonite is about 2.5 ‰.

10.3. Discussion

10.3.1. Effect of early *recrystallization* and *secondary precipitation* on the Mexican microbialites carbonate record

Among the microbialites studied, different phases and steps of carbonate precipitation were evidenced from petrographic observations. Some of the carbonates were primary (*e.g.* the aragonite in Alchichica, or some of the aragonite in Atexcac), while others were secondary (Chapter 9). In the secondary phases, some allowed the preservation of primary biogenic remnants (*e.g.* aragonite replacing Mg-silicates in Atexcac, but preserving filaments and diatoms), while others mostly induced their loss (*e.g.* replacement hydromagnesite in Alchichica), along with the possible formation of new characteristic fabrics (*e.g.* "recrystallized" facies in Atexcac). This first subsection will investigate whether these different recrystallization processes and degrees of carbonate replacement can be identified and differentiated based on carbonates isotopic signatures.

10.3.1.1. Isotopic changes related to carbonates recrystallization and early replacement in Atexcac

10.3.1.1.1. *Isotopic signatures of the "recrystallized facies", and the hydrological history of Lake Atexcac*

From the cross plot of carbonates C and O isotopes, it is evident that the "recrystallized facies" strongly differs from all the other samples (Fig. 10.3). Within "recrystallized" microbialites, three samples differ from the others by having lower $\delta^{13}C_{carb}$ and $\delta^{18}O_{carb}$ values (Fig. 10.3a). Interestingly, they are the three samples whose carbonate matrix is made of calcite (ATX-C11, -C15 and -C16). Once the mineralogy-dependent isotopic fractionations are accounted for, a cross-plot of $\delta^{13}C_{DIC\text{-}eq}$ and $\delta^{18}O_{H2O\text{-}eq}$ erases most of the variability found between the two sub-groups (Figs. 10.3b and 10.9b). Consistently with petrographic observations, the distinctive and homogeneous isotopic signatures of the "recrystallized facies" suggest that they were re-equilibrated and recrystallized from an external fluid, probably since the microbialites became emerged above the lake water level.

The $\delta^{13}C_{DIC\text{-}eq}$ and $\delta^{18}O_{H2O\text{-}eq}$ values may help uncovering what the fluid of recrystallization was, as they should reflect a mix between the late fluid and the lake water from which the

microbialites initially precipitated. Oxidation of the microbialite organic carbon would drive $\delta^{13}C$ towards lower, and not higher values. Groundwater or hydrothermal fluids would also bear lower C and O isotope compositions than what is observed (Chapter 5). These latter sources are also inconsistent with the microbialites high position on the crater walls. By contrast, emerged microbialites would easily be in contact with rain water. In the area, oxygen from rain was predicted to have an isotopic composition up to ~ -6 ‰ SMOW (Fig. 10.9b; Chapter 5). The calcite samples – which experienced quantitative dissolution before reprecipitation – should record an isotopic composition close to that of this fluid; for temperatures between 12 and 16 °C (corresponding to the average range of air temperatures in the area since 1960, Silva-Aguilera *et al.*., 2022a), their $\delta^{18}O_{H2O\text{-}eq}$ ranges between -5.4 and -6.3 ‰, consistent with a meteoric water source. Carbon in rainwater should come from atmospheric CO_2, with an average isotopic composition between -6.5 and -8.5 ‰ (Graven *et al.*., 2020). The isotopic composition of DIC coming from this CO_{2atm} would range from ~0.4 to 2.8 ‰ (for temperatures between 12 and 16 °C; Emrich *et al.*., 1970), which overlaps with the composition of most recrystallized microbialites (Fig. 10.9).

Figure 10.9: Distribution of the C and O isotope signatures from Atexcac microbialites. A) Isotope-stratigraphic profiles of the bulk microbialite carbonates in Atexcac, expressed in ‰ *vs*. VPDB. The height depicted on the ordinate axis is not scaled to the picture in the background. The microbialites samples were not collected on this exact crater wall, but it illustrates how similar microbialites buildups were sampled relative to the lake water level (below 0 are the living microbialites sampled from 5 to 20 m depth in the water column; ATX-C1 was the only of the ATX-C series to be sample underwater). Emerged microbialites over ~11m clearly evidence the lake level fluctuations, notably as a result of evaporation. B) Isotope compositions of the precipitation fluid in equilibrium with solid carbonates. These compositions were calculated for a temperature of 18 °C for emerged samples, and from 18 to 15 °C for samples in the water column. One can see a clear covariation trend from "ATX-C9" (6m above current water level) and "ATX19-5m" (5m within the water column), consistent with an evaporation trend. "Recrystallized" microbialites isotopic signatures from "ATX-C11/-C13" to "ATX-C21" (from ~7.5 to 11 m above water level) plot separately and were re-equilibrated with a subsequent, external fluid. In the graphic in B, a single temperature was used in the calculation of $\delta^{13}C_{DIC\text{-}eq}$ and $\delta^{18}O_{H2O\text{-}eq}$ to easily compare between the different samples. But calcite "recrystallized" samples (reprecipitated after dissolution from meteoric water) likely formed at temperatures closer to air temperatures from 12 to 16 °C, and would thus be characterized by even lower $\delta^{18}O_{H2O\text{-}eq}$. In this early alteration process, a low water to rock ratio (W/R) would significantly decrease the $\delta^{18}O$ signatures, but the $\delta^{13}C$ would have remained largely unaffected, although possibly homogenized among "recrystallized" microbialites. Hence, the putative composition of $\delta^{13}C$ before and after recrystallization should fall on the same line on the y-axis.

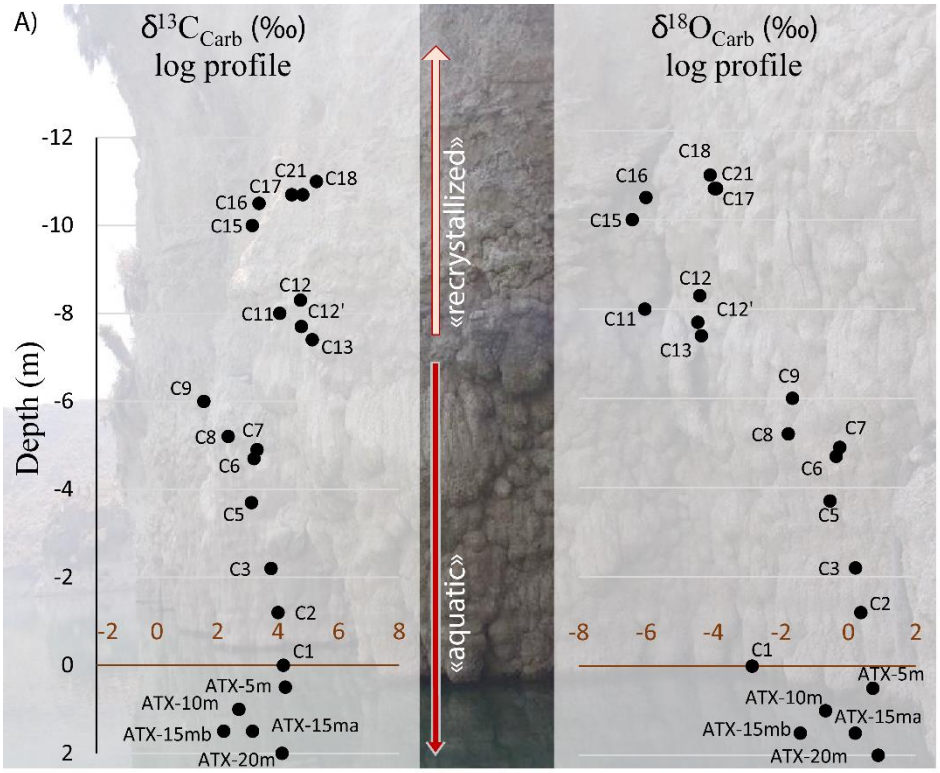
A)
δ13CCarb (‰)
log profile
δ18OCarb (‰)
log profile
«recrystallized»
«aquatic»
Depth (m)
-12
-10
-8
-6
-4
-2
0
2
-2 0 2 4 6 8
-8 -6 -4 -2 0 2
C21
C18
C17
C16
C15
C12
C11
C12'
C13
C9
C8
C7
C6
C5
C3
C2
C1
ATX-5m
ATX-10m
ATX-15ma
ATX-15mb
ATX-20m

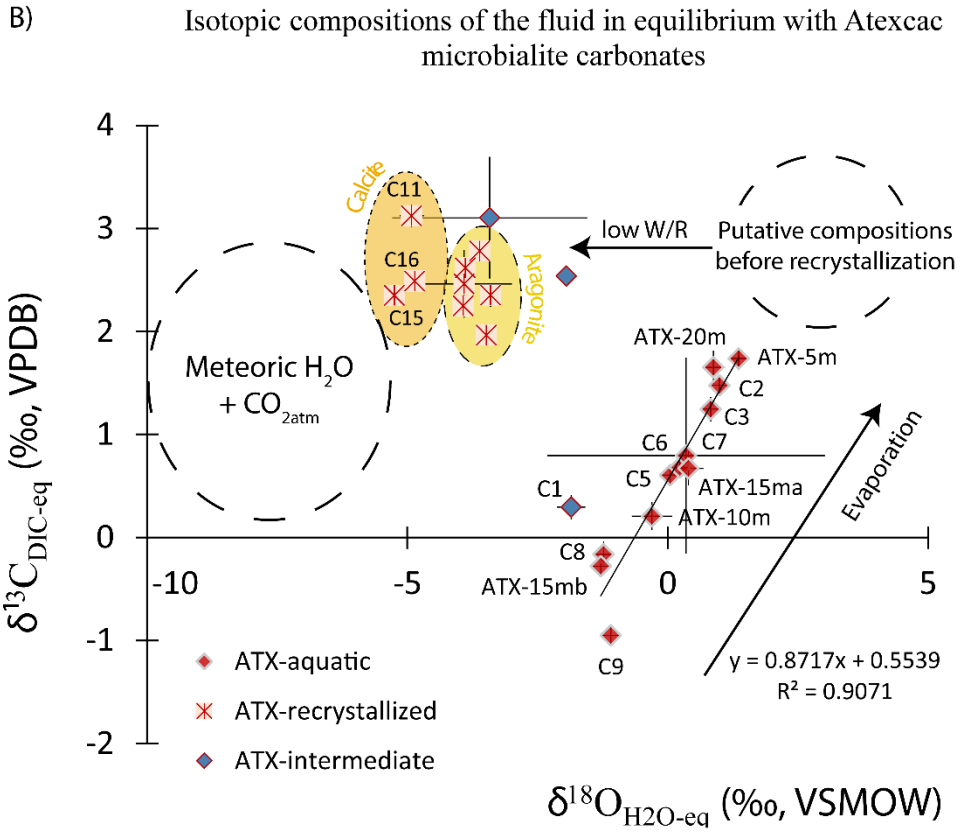
B)
Isotopic compositions of the fluid in equilibrium with Atexcac microbialite carbonates
δ13CDIC-eq (‰, VPDB)
δ18OH2O-eq (‰, VSMOW)
Calcite
Aragonite
C11
C16
C15
low W/R
Putative compositions before recrystallization
Meteoric H2O + CO2atm
ATX-20m
ATX-5m
C2
C3
C6
C7
C5
ATX-15ma
ATX-10m
C1
C8
ATX-15mb
C9
Evaporation
y = 0.8717x + 0.5539
R² = 0.9071
ATX-aquatic
ATX-recrystallized
ATX-intermediate

The magnitude of isotopic shifts due to secondary fluids strongly depend on the water to rock ratio (W/R), such that O is easily re-equilibrated whereas it takes more time for C, or requires the action of a DIC-enriched fluid (Sharp, 2017; Fig. 10.2). Rainwater is not concentrated in DIC, so if the fluid that interacted with the "recrystallized" microbialites once was, it would have been due to the dissolution of microbialite carbonates. Therefore, the $\delta^{13}C$ of the "recrystallized facies" is mostly reflecting the microbialites original signal – although it was potentially homogenized during recrystallization – whereas O was strongly shifted to more negative values. It follows that samples from ATX-C21 to ATX-C11/13 (high on the crater wall) had original $\delta^{13}C$ values higher than the better preserved and currently active microbialites below, from ATX-C9 to ATX19-20m (Fig. 10.9).

The transition between the "recrystallized" and "aquatic" facies is abrupt (< 2 m from ATX-C13 to ATX-C9) (Fig. 10.9). It implies that the lake level stayed around that of ATX-C9 for a prolonged period of time (~6 m above the current level). During that time, emerged microbialites were altered by rain water and recrystallized, but those underwater remained active and in equilibrium with the lake water. A slow water level decrease by evaporation from ATX-C21 to ATX-C9 would have progressively increased the lake $\delta^{13}C_{DIC}$, as seen between ATX-C9 and -C1, but not ATX-C21 and -C9 (Fig. 10.9). On the contrary, the ATX-C13/-C9 transition is associated with a drop in $\delta^{13}C_{carb}$ from ~5.1 to 1.6 ‰ (Fig. 10.9a). This suggests that the water level decrease between ATX-C21 and ATX-C9 could have been rapid, and associated to the input of a new, ^{13}C-depleted source of DIC, recorded in ATX-C9 (Fig. 10.9).

Such a rapid decrease of the lake level should be related to a sudden increase of the groundwater discharge. The studied area has remained seismically active since the crater's formation, and until the very last century (Carrasco-Núñez *et al.*., 2010; Suter, 2022). Although highly speculative, a destabilization of the lakes basement due to an earthquake could affect the way groundwater outflows the lake, potentially leading to a water level decrease until a new steady state is attained. In such a scenario, the carbonate record in Lake Atexcac microbialites would have experienced a first episode with relatively "high" $\delta^{13}C_{DIC}$ of ~ +3 ‰ values (*e.g.* as a result of a long-stand evaporation period), recorded in samples ATX-C21 to -C11/13, before a rapid "flush" event happened at the transition between sample ATX-C13 to -C9. After that, increasing proportions – due to a smaller lake volume – of groundwater DIC inflow, and/or possibly of degassing volcanic-CO_2, would tend to decrease the $\delta^{13}C_{DIC}$ and increase the lake pCO_2, to values observed today (Havas *et al.*., 2023a). Back to a more stable state, a second progressive evaporation phase would have decreased the lake level from ATX-C9 to its current

level, thereby generating the $\delta^{13}C$–$\delta^{18}O$ correlation seen in the more recent samples (section 10.3.3; Fig. 10.9). It would be interesting to test this hypothetic scenario by dating the emerged microbialite surfaces with cosmogenic isotopes for example, or by sampling/analyzing a deeper sediment core at the bottom of the lake, to attest if such an event was recorded in the sediments of Lake Atexcac.

10.3.1.1.2. *Micro-drilling results: effects of recrystallization in Atexcac at the scale of a single microbialite*

The recrystallized "ATX-C21" sample preserved a laminated structure, but carries relatively homogeneous isotopic signatures over a ~6cm-long transect (Fig. 10.6). Several distinct colored-phases have very close isotopic compositions, implying that some of the primary signatures are likely homogenized (Fig. 10.6). More negative values towards the top suggest that the microbialite's surface is more altered than the core. A $\delta^{13}C$–$\delta^{18}O$ correlation is recorded, with the largest variations found near the middle of the transect, where the microbialite's lamination is mostly visible (Fig. 10.6a, f, g, h). At the scale of carbonate sequences spanning millions of years, $\delta^{13}C$–$\delta^{18}O$ covariations are usually interpreted to reflect secondary fluid alteration (*e.g.* Knauth and Kennedy, 2009). At the centimetric scale of this sample however, the heterogeneity of the secondary fluids affecting this microbialite may have been limited. Moreover, the aliquot recording the highest $\delta^{13}C$ value (but also highest $\delta^{18}O$) was sampled in the "dirty white" layer, which shows the best-preserved texture, and thickest organic content (Fig. 10.6d, f, g). Hence, the covariation recorded is more likely primary than diagenetic, implying that some of the microbialite isotopic features may be conserved despite the average isotopic signatures being shifted. A tighter coupling between isotopic measurements and the analyzed carbonate fabrics (*e.g. via* SIMS analyses) will be necessary to further interpret how the isotopic signals of primary fabrics are progressively altered.

The "intermediate" microbialites plot in-between the "recrystallized" and "aquatic" facie (Figs. 10.3, 10.7 and 10.9) consistently with their petrographic description (Chapter 9). In ATX-C1, all the micro-drilling analyses but one plot near the "recrystallized" samples composition, in agreement with the carbonate fabrics that were sampled (Fig. 10.7). The microdrilled aliquot sampled at the very bottom (ATX-C1_H1) shows isotopic signatures closer to the presently forming microbialites (Figs. 10.7 and 10.9). This confirms the strong link there is between recrystallized carbonate fabrics and the non-primary nature of their O isotope

signature. Besides, it shows that the primary signal of this microbialite is better preserved at the core than at the rim.

10.3.1.1.3. *Isotopic signatures in relation with early Mg-silicate replacement by aragonite in Atexcac*

In Atexcac, carbonates from the "aquatic facies" record a lot of primary features (*e.g.* diatom frustules, filaments), but at least partly correspond to "secondary" precipitates as some of the carbonates in these microbialites replace precursor Mg-silicate phases. Microbialites from this facies are mostly in isotopic equilibrium with the lake's $\delta^{13}C_{DIC}$ (Fig. 10.10). They follow a clear $\delta^{13}C_{DIC\text{-}eq}$–$\delta^{18}O_{H2O\text{-}eq}$ trend suggestive of a primary evaporation-influenced record (section 10.3.3). This suggests that the replacement of Mg-silicates by aragonite occurs relatively rapidly in the microbialite formation, and allows for a good preservation of the lake $\delta^{13}C_{DIC}$ and $\delta^{18}O_{H2O}$ evolution through time. This further differentiates these *secondary replacement precipitates* from *recrystallized fabrics*, with isotopic evidences on top of petrographic ones (Chapter 9).

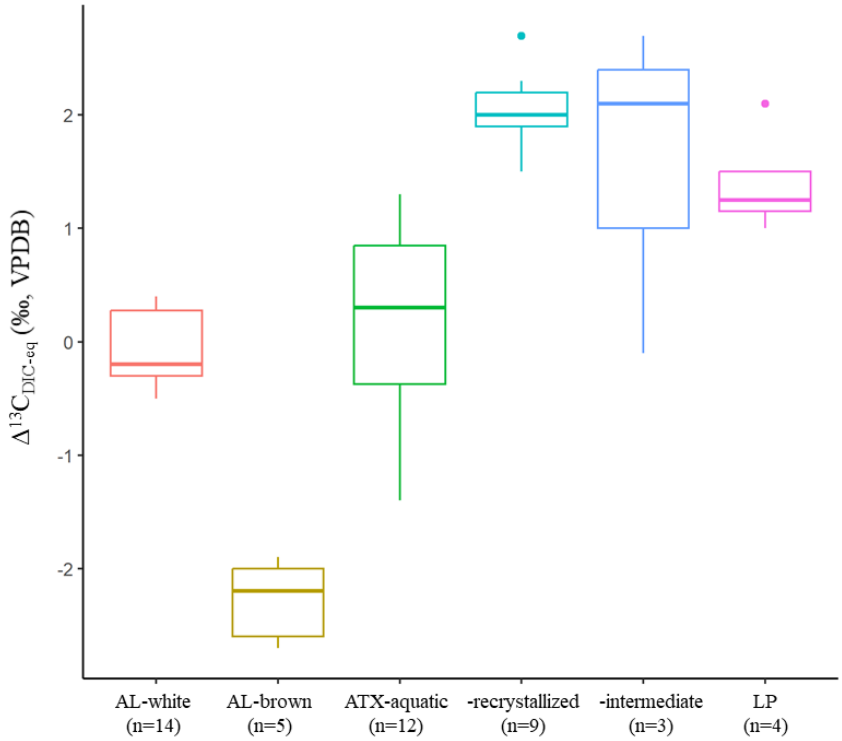

Figure 10.10: Boxplots of the difference between the current lake DIC isotope composition and that of the DIC from which microbialite carbonates precipitated in equilibrium, represented for each microbialite facies in the SOB lakes.

10.3.1.2. How does secondary replacement of aragonite by hydromagnesite alter the isotopic signatures in Alchichica microbialites?

Hydromagnesite (and more broadly Mg-carbonates), is the predominant mineralogical phase of "white microbialites" in Alchichica (Table 10.1). It has been suggested to precipitate abiotically, as a replacement of biogenic aragonite (Chapter 9; Kaźmierczak *et al.*., 2011; Gérard *et al.*., 2013). It is interesting to note that hydromagnesian microbialites (both underwater and subfossil) are in equilibrium with the lake $\delta^{13}C_{DIC}$, whereas aragonitic ones (suggested to be less affected by secondary processes, *cf.* Chapter 9), have significantly ^{13}C-depleted signatures (Fig. 10.10). This observation is consistent with spontaneous hydromagnesite precipitation, in equilibrium with the lake DIC, and potentially overwriting the primary carbonates, precipitated in the vicinity of the microbial mat at the microbialites surface. A similar process has been evidenced in Pavilion Lake microbialites, where the initial ^{13}C-enriched biosignatures of surficial carbonates resulting from photosynthesis activity are erased by secondary precipitation towards the microbialite's core (Belan *et al.*., 2019). The secondary carbonates were suggested to precipitate in equilibrium with the lake bulk DIC, and/or under the local influence of heterotrophy-derived DIC. These authors suggested that the initial biosignature disappeared in less than 20–400 years.

The fact that subfossil microbialites record $\delta^{13}C_{carb}$ close to equilibrium with modern $\delta^{13}C_{DIC}$ supports that DIC in Alchichica is a highly buffered reservoir (Havas *et al.*., 2023a), and did not evolve much over the past thousand years, as suggested from the stable sedimentary $\delta^{13}C_{carb}$ for the last ~340 years (Chapter 6). Accordingly, micro-drilling of the microbialites from 20m- and 40m-depths in Lake Alchichica show relatively homogeneous C and O isotope compositions (Figs. 10.4 and 10.11; standard deviation of less than 0.2 and 0.5 ‰ for C and O, respectively). In comparison, AL-T-9, from the "brown facies", shows higher variability over a smaller area (Figs. 10.5 and 10.11; SD of 0.7 ‰ for C and O, respectively), suggestive of more pristine signatures.

The occurrence of hydromagnesite as a replacing precipitate prevents the preservation of primary biosignatures (*i.e*. the metabolic effects on carbonate isotopic composition). However, by contrast with Atexcac "recrystallized" microbialites (whose transformation involved the action of external fluids), hydromagnesite precipitation in Alchichica occurs and takes root in the lake water. Thence, the secondary nature of hydromagnesite in "white microbialites" does not preclude them to faithfully archive hydrological and climatic changes.

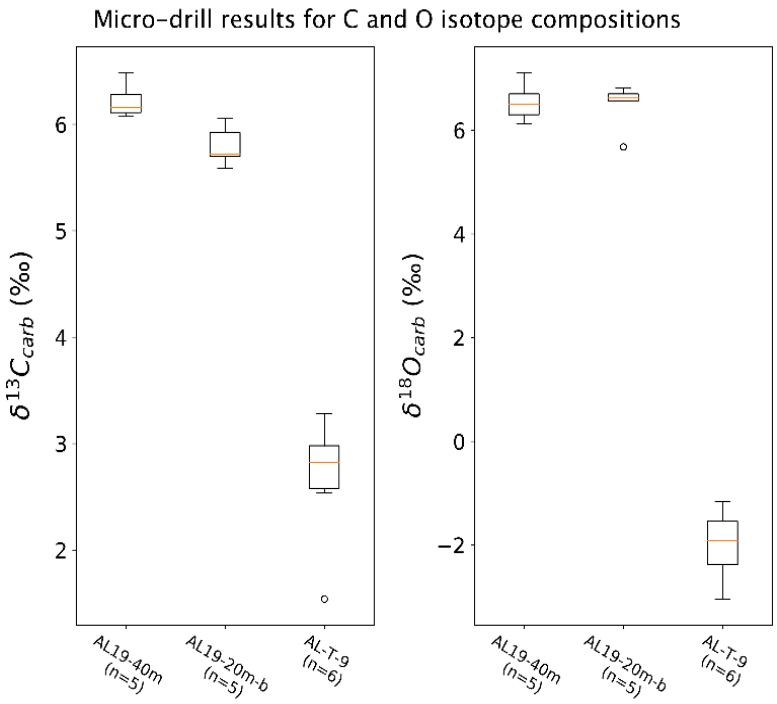

Figure 10.11 : Boxplots of the C and O isotope compositions from micro drill sampling in three microbialites from Alchichica: AL19-40m, AL19-20m-b and AL-T-9 (*cf.* Figs. 10.4 and 10.5 for a visualization of the sampling. For $\delta^{13}C_{carb}$, standard deviation (SD) were 0.19, 0.16, and 0.61, respectively. For $\delta^{18}O_{carb}$, SD were 0.46, 0.37, and 0.69, respectively. The small variability shown by AL19-40m and AL19-20m-b samples illustrates the homogenizing effect of secondary hydromagnesite precipitation as a replacing material in "white microbialites".

10.3.2. Biosignatures and local environments record by microbialites

The $\delta^{13}C_{carb}$ of the SOB lake sediments were in equilibrium with the $\delta^{13}C_{DIC}$, and followed the alkalinity gradient with increasing values from La Preciosa to Atexcac to Alchichica. By contrast, the microbialite record can be more variable and is not always in equilibrium with the current lake $\delta^{13}C_{DIC}$ (Fig. 10.10). In Alchichica, the $\delta^{13}C_{carb}$ of "brown" and "white" microbialites (sometimes adjacent) average 2.1 and 6.2 ‰, respectively, with the latter being in equilibrium with $\delta^{13}C_{DIC}$ but the former being lower (Fig. 10.10). In contrast, the $\delta^{13}C_{DIC\text{-}eq}$ in La Preciosa microbialites (either active or subfossil) are systematically heavier than the equilibrium value (*i.e.* $\Delta^{13}C_{DIC\text{-}eq} > 0$; Fig. 10.10).

A positive $\Delta^{13}C_{DIC\text{-}eq}$ shift cannot be explained by a change of the lake $\delta^{13}C_{DIC}$ over time. Indeed, evaporative conditions in the SOB area should drive the lakes $\delta^{13}C_{DIC}$ to higher values with time, as seen in the sediment carbonate records of La Preciosa and Atexcac (Chapter 6). Active (*i.e.* immerged) and recently emerged microbialites in La Preciosa should thus bear an isotopic composition in equilibrium, or lower than equilibrium with the lake DIC. Therefore, other processes than evaporation or a change of $\delta^{13}C_{DIC}$ over time influence the microbialites carbonate record.

After the samples affected by recrystallization have been put aside (*i.e.* the "recrystallized facies" in Atexcac), the following processes could explain the observed positive and negative $\Delta^{13}C_{DIC\text{-}eq}$ shifts: (i) temperature changes, (ii) rapid precipitation resulting in isotopic disequilibrium (Sumner, 2001; Houghton *et al.*., 2014), and (iii) precipitation from a DIC reservoir locally affected by other DIC sources. (i) In the contexts studied, small temperature variations (~ from 10 to 20 °C) could have a visible impact on the carbonate O isotopes, but would not generate several-‰ deviations in $\delta^{13}C$ (Chacko *et al.*., 2001 and references therein). (ii) Disequilibrium effects could occur due to microbially enhanced precipitation rates. They would induce a negative $\delta^{13}C_{carb}$ signature if precipitation was enhanced by heterotrophic activity (but would be cancelled out in case of autotrophy-driven precipitation; Sumner, 2001). The third possibility could occur if, (iiia) an external DIC source feeds in the lake near the location of microbialite formation, or (iiib), autotrophic or heterotrophic activity locally shift the $\delta^{13}C_{DIC}$ (Figs. 10.1 and 10.2).

Both autotrophic and heterotrophic metabolisms can trigger carbonate precipitation (*e.g.* Dupraz *et al.*., 2009) and have opposite isotopic effects on the DIC reservoir they exchange with (Figs. 10.1). For example, autotrophic photosynthesis increases pH *via* the consumption of ^{12}C-rich CO_2 (*e.g.* Breitbart *et al.*., 2009), which raises alkalinity and favors carbonatogenesis (Fig. 10.1) (*e.g.* Visscher and Stolz, 2005; Dupraz *et al.*., 2009). Microbial sulfate reduction (MSR) respires ^{12}C-rich organic matter, generating $H^{12}CO_3^-$, which favors carbonate precipitation as well (Visscher and Stolz, 2005), but bearing a comparatively light isotopic signature (Fig. 10.1). Accordingly, C isotope deviations of carbonates $\delta^{13}C$ from canonical equilibrium values (*i.e.* assuming or determining a reference $\delta^{13}C_{DIC}$) in both modern and fossil microbialites have been often interpreted to reflect the presence of heterotrophic (*e.g.* Andres *et al.*., 2006; Breitbart *et al.*., 2009; Pace *et al.*., 2016), or autotrophic organisms (*e.g.* Planavsky *et al.*., 2009; Brady *et al.*., 2010; Louyakis *et al.*., 2017; Friesenbichler *et al.*., 2018), or both (Sumner, 2001; Nitti *et al.*., 2012).

Following a purely isotopic mass balance logic, Alchichica "brown microbialites" should have precipitated influenced by heterotrophic activity, those in La Preciosa following autotrophic activity, and those in Atexcac as a variable mixture of both type of metabolisms (Fig. 10.10). Next I unravel the actual history of formation of these microbialites combining microbiological, mineralogical, geological, and geochemical data to assess whether the above "isotopic conclusions" are consistent or not.

10.3.2.1. Autotrophic biosignatures: La Preciosa (and Atexcac) microbialites

Iniesto *et al.*. (2021b) found that a common core of prokaryotic (and eukaryotic) organisms was shared across the microbialites of ten Mexican crater lakes following an alkalinity gradient (including La Preciosa, Atexcac and Alchichica). The shared prokaryotic OTUs represented ~40% of the total diversity in microbialites community in Alchichica and Atexcac, and 25% in La Preciosa. Based on the metabolic potential of dominant taxa, major metabolisms for carbonatogenesis are clearly dominated by oxygenic and anoxygenic photosynthesis in the three lakes, while microbial sulfate-reduction only plays a minor role (Iniesto *et al.*., 2021b). Anoxygenic phototrophs and heterotrophs are likely more abundant in La Preciosa than in the other two lakes (Iniesto *et al.*., 2021b; Fig. 10.12a).

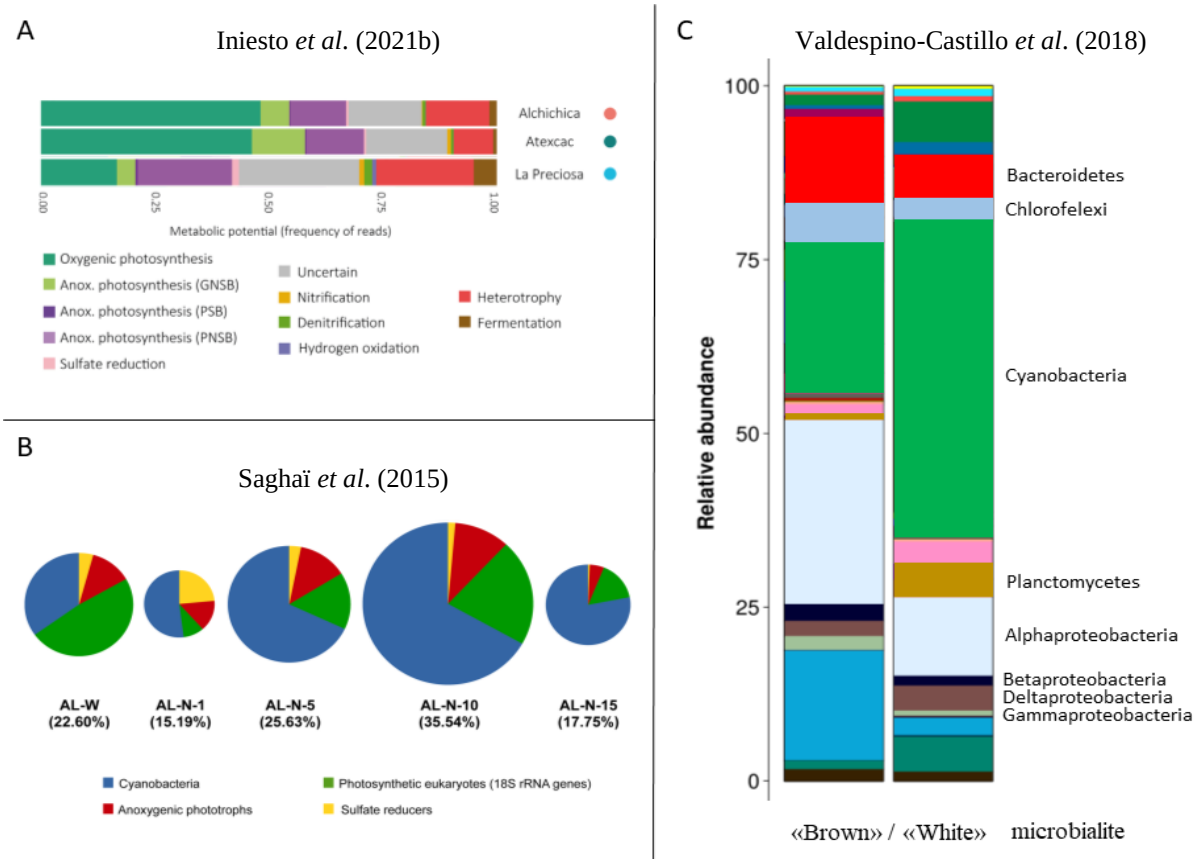

Figure 10.12 : Metagenomic diversity data for Alchichica microbialites from Saghaï *et al.*. (2015) and Valdespino-Castillo *et al.*. (2018), as well as for Atexcac and La Preciosa from Iniesto *et al.*. (2021b). The data from Iniesto *et al.*. Shows the different metabolisms contribution based on the dominant microbial taxon abundances. The samples from Saghaï and Iniesto *et al.*. correspond to white microbialites from the western and northen shore, with aragonite content up to 50% (AL-N-15). « Brown » columnar from Valespino-Castillo *et al.*. contain 97 wt. % of

aragonite. The carbonate-promotting metabolisms are clearly dominated by photosynthesis, with small contribution of sulfate reduction. According to Saghaï *et al.*. (2015) and Iniesto *et al.*. (2021b), anoxygenic photosynthesis is performed by Chloroflexi, along with Alpha- and Gammaproteobacteria mainly. Bacteroidetes and Planctomycetes are typical EPS-degrading bacterial groups, while Deltaproteobacteria contain several sulfate reducer species (Saghaï *et al.*., 2015, although the gene associated with sulfate reduction was found in very low abundance (Saghaï *et al.*., 2016). The bottom blue color in 'C' are unassigned OTUs.

Organic C isotope signatures agree with a primary photosynthetic origin of the microbialites biomass in the three lakes with $\Delta^{13}C_{org\text{-}DICeq}$ averaging -25, -28 and -26 in La Preciosa, Atexcac, and Alchichica, respectively (Fig. 10.13). Comparable signatures were similarly interpreted in Pavilion Lake (-26.8 ‰; Brady *et al.*., 2010), in Cuatro Ciénagas (-30 to -31 ‰; Breitbart *et al.*., 2009), and Kelly Lake (-26 to -29‰; White III *et al.*., 2020). Photosynthetic-dominated biomass is also consistent with the numerous remains of autotrophic organisms found in microbialites from La Preciosa and the "brown" and "aquatic" facies in Alchichica and Atexcac (Chapter 9; Zeyen *et al.*., 2015).

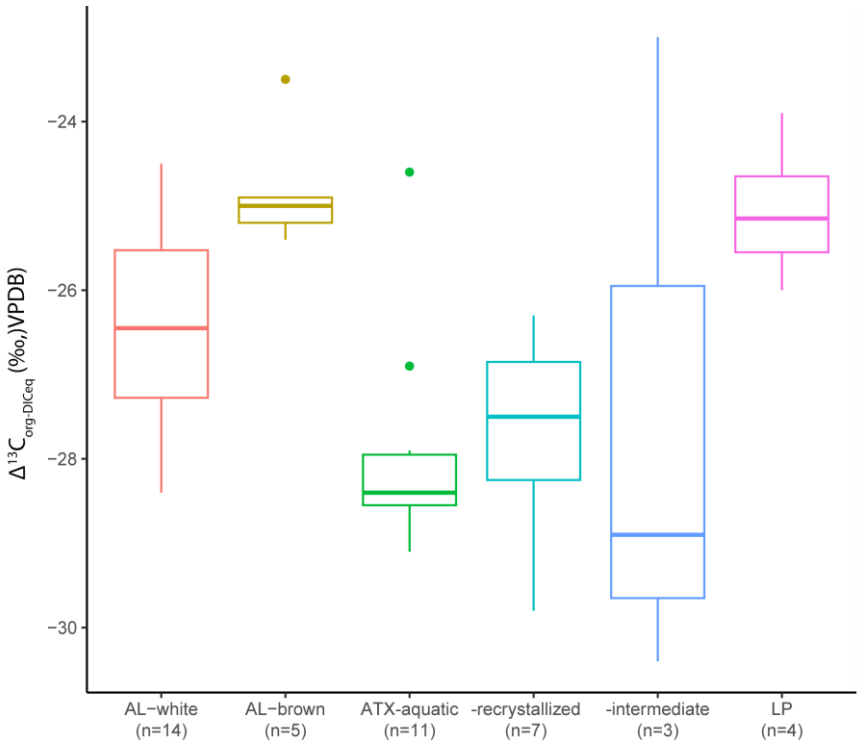

Figure 10.13 : Boxplots of the isotopic fractionation between microbialites bulk organic C and the DIC in equilibrium with the carbonates, represented for each microbialite facies in the SOB lakes.

In La Preciosa, the connection between microbial activity and the positive isotopic shift is directly evidenced by "PR-2" sample micro-drilling. Indeed, aliquots of the microbial shrubs show systematic ^{13}C-enrichment compared to the lake $\delta^{13}C_{DIC}$, and to the $\delta^{13}C$ of porosity in-filling detrital carbonates (Fig. 10.8). Most interestingly, the detrital aliquots surround the $\delta^{13}C$–$\delta^{18}O$ values of the bottom lake sediments (Fig. 10.8), suggesting a different formation pathway for the microbialite carbonate shrubs, and detrital grains and bottom lake carbonates. This reinforces the identification of these bottom lake carbonates as abiotic products (*i.e.* in the sense that it precipitated from an oversaturated water with little metabolic influence), faithfully recording the evolution of the lake's $\delta^{13}C_{DIC}$ and $\delta^{18}O_{H2O}$ (Chapters 4 and 6). However, the signatures of 'H8' and 'H7' detrital aliquots lean towards the microbial aliquots composition, suggesting some reworking of the microbialite actual material, and inclusion into the detrital matrix. In consequence, the $\delta^{13}C$–$\delta^{18}O$ correlation recorded by detrital grains has a steeper slope than the bottom sediments because, in contrast to O, carbon is more heavily shifted than if there was no microbial influence at all in the microbialites detrital grains. Microbialites in La Preciosa also have the highest TOC content of all three lakes, evidencing the importance of autotrophic metabolisms in this lake, and their impact on carbonatogenesis (Fig. 10.14).

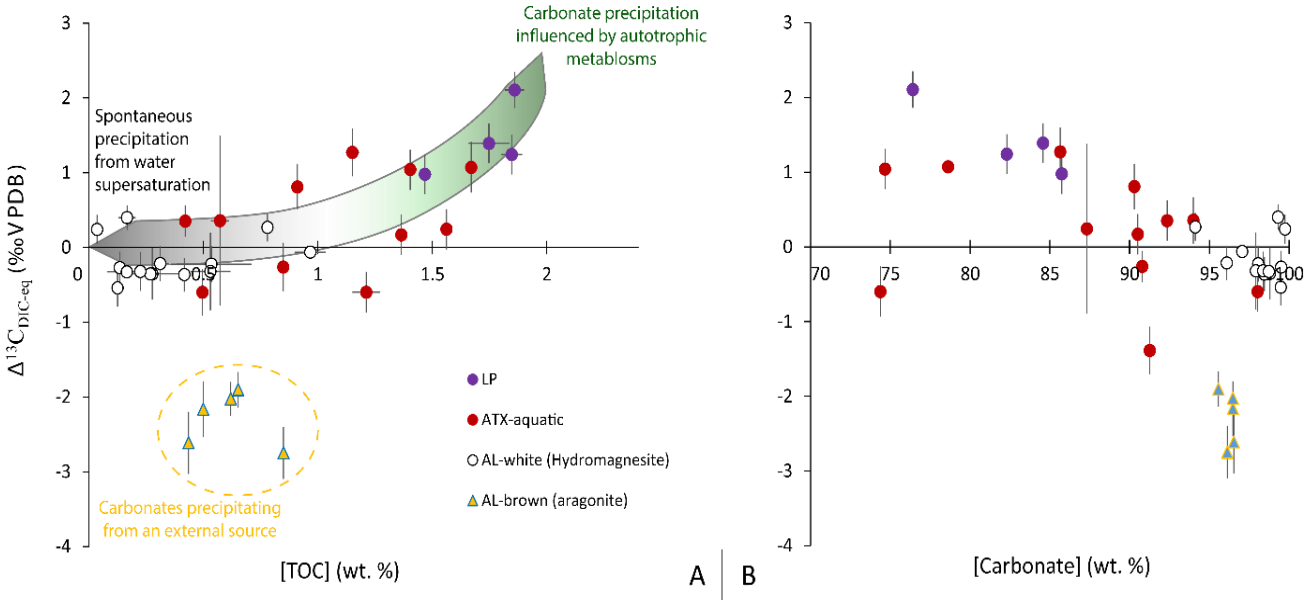

Figure 10.14 : Isotopic disequilibrium between the lakes $\delta^{13}C_{DIC}$ and microbialites $\delta^{13}C_{DIC\text{-}eq}$ as a function of the microbialites total organic carbon (A) and bulk carbonate contents (B) in weight percent (wt. %). Microbialites carbonates with $\Delta^{13}C_{DIC\text{-}eq}$ close to 0 precipitate near equilibrium with the lakes $\delta^{13}C_{DIC}$; those deviating from 0 have been affected by other processes (autotrophic influence on carbonatogenesis in La Preciosa) or sources (*e.g.* "brown" aragonitic microbialites in Alchichica). These deviations have more or less chances to be expressed and preserved depending on the alkalinity-buffer capacity of each lake water, and how much carbonate spontaneously precipitate.

In Atexcac microbialites, the carbonate isotopic signatures approach a value near equilibrium with the lake DIC as the TOC content decreases (Fig. 10.14a). Atexcac samples connect within a trend from La Preciosa microbialites to "white microbialites" in Alchichica (Fig. 10.14a). This trend can be interpreted as the reflect of dominant autotrophic biosignatures preserved in samples with high TOC content, but obscured in microbialites with higher carbonate content (Fig. 10.14b). High carbonate contents (and microbialite abundance) are fostered where physico-chemical constraints (*e.g.* evaporation, ion-rich groundwaters) favor high saturation indexes with respect to carbonate phases (Caumartin *et al.*., 2023). In such environments, spontaneous carbonate precipitation is more likely to occur without an influence of biological processes, and thus would proceed near equilibrium with the whole lake DIC (*i.e.* $\Delta^{13}C_{org\text{-}DICeq} \approx 0$ ‰). In Figure 10.14, these carbonates correspond mainly to the previously discussed "replacement-hydromagnesite" found in Alchichica (section 10.3.1.1.3). Consistently, this latter lake presents the most alkaline conditions, and the highest carbonate saturation indexes of the lakes studied (Zeyen *et al.*., 2021). On the lower hand of the alkalinity gradient, microbialites in La Preciosa have smaller carbonate contents, and their C isotope signatures are more easily influenced by biological processes (Fig. 10.14b).

Therefore, the microbialite carbonate records highlight the importance of distinct buffering capacities of the DIC/alkalinity reservoirs, similarly to our inferences about the water column (Havas *et al.*., 2023a). The marked positive $\Delta^{13}C_{DIC\text{-}eq}$ shift in La Preciosa is thus well explained by the influence of photosynthetic organisms triggering carbonate precipitation, and a lower buffering potential allowing the record of biosignatures (Fig. 10.14). These results suggest that microbialites forming in highly alkaline/saline water bodies are weakly susceptible to preserve diagnostic C isotopic biosignatures in their carbonates.

10.3.2.2. Alchichica "brown microbialites": the influence of an external source.

The interpretation of heterotrophy-driven precipitation for aragonitic "brown microbialites" based on a negative bulk $\Delta^{13}C_{DIC\text{-}eq}$ shift contrasts with the results of Iniesto *et al.*. (2021b) (Fig. 10.12a). Other metagenomic and metatranscriptomic studies – dedicated to the microbialites in Alchichica – also support that carbonate-promoting metabolisms are dominated by photosynthesis (oxygenic and anoxygenic) photosynthesis, while the contribution

of MSR is minor (*e.g.* Fig. 10.12b and c; Saghaï *et al.*., 2015, 2016; Valdespino-Castillo *et al.*., 2018; Iniesto *et al.*., 2021a). In some of the "brown microbialites", Kaźmierzack *et al.*. (2011) specifically report the encrustation of filamentous cyanobacteria by aragonite, which is also the most recurrent association found in presently forming microbialites. Indeed, Couradeau *et al.*. (2013) and Gérard *et al.*. (2013) found that aragonite in the surface mats of "white microbialites" sampled at depths between 4 to 14 m is actively precipitated by cyanobacteria growing cells (mostly Pleurocapsales).

The discrepancy between microscopic observations, metagenomic findings, and bulk isotopic results for "brown microbialites" is all the more surprising that micro-drilling analyses of aragonite fabrics in a "white microbialite" sample does record a biosignature characteristic of autotrophic organisms (Fig. 10.5c). As a reminder of the classification presented in Chapter 9, the carbonate mineralogy in "brown microbialites" consists almost exclusively in aragonite (>96% with less than 2% hydromagnesite), whereas "white" ones contain mostly hydromagnesite, but sometimes with appreciable amounts of aragonite (up to 27%) (Table 10.1). In "AL-T-11", a clear separate micro-sampling of aragonite and hydromagnesite phases was possible. The $\delta^{13}C_{DIC\text{-}eq}$ from micro-drilled aragonite aliquots record a 1-2 ‰ ^{13}C-enrichment compared with the $\delta^{13}C_{DIC\text{-}eq}$ from abiotic hydromagnesite nodules, which is most consistent with an autotrophy-driven precipitation of aragonite in this sample (Fig. 10.5c), but differs from the bulk $\Delta^{13}C_{DIC\text{-}eq}$ values of "brown microbialites".

To explain the isotopic compositions of "brown microbialites", Kaźmierczak *et al.*. (2011) suggested that they precipitated from a less evaporated lake water (*i.e.* having a lower $\delta^{13}C$ and $\delta^{18}O$). In other words, these microbialites would record negative bulk $\Delta^{13}C_{DIC\text{-}eq}$ because they precipitated at a time when the water level was higher, and the lake $\delta^{13}C_{DIC}$ lower. However, it is in contradiction with the contiguous arrangement of "brown" and "white" samples (Chapter 9; Fig. 10.15), or the fact that some presently immerged microbialites have lower isotopic compositions than emerged subfossil ones (Fig. 10.3). Furthermore, it is unlikely that a 4-7 ‰ difference in $\delta^{18}O_{H2O}$ would have been induced by lake level variations (*i.e.* by evaporation) and recorded by microbialite deposits that grew at the same level. For example, 0-6 ‰ variations in the $\delta^{18}O_{carb}$ of sediments and microbialites from the Great Salt Lake have been related to water level fluctuations of nearly 20 m, due to water inflow and evaporation balance (Newell *et al.*., 2017). Similarly, microbialites separated from more than 10 m on the

crater walls of Atexcac have $\delta^{18}O_{carb}$ spreading "only" over ~ 3 ‰ (Fig. 10.9). Evaporation thus seems unlikely to explain the different microbialite isotopic compositions in Alchichica.

A possible unifying explanation is that sulfate-reducing bacteria (SRB) have a stronger impact on carbonate precipitation than photosynthesizers despite being less abundant. "Brown microbialites" have much higher pyrite concentrations than "white" ones, and than most of the other analyzed samples (Chapter 11). The combined equation of sulfate reduction and carbonate precipitation,

$$Ca^{2+} + OH^- + SO_4^{2-} \rightarrow CaCO_3 + CO_2 + HS^- + 2H_2O \qquad (10.1),$$

suggests a 1:1 carbonate precipitation to sulfide production ratio (*e.g.* Dupraz *et al.*., 2009). Considering carbonate and solid sulfide (pyrite) concentrations measured in the aragonitic samples, this ratio varies between 150 and 2500. Therefore, even if some of the sulfide production was not recorded in pyrites due for example to a lack of dissolved Fe, MSR was likely insufficient to significantly contribute to the bulk carbonate C isotope compositions of "brown microbialites". Moreover, the "brown microbialites" plot far off the main trends in figure 10.14, suggesting that their carbonate signatures reflect something else than a strong alkalinity buffer effect (alike the hydromagnesian samples), or an autotrophic influence (alike La Preciosa samples). Rather, these ^{13}C-depleted signatures could sign a different water/DIC supply to the western/south-western shore of Lake Alchichica.

Petrographic observations evidenced a great abundance of autotrophic and heterotrophic organisms in the "brown microbialites", suggestive of potentially more productive waters than in the rest of the lake (Chapter 9). This supports that at the time, and/or location, of "brown microbialites" formation, the precipitation water was fueled by a source with a distinct chemical composition, probably richer in nutrients. This is not directly testable by trace element signatures in our samples, which were not determined. However, Zeyen *et al.*. (2021) reported such data for a microbialite sample that is similar to the "brown microbialites" from this PhD ("AL2012-17" from the NW shore of the lake with an aragonite content of 98%). A principal component analysis (PCA) of 63 bulk chemical composition variables from 18 Mexican microbialites (Zeyen *et al.*., 2021) showed that this sample significantly differed from the others (including several from Alchichica , Atexcac, and La Preciosa), harboring prominent positive Eu and Gd anomalies, Y/Ho ratio, and Fe content, interpreted as the result of chemical enrichment from groundwater infiltrating adjacent volcanic rocks (Zeyen *et al.*., 2019, 2021).

The influence of an external source on "brown microbialites" formation is also suggested by the common occurrence of bubbling rising from these columnar "brown microbialites" (Chapter 9; Saghaï *et al.*., 2015). The bubbling could result from the release of volcanic- or groundwater-fluids on this side of the lake (Chapter 5; Silva-Aguilera, 2019). The delivery of much lower Mg:Ca groundwater (~2; Lelli *et al.*., 2021) relative to the lake (~120) could have a primary control on the precipitation of massive aragonite on this side of the crater, compared with the rest of the lake where hydromagnesite mostly precipitates. Besides, "brown microbialites" are predominantly located on the same side as the steep crater wall (Chapter 9). Alteration of volcanic deposits by meteoric fluids followed by their infiltration/runoff may (have) strongly impact(ed) the water chemistry near the western/south-western shore of Alchichica. Leaching of Fe-rich volcanic minerals is consistent with the general brown color of these samples, the multiple red-orange oxidized surfaces found in optical microscopy, and the much higher Fe content measured in Alchichica aragonite microbialites (Zeyen *et al.*., 2021). An XRD analysis of an outcropping basalt sample (AL-T-4) showed the presence of hematite, chloritoid, and diopside minerals, which can be Fe-rich (Fig. S10.1). An external source from groundwater and/or rainwater would also explain the different ^{18}O signatures of "brown microbialite" carbonates, which would thus have precipitated from a mix between the lake water and a ^{18}O-depleted source.

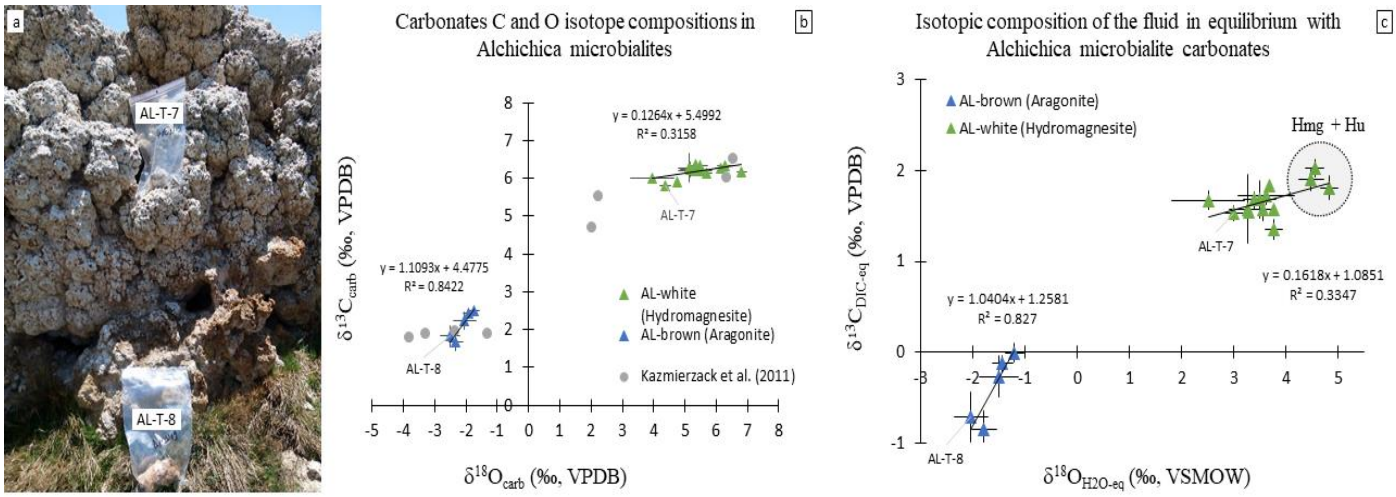

Figure 10.15: Distribution of the C and O isotope signatures from Alchichica microbialites. a) Photograph of a "white microbialite" overlying a "brown microbialite". b) Carbonates C and O isotope compositions in microbialites analyzed in this PhD and by Kaźmierzack *et al.*. (2011). c) Isotopic compositions of the precipitation fluid in equilibrium with solid carbonates, calculated for a temperature of 18 °C for emerged samples, and from 18 to 15 °C for samples in the water column. Kaźmierzack *et al.*. samples are not represented in 'c' because their precise mineralogy is not known. If the two gray dots in the middle of the cross-plot in 'b' had aragonite and

hydromagnesite proportions of about 60-40, they would plot with the green cluster in 'c'. The three samples with the most positive $\delta^{18}O_{DIC\text{-}eq}$ values in 'c' correspond to samples at 20m depth or more, and contain huntite, explaining why they plot separately (black circle area). If evaporation primarily drove the isotopic signals of brown and white microbialites, AL-T-7, which is above AL-T-8, should have lower $\delta^{18}O$ and $\delta^{13}C$ than AL-T-8. Instead, its compositions are higher because its mineralogy mainly consists of hydromagnesite.

10.3.3. Microbialite carbonates as climatic/environmental archives

The $\delta^{13}C_{carb}$ of the SOB lake sediments followed the alkalinity gradient and thus reflected the integrated environmental factors creating that gradient (Chapter 6). In the two preceding subsections, I have shown that the Mexican microbialites do not record that gradient as consistently, due to local recrystallization, biological or external fluid effects. I now investigate how the microbialites may, or not, preserve a pristine climatic- and hydrologic-related signature across different alkalinity conditions.

Alchichica microbialites were interpreted to reflect different stages of formation at distinct evaporation levels, based on a covariation of C and O isotopes in carbonates (Kaźmierczak *et al.*., 2011; Fig. 10.15). The correlation seen in the $\delta^{13}C_{carb}$–$\delta^{18}O_{carb}$ dataset actually reflects the existence of two microbialite endmembers having a separate history of formation, as discussed above, rather than a continuous evaporation trend (Fig. 10.15). The two subgroups exhibit very different $\delta^{13}C$–$\delta^{18}O$ relationships (Fig. 10.15), reflecting the different mechanisms that influence their formation, that is: biology/source driven for "brown microbialites" (subsection 10.3.2.2), and abiotic alkalinity-buffered/evaporation-driven precipitation for "white" ones (subsection 10.3.1.2; Fig. 10.14b).

In the "AL-T-11" sample, hydromagnesite nodules record extreme isotopic enrichments ($\delta^{13}C$ and $\delta^{18}O$ up to +9 and +13 ‰, respectively), compatible with a formation pathway through intense evaporation in an isolated basin or "puddle", where water can undergo a Rayleigh-type distillation process. It exemplifies the importance of local environmental conditions in controlling lateral and temporal carbonates isotopic variability as previously suggested (Ingalls *et al.*., 2020). It is interesting to note that this evaporation-driven $\delta^{13}C_{DIC\text{-}eq}$–$\delta^{18}O_{DIC\text{-}eq}$ trend has a slope of 0.31, similar to the slopes found for Atexcac and La Preciosa sediments (0.29 and 0.42, respectively), which precipitate in equilibrium with the lakes $\delta^{13}C_{DIC}$, and likely reflect an evaporation trend (Chapter 6).

By contrast, the slope recorded by micro-drilled aragonite layers from "AL-T-9" sample (of the "brown" facies) lies on a higher end (s=0.77), closer to that recorded by the overall "brown" facies (s=1.04) (Figs. 10.5 and 10.15). The first order control on the bulk carbonate signatures of this facies is the composition of the external source from which they precipitate (section 10.3.2.2). Nonetheless, these microbialites are also characterized by a formation in more productive waters and biologically-dynamic conditions than the "white microbialites" (Chapter 9). These conditions of formation could show through the isotopic signal of the "brown" facies *via* a steeper slope around 1. As described earlier for the "PR-2" sample in La Preciosa, this is explained by a greater influence of biological activity on C over O isotopes. Therefore, these patterns between the carbonates $\delta^{13}C$–$\delta^{18}O$ trend and their formation pathway gives a quantitative frame for distinguishing between a primary biotic or abiotic origin of the microbialite carbonates in the Mexican alkaline lakes.

In Atexcac, microbialites outcropping on the crater walls over a height of ~10 m should allow a clear assessment of the lake level fluctuations' impact on the microbialite carbonates isotopic record. As expected, samples with pristine signatures (from 6 m above the water level down to 20 m in the water column; Fig. 10.9) show a strong $\delta^{13}C$–$\delta^{18}O$ correlation (R^2=0.87). The progressive increase in $\delta^{13}C$ and $\delta^{18}O$ from "ATX-C9" (6m above water) to "ATX19-5m" (5m in depth) is very consistent with a higher lake level recorded by "ATX-C9", and evaporation leading to the currently lower water level (Fig. 10.9).

The slope for Atexcac "aquatic" microbialites amounts 0.83, which is higher than the slope recorded in the bottom sediments of the same lake (0.29), and falls in between the "evaporation-type" and "biology-influenced-type" slopes (see above). Many diatom and cyanobacteria remains were observed in these samples thin sections (Chapter 9). Autotrophic metabolic activity would act to increase the medium $\delta^{13}C_{DIC}$ (Fig. 10.2), and therefore steepen the $\delta^{13}C$–$\delta^{18}O$ slope (Figs. 10.3 and 10.9). Therefore, the microbialite log section in Atexcac does not provide a perfectly faithful record of the lake's chemistry, despite spreading over a clear "evaporation profile", due to a microbial influence on the local medium.

The interpretation of Kaźmierczak *et al.*. (2011) is a good example of the biased view that can stem from $\delta^{13}C$–$\delta^{18}O$ microbialite carbonate data. The isotopic difference between "brown" and "white" microbialites is furthermore exacerbated by a mineralogical bias. Accounting for the different aragonite and hydromagnesite proportions in each sample, the calculated range of

$\delta^{13}C_{DIC\text{-}eq}$ and $\delta^{18}O_{H2O\text{-}eq}$ is 2 ‰ narrower than the measured $\delta^{13}C_{carb}$–$\delta^{18}O_{carb}$ range (Fig. 10.15). Besides, it changes the distribution of "white microbialites" such that they actually cluster in two distinct groups, instead of forming a continuous trend (Fig. 10.15). The three samples on the right side of the plot actually correspond to those which contain huntite ($MgCa(CO_3)$; only found in samples at 20 and 40m depths). Huntite is a secondary phase replacing both aragonite ($CaCO_3$) and hydromagnesite ($Mg_5(CO_3)_4(OH)_2{\cdot}4H_2O$) (Chapter 9). It could inherit a cryptic isotopic signature, recording both "its own" fractionation (*i.e.* related to huntite precipitation), and that of the primary carbonate phases. Hence, huntite would be isotopically heavier than if it directly precipitated from the lake water. The isotopic signatures of these samples thus represent an additional mineralogical bias, and not a primary hydrological marker.

Still, the calculated $\delta^{18}O_{H2O\text{-}eq}$ for the hydromagnesian samples is higher than the actual lake $\delta^{18}O_{H2O}$ (~1 ‰; Lelli *et al.*., 2021) by 2.5 ‰ on average. While there is no clear explanation for this discrepancy, many factors can impact O isotope signals. They include temperature variations and an insufficient knowledge of O isotope fractionations, especially for hydromagnesite which is an uncommon phase, and harbors several O-bearing chemical groups. The effect of salinity on this fractionation is for example unknown, and the precipitation temperature is not precisely known, although it can be critical (O'Neil and Barnes, 1971; Aharon, 1988). Finally, if hydromagnesite does form as a replacement material, it is not known how it exchanges with the initial aragonite minerals (similarly to the process presented for huntite).

Overall, this underlines the importance of identifying the specific carbonate petrographic facies and mineralogy as primary context information before any isotopic interpretations are made (Arenas *et al.*., 2019). Chagas *et al.*. (2016) described the ^{13}C-enrichment of Alchichica's "white microbialites" as "unusual for a condition of high alkalinity wherein photosynthesis should not drive precipitation". This enrichment is actually well explained considering the high C isotope fractionation associated with hydromagnesite precipitation (Aharon, 1988; Harrison *et al.*., 2021), and is not primarily driven by photosynthesis. In Eocene stromatolites from the Green River Formation, different carbonate facie were interpreted to record drastic evaporation and hydrological changes based on ^{13}C- and ^{18}O-isotope- and Na-enrichments found in micrite layers (Frantz *et al.*., 2014). However, all samples from these micrite layers, are composed of dolomite, or calci-dolomite, while the other facies contains only calcite. At 20 °C, dolomite and

calcite would precipitate with a ~5‰-difference in $\delta^{18}O$ (Chacko *et al.*, 2001 and references therein). Similarly, dolomite was found to incorporate much higher proportions of Na than calcite at room temperature (Oomori *et al.*, 1985). It underlines that small isotopic variations in the geological record, for instance in Precambrian formations containing both calcite and dolomite (*e.g.* Tang *et al.*, 2022), should be interpreted with caution.

10.3.4. How does the redox stratification impact the microbialites organic carbon signatures?

The sampling and analysis of microbialites from 5 to 40 m depths in Lake Alchichica allow the investigation of potential organic C isotope signatures changes in microbialites through a redox gradient, down to waters that stay anoxic for most of the year (*e.g.* Macek *et al.*, 2020). In Atexcac, microbialites at a 20-m depth are located in the transition from oxic to anoxic waters. Microbialites OC isotopes show systematically enriched compositions compared with the plankton values measured in 2019 (+1-3 ‰ in Alchichica, +0.5-4 ‰ in Atexcac). Planktonic communities in Alchichica significantly differed from benthic communities sampled in surface microbialites (Iniesto *et al.*, 2022), which could cause differences in C isotope signatures. However, planktonic communities sampled in Atexcac in 2019 are much closer to what is found in the microbialite communities at 20m depth (Fig. 10.16). The higher $\delta^{13}C_{org}$ in microbialites than in plankton (and smaller $\Delta^{13}C_{OC\text{-}DICeq}$) can be explained by a difference in CO_2 diffusion, usually being slower in microbial mats than in plankton, reducing the overall isotopic fractionation recorded (*e.g.* Des Marais *et al.*, 1989; Houghton *et al.*, 2014; Louyakis *et al.*, 2017).

In Alchichica, there is a clear increase of microbialite $\delta^{13}C_{org}$ with depth, parallel with the pattern observed in $\delta^{13}C_{plankton}$ (Fig. 10.16). Although plankton values in Atexcac showed the same increasing trend as in Alchichica, Atexcac microbialites $\delta^{13}C_{org}$ do not follow this depth pattern (Fig. 10.16). In contrast with Atexcac, the interior of hydromagnesian microbialites in Alchichica is mostly devoid of organics. Hence, bulk OM is restricted to the microbialites surface, where “active mats” can record a more accurate description of their contemporary environment. Meta-genomic and -transcriptomic analyzes from the same field campaign showed an increase of heterotrophs towards 40m depth in Alchichica (Fig. 10.16) and of secondary metabolite biosynthesis function expression (Microbialite-ANR-project, unpublished data). A preferential consumption of ^{13}C-enriched molecules by heterotrophs

(Williams and Gordon, 1970; Hayes *et al.*., 1989; Lehmann *et al.*., 2002; Jiao *et al.*., 2010) is consistent with this trend.

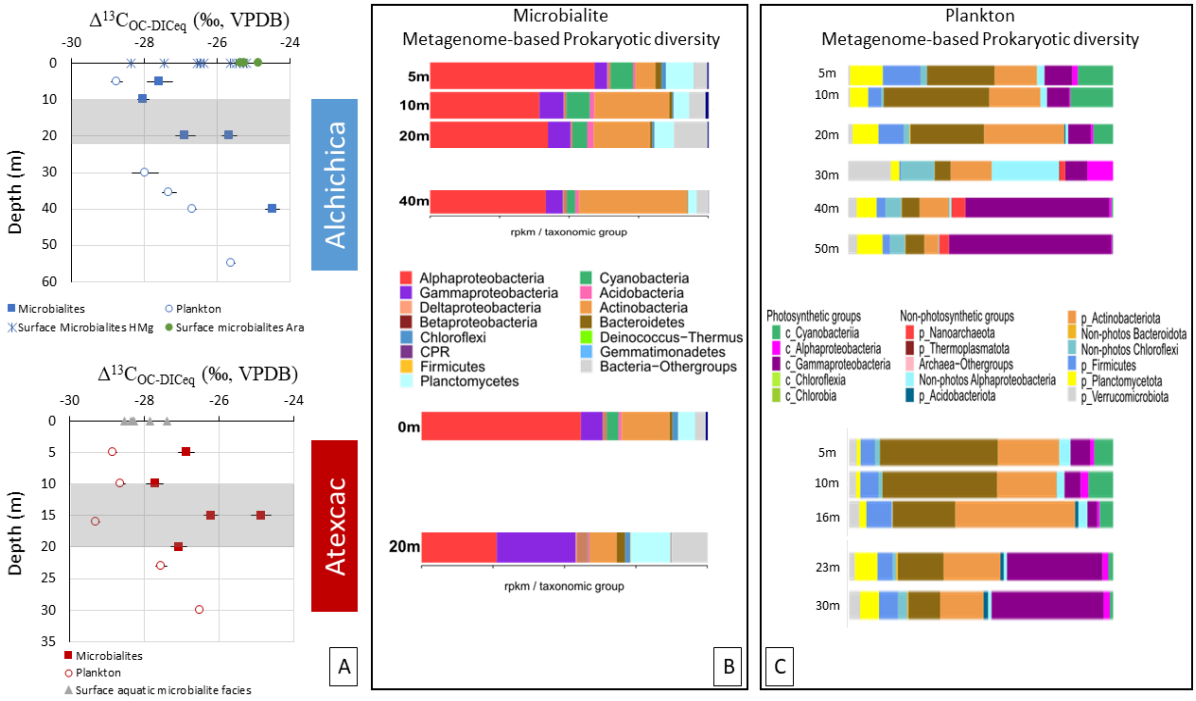

Figure 10.16 : Isotopic and metagenomic data comparison in Alchichica and Atexcac lakes. A) Isotopic fractionation between organic and inorganic C in the microbialites and in the plankton at different depths in the two lakes sampled in 2019. The gray-shaded area depicts the redox gradient in 2019, with anoxic waters below it. B) Relative abundance of prokaryotic OTUs in microbialites based on amplified 16S and 18S rRNA genes, ordered by phyla classes. C) Relative abundance of prokaryotic OTUs in water column plankton based on amplified 16S rRNA genes, ordered by phyla classes in photo- or non-photosynthetic groups. The microbial data were acquired by our partners from the "Microbialite-ANR-project".

The bulk (C:N) ratios measured in the OM of Alchichica microbialites and plankton show the same values and decreasing trend, while, again, the same trend is found in the plankton of Lake Atexcac, but not in its microbialites (Fig. 10.17). Instead the microbialites in Atexcac show no specific $(C:N)_{OM}$ trend, and very variable values in two samples from 15m (Fig. 10.17). In comparison, the two samples at 20m in Alchichica have very similar $(C:N)_{OM}$ ratios.

Therefore, the current stratification is well recorded in Alchichica $\delta^{13}C_{org}$ and $(C:N)_{OM}$ proxies, but mostly because the bulk of its organic content is limited to the microbialites' surface, while in their interior it is progressively lost in favor of massive hydromagnesite precipitation; organic matter is thus "permanently up to date". On the contrary, organics in Atexcac microbialites likely record a longer and more complex history, which blurs their

geochemical signal (*n.b.*: the same observation is made for nitrogen isotopes – Fig. S10.2 – but will not be discussed further).

The isotopic variability recorded in the microbialites of these stratified lakes nonetheless remain quite small (less than 4 ‰), and would be difficult to preserve and interpret in the geological record. Microbialites from surface and anoxic hypolimnetic waters in Atexcac have almost identical isotopic signatures (Fig. 10.16a) despite clear changes in the diversity of both planktonic and microbialite communities (Fig. 10.16b and c; Iniesto *et al.*., 2021b). In Alchichica, the signatures recorded in subfossil microbialites at the surface, overlap most of those formed in the water column (Fig. 10.16a). It shows that local processes at the mat scale (including redox), may be just as critical for setting the microbialites organic geochemical signatures, as redox condition of the whole environment. Nonetheless, the microbialite sampled in "the most extreme conditions" (*i.e.* at 40m, in the most reducing conditions) does show "the most extreme isotopic signatures" (here the highest $\delta^{13}C$ values) of our sample set. It would thus be interesting to obtain similar type of data in microbialites from permanently stratified water bodies showing stronger redox gradients to see if more active sulfur or methane cycling, for example, enables the record of more extreme and straightforward isotopic signatures. For example, it would be interesting to sample microbialites from Lake Dziani Dzaha (Mayotte, France) across its stratification (they were only sampled in the oxic zone so far; Gérard *et al.*., 2018), as it depicts extreme C and S cycling and isotopic signatures (Cadeau *et al.*., 2020, 2022).

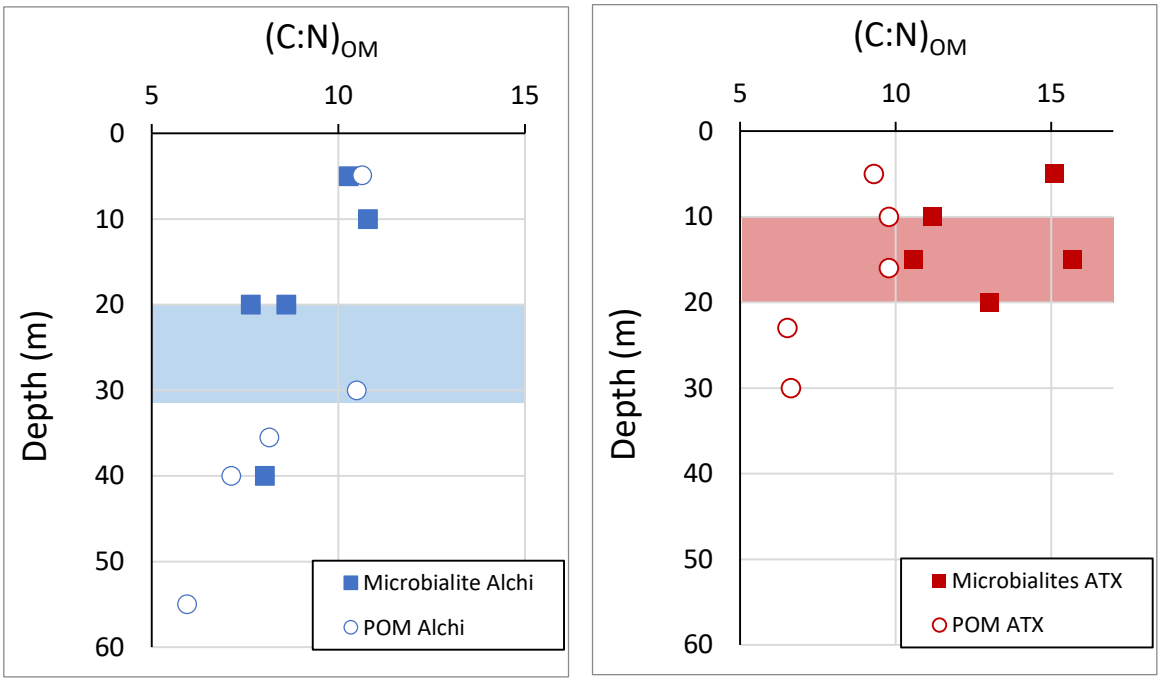

Figure 10.17: Water-column depth profiles of organic matter C:N ratios in the microbialite and plankton samples from Alchichica (blue) and Atexcac (red) lakes. The 2019 redox gradient from oxic to anoxic waters is shown by the colored layers.

The isotopic fractionation between organic C and the DIC source recorded by "brown microbialites" at the surface, tends to be higher, but remains close to that of "white microbialites" (Fig. 10.13, 10.16). This can result from a more limited access to CO_2 in the microbial mat, the impact of heterotrophic organisms, or C fixation pathways inducing a smaller isotopic fractionation. Notably, the ratio of cyanobacteria to alpha- and gamma-proteobacteria is much smaller in "brown" compared to "white microbialites" (Fig. 10.12; Valdespino-Castillo *et al.*, 2018), implying a larger role of anoxygenic photosynthesis in "brown" microbialite. However, this cannot be distinguished from $\Delta^{13}C_{OC\text{-}DICeq}$ data because photosynthesis by either group of bacteria can result in very similar isotopic fractionations (*e.g.* Thomas *et al.*, 2019). Bulk organic carbon isotopes are thus not discriminant enough to distinguish specific metabolisms, and to an even lower degree, specific phyla.

Microbial mats result from complex interactions of very diverse microorganisms at a small scale, and isotopic fractionations inherent to different metabolisms/microbial groups may not always strongly differ (*e.g.* Houghton *et al.*, 2014; Thomas *et al.*, 2019). Thus, it may already prove challenging to properly relate an isotopic signal to a specific metabolic group in layered modern mats, without more compound-specific analyses: for example, fatty acid isotopic compositions (White III *et al.*, 2020), pigment-specific concentrations and isotopic compositions (Houghton *et al.*, 2014; Fulton *et al.*, 2018). The results presented here demonstrate further that bulk organic C isotopes alone may be limited as metabolic specific biosignatures alone, which is essential to keep in mind when interpreting geological samples.

10.4. Conclusions

The carbonate and organic matter geochemical signatures of the Mexican microbialites record the influence of numerous processes and C sources. For carbonates it includes diagenetic recrystallization, biological influence, local DIC sources, hydrological changes, and mineralogical effects. For organic matter it includes the complex microbial diversity forming

the mats, the redox conditions at the lake- and mat-scale, as well as the preservation of organic matter in time.

Emerged microbialites exposed to meteoric fluids and experiencing recrystallization may have their O isotopic signatures strongly shifted. However, micro-sampling of specific carbonate fabrics may help finding primary signatures. The C isotope signal of recrystallized carbonates has more chance to be preserved than O, although it may be homogenized among different microbialites. These samples altered by meteoric fluids have more chance to be *altered* at their rim, while those reprecipitating directly in the lake waters tend to *better preserve* primary isotopic signatures at their rim.

Massive spontaneous carbonate precipitation at the expense of primary "biogenic" carbonates (*cf*. the replacement of aragonite by hydromagnesite in Alchichica) enables a good record of environmental abiotic factors, but tend to erase primary biosignatures, except towards the rim of the microbialites. Thus, phase specific and small-scale analyses may help circumvent this issue.

Alkaline conditions have a contrasting effect on the potential record of bio- or environmental-signatures by microbialites. High alkalinity waters will favor spontaneous abiotic precipitation, and thus faithfully record the changes in fluid composition. These changes, however, are more likely to occur at longer than shorter timescales, because of the important buffer effect of high-alkalinity settings. In lower alkalinity waters, biological activity is more likely to trigger carbonate precipitation and to be recorded as isotopic biosignatures (*e.g.* in La Preciosa microbialites). External and local fluid inputs can generate important lateral variability, complexifying the record of microbialites, and generating signatures that can be incorrectly interpreted as primary biological or climatic processes. Nevertheless, for the same reason, microbialites represent a complementary and more specific record than the gravitational sediments, whose signatures average the whole basin.

Overall, this work brings to light the requirement of providing substantial facies, mineralogical, and geological context information for the interpretation of microbialite geochemical data. Besides, it shows how crucial it can be to identify a good reference reservoir to properly understand the signatures of authigenic phases; for instance, the detrital grains in "PR-2" sample, the hydromagnesite nodules or bulk microbialite in Alchichica, or more generally, the lake sediments appeared to be appropriately in equilibrium with the lake water.

Combining all this information, a good understanding of these modern microbialites' history of formation was possible. Notably, the balance between biotic and abiotic influences produced distinguishable carbonate $\delta^{13}C$–$\delta^{18}O$ covariation; at the locations studied, slopes between 0.2 and 0.5 result mostly from abiotic precipitation, and those close to 1 from biological controls.

Organic carbon of microbialites reflect mostly the isotopic composition of primary photosynthetic producers. The signatures can fluctuate due to changes in microbial community and to the microbialites location, growing in more or less oxidizing/reducing conditions. However, the isotopic variations are small, and would be challenging to interpret in the geological record. It is indeed difficult to distinguish between the impact of specific metabolisms or environmental constraints without more specific analyses.

10.5. Supplementary figures

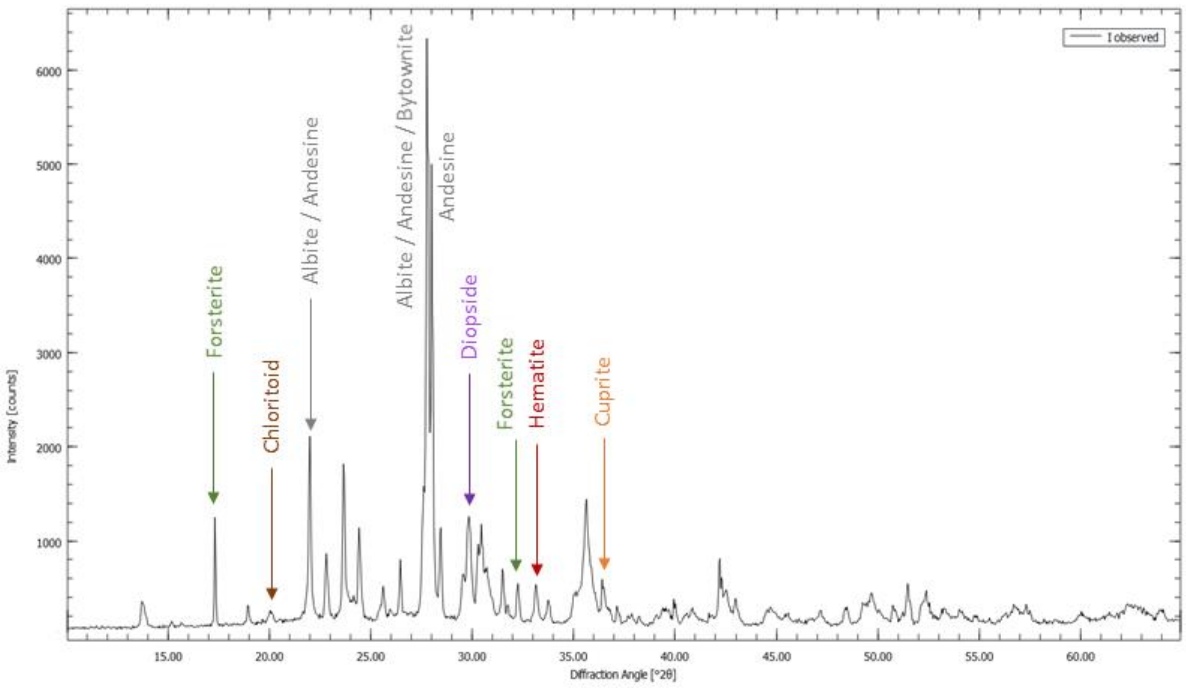

Figure S10.1: XRD diffractogram of 'AL-T-4' sample. The main peaks of the phases identified are pointed out.

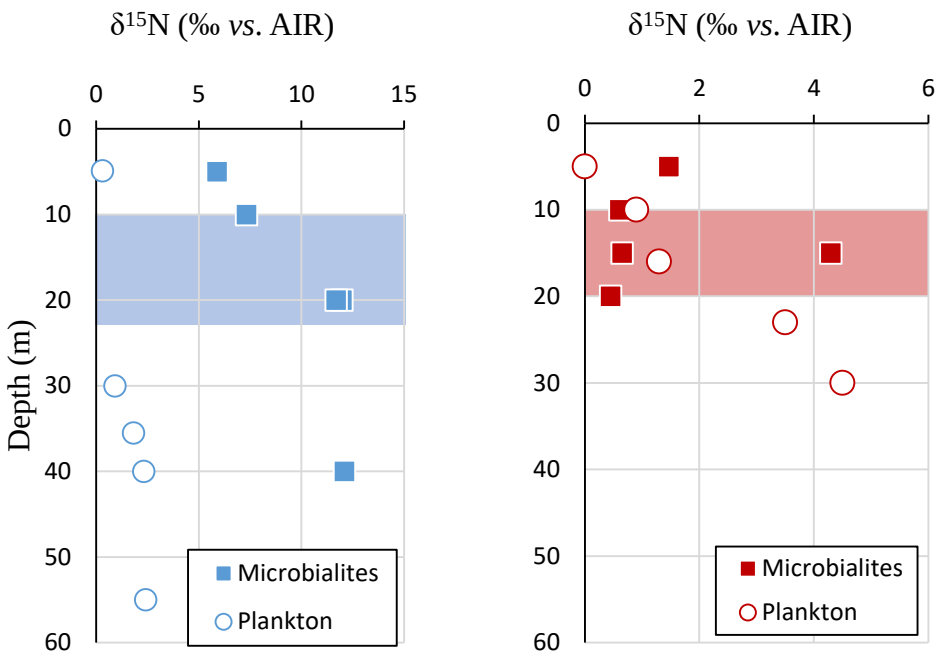

Figure S10.2: Bulk nitrogen isotope composition in the plankton and microbialites from Alchichica and Atexcac represented with depth in the two lakes. The coloured bands represent the redoxcline of each lake.

Chapter 11
Multiple sulfur isotope signatures in microbialites across a redox-stratified water column

As part of a preliminary work about multiple sulfur isotopes in microbialites, this chapter summarizes a poster presented at the Goldschmidt conference in Lyon in 2023.

While the major S isotopes have been regularly analyzed from microbialite samples, ^{33}S and ^{36}S data for such objects are relatively few in the geological record, and to the best of my knowledge, are inexistent for modern microbialites. During my stay in Tokyo, I carried out quadruple S isotopes analyses for more 20 bulk pyrite samples from the Mexican microbialites, as well as for a few carbonate-associated sulfate (CAS) samples. In the poster, I present the $\delta^{34}S$ and $\Delta^{33}S$' data for pyrite and CAS extracts from Alchichica microbialites in the "brown" and "white" facies, including those from the anoxic part of the water column (at a 40-m depth).

Consistently with microscope observations, the "brown microbialites" contained much more pyrite than the "white" ones with FeS_2 averaging 1650 and 45 ppm, respectively (Fig. 1). Besides, the "white facies" harbored less negative and more variable $\delta^{34}S_{py}$ (-20 ± 4.3 ‰) than the "brown facies" (-36.7 ± 2.4 ‰; Fig. 1). Considering the present lake sulfate $\delta^{34}S$ (+ ~19 ‰), the $\Delta^{34}S_{py\text{-}SO4}$ recorded by the two microbialite groups is consistent with a MSR-fractionation, however, with much larger values for the "brown" compared to "white microbialites" (-56 *vs*. -39 ‰; Fig. 2).

Three main explanations can be suggested to explain these differences: (i) they form from a different source of sulfate, (ii) the fractionation imparted by their respective sulfate reducers differs, and/or (iii) secondary processes affect their isotopic signal.

A different source of sulfate is possible, because "brown microbialites" were shown to form under the influence of groundwater and/or runoff water from the crater wall (Chapters 9 and 10). A conglomerate containing detrital pyrites was sampled from this crater wall, and shows $\delta^{34}S \approx 0$ ‰ and $\Delta^{33}S' \approx -0.055$ ‰ (consistent with the present volcanic context). Oxidation of these detrital pyrites, followed by sulfate reduction would result in a $\Delta^{34}S_{SO4\text{-}py}$ of ~ -37‰,

Multiple sulfur isotope signatures in microbialites across a redox stratified water-column

Robin Havas[a,*], Christophe Thomazo[a], Purificación López-García[b], Jakub Surma[c], Mayuko Nakagawa[c], Didier Jézéquel[d], Miguel Iniesto[b], David Moreira[b], Rosaluz Tavera[e], Jeanne Caumartin[f], Karim Benzerara[f], Yuichiro Ueno[c]

Introduction

Microbialites are among the **oldest traces of life on Earth** and result from complex microbial interactions in biofilms with **steep redox gradients.** Sulfur **major isotope signatures** (as $\delta^{34}S$) have often been used to characterize ancient and modern microbialites (*e.g.* Gomes *et al.*, 2018; Marin-Carbonne *et al.*, 2022).

Multiple S isotope data (as $\Delta^{33}S$ and $\Delta^{36}S$) in microbialites have yet received very little attention (*e.g.* Thomazo et al., 2009). These data are **inexistent in modern contexts**, although modern environments can be better constrained. More broadly, the geochemical characterization of microbialites from **natural anoxic environments** remains to be carried out.

We analyzed the **minor S isotope signals in living and subfossil microbialites from a modern redox-stratified lake in Mexico.**

Methods

Bulk pyrite --> Ag_2S by chromium-reducible sulfur **(CRS)** distillation.
Dissolved sulfate --> $BaSO_4$, reacted with a Kiba solution --> Ag_2S.
CAS --> $BaSO_4$ (Wotte *et al.*, 2012), then converted to Ag_2S or directly fluorinated and analyzed as SO_2F_2 (Ultra HR-IRMS, Thermo Scientific™).

All four S isotopes were analysed on a MAT253 (ThermoScientific™) after **fluorination of Ag_2S by flash heating with CoF_3** with a Curie-point pyroliser (Ueno *et al.*, 2015), with 2σ uncertainties on S1 standard of 0.25, 0.007, and 0.071 ‰ for $\delta^{34}S$, $\Delta^{33}S'$, and $\Delta^{36}S'$.

Limnology and microbialites in Lake Alchichica

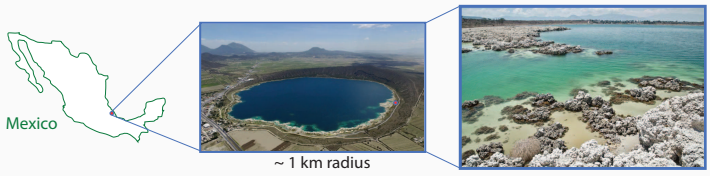

Alchichica is a 62m-deep **alkaline** lake (pH ~9.2), **redox-stratified** mixing once a year (**monomictic**), with **hyposaline** water (8 psu), high **alkalinity** ~34 mM, and **[SO_4^{2-}]** around 12 mM.

Subfossil microbialites
<=> «White» and «Brown» facies

Living microbialites
<=> «White» facies»

«WM» facies
>80% hydromagnesite (HMg)
<20% aragonite (Ara)
very low TOC, and Fe
HMg secondary precipitation over Ara
Located all around the crater

«BM» facies
>95% aragonite,
high TOC and Fe
Pristine textures, visible framboids, microbial mats, *etc.*
Restricted to W shore, next to the crater wall

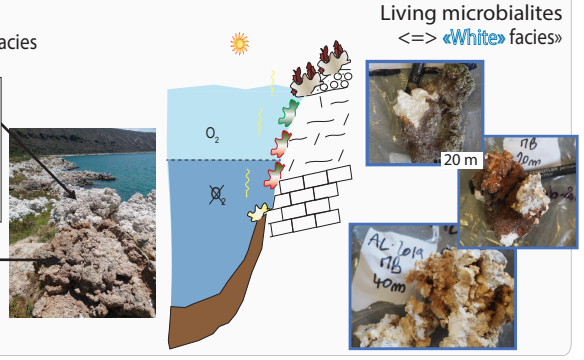

Results

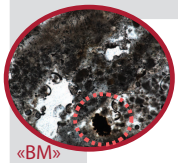

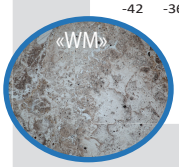

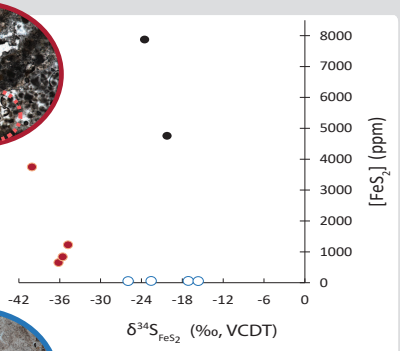

Fig. 1: Major sulfur isotope composition *vs.* the bulk pyrite S concentration.

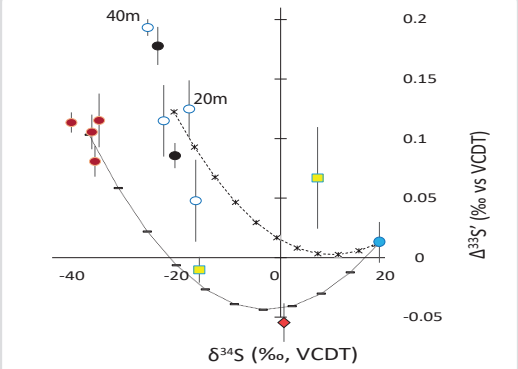

Fig. 2: $\Delta^{33}S$ *vs.* $\delta^{34}S$ isotopic signatures in the microbialite, detrital, and bottom sediment pyrites, and microbialite CAS and lake dissolved SO_4^{2-}. Error bars represent 2σ errors. The two mixing lines connect the lake sulfate and microbialites average compositions.

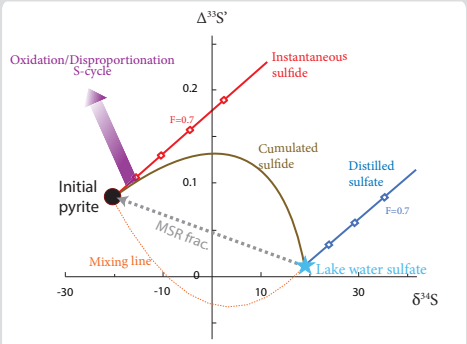

Fig. 3: conceptual frame to interpret the S isotope data. Intial fractionation by microbial sulfate reduction (gray); a mixing trend line between microbial pyrite and lake SO_4^{2-} compositions (orange); Rayleigh distillation in a closed system (red, brown, blue); oxidation and disproportionation reactions in purple (following a trend found in Alchichica bottom sediments (Havas *et al.*, in prep; Fig. 2) and by Liu *et al.* (2022).

FeS_2: ○ «White» microbialite facies (WM) ● «Brown» microbialite facies (BM) ● Bottom lake sediment ◆ Crater detrital pyrite
SO_4^{2-}: ■ Carbonate associateed sulfate (CAS) ● Dissolved sulfate

Discussion

o **Clear distinction** between the **two microbialite groups** (Fig. 1). The bottom sediments (always under anoxic conditions) show higher pyrite contents.

o Higher [FeS_2] in «brown» compared to «white» microbialites (~1650 vs. 45 ppm) ==> **BM** facies: **higher H_2S prod.** and **better preserved primary features** (*e.g.* pyrite framboids).
==> WM facies: smaller H_2S prod. and more affected by **secondary processes** (*e.g.* carbonate reprecipitation, pyrite oxidation?).

o The **net $\Delta^{34}S_{FeS_2\text{-}SO_4}$ fractionation** for all samples (between -35 and -60 ‰) is consistent with **microbial sulfate reduction** (Fig. 2).

Differences in $\delta^{34}S_{FeS_2}$ between the two facies suggest different **(i)** sources of sulfate, (**ii**) fractionations, and/or **(iii)** that secondary processes affecting the WM isotopic signatures.

(i) The BM facies is influenced by underground and/or runoff waters (Havas *et al.*, in prep) => oxidation of detrital pyrite to SO_4 ($\delta^{34}S$ ~0 ‰) before MSR can explain more negative $\delta^{34}S_{FeS2}$ in BM (Fig. 2). The CAS in BM samples is consistent with a **mixing between the oxidation of microbial and detrital pyrites** (and/or with the lake sulfate) (Fig. 2).

(ii) Higher TOC and FeS_2 content in BM, suggest higher cell-specific reduction rates and thus smaller fractionations (Sim et al., 2011) recorded by BM pyrites than WM, not higher (Fig. 2).

(iii) Low pyrite content, and carbonate reworking in WM suggest a **possible reoxidation of pyrite** (Fig. 1)**.** The WM multi-S signal follows that of bottom sediment pyrites, interpreted to reflect a **reoxidative S cycle and disproportionation** (Fig. 2 and 3; Havas *et al.*, in prep).
. The sample mainly growing under anoxia at 40m shows the highest $\Delta^{33}S'$ (Fig. 2). Switch in **anoxic/oxic conditions** during water column mixing may **enhance reoxidation/disproportionation effects**.
. The CAS isotopic signatures in WM do not simply plot on a mixing line with lake sulfates. The direction of the shift in CAS of WM samples is consistent with oxidation/diproporitonation cycles (Havas *et al.*, in pep).

Conclusion

o Different source effects and microbial processes are identified based on mutli-S isotope signatures in the Mexican microbialites.
o Seasonal variation of the redox-stratification favors reoxidation/disproportionation in the microbialites.
o Paired sulfide and CAS within microbialtes may help recognizing such processes.

a, CNRS UMR 6282, Université de Bourgogne, France
b, CNRS UMR 8079, Université Paris Sud, France
c, Tokyo Institute of Technology, Japan
d, IPGP, CNRS UMR 7154, Université de Paris, France
e, Universidad Nacional Autonoma de Mexico, Mexico
f, IMPMC, CNRS UMR 7590, Sorbonne Université, MNHN, France

Gomes et al., doi.org/10.1111/gbi.12265, Geobiology, 2018.
Marin-Carbonne et al., 10.7185/geochemlet.2209, Geochem. Persp. Letters, 2022.
Thomazo et al., doi.org/10.1016/j.epsl.2008.12.036, 2009.
Wotte et al., doi.org/10.1016/j.chemgeo.2012.07.020, Chem. Geology, 2012.
Ueno et al., doi.org/10.1016/j.chemgeo.2015.10.032, Chem. Geology, 2015.
Liu et al., doi.org/10.1016/j.gca.2021.09.026, GCA, 2022.
Sim et al., 10.1126/science.1205103, 2011.

similar to the value recorded by presently forming pyrites (*i.e.*, in the bottom sediments and "white microbialites" underwater).

Explanation (ii) requires that the fractionation recorded by "brown microbialites" is larger than for "white microbialites". Yet, the higher TOC and FeS_2 content found in the "brown facies" suggests a higher cell-specific sulfate reduction rates (csSRR) and thus smaller, rather than larger, isotopic fractionations for "brown microbialites". Scenario (ii) is therefore unlikely.

The very low pyrite content in "white microbialites" together with the secondary replacement history of hydromagnesite described before (Chapters 9 and 10) suggest that pyrites in these samples may have been oxidized after their precipitation. Whereas the "brown microbialites" show homogeneous $\Delta^{33}S'$ (0.1 ± 0.02 ‰), the white ones are again more heterogeneous (0.12 ± 0.02 ‰), and importantly, follow the same trend as found in the bottom sediment pyrites (Fig. 2). This latter was also interpreted to result from sulfides reoxidation, and disproportionation (Fig. 3; Chapter 7). Interestingly, the CAS sample associated to the "brown facies" lies directly on a mixing line between detrital pyrites and brown pyrites (and lake sulfate). It implies an abiotic oxidation of pyrites from the "brown microbialites", directly mixing with the sulfate source (*i.e.* oxidized detrital pyrites plus lake sulfates). By contrast the CAS from the "white facies" lies above the mixing line, in the direction that was suggested for sulfate resulting from the cryptic oxidation/disproportionation cycle presented in Alchichica sediments (Chapter 7).

Interestingly, the highest $\Delta^{33}S'$ value in that trend corresponds to the microbialite sample residing mostly in anoxic conditions at 40 m in the water column (Fig. 2). Because the lake is monomictic (mixes once a year), it is possible that the alternation of anaerobic and aerobic conditions favors the reactions presented above. In samples that are closer to the surface, the sulfide produced by MSR would be more completely oxidized back to sulfate, preventing the action of disproportionation for example. Because there is more Fe available in the local environments of the "brown" samples (which are near surface level), they may preserve MSR-type signatures, because dissolved sulfides are efficiently captured in pyrites within the microbialites microenvironments, before being significantly oxidized.

While this is still a preliminary work, it gives interesting perspectives about the variability of the S isotope record in microbialites, depending on redox conditions and

stratification, Fe availability, and perhaps microbial communities. These results further identify the two microbialite facies as two clearly different groups, forming after very different processes. Compared with the bottom sediments, the precipitation of carbonate in the microbialites gives a potential mean to identify cryptic S cycles because it provides constraint on an additional S reservoir (namely, the sulfate resulting from the oxidation of microbial pyrites and mixing with the lake sulfate). Finally, these results suggest that the redox-stratification and its variations with time may have had a strong impact on the S sedimentary record.

Part 3
Intermediate conclusion

In this last part, I assessed the diversity of the Mexican microbialites from Alchichica, Atexcac, and La Preciosa, based on petrographic, mineralogical, and geochemical data, together with genetic microbial data. The petrographic observations allowed establishing microbialite groups according to their degree of preservation, the potential differences in their geological context, and the sources of water from which they form. Highlighting secondary and recrystallized carbonate facies, mineralogies, and specific associations with biogenic remains, this preliminary characterization proved to be a useful, and necessary step before interpretation of the microbialites isotopic signatures.

Isotope data agree and complement the microscopic observations. More alkaline conditions favor the precipitation of carbonates, thus being in isotopic equilibrium with the lake water, giving them the possibility to record potential shifts in the lake's chemistry. However, spontaneous precipitation and replacement of primary carbonates may overprint metabolic isotopic biosignatures of carbonates forming in the vicinity of the microbial mat. In the lower alkalinity setting studied (La Preciosa), carbonates isotopic composition record the role of photosynthesis in carbonatogenesis, supporting previous microbial studies which suggested a minor role for microbial sulfate reduction in the formation of the Mexican microbialites. Carbonates isotopic signatures of the "brown microbialites", on the western shore of Alchichica, evidence the role of external fluids in their formation (groundwater, runoff water, and/or volcanic fluids), corroborating the observations made from thin sections. Changes in carbonates mineralogy strongly impact the microbialites isotopic signals, and should be carefully assessed. Bulk organic C analyses agree with a dominantly photosynthetic biomass, but more compounds specific analyses are required to retrace the metabolic pathways on a finer scale (*e.g.* anoxygenic *vs.* oxygenic). Nonetheless, the bulk signatures measured differ from those in planktonic communities (possibly due to slower CO_2 diffusion in the microbial mat), and vary according to the redox-stratification in Alchichica. Microbialites thus represent valuable archives to assess the vertical and lateral variability found in stratified environments.

Sulfur isotope data provide significant insights to the biotic and abiotic reactions operating in the Mexican microbialites. They confirm the influence of a S and water source different than

the lake water for “brown microbialites” in Alchichica, supporting that they formed under less oligotrophic conditions. By contrast, lower Fe availability, and possibly lower sulfide production/precipitation rates give a higher chance for oxidation/disproportionation reactions to occur. Variations in the water column redox stratification seems to hold a critical role in the isotopic signal they record. Overall, it demonstrates microbialites as powerful environmental archives of the C and S cycles, despite secondary processes affecting them. Applying a multi-disciplinary approach to their study (geochemistry, mineralogy, sedimentology, and microbiology) allows approaching a comprehensive understanding of their history and environment of formation.

Chapter 12

Conclusion, summary, and perspectives

A geochemical overview of reactions affecting the C and S cycles in four redox stratified alkaline lakes from Mexico and their microbialites was achieved. Some key processes occurring in these environments could be evidenced *via* the analysis of dissolved phases only (lake waters and pore waters), but were not preserved in the perennial geological reservoirs (*i.e.* the bottom lake sediments and microbialite deposits). Similarly, by untangling the processes presently occurring in the four systems, this study highlights the biased conclusions that can arise from their sedimentary record, and how these records are altered by early diagenetic processes. Additionally, this work contributes to a better understanding of the C cycle in modern stratified alkaline environments in general, notably how the DOC reservoir is cycled, what environmental parameters lead to distinct alkalinity levels, and how these different levels favor or not the record of primary biological and climatic signatures. It also shows what are the primary factors influencing the (final) S isotope signatures recorded in sedimentary pyrites. These conclusions are summarized chapter by chapter (referred to with the numbers in brackets), before the implications and perspectives to this work are given.

Part I

The more alkaline an aqueous medium, the less sensitive it is to record short-term climatic, hydrologic, and especially biological influences, because it will feature a large and buffered DIC reservoir (4, 6, 10). High alkalinity systems favor the saturation with, and precipitation of carbonate minerals, in isotopic equilibrium with the lake water (4, 6, 10). These carbonates thus represent a faithful isotopic archive with the potential to effectively record environmental changes on longer time scales (10^3 to 10^6 years). However, alkaline settings represent extreme environments, where, a decrease in pH (which was always observed going from the water column to the bottom sediments) may involve critical rearrangement of carbonate (and Mg-silicate) minerals. This process leads to a geochemical (and isotopic) record that is secondary, representing the sediment porewater rather than the water column (6). On the contrary, if no diagenetic reprecipitation occurs, a primary signal may be preserved, but only the upper water column part is recorded by the carbonates, missing out important environmental

aspects going on in the lower part of the stratified basin, and in the sediments (*e.g.* methanogenesis in Alberca; 4, 6).

The dominant sources and C-related processes were quantitatively constrained in Lake Alchichica by modeling the C cycle evolution over the last 60 years (5). The results show a significant contribution of volcanic CO_2 to the C mass balance in Alchichica (5). Besides, this work highlights the importance of the downstream position of Alchichica, compared to La Preciosa and Atexcac, influencing the chemical composition of groundwater feeding the lake, and the importance of anthropic groundwater use over the last decades (5). Importantly, the identification of a volcanic-CO_2 source was made possible by having access to hydrological and aquifer waters (external to the lakes), highlighting again the poor sensitivity of the DIC reservoir in high alkalinity contexts, and the necessity to zoom out a specific study site, in order to grasp a broader vision of it.

The DOC reservoir – which is not recorded in the sediments – appeared to be key in the C cycle of the lakes studied. Its concentration and isotope composition evidenced several processes happening in the water columns, but hardly visible from DIC and POC data (4). Based on extreme positive isotopic shifts, the DOC data evidenced that a combination of strong UV radiation, high CO_2 availability, and low nutrient levels, promotes the highest production of autochthonous DOC (4). The bacterial communities most actively cycling carbon were evidenced: mainly oxygenic and/or anoxygenic photosynthesizers, and possibly heterotrophic bacteria, at and below the redoxcline. The respective activity of these groups was very different in each lake, which contributed to heterogeneity of sedimentary OM record (SOM) coming from different parts of each redox stratified water column (4, 6). Different degrees of SOM reworking were evidenced in the four systems, with maximum induced isotopic shifts of +4 ‰. The characterization of the bottom lake sediments showed that higher isotopic shifts should be linked to lower primary productivity (*i.e.* more oligotrophic conditions), lower sedimentation rates, and higher oxidant availability in the system (6).

Part II

The main factors influencing the sulfur isotopic record varied in the four lakes sedimentary sequences (7, 8). In Alchichica, a cryptic reoxidative S cycle was identified based on multiple-S isotopes of pyrites and porewater sulfates (7). The MSR-produced sulfides are reoxidized to intermediate sulfur species which are then disproportionated to dissolved sulfides

and sulfates. Repeated cycles of this process shift the final pyrite isotopic record to more negative $\delta^{34}S$, and more positive $\Delta^{33}S$' signals than what would be recorded if only the pooling of porewater sulfide during MSR proceeded. Environmental reconstructions based on the sedimentary pyrite record alone would likely interpret, *a posteriori*, an open porewater system with abundant sulfate concentrations, whereas it actually experiences a closed-system Rayleigh distillation with porewater $\delta^{34}S_{H2S}$ progressively approaching that of the lake $\delta^{34}S_{SO4}$ (7). In other words, the occurrence of a reoxidative cycle was identified based on porewater data, but would have been hardly detected if only the perennial pyrite reservoir was available.

In the other lakes, the csSRR and sulfate concentration were shown as primary controls in shaping the $\Delta^{34}S_{SO4\text{-}py}$ fractionations induced by MSR (8). Combining the four lakes record, however, the underlying constraint on the final pyrite isotopic record was the size of each lake sulfate reservoir. Following the "reservoir effect", the overall $\Delta^{34}S_{SO4\text{-}py}$ is modulated, and more or less expressed depending on the degree of sulfate consumption (8). The sulfate isotopic signatures of the four lakes evidenced the influence of volcanic sulfur sources to the lakes. In Atexcac, it has a mantle-like signal, and strongly suggests a continuous contribution of volcanic sources to that lake (8).

Part III

The petrographic and isotopic descriptions made of the Mexican microbialites allowed a better comprehension of their history of formation, how they were modified by secondary precipitation, and early diagenesis after emersion (9, 10). Petrographic observations allow: the recognition of the lakes dynamic hydrology with usually multiple steps of immersion and emersion evidenced, the identification of successive carbonate precipitation steps from primary phases to complete recrystallized ones, and the assessment of the lateral diversity that can exist within a single lake due to changing fluid sources and biological influences (9). Whereas high alkalinity favors the growth of microbialites, it also fosters a loss of their primary isotopic biosignatures *via* spontaneous ("abiotic") precipitation and replacement. Alike the bottom lake sediments, microbialite carbonates formed in high alkalinity settings may thus represent a good record of climatic changes on the longer rather than shorter term (10) (provided that they are not subsequently altered, by meteoric fluids for example). Due to secondary replacement in the microbialite's core (under high alkalinity settings), biosignatures in carbonate isotopic compositions have more chances to be preserved at its rim. By contrast, in lower alkalinity Lake La Preciosa, isotopic biosignatures typical of photosynthesis are clearly identified from both bulk and local carbonate isotopic analyses (10). However, after emersion of some of the

microbialites, early alteration *via* meteoric fluids is clearly evidenced from combined petrographic/isotopic analyses (9, 10). It causes a clear loss of the primary biogenic microfossils (diatom frustules, microbial filamentous mats), carbonate textures, and isotopic signals, especially for O. This time, the microbialites initial messages are better preserved towards their core.

Similar to the bottom sediments, primary and secondary carbonates mineralogy in microbialites is of prime importance for the interpretation of their isotopic signals (10). Using a correct isotopic reference for the source of C forming the microbialites is also determinant to correctly interpret potential biosignatures, mechanisms of formation, and environmental records (10).

Although bulk organic matter of the microbialites mostly inherits geochemical signatures form primary photosynthetic producers, it is sensitive to the microbialite's position relative to the lake redox gradient, raising interest in targeting microbialites through stratigraphic gradients, in order to grasp the full lateral and vertical variability of a paleo-environment (10). Microbialites may be more sensitive to biological influences, and are bound to a specific position relative to the redox stratification, rising interest in analyzing them in complement to the sediments at the bottom of a basin (10).

Multiple S isotope data from Alchichica microbialites (11) corroborate the inferences from previous chapters about microbialites (9, 10) and the S cycle in the sediments (7, 8). These data suggest a distinct source of S for "brown microbialites" coming from the oxidation of detrital pyrite and from the crater or basement rocks, consistent with the influence of underground or runoff waters (11). Thence, it supports that these microbialites formed under distinct local environments compared with the majority of the lake's ("white") microbialites (9, 10). Whereas "brown microbialites" S isotopes evidence an efficient record of MSR-produced sulfides in pyrite, "white microbialites" show similar signatures as in the lake's bottom sediments (7), suggestive of reoxidation/disproportionation reactions (11). An advantage of microbialite deposits to identify these processes is that they precipitate carbonate *in situ*, providing a local record of sulfate that is not available from bottom lake sediment porewaters. Finally, the microbialite S isotope record seems to be noticeably impacted by the lake redox-stratification (and mixing regime).

One of the central objectives of this work was to assess the reliability of geochemical records within sedimentary archives of redox stratified environments. The main conclusions of this study bring to light a number of biases and cryptic processes that may be detected when studying modern stratified environments, as summarized in Table 12.1. It shows notably that a number of important processes and metabolisms are active, but not recorded in the sedimentary archives, raising our awareness when interpreting ancient geochemical records. This work renews the importance of constraining geological, stratigraphic, and petrographic contexts in addition to the geochemical data. Besides, it opens promising ways to interdisciplinary microbiological, mineralogical, geological, and geochemical approaches. Such modern environments should thus be further investigated in such integrative and comparative studies.

Specific perspectives to each of the problematics discussed are presented in the respective chapter, but more general possible extensions to this work are presented in this final paragraph.

As a follow up, the thorough isotopic constraints provided in this PhD for stratified environments and their microbialites should be further combined to the available "omics" data. It will be a pioneering work to establish a full picture from specific microbial and physico-chemical contexts to mineralogical and geochemical records. A further characterization of these Mexican systems through powerful geochemical proxies like ^{33}S and ^{36}S isotopes should also be more systematically performed. *In situ* analyses, for example *via* (nano-)SIMS techniques, open complementary ways to understand how a primary signature might be preserved locally, despite the alteration of the bulk sample signals (Marin-Carbonne *et al.,* 2022). These approaches should be applied on the Mexican objects, and compared with other lacustrine stratified water bodies from various geological contexts (such as Lake Dziani Dzaha in the Indian Ocean, or Lake Cadagno in the Alps). Finally, a greater effort should be dedicated to seek how the previous conclusions apply to larger scale basins, such as the past open oceans, possibly starting from present days oxygen-minimum zones in continental margins.

Table 12.1 (below): Summary table of biases potentially arising when interpreting C and S geochemical proxies from the water column and sediment reservoirs of stratified environments, together with suggestions to resolve these issues.

Table 12.1 (continued)

Biased and/or partial interpretations	Concerned reservoir	Concerned phases and elements	Concerned proxy	Description of the problem	"Solution type"	Ways to improve our interpretations of geological samples
Partial record of the stratified water column	Sediments at the bottom of a stratified basin	Organic matter (C, and N?)	Isotopes	Gravitational sediments receive organic particles coming from different layers of the stratified water column depending on the size, weight, and respective abundance of the aerobic and anaerobic organisms.	"stratigraphic"	• Sample across the redox gradients. • Microbial mats from microbialites (although influenced by micro-scale specificities) develop at a given depth. • Microbialites are more likely to reflect a specific redox layer. In a wide basin, sample from proximal to distal settings to assess the lateral redox variability.
		Carbonates (C and O)	Isotopes and concentration	Carbonates precipitate mainly in the upper water column where higher pH prevails, while pH decreases towards the bottom of the lake and sediment porewaters, preventing the record of anoxic layers.		• Assess the pH gradient by estimating flux of carbonate deposition across the stratification (stratigraphic gradient). • If pH does not decrease enough to lead to undersaturation, sampling across that gradient provides a carbonate record of the different redox layers. • Microbialites can provide records specific to their depth of formation. They can trigger carbonate precipitation despite unfavorable pH conditions. In that case however, carbonates might also reflect a biological influence.
Masked processes due to buffered alkalinity	Water column DIC and carbonate precipitates	Carbonates (C)	Isotopes and concentration	High alkalinity contexts buffer the effects of processes recorded by the DIC and solid carbonate reservoirs. These processes include hydrologic and climatic changes such as evaporation, inputs of external sources like volcanic CO_2, and changes induced by biological activity (*i.e.* primary productivity).	"contextual and geologic"	• A thorough geological context evaluation should facilitate the identification of processes that are the most likely. • Extend the sampling and analysis of deposits exterior to the locus of study (which can record potential sources) to have a complete view of a given system. • Modeling approaches, and characterization of longer time-series should allow the identification of processes significant enough the shift a buffered reservoir over time.

Masked microbial isotopic fractionation from primary producers	Water column and sedimentary organic matter	Dissolved and particulate organic matter (C)	Isotopes and concentration	The particulate matter represents a partial inventory of organics produced by primary production. Dissolved organic compounds are not archived in the sedimentary record, but can record isotopic signals better reflecting the environments and microbes physiology than particulate organic C.	"Modeling?"	Knowing the chemical parameters of the water column biological diversity in various environmental contexts may help to build inverse model in the future?
Mineralogical biases	Carbonate precipitates	Carbonates (C and O)	Isotopes	The carbonate mineralogy (of both primary and secondary phases) can generate isotopic differences > 5 ‰ leading to false interpretation of isotopic results if mineralogy is not accounted for. Transformation of an initial mineralogy can potentially drive additional fractionations if the secondary phase is not fully reequilibrated with medium water.	"mineralogical and petrographic"	• The isotopic composition of the fluid from which carbonates precipitated should be determined. • A detailed assessment of carbonates mineralogy is required, especially when there are mutiple carbonate phases in a sample. • *In situ* analyses can help differentiating the respective mineralogy isotopic effect, and history of formation. • Primary carbonates are often replaced, caution should be paid about potential succession of carbonate replacements in geological samples, and fractionations associated with it.
Secondary (re)precipitation, Recrystalization	Carbonate precipitates	Carbonates (C and O)	Isotopes	- Oversaturation leads to spontaneous carbonate precipitation that can erase primary biological remains (fossils), fabrics, and isotopic signals from primary carbonates more influenced by biological activity. Carbonate biosignatures may be lost, especially towards the microbialite's core. - Recrystalization from an external source, like meteoric waters after emersion, may erase the primary carbonate textures and isotopic signals.	"mineralogical and petrographic"	• From microscopic observations, identify areas of higher microfossil preservation, representing ideal targets for local analyses, and recrystallized fabrics should be avoided. • The underwater replacement process preferentially occurs where the microbial mat is no longer active; hence the microbialites rim should be targeted to find primary signatures. • However, in case of meteoric alteration and recrystallization the microbialite's surface will also be secondary.

Table 12.1 (continued)

Cryptic sulfur cycling	Sedimentary pyrites	Pyrites (S)	Isotopes and concentration	Complex successive S reduction / oxidation / disproportionation reactions can mimic "simple" MSR-like isotopic fractionation and leave indistinguishable isotopic signatures in the pyrite record, even including minor S isotopes.	"petrographic, geochemical, and experimental"	• Other isotopic systems involved in the reoxidation of sulfides, like Fe isotopes, can be looked for in addition to multiple-S isotopes. • Microscopic observations, followed by *in situ* isotope analyses, may help discerning early pyrites forming after MSR from pyrites precipitating after cryptic reactions. • More pure culture experiments constraining the isotopic fractionation produced by sulfide oxidizing and S disproportioning bacteria are required.
Masked primary S isotope fractionation under low sulfate conditions	Sedimentary pyrites and sulfates	Pyrites and sulfates bearing minerals (S)	Isotopes and concentration	Below concentrations of a few mM, the sulfate pool tends to approach a full consumption by sulfate reducing organisms, leading to a net bulk isotopic fractionation approaching 0 ‰ between sulfates (inherited from the upper water column) and pyrites, masking the intrinsic microbial fractionations.	"petrographic and geochemical"	• The use of *in situ* analyses, may allow finding isotopic fractionations at a small scale that cannot be distinguish at the bulk scale within low sulfate content (paleo)environment. • In these environments, bulk analyses are complementary to assess the sulfate reservoir effect and constrain the system at a broader scale.

Bibliography

Adame, M.F., Alcocer, J., Escobar, E., 2008. Size-fractionated phytoplankton biomass and its implications for the dynamics of an oligotrophic tropical lake. Freshwater Biol 53, 22–31. https://doi.org/10.1111/j.1365-2427.2007.01864.x

Ader, M., Macouin, M., Trindade, R.I.F., Hadrien, M.-H., Yang, Z., Sun, Z., Besse, J., 2009. A multilayered water column in the Ediacaran Yangtze platform? Insights from carbonate and organic matter paired δ13C. Earth and Planetary Science Letters 288, 213–227. https://doi.org/10.1016/j.epsl.2009.09.024

Ader, M., Sansjofre, P., Halverson, G.P., Busigny, V., Trindade, R.I.F., Kunzmann, M., Nogueira, A.C.R., 2014. Ocean redox structure across the Late Neoproterozoic Oxygenation Event: A nitrogen isotope perspective. Earth and Planetary Science Letters 396, 1–13. https://doi.org/10.1016/j.epsl.2014.03.042

Ader, M., Thomazo, C., Sansjofre, P., Busigny, V., Papineau, D., Laffont, R., Cartigny, P., Halverson, G.P., 2016. Interpretation of the nitrogen isotopic composition of Precambrian sedimentary rocks: Assumptions and perspectives. Chemical Geology 429, 93–110. https://doi.org/10.1016/j.chemgeo.2016.02.010

Águila, B., Alcántara-Hernández, R.J., Montejano, G., López-Martínez, R., Falcón, L.I., Becerra-Absalón, I., 2021. Cyanobacteria in microbialites of Alchichica Crater Lake: a polyphasic characterization. European Journal of Phycology 56, 428–443. https://doi.org/10.1080/09670262.2020.1853815

Aharon, P., 1988. A stable-isotope study of magnesites from the Rum Jungle Uranium Field, Australia: Implications for the origin of strata-bound massive magnesites. Chemical Geology 69, 127–145. https://doi.org/10.1016/0009-2541(88)90164-7

Alcalá, A., 2004. Estudio hidrogeológico de Alchichica, estado de Puebla. BE Thesis 52.

Alcántara-Hernández, R., Valdespino-Castillo, P., Centeno, C., Alcocer, J., Merino-Ibarra, M., Falcón, L., 2017. Genetic diversity associated with N-cycle pathways in microbialites from Lake Alchichica, Mexico. Aquat. Microb. Ecol. 78, 121–133. https://doi.org/10.3354/ame01806

Alcocer, J., 2021. Lake Alchichica Limnology, Springer Nature. ed.

Alcocer, J., 2019. Lago Alchichica, Una joya de biodiversidad.

Alcocer, J., Lugo, A., Escobar, E., Sànchez, M.R., Vilaclara, G., 2000. Water column stratification and its implications in the tropical warm monomictic Lake Alchichica, Puebla, Mexico. SIL Proceedings, 1922-2010 27, 3166–3169. https://doi.org/10.1080/03680770.1998.11898262

Alcocer, J., Ruiz-Fernández, A.C., Escobar, E., Pérez-Bernal, L.H., Oseguera, L.A., Ardiles-Gloria, V., 2014. Deposition, burial and sequestration of carbon in an oligotrophic, tropical lake. J Limnol 73. https://doi.org/10.4081/jlimnol.2014.783

Algeo, T.J., Luo, G.M., Song, H.Y., Lyons, T.W., Canfield, D.E., 2015. Reconstruction of secular variation in seawater sulfate concentrations. Biogeosciences 12, 2131–2151. https://doi.org/10.5194/bg-12-2131-2015

Allwood, A.C., Walter, M.R., Kamber, B.S., Marshall, C.P., Burch, I.W., 2006. Stromatolite reef from the Early Archaean era of Australia. Nature 441, 714–718. https://doi.org/10.1038/nature04764

Andres, M.S., Sumner, D.Y., Reid, R.P., Swart, P.K., 2006. Isotopic fingerprints of microbial respiration in aragonite from Bahamian stromatolites. Geology 34, 973. https://doi.org/10.1130/G22859A.1

Antunes, G.C., Warren, L.V., Okubo, J., Fairchild, T.R., Varejão, F.G., Uhlein, G.J., Inglez, L., Poiré, D.G., Bahniuk, A.M., Simões, M.G., 2022. The rise and fall of the giant stromatolites of the Lower Permian Irati Formation (Paraná Basin, Brazil): A multi-proxy based paleoenvironmental reconstruction. Palaeogeography, Palaeoclimatology, Palaeoecology 606, 111246. https://doi.org/10.1016/j.palaeo.2022.111246

Aoyama, S., Nishizawa, M., Takai, K., Ueno, Y., 2014. Microbial sulfate reduction within the Iheya North subseafloor hydrothermal system constrained by quadruple sulfur isotopes. Earth and Planetary Science Letters 398, 113–126. https://doi.org/10.1016/j.epsl.2014.04.039

Appleby, P.G., Nolan, P.J., Gifford, D.W., Godfrey, M.J., Oldfield, F., Anderson, N.J., Battarbee, R.W., 1986. 210Pb dating by low background gamma counting. Hydrobiologia 143, 21–27. https://doi.org/10.1007/BF00026640

Appleby, P.G., Richardson, N., Nolan, P.J., 1992. Self-absorption corrections for well-type germanium detectors. Nuclear Instruments and Methods in Physics Research Section B: Beam Interactions with Materials and Atoms 71, 228–233. https://doi.org/10.1016/0168-583X(92)95328-O

Ardiles, V., Alcocer, J., Vilaclara, G., Oseguera, L.A., Velasco, L., 2012. Diatom fluxes in a tropical, oligotrophic lake dominated by large-sized phytoplankton. Hydrobiologia 679, 77–90. https://doi.org/10.1007/s10750-011-0853-7

Arenas, C., Osácar, M.C., Auqué, L., Sancho, C., 2019. Coupling textural and stable-isotope variations in fluvial stromatolites: Comparison of Pleistocene and recent records in NE Spain. Journal of Palaeogeography 8, 13. https://doi.org/10.1186/s42501-019-0021-y

Armienta, M.A., Vilaclara, G., De la Cruz-Reyna, S., Ramos, S., Ceniceros, N., Cruz, O., Aguayo, A., Arcega-Cabrera, F., 2008. Water chemistry of lakes related to active and inactive Mexican volcanoes. Journal of Volcanology and Geothermal Research 178, 249–258. https://doi.org/10.1016/j.jvolgeores.2008.06.019

Arp, G., Reimer, A., Reitner, J., 2001. Photosynthesis-Induced Biofilm Calcification and Calcium Concentrations in Phanerozoic Oceans. Science 292, 1701–1704. https://doi.org/10.1126/science.1057204

Assayag, N., Rivé, K., Ader, M., Jézéquel, D., Agrinier, P., 2006. Improved method for isotopic and quantitative analysis of dissolved inorganic carbon in natural water samples. Rapid Commun. Mass Spectrom. 20, 2243–2251. https://doi.org/10.1002/rcm.2585

Au Yang, D., Bardoux, G., Assayag, N., Laskar, C., Widory, D., Cartigny, P., 2018. Atmospheric SO2 oxidation by NO_2 plays no role in the mass independent sulfur isotope fractionation of urban aerosols. Atmospheric Environment 193, 109–117. https://doi.org/10.1016/j.atmosenv.2018.09.007

Awramik, S.M., Riding, R., 1988. Role of algal eukaryotes in subtidal columnar stromatolite formation. Proceedings of the National Academy of Sciences 85, 1327–1329. https://doi.org/10.1073/pnas.85.5.1327

Bahniuk, A.M., Anjos, S., França, A.B., Matsuda, N., Eiler, J., Mckenzie, J.A., Vasconcelos, C., 2015. Development of microbial carbonates in the Lower Cretaceous Codó Formation (north-east Brazil): Implications for interpretation of microbialite facies associations and palaeoenvironmental conditions. Sedimentology 62, 155–181. https://doi.org/10.1111/sed.12144

Belan, M.A., Brady, A.L., Kim, S.-T., Lim, D.S.S., Slater, G.F., 2019. Spatial Distribution and Preservation of Carbon Isotope Biosignatures in Freshwater Microbialite Carbonate. ACS Earth Space Chem. 3, 335–343. https://doi.org/10.1021/acsearthspacechem.8b00182

Benzerara, K., Menguy, N., López-García, P., Yoon, T.-H., Kazmierczak, J., Tyliszczak, T., Guyot, F., Brown, G.E., 2006. Nanoscale detection of organic signatures in carbonate microbialites. Proc. Natl. Acad. Sci. U.S.A. 103, 9440–9445. https://doi.org/10.1073/pnas.0603255103

Benzerara, K., Skouri-Panet, F., Li, J., Férard, C., Gugger, M., Laurent, T., Couradeau, E., Ragon, M., Cosmidis, J., Menguy, N., Margaret-Oliver, I., Tavera, R., López-García, P., Moreira, D., 2014. Intracellular Ca-carbonate biomineralization is widespread in cyanobacteria. Proc. Natl. Acad. Sci. U.S.A. 111, 10933–10938. https://doi.org/10.1073/pnas.1403510111

Berner, R.A., Scott, M.R., Thomlinson, C., 1970. Carbonate Alkalinity in the Pore Waters of Anoxic Marine Sediments1. Limnology and Oceanography 15, 544–549. https://doi.org/10.4319/lo.1970.15.4.0544

Bertran, E., Leavitt, W.D., Pellerin, A., Zane, G.M., Wall, J.D., Halevy, I., Wing, B.A., Johnston, D.T., 2018. Deconstructing the Dissimilatory Sulfate Reduction Pathway: Isotope Fractionation of a Mutant Unable of Growth on Sulfate. Frontiers in Microbiology 9.

Blanc, Ph., Lassin, A., Piantone, P., Azaroual, M., Jacquemet, N., Fabbri, A., Gaucher, E.C., 2012. Thermoddem: A geochemical database focused on low temperature water/rock interactions and waste materials. Applied Geochemistry 27, 2107–2116. https://doi.org/10.1016/j.apgeochem.2012.06.002

Blaser, M., Conrad, R., 2016. Stable carbon isotope fractionation as tracer of carbon cycling in anoxic soil ecosystems. Current Opinion in Biotechnology 41, 122–129. https://doi.org/10.1016/j.copbio.2016.07.001

Borges, A.V., Morana, C., Bouillon, S., Servais, P., Descy, J.-P., Darchambeau, F., 2014. Carbon Cycling of Lake Kivu (East Africa): Net Autotrophy in the Epilimnion and Emission of CO2 to the Atmosphere Sustained by Geogenic Inputs. PLoS ONE 9, e109500. https://doi.org/10.1371/journal.pone.0109500

Bosence, D., Gallois, A., 2022. How do thrombolites form? Multiphase construction of lacustrine microbialites, Purbeck Limestone Group, (Jurassic), Dorset, UK. Sedimentology 69, 914–953. https://doi.org/10.1111/sed.12933

Bougeault, C., Durlet, C., Vennin, E., Muller, E., Ader, M., Ghaleb, B., Gérard, E., Virgone, A., Gaucher, E.C., 2020. Variability of Carbonate Isotope Signatures in a Hydrothermally Influenced System: Insights from the Pastos Grandes Caldera (Bolivia). Minerals 10, 989. https://doi.org/10.3390/min10110989

Bourg, I.C., 2008. Comment on “Modeling sulfur isotope fractionation and differential diffusion during sulfate reduction in sediments of the Cariaco Basin” by M.A. Donahue, J.P. Werne, C. Meile and T.W. Lyons. Geochimica et Cosmochimica Acta 72, 5852–5854. https://doi.org/10.1016/j.gca.2008.06.033

Boussagol, P., Vennin, E., Bouton, A., Roche, A., Thomazo, C., Kolodka, C., Buoncristiani, J., Monna, F., Musset, O., Visscher, P.T., 2023. Quaternary lacustrine carbonate deposits of the Great Basin, USA : Impact of climate, tectonics and substrate. Sedimentology 70, 969–1007. https://doi.org/10.1111/sed.13068

Bouton, A., Vennin, E., Amiotte-Suchet, P., Thomazo, C., Sizun, J., Virgone, A., Gaucher, E.C., Visscher, P.T., 2020a. Prediction of the calcium carbonate budget in a sedimentary basin: A “source-to-sink” approach applied to Great Salt Lake, Utah, USA. Basin Res 32, 1005–1034. https://doi.org/10.1111/bre.12412

Bouton, A., Vennin, E., Boulle, J., Pace, A., Bourillot, R., Thomazo, C., Brayard, A., Désaubliaux, G., Goslar, T., Yokoyama, Y., Dupraz, C., Visscher, P.T., 2016a. Linking the distribution of microbial deposits from the Great Salt Lake (Utah, USA) to tectonic and climatic processes. Biogeosciences 13, 5511–5526. https://doi.org/10.5194/bg-13-5511-2016

Bouton, A., Vennin, E., Mulder, T., Pace, A., Bourillot, R., Thomazo, C., Brayard, A., Goslar, T., Buoncristiani, J.-F., Désaubliaux, G., Visscher, P.T., 2016b. Enhanced development of lacustrine microbialites on gravity flow deposits, Great Salt Lake, Utah, USA. Sedimentary Geology 341, 1–12. https://doi.org/10.1016/j.sedgeo.2016.05.004

Bouton, A., Vennin, E., Pace, A., Bourillot, R., Dupraz, C., Thomazo, C., Brayard, A., Désaubliaux, G., Visscher, P.T., 2016c. External controls on the distribution, fabrics and mineralization of modern microbial mats in a coastal hypersaline lagoon, Cayo Coco (Cuba). Sedimentology 63, 972–1016. https://doi.org/10.1111/sed.12246

Bouton, A., Vennin, E., Thomazo, C., Mathieu, O., Garcia, F., Jaubert, M., Visscher, P., 2020b. Microbial Origin of the Organic Matter Preserved in the Cayo Coco Lagoonal Network, Cuba. Minerals 10, 143. https://doi.org/10.3390/min10020143

Bradley, A.S., Leavitt, W.D., Schmidt, M., Knoll, A.H., Girguis, P.R., Johnston, D.T., 2016. Patterns of sulfur isotope fractionation during microbial sulfate reduction. Geobiology 14, 91–101. https://doi.org/10.1111/gbi.12149

Bradley, J.A., Arndt, S., Amend, J.P., Burwicz, E., Dale, A.W., Egger, M., LaRowe, D.E., 2020. Widespread energy limitation to life in global subseafloor sediments. Science Advances 6, eaba0697. https://doi.org/10.1126/sciadv.aba0697

Brady, A.L., Slater, G.F., Omelon, C.R., Southam, G., Druschel, G., Andersen, D.T., Hawes, I., Laval, B., Lim, D.S.S., 2010. Photosynthetic isotope biosignatures in laminated micro-stromatolitic and non-laminated nodules associated with modern, freshwater microbialites in Pavilion Lake, B.C. Chemical Geology 274, 56–67. https://doi.org/10.1016/j.chemgeo.2010.03.016

Braissant, O., Decho, A.W., Dupraz, C., Glunk, C., Przekop, K.M., Visscher, P.T., 2007. Exopolymeric substances of sulfate-reducing bacteria: Interactions with calcium at alkaline pH and implication for formation of carbonate minerals. Geobiology 5, 401–411. https://doi.org/10.1111/j.1472-4669.2007.00117.x

Bralower, T.J., Thierstein, H.R., 1984. Low productivity abnd slow deep-water circulation in mid-Cretaceous oceans 614–618.

Brečević, L., Nielsen, A.E., 1989. Solubility of amorphous calcium carbonate. Journal of Crystal Growth 98, 504–510. https://doi.org/10.1016/0022-0248(89)90168-1

Breitbart, M., Hoare, A., Nitti, A., Siefert, J., Haynes, M., Dinsdale, E., Edwards, R., Souza, V., Rohwer, F., Hollander, D., 2009. Metagenomic and stable isotopic analyses of modern freshwater microbialites in Cuatro Ciénegas, Mexico. Environmental Microbiology 11, 16–34. https://doi.org/10.1111/j.1462-2920.2008.01725.x

Briones, E.E., Alcocer, J., Cienfuegos, E., Morales, P., 1998. Carbon stable isotopes ratios of pelagic and littoral communities in Alchichica crater-lake, Mexico. International Journal of Salt Lake Research 7, 345–355. https://doi.org/10.1007/BF02442143

Brunner, B., Bernasconi, S.M., 2005. A revised isotope fractionation model for dissimilatory sulfate reduction in sulfate reducing bacteria. Geochimica et Cosmochimica Acta 69, 4759–4771. https://doi.org/10.1016/j.gca.2005.04.015

Brunner, B., Bernasconi, S.M., Kleikemper, J., Schroth, M.H., 2005. A model for oxygen and sulfur isotope fractionation in sulfate during bacterial sulfate reduction processes. Geochimica et Cosmochimica Acta 69, 4773–4785. https://doi.org/10.1016/j.gca.2005.04.017

Buongiorno, J., Gomez, F.J., Fike, D.A., Kah, L.C., 2018. Mineralized microbialites as archives of environmental evolution, Laguna Negra, Catamarca Province, Argentina. Geobiology gbi.12327. https://doi.org/10.1111/gbi.12327

Burdige, D.J., Komada, T., Magen, C., Chanton, J.P., 2016. Modeling studies of dissolved organic matter cycling in Santa Barbara Basin (CA, USA) sediments. Geochimica et Cosmochimica Acta 195, 100–119. https://doi.org/10.1016/j.gca.2016.09.007

Burne, R.V., Moore, L.S., 1987. Microbialites: Organosedimentary Deposits of Benthic Microbial Communities. PALAIOS 2, 241–254. https://doi.org/10.2307/3514674

Burne, R.V., Moore, L.S., Christy, A.G., Troitzsch, U., King, P.L., Carnerup, A.M., Hamilton, P.J., 2014. Stevensite in the modern thrombolites of Lake Clifton, Western Australia: A missing link in microbialite mineralization? Geology 42, 575–578. https://doi.org/10.1130/G35484.1

Busigny, V., Planavsky, N.J., Jézéquel, D., Crowe, S., Louvat, P., Moureau, J., Viollier, E., Lyons, T.W., 2014. Iron isotopes in an Archean ocean analogue. Geochimica et Cosmochimica Acta 133, 443–462. https://doi.org/10.1016/j.gca.2014.03.004

Caballero, M., Vilaclara, G., Rodríguez, A., Juárez, D., 2003. Short-term climatic change in lake sediments from lake Alchichica, Oriental, Mexico. GeoInt 42, 529–537. https://doi.org/10.22201/igeof.00167169p.2003.42.3.942

Cadeau, P., Cartigny, P., Thomazo, C., Jézéquel, D., Leboulanger, C., Sarazin, G., Ader, M., 2022. The Dziani Dzaha Lake: A long-awaited modern analogue for superheavy pyrites. Geobiology 20, 444–461. https://doi.org/10.1111/gbi.12486

Cadeau, P., Jézéquel, D., Leboulanger, C., Fouilland, E., Le Floc'h, E., Chaduteau, C., Milesi, V., Guélard, J., Sarazin, G., Katz, A., d'Amore, S., Bernard, C., Ader, M., 2020. Carbon isotope evidence for large methane emissions to the Proterozoic atmosphere. Sci Rep 10, 18186. https://doi.org/10.1038/s41598-020-75100-x

Calver, C.R., 2000. Isotope stratigraphy of the Ediacarian (Neoproterozoic III) of the Adelaide Rift Complex, Australia, and the overprint of water column stratification. Precambrian Research 100, 121–150. https://doi.org/10.1016/S0301-9268(99)00072-8
Canfield, D.E., 2004. The evolution of the Earth surface sulfur reservoir. American Journal of Science 304, 839–861. https://doi.org/10.2475/ajs.304.10.839
Canfield, D.E., 2001. Biogeochemistry of Sulfur Isotopes | Reviews in Mineralogy and Geochemistry | GeoScienceWorld. Reviews in Mineralogy and Geochemistry 43, 607–636. https://doi.org/10.2138/gsrmg.43.1.607
Canfield, D.E., 1998. A new model for Proterozoic ocean chemistry. Nature 396, 450–453. https://doi.org/10.1038/24839
Canfield, D.E., Farquhar, J., 2009. Animal evolution, bioturbation, and the sulfate concentration of the oceans. Proc. Natl. Acad. Sci. U.S.A. 106, 8123–8127. https://doi.org/10.1073/pnas.0902037106
Canfield, D.E., Farquhar, J., Zerkle, A.L., 2010. High isotope fractionations during sulfate reduction in a low-sulfate euxinic ocean analog. Geology 38, 415–418. https://doi.org/10.1130/G30723.1
Canfield, D.E., Teske, A., 1996. Late Proterozoic rise in atmospheric oxygen concentration inferred from phylogenetic and sulphur-isotope studies. Nature 382, 127–132. https://doi.org/10.1038/382127a0
Canfield, D.E., Thamdrup, B., 2009. Towards a consistent classification scheme for geochemical environments, or, why we wish the term ‘suboxic’ would go away. Geobiology 7, 385–392. https://doi.org/10.1111/j.1472-4669.2009.00214.x
Canfield, D.E., Thamdrup, B., 1994. The Production of 34S-Depleted Sulfide During Bacterial Disproportionation of Elemental Sulfur. Science 266, 1973–1975. https://doi.org/10.1126/science.11540246
Carrasco-Núñez, G., Chako-Tchamabé, B., 2022. Geological Evolution of the Alchichica Crater, in: Alcocer, J. (Ed.), Lake Alchichica Limnology: The Uniqueness of a Tropical Maar Lake. Springer International Publishing, Cham, pp. 15–32. https://doi.org/10.1007/978-3-030-79096-7_2
Carrasco-Núñez, G., Hernández, J., Cavazos-Álvarez, J., Norini, G., Orozco-Esquivel, T., López-Quiroz, P., Jáquez, A., De León-Barragán, L., 2021. Volcanic geology of the easternmost sector of the Trans-Mexican Volcanic Belt, Mexico. Journal of Maps 17, 486–496. https://doi.org/10.1080/17445647.2021.1970037
Carrasco-Núñez, G., Ort, M.H., Romero, C., 2007. Evolution and hydrological conditions of a maar volcano (Atexcac crater, Eastern Mexico). Journal of Volcanology and Geothermal Research 159, 179–197. https://doi.org/10.1016/j.jvolgeores.2006.07.001
Carrasco-Núñez, G., Siebert, L., Díaz-Castellón, R., Vázquez-Selem, L., Capra, L., 2010. Evolution and hazards of a long-quiescent compound shield-like volcano: Cofre de Perote, Eastern Trans-Mexican Volcanic Belt. Journal of Volcanology and Geothermal Research 197, 209–224. https://doi.org/10.1016/j.jvolgeores.2009.08.010
Cartigny, P., 2005. Stable Isotopes and the Origin of Diamond. Elements 1, 79–84. https://doi.org/10.2113/gselements.1.2.79
Catling, D.C., Zahnle, K.J., 2020. The Archean atmosphere. Sci. Adv. 6, eaax1420. https://doi.org/10.1126/sciadv.aax1420
Caumartin, J., Benzerara, K., Havas, R., Thomazo, C., Lòpez-García, P., Duprat, E., 2023. The chemical conditions necessary for the formation of microbialites. Geochemical Perspectives Letters 25, 30–35. https://doi.org/10.7185/geochemlet.2311
Chacko, T., Cole, D.R., Horita, J., 2001. Equilibrium Oxygen, Hydrogen and Carbon Isotope Fractionation Factors Applicable to Geologic Systems, in: Valley, J.W., Cole, D.R. (Eds.), Stable Isotope Geochemistry. De Gruyter, pp. 1–82. https://doi.org/10.1515/9781501508745-004
Chagas, A.A.P., Webb, G.E., Burne, R.V., Southam, G., 2016. Modern lacustrine microbialites: Towards a synthesis of aqueous and carbonate geochemistry and mineralogy. Earth-Science Reviews 162, 338–363. https://doi.org/10.1016/j.earscirev.2016.09.012

Chahi, A., Fritz, B., Duplay, J., Weber, F., Lucas, J., 1997. Textural Transition and Genetic Relationship between Precursor Stevensite and Sepiolite in Lacustrine Sediments (Jbel Rhassoul, Morocco). Clays Clay Miner. 45, 378–389. https://doi.org/10.1346/CCMN.1997.0450308

Chako Tchamabé, B., Carrasco-Núñez, G., Miggins, D.P., Németh, K., 2020. Late Pleistocene to Holocene activity of Alchichica maar volcano, eastern Trans-Mexican Volcanic Belt. Journal of South American Earth Sciences 97, 102404. https://doi.org/10.1016/j.jsames.2019.102404

Chakrabarti, G., Shome, D., Kumar, S., Armstrong-Altrin, J.S., Sial, A.N., 2011. Carbon and oxygen isotopic variations in stromatolitic dolomites of Palaeoproterozoic Vempalle Formation, Cuddapah Basin, India. Carbonates Evaporites 26, 181–191. https://doi.org/10.1007/s13146-011-0054-5

Chambers, L.A., Trudinger, P.A., 1979. Microbiological fractionation of stable sulfur isotopes: A review and critique. Geomicrobiology Journal 1, 249–293. https://doi.org/10.1080/01490457909377735

Chédeville, C., Guilbaud, M.-N., Siebe, C., 2020. Stratigraphy and radiocarbon ages of late-Holocene Las Derrumbadas rhyolitic domes and surrounding vents in the Serdán-Oriental basin (Mexico): Implications for archeology, biology, and hazard assessment. The Holocene 30, 402–419. https://doi.org/10.1177/0959683619887417

Coffey, J.M., Flannery, D.T., Walter, M.R., George, S.C., 2013. Sedimentology, stratigraphy and geochemistry of a stromatolite biofacies in the 2.72Ga Tumbiana Formation, Fortescue Group, Western Australia. Precambrian Research 236, 282–296. https://doi.org/10.1016/j.precamres.2013.07.021

Cole, J.J., Caraco, N.F., 1998. Atmospheric exchange of carbon dioxide in a low-wind oligotrophic lake measured by the addition of SF6. Limnology and Oceanography 43, 647–656. https://doi.org/10.4319/lo.1998.43.4.0647

Cole, J.J., Caraco, N.F., Kling, G.W., Kratz, T.K., 1994. Carbon Dioxide Supersaturation in the Surface Waters of Lakes. Science 265, 1568–1570. https://doi.org/10.1126/science.265.5178.1568

Corkeron, M., Webb, G.E., Moulds, J., Grey, K., 2012. Discriminating stromatolite formation modes using rare earth element geochemistry: Trapping and binding versus in situ precipitation of stromatolites from the Neoproterozoic Bitter Springs Formation, Northern Territory, Australia. Precambrian Research 212–213, 194–206. https://doi.org/10.1016/j.precamres.2012.04.019

Couradeau, E., Benzerara, K., Gérard, E., Estève, I., Moreira, D., Tavera, R., López-García, P., 2013. Cyanobacterial calcification in modern microbialites at the submicrometer scale. Biogeosciences 10, 5255–5266. https://doi.org/10.5194/bg-10-5255-2013

Couradeau, E., Benzerara, K., Gérard, E., Moreira, D., Bernard, S., Brown, G.E., López-García, P., 2012. An Early-Branching Microbialite Cyanobacterium Forms Intracellular Carbonates. Science 336, 459–462. https://doi.org/10.1126/science.1216171

Couradeau, E., Benzerara, K., Moreira, D., Gérard, E., Kaźmierczak, J., Tavera, R., López-García, P., 2011. Prokaryotic and Eukaryotic Community Structure in Field and Cultured Microbialites from the Alkaline Lake Alchichica (Mexico). PLoS ONE 6, e28767. https://doi.org/10.1371/journal.pone.0028767

Crémière, A., Pellerin, A., Wing, B.A., Lepland, A., 2020. Multiple sulfur isotopes in methane seep carbonates track unsteady sulfur cycling during anaerobic methane oxidation. Earth and Planetary Science Letters 532, 115994. https://doi.org/10.1016/j.epsl.2019.115994

Crowe, S.A., Katsev, S., Leslie, K., Sturm, A., Magen, C., Nomosatryo, S., Pack, M.A., Kessler, J.D., Reeburgh, W.S., Roberts, J.A., González, L., Douglas Haffner, G., Mucci, A., Sundby, B., Fowle, D.A., 2011. The methane cycle in ferruginous Lake Matano: Methane cycle in ferruginous Lake Matano. Geobiology 9, 61–78. https://doi.org/10.1111/j.1472-4669.2010.00257.x

Crowe, S.A., Paris, G., Katsev, S., Jones, C., Kim, S.-T., Zerkle, A.L., Nomosatryo, S., Fowle, D.A., Adkins, J.F., Sessions, A.L., Farquhar, J., Canfield, D.E., 2014. Sulfate was a trace constituent of Archean seawater. Science 346, 735–739. https://doi.org/10.1126/science.1258966

Dauphas, N., Schauble, E.A., 2016. Mass Fractionation Laws, Mass-Independent Effects, and Isotopic Anomalies. Annu. Rev. Earth Planet. Sci. 44, 709–783. https://doi.org/10.1146/annurev-earth-060115-012157

De Choudens-Sanchez, V., Gonzalez, L.A., 2009. Calcite and Aragonite Precipitation Under Controlled Instantaneous Supersaturation: Elucidating the Role of CaCO3 Saturation State and Mg/Ca Ratio on Calcium Carbonate Polymorphism. Journal of Sedimentary Research 79, 363–376. https://doi.org/10.2110/jsr.2009.043

de Moor, J.M., Fischer, T.P., Plank, T., 2022. Constraints on the sulfur subduction cycle in Central America from sulfur isotope compositions of volcanic gases. Chemical Geology 588, 120627. https://doi.org/10.1016/j.chemgeo.2021.120627

De Visscher, A., Vanderdeelen, J., 2003. Estimation of the Solubility Constant of Calcite, Aragonite, and Vaterite at 25°C Based on Primary Data Using the Pitzer Ion Interaction Approach. Monatshefte für Chemie 134, 769–775. https://doi.org/10.1007/s00706-002-0587-3

De Wever, A., 2019. Etude de la biominéralisation de carbonates intracellulaires et de silicates dfe magnésium hydratés dans les environnements lacustres alcalins. Sorbonne Université, Paris.

Decho, A.W., 2000. Exopolymer Microdomains as a Structuring Agent for Heterogeneity Within Microbial Biofilms, in: Riding, R.E., Awramik, S.M. (Eds.), Microbial Sediments. Springer, Berlin, Heidelberg, pp. 9–15. https://doi.org/10.1007/978-3-662-04036-2_2

Della Porta, G., 2015. Carbonate build-ups in lacustrine, hydrothermal and fluvial settings: comparing depositional geometry, fabric types and geochemical signature. SP 418, 17–68. https://doi.org/10.1144/SP418.4

Des Marais, D.J., Nguyen, H., Cheatham, M., Cheatham, T., Munoz, E., Cohen, Y., 1989. Carbon isotopic trends in the hypersaline ponds and microbial mats at Guerrero Negro, Baja California Sur, Mexico - Implications for precambrian stromatolites, Amer. Soc. Microbiology. ed. Washington DC.

Döbelin, N., Kleeberg, R., 2015. Profex : a graphical user interface for the Rietveld refinement program BGMN. J Appl Crystallogr 48, 1573–1580. https://doi.org/10.1107/S1600576715014685

Donahue, M.A., Werne, J.P., Meile, C., Lyons, T.W., 2008a. Modeling sulfur isotope fractionation and differential diffusion during sulfate reduction in sediments of the Cariaco Basin. Geochimica et Cosmochimica Acta 72, 2287–2297. https://doi.org/10.1016/j.gca.2008.02.020

Donahue, M.A., Werne, J.P., Meile, C., Lyons, T.W., 2008b. Response to comment by I.C. Bourg on “Modeling sulfur isotope fractionation and differential diffusion during sulfate reduction in sediments of the Cariaco Basin” by M.A. Donahue, J.P. Werne, C. Meile, and T.W. Lyons. Geochimica et Cosmochimica Acta 72, 5855–5856. https://doi.org/10.1016/j.gca.2008.09.016

Dos Santos Afonso, M., Stumm, W., 1992. Reductive dissolution of iron(III) (hydr)oxides by hydrogen sulfide. Langmuir 8, 1671–1675. https://doi.org/10.1021/la00042a030

Duarte, C.M., Prairie, Y.T., Montes, C., Cole, J.J., Striegl, R., Melack, J., Downing, J.A., 2008. CO_2 emissions from saline lakes: A global estimate of a surprisingly large flux: CO_2 FLUXES FROM SALINE LAKES. J. Geophys. Res. 113. https://doi.org/10.1029/2007JG000637

Dupraz, C., Reid, R.P., Braissant, O., Decho, A.W., Norman, R.S., Visscher, P.T., 2009a. Processes of carbonate precipitation in modern microbial mats. Earth-Science Reviews 96, 141–162. https://doi.org/10.1016/j.earscirev.2008.10.005

Dupraz, C., Reid, R.P., Braissant, O., Decho, A.W., Norman, R.S., Visscher, P.T., 2009b. Processes of carbonate precipitation in modern microbial mats. Earth-Science Reviews 96, 141–162. https://doi.org/10.1016/j.earscirev.2008.10.005

Eldridge, D.L., Farquhar, J., 2018. Rates and multiple sulfur isotope fractionations associated with the oxidation of sulfide by oxygen in aqueous solution. Geochimica et Cosmochimica Acta 237, 240–260. https://doi.org/10.1016/j.gca.2018.06.030

Eldridge, D.L., Kamyshny, A., Farquhar, J., 2021. Theoretical estimates of equilibrium sulfur isotope effects among aqueous polysulfur and associated compounds with applications to authigenic

pyrite formation and hydrothermal disproportionation reactions. Geochimica et Cosmochimica Acta 310, 281–319. https://doi.org/10.1016/j.gca.2021.05.051
Emrich, K., Ehhalt, D.H., Vogel, J.C., 1970. Carbon isotope fractionation during the precipitation of calcium carbonate. Earth and Planetary Science Letters 8, 363–371. https://doi.org/10.1016/0012-821X(70)90109-3
Farquhar, J., Bao, H., Thiemens, M., 2000. Atmospheric Influence of Earth's Earliest Sulfur Cycle. Science 289, 756–758. https://doi.org/10.1126/science.289.5480.756
Farquhar, J., Canfield, D.E., Masterson, A., Bao, H., Johnston, D., 2008. Sulfur and oxygen isotope study of sulfate reduction in experiments with natural populations from Fællestrand, Denmark. Geochimica et Cosmochimica Acta 72, 2805–2821. https://doi.org/10.1016/j.gca.2008.03.013
Farquhar, J., Johnston, D.T., Wing, B.A., Habicht, K.S., Canfield, D.E., Airieau, S., Thiemens, M.H., 2003. Multiple sulphur isotopic interpretations of biosynthetic pathways: implications for biological signatures in the sulphur isotope record. Geobiology 1, 27–36. https://doi.org/10.1046/j.1472-4669.2003.00007.x
Farquhar, J., Zerkle, A.L., Bekker, A., 2011. Geological constraints on the origin of oxygenic photosynthesis. Photosynth Res 107, 11–36. https://doi.org/10.1007/s11120-010-9594-0
Fedorchuk, N.D., Dornbos, S.Q., Corsetti, F.A., Isbell, J.L., Petryshyn, V.A., Bowles, J.A., Wilmeth, D.T., 2016. Early non-marine life: Evaluating the biogenicity of Mesoproterozoic fluvial-lacustrine stromatolites. Precambrian Research 275, 105–118. https://doi.org/10.1016/j.precamres.2016.01.015
Ferrari, L., Orozco-Esquivel, T., Manea, V., Manea, M., 2012. The dynamic history of the Trans-Mexican Volcanic Belt and the Mexico subduction zone. Tectonophysics 522–523, 122–149. https://doi.org/10.1016/j.tecto.2011.09.018
Fike, D.A., Bradley, A.S., Rose, C.V., 2015. Rethinking the Ancient Sulfur Cycle. Annu. Rev. Earth Planet. Sci. 43, 593–622. https://doi.org/10.1146/annurev-earth-060313-054802
Fike, D.A., Finke, N., Zha, J., Blake, G., Hoehler, T.M., Orphan, V.J., 2009. The effect of sulfate concentration on (sub)millimeter-scale sulfide δ34S in hypersaline cyanobacterial mats over the diurnal cycle. Geochimica et Cosmochimica Acta 73, 6187–6204. https://doi.org/10.1016/j.gca.2009.07.006
Fike, D.A., Grotzinger, J.P., Pratt, L.M., Summons, R.E., 2006. Oxidation of the Ediacaran Ocean. Nature 444, 744–747. https://doi.org/10.1038/nature05345
Filonov, A., Tereshchenko, I., Alcocer, J., 2006. Dynamic response to mountain breeze circulation in Alchichica, a crater lake in Mexico. Geophys. Res. Lett. 33, L07404. https://doi.org/10.1029/2006GL025901
Filonov, A., Tereshchenko, I., Barba-Lopez, M. del R., Alcocer, J., Ladah, L., 2022. Meteorological Regime, Local Climate, and Hydrodynamics of Lake Alchichica, in: Alcocer, J. (Ed.), Lake Alchichica Limnology. Springer International Publishing, Cham, pp. 75–99. https://doi.org/10.1007/978-3-030-79096-7_6
Fischer, W.W., Fike, D.A., Johnson, J.E., Raub, T.D., Guan, Y., Kirschvink, J.L., Eiler, J.M., 2014. SQUID–SIMS is a useful approach to uncover primary signals in the Archean sulfur cycle. Proc. Natl. Acad. Sci. U.S.A. 111, 5468–5473. https://doi.org/10.1073/pnas.1322577111
Fischer, W.W., Schroeder, S., Lacassie, J.P., Beukes, N.J., Goldberg, T., Strauss, H., Horstmann, U.E., Schrag, D.P., Knoll, A.H., 2009. Isotopic constraints on the Late Archean carbon cycle from the Transvaal Supergroup along the western margin of the Kaapvaal Craton, South Africa. Precambrian Research 169, 15–27. https://doi.org/10.1016/j.precamres.2008.10.010
Fouke, B.W., 2011. Hot-spring Systems Geobiology: abiotic and biotic influences on travertine formation at Mammoth Hot Springs, Yellowstone National Park, USA: Hot-spring systems geobiology. Sedimentology 58, 170–219. https://doi.org/10.1111/j.1365-3091.2010.01209.x
Frantz, C.M., Petryshyn, V.A., Marenco, P.J., Tripati, A., Berelson, W.M., Corsetti, F.A., 2014. Dramatic local environmental change during the Early Eocene Climatic Optimum detected using high

resolution chemical analyses of Green River Formation stromatolites. Palaeogeography, Palaeoclimatology, Palaeoecology 405, 1–15. https://doi.org/10.1016/j.palaeo.2014.04.001
Friedlingstein, P., *et al*., 2019. Global Carbon Budget 2019. Earth System Science Data 11, 1783–1838. https://doi.org/10.5194/essd-11-1783-2019
Friesenbichler, E., Richoz, S., Baud, A., Krystyn, L., Sahakyan, L., Vardanyan, S., Peckmann, J., Reitner, J., Heindel, K., 2018. Sponge-microbial build-ups from the lowermost Triassic Chanakhchi section in southern Armenia: Microfacies and stable carbon isotopes. Palaeogeography, Palaeoclimatology, Palaeoecology 490, 653–672. https://doi.org/10.1016/j.palaeo.2017.11.056
Froelich, P., Klinkhammer, G.P., Bender, M.L., Luedtke, N.A., Heath, G.R., Cullen, D., Dauphin, P., Hammond, D., Hartman, B., Maynard, V., 1979. Early oxidation of organic matter in pelagic sediments of the eastern equatorial Atlantic: suboxic diagenesis. Geochimica et cosmochimica acta 43, 1075–1090.
Fry, B., Jannasch, H.W., Molyneaux, S.J., Wirsen, C.O., Muramoto, J.A., King, S., 1991. Stable isotope studies of the carbon, nitrogen and sulfur cycles in the Black Sea and the Cariaco Trench. Deep Sea Research Part A. Oceanographic Research Papers 38, S1003–S1019. https://doi.org/10.1016/S0198-0149(10)80021-4
Fukushi, K., Matsumiya, H., 2018. Control of Water Chemistry in Alkaline Lakes: Solubility of Monohydrocalcite and Amorphous Magnesium Carbonate in CaCl2–MgCl2–Na2CO3 Solutions. ACS Earth Space Chem. 2, 735–744. https://doi.org/10.1021/acsearthspacechem.8b00046
Fulton, J.M., Arthur, M.A., Thomas, B., Freeman, K.H., 2018. Pigment carbon and nitrogen isotopic signatures in euxinic basins. Geobiology 16, 429–445. https://doi.org/10.1111/gbi.12285
Gallagher, K.L., Dupraz, C., Visscher, P.T., 2014. Two opposing effects of sulfate reduction on carbonate precipitation in normal marine, hypersaline, and alkaline environments. Geology Forum e313–e314. https://doi.org/10.1130/G34639C.1
García-Sánchez, B.E., 2022. Organic compounds in surface and groundwaters in the surrounding of a Mexican geothermal reservoir; case study Los Humeros, Puebla. Applied Geochemistry.
Gargaud, M., Martin, H., López-García, P., Montmerle, T., Pascal, R., 2009. Le Soliel, la Terre... La Vie, La quête des origines, Belin. ed, Belin: pour la science.
Ge, Y., Della Porta, G., Pederson, C.L., Lokier, S.W., Hoffmann, R., Immenhauser, A., 2021. Botryoidal and Spherulitic Aragonite in Carbonates Associated with Microbial Mats: Precipitation or Diagenetic Replacement Product? Front. Earth Sci. 9, 698952. https://doi.org/10.3389/feart.2021.698952
Gérard, E., De Goeyse, S., Hugoni, M., Agogué, H., Richard, L., Milesi, V., Guyot, F., Lecourt, L., Borensztajn, S., Joseph, M.-B., Leclerc, T., Sarazin, G., Jézéquel, D., Leboulanger, C., Ader, M., 2018. Key Role of Alphaproteobacteria and Cyanobacteria in the Formation of Stromatolites of Lake Dziani Dzaha (Mayotte, Western Indian Ocean). Front. Microbiol. 9, 796. https://doi.org/10.3389/fmicb.2018.00796
Gérard, E., Ménez, B., Couradeau, E., Moreira, D., Benzerara, K., Tavera, R., López-García, P., 2013. Specific carbonate–microbe interactions in the modern microbialites of Lake Alchichica (Mexico). ISME J 7, 1997–2009. https://doi.org/10.1038/ismej.2013.81
Gerdes, G., 2007. Structures left by modern microbial mats in their host sediments, -38.
Ghosh, P., Bhattacharya, S.K., Chakrabarti, A., 2001. Stable isotopic studies of microbial carbonates from Talchir sediments of east-central India. Current Science 80, 1326–1330.
Gibson, J.J., Birks, S.J., Yi, Y., 2016. Stable isotope mass balance of lakes: a contemporary perspective. Quaternary Science Reviews 131, 316–328. https://doi.org/10.1016/j.quascirev.2015.04.013
Goevert, D., Conrad, R., 2010. Stable carbon isotope fractionation by acetotrophic sulfur-reducing bacteria. FEMS Microbiology Ecology 71, 218–225. https://doi.org/10.1111/j.1574-6941.2009.00811.x
Gomes, M.L., Hurtgen, M.T., 2015. Sulfur isotope fractionation in modern euxinic systems: Implications for paleoenvironmental reconstructions of paired sulfate–sulfide isotope

records. Geochimica et Cosmochimica Acta 157, 39–55. https://doi.org/10.1016/j.gca.2015.02.031
Gomes, M.L., Hurtgen, M.T., 2013. Sulfur isotope systematics of a euxinic, low-sulfate lake: Evaluating the importance of the reservoir effect in modern and ancient oceans. Geology 41, 663–666. https://doi.org/10.1130/G34187.1
Gonfiantini, R., 1986. ENVIRONMENTAL ISOTOPES IN LAKE STUDIES, in: The Terrestrial Environment, B. Elsevier, pp. 113–168. https://doi.org/10.1016/B978-0-444-42225-5.50008-5
Gonzales-Partida, E., Barragan-R, R.M., Nieva-G, D., 1993. Analisis geoquimico-isotopico de las especies carbonicas del fluido geotermico de Los Humeros, Puebla, México. Geofisica Internacional 32, 299–309.
Graven, H., Keeling, R.F., Rogelj, J., 2020. Changes to Carbon Isotopes in Atmospheric CO_2 Over the Industrial Era and Into the Future. Global Biogeochem. Cycles 34. https://doi.org/10.1029/2019GB006170
Grey, K., Awramik, S.M., 2020. HANDBOOK FOR THE STUDY AND DESCRIPTION OF MICROBIALITES, Geological Survey of Western Australia. ed, Geological Survey of Western Australia: Bulletin 147.
Gröger, J., Franke, J., Hamer, K., Schulz, H.D., 2009. Quantitative Recovery of Elemental Sulfur and Improved Selectivity in a Chromium-Reducible Sulfur Distillation. Geostandards and Geoanalytical Research 33, 17–27. https://doi.org/10.1111/j.1751-908X.2009.00922.x
Grossman, E.L., 1998. oxygen isotopesOxygen isotopes, in: Geochemistry, Encyclopedia of Earth Science. Springer Netherlands, Dordrecht, pp. 469–474. https://doi.org/10.1007/1-4020-4496-8_234
Grotzinger, J.P., 1990. Geochemical model for Proterozoic stromatolite decline. American Journal of Science 290-A, 80–103.
Guibourdenche, L., 2022. Multiple sulfur isotopes insights on the biogeochemistry of the Mediterranean during Messinian Salinity Crisis. Université Paris Cité, Institut de Physique du Globe de Paris, Paris.
Guibourdenche, L., Cartigny, P., Dela Pierre, F., Natalicchio, M., Aloisi, G., 2022. Cryptic sulfur cycling during the formation of giant gypsum deposits. Earth and Planetary Science Letters 593, 117676. https://doi.org/10.1016/j.epsl.2022.117676
Guilbaud, M.-N., Chédeville, C., Molina-Guadarrama, Á.N., Pineda-Serrano, J.C., Siebe, C., 2023. Volcano-sedimentary processes at Las Derrumbadas rhyolitic twin domes, Serdán-Oriental Basin, Eastern Trans-Mexican Volcanic Belt. SP 520, 165–189. https://doi.org/10.1144/SP520-2021-144
Guilbaud, R., Poulton, S.W., Butterfield, N.J., Zhu, M., Shields-Zhou, G.A., 2015. A global transition to ferruginous conditions in the early Neoproterozoic oceans. Nature Geosci 8, 466–470. https://doi.org/10.1038/ngeo2434
Halevy, I., Bachan, A., 2017. The geologic history of seawater pH. Science 355, 1069–1071. https://doi.org/10.1126/science.aal4151
Halevy, I., Peters, S.E., Fischer, W.W., 2012. Sulfate Burial Constraints on the Phanerozoic Sulfur Cycle. Science 337, 331–334. https://doi.org/10.1126/science.1220224
Harerimana, C., Harbi, B., Vasel, J.-L., 2010. Développement d'un modèle stœchiométrique de la sulfato-réduction par des bactéries sulfato-réductrices en lagunage anaérobie. Biotechnol. Agron. Soc. Environ.
Harrison, A.L., Bénézeth, P., Schott, J., Oelkers, E.H., Mavromatis, V., 2021. Magnesium and carbon isotope fractionation during hydrated Mg-carbonate mineral phase transformations. Geochimica et Cosmochimica Acta 293, 507–524. https://doi.org/10.1016/j.gca.2020.10.028
Hayes, J.M., 2001. Fractionation of Carbon and Hydrogen Isotopes in Biosynthetic Processes*. Reviews in Mineralogy and Geochemistry 43, 225–277. https://doi.org/10.2138/gsrmg.43.1.225
Hayes, J.M., Popp, B.N., Takigiku, R., Johnson, M.W., 1989. An isotopic study of biogeochemical relationships between carbonates and organic carbon in the Greenhorn Formation.

Geochimica et Cosmochimica Acta 53, 2961–2972. https://doi.org/10.1016/0016-7037(89)90172-5
Hayes, J.M., Waldbauer, J.R., 2006. The carbon cycle and associated redox processes through time. Philosophical Transactions of the Royal Society B: Biological Sciences 361, 931–950. https://doi.org/10.1098/rstb.2006.1840
Herczeg, A.L., Leaney, F.W., Dighton, J.C., Lamontagne, S., Schiff, S.L., Telfer, A.L., English, M.C., 2003. A modern isotope record of changes in water and carbon budgets in a groundwater-fed lake: Blue Lake, South Australia. Limnol. Oceanogr. 48, 2093–2105. https://doi.org/10.4319/lo.2003.48.6.2093
Holgerson, M.A., Farr, E.R., Raymond, P.A., 2017. Gas transfer velocities in small forested ponds. JGR Biogeosciences 122, 1011–1021. https://doi.org/10.1002/2016JG003734
Holgerson, M.A., Zappa, C.J., Raymond, P.A., 2016. Substantial overnight reaeration by convective cooling discovered in pond ecosystems: OVERNIGHT REAERATION IN PONDS. Geophys. Res. Lett. 43, 8044–8051. https://doi.org/10.1002/2016GL070206
Holmer, M., Storkholm, P., 2001. Sulphate reduction and sulphur cycling in lake sediments: a review: Sulphate cycling in lake sediments. Freshwater Biology 46, 431–451. https://doi.org/10.1046/j.1365-2427.2001.00687.x
Horton, T.W., Defliese, W.F., Tripati, A.K., Oze, C., 2016. Evaporation induced 18O and 13C enrichment in lake systems: A global perspective on hydrologic balance effects. Quaternary Science Reviews 131, 365–379. https://doi.org/10.1016/j.quascirev.2015.06.030
Horton, T.W., Oze, C., 2012. Are two elements better than one? Dual isotope-ratio detrending of evaporative effects on lake carbonate paleoelevation proxies: ^{13} C-EXCESS DETRENDING OF EVAPORATION. Geochem. Geophys. Geosyst. 13, n/a-n/a. https://doi.org/10.1029/2012GC004132
Houghton, J., Fike, D., Druschel, G., Orphan, V., Hoehler, T.M., Des Marais, D.J., 2014. Spatial variability in photosynthetic and heterotrophic activity drives localized $\delta^{13}C_{org}$ fluctuations and carbonate precipitation in hypersaline microbial mats. Geobiology 12, 557–574. https://doi.org/10.1111/gbi.12113
Houghton, J., Scarponi, D., Capraro, L., Fike, D.A., 2022. Impact of sedimentation, climate and sea level on marine sedimentary pyrite sulfur isotopes: Insights from the Valle di Manche section (Lower-Middle Pleistocene, southern Italy). Palaeogeography, Palaeoclimatology, Palaeoecology 585, 110730. https://doi.org/10.1016/j.palaeo.2021.110730
Hurowitz, J.A., Grotzinger, J.P., Fischer, W.W., McLennan, S.M., Milliken, R.E., Stein, N., Vasavada, A.R., Blake, D.F., Dehouck, E., Eigenbrode, J.L., Fairén, A.G., Frydenvang, J., Gellert, R., Grant, J.A., Gupta, S., Herkenhoff, K.E., Ming, D.W., Rampe, E.B., Schmidt, M.E., Siebach, K.L., Stack-Morgan, K., Sumner, D.Y., Wiens, R.C., 2017. Redox stratification of an ancient lake in Gale crater, Mars. Science 356, eaah6849. https://doi.org/10.1126/science.aah6849
Ingalls, M., Frantz, C.M., Snell, K.E., Trower, E.J., 2020. Carbonate facies-specific stable isotope data record climate, hydrology, and microbial communities in Great Salt Lake, UT. Geobiology 18, 566–593. https://doi.org/10.1111/gbi.12386
Iniesto, M., Moreira, D., Benzerara, K., Muller, E., Bertolino, P., Tavera, R., López-García, P., 2021a. Rapid formation of mature microbialites in Lake Alchichica, Mexico. Environmental Microbiology Reports 13, 600–605. https://doi.org/10.1111/1758-2229.12957
Iniesto, M., Moreira, D., Benzerara, K., Reboul, G., Bertolino, P., Tavera, R., López-García, P., 2022. Planktonic microbial communities from microbialite-bearing lakes sampled along a salinity-alkalinity gradient. Limnology & Oceanography lno.12233. https://doi.org/10.1002/lno.12233
Iniesto, M., Moreira, D., Reboul, G., Deschamps, P., Benzerara, K., Bertolino, P., Saghaï, A., Tavera, R., López-García, P., 2021b. Core microbial communities of lacustrine microbialites sampled along an alkalinity gradient. Environ Microbiol 23, 51–68. https://doi.org/10.1111/1462-2920.15252
Jahnke, R.A., 1996. The global ocean flux of particulate organic carbon: Areal distribution and magnitude. Global Biogeochem. Cycles 10, 71–88. https://doi.org/10.1029/95GB03525

Jaramillo-Vogel, D., Foubert, A., Braga, J.C., Schaegis, J.-C., Atnafu, B., Grobety, B., Kidane, T., 2019. Pleistocene sea-floor fibrous crusts and spherulites in the Danakil Depression (Afar, Ethiopia). Sedimentology 66, 480–512. https://doi.org/10.1111/sed.12484

Jenkyns, H.C., 2010. Geochemistry of oceanic anoxic events: REVIEW. Geochem. Geophys. Geosyst. 11, n/a-n/a. https://doi.org/10.1029/2009GC002788

Jiao, N., Herndl, G.J., Hansell, D.A., Benner, R., Kattner, G., Wilhelm, S.W., Kirchman, D.L., Weinbauer, M.G., Luo, T., Chen, F., Azam, F., 2010. Microbial production of recalcitrant dissolved organic matter: long-term carbon storage in the global ocean. Nat Rev Microbiol 8, 593–599. https://doi.org/10.1038/nrmicro2386

Johnson, C.M., Beard, B.L., Albarède, F., 2018. Geochemistry of Non-Traditional Stable Isotopes. Walter de Gruyter GmbH & Co KG.

Johnston, D.T., 2011. Multiple sulfur isotopes and the evolution of Earth's surface sulfur cycle. Earth-Science Reviews 106, 161–183. https://doi.org/10.1016/j.earscirev.2011.02.003

Johnston, D.T., 2005. Multiple sulfur isotope fractionations in biological systems: A case study with sulfate reducers and sulfur disproportionators. American Journal of Science 305, 645–660. https://doi.org/10.2475/ajs.305.6-8.645

Johnston, D.T., Farquhar, J., Canfield, D.E., 2007. Sulfur isotope insights into microbial sulfate reduction: When microbes meet models. Geochimica et Cosmochimica Acta 71, 3929–3947. https://doi.org/10.1016/j.gca.2007.05.008

Johnston, D.T., Farquhar, J., Habicht, K.S., Canfield, D.E., 2008. Sulphur isotopes and the search for life: strategies for identifying sulphur metabolisms in the rock record and beyond. Geobiology 6, 425–435. https://doi.org/10.1111/j.1472-4669.2008.00171.x

Johnston, D.T., Farquhar, J., Wing, B.A., Kaufman, A.J., Canfield, D.E., Habicht, K.S., 2005a. Multiple sulfur isotope fractionations in biological systems: A case study with sulfate reducers and sulfur disproportionators. American Journal of Science 305, 645–660. https://doi.org/10.2475/ajs.305.6-8.645

Johnston, D.T., Wing, B.A., Farquhar, J., Kaufman, A.J., Strauss, H., Lyons, T.W., Kah, L.C., Canfield, D.E., 2005b. Active Microbial Sulfur Disproportionation in the Mesoproterozoic. Science 310, 1477–1479. https://doi.org/10.1126/science.1117824

Jones, B.F., Galan, E., 1988. Sepiolite and Palygorskite, in: Hydrous Phyllosilicates, Reviews in Mineralogy. pp. 631–674.

Jørgensen, B.B., 2021. SULFUR BIOGEOCHEMICAL CYCLE OF MARINE SEDIMENTS. Geochemical Perspectives 10, 145–146.

Jørgensen, B.B., 1979. A theoretical model of the stable sulfur isotope distribution in marine sediments. Geochimica et Cosmochimica Acta 43, 363–374. https://doi.org/10.1016/0016-7037(79)90201-1

Jovovic, I., Grossi, V., Adam, P., Simon, L., Antheaume, I., Gelin, F., Ader, M., Cartigny, P., 2020. Quantitative and specific recovery of natural organic and mineral sulfur for (multi-)isotope analysis. Organic Geochemistry 146, 104055. https://doi.org/10.1016/j.orggeochem.2020.104055

Kamber, B.S., Bolhar, R., Webb, G.E., 2004. Geochemistry of late Archaean stromatolites from Zimbabwe: evidence for microbial life in restricted epicontinental seas. Precambrian Research 132, 379–399. https://doi.org/10.1016/j.precamres.2004.03.006

Kamennaya, N.A., Ajo-Franklin, C.M., Northen, T., Jansson, C., 2012. Cyanobacteria as Biocatalysts for Carbonate Mineralization. Minerals 2, 338–364. https://doi.org/10.3390/min2040338

Kaźmierczak, J., Kempe, S., Kremer, B., López-García, P., Moreira, D., Tavera, R., 2011. Hydrochemistry and microbialites of the alkaline crater lake Alchichica, Mexico. Facies 57, 543–570. https://doi.org/10.1007/s10347-010-0255-8

Kellermeier, M., Picker, A., Kempter, A., Cölfen, H., Gebauer, D., 2014. A Straightforward Treatment of Activity in Aqueous CaCO3 Solutions and the Consequences for Nucleation Theory. Advanced Materials 26, 752–757. https://doi.org/10.1002/adma.201303643

Kempe, S., Degens, E.T., 1985. An early soda ocean? Chemical Geology 53, 95–108. https://doi.org/10.1016/0009-2541(85)90023-3
Kempe, S., Kazmierczak, J., Landmann, G., Konuk, T., Reimer, A., Lipp, A., 1991. Largest known microbialites discovered in Lake Van, Turkey. Nature 349, 605–608. https://doi.org/10.1038/349605a0
Kendall, B., Reinhard, C.T., Lyons, T.W., Kaufman, A.J., Poulton, S.W., Anbar, A.D., 2010. Pervasive oxygenation along late Archaean ocean margins. Nature Geosci 3, 647–652. https://doi.org/10.1038/ngeo942
Kesler, S.E., Jones, L.M., 1980. Sulfur- and strontium-isotopic geochemistry of celestite, barite and gypsum from the Mesozoic basins of northeastern Mexico. Chemical Geology 31, 211–224. https://doi.org/10.1016/0009-2541(80)90087-X
Khelen, A.C., Manikyamba, C., Ganguly, S., Singh, Th.D., Subramanyam, K.S.V., Ahmad, S.M., Reddy, M.R., 2017. Geochemical and stable isotope signatures of Proterozoic stromatolitic carbonates from the Vempalle and Tadpatri Formations, Cuddapah Supergroup, India: Implications on paleoenvironment and depositional conditions. Precambrian Research 298, 365–384. https://doi.org/10.1016/j.precamres.2017.05.021
Kiba, T., Takagi, T., Yoshimura, Y., Kishi, I., 1955. Tin (II)-Strong Phosphoric Acid. A New Reagent for the Determination of Sulfate by Reduction to Hydrogen Sulfide. BCSJ 28, 641–644. https://doi.org/10.1246/bcsj.28.641
Killingsworth, B.A., Sansjofre, P., Philippot, P., Cartigny, P., Thomazo, C., Lalonde, S.V., 2019. Constraining the rise of oxygen with oxygen isotopes. Nat Commun 10, 4924. https://doi.org/10.1038/s41467-019-12883-2
Kim, S.-T., O'Neil, J.R., 1997. Equilibrium and nonequilibrium oxygen isotope effects in synthetic carbonates. Geochimica et Cosmochimica Acta 61, 3461–3475. https://doi.org/10.1016/S0016-7037(97)00169-5
Kim, S.-T., O'Neil, J.R., Hillaire-Marcel, C., Mucci, A., 2007. Oxygen isotope fractionation between synthetic aragonite and water: Influence of temperature and Mg2+ concentration. Geochimica et Cosmochimica Acta 71, 4704–4715. https://doi.org/10.1016/j.gca.2007.04.019
Knauth, L.P., Kennedy, M.J., 2009. The late Precambrian greening of the Earth. Nature 460, 728–732. https://doi.org/10.1038/nature08213
Knoll, A.H., Bergmann, K.D., Strauss, J.V., 2016. Life: the first two billion years. Philosophical Transactions of the Royal Society B: Biological Sciences 371, 20150493. https://doi.org/10.1098/rstb.2015.0493
Koegler, F.C., 1967. Geotechnical properties of recent marine sediments from the Arabian Sea and the Baltic Sea. University of Illinois Press., A.F. Richards (ed.) Geotechnique 170–176.
Kramer, R.T., Herrmann, N., Bartelink, E., Spradley, K., Bataille, C., 2018. Application of stable isotopes and geostatistics to predict region of geographic origin for deceased migrants recovered in southern Texas. https://doi.org/10.13140/RG.2.2.16931.27683
Kremer, B., Kazmierczak, J., Łukomska-Kowalczyk, M., Kempe, S., 2012. Calcification and Silicification: Fossilization Potential of Cyanobacteria from Stromatolites of Niuafo'ou's Caldera Lakes (Tonga) and Implications for the Early Fossil Record. Astrobiology 12, 535–548. https://doi.org/10.1089/ast.2011.0742
Krissansen-Totton, J., Arney, G.N., Catling, D.C., 2018. Constraining the climate and ocean pH of the early Earth with a geological carbon cycle model. Proc. Natl. Acad. Sci. U.S.A. 115, 4105–4110. https://doi.org/10.1073/pnas.1721296115
Krissansen-Totton, J., Buick, R., Catling, D.C., 2015. A statistical analysis of the carbon isotope record from the Archean to Phanerozoic and implications for the rise of oxygen. American Journal of Science 315, 275–316. https://doi.org/10.2475/04.2015.01
Kshirsagar, P., Siebe, C., Guilbaud, M.N., Salinas, S., 2016. Geological and environmental controls on the change of eruptive style (phreatomagmatic to Strombolian-effusive) of Late Pleistocene El Caracol tuff cone and its comparison with adjacent volcanoes around the Zacapu basin

(Michoacán, México). Journal of Volcanology and Geothermal Research 318, 114–133. https://doi.org/10.1016/j.jvolgeores.2016.03.015
Kshirsagar, P., Siebe, C., Guilbaud, M.N., Salinas, S., Layer, P.W., 2015. Late Pleistocene Alberca de Guadalupe maar volcano (Zacapu basin, Michoacán): Stratigraphy, tectonic setting, and paleo-hydrogeological environment. Journal of Volcanology and Geothermal Research 304, 214–236. https://doi.org/10.1016/j.jvolgeores.2015.09.003
Kuntz, L.B., Laakso, T.A., Schrag, D.P., Crowe, S.A., 2015. Modeling the carbon cycle in Lake Matano. Geobiology 13, 454–461. https://doi.org/10.1111/gbi.12141
Kusakabe, M., Komoda, Y., Takano, B., Abiko, T., 2000. Sulfur isotopic effects in the disproportionation reaction of sulfur dioxide in hydrothermal fluids: implications for the d 34S variations of dissolved bisulfate and elemental sulfur from active crater lakes. Journal of Volcanology and Geothermal Research 97, 287–307. https://doi.org/10.1016/S0377-0273(99)00161-4
Labidi, J., Cartigny, P., Jackson, M.G., 2015. Multiple sulfur isotope composition of oxidized Samoan melts and the implications of a sulfur isotope 'mantle array' in chemical geodynamics. Earth and Planetary Science Letters 417, 28–39. https://doi.org/10.1016/j.epsl.2015.02.004
Leavitt, W.D., Halevy, I., Bradley, A.S., Johnston, D.T., 2013. Influence of sulfate reduction rates on the Phanerozoic sulfur isotope record. Proc. Natl. Acad. Sci. U.S.A. 110, 11244–11249. https://doi.org/10.1073/pnas.1218874110
Lehmann, M.F., Bernasconi, S.M., Barbieri, A., McKenzie, J.A., 2002. Preservation of organic matter and alteration of its carbon and nitrogen isotope composition during simulated and in situ early sedimentary diagenesis. Geochimica et Cosmochimica Acta 66, 3573–3584. https://doi.org/10.1016/S0016-7037(02)00968-7
Lelli, M., Kretzschmar, T.G., Cabassi, J., Doveri, M., Sanchez-Avila, J.I., Gherardi, F., Magro, G., Norelli, F., 2021. Fluid geochemistry of the Los Humeros geothermal field (LHGF - Puebla, Mexico): New constraints for the conceptual model. Geothermics 90, 101983. https://doi.org/10.1016/j.geothermics.2020.101983
Lepot, K., 2020. Signatures of early microbial life from the Archean (4 to 2.5 Ga) eon. Earth-Science Reviews 209, 103296. https://doi.org/10.1016/j.earscirev.2020.103296
Lepot, K., Benzerara, K., Rividi, N., Cotte, M., Brown, G.E., Philippot, P., 2009. Organic matter heterogeneities in 2.72 Ga stromatolites: Alteration versus preservation by sulfur incorporation. Geochimica et Cosmochimica Acta 73, 6579–6599. https://doi.org/10.1016/j.gca.2009.08.014
Lepot, K., Williford, K.H., Philippot, P., Thomazo, C., Ushikubo, T., Kitajima, K., Mostefaoui, S., Valley, J.W., 2019. Extreme 13C-depletions and organic sulfur content argue for S-fueled anaerobic methane oxidation in 2.72 Ga old stromatolites. Geochimica et Cosmochimica Acta 244, 522–547. https://doi.org/10.1016/j.gca.2018.10.014
Li, H.-C., Ku, T.-L., 1997. $\delta^{13}C$–$\delta^{18}C$ covariance as a paleohydrological indicator for closed-basin lakes. Palaeogeography, Palaeoclimatology, Palaeoecology 133, 69–80. https://doi.org/10.1016/S0031-0182(96)00153-8
Lin, Z., Sun, X., Strauss, H., Lu, Y., Gong, J., Xu, L., Lu, H., Teichert, B.M.A., Peckmann, J., 2017. Multiple sulfur isotope constraints on sulfate-driven anaerobic oxidation of methane: Evidence from authigenic pyrite in seepage areas of the South China Sea. Geochimica et Cosmochimica Acta 153–173. https://doi.org/10.1016/j.gca.2017.05.015
Liu, J., Antler, G., Pellerin, A., Izon, G., Dohrmann, I., Findlay, A.J., Røy, H., Ono, S., Turchyn, A.V., Kasten, S., Jørgensen, B.B., 2021. Isotopically "heavy" pyrite in marine sediments due to high sedimentation rates and non-steady-state deposition. Geology 49, 816–821. https://doi.org/10.1130/G48415.1
Liu, J., Pellerin, A., Antler, G., Kasten, S., Findlay, A.J., Dohrmann, I., Røy, H., Turchyn, A.V., Jørgensen, B.B., 2020a. Early diagenesis of iron and sulfur in Bornholm Basin sediments: The role of near-surface pyrite formation. Geochimica et Cosmochimica Acta 284, 43–60. https://doi.org/10.1016/j.gca.2020.06.003

Liu, J., Pellerin, A., Izon, G., Wang, J., Antler, G., Liang, J., Su, P., Jørgensen, B.B., Ono, S., 2020b. The multiple sulphur isotope fingerprint of a sub-seafloor oxidative sulphur cycle driven by iron. Earth and Planetary Science Letters 536, 116165. https://doi.org/10.1016/j.epsl.2020.116165

Liu, J., Pellerin, A., Wang, J., Rickard, D., Antler, G., Zhao, J., Wang, Z., Jørgensen, B.B., Ono, S., 2022. Multiple sulfur isotopes discriminate organoclastic and methane-based sulfate reduction by sub-seafloor pyrite formation. Geochimica et Cosmochimica Acta 316, 309–330. https://doi.org/10.1016/j.gca.2021.09.026

Londry, K.L., Des Marais, D.J., 2003. Stable Carbon Isotope Fractionation by Sulfate-Reducing Bacteria. Appl Environ Microbiol 69, 2942–2949. https://doi.org/10.1128/AEM.69.5.2942-2949.2003

Lorenz, V., 1986. On the growth of maars and diatremes and its relevance to the formation of tuff rings. Bull Volcanol 48, 265–274. https://doi.org/10.1007/BF01081755

Louyakis, A.S., Mobberley, J.M., Vitek, B.E., Visscher, P.T., Hagan, P.D., Reid, R.P., Kozdon, R., Orland, I.J., Valley, J.W., Planavsky, N.J., Casaburi, G., Foster, J.S., 2017. A Study of the Microbial Spatial Heterogeneity of Bahamian Thrombolites Using Molecular, Biochemical, and Stable Isotope Analyses. Astrobiology 17, 413–430. https://doi.org/10.1089/ast.2016.1563

Lugo, A., Alcocer, J., Sánchez, Ma. del R., Escobar, E., Macek, M., 2000. Temporal and spatial variation of bacterioplankton abundance in a tropical, warm-monomictic, saline lake: Alchichica, Puebla, Mexico. SIL Proceedings, 1922-2010 27, 2968–2971. https://doi.org/10.1080/03680770.1998.11898217

Lyons, T.W., Reinhard, C.T., Planavsky, N.J., 2014. The rise of oxygen in Earth's early ocean and atmosphere. Nature 506, 307–315. https://doi.org/10.1038/nature13068

Macek, M., Medina, X.S., Picazo, A., Peštová, D., Reyes, F.B., Hernández, J.R.M., Alcocer, J., Ibarra, M.M., Camacho, A., 2020. Spirostomum teres: A Long Term Study of an Anoxic-Hypolimnion Population Feeding upon Photosynthesizing Microorganisms. Acta Protozool. 59, 13–38. https://doi.org/10.4467/16890027AP.20.002.12158

Mackenzie, F.T., Kump, L.R., 1995. Reverse Weathering, Clay Mineral Formation, and Oceanic Element Cycles. Science 270, 586–586. https://doi.org/10.1126/science.270.5236.586

Marin-Carbonne, J., Decraene, M.-N., Havas, R., Remusat, L., Pasquier, V., Alléon, J., Zeyen, N., Bouton, A., Bernard, S., Escrig, S., Olivier, N., Vennin, E., Meibom, A., Benzerara, K., Thomazo, C., 2022. Early precipitated micropyrite in microbialites: A time capsule of microbial sulfur cycling. Geochem. Persp. Let. 21, 7–12. https://doi.org/10.7185/geochemlet.2209

Mason, E., Edmonds, M., Turchyn, A.V., 2017. Remobilization of crustal carbon may dominate volcanic arc emissions. Science 357, 290–294. https://doi.org/10.1126/science.aan5049

Masterson, A., Alperin, M.J., Berelson, W.M., Johnston, D.T., 2018. Interpreting multiple sulfur isotope signals in modern anoxic sediments using a full diagenetic model (California-Mexico margin: Alfonso Basin). Am J Sci 318, 459–490. https://doi.org/10.2475/05.2018.02

Masterson, A.L., Alperin, M.J., Arnold, G.L., Berelson, W.M., Jørgensen, B.B., Røy, H., Johnston, D.T., 2022. Understanding the isotopic composition of sedimentary sulfide: A multiple sulfur isotope diagenetic model for Aarhus Bay. Am J Sci 322, 1–27. https://doi.org/10.2475/01.2022.01

Masterson, A.L., Wing, B.A., Paytan, A., Farquhar, J., Johnston, D.T., 2016. The minor sulfur isotope composition of Cretaceous and Cenozoic seawater sulfate. Paleoceanography 31, 779–788. https://doi.org/10.1002/2016PA002945

McCormack, J., Kwiecien, O., 2021. Coeval primary and diagenetic carbonates in lacustrine sediments challenge palaeoclimate interpretations. Sci Rep 11, 7935. https://doi.org/10.1038/s41598-021-86872-1

Meister, P., 2014. Two opposing effects of sulfate reduction on carbonate precipitation in normal marine, hypersaline, and alkaline environments. Geology Forum e315. https://doi.org/10.1130/G35240Y.1

Meister, P., 2013. Two opposing effects of sulfate reduction on carbonate precipitation in normal marine, hypersaline, and alkaline environments. Geology 41, 499–502. https://doi.org/10.1130/G34185.1

Mendonça, R., Müller, R.A., Clow, D., Verpoorter, C., Raymond, P., Tranvik, L.J., Sobek, S., 2017. Organic carbon burial in global lakes and reservoirs. Nat Commun 8, 1694. https://doi.org/10.1038/s41467-017-01789-6

Milesi, V.P., Debure, M., Marty, N.C.M., Capano, M., Jézéquel, D., Steefel, C., Rouchon, V., Albéric, P., Bard, E., Sarazin, G., Guyot, F., Virgone, A., Gaucher, É.C., Ader, M., 2020. Early Diagenesis of Lacustrine Carbonates in Volcanic Settings: The Role of Magmatic CO_2 (Lake Dziani Dzaha, Mayotte, Indian Ocean). ACS Earth Space Chem. 4, 363–378. https://doi.org/10.1021/acsearthspacechem.9b00279

Millero, F.J., Graham, T.B., Huang, F., Bustos-Serrano, H., Pierrot, D., 2006. Dissociation constants of carbonic acid in seawater as a function of salinity and temperature. Marine Chemistry 100, 80–94. https://doi.org/10.1016/j.marchem.2005.12.001

Mills, B.J.W., Krause, A.J., Scotese, C.R., Hill, D.J., Shields, G.A., Lenton, T.M., 2019. Modelling the long-term carbon cycle, atmospheric CO2, and Earth surface temperature from late Neoproterozoic to present day. Gondwana Research 67, 172–186. https://doi.org/10.1016/j.gr.2018.12.001

Mulholland, P.J., Elwood, J.W., 1982. The role of lake and reservoir sediments as sinks in the perturbed global carbon cycle. Tellus 34, 490–499. https://doi.org/10.1111/j.2153-3490.1982.tb01837.x

Muller, E., Ader, M., Aloisi, G., Bougeault, C., Durlet, C., Vennin, E., Benzerara, K., Gaucher, E.C., Virgone, A., Chavez, M., Souquet, P., Gérard, E., 2022. Successive Modes of Carbonate Precipitation in Microbialites along the Hydrothermal Spring of La Salsa in Laguna Pastos Grandes (Bolivian Altiplano). Geosciences 12, 88. https://doi.org/10.3390/geosciences12020088

Muller, E., Rapin, W., Caumartin, J., Jézéquel, D., De Wever, A., Thomazo, C., Havas, R., López-García, P., Moreira, D., Tavera, R., Benzerara, K., 2023. Diagenetic formation of stevensite by replacement of diatom frustules in the sediments of the alkaline Lake Alchichica (Mexico). Sedimentology sed.13069. https://doi.org/10.1111/sed.13069

Müller, G., Irion, G., Förstner, U., 1972. Formation and diagenesis of inorganic Ca?Mg carbonates in the lacustrine environment. Naturwissenschaften 59, 158–164. https://doi.org/10.1007/BF00637354

Newell, D.L., Jensen, J.L., Frantz, C.M., Vanden Berg, M.D., 2017. Great Salt Lake (Utah) Microbialite δ13C, δ18O, and δ15N Record Fluctuations in Lake Biogeochemistry Since the Late Pleistocene. Geochemistry, Geophysics, Geosystems 18, 3631–3645. https://doi.org/10.1002/2017GC007078

Nielsen, H., 1974. Isotopic composition of the major contributors to atmospheric sulfur. Tellus 26, 213–221. https://doi.org/10.1111/j.2153-3490.1974.tb01969.x

Nitti, A., Daniels, C.A., Siefert, J., Souza, V., Hollander, D., Breitbart, M., 2012. Spatially Resolved Genomic, Stable Isotopic, and Lipid Analyses of a Modern Freshwater Microbialite from Cuatro Ciénegas, Mexico. Astrobiology 12, 685–698. https://doi.org/10.1089/ast.2011.0812

Noffke, N., Awramik, S.M., 2013. Stromatolites and MISS—Differences between relatives. GSAT 23, 4–9. https://doi.org/10.1130/GSATG187A.1

Nöthen, K., Kasten, S., 2011. Reconstructing changes in seep activity by means of pore water and solid phase Sr/Ca and Mg/Ca ratios in pockmark sediments of the Northern Congo Fan. Marine Geology 287, 1–13. https://doi.org/10.1016/j.margeo.2011.06.008

Ohkouchi, N., Nakajima, Y., Ogawa, N.O., Chikaraishi, Y., Suga, H., Sakai, S., Kitazato, H., 2008. Carbon isotopic composition of the tetrapyrrole nucleus in chloropigments from a saline meromictic lake: A mechanistic view for interpreting the isotopic signature of alkyl porphyrins in geological samples. Organic Geochemistry 39, 521–531. https://doi.org/10.1016/j.orggeochem.2007.11.002

Ollivier, B., Zeyen, N., Gales, G., Hickman-Lewis, K., Gaboyer, F., Benzerara, K., Westall, F., 2018. Importance of Prokaryotes in the Functioning and Evolution of the Present and Past Geosphere and Biosphere, in: Bertrand, J.-C., Normand, P., Ollivier, B., Sime-Ngando, T. (Eds.), Prokaryotes and Evolution. Springer International Publishing, Cham, pp. 57–129. https://doi.org/10.1007/978-3-319-99784-1_3

O'Neil, J.R., Barnes, I., 1971. C13 and O18 compositions in some fresh-water carbonates associated with ultramafic rocks and serpentinites: western United States. Geochimica et Cosmochimica Acta 35, 687–697. https://doi.org/10.1016/0016-7037(71)90067-6

Ono, S., Wing, B., Johnston, D., Farquhar, J., Rumble, D., 2006. Mass-dependent fractionation of quadruple stable sulfur isotope system as a new tracer of sulfur biogeochemical cycles. Geochimica et Cosmochimica Acta 70, 2238–2252. https://doi.org/10.1016/j.gca.2006.01.022

Oomori, T., Nakasone, M., Kaneshima, K., Kitano, Y., 1985. Incorporation of Sodium into Calcium Carbonate and Protodolomite. Bulletin of the College of Science 51–56.

Ossa Ossa, F., Hofmann, A., Wille, M., Spangenberg, J.E., Bekker, A., Poulton, S.W., Eickmann, B., Schoenberg, R., 2018. Aerobic iron and manganese cycling in a redox-stratified Mesoarchean epicontinental sea. Earth and Planetary Science Letters 500, 28–40. https://doi.org/10.1016/j.epsl.2018.07.044

Osterhout, J.T., Czaja, A.D., Bartley, J.K., Fralick, P.W., 2019. Preservation of carbon isotopes in kerogen from thermally altered Mesoproterozoic lacustrine microbialites. Can. J. Earth Sci. 56, 1017–1026. https://doi.org/10.1139/cjes-2018-0309

Pace, A., Bourillot, R., Bouton, A., Vennin, E., Galaup, S., Bundeleva, I., Patrier, P., Dupraz, C., Thomazo, C., Sansjofre, P., Yokoyama, Y., Franceschi, M., Anguy, Y., Pigot, L., Virgone, A., Visscher, P.T., 2016. Microbial and diagenetic steps leading to the mineralisation of Great Salt Lake microbialites. Sci Rep 6, 31495. https://doi.org/10.1038/srep31495

Parkhurst, D.L., Appelo, C., 2013. Description of input and examples for PHREEQC version 3: a computer program for speciation, batch-reaction, one-dimensional transport, and inverse geochemical calculations (Technical Report No. 7676153). U.S. Geological Survey, Denver, CO.

Pasquier, V., Bryant, R.N., Fike, D.A., Halevy, I., 2021a. Strong local, not global, controls on marine pyrite sulfur isotopes. Sci. Adv. 7, eabb7403. https://doi.org/10.1126/sciadv.abb7403

Pasquier, V., Fike, D.A., Halevy, I., 2021b. Sedimentary pyrite sulfur isotopes track the local dynamics of the Peruvian oxygen minimum zone. Nat Commun 12, 4403. https://doi.org/10.1038/s41467-021-24753-x

Pasquier, V., Sansjofre, P., Rabineau, M., Revillon, S., Houghton, J., Fike, D.A., 2017. Pyrite sulfur isotopes reveal glacial–interglacial environmental changes. Proc. Natl. Acad. Sci. U.S.A. 114, 5941–5945. https://doi.org/10.1073/pnas.1618245114

Pecoraino, G., D'Alessandro, W., Inguaggiato, S., 2015. The Other Side of the Coin: Geochemistry of Alkaline Lakes in Volcanic Areas, in: Rouwet, D., Christenson, B., Tassi, F., Vandemeulebrouck, J. (Eds.), Volcanic Lakes, Advances in Volcanology. Springer Berlin Heidelberg, Berlin, Heidelberg, pp. 219–237. https://doi.org/10.1007/978-3-642-36833-2_9

Peiffer, L., Carrasco-Núñez, G., Mazot, A., Villanueva-Estrada, R.E., Inguaggiato, C., Bernard Romero, R., Rocha Miller, R., Hernández Rojas, J., 2018. Soil degassing at the Los Humeros geothermal field (Mexico). Journal of Volcanology and Geothermal Research 356, 163–174. https://doi.org/10.1016/j.jvolgeores.2018.03.001

Pellerin, A., Bui, T.H., Rough, M., Mucci, A., Canfield, D.E., Wing, B.A., 2015. Mass-dependent sulfur isotope fractionation during reoxidative sulfur cycling: A case study from Mangrove Lake, Bermuda. Geochimica et Cosmochimica Acta 149, 152–164. https://doi.org/10.1016/j.gca.2014.11.007

Pentecost, A., 2005. Travertine. Springer Science & Business Media, Berlin.

Pérez, N.M., Hernandez, P.A., Padilla, G., Nolasco, D., Barrancos, J., Melian, G., Padron, E., Dionis, S., Calvo, D., Rodriguez, F., Notsu, K., Mori, T., Kusakabe, M., Arpa, M.C., Reniva, P., Ibarra, M.,

2011. Global CO2 emission from volcanic lakes. Geology 39, 235–238. https://doi.org/10.1130/G31586.1
Peters, M., Strauss, H., Farquhar, J., Ockert, C., Eickmann, B., Jost, C.L., 2010. Sulfur cycling at the Mid-Atlantic Ridge: A multiple sulfur isotope approach. Chemical Geology 269, 180–196. https://doi.org/10.1016/j.chemgeo.2009.09.016
Petrash, D.A., Steenbergen, I.M., Valero, A., Meador, T.B., Pačes, T., Thomazo, C., 2022. Aqueous system-level processes and prokaryote assemblages in the ferruginous and sulfate-rich bottom waters of a post-mining lake. Biogeosciences 19, 1723–1751. https://doi.org/10.5194/bg-19-1723-2022
Planavsky, N., Bekker, A., Rouxel, O.J., Kamber, B., Hofmann, A., Knudsen, A., Lyons, T.W., 2010. Rare Earth Element and yttrium compositions of Archean and Paleoproterozoic Fe formations revisited: New perspectives on the significance and mechanisms of deposition. Geochimica et Cosmochimica Acta 74, 6387–6405. https://doi.org/10.1016/j.gca.2010.07.021
Planavsky, N., Rouxel, O., Bekker, A., Shapiro, R., Fralick, P., Knudsen, A., 2009. Iron-oxidizing microbial ecosystems thrived in late Paleoproterozoic redox-stratified oceans. Earth and Planetary Science Letters 286, 230–242. https://doi.org/10.1016/j.epsl.2009.06.033
Planavsky, N.J., Asael, D., Hofmann, A., Reinhard, C.T., Lalonde, S.V., Knudsen, A., Wang, X., Ossa Ossa, F., Pecoits, E., Smith, A.J.B., Beukes, N.J., Bekker, A., Johnson, T.M., Konhauser, K.O., Lyons, T.W., Rouxel, O.J., 2014. Evidence for oxygenic photosynthesis half a billion years before the Great Oxidation Event. Nature Geosci 7, 283–286. https://doi.org/10.1038/ngeo2122
Planavsky, N.J., McGoldrick, P., Scott, C.T., Li, C., Reinhard, C.T., Kelly, A.E., Chu, X., Bekker, A., Love, G.D., Lyons, T.W., 2011. Widespread iron-rich conditions in the mid-Proterozoic ocean. Nature 477, 448–451. https://doi.org/10.1038/nature10327
Portugal, E., Verma, M.P., Barragan, M., 1994. Geoquimica isotópica de 13C, D y 18O de fluidos del sistema geotérmico Los Humeros, Puebla (México). Geofis. Int. 33, 607–618.
Posth, N.R., Bristow, L.A., Cox, R.P., Habicht, K.S., Danza, F., Tonolla, M., Frigaard, N. -U., Canfield, D.E., 2017. Carbon isotope fractionation by anoxygenic phototrophic bacteria in euxinic Lake Cadagno. Geobiology 15, 798–816. https://doi.org/10.1111/gbi.12254
Poulton, S.W., Fralick, P.W., Canfield, D.E., 2010. Spatial variability in oceanic redox structure 1.8 billion years ago. Nature Geosci 3, 486–490. https://doi.org/10.1038/ngeo889
Pratt, B.R., 1982. Stromatolitic Framework of Carbonate Mud-Mounds. SEPM JSR Vol. 52, 1203–11227. https://doi.org/10.1306/212F80FD-2B24-11D7-8648000102C1865D
Raven, M.R., Fike, D.A., Gomes, M.L., Webb, S.M., Bradley, A.S., McClelland, H.-L.O., 2018. Organic carbon burial during OAE2 driven by changes in the locus of organic matter sulfurization. Nat Commun 9, 3409. https://doi.org/10.1038/s41467-018-05943-6
Raven, M.R., Sessions, A.L., Fischer, W.W., Adkins, J.F., 2016. Sedimentary pyrite δ34S differs from porewater sulfide in Santa Barbara Basin: Proposed role of organic sulfur. Geochimica et Cosmochimica Acta 186, 120–134. https://doi.org/10.1016/j.gca.2016.04.037
Reid, R.P., James, N.P., Macintyre, I.G., Dupraz, C.P., Burne, R.V., 2003. Shark Bay stromatolites: Microfabrics and reinterpretation of origins. Facies 49, 299–324. https://doi.org/10.1007/s10347-003-0036-8
Rendon-Lopez, M.J., 2008. Limnologia fisica del lago crater los Espinos, Municipio de Jiménez Michoacan.
Riding, R., 2011. Microbialites, Stromatolites, and Thrombolites, in: Reitner, J., Thiel, V. (Eds.), Encyclopedia of Geobiology, Encyclopedia of Earth Sciences Series. Springer Netherlands, Dordrecht, pp. 635–654. https://doi.org/10.1007/978-1-4020-9212-1_196
Riding, R., 2008. Abiogenic, microbial and hybrid authigenic carbonate crusts: components of Precambrian stromatolites. Geologia Croatica 61/2–3, 73–103.
Riding, R., 2006. Microbial carbonate abundance compared with fluctuations in metazoan diversity over geological time. Sedimentary Geology 185, 229–238. https://doi.org/10.1016/j.sedgeo.2005.12.015

Riding, R., 1991. Classification of Microbial Carbonates, in: Riding, Robert (Ed.), Calcareous Algae and Stromatolites. Springer, Berlin, Heidelberg, pp. 21–51. https://doi.org/10.1007/978-3-642-52335-9_2

Roche, A., Vennin, E., Bouton, A., Olivier, N., Wattinne, A., Bundeleva, I., Deconinck, J.-F., Virgone, A., Gaucher, E.C., Visscher, P.T., 2018. Oligo-Miocene lacustrine microbial and metazoan buildups from the Limagne Basin (French Massif Central). Palaeogeography, Palaeoclimatology, Palaeoecology 504, 34–59. https://doi.org/10.1016/j.palaeo.2018.05.001

Romanek, C.S., Grossman, E.L., Morse, J.W., 1992. Carbon isotopic fractionation in synthetic aragonite and calcite: Effects of temperature and precipitation rate. Geochimica et Cosmochimica Acta 56, 419–430. https://doi.org/10.1016/0016-7037(92)90142-6

Rouwet, D., Tassi, F., Mora-Amador, R., Sandri, L., Chiarini, V., 2014. Past, present and future of volcanic lake monitoring. Journal of Volcanology and Geothermal Research 272, 78–97. https://doi.org/10.1016/j.jvolgeores.2013.12.009

Rye, R.O., Luhr, J.F., Wasserman, M.D., 1984. Sulfur and oxygen isotopic systematics of the 1982 eruptions of El Chichón Volcano, Chiapas, Mexico. Journal of Volcanology and Geothermal Research 23, 109–123. https://doi.org/10.1016/0377-0273(84)90058-1

Saghaï, A., Zivanovic, Y., Moreira, D., Benzerara, K., Bertolino, P., Ragon, M., Tavera, R., López-Archilla, A.I., López-García, P., 2016. Comparative metagenomics unveils functions and genome features of microbialite-associated communities along a depth gradient: Comparative metagenomics of microbialites from Lake Alchichica. Environmental Microbiology 18, 4990–5004. https://doi.org/10.1111/1462-2920.13456

Saghaï, A., Zivanovic, Y., Zeyen, N., Moreira, D., Benzerara, K., Deschamps, P., Bertolino, P., Ragon, M., Tavera, R., López-Archilla, A.I., López-García, P., 2015. Metagenome-based diversity analyses suggest a significant contribution of non-cyanobacterial lineages to carbonate precipitation in modern microbialites. Front. Microbiol. 6. https://doi.org/10.3389/fmicb.2015.00797

Saitoh, M., Ueno, Y., Isozaki, Y., Shibuya, T., Yao, J., Ji, Z., Shozugawa, K., Matsuo, M., Yoshida, N., 2015. Authigenic carbonate precipitation at the end-Guadalupian (Middle Permian) in China: Implications for the carbon cycle in ancient anoxic oceans. Prog. in Earth and Planet. Sci. 2, 41. https://doi.org/10.1186/s40645-015-0073-2

Satkoski, A.M., Beukes, N.J., Li, W., Beard, B.L., Johnson, C.M., 2015. A redox-stratified ocean 3.2 billion years ago. Earth and Planetary Science Letters 430, 43–53. https://doi.org/10.1016/j.epsl.2015.08.007

Schidlowski, M., 2001. Carbon isotopes as biogeochemical recorders of life over 3.8 Ga of Earth history: evolution of a concept. Precambrian Research 106, 117–134. https://doi.org/10.1016/S0301-9268(00)00128-5

Schiff, S.L., Tsuji, J.M., Wu, L., Venkiteswaran, J.J., Molot, L.A., Elgood, R.J., Paterson, M.J., Neufeld, J.D., 2017. Millions of Boreal Shield Lakes can be used to Probe Archaean Ocean Biogeochemistry. Sci Rep 7, 46708. https://doi.org/10.1038/srep46708

Sharp, Z., 2017. Principles of Stable Isotope Geochemistry, 2nd Edition.

Shields, G.A., Mills, B.J.W., 2017. Tectonic controls on the long-term carbon isotope mass balance. Proceedings of the National Academy of Sciences 114, 4318–4323. https://doi.org/10.1073/pnas.1614506114

Siebe, C., Guilbaud, M.-N., Salinas, S., Chédeville-Monzo, C., 2012. Eruption of Alberca de los Espinos tuff cone causes transgression of Zacapu lake ca. 25,000 yr BP in Michoacán, México. Presented at the IAS 4IMC Conference, Auckland, New Zeland, pp. 74–75.

Siebe, C., Guilbaud, M.-N., Salinas, S., Kshirsagar, P., Chevrel, M.O., Jiménez, A.H., Godínez, L., 2014. Monogenetic volcanism of the Michoacán-Guanajuato Volcanic Field: Maar craters of the Zacapu basin and domes, shields, and scoria cones of the Tarascan highlands (Paracho-Paricutin region). Presented at the Pre-meeting field guide for the 5th international Maar Conference, Querétaro, México, pp. 1–37.

Sigala, I., Caballero, M., Correa-Metrio, A., Lozano-García, S., Vázquez, G., Pérez, L., Zawisza, E., 2017. Basic limnology of 30 continental waterbodies of the Transmexican Volcanic Belt across climatic and environmental gradients. BSGM 69, 313–370. https://doi.org/10.18268/BSGM2017v69n2a3

Silva Aguilera, R.A., 2019. Analisis del descenso del nivel de agua del lago Alchichica, Puebla, México 120.

Silva-Aguilera, Raúl Alberto, Escolero, Ó., Alcocer, J., 2022. Recent Climate of Serdán-Oriental Basin, in: Alcocer, J. (Ed.), Lake Alchichica Limnology: The Uniqueness of a Tropical Maar Lake. Springer International Publishing, Cham, pp. 51–61. https://doi.org/10.1007/978-3-030-79096-7_4

Silva-Aguilera, Raúl A., Vilaclara, G., Armienta, M.A., Escolero, Ó., 2022a. Hydrogeology and Hydrochemistry of the Serdán-Oriental Basin and the Lake Alchichica, in: Alcocer, J. (Ed.), Lake Alchichica Limnology: The Uniqueness of a Tropical Maar Lake. Springer International Publishing, Cham, pp. 63–74. https://doi.org/10.1007/978-3-030-79096-7_5

Silva-Aguilera, Raúl A., Vilaclara, G., Armienta, M.A., Escolero, Ó., 2022b. Hydrogeology and Hydrochemistry of the Serdán-Oriental Basin and the Lake Alchichica, in: Alcocer, J. (Ed.), Lake Alchichica Limnology. Springer International Publishing, Cham, pp. 63–74. https://doi.org/10.1007/978-3-030-79096-7_5

Sim, M.S., Bosak, T., Ono, S., 2011a. Large Sulfur Isotope Fractionation Does Not Require Disproportionation. Science 333, 74–77. https://doi.org/10.1126/science.1205103

Sim, M.S., Ono, S., Donovan, K., Templer, S.P., Bosak, T., 2011b. Effect of electron donors on the fractionation of sulfur isotopes by a marine Desulfovibrio sp. Geochimica et Cosmochimica Acta 75, 4244–4259. https://doi.org/10.1016/j.gca.2011.05.021

Sobek, S., Durisch-Kaiser, E., Zurbrügg, R., Wongfun, N., Wessels, M., Pasche, N., Wehrli, B., 2009. Organic carbon burial efficiency in lake sediments controlled by oxygen exposure time and sediment source. Limnol. Oceanogr. 54, 2243–2254. https://doi.org/10.4319/lo.2009.54.6.2243

Soetaert, K., Hofmann, A.F., Middelburg, J.J., Meysman, F.J.R., Greenwood, J., 2007. Reprint of "The effect of biogeochemical processes on pH." Marine Chemistry, Special issue: Dedicated to the memory of Professor Roland Wollast 106, 380–401. https://doi.org/10.1016/j.marchem.2007.06.008

Solari, M.A., Hervé, F., Le Roux, J.P., Airo, A., Sial, A.N., 2010. Paleoclimatic significance of lacustrine microbialites: A stable isotope case study of two lakes at Torres del Paine, southern Chile. Palaeogeography, Palaeoclimatology, Palaeoecology 297, 70–82. https://doi.org/10.1016/j.palaeo.2010.07.016

Stoessell, R.K., 1988. 25°C and 1 atm dissolution experiments of sepiolite and kerolite. Geochimica et Cosmochimica Acta 52, 365–374. https://doi.org/10.1016/0016-7037(88)90092-0

Stramma, L., Johnson, G.C., Sprintall, J., Mohrholz, V., 2008. Expanding Oxygen-Minimum Zones in the Tropical Oceans. Science 320, 655–658. https://doi.org/10.1126/science.1153847

Strauss, H., 1997. The isotopic composition of sedimentary sulfur through time. Palaeogeography, Palaeoclimatology, Palaeoecology 132, 97–118. https://doi.org/10.1016/S0031-0182(97)00067-9

Strauss, H., Bast, R., Cording, A., Diekrup, D., Fugmann, A., Garbe-Schönberg, D., Lutter, A., Oeser, M., Rabe, K., Reinke, D., Teichert, B.M.A., Westernströer, U., 2012. Sulphur diagenesis in the sediments of the Kiel Bight, SW Baltic Sea, as reflected by multiple stable sulphur isotopes. Isotopes in Environmental and Health Studies 48, 166–179. https://doi.org/10.1080/10256016.2012.648930

Stüeken, E.E., Buick, R., Anderson, R.E., Baross, J.A., Planavsky, N.J., Lyons, T.W., 2017. Environmental niches and metabolic diversity in Neoarchean lakes. Geobiology 15, 767–783. https://doi.org/10.1111/gbi.12251

Sumner, D.Y., 2002. Decimetre-Thick Encrustations of Calcite and Aragonite on the Sea-Floor and Implications for Neoarchaean and Neoproterozoic Ocean Chemistry, in: Precambrian

Sedimentary Environments. John Wiley & Sons, Ltd, pp. 107–120. https://doi.org/10.1002/9781444304312.ch5
Sumner, D.Y., 2001. Microbial Influences on Local Carbon Isotopic Ratios and Their Preservation in Carbonate. Astrobiology 1, 57–70. https://doi.org/10.1089/153110701750137431
Sumner, D.Y., Grotzinger, J.P., 2004. Implications for Neoarchaean ocean chemistry from primary carbonate mineralogy of the Campbellrand-Malmani Platform, South Africa. Sedimentology 51, 1273–1299. https://doi.org/10.1111/j.1365-3091.2004.00670.x
Suter, M., 2022. The Historical Seismicity of the Puebla-Tlaxcala Region (Trans-Mexican Volcanic Belt) during Early Novohispanic Times (A.D. 1542–1740) and the Structure of the Tlaxcala-Huamantla Half-Graben. Seismological Research Letters 93, 296–314. https://doi.org/10.1785/0220210200
Sutherland, I.W., 2001. Biofilm exopolysaccharides: a strong and sticky framework. Microbiology 147, 3–9. https://doi.org/10.1099/00221287-147-1-3
Szaran, J., 1997. Achievement of carbon isotope equilibrium in the system HCO3− (solution)-CO2(gas). Chemical Geology 142, 79–86. https://doi.org/10.1016/S0009-2541(97)00077-6
Talbot, M.R., 1990. A review of the palaeohydrological interpretation of carbon and oxygen isotopic ratios in primary lacustrine carbonates. Chemical Geology: Isotope Geoscience section 80, 261–279. https://doi.org/10.1016/0168-9622(90)90009-2
Tang, P., Chen, D., Wang, Y., Ding, Y., El-Shafeiy, M., Yang, B., 2022. Diagenesis of microbialite-dominated carbonates in the Upper Ediacaran Qigebrak Formation, NW Tarim Basin, China: Implications for reservoir development. Marine and Petroleum Geology 136, 105476. https://doi.org/10.1016/j.marpetgeo.2021.105476
Tarpgaard, I.H., Røy, H., Jørgensen, B.B., 2011. Concurrent low- and high-affinity sulfate reduction kinetics in marine sediment. Geochimica et Cosmochimica Acta 75, 2997–3010. https://doi.org/10.1016/j.gca.2011.03.028
Taylor, E.H., 1943. A New Ambystomid Salamander Adapted to Brackish Water. Copeia 1943, 151. https://doi.org/10.2307/1438606
Templeton, C.C., 1960. Solubility of Barium Sulfate in Sodium Chloride Solutions from 25° to 95° C. J. Chem. Eng. Data 5, 514–516. https://doi.org/10.1021/je60008a028
Teng, F.-Z., Dauphas, N., Watkins, J.M., 2017. Non-Traditional Stable Isotopes: Retrospective and Prospective. Reviews in Mineralogy and Geochemistry 82, 1–26. https://doi.org/10.2138/rmg.2017.82.1
Teranes, J.L., Bernasconi, S.M., 2000. The record of nitrate utilization and productivity limitation provided by δ ^{15} N values in lake organic matter-A study of sediment trap and core sediments from Baldeggersee, Switzerland. Limnol. Oceanogr. 45, 801–813. https://doi.org/10.4319/lo.2000.45.4.0801
Thomas, P.J., Boller, A.J., Satagopan, S., Tabita, F.R., Cavanaugh, C.M., Scott, K.M., 2019. Isotope discrimination by form IC RubisCO from *Ralstonia eutropha* and *Rhodobacter sphaeroides* , metabolically versatile members of ' *Proteobacteria* ' from aquatic and soil habitats. Environ Microbiol 21, 72–80. https://doi.org/10.1111/1462-2920.14423
Thomazo, C., Ader, M., Philippot, P., 2011. Extreme ^{15}N-enrichments in 2.72-Gyr-old sediments: evidence for a turning point in the nitrogen cycle. Geobiology 9, 107–120. https://doi.org/10.1111/j.1472-4669.2011.00271.x
Thomazo, C., Pinti, D.L., Busigny, V., Ader, M., Hashizume, K., Philippot, P., 2009. Biological activity and the Earth's surface evolution: Insights from carbon, sulfur, nitrogen and iron stable isotopes in the rock record. Comptes Rendus Palevol 8, 665–678. https://doi.org/10.1016/j.crpv.2009.02.003
Tosca, N.J., Macdonald, F.A., Strauss, J.V., Johnston, D.T., Knoll, A.H., 2011. Sedimentary talc in Neoproterozoic carbonate successions. Earth and Planetary Science Letters 306, 11–22. https://doi.org/10.1016/j.epsl.2011.03.041

Tosca, N.J., Masterson, A.L., 2014. Chemical controls on incipient Mg-silicate crystallization at 25°C: Implications for early and late diagenesis. Clay Minerals 49, 165–194. https://doi.org/10.1180/claymin.2014.049.2.03

Treude, T., Hamdan, L.J., Lemieux, S., Dale, A.W., Sommer, S., 2021. Rapid sulfur cycling in sediments from the Peruvian oxygen minimum zone featuring simultaneous sulfate reduction and sulfide oxidation. Limnology and Oceanography 66, 2661–2671. https://doi.org/10.1002/lno.11779

Treude, T., Niggemann, J., Kallmeyer, J., Wintersteller, P., Schubert, C.J., Boetius, A., Jørgensen, B.B., 2005. Anaerobic oxidation of methane and sulfate reduction along the Chilean continental margin. Geochimica et Cosmochimica Acta 69, 2767–2779. https://doi.org/10.1016/j.gca.2005.01.002

Truesdell, A.H., Jones, B.F., 1974. Wateq, a computer program for calculating chemical equilibria of natural waters. J. R. US Geol. Surv. 2, 233–248.

Truesdell, A.H., Quijano, J.L., 1988. Datos isotópicos de CO2 en la descarga total de pozos en Los Humeros Pue. Comisión Federal de Electricidad, México, Reporte Interno 5.

Turner, J.V., Allison, G.B., Holmes, J.W., 1983. Environmental isotope methods for the determination of lake-groundwater relations: applications to determine the effects of man's activities. Volume 1: Investigation and assessment of groundwater resources.

Tyson, R.V., 2001. Sedimentation rate, dilution, preservation and total organic carbon: some results of a modelling study. Organic Geochemistry 32, 333–339. https://doi.org/10.1016/S0146-6380(00)00161-3

Tziperman, E., Halevy, I., Johnston, D.T., Knoll, A.H., Schrag, D.P., 2011. Biologically induced initiation of Neoproterozoic snowball-Earth events. Proc. Natl. Acad. Sci. U.S.A. 108, 15091–15096. https://doi.org/10.1073/pnas.1016361108

Ueno, Y., Aoyama, S., Endo, Y., Matsu'ura, F., Foriel, J., 2015. Rapid quadruple sulfur isotope analysis at the sub-micromole level by a flash heating with CoF3. Chemical Geology 419, 29–35. https://doi.org/10.1016/j.chemgeo.2015.10.032

Ueno, Y., Ono, S., Rumble, D., Maruyama, S., 2008. Quadruple sulfur isotope analysis of ca. 3.5 Ga Dresser Formation: New evidence for microbial sulfate reduction in the early Archean. Geochimica et Cosmochimica Acta 72, 5675–5691. https://doi.org/10.1016/j.gca.2008.08.026

Ueno, Y., Yamada, K., Yoshida, N., Maruyama, S., Isozaki, Y., 2006. Evidence from fluid inclusions for microbial methanogenesis in the early Archaean era. Nature 440, 516–519. https://doi.org/10.1038/nature04584

Valdespino-Castillo, P.M., Alcántara-Hernández, R.J., Alcocer, J., Merino-Ibarra, M., Macek, M., Falcón, L.I., 2014. Alkaline phosphatases in microbialites and bacterioplankton from Alchichica soda lake, Mexico. FEMS Microbiol Ecol n/a-n/a. https://doi.org/10.1111/1574-6941.12411

Valdespino-Castillo, P.M., Hu, P., Merino-Ibarra, M., López-Gómez, L.M., Cerqueda-García, D., González-De Zayas, R., Pi-Puig, T., Lestayo, J.A., Holman, H.-Y., Falcón, L.I., 2018. Exploring Biogeochemistry and Microbial Diversity of Extant Microbialites in Mexico and Cuba. Front. Microbiol. 9, 510. https://doi.org/10.3389/fmicb.2018.00510

van Lith, Y., Vasconcelos, C., Warthmann, R., Martins, J.C.F., McKenzie, J.A., 2002. Bacterial sulfate reduction and salinity: two controls on dolomite precipitation in Lagoa Vermelha and Brejo do Espinho (Brazil). Hydrobiologia 485, 35–49.

van Zuilen, M.A., Lepland, A., Arrhenius, G., 2002. Reassessing the evidence for the earliest traces of life. Nature 418, 627–630. https://doi.org/10.1038/nature00934

Varekamp, J.C., Kreulen, R., 2000. The stable isotope geochemistry of volcanic lakes, with examples from Indonesia. Journal of Volcanology and Geothermal Research 97, 309–327. https://doi.org/10.1016/S0377-0273(99)00175-4

Vennin, E., Bouton, A., Bourillot, R., Pace, A., Roche, A., Brayard, A., Thomazo, C., Virgone, A., Gaucher, E.C., Desaubliaux, G., Visscher, P.T., 2019. The lacustrine microbial carbonate

factory of the successive Lake Bonneville and Great Salt Lake, Utah, USA. Sedimentology 66, 165–204. https://doi.org/10.1111/sed.12499
Vennin, E., Bouton, A., Roche, A., Gérard, E., Bundeleva, I., Boussagol, P., Wattinne, A., Kolodka, C., Gaucher, E., Virgone, A., Visscher, P.T., 2021. The Limagne Basin: a journey through modern and fossil microbial deposits. BSGF - Earth Sci. Bull. 192, 41. https://doi.org/10.1051/bsgf/2021030
Vilaclara, G., Chávez, M., Lugo, A., González, H., Gaytán, M., 1993. Comparative description of crater-lakes basic chemistry in Puebla State, Mexico. SIL Proceedings, 1922-2010 25, 435–440. https://doi.org/10.1080/03680770.1992.11900158
Visscher, P.T., Stolz, J.F., 2005. Microbial mats as bioreactors: populations, processes, and products. Palaeogeography, Palaeoclimatology, Palaeoecology 219, 87–100. https://doi.org/10.1016/j.palaeo.2004.10.016
Wacey, D., 2010. Stromatolites in the ~3400 Ma Strelley Pool Formation, Western Australia: Examining Biogenicity from the Macro- to the Nano-Scale. Astrobiology 10, 381–395. https://doi.org/10.1089/ast.2009.0423
Wanninkhof, R., Asher, W.E., Ho, D.T., Sweeney, C., McGillis, W.R., 2009. Advances in Quantifying Air-Sea Gas Exchange and Environmental Forcing. Annu. Rev. Mar. Sci. 1, 213–244. https://doi.org/10.1146/annurev.marine.010908.163742
Wanninkhof, R., Knox, M., 1996. Chemical enhancement of CO_2 exchange in natural waters. Limnol. Oceanogr. 41, 689–697. https://doi.org/10.4319/lo.1996.41.4.0689
Wassenaar, L.I., Van Wilgenburg, S.L., Larson, K., Hobson, K.A., 2009. A groundwater isoscape (δD, δ18O) for Mexico. Journal of Geochemical Exploration 102, 123–136. https://doi.org/10.1016/j.gexplo.2009.01.001
Weiss, R.F., 1974. Carbon dioxide in water and seawater: the solubility of a non-ideal gas. Marine Chemistry 2, 203–215. https://doi.org/10.1016/0304-4203(74)90015-2
Werne, J.P., Hollander, D.J., 2004. Balancing supply and demand: controls on carbon isotope fractionation in the Cariaco Basin (Venezuela) Younger Dryas to present. Marine Chemistry 92, 275–293. https://doi.org/10.1016/j.marchem.2004.06.031
White III, R.A., Soles, S.A., Brady, A.L., Southam, G., Lim, D.S.S., Slater, G.F., 2020. Biosignatures Associated with Freshwater Microbialites. Life 10, 66. https://doi.org/10.3390/life10050066
Williams, P.M., Gordon, L.I., 1970. Carbon-13: carbon-12 ratios in dissolved and particulate organic matter in the sea. Deep Sea Research and Oceanographic Abstracts 17, 19–27. https://doi.org/10.1016/0011-7471(70)90085-9
Wing, B.A., Halevy, I., 2014. Intracellular metabolite levels shape sulfur isotope fractionation during microbial sulfate respiration. Proc. Natl. Acad. Sci. U.S.A. 111, 18116–18125. https://doi.org/10.1073/pnas.1407502111
Wollast, R., Mackenzie, F.T., Bricker, O.P., 1968. Experimental precipitation and genesis of sepiolite at earth-surface conditions. American Mineralogist 53, 1645–1662.
Wortmann, U.G., Paytan, A., 2012. Rapid Variability of Seawater Chemistry Over the Past 130 Million Years. Science 337, 334–336. https://doi.org/10.1126/science.1220656
Wotte, T., Shields-Zhou, G.A., Strauss, H., 2012. Carbonate-associated sulfate: Experimental comparisons of common extraction methods and recommendations toward a standard analytical protocol. Chemical Geology 326–327, 132–144. https://doi.org/10.1016/j.chemgeo.2012.07.020
Xu, B., 2011. Microfacies, Carbon and Oxygen Isotopes of the Late Archean Stromatolitic Carbonate Platform of the Kaapvaal Craton, South Africa: Implications for Changes in Paleo-environment. Ludwig-Maximilians-Universität München.
Young, E.D., Galy, A., Nagahara, H., 2002. Kinetic and equilibrium mass-dependent isotope fractionation laws in nature and their geochemical and cosmochemical significance. Geochimica et Cosmochimica Acta 66, 1095–1104. https://doi.org/10.1016/S0016-7037(01)00832-8

Yücel, M., Luther, G.W., Moore, W.S., 2010. Earthquake-induced turbidite deposition as a previously unrecognized sink for hydrogen sulfide in the Black Sea sediments. Marine Chemistry 121, 176–186. https://doi.org/10.1016/j.marchem.2010.04.006

Zerkle, A.L., Farquhar, J., Johnston, D.T., Cox, R.P., Canfield, D.E., 2009. Fractionation of multiple sulfur isotopes during phototrophic oxidation of sulfide and elemental sulfur by a green sulfur bacterium. Geochimica et Cosmochimica Acta 73, 291–306. https://doi.org/10.1016/j.gca.2008.10.027

Zerkle, A.L., Jones, D.S., Farquhar, J., Macalady, J.L., 2016. Sulfur isotope values in the sulfidic Frasassi cave system, central Italy: A case study of a chemolithotrophic S-based ecosystem. Geochimica et Cosmochimica Acta 173, 373–386. https://doi.org/10.1016/j.gca.2015.10.028

Zerkle, A.L., Kamyshny, A., Kump, L.R., Farquhar, J., Oduro, H., Arthur, M.A., 2010. Sulfur cycling in a stratified euxinic lake with moderately high sulfate: Constraints from quadruple S isotopes. Geochimica et Cosmochimica Acta 74, 4953–4970. https://doi.org/10.1016/j.gca.2010.06.015

Zeyen, N., 2017. Etude de microbialites lacustres actuels du Mexique: traçage de l'activité biologique et des conditions environnementales de formation, Sorbonne Université, Paris, 316.

Zeyen, N., Benzerara, K., Beyssac, O., Daval, D., Muller, E., Thomazo, C., Tavera, R., López-García, P., Moreira, D., Duprat, E., 2021. Integrative analysis of the mineralogical and chemical composition of modern microbialites from ten Mexican lakes: What do we learn about their formation? Geochimica et Cosmochimica Acta 305, 148–184. https://doi.org/10.1016/j.gca.2021.04.030

Zeyen, N., Benzerara, K., Li, J., Groleau, A., Balan, E., Robert, J.-L., Estève, I., Tavera, R., Moreira, D., López-García, P., 2015. Formation of low-T hydrated silicates in modern microbialites from Mexico and implications for microbial fossilization. Front. Earth Sci. 3. https://doi.org/10.3389/feart.2015.00064

Zeyen, N., Benzerara, K., Menguy, N., Brest, J., Templeton, A.S., Webb, S.M., Gérard, E., Moreira, D., López-García, P., Tavera, R., Morin, G., 2019. Fe-bearing phases in modern lacustrine microbialites from Mexico. Geochimica et Cosmochimica Acta 253, 201–230. https://doi.org/10.1016/j.gca.2019.03.021

Zhang, G., Zhang, X., Li, D., Farquhar, J., Shen, S., Chen, X., Shen, Y., 2015. Widespread shoaling of sulfidic waters linked to the end-Guadalupian (Permian) mass extinction. Geology 43, 1091–1094. https://doi.org/10.1130/G37284.1

Zhang, X.-Y., Li, Y., Wang, G., Yang, H.-Q., 2021. Different accretion and diagenetic patterns within the fabrics of the Permian–Triassic boundary microbialites on the Leye isolated carbonate platform, South China Block. Journal of Palaeogeography 10, 11. https://doi.org/10.1186/s42501-021-00091-3

Zhang, Z., Li, C., Cheng, M., Algeo, T.J., Jin, C., Tang, F., Huang, J., 2018. Evidence for Highly Complex Redox Conditions and Strong Water-Column Stratification in an Early Cambrian Continental-Margin Sea. Geochemistry, Geophysics, Geosystems 19, 2397–2410. https://doi.org/10.1029/2018GC007666

Zhu, D., Liu, Q., Wang, J., Ding, Q., He, Z., 2021. Stable carbon and oxygen isotope data of Late Ediacaran stromatolites from a hypersaline environment in the Tarim Basin (NW China) and their reservoir potential. Facies 67, 25. https://doi.org/10.1007/s10347-021-00633-0

Zopfi, J., Ferdelman, T.G., Fossing, H., 2004. Distribution and fate of sulfur intermediates—sulfite, tetrathionate, thiosulfate, and elemental sulfur—in marine sediments, in: Amend, J.P., Edwards, K.J., Lyons, T.W. (Eds.), Sulfur Biogeochemistry - Past and Present. Geological Society of America, pp. 97–116. https://doi.org/10.1130/0-8137-2379-5.97

Annex

This annex section contains the three papers that I coauthored and are related to my PhD.

Annex 1:

Marin-Carbonne, J., Decraene, M.N., Havas, R., Remusat, L., Pasquier, V., Alléon, J., Zeyen, N., Bouton, A., Bernard, S., Escrig, S. and Olivier, N., 2022. Early precipitated micropyrite in microbialites: a time capsule of microbial sulfur cycling. *Geochemical Perspectives Letters*, *21*, pp.7-12.

Annex 2:

Muller, E., Rapin, W., Caumartin, J., Jézéquel, D., De Wever, A., Thomazo, C., Havas, R., López-García, P., Moreira, D., Tavera, R. and Benzerara, K., 2023. Diagenetic formation of stevensite by replacement of diatom frustules in the sediments of the alkaline Lake Alchichica (Mexico). *Sedimentology*.

Annex 3:

Caumartin, J., Benzerara, K., Havas, R., Thomazo, C., Lòpez-García, P. and Duprat, E., 2023. The chemical conditions necessary for the formation of microbialites. *Geochemical Perspectives Letters*, *25*, pp.30-35.

Geochemical Perspectives Letters

Early precipitated micropyrite in microbialites: A time capsule of microbial sulfur cycling

J. Marin-Carbonne[1*], M.-N. Decraene[1], R. Havas[2], L. Remusat[3], V. Pasquier[4], J. Alléon[1], N. Zeyen[5], A. Bouton[2], S. Bernard[3], S. Escrig[6], N. Olivier[7], E. Vennin[2], A. Meibom[6,1], K. Benzerara[3], C. Thomazo[2,8]

https://doi.org/10.7185/geochemlet.2209

Abstract

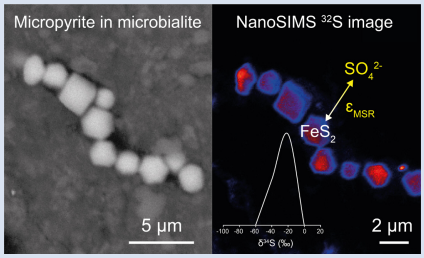

Microbialites are organosedimentary rocks that have occurred throughout the Earth's history. The relationships between diverse microbial metabolic activities and isotopic signatures in biominerals forming within these microbialites are key to understanding modern biogeochemical cycles, but also for accurate interpretation of the geologic record. Here, we performed detailed mineralogical investigations coupled with NanoSIMS (Nanoscale Secondary Ion Mass Spectrometry) analyses of pyrite S isotopes in mineralising microbial mats from two different environments, a hypersaline lagoon (Cayo Coco, Cuba) and a volcanic alkaline crater lake (Atexcac, Mexico). Both microbialite samples contain two distinct pyrite morphologies: framboids and euhedral micropyrites, which display distinct ranges of $\delta^{34}S$ values[1]. Considering the sulfate-sulfur isotopic compositions associated with both environments, micropyrites display a remarkably narrow range of Δ_{pyr} (*i.e.* $\Delta_{pyr} \equiv \delta^{34}S_{SO_4} - \delta^{34}S_{pyr}$) between 56 and 62 ‰. These measured Δ_{pyr} values agree with sulfate-sulfide equilibrium fractionation, as observed in natural settings characterised by low microbial sulfate reduction respiration rates. Moreover, the distribution of S isotope compositions recorded in the studied micropyrites suggests that sulfide oxidation also occurred at the microbialite scale. These results highlight the potential of micropyrites to capture signatures of microbial sulfur cycling and show that S isotope composition in pyrites record primarily the local micro-environments induced by the microbialite.

Received 21 October 2021 | Accepted 14 February 2022 | Published 21 March 2022

Introduction

Sulfate-reducing bacteria, *i.e.* microorganisms that use sulfate as a terminal electron acceptor, are ubiquitous in Earth environments where they play a major role both in S and C biogeochemical cycles (*e.g.*, Jørgensen *et al.*, 2019). Microbial sulfate reduction (MSR) reduces sulfate to dissolved S species, such as HS^- and H_2S, and discriminates against heavy sulfur isotopes. The resulting sulfide $\delta^{34}S$ values are relatively light and can be as much as −70 ‰ relative to sulfate (Jørgensen *et al.*, 2019). The fractionation induced by this metabolic activity ($^{34}\varepsilon_{mic}$ hereafter) depends on the sulfate concentration, identity of the electron donor, bioavailable carbon (content and chemical form) and, perhaps most importantly, the cell-specific sulfate reduction rates (csSRR; Bradley *et al.*, 2016). In modern environments, MSR can be identified by rate measurements with radiotracers or genomic and proteomic approaches. However, since genetic markers are not preserved in the geological record, the recognition of MSR in palaeoenvironments mostly relies on the sulfur isotopic compositions of sedimentary sulfide and sulfate minerals (Visscher *et al.*, 2000; Fike *et al.*, 2008).

MSR plays a key role in carbonate mineralisation, especially identified in microbialites and microbial mats (Visscher *et al.*, 2000). Microbial mats are stratified microbial communities whose metabolic activities produce geochemical gradients and drive elemental cycling (Canfield and Des Marais, 1993; Paerl and Pinckney, 1996). In the geological record, such deposits (often referred to as stromatolites) are considered among the oldest trace of life on Earth (Allwood *et al.*, 2009). Some Archaean stromatolites contain carbonaceous laminae that have been interpreted as fossil microbial mats or biofilms based on textural evidence (Awramik, 1992; Lepot, 2020). Interestingly, determining the precise nature of the fossil microbial community

1. Institute of Earth Sciences, Université de Lausanne, Geopolis, Mouline 1015 Lausanne, Switzerland
2. UMR CNRS/uB6282 Biogéosciences, UFR Science Vie Terre Environnement, Université de Bourgogne Franche Comté, Dijon, France
3. Muséum National d'Histoire Naturelle, Sorbonne Université, CNRS UMR7590, Institut de Minéralogie, de Physique des Matériaux et de Cosmochimie (IMPMC), Paris, France
4. Earth and Planetary Sciences, Weizmann Institute of Sciences, Rehovot, Israel
5. Department of Earth and Atmospheric Sciences, University of Alberta, T6G 2E3, Canada
6. Laboratory for Biological Geochemistry, School of Architecture, Civil and Environmental Engineering, Ecole PolytechniqueFédérale de Lausanne, CH-1015 Lausanne, Switzerland
7. Université Clermont Auvergne, CNRS, IRD, Laboratoire Magmas et Volcans, F-63000 Clermont-Ferrand, France
8. Institut Universitaire de France, Paris, France
* Corresponding author (email: johanna.marincarbonne@unil.ch)

[1] $\delta^{34}S = ((^{34}S/^{32}S)_{sample}/(^{34}S/^{32}S)_{reference} - 1) \times 1000$ in ‰, with Vienna Canyon Diablo Troilite as the reference.

is challenging because these organosedimentary rocks resulted from a complex balance between microbial activities, sedimentation and intermittent lithification (Reid *et al.*, 2000). In addition, the biosignatures preserved in fossil biofilms are ambiguous, especially after diagenesis and post-depositional history (Javaux, 2019; Alleon *et al.*, 2021). The oldest evidence for MSR in the Archaean geological record are sulfur isotopic signatures from deep marine sediments (Kamber and Whitehouse, 2007; Shen *et al.*, 2009) and stromatolites (Shen and Buick, 2004). In modern microbialites, numerous studies have reported dynamic MSR activity based on H_2S labelling (Visscher *et al.*, 2000; Fike *et al.*, 2008; Pace *et al.*, 2018; Gomes *et al.*, 2021), but only a few studies have investigated sulfur isotope signatures of individual pyrite grains (Gomes *et al.*, 2021).

The primary S isotopic signatures of pyrites (FeS_2) are often modified by fluid circulation during metasomatism or metamorphism (Marin-Carbonne *et al.*, 2020; Slotznick *et al.*, 2022), occurring millions or billions of years after sediment deposition. While late diagenesis can modify both pyrite crystallinity and S isotope composition (Williford *et al.*, 2011; Gomes *et al.*, 2018; Marin-Carbonne *et al.*, 2020), early diagenesis in microbial mats is thought to have a limited effect on the S isotopic composition of pyrite, meaning that microbialitic pyrites may preserve 'pristine' isotopic signatures. However, the observation of large isotopic differences of about ~30 ‰ (Raven *et al.*, 2016) between pore water sulfur species (SO_4^{2-} and H_2S) and pyrite shows that other S-bearing pools, such as organic matter, should be considered in order to quantitatively and isotopically describe sulfur cycling in microbialites. Pyrite often precipitates at the microbial mat surface (Gomes *et al.*, 2021) and its isotopic composition is more representative of the local setting rather than global environmental conditions, *e.g.*, water column (Lang *et al.*, 2020; Pasquier *et al.*, 2021). Decoding pyrite S isotopes at the microscale in sedimentary rocks is required to better understand how local conditions may affect the isotopic composition of microbialite pyrites. Here, we focus our investigation on two geographically independent modern microbial mats, which have not yet undergone (complete) lithification, and/or metasomatism.

Syngenetic Microbialitic Pyrites

We studied two samples from 1) the Atexcac Lake, a monomictic volcanic crater lake (Mexico; Zeyen *et al.*, 2021) and 2) Cayo Coco Lake, a shallow hypersaline lagoon in Cuba (Pace *et al.*, 2018; Bouton *et al.*, 2020). These two depositional settings exhibit contrasting water column sulfate concentrations of 2.1 and 62 mM for Lake Atexcac and Cayo Coco, respectively (Figs. S-1 and S-2, SI). Both samples were produced by mineralising microbial mats and contained authigenic aragonite, Mg-rich calcite, dolomite, authigenic hydrated Mg-silicates/silica such as kerolite, and detrital phases such as feldspars and illite (Figs S-1 and S-2, SI). In each locality, pyrite morphologies fall into two different categories (Fig. 1): framboidal pyrites, ranging from 3 to 15 µm, and mono-crystal pyrites of a few micrometres (>3 µm), hereafter called micropyrites (Figs. 1 and 2, SI). Transmission electron microscopy analyses revealed an early origin of the micropyrite grains (SI). Considering both the

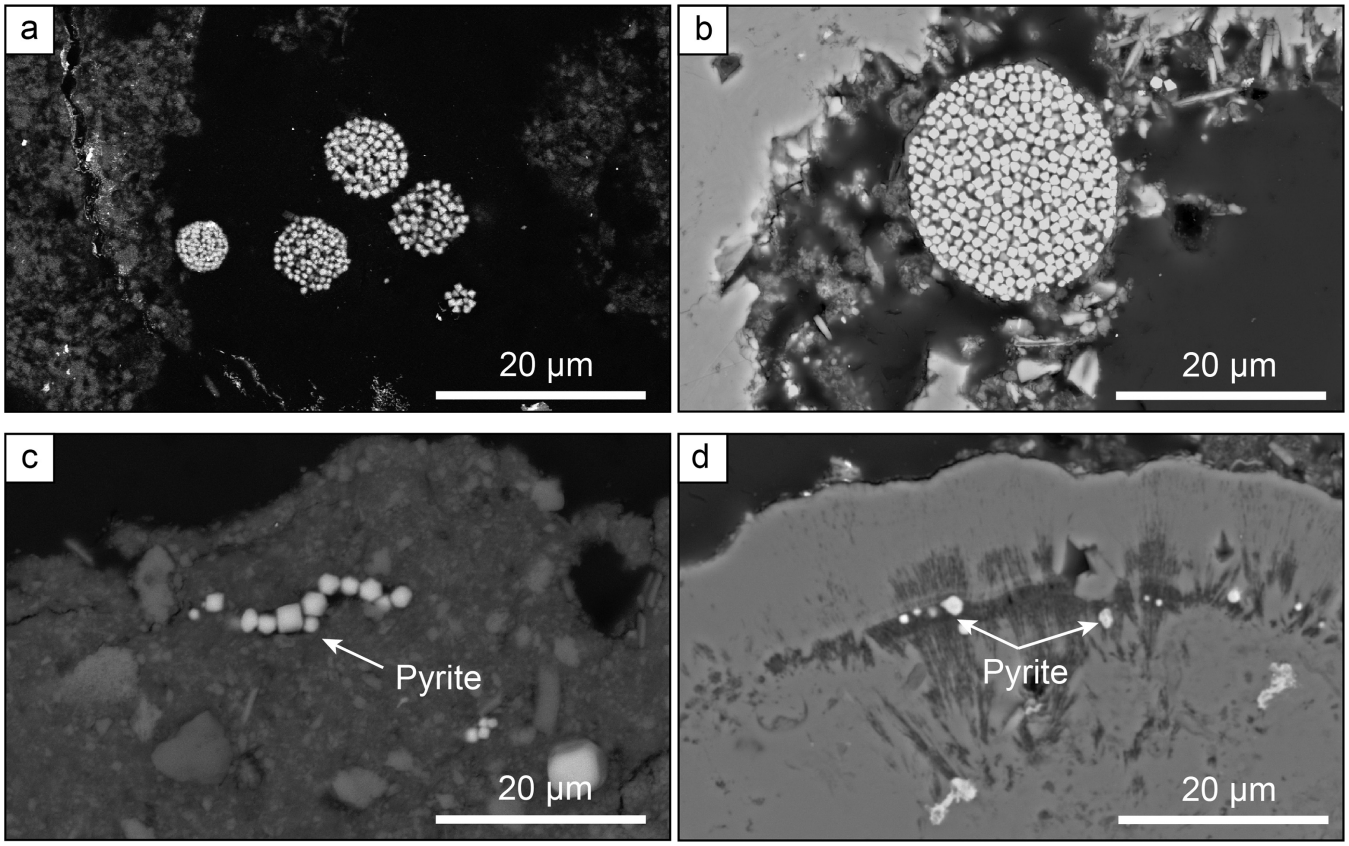

Figure 1 Secondary Electron microscopy pictures of **(a, b)** framboidal pyrites and **(c, d)** micropyrites from **(a, c)** Cayo Coco Lagoon and **(b, d)** Atexcac. Framboidal pyrites are located at the surface of the mineralised microbialite (in dark) while micropyrites are entombed within aragonite (in light grey) or Mg rich silicate (dark grey).

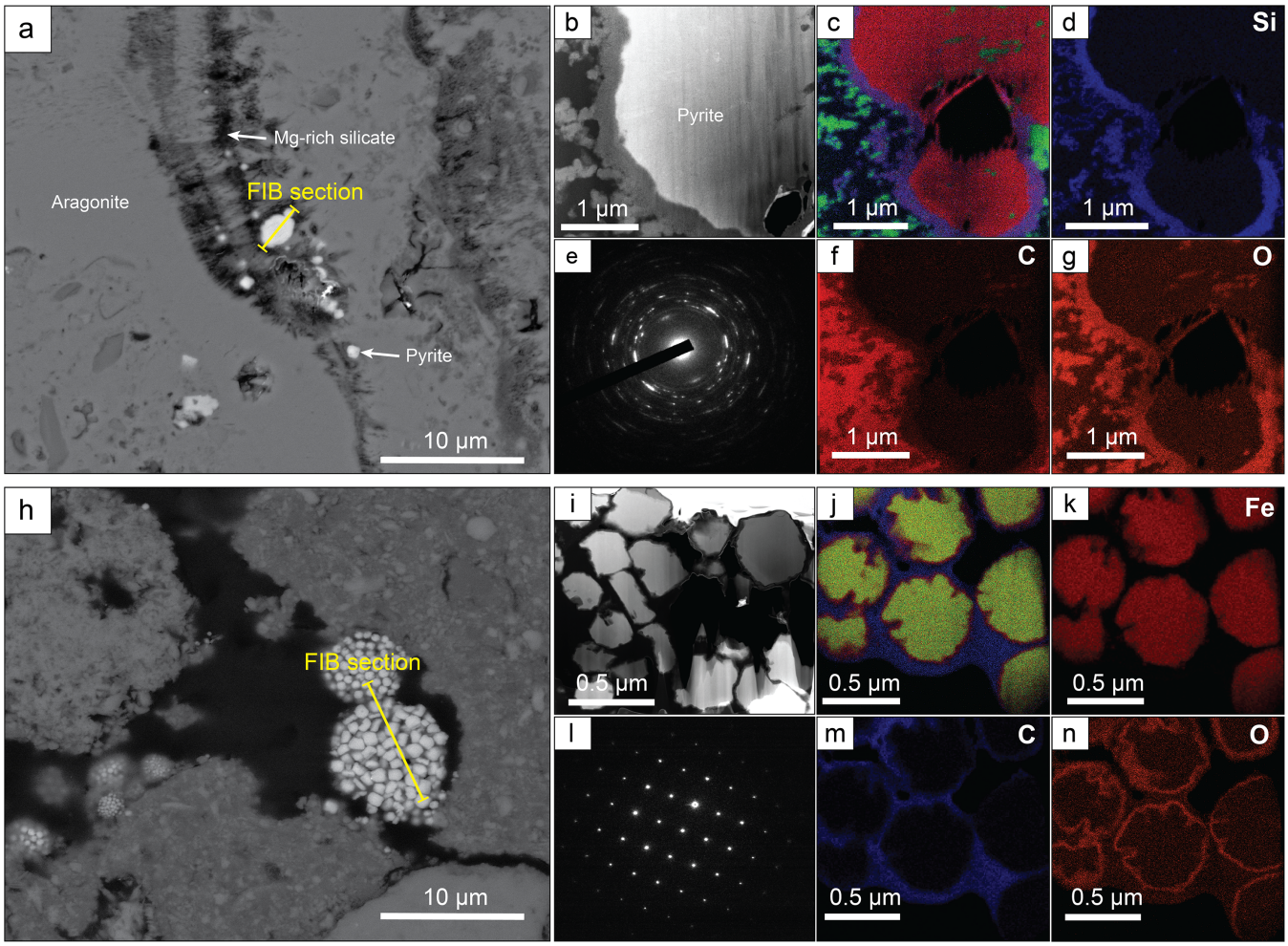

Figure 2 **(a)** SEM picture of micropyrites. Location where FIB section was extracted is shown by the yellow line, **(b)** TEM picture of the pyrite crystal and **(e)** its associated powder-like diffraction pattern, **(c)** false colour STEM EDXS image (Si in blue, Ca in green, Fe in red) and **(d, f, g)** Si, C and O images of the submicrometric pyrites, respectively. **(h)** SEM picture of framboidal pyrite with FIB section location (yellow line), **(i)** TEM image and **(l)** associated single crystal diffraction pattern along the [112] zone axis of pyrite, **(j)** false colour STEM EDXS image of pyrite crystallites (Fe in red, S in green, C in blue) and **(k, m, n)** Fe, C and O images, respectively.

alignment of the micropyrites within the organic lamination and their crystallinity, micropyrites are likely formed during an early lithification stage (SI).

NanoSIMS S Isotope Composition of Pyrites

The S isotope compositions of 66 framboidal pyrites and 55 individual micropyrites were measured by NanoSIMS with a reproducibility better than 2 ‰ (2σ, see SI). Framboidal pyrites display a ~20–30 ‰ range in $\delta^{34}S$ values with an average of −26.1 ± 7 ‰ and −26.4 ± 9 ‰ (2 s.d.) for Atexcac and Cayo Coco, respectively (Figs. 3 and 4). We have extracted S isotope composition of individual crystallites from four framboids (Fig. 3, SI). All framboidal pyrites (n = 4) show a large internal $\delta^{34}S$ variability (~40 ‰, Fig. 3) characterised by a gradient from ~+8.5 ± 1.5 ‰ to more ^{34}S-depleted values ranging from −42 to −69 ‰. Micropyrites also show large S isotope heterogeneities with $\delta^{34}S$ values ranging from −86 to −17 ‰ with an average value of −61.4 ± 17 ‰ for Atexcac, and from −53 to −21 ‰ with an average value of −34.5 ± 29 ‰ in Cayo Coco (Fig. 4).

Framboidal Pyrites Record a Mixing of Reduction and Oxidation Processes

Framboidal pyrites display a large range of $\delta^{34}S$ values but also an internal isotope variation across the length scale of individual framboidal grains (Fig. 3), best explained by a combination of MSR and partial sulfide oxidation (Fig. 3; Pellerin *et al.*, 2019). As framboidal pyrites are mostly observed at the surface of the mat, S isotope variations reflect the mixing of in situ production, upward diffusion of sulfide in the mat and its subsequent reoxidation at the mat surface. The fractionation required to produce such an isotopic gradient is well above abiotic sulfide oxidation (*i.e.* ~+5 ‰; Fry *et al.*, 1988), yet can also be consistent with microbial sulfide oxidation in high pH environments (Pellerin *et al.*, 2019). Both sites are characterised by high pH (pH > 8, see SI), which is known to promote large isotope fractionation during sulfide oxidation (Pellerin *et al.*, 2019). Consequently, part of the observed range of $\delta^{34}S$ values may be attributed to local variation of S speciation associated with pH. As such, the internal gradient may be the result of microbially mediated surface H_2S oxidation. Alternatively, the internal isotope gradient across the framboidal pyrites (Fig. 2, SI) can be due to Rayleigh isotope fractionation, as even under

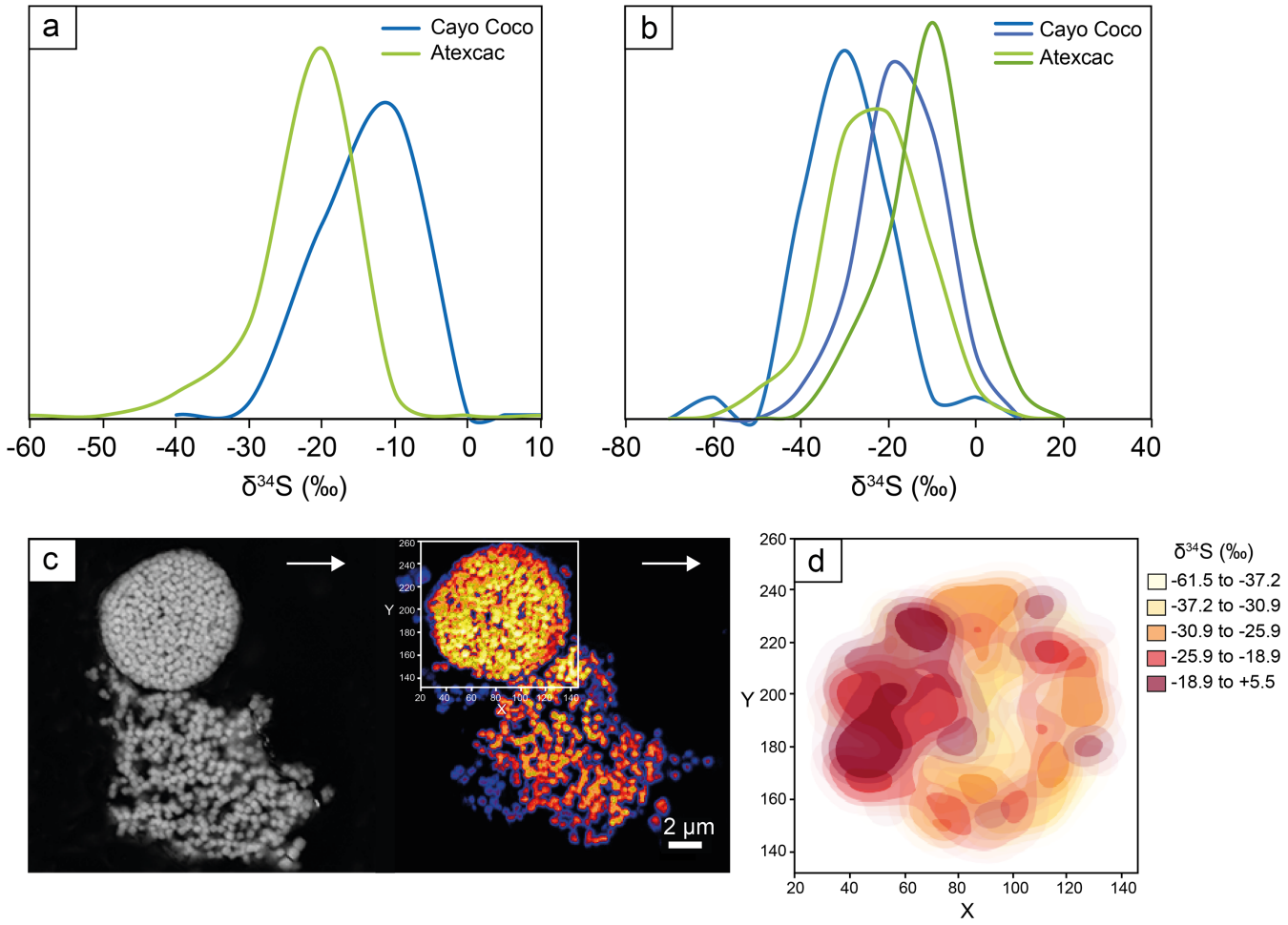

Figure 3 **(a)** $\delta^{34}S$ probability density function of all framboidal pyrites from Atexcac and Cayo Coco uncertainties of analyses ranges from 0.4 to 4 ‰, **(b)** $\delta^{34}S$ probability density function of four individual framboidal pyrites containing up to 100 pyrite crystallites, **(c)** SEM and corresponding NanoSIMS ^{32}S image of one framboidal pyrite; the arrow indicates the top of the mat, and **(d)** $\delta^{34}S$ values reconstructed for individual pyrite crystallites showing strong variations in S isotope composition across the framboidal pyrite.

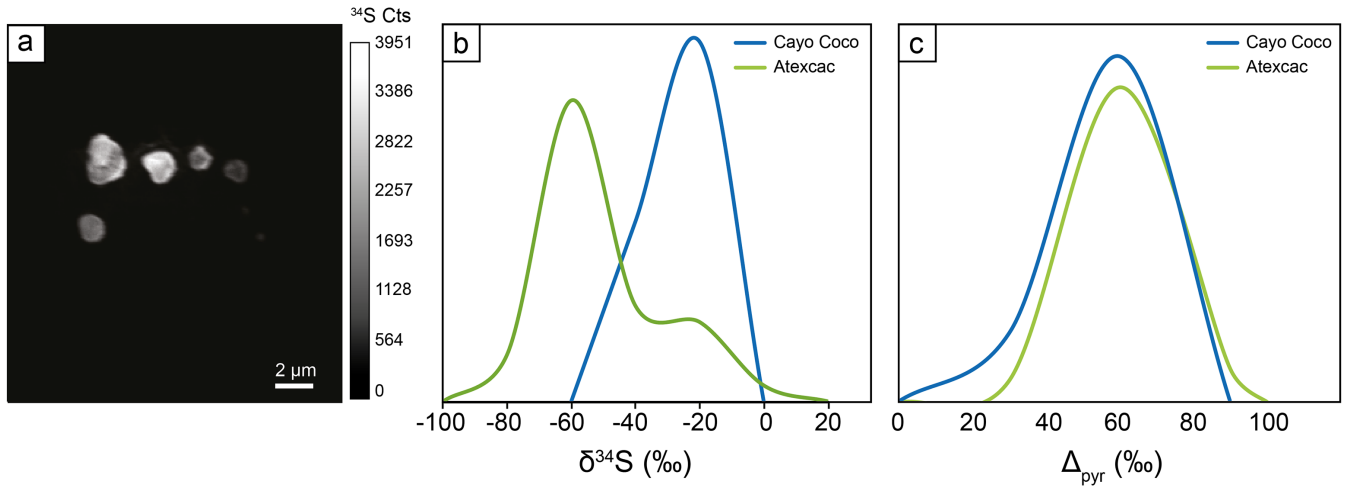

Figure 4 **(a)** NanoSIMS ^{32}S image of submicrometric pyrites, **(b)** $\delta^{34}S$ probability density function, taking account of the range of uncertainties from 1 ‰ to 8 ‰ of micropyrites from Cayo Coco and Atexcac, **(c)** Δ_{pyr} distribution calculated for both environments.

oxidising (abundant sulfate) conditions, consumption can occur faster than diffusive replenishment (Goldhaber and Kaplan, 1980). Rather than reflecting water column conditions, the S isotope composition of framboidal pyrites appears to be strongly influenced by local redox conditions (*i.e.* at the microbial mat scale).

Microbialitic Micropyrite Preserve Primary Isotopic Microbial Fractionation Signatures

The presence of Mg silicate rich rims (SI) suggests that micropyrites were probably formed very early during lithification (Fig. 2). Moreover, the small crystal size of micropyrites composed of nanocrystals with different orientations has been highlighted as a possible biogenic signature (Picard *et al.*, 2018). The $\delta^{34}S$ values of dissolved sulfate are +0.52 ‰ in Atexcac and are assumed to be close to seawater composition (+21 ‰) for Cayo Coco (SI). Considering these hugely contrasting isotopic compositions of sulfate, micropyrites display surprisingly similar Δ_{pyr} values (*i.e.* $\Delta_{pyr} = \delta^{34}S_{SO_4} - \delta^{34}S_{pyr}$) of 62 ± 17 ‰ and 56 ± 29 ‰ for Atexcac and Cayo Coco, respectively (Fig. 4). These Δ_{pyr} values are consistent with near thermodynamic equilibrium fractionation as observed in *i*) MSR batch culture experiments characterised by low growth rate and csSRR (Leavitt *et al.*, 2013; Bradley *et al.*, 2016) and *ii*) natural environments (*e.g.*, Cadagno Lake; Canfield *et al.*, 2010). High $^{34}\varepsilon_{mic}$ has been observed in sulfate reducing strains only partially oxidising their carbon substrate and is sometimes associated with the degradation of carbohydrate components, including exopolymeric substances (EPS) (Sim *et al.*, 2011), which are abundant in microbialite-forming mats. Atexcac waters have a high dissolved organic carbon content (over 15 times that of the modern ocean) which can sustain MSR activity, while Cayo Coco harbours conspicuous suspended EPS-rich organic slimes (Bouton *et al.*, 2016). Despite abundant sulfate (at Cayo Coco) and organic matter, csSRR in these mats are intriguingly low and contrast with previous occurrences of high SRR in surface microbial mats (Canfield and Des Marais, 1993). Low csSRR and high S isotope fractionations in both lakes could be explained by the refractory nature of this organic matter (Bouton *et al.*, 2020; Gomes *et al.*, 2021). At the microbial mat scale, strong gradients of sulfate reduction within layered mats (Visscher *et al.*, 2000; Fike *et al.*, 2009; Pace *et al.*, 2018) have been attributed to small scale variations in csSRR and/or localised MSR micro-niches (Fike *et al.*, 2009; Gomes *et al.*, 2021). The observed laminations, which contain micropyrites, likely reflect local high density microbe spots, which can result from a more pronounced local distillation of $\delta^{34}S$ (Pasquier *et al.*, 2021). Alternatively, the composition of microbial consortia may affect the range of csSRR at the microbial mat scale (Bradley *et al.*, 2016), with guild diversity having opposite effects on trophic group functions, thus modulating csSRR (Bell *et al.*, 2005; Peter *et al.*, 2011).

Conclusions

Here, we have shown that the S isotope composition of framboids and micropyrites reflects sulfur cycling at the scale of the mat environment. While S isotope signatures in microbialite micropyrites are primarily controlled by MSR, they can also be influenced by oxidative sulfur cycling in high pH environments. Notably, microbialites growing at different dissolved sulfate concentrations and in marine versus lacustrine environments display similar micropyrite morphologies and comparable Δ_{pyr}. Such observations demonstrate that microbialites have the potential to record the isotopic fractionation associated with MSR irrespective of the depositional environment and sulfate level. Consequently, we propose that microbialite micropyrites can be used as a mineral signature for reconstructing past Earth surface and microbial environments, as already suggested for Archaean stromatolites (Marin-Carbonne *et al.*, 2018). In addition, this study clearly shows that caution should be used in reconstructing past environmental parameters, such as water body sulfate levels, from Δ_{pyr}. Finally, the respective influence of different electron donors, sulfate concentration, and non-actualistic microbial communities on the csSRR and associated sedimentary pyrites $\delta^{34}S$ remains to be explored in order to deepen our understanding of the evolutionary trajectory of biogeochemical sulfur cycling on Earth.

Author contributions

JMC, LR, SB and CT designed the study, KB, EV, CT and AB collected samples in the field. JMC, LR, MND and SE conducted the NanoSIMS analyses, CT and RH conducted the bulk S isotope analyses. JMC, MND, JA, AB, NZ and KB conducted the microscope observations. All authors have contributed to the data interpretation. JMC wrote the manuscript with important contributions of all co-authors.

Competing interests

Authors declare no competing interests.

Data and materials availability

All data is available in the main text or the supplementary materials.

Additional Information

Supplementary Information accompanies this letter at https://www.geochemicalperspectivesletters.org/article2209.

Acknowledgements

This research was supported through the European Research council (ERC) under the European Union's Horizon H2020 research and innovation programme (STROMATA grant agreement 759289). The NanoSIMS facility at the Museum National d'Histoire Naturelle in Paris was established by funds from the CNRS, region ile de France, Ministère délégué à l'enseignement et à la recherche and the Museum National d'Histoire Naturelle. We thank Kevin McKeegan and Jasmine Berg for their proofreading of the manuscript and for fruitful discussions.

Editor: Tanja Bosak

Cite this letter as: Marin-Carbonne, J., Decraene, M.-N., Havas, R., Remusat, L., Pasquier, V., Alléon, J., Zeyen, N., Bouton, A., Bernard, S., Escrig, S., Olivier, N., Vennin, E., Meibom, A., Benzerara, K., Thomazo, C. (2022) Early precipitated micropyrite in microbialites: A time capsule of microbial sulfur cycling. *Geochem. Persp. Let.* 21, 7–12. https://doi.org/10.7185/geochemlet.2209

References

Alleon, J., Bernard, S., Olivier, N., Thomazo, C., Marin-Carbonne, J. (2021) Inherited geochemical diversity of 3.4 Ga organic films from the Buck Reef Chert, South Africa. *Communications Earth & Environment* 2, 6. https://doi.org/10.1038/s43247-020-00066-7

Allwood, A.C., Grotzinger, J.P., Knoll, A.H., Burch, I.W., Anderson, M.S., Coleman, M.L., Kanik, I. (2009) Controls on development and diversity of Early Archean stromatolites. *Proceedings of the National Academy of Sciences* 106, 9548–9555. https://doi.org/10.1073/pnas.0903323106

Awramik, S.M. (1992) The history and significance of stromatolite. In: Schidlowski, M., Golubic, S., Kimberley, M.M., McKirdy, D.M., Trudinger, P.A. (Eds.) *Early organic evolution*. Springer, Berlin, 435–449. https://doi.org/10.1007/978-3-642-76884-2_34

Bell, T., Newman, J.A., Silverman, B.W., Turner, S.L., Lilley, A.K. (2005) The contribution of species richness and composition to bacterial services. *Nature* 436, 1157–1160. https://doi.org/10.1038/nature03891

Bouton, A., Vennin, E., Pace, A., Bourillot, R., Dupraz, C., Thomazo, C., Brayard, A., Désaubliaux, G., Visscher, P.T. (2016) External controls on the distribution, fabrics and mineralization of modern microbial mats in a coastal hypersaline lagoon, Cayo Coco (Cuba). *Sedimentology* 63, 972–1016. https://doi.org/10.1111/sed.12246

Bouton, A., Vennin, E., Thomazo, C., Mathieu, O., Garcia, F., Jaubert, M., Visscher, P. (2020) Microbial Origin of the Organic Matter Preserved in the Cayo Coco Lagoonal Network, Cuba. *Minerals* 10, 143. https://doi.org/10.3390/min10020143

Bradley, A.S., Leavitt, W.D., Schmidt, M., Knoll, A.H., Girguis, P.R., Johnston, D.T. (2016) Patterns of sulfur isotope fractionation during microbial sulfate reduction. *Geobiology* 14, 91–101. https://doi.org/10.1111/gbi.12149

Canfield, D.E., Des Marais, D.J. (1993) Biogeochemical cycles of carbon, sulfur, and free oxygen in a microbial mat. *Geochimica et Cosmochimica Acta* 57, 3971–3984. https://doi.org/10.1016/0016-7037(93)90347-Y

Canfield, D.E., Farquhar, J., Zerkle, A.L. (2010) High isotope fractionations during sulfate reduction in a low-sulfate euxinic ocean analog. *Geology* 38, 415–418. https://doi.org/10.1130/G30723.1

Fike, D.A., Finke, N., Zha, J., Blake, G., Hoehler, T.M., Orphan, V.J. (2009) The effect of sulfate concentration on (sub)millimeter-scale sulfide $\delta^{34}S$ in hypersaline cyanobacterial mats over the diurnal cycle. *Geochimica et Cosmochimica Acta* 73, 6187–6204. https://doi.org/10.1016/j.gca.2009.07.006

Fike, D.A., Gammon, C.L., Ziebis, W., Orphan, V.J. (2008) Micron-scale mapping of sulfur cycling across the oxycline of a cyanobacterial mat: a paired nanoSIMS and CARD-FISH approach. *The ISME Journal* 2, 749–759. https://doi.org/10.1038/ismej.2008.39

Fry, B., Ruf, W., Gest, H., Hayes, J.M. (1988) Sulfur isotope effects associated with oxidation of sulfide by O_2 in aqueous solution. *Chemical Geology: Isotope Geoscience section* 73, 205–210. https://doi.org/10.1016/0168-9622(88)90001-2

Goldhaber, M.B., Kaplan, I.R. (1980) Mechanisms of sulfur incorporation and isotope fractionation during early diagenesis in sediments of the Gulf of California. *Marine Chemistry* 9, 95–143. https://doi.org/10.1016/0304-4203(80)90063-8

Gomes, M.L., Fike, D.A., Bergmann, K.D., Jones, C., Knoll, A.H. (2018) Environmental insights from high-resolution (SIMS) sulfur isotope analyses of sulfides in Proterozoic microbialites with diverse mat textures. *Geobiology* 16, 17–34. https://doi.org/10.1111/gbi.12265

Gomes, M.L., Klatt, J.M., Dick, G.J., Grim, S.L., Rico, K.I., Medina, M., Ziebis, W., Kinsman-Costello, L., Sheldon, N.D., Fike, D.A. (2021) Sedimentary pyrite sulfur isotope compositions preserve signatures of the surface microbial mat environment in sediments underlying low-oxygen cyanobacterial mats. *Geobiology* 20, 60–78. https://doi.org/10.1111/gbi.12466

Javaux, E.J. (2019) Challenges in evidencing the earliest traces of life. *Nature* 572, 451–460. https://doi.org/10.1038/s41586-019-1436-4

Jørgensen, B.B., Findlay, A.J., Pallerin, A. (2019) The Biogeochemical Sulfur Cycle of Marine Sediments. *Frontiers in Microbiology* 10, 849. https://doi.org/10.3389/fmicb.2019.00849

Kamber, B.S., Whitehouse, M.J. (2007) Micro-scale sulphur isotope evidence for sulphur cycling in the late Archean shallow ocean. *Geobiology* 5, 5–17. https://doi.org/10.1111/j.1472-4669.2006.00091.x

Lang, X., Tang, W., Ma, H., Shen, B. (2020) Local environmental variation obscures the interpretation of pyrite sulfur isotope records. *Earth and Planetary Science Letters* 533, 116056. https://doi.org/10.1016/j.epsl.2019.116056

Leavitt, W.D., Halevy, I., Bradley, A.S., Johnston, D.T. (2013) Influence of sulfate reduction rates on the Phanerozoic sulfur isotope record. *Proceedings of the National Academy of Sciences* 110, 11244–11249. https://doi.org/10.1073/pnas.1218874110

Lepot, K. (2020) Signatures of early microbial life from the Archean (4 to 2.5 Ga) eon. *Earth-Science Reviews* 209, 103296. https://doi.org/10.1016/j.earscirev.2020.103296

Marin-Carbonne, J., Busigny, V., Miot, J., Rollion-Bard, C., Muller, E., Drabon, N., Jacob, D., Pont, S., Robyr, M., Bontognali, T.R.R., François, C., Reynaud, S., Van Zuilen, M., Philippot, P. (2020) In Situ Fe and S isotope analyses in pyrite from the 3.2 Ga Mendon Formation (Barberton Greenstone Belt, South Africa): Evidence for early microbial iron reduction. *Geobiology* 18, 306–325. https://doi.org/10.1111/gbi.12385

Marin-Carbonne, J., Remusat, L., Sforna, M.C., Thomazo, C., Cartigny, P., Philippot, P. (2018) Sulfur isotope's signal of nanopyrites enclosed in 2.7 Ga stromatolitic organic remains reveal microbial sulfate reduction. *Geobiology* 16, 121–138. https://doi.org/10.1111/gbi.12275

Pace, A., Bourillot, R., Bouton, A., Vennin, E., Braissant, O., Dupraz, C., Duteil, T., Bundeleva, I., Patrier, P., Galaup, S., Yokoyama, Y., Franceschi, M., Virgone, A., Visscher, P.T. (2018) Formation of stromatolite lamina at the interface of oxygenic-anoxygenic photosynthesis. *Geobiology* 16, 378–398. https://doi.org/10.1111/gbi.12281

Paerl, H.W., Pinckney, J.L. (1996) A mini-review of microbial consortia: their roles in aquatic production and biogeochemical cycling. *Microbial Ecology* 31, 225–247. https://doi.org/10.1007/BF00171569

Pasquier, V., Bryant, R.N., Fike, D.A., Halevy, I. (2021) Strong local, not global, controls on marine pyrite sulfur isotopes. *Science Advances* 7, eabb7403. https://doi.org/10.1126/sciadv.abb7403

Pellerin, A., Antler, G., Holm, S.A., Findlay, A.J., Crockford, P.W., Turchyn, A.V., Jørgensen, B.B., Finster, K. (2019) Large sulfur isotope fractionation by bacterial sulfide oxidation. *Science Advances* 5, eaaw1480. https://doi.org/10.1126/sciadv.aaw1480

Peter, H., Beier, S., Bertilsson, S., Lindström, E.S., Langenheder, S., Tranvik, L.J. (2011) Function-specific response to depletion of microbial diversity. *The ISME Journal* 5, 351–361. https://doi.org/10.1038/ismej.2010.119

Picard, A., Gartman, A., Clarke, D.R., Girguis, P.R. (2018) Sulfate-reducing bacteria influence the nucleation and growth of mackinawite and greigite. *Geochimica et Cosmochimica Acta* 220, 367–384. https://doi.org/10.1016/j.gca.2017.10.006

Raven, M.R., Sessions, A.L., Fischer, W.W., Adkins, J.F. (2016) Sedimentary pyrite $\delta^{34}S$ differs from porewater sulfide in Santa Barbara Basin: Proposed role of organic sulfur. *Geochimica et Cosmochimica Acta* 186, 120–134. https://doi.org/10.1016/j.gca.2016.04.037

Reid, R.P., Visscher, P.T., Decho, A.W., Stolz, J.F., Bebout, B.M., Dupraz, C., Macintyre, I.G., Paerl, H.W., Pinckney, J.L., Prufert-Bebout, L., Steppe, T.F., DesMarais, D.J. (2000) The role of microbes in accretion, lamination and early lithification of modern marine stromatolites. *Nature* 406, 989–992. https://doi.org/10.1038/35023158

Shen, Y., Farquhar, J., Masterson, A., Kaufman, A.J., Buick, R. (2009) Evaluating the role of microbial sulfate reduction in the early Archean using quadruple isotope systematics. *Earth and Planetary Science Letters* 279, 383–391. https://doi.org/10.1016/j.epsl.2009.01.018

Shen, Y., Buick, R. (2004). The antiquity of microbial sulfate reduction. *Earth-Science Reviews* 64, 243–272. https://doi.org/10.1016/S0012-8252(03)00054-0

Sim, M.S., Ono, S., Donovan, K., Templer, S.P., Bosak, T. (2011) Effect of electron donors on the fractionation of sulfur isotopes by a marine *Desulfovibrio* sp. *Geochimica et Cosmochimica Acta* 75, 4244–4259. https://doi.org/10.1016/j.gca.2011.05.021

Slotznick, S.P., Johnson, J.E., Rasmussen, B., Raub, T.D., Webb, S.M., Zi, J.-W., Kirschvink, J.L., Fischer, W.W. (2022) Reexamination of 2.5-Ga "whiff" of oxygen interval points to anoxic ocean before GOE. *Science Advances* 8, eabj7190. https://doi.org/10.1126/sciadv.abj7190

Visscher, P.T., Reid, R.P., Bebout, B.M. (2000) Microscale observations of sulfate reduction: Correlation of microbial activity with lithified micritic laminae in modern marine stromatolites. *Geology* 28, 919–922. https://doi.org/10.1130/0091-7613(2000)28<919:MOOSRC>2.0.CO;2

Williford, K.H., Van Kranendonk, M.J., Ushikubo, T., Kozdon, R., Valley, J.W. (2011) Constraining atmospheric oxygen and seawater sulfate concentrations during Paleoproterozoic glaciation: In situ sulfur three-isotope microanalysis of pyrite from the Turee Creek Group, Western Australia. *Geochimica et Cosmochimica Acta* 75, 5686–5705. https://doi.org/10.1016/j.gca.2011.07.010

Zeyen, N., Benzerara, K., Beyssac, O., Daval, D., Muller, E., Thomazo, C., Tavera, R., López-García, P., Moreira, D., Duprat, E. (2021) Integrative analysis of the mineralogical and chemical composition of modern microbialites from ten Mexican lakes: What do we learn about their formation. *Geochimica et Cosmochimica Acta* 305, 148–184. https://doi.org/10.1016/j.gca.2021.04.030

SEDIMENTOLOGY the journal of the International Association of Sedimentologists

Sedimentology (2023) doi: 10.1111/sed.13069

Diagenetic formation of stevensite by replacement of diatom frustules in the sediments of the alkaline Lake Alchichica (Mexico)

ELODIE MULLER* , WILLIAM RAPIN*,†, JEANNE CAUMARTIN*, DIDIER JÉZÉQUEL‡, ALEXIS DE WEVER*, CHRISTOPHE THOMAZO§,¶ , ROBIN HAVAS§, PURIFICACIÓN LÓPEZ-GARCÍA**, DAVID MOREIRA**, ROZALUZ TAVERA†† and KARIM BENZERARA*

**Muséum National d'Histoire Naturelle, UMR CNRS 7590, Institut de Minéralogie, de Physique des Matériaux et de Cosmochimie (IMPMC), Sorbonne Université, 4 Place Jussieu, 75005, Paris, France (E-mail: karim.benzerara@upmc.fr)*

†IRAP, CNRS UMR 5277, OMP, Université de Toulouse, Toulouse, France

‡IPGP, CNRS UMR 7154, Université de Paris & UMR CARRTEL, INRAE-USMB, Paris, France

§UMR CNRS/uB6282 Biogéosciences, Université de Bourgogne Franche-Comté, 6 Bd Gabriel, 21000, Dijon, France

¶Institut Universitaire de France, Paris, France

***Ecologie, Systématique et Evolution, CNRS, Université Paris-Saclay, AgroParisTech, Orsay, France*

††Departamento de Ecología y Recursos Naturales, Universidad Nacional Autónoma de México, DF México, Mexico

Associate Editor – Andrea Martin Pérez

ABSTRACT

Better understanding the conditions of formation of authigenic Mg-silicates and their reactivity is key to interpret the palaeoenvironmental message carried by the sedimentary record and evaluate the effect of reverse weathering, a process involved in long-term climate evolution. Microbialites from most alkaline crater lakes in Mexico contain Mg-silicates except those in Lake Alchichica, where concentration of orthosilicic acid is low (<26 μM). This study investigated the first metre of sediments in Lake Alchichica in order to check how their mineralogy compared with that of shoreline microbialites. The mineralogy and chemistry of the sediment column were determined, together with the pore water chemistry, providing insights on the processes occurring during early diagenesis. Below *ca* 3 cm in depth, diatom frustules are progressively pseudomorphized into Al-poor Mg-silicates with a composition corresponding to stevensite. This diagenetic process is massive and the resulting silicate represents between 30 and 53 wt.% of the sediment content at all depths. This observation questions the possibility to infer lake palaeochemistry from the presence/absence of Mg-silicates in the sedimentary record. Moreover, it allowed refinement of the conditions under which Mg-silicates authigenesis occurs: the saturation of the solution should be higher or equal to the solubility of a Mg-silicate phase close to that of 'amorphous sepiolite'. Although the solubility of authigenic silicates is a key parameter of reverse weathering modelling during geological times, it is still debated. In this study, a solubility constant deduced from a natural system is proposed that should be considered when modelling the formation of Mg-silicates in a natural environment. The proportion of reverse weathering associated with this solubility constant could be higher than previously predicted based on experiments and thus have a greater impact on climate stability over geological timescales.

Keywords Diagenesis, diatoms, Mg-silicates, reverse weathering, solubility.

INTRODUCTION

Authigenic clays are reported in various sedimentary environments from marine (e.g. Tosca *et al.*, 2011) to soils (e.g. Cuadros *et al.*, 2016), speleothems (e.g. Léveillé *et al.*, 2002) and lacustrine environments (e.g. Deocampo, 2015; Wright & Barnett, 2015). They form either through direct precipitation from solution (i.e. neoformation) or by transformation of precursor minerals (also called neoformation by addition; Jones & Mumpton, 1986; Galán & Pozo, 2011). In the sedimentary environment, transformation is mostly related to diagenesis, whereas neoformation can take place in both syngenetic (depositional) and diagenetic environments (Galán & Pozo, 2011). Clays forming in evaporitic closed basins where parent rocks are enriched in ferromagnesian minerals, tend to be Mg-rich minerals, as reported in the American Great Salt Lake (Jones & Spencer, 1999) and Lake Abert (Jones & Weir, 1983), in several modern East African lake basins (Jones & Mumpton, 1986; Deocampo, 2005, 2015) and in Mexican crater lakes (Zeyen *et al.*, 2015). Hereafter, they are referred to as Mg-silicates (Jones, 1986). They constitute a significant part of the Mg-rich phyllosilicate family. They structurally and chemically encompass diverse phases, either rich in Al such as saponite and palygorskite or poor in Al such as sepiolite, stevensite and kerolite (Pozo & Calvo, 2018). The latter, not listed as a valid mineral species by the International Mineralogical Association, is considered as a stacking-disordered talc phase (Brindley *et al.*, 1977).

Aluminium-poor Mg-silicates have been studied extensively in modern lakes from different localities such as the Satonda crater lake (Indonesia; Arp *et al.*, 2003; Benzerara *et al.*, 2010), Eyasi and Ngorongoro crater lakes (Tanzania; Deocampo, 2005), Lake Van (eastern Anatolia; Reimer *et al.*, 2009), Lake Clifton (western Australia; Burne *et al.*, 2014), Atexcac, Quechulac and La Preciosa lakes (Mexico; Zeyen *et al.*, 2015), Dziani Dzaha Lake (Mayotte; Gérard *et al.*, 2018; Milesi *et al.*, 2019, 2020), Mono Lake and Great Salt Lake (USA; Souza-Egipsy *et al.*, 2005; Pace *et al.*, 2016), as well as peri-marine environments (e.g. Léveillé *et al.*, 2000a,b; Warren, 2016). Last but not least, such authigenic Mg-silicate phases have been observed in some ancient marine and lacustrine formations showing that they can be traced back in the geological record. For example, Tosca *et al.* (2011) reported occurrences of talc in two early Neoproterozoic carbonate formations located in the Akademikerbreen Group (Svalbard) and in the upper Fifteenmile Group of the Ogilvie Mountains (north-west Canada), which they interpreted as the product of dehydration of authigenic hydrous Mg-silicates, including kerolite. It has been shown that the identity of these phases in modern environments depends on specific geochemical factors, such as pH, dissolved CO_2, salinity, alkalinity, dissolved element concentration ratios, and the activities of Mg^{2+}, H_4SiO_4, Al^{3+}, Ca^{2+} and Fe^{3+} in solution (Jones & Galan, 1988; Weaver, 1989; Deocampo, 2005; Bristow & Milliken, 2011). Several experimental studies have investigated the conditions allowing their formation (e.g. Wollast *et al.*, 1968; Tosca *et al.*, 2011). They have shown that high pH > 8.2 and high concentrations of Si and/or Mg are required for their precipitation (Tosca *et al.*, 2011; Zeyen *et al.*, 2015). In addition, high salinity favours the formation of stevensite, whereas sepiolite and kerolite are formed under lower saline conditions, with a high Si/Mg ratio favouring the formation of sepiolite. Likewise, precipitation of kerolite instead of sepiolite is favoured by an increase of pH and dissolved Mg concentration (Pozo & Calvo, 2018). Last, Millot (1970) proposed that the Al content of Mg-silicates could be indicative of the distance to the detrital source. The Millot (1970) model shows that detrital clay inputs, mainly kaolinite, illite, chlorite and Al-rich smectite, preferentially occur in the margins of saline lake basins and transition to fibrous clays (palygorskite, sepiolite) that precipitate in the centre of lakes.

Overall, these minerals have received considerable attention as potential palaeoenvironmental recorders of the geochemistry of the solution in which they precipitated. In addition to their value for palaeoenvironmental reconstruction, better understanding the conditions of Mg-silicates formation and their reactivity is interesting for two broad reasons. First, they can have a crucial role in the control of carbonate fabrics and porosity as exemplified by the study of offshore Barra Velha Formation carbonate

reservoirs in Brazil (Tosca & Wright, 2018; Wright & Barnett, 2020). Second, their precipitation feeds a process called reverse weathering, which consumes alkalinity without consuming carbon and may therefore have a significant role in the evolution of climates at the geological timescale (Isson & Planavsky, 2018; Krissansen-Totton & Catling, 2020). However, there remain a few difficulties for their use as a proxy. First, there is some uncertainty about the exact value of the solubility constant of the amorphous Mg-silicates, commonly considered as precursors to the formation of Mg-silicates in laboratory experiments (i.e. sepiolite, kerolite, stevensite; e.g. Tosca *et al.*, 2011). Second, Mg-silicates may form either in the water column or in sediments during early diagenesis (Işik Ece, 1998; Bristow *et al.*, 2009; Milesi *et al.*, 2019, 2020). In the latter case, they do not reflect the chemistry of the waters in the depositional basin but instead that in the sediment pore waters. Moreover, several authors have suggested that some biogeochemical processes may trigger Mg-silicate formation, possibly obscuring the relationship between the identity and presence/absence of Mg-silicates and bulk chemical conditions. For instance, recent studies reported Mg-silicates formed by a local pH increase and/or nucleation on extracellular polymeric substances within microbial mats, acting as precursors of carbonate precipitation in microbialites (Bontognali *et al.*, 2010; Burne *et al.*, 2014; Zeyen *et al.*, 2015; Pace *et al.*, 2016). The association of Mg-silicates and biofilms has also been evidenced in certain speleothems (Melim & Spilde, 2018), mostly in volcanic caves (Léveillé *et al.*, 2002; Miller *et al.*, 2014). In some cases, Mg-silicates were shown to develop at the surface of diatom frustules (Badaut & Risacher, 1983; Bentz & Peterson, 2020). Yet, although Mg-silicates have shown a strong potential for fossilization of microbes and organic matter (Zeyen *et al.*, 2015), the role of the microorganisms in the formation of these phases remains unclear.

Magnesium-silicates, characterized as poorly crystalline hydrated talc phases similar to kerolite, were reported in shallow microbialites from numerous alkaline crater lakes in Mexico (e.g. Atexcac, La Preciosa, Quechulac; Zeyen *et al.*, 2015, 2021). By contrast, the shallow microbialites of the Mexican Lake Alchichica were essentially composed of hydromagnesite and aragonite, but did not contain kerolite, possibly because lake water had a low concentration in orthosilicic acid (<26 μM). This study investigated deep sediments in Lake Alchichica in order to check how their mineralogy compared with that of shoreline microbialites. The mineralogy and chemistry of the first metre of the sediment column were studied together with the pore water chemistry, providing insights on the processes occurring during early diagenesis.

GEOLOGICAL SETTING

Alchichica is a crater lake located in the eastern part of the trans-Mexican volcanic belt (TMVB) in the Cuenca de Oriental region (19°24′N and 97°24′W; Fig. 1A). The TMVB is a seismically and volcanically active zone resulting from the subduction of the Rivera and Cocos plates beneath North America at the Middle American Trench during the Neogene period (Ferrari *et al.*, 2012). It is composed of diverse volcanic structures formed on a basement predominately composed of highly folded and faulted Cretaceous limestones and shales, as well as small plutonic intrusions of granodiorite, monzonite and syenite emplaced during the Oligocene and the Miocene (Negendank *et al.*, 1985). These basement rocks are covered by Miocene to Pleistocene andesitic rocks, which are themselves overlain by: (i) widespread pyroclastic deposits derived from both local phreatomagmatic volcanoes and large eruptions from nearby volcanoes; as well as (ii) lacustrine deposits. The crater of Alchichica is surrounded by an asymmetrical ring of tephra, deposited by several Hawaiian, strombolian and phreatomagmatic eruptions dated from >114 ka to 6.3 ± 5.1 ka by $^{40}Ar/^{39}Ar$ methods (Tchamabé *et al.*, 2020). The crater rim is mainly composed of maar deposits (i.e. pyroclastic rocks including 44 to 73 wt.% of juvenile clasts) and basaltic andesite lava flow and scoriaceous pre-maar deposits cropping out only on the west side of the crater (Fig. 1; Tchamabé *et al.*, 2020).

With a maximum depth of 65 m (Arredondo-Figueroa *et al.*, 1983; Vilaclara *et al.*, 1993), Alchichica is the deepest crater lake in Mexico. It is located at 2320 m above sea level (a.s.l.) on a high-altitude plateau called Los Llanos de San Juan. The climate is semi-arid with an annual precipitation regime of less than 400 mm and an annual evaporation rate of about 1700 mm (Alcocer, 2021). The air temperature seasonally ranges from −5.5 to 30°C (Alcocer & Hammer, 1998). The lake is supplied by rainfall and groundwaters as suggested by Armienta

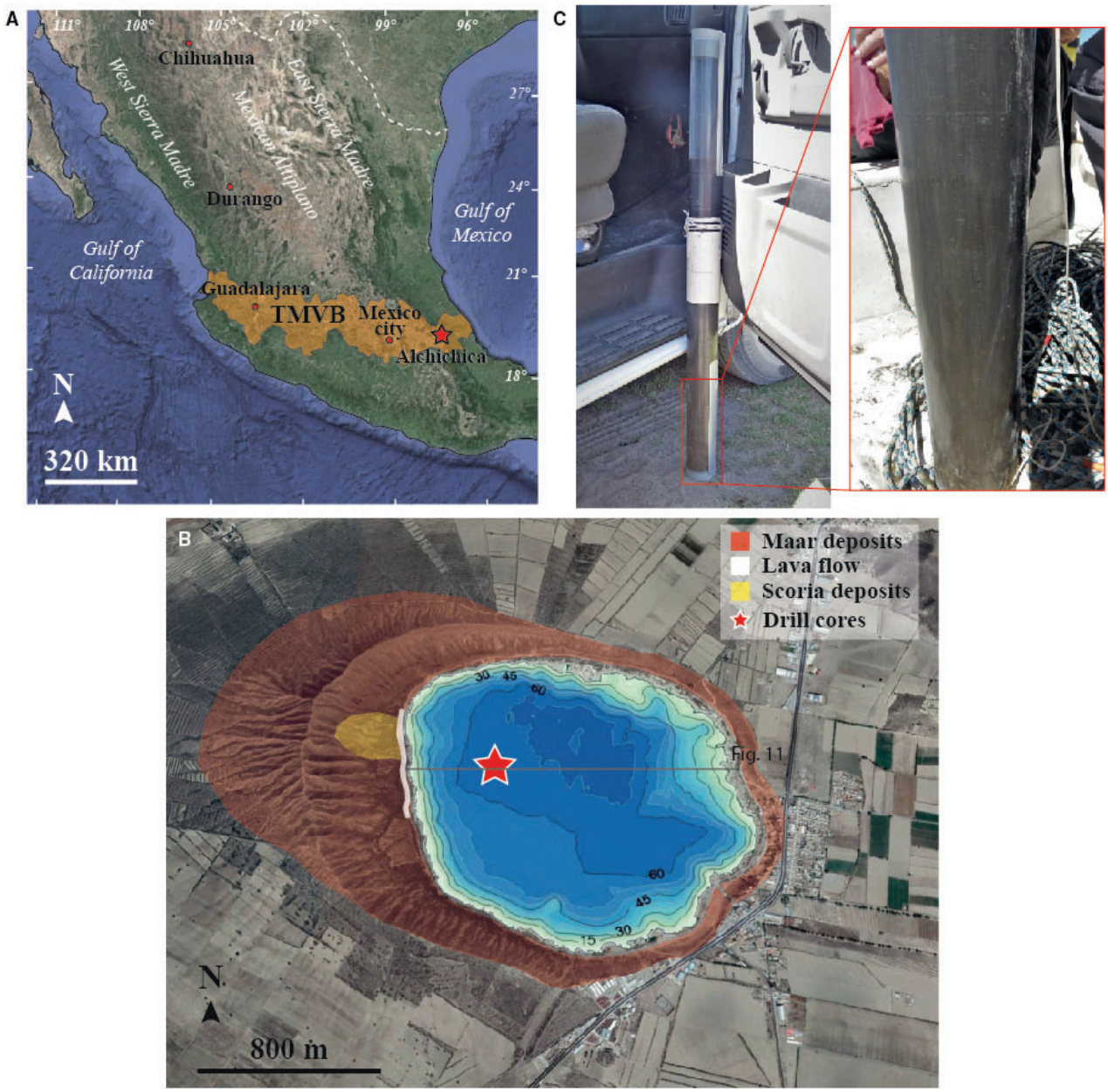

Fig. 1. (A) Relief map of Mexico representing the location of the lake Alchichica in the trans-Mexican volcanic belt (TMVB, orange area; modified from Ferrari *et al.*, 2012). (B) Google Earth image of Lake Alchichica showing the surrounding volcanic deposits (from Tchamabé *et al.*, 2020), bathymetrical data (from Alcocer & Oseguera, 2019) and the location of the drill core (red star). (C) Pictures of the 85.5 cm long sediment core.

et al. (2008) for all maar lakes. The water deficit between evaporation and rainfall could be partially balanced by underground sources and outflows (García Martínez, 2010), yet the lake water level has decreased to a rate of about 8 cm.yr^{-1} for several decades (Alcocer, 2021). Water in Lake Alchichica is alkaline (pH > 9), subsaline (*ca* 7.9 g l^{-1}) and dominated by Na^+, Cl^-, HCO_3^- and Mg^{2+} ions. Two main factors control its chemical composition: (i) the weathering of surrounding bedrocks (basalts and Cretaceous limestones) through groundwater supply; and (ii) the evaporation of the lake due to the semi-arid climate (Zeyen *et al.*, 2021). Alchichica is a monomictic lake stratified during most of the year and homogenized during winter

(Arredondo-Figueroa, 2002). Two annual blooms of primary producers were observed by previous studies: a diatom bloom during the winter mixing (December–January) and a cyanobacteria bloom at the onset of the stratification period (April–May; Vilaclara *et al.*, 1993; Alcocer *et al.*, 2000). Microbialites were studied extensively in Lake Alchichica and are mainly composed of hydromagnesite and aragonite in varying proportions (Couradeau *et al.*, 2011, 2013; Kaźmierczak *et al.*, 2011; Gérard *et al.*, 2013; Saghaï *et al.*, 2015; Valdespino-Castillo *et al.*, 2018; Zeyen *et al.*, 2021). They are covered by complex microbial communities dominated by oxygenic and anoxygenic photosynthesizers (Couradeau *et al.*, 2011; Saghaï *et al.*, 2016; Iniesto *et al.*, 2021).

MATERIAL AND METHODS

Sample collection

Lake water was sampled with a Niskin bottle in May 2019 in the centre of the lake at 0, 5, 10, 20, 30, 40, 50, 55 and 60 m depth. Temperature, pH and salinity were measured *in situ* with a YSI Exo 2 multi-parameter probe (YSI Incorporated, Yellow Springs, OH, USA). Hundreds of millilitres of solution were systematically filtered using 0.22 μm Filtropur S filters (Sarstedt AG & Co. KG, Nümbrecht, Germany). For major cation analysis, 30 ml of solution were acidified with nitric acid (2%). One hundred and thirty millilitres were used for measurements of anion and orthosilicic acid (H_4SiO_4) concentrations, without pre-acidification. For dissolved inorganic carbon (DIC) analysis, 12 ml were placed in airtight Labco Exetainer® tubes (Labco Limited, Ceredigion, UK) in order to avoid exchange of DIC with atmospheric CO_2.

The sediment core was collected from the bottom of the lake at 61 m depth during the same field campaign in May 2019, using a gravitational Uwitec corer (Uwitec GmbH, Mondsee, Austria) with a diameter of 90 mm. The total length of the recovered core was 85.5 cm (Fig. 1C). The sediment core was then cut in two in order to allow its processing in a glove-bag. The two cores were transferred into a glove-bag and placed under anoxic conditions (N_2 atmosphere) immediately after collection. They were then processed and split into centimetre-scale fractions along the core's vertical axis. The pore water was separated from the solid phases once extracted from the core barrel using Rhizon samplers (Rhizosphere Research Products B.V., Wageningen, The Netherlands) connected via tubing to syringes (filtration to 0.2 μm). During all of the slicing process, oxygen levels were monitored with a Multi 3630 IDS WTW oxygen meter (equipped with a FDO 925-3 O_2 optode; Xylem Analytics Germany GmbH, Weilheim, Germany) and were always below the detection limit of 0.1 mg l^{-1}. The pH of the pore waters was measured (with a Sentix 940 IDS WTW electrode; Xylem Analytics) immediately after water collection within the glove-bag. Sediments were packaged under nitrogen and transported in heat sealed airtight bags (PP016 H Protective Packaging Limited, Manchester, UK) with O_2 trap (Anaerocult® A), then fully dried in an anoxic N_2-filled glove-box in the laboratory.

Chemical analyses of solutions

Chemical analyses for major elements (Al, B, Ca, K, Li, Mg, Na, Mn, Si, S and Cl) are summarized in Table 1. They were carried out at the Laboratoire Géoscience Océan (UBO, Brest, France) using inductively coupled plasma–atomic emission spectroscopy (ICP-AES). Anion concentrations (F^-, Cl^-, Br^- and SO_4^{2-}) were measured by ion chromatography and orthosilicic acid (H_4SiO_4) concentrations were determined by continuous flow colorimetric analyses at the Institut de physique du globe de Paris (IPGP, Paris, France). The uncertainty on the concentration measurements of cations, anions and orthosilicic acid was lower than ±5%.

Dissolved inorganic carbon concentrations were determined at the IPGP, using an 'Analytical Precision 2003' Gas Chromatograph – Isotope Ratio Mass Spectrometer (running under He-continuous flow) following the analytical protocol detailed in Assayag *et al.* (2006). An aliquot of the water sample was injected into a Labco Exetainer® tube pre-loaded with H_3PO_4 and He. After the dissolved CO_2 has equilibrated with the head-space gas (for one night), gases (i.e. He and CO_2) were sampled and quantified with the GC-IRMS by comparison with internal standards of known concentrations. Each measurement represents an average of four injections in the mass spectrometer and all samples were duplicated (including chemical preparation and analysis). Standard deviation for [DIC] is 1 mM (n = 33), on average.

Activities of cations, anions and orthosilicic acid, as well as saturation indices of the

Table 1. pH, DIC and major element concentrations measured in lake and pore waters. Relative standard deviation is ≤5% for DIC and element concentrations and ±0.02 units for pH values. Charge balance (Bal.) in % is calculated as 100*(Σcations − Σanions)/((Σcations + Σanions)/2).

	Depth	pH	T (°C)	DIC (mM)	Cl (mM)	Na (mM)	Mg (mM)	SO_4^{2-} (mM)	K (mM)	B (mM)	Li (mM)	Ca (mM)	Mn (mM)	H_4SiO_4 (mM)	Al (μM)	Bal. (%)
Lake water																
AL19_0m-ext	0 m	9.19	19.6	34.1	116	108	19.1	12.8	4.96	3.79	0.35	0.16	<DL	<DL	<DL	−14.2
AL19_4.9m	4.9	9.14	19.2	34.5	107	106	18.8	11.8	4.91	3.79	0.35	0.16	<DL	<DL	0.96	−9.5
AL19_5m	5	9.14	19.2	–	107	108	19.3	11.9	5.01	3.84	0.35	0.16	<DL	<DL	<DL	−8.0
AL19_10m	10	9.22	19.2	32.8	106	107	19.1	11.8	5.00	3.83	0.35	0.16	<DL	<DL	<DL	−7.3
AL19_20m	20	9.23	16.7	34.0	106	105	18.6	11.8	4.90	3.75	0.34	0.15	<DL	<DL	<DL	−10.0
AL19_30m	30	9.22	15.5	34.0	106	105	18.7	11.7	4.90	3.75	0.34	0.15	<DL	0.002	<DL	−9.7
AL19_40m	40	9.24	15.3	32.8	106	106	18.8	11.8	4.87	3.74	0.35	0.15	<DL	0.005	<DL	−9.0
AL19_50m	50	9.17	15.2	34.3	108	104	18.7	12.0	4.82	3.75	0.34	0.14	<DL	0.018	<DL	−12.6
AL19_55m	55	9.18	15.2	34.3	109	100	17.9	12.0	4.62	3.58	0.32	0.14	<DL	0.013	<DL	−16.9
AL19_60m	60	9.25	15.2	34.1	112	104	18.7	12.2	4.84	3.75	0.34	0.15	<DL	0.026	<DL	−14.3
Sediment pore water																
AL19_C2a_0.5cm	0–1 cm	8.95	N.D.	35.8	97.4	109	18.1	9.92	5.05	3.85	0.35	0.13	0.02	0.76	2.01	2.4
AL19_C2a_2cm	1–3	8.76	N.D.	36.2	99.8	105	16.6	9.50	5.03	3.71	0.34	0.10	0.012	0.75	<DL	8.0
AL19_C2a_4cm	3–5	8.61	N.D.	36.8	99.0	106	16.3	9.21	5.03	3.74	0.34	0.10	0.012	0.69	<DL	5.9
AL19_C2a_6cm	5–7	8.53	N.D.	34.5	99.6	105	15.9	9.09	5.06	3.68	0.33	0.10	0.013	0.67	0.08	7.7
AL19_C2a_8.5cm	7–10	8.45	N.D.	34.6	100.2	104	15.7	8.70	5.06	3.72	0.33	0.11	0.022	0.66	1.16	8.1
AL19_C2a_11.5cm	10–13	8.42	N.D.	34.9	98.9	105	15.4	8.26	5.08	3.77	0.33	0.12	0.028	0.64	0.45	8.8
AL19_C2a_17.5cm	16–19	8.4	N.D.	38.2	98.2	103	15.2	8.06	5.02	3.71	0.32	0.11	0.036	0.59	0.47	10.2
AL19_C2a_23.5cm	22–25	8.45	N.D.	39.0	96.2	103	15.6	7.40	5.02	3.74	0.31	0.11	0.011	0.49	<DL	8.1
AL19_C2a_29.3cm	28–30.5	8.48	N.D.	39.8	94.6	100	16.0	7.00	4.96	3.68	0.30	0.09	0.011	0.38	<DL	9.1
AL19_C2a_37.3cm	34.5–40	8.5	N.D.	42.2	93.2	102	17.1	6.16	5.06	3.80	0.30	0.09	0.011	0.39	<DL	4.4
AL19_C2a_41.5cm	40–43	8.56	N.D.	42.4	94.4	100	17.0	5.56	4.93	3.62	0.29	0.09	0.011	0.42	<DL	6.1
AL19_C2b_44.5cm	43–46	8.5	N.D.	42.9	96.6	99.4	16.7	5.62	4.89	3.59	0.29	0.09	0.012	0.47	0.44	8.9
AL19_C2b_50.5cm	49–52	8.46	N.D.	43.2	97.2	99.4	16.4	5.47	4.87	3.57	0.28	0.11	0.012	0.54	0.34	9.6
AL19_C2b_56.5cm	55–58	8.44	N.D.	43.4	95.3	97.8	16.2	5.13	4.81	3.56	0.28	0.12	0.013	0.57	<DL	8.5
AL19_C2b_62.5cm	61–64	8.47	N.D.	41.8	95.4	97.0	15.8	4.84	4.79	3.52	0.27	0.12	0.013	0.59	0.27	10.2
AL19_C2b_68.5cm	67–70	8.47	N.D.	43.1	94.6	96.3	15.7	4.90	4.71	3.48	0.27	0.13	0.002	0.60	0.50	10.3
AL19_C2b_74.5cm	73–76	8.47	N.D.	43.0	96.7	96.2	15.5	4.49	4.74	3.50	0.26	0.14	0.002	0.63	0.71	11.4
AL19_C2b_80.5cm	79–82	8.47	N.D.	43.0	94.2	95.6	15.3	4.20	4.68	3.52	0.26	0.14	0.002	0.63	0.31	10.3
AL19_C2b_83cm	82–84	8.46	N.D.	43.2	93.8	95.9	15.1	4.09	4.65	3.48	0.26	0.13	0.002	0.62	0.03	2.1

solutions were calculated using the software PHREEQC 3 (Parkhurst & Appelo, 2013) and the thermodynamic database 'thermoddem.dat' (Blanc *et al.*, 2012).

Bulk analyses of sediments

A quantity of about 10 g for each sediment sample was finely ground and homogenized in an agate mortar and aliquots of the same powdered sample were used for the different bulk analyses.

X-ray powder diffraction

For X-ray diffraction (XRD) analyses, each core sample powder was placed onto 3 cm diameter sample holders and levelled to form a flat surface for analysis. XRD analyses were performed using a Panalytical Xpert Pro transmission diffractometer (Malvern Panalytical Limited, Malvern, UK) with a cobalt anode operated at 45 kV and 40 mA and a slit of 0.5° at 240 mm radius distance. The 2θ scan was performed in the continuous mode from 4° to 110° (2θ) with a step of 0.024°.

Each diffractogram was corrected for small relative displacements of sample height using the alignment with major aragonite diffraction peaks (2θ-Co angles 30.52° and 53.77°), dominant in all samples. The background signal was fit so that the contribution of X-ray low crystalline phases could be removed from peak analysis. Automatic background determination did not produce adequate results, given the presence of magnesium silicate and opaline silica in the sample generating broad diffraction signals, but these were used to assess the relative presence of the two low crystalline materials (Fig. S1). The background signal was manually fit with an interpolated spline for each diffractogram. Peak identification was performed using pattern search on the XRD database of reference spectra 'Crystallography Open Database (COD)' (from http://www.crystallography.net/).

Structural data of identified minerals were obtained from the COD. The structure and abundance of crystalline minerals were estimated using a Rietveld refinement analysis implemented in the Highscore Plus software (Fig. S2). XRD identifications were cross-checked back and forth with results from energy dispersive X-ray spectrometry (EDXS) elemental composition data obtained by scanning electron microscopy (SEM) to more confidently identify the mineralogy of (core) samples.

Fourier transform infrared spectroscopy analyses

For attenuated total reflectance (ATR) – Fourier transform infrared (FTIR) spectroscopy analyses, *ca* 1 mg of sediment powder was pressed against a single-reflection diamond prism. ATR spectra were recorded between 400 and 4000 cm^{-1} with a resolution of 1 cm^{-1}, using a Nicolet 6700 FTIR spectrometer (Thermo Fisher Scientific, Waltham, MA, USA) equipped with a deuterated triglycine sulphate detector. Spectra were corrected from the atmospheric signal.

Bulk chemical analyses of sediments

Concentrations of major elements were measured on 30 sediment samples using an ICP-AES ICap 6500 (Thermo Fisher) after alkali fusion of rock samples with $LiBO_2$ followed by dissolution in HNO_3 at the Service d'Analyse des Roches et Minéraux (Centre de Recherches Pétrographiques et Géochimiques, Nancy, France). About two grams of ground powder were used for these analyses. The uncertainties on the major element measurements, between 1% and 25% depending on their concentrations, were assessed from relative standard deviations calculated on a minimum of 30 measurements of reference geochemical standards.

Microscopy analyses of sediments

Around 5 mm^3 of powder (<100 μm) from eight samples (at 0.5, 2.0, 4.0, 8.5, 37.3, 41.5, 44.5 and 84.8 cm) collected all the way along the core length were progressively impregnated in hard grade LR-white resin (Polysciences Inc., Warrington, PA, USA) by incubating them at 6°C for 18 h in (1 : 2) then (2 : 1) mixture of LR-white/ethanol and finally in pure LR-white resin. After 1 h at room temperature, the resin was polymerized by incubation at 40°C for 1 h and at 60°C for 24 h. Once polymerization was completed, inclusions were polished with diamond polishing paper with a grain size down to a one quarter of a micrometre and rinsed in deionized water with ultrasound for 10 min. SEM analyses were performed using a Zeiss Ultra 55 field emission gun (FEG) SEM (Carl Zeiss AG, Oberkochen, Germany). Backscattered electron (BSE) images were acquired using an angle selective backscattered (AsB) detector at an accelerating voltage of 15 kV, a working distance of *ca* 7.5 mm and a 60 mm aperture at high current. The elemental composition of mineral phases was determined by EDXS using an EDS QUANTAX detector after copper calibration. Semi-

quantification of the spectra was achieved using the ESPRIT software package (Bruker, Billerica, MA, USA) and the phi-rho-z method.

An electron-transparent foil (*ca* 100 nm in thickness) was cut by focused ion beam (FIB) milling from one of the embedded samples, to further analyse by transmission electron microscopy (TEM) a diatom replaced by Mg-silicates (at 16 to 19 cm in depth). This was performed at IMPMC using a Zeiss Crossbeam Neon40. The lift-out procedure as described by Benzerara *et al.* (2005) was used. A FIB-assisted Pt deposit was first made. A 30 kV Ga + beam operated at *ca* 5 nA was then used for initial milling, resulting in rough excavation from both sides of the thin foil. An *in situ* micromanipulator was attached to the foil by FIB-assisted platinum deposition prior to separation of the foil (at *ca* 100 pA). The thin foil was transferred to a TEM grid and welded to it. Further thinning of the foil was performed with the beam operated at a low, *ca* 100 pA current. A last cleaning step was performed at low acceleration tension (*ca* 3 kV).

The electron-transparent foil was then analysed by TEM using a JEOL 2100F (JEOL Limited, Tokyo, Japan) operating at 200 kV and equipped with a field emission gun (FEG-TEM). Scanning transmission electron microscopy (STEM) observations were performed in the high-angle annular dark field mode (HAADF) and a probe size of 1 nm. EDXS mapping was performed using the STEM mode.

RESULTS

Solution chemistry of the water column and the sediment pore water

Solutions at all depths in the water column of Lake Alchichica are dominated by sodium, chloride and magnesium (Fig. 2; Table 1). In the water column, the temperature decreases from 19.5 to 15.2°C with depth and the chemical composition remains stable, with a pH of 9.2 and concentrations of DIC at 33.9 mM, Mg at 18.8 mM and Ca at 0.1 mM (Fig. 2; Table 1). The concentration of orthosilicic acid in the water column is below the detection limit (0.1 μM) from the surface down to 30 m in depth, then increases to 26 μM at 60 m (maximum depth of the lake). In the sediments, pore waters are also dominated by sodium, chloride and magnesium (Fig. 2; Table 1). The [Mg] decreases in the first 20 cm from 18.1 to 15.2 mM and then remains constant with a peak at 17.1 mM at 34.5 to 40.0 cm depth. The pH also decreases down to 8.47 in the first 10 cm of the sediments and then remains constant. The concentration of orthosilicic acid in pore water is significantly higher than in the lake water. It decreases from 760 μM at 0.5 cm down to 380 μM at 28 to 40 cm and raises again to 620 μM at 83 cm deep. The DIC concentration globally increases from the top to the bottom of the core, from 35.8 to 43.2 mM. The [Ca] varies non-monotonously between 0.09 mM and 0.14 mM (Fig. 2; Table 1).

Saturations of the solutions with respect to authigenic silicate and silica phases are best visualized in a diagram, where the logarithm of the $a(Mg^{2+})/a(H^{+})^2$ activity ratio is plotted against the logarithm of the orthosilicic acid activity ($a(H_4SiO_4)$; Fig. 3). As the orthosilicic acid concentration increases with depth in the water column, the lake water reaches saturation with respect to several low-temperature Mg-silicates such as sepiolite, kerolite, talc and stevensite below 30 m in depth. However, all lake waters down to 60 m remain undersaturated with respect to 'amorphous sepiolite', as defined by Wollast *et al.* (1968). By contrast, all sediment pore solutions are saturated/supersaturated with respect to 'amorphous sepiolite'. Two trends can be detected: (i) from 0 to 11.5 cm in depth, pore waters align along a vertical trend, i.e. at a constant $a(H_4SiO_4)$, located between the solubility lines of quartz and amorphous silica (arrow 1 in Fig. 3); and (ii) from 11.5 to 84.8 cm, pore waters follow a trend parallel to the 'amorphous sepiolite' solubility line (arrow 2 in Fig. 3). Only one sample of pore water from the top of the sediments (0 to 1 cm) lies above the critical supersaturation line for homogeneous nucleation of Mg-silicates as defined by Tosca *et al.* (2011) and Tosca & Masterson (2014).

Saturations of solutions with respect to several carbonate phases are visualized in other diagrams, where the logarithms of $a(Ca^{2+})$ or $a(Mg^{2+})$ are plotted against the log of $a(CO_3^{2-})$ (Fig. S3). These diagrams clearly show that lake and pore waters are supersaturated with respect to calcite and aragonite at all depths but only lake waters reach saturation with monohydrocalcite (MHC; Fig. S3a). The water column of Lake Alchichica is oversaturated at all depths with amorphous Mg carbonate (AMC), as defined by Fukushi & Matsumiya (2018) (Fig. S3b), and therefore with hydromagnesite as well. All pore waters except those between 8.5 cm and 23.5 cm, are saturated or supersaturated with hydromagnesite.

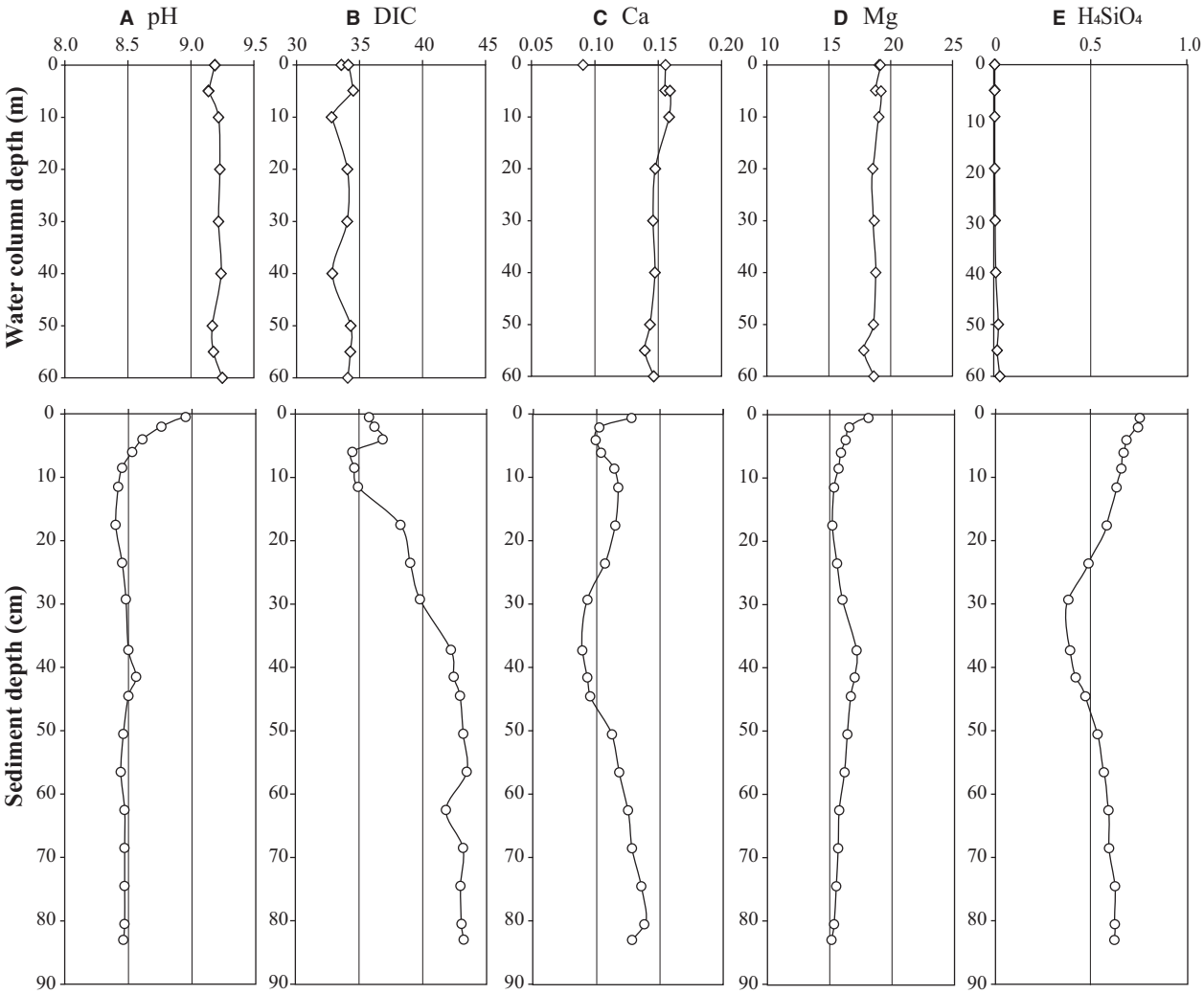

Fig. 2. Depth profiles of (A) pH, (B) dissolved inorganic carbon (DIC), (C) Ca, (D) Mg and (E) H_4SiO_4 concentrations in mM along the water column (top part, diamonds) versus in pore water in the first 83 cm of sediments (bottom part, circles).

Bulk mineralogy

X-ray diffraction analyses highlight that aragonite is the dominant mineral species in the sediments with an abundance varying between 40 wt.% and 80 wt.% (amorphous-free) as estimated by Rietveld (Figs 4 and S4; Table S1). Detrital silicate minerals (albite, bytownite, quartz and pigeonite) are also detected in all diffractograms, their total abundance varying from 15 to 48 wt.% (amorphous-free). The relative abundance of aragonite and detrital species is anticorrelated to some degree along the core, but other mineral phases exhibit key variations with depth. In particular, a substantial amount of hydromagnesite is identified in the first two samples near the sediment surface (up to 15 wt.% in the top 3 cm of the core), but is absent at depth (<1 wt.%) except within a specific interval near 35 cm in depth where hydromagnesite is clearly detected (*ca* 8 wt.%) along with huntite (*ca* 11 wt.%), a trigonal carbonate phase of formula $Mg_3Ca(CO_3)_4$. Poorly crystalline magnesium silicates and opaline silica can also be detected by XRD (Fig. S1). The estimation of the intensity of the broad X-ray scattering signal related to silica reveals that it is most intense near the surface but significantly decreases within the sediment beneath, with the lowest signal near 35 cm. By contrast, the magnesium silicate, identified as a kerolite or a

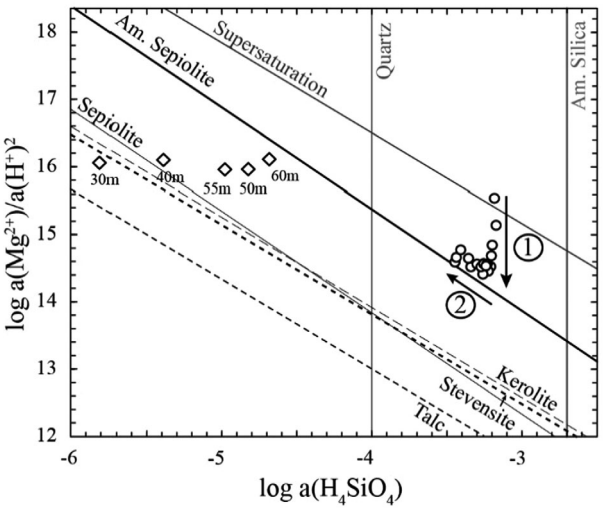

Fig. 3. Solubility diagram in the $\log[a(Mg^{2+})/a(H^{+})^2]$ – $\log[a(H_4SiO_4)]$ space determined at 25°C. Lake (diamond) and pore waters (dots) of Alchichica are plotted against the solubility lines of talc (Jones & Galan, 1988), stevensite (Chahi *et al.*, 1997), kerolite and sepiolite (Stoessell, 1988), amorphous sepiolite (Wollast *et al.*, 1968), quartz and amorphous silica (Truesdell & Jones, 1974). The 'supersaturation' line results from experiments conducted by Tosca *et al.* (2011) and Tosca & Masterson (2014), and relates to homogeneous nucleation of Mg-silicate phases from solution. The arrows 1 and 2 show the main trends followed by Alchichica sediment pore waters, respectively, between 0 cm and 11.5 cm and between 11.5 cm and 84.8 cm. Above 30 m in the lake waters, silica is below the detection limit and hence data are not represented in this diagram.

stevensite, based on broad diffraction peaks at 22.7°, 41.2° and 71.8° 2θ angles (see Zeyen *et al.*, 2015, for more details about XRD identification), is not detected in the first two samples at the surface but clearly detected deeper down, with a low relative intensity near 35 cm. Other minor minerals are detected by XRD in all samples, such as calcite (average abundance of 2.6 wt.% as suggested by Rietveld), and halite, which likely formed when the samples containing Cl-rich pore waters were dried.

The FTIR analyses of the sediment samples show an evolution of their mineralogical composition with depth in perfect agreement with XRD analyses (Figs 5, S4 and S5). The aragonite signal is present in all samples at all depths (Fig. S5), as attested to by bands at 700, 713, 845, 855, 1083, 1464 and 1512 cm^{-1} (Zeyen *et al.*, 2015). In surface sediment spectra (down to 10 cm), bands at 796, 1059 and 1230 cm^{-1}, characteristic of amorphous silica (d'Espinose de la Caillerie *et al.*, 1995; Nied *et al.*, 2016), are detected as well as bands at 887, 1420 and 1477 cm^{-1}, characteristic of hydromagnesite (Farmer, 1974). These bands disappear in deeper samples except for those at 37.3 cm depth. By contrast, Mg-silicates (for example, kerolite or stevensite) are absent in surface samples but detected in FTIR spectra of all sediments deeper than 10 cm as shown by the presence of OH absorption bands at 662 and 670 cm^{-1} (Tosca & Masterson, 2014), a Si–OH stretching band at 892 cm^{-1} and a Si–O stretching band at 981 cm^{-1} (Zeyen *et al.*, 2015). Only the sediment samples at 34.5 to 40.0 cm in depth appeared anomalous in that trend: in particular it notably shows the reappearance of hydromagnesite as attested to by the bands at 887 and 1420 cm^{-1}, but also the presence of huntite as attested to by the bands at 870, 878, 891, 1442, 1511 and 1551 cm^{-1} (Kangal *et al.*, 2005; Hollingbery & Hull, 2012).

Observations by SEM and EDXS analyses of eight samples also confirm the evolution of the mineralogical composition of the sediments with depth in total agreement with FTIR and XRD data. SEM-EDXS analyses show that the sediments contain abundant fine-grained Ca-carbonates chemically consistent with aragonite at all depths. By contrast, Mg-rich non-silicate minerals (containing Mg, O and C only) are detected only in the first 10 cm of sediments and at 34.5 to 40.0 cm and likely correspond to hydromagnesite as supported by XRD and FTIR analyses (Fig. 6). A Ca-rich and Mg-rich mineral interpreted as huntite based on a Mg/Ca ratio of about three is locally observed in samples C2a-05 (7 to 10 cm), C2a-10 (34.5 to 40.0 cm), C2a-11 (40 to 43 cm) and C2b-12 (43 to 46 cm). Huntite grains are relatively small, measuring less than 20 μm in size. Regarding Si-rich mineral phases, various grains are best interpreted as detrital minerals. The stoichiometry of these grains together with XRD analyses allowed to identify them as alkaline feldspars and quartz (Table S2). Other detrital minerals rich in Mg, Al, Si and K show elemental Si/Al and Mg/Al ratios consistent with olivine and pyroxenes (Table S2). Last, SEM images show that diatom frustules are very abundant in the sediments at all depths, most of them are broken (and potentially degraded during sample preparation) but show a nicely preserved fine ultrastructure with, for example, visible nanopores (Figs 6 to 8). However, notable chemical differences are observed, depending on depth in the sediments. In the first 10 cm, the

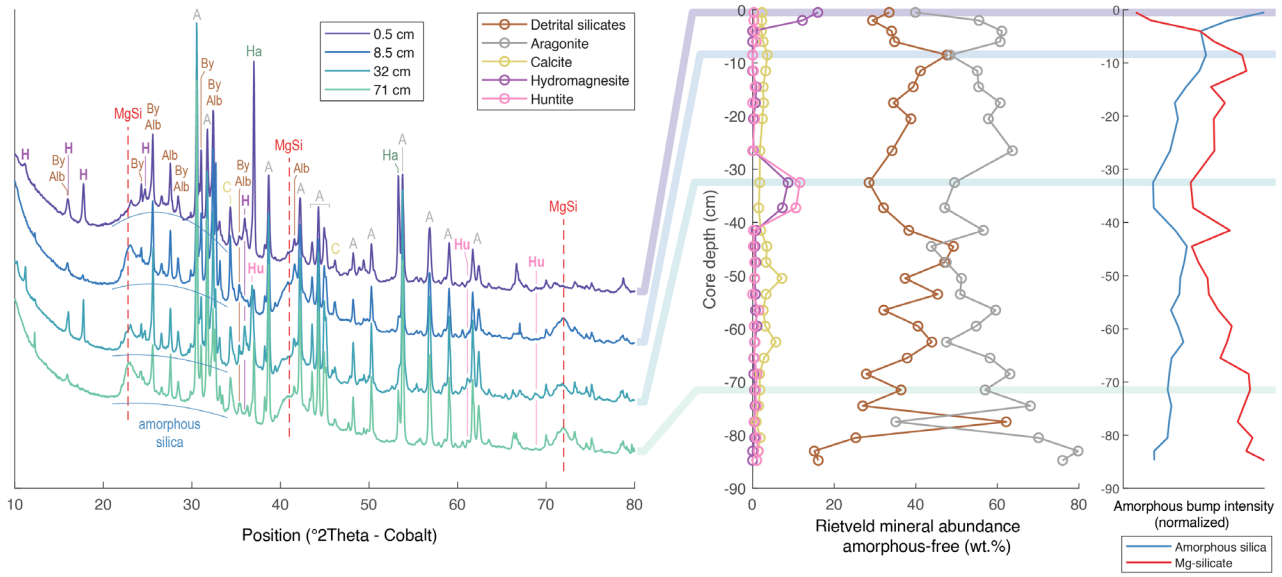

Fig. 4. X-ray diffraction analyses of Alchichica sediment core samples. (Left panel) Selected diffraction patterns (at 0.5, 8.5, 32.5 cm and 71.5 cm depth) highlighting the key crystalline mineral assemblages used for Rietveld refinement analysis (A: aragonite, Alb: albite, By: bytownite, H: hydromagnesite, Hu: huntite, Ha: halite, C: calcite, see Fig. S4 for all patterns), along with the broad diffraction signals of poorly crystalline magnesium silicate (MgSi, kerolite or stevensite) and amorphous silica. (Middle panel) Estimated crystalline mineral relative abundances and (Right panel) relative intensity of XRD signals affiliated to poorly crystalline phases (see also Fig. S1) in the core with depth.

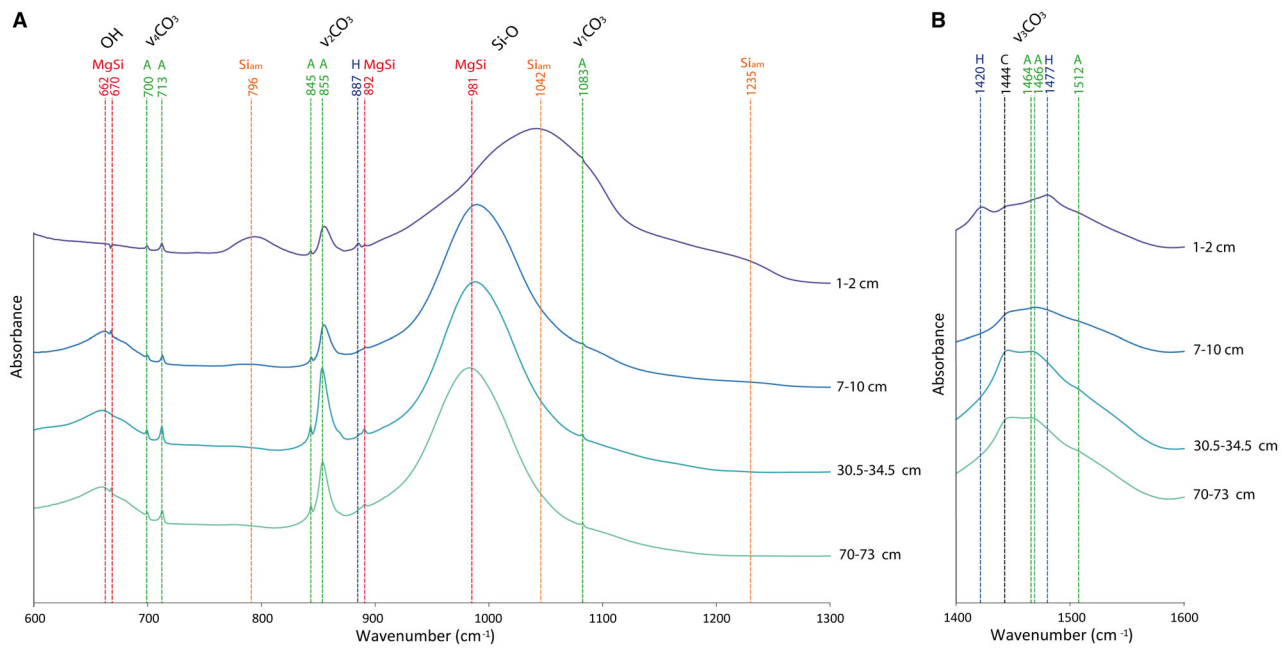

Fig. 5. Selected Fourier transform infrared (FTIR) spectra of Alchichica sediment samples (at increasing depth from top to bottom, same depths as those shown in Fig. 4). (A) Spectra in the 600 to 1300 cm^{-1} wavenumber range. (B) Spectra of the same samples from 1400 to 1600 cm^{-1}. The dashed lines show characteristic bands of silicates [red for authigenic magnesium silicates (MgSi), orange for amorphous silicates (Siam)] and carbonates [green for aragonite (A), black for calcite (C), blue for hydromagnesite (H)] in the samples.

frustules are composed of silica. Morphologically well-preserved frustules become less abundant below 10 cm depth and the silica composing them gradually transforms to a poorly crystalline Mg-silicate phase, as shown by SEM-EDXS and TEM-EDXS as well as SAED (Figs 6, 7 and 8). Despite this chemical/mineralogical transformation, the ultrastructure sometimes remains finely preserved, showing that this mineralogical transformation is pseudomorphic. The average Mg/Si ratio of this phase as analysed by EDXS is 0.74 ± 0.18 (n = 12), which is consistent with kerolite [$Mg_3Si_4O_{10}(OH)_2{\cdot}H_2O$] and stevensite [$(Ca,Na)_xMg_{3-x}(Si_4O_{10})(OH)_2{\cdot}nH_2O$]. The stoichiometry estimated more precisely as $Na_{0.12}K_{0.009}Ca_{0.31}Fe_{0.2}Al_{0.15}Mg_{2.65}Si_4O_{10}(OH)_2{\cdot}nH_2O$ is more consistent with Al-poor stevensite (Al = 0.19 ± 0.26 at.%, n = 12).

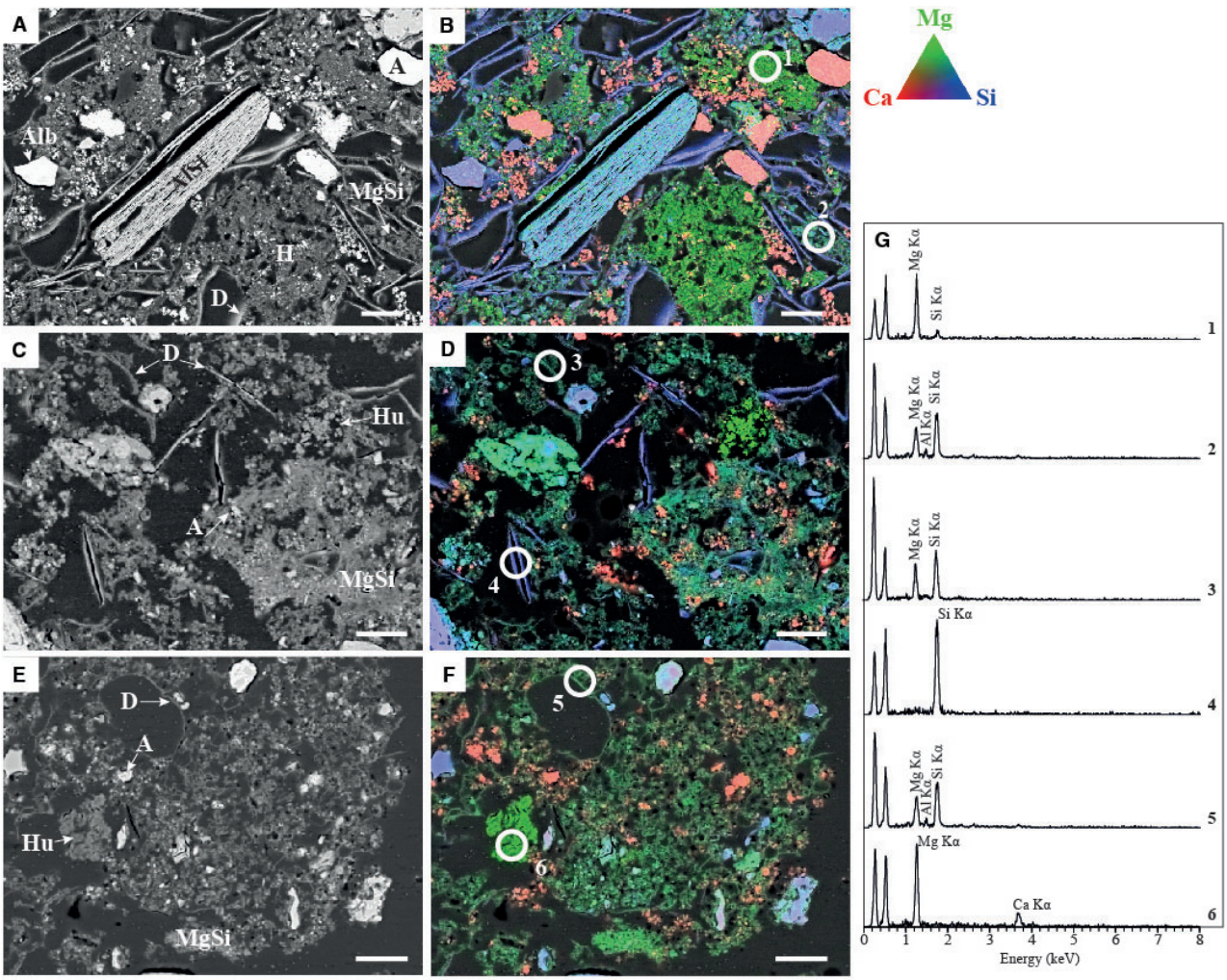

Fig. 6. Evolution of the sediment mineralogy with depth. Backscattered electron (BSE) images (left) and corresponding energy dispersive X-ray spectrometry (EDXS) maps (right) of Mg (green), Ca (red) and Si (blue) at 1 to 3 cm (A) and (B), 7 to 10 cm (C) and (D), and 34.5 to 40.0 cm depth in the sediment core (E) and (F). (G) EDXS spectra of areas circled in white. On the chemical composition maps, aragonite appears in red, silica in blue, huntite and hydromagnesite in light green and Mg-silicates in dark green. Hydromagnesite is mainly observed at 1 to 3 cm (spectra 1), whereas huntite is only detected at 7 to 10 cm and 34.5 to 40.0 cm (spectra 6). Mg-silicates with very low amount of Al (0.19 ± 0.26 wt.% in average, n = 12) are detected in all of the samples (spectra 2). Diatoms are progressively transformed into Mg-silicate. At 1 to 3 cm depth, they are mostly composed of silica, whereas at 7 to 10 cm depth, some are transformed into Mg-silicates (spectra 3) while others are not (spectra 4). Then, at 34.5 to 40.0 cm depth, all diatoms are replaced by Mg-silicates (spectra 5). Scale bars correspond to 20 μm. H: hydromagnesite; MgSi: Mg-silicate; D: diatom; A: aragonite; Hu: huntite; AlSi: detrital Al-silicate (containing Al, Si, Fe, K, Na and Mg).

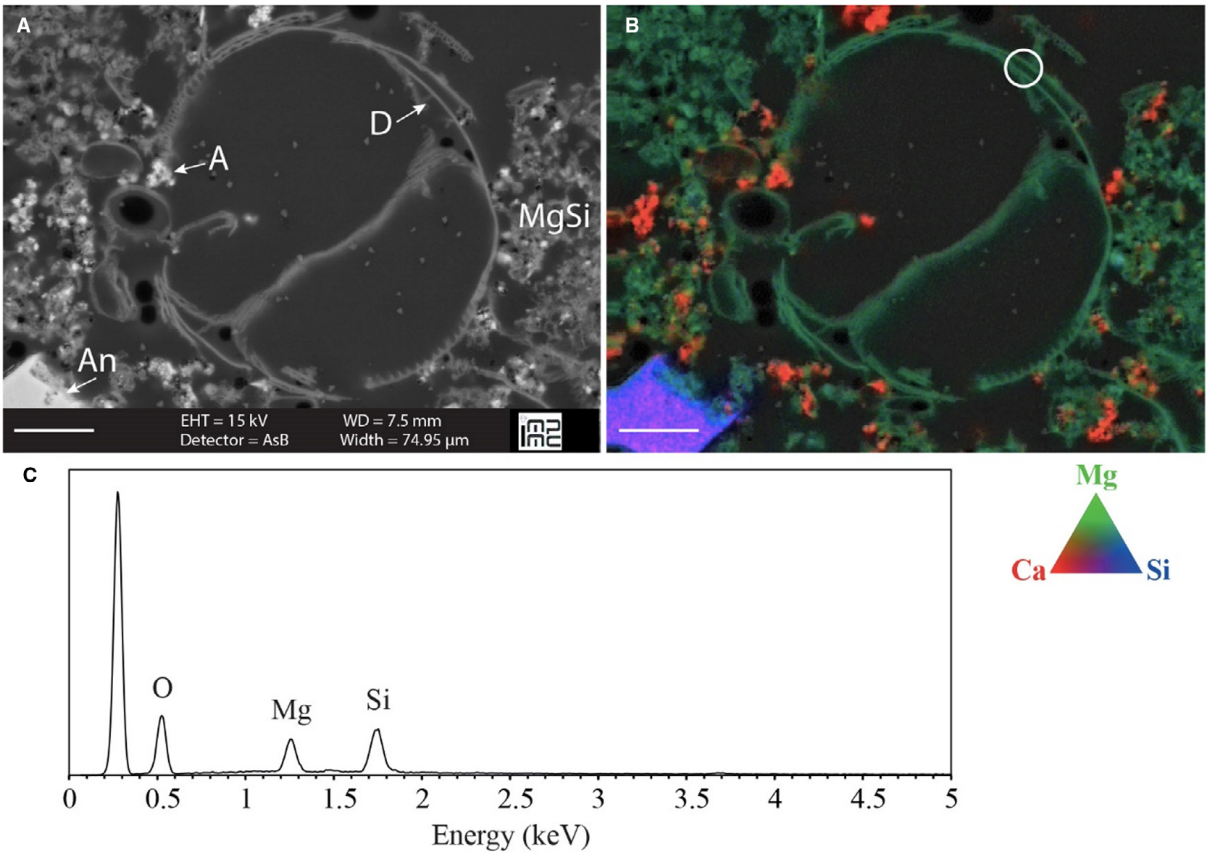

Fig. 7. Remnants of diatom frustule composed of Mg-silicates at a 41.5 cm depth in the sediment core. (A) Backscattered electron (BSE) image, (B) corresponding energy dispersive X-ray spectrometry (EDXS) map of Mg (green), Ca (red) and Si (blue) and (C) EDXS spectra of the zone highlighted by a white circle. On the chemical composition map, aragonite appears in red, Mg-silicates in dark green and anorthite in pink-blue (at bottom left corner). Scale bars correspond to 10 µm. An: anorthite, A: aragonite, D: diatom, MgSi: Mg-silicate.

Some grains of this phase are also observed away of the diatoms and not just replacing them. In a few cases, Al-containing Mg-silicates were detected but mostly in the vicinity of detrital grains in Lake Alchichica sediments (Al = 2.41 ± 0.85 at.%, n = 20; Fig. S6). In the literature, up to 1 wt.% of Al is commonly reported in sepiolite, kerolite and stevensite (e.g. Stoessell, 1988; Capet, 1990), sometimes reaching up to 5 wt.% (e.g. Rhouta *et al.* 2008, and references therein).

Bulk chemistry of the sediment solid phases

The bulk chemical composition of the sediments mostly consists of silicon, calcium, magnesium and aluminium (Table 2). Titanium content shows a strong positive correlation with aluminium with a y-intercept of about 0 in all sediments interpreted as a result of the shared detrital origin of these two elements (Fig. 9B). SiO_2 and Al_2O_3 also correlate positively for most of the samples suggesting that Al is mostly found in silicates (Fig. 9A). However, since [SiO_2] = 25.78 wt.% when [Al_2O_3] = 0, phases other than detritic Al-containing silicates contribute massively to the total concentration of silica in the sediments. Based on all mineralogical analyses shown above, the authors suggest that those phases are the amorphous silica of diatoms and/or authigenic Mg-silicates, depending on the depth in the core. Moreover, Fig. 9 suggests that the top sediments (from 0 to 11.5 cm) are enriched in non-detrital silica, possibly due to the accumulation of diatoms, whereas samples at 37.3 cm and 71.5 cm are depleted in non-detrital silica, in agreement with FTIR and XRD data.

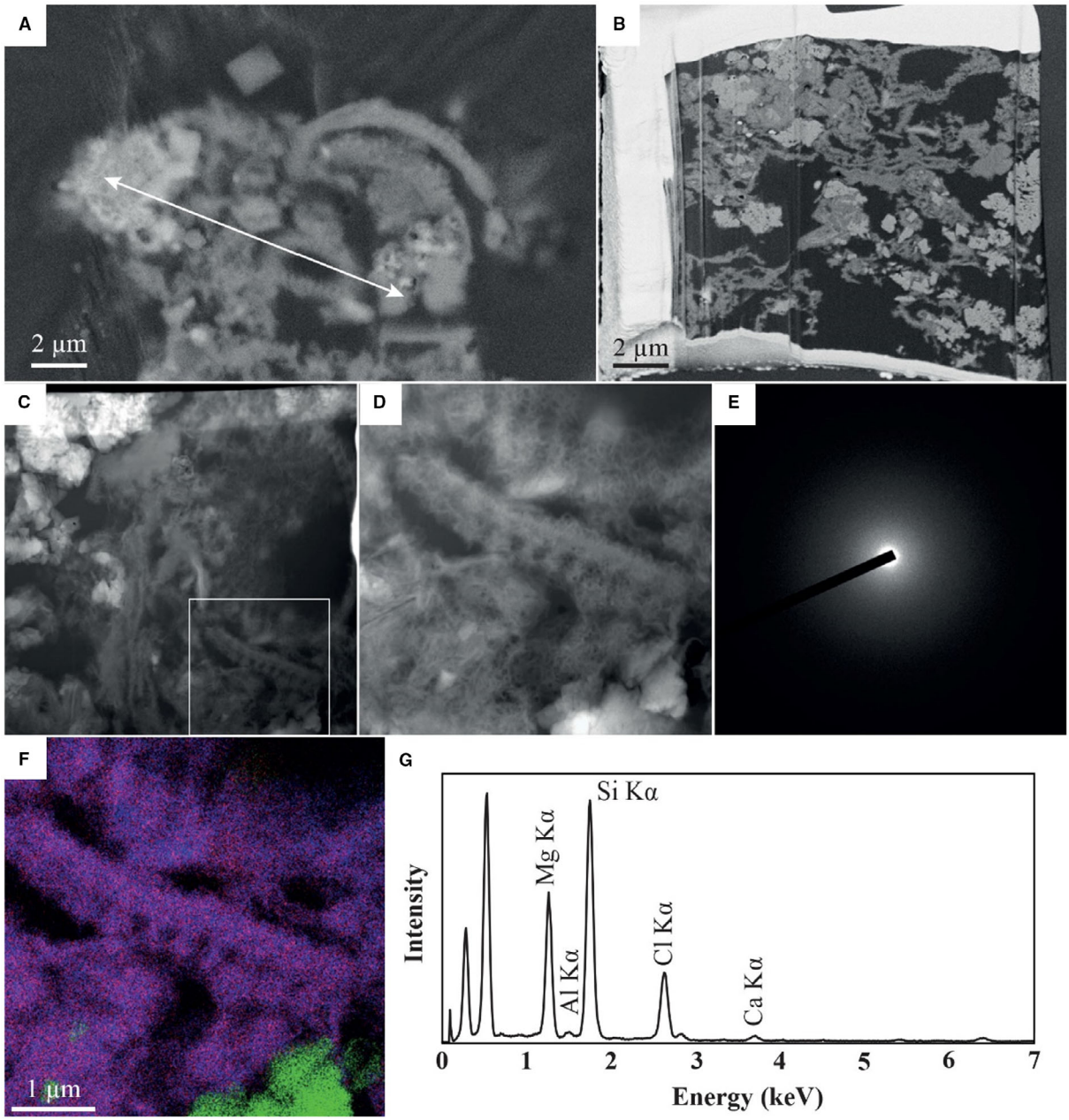

Fig. 8. Scanning transmission electron microscopy (STEM) analyses of a diatom pseudomorphozed into Mg-silicates. (A) SEM image showing sediment particles collected at 16 to 19 cm and embedded in resin. The white line indicates where the focused ion beam (FIB) section was excavated. (B) Image of the FIB foil. Aragonite appears in bright and Mg-silicates in grey. (C) STEM image in high-angle annular dark field mode (HAADF) showing sediment particles. (D) Zoom showing a diatom fragment with a fibrous texture. (E) Electron diffraction pattern measured on the diatom fragment, indicating that it is amorphous. (F) Overlay of magnesium (red), silicon (blue) and calcium (green) elemental maps as measured by energy dispersive X-ray spectrometry (EDXS). (G) EDXS spectrum obtained on the diatom fragment showing major Mg and Si peaks. Cl is attributed to resin. A small Al peak can be observed.

The semi-quantitative evolution of the mineral composition with depth was assessed based on bulk chemical analyses of the sediments and relying on XRD and FTIR analyses (Fig. 10; Table S3). The feldspars (albite and bytownite) and aragonite contents are

Table 2. Elemental composition of the sediments determined by inductively coupled plasma – atomic emission spectroscopy (ICP–AES) in wt.%. LOI (loss on ignition) refers to the mass difference before and after ignition and represents the amount of water, organic carbon and volatile elements contained in the sediment.

	Depth (cm)	SiO_2	Al_2O_3	MgO	CaO	Na_2O	Fe_2O_3	K_2O	TiO_2	P_2O_5	MnO	LOI	Total
AL19_C2a_0.5cm	0–1	40.97	4.67	6.34	8.35	5.01	1.81	1.09	0.17	0.21	0.04	31.9	100.5
AL19_C2a_2cm	1–3	38.47	4.89	7.14	12.12	2.88	1.87	0.94	0.18	0.18	0.05	31.3	100.0
AL19_C2a_4cm	3–5	39.57	5.04	8.15	12.24	3.01	1.87	0.95	0.19	0.17	0.05	28.9	100.1
AL19_C2a_6cm	5–7	39.08	5.34	8.60	12.71	2.96	1.88	0.98	0.19	0.16	0.05	28.1	100.1
AL19_C2a_8.5cm	7–10	42.78	5.92	10.28	9.62	2.94	2.02	1.04	0.22	0.16	0.06	24.4	99.4
AL19_C2a_11.5cm	10–13	39.61	5.28	10.68	10.74	2.53	1.88	0.90	0.20	0.15	0.05	27.6	99.6
AL19_C2a_14.5cm	13–16	36.63	5.41	9.06	13.55	2.83	1.83	0.93	0.20	0.14	0.05	29.2	99.8
AL19_C2a_17.5cm	16–19	36.73	5.25	9.81	14.31	2.63	1.74	0.90	0.20	0.14	0.05	20.1	99.9
AL19_C2a_20.5cm	19–22	37.46	5.99	9.12	14.39	2.95	1.89	1.01	0.22	0.15	0.06	26.8	100.1
AL19_C2a_23.5cm	22–25	36.44	5.80	9.42	14.87	2.57	1.86	0.95	0.22	0.15	0.06	27.3	99.6
AL19_C2a_26.5cm	25–28	36.13	5.58	9.68	14.19	2.62	1.75	0.93	0.20	0.13	0.05	29.1	100.4
AL19_C2a_29.3cm	28–30.5	35.26	5.12	10.53	15.49	2.55	1.69	0.84	0.19	0.15	0.05	28.0	99.8
AL19_C2a_32.5cm	30.5–34.5	34.61	5.23	10.35	15.13	3.10	1.72	0.89	0.19	0.13	0.05	28.5	99.9
AL19_C2a_37.3cm	34.5–40	30.81	5.35	11.90	16.28	2.02	1.69	0.84	0.20	0.14	0.05	30.6	99.9
AL19_C2a_41.5cm	40–43	38.40	5.93	10.49	14.11	2.34	1.90	0.94	0.22	0.15	0.06	25.1	99.6
AL19_C2b_44.5cm	43–46	41.90	8.14	7.69	12.79	2.65	2.45	1.29	0.30	0.16	0.06	22.3	99.7
AL19_C2b_47.5cm	46–49	39.49	7.45	7.76	13.00	3.35	2.30	1.23	0.28	0.15	0.06	24.6	99.7
AL19_C2b_50.5cm	49–52	38.96	6.54	9.09	14.22	2.46	2.13	1.05	0.25	0.16	0.06	24.6	99.5
AL19_C2b_53.5cm	52–55	38.56	6.61	8.62	12.95	3.33	2.17	1.11	0.25	0.15	0.05	25.4	99.2
AL19_C2b_56.5cm	55–58	36.74	5.68	9.75	14.40	2.91	1.95	0.95	0.22	0.16	0.05	27.1	99.9
AL19_C2b_59.5cm	58–61	36.63	5.57	9.44	11.92	2.94	1.91	0.94	0.21	0.14	0.05	29.4	99.1
AL19_C2b_62.5cm	61–64	40.69	6.56	9.60	12.60	2.59	2.15	1.07	0.25	0.14	0.05	24.5	100.2
AL19_C2b_65.5cm	64–67	38.06	5.85	9.68	12.71	3.24	1.97	1.01	0.22	0.13	0.05	26.7	99.6
AL19_C2b_68.5cm	67–70	35.56	4.34	11.40	14.08	2.64	1.61	0.75	0.17	0.15	0.05	28.9	99.6
AL19_C2b_71.5cm	70–73	27.31	3.15	8.99	10.68	2.88	1.26	0.63	0.13	0.10	0.03	45.4	100.5
AL19_C2b_74.5cm	73–76	35.19	4.13	11.36	15.61	2.19	1.59	0.69	0.16	0.15	0.05	28.8	99.9
AL19_C2b_77.5cm	76–79	35.00	4.27	11.08	13.51	3.22	1.59	0.78	0.17	0.13	0.05	30.2	100.0
AL19_C2b_80.5cm	79–82	34.05	3.81	11.60	15.75	2.18	1.49	0.64	0.15	0.14	0.05	30.5	100.3
AL19_C2b_83cm	82–84	31.30	2.50	12.65	17.89	2.03	1.11	0.46	0.10	0.14	0.04	32.3	100.5
AL19_C2b_84.8cm	84–85.5	30.36	2.27	12.35	15.88	3.05	1.02	0.51	0.10	0.12	0.04	33.7	99.3

relatively constant along the core, between 40 wt.% and 60 wt.%. The uppermost sediments (0 to 3 cm) also show more than 30 wt.% of amorphous silica and 20 wt.% of hydromagnesite. Then, amorphous silica decreases with depth down to 3 wt.% on average, while Mg-silicates accumulate to reach up to 40 wt.% on average. Because hydromagnesite is not detected by XRD (Fig. S4), FTIR (Fig. S5) or SEM (Fig. 6) below 3 cm in depth, it is no longer considered in the calculations. Between 30 cm and 40 cm in depth, sediments are devoid of silica. Concurrently, between 35 cm and 40 cm, they show a lower Mg-silicates content (34 wt.%) and a relatively high amount of Mg carbonates (10 wt.%. of huntite and hydromagnesite).

DISCUSSION

Massive formation of Mg-silicates in the sediments of Lake Alchichica

The uppermost sediments (0 to 3 cm) are dominated by hydromagnesite, aragonite, diatom frustules which settled down the water column, detrital alkaline feldspars and quartz inherited from the erosion of the surrounding volcanic rocks (Figs 10 and 11). The presence of aragonite and hydromagnesite in the first centimetres of sediment suggests that they precipitated in the water column or at the sediment–water interface, where solutions are oversaturated with all calcium and magnesium carbonate phases, including their potential precursors, i.e.

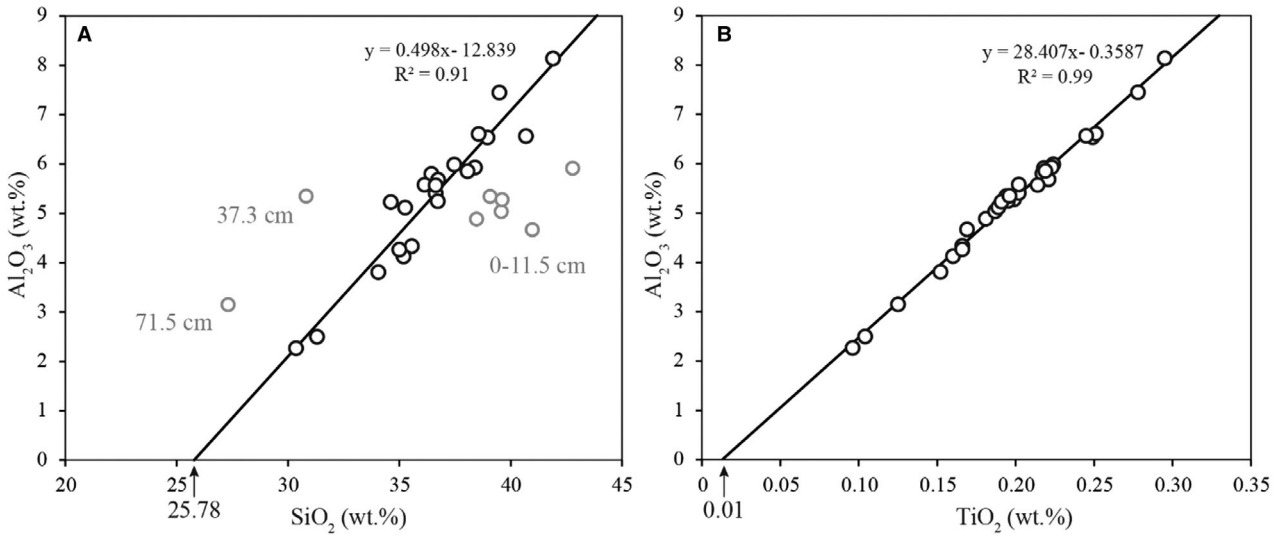

Fig. 9. Correlation between bulk concentrations of: (A) Al_2O_3 and SiO_2; and (B) Al_2O_3 and TiO_2 in the sediments of Alchichica. Symbolized by grey dots, the top sediments (from 0 to 11.5 cm) are enriched in non-detrital silica possibly due to the accumulation of diatoms, whereas samples at 37.3 cm and 71.5 cm are depleted in non-detrital silica, in agreement with FTIR and XRD data.

amorphous phases (Zeyen *et al.*, 2021). This is also consistent with the fact that these phases are found in shallow microbialites populating Lake Alchichica (Zeyen *et al.*, 2021). However, below *ca* 3 cm depth, hydromagnesite rapidly disappears, and diatom frustules are progressively replaced by Al-poor Mg-silicates with a composition corresponding to stevensite, as evidenced by SEM-EDXS and STEM (Figs 6 to 8). These Mg-silicates then rapidly become a dominant phase detected by XRD, FTIR and SEM-EDXS (Figs 4 to 6), and represent between 30 wt.% and 53 wt.% of the sediment content at all depths below *ca* 3 cm, as calculated from the bulk chemistry and relying on FTIR and XRD results (Fig. 10). Thereafter, the authors explain how this massive amount of Mg-silicates results from a diagenetic process occurring within the sediments and not past variations of the nature of the mineral phases settling down in the water column.

Large amounts of authigenic Mg-silicates in modern environments are rarely described in the literature. Badaut & Risacher (1983), and more recently Bentz & Peterson (2020), reported authigenesis of Mg-silicates from diatom frustules (from 25 to 100% of the total diatom content) in the sediments of Bolivian salars. High amounts of Mg-silicates (*ca* 296 μmol Si g^{-1} sediments) were also described in the Amazon delta sediments (Michalopoulos & Aller, 1995, 2004) and in Lake Dziani Dzaha (Mayotte), including Al-poor Mg-silicate associated with shallow microbialites and up to 20 wt.% of Mg-saponite in the sediments (Gérard *et al.*, 2018; Milesi *et al.*, 2019, 2020). Interestingly, the high proportion of Mg-silicates in Lake Alchichica sediments contrasts with the absence of authigenic Mg-silicates in Alchichica shallow microbialites (Zeyen *et al.*, 2019). Zeyen *et al.* (2021) systematically assessed the presence/absence of authigenic Mg-silicates in microbialites from 10 Mexican alkaline crater lakes. They showed that microbialites from most lakes contained Mg-silicates except those in Lake Alchichica. Those authors suggested that this difference may result from the very low orthosilicic acid concentration in Lake Alchichica (64 ± 94 μM) compared with other lakes (for example, 1.10 mM and 0.58 mM in Lakes Atexcac and La Preciosa, respectively; Zeyen *et al.*, 2021), and therefore that water was not saturated enough to allow spontaneous precipitation. They also speculated about the potential causes for a lower acid orthosilicic acid concentration in the water column of Lake Alchichica, mentioning variations in the nature of the weathered protolith and the active extraction of orthosilicic acid by diatoms, similar to what has been shown in oceans (Conley *et al.*, 2017). As explained thereafter, the formation of

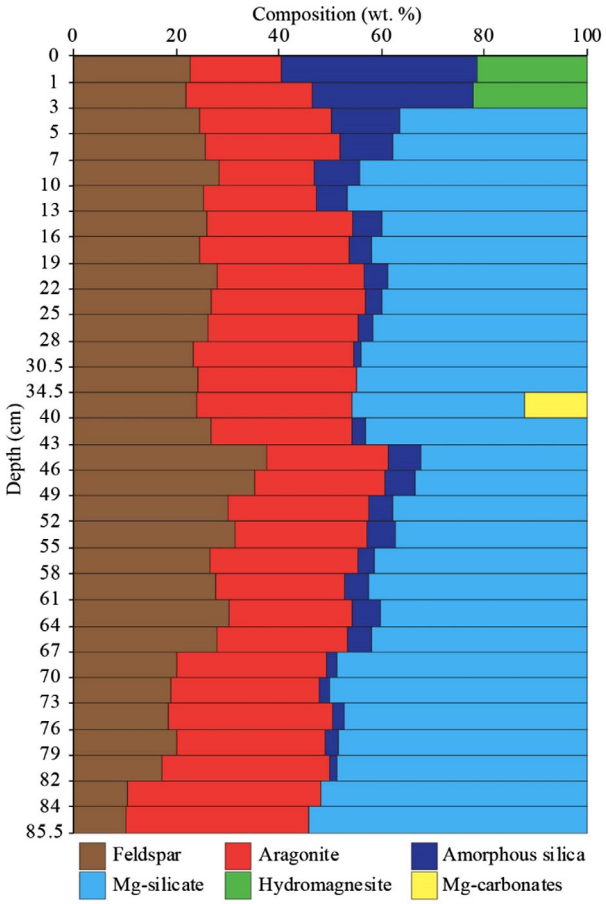

Fig. 10. Estimated mineral content of the sediment (wt. %) as function of depth based on bulk chemical analyses. Mineral stoichiometry used for the quantification of mineral phases is given in Table S3.

Mg-silicates in Lake Alchichica sediments results from a diagenetic process which locally increases the orthosilicic acid concentrations highly enough to allow the precipitation of these phases. The source of the orthosilicic acid is discussed in the next section.

Geochemical processes involved in the formation of Mg-silicates

This section discusses the processes that may explain the evolution at depth of the mineralogical composition of Lake Alchichica sediments, i.e. the correlated disappearance of Mg-carbonates and amorphous silica and appearance of Mg-silicates. In the sediments of Lake Alchichica, the formation of Mg-silicates may result from three different mechanisms providing alternate Mg and/or Si sources:

1 A reaction between detrital silicates as the main source of Si and hydromagnesite as the source of Mg, along the same mechanism as that mentioned by Milesi *et al.* (2019) for the sediments of Lake Dziani Dzaha (Mayotte), and following the equation:

$$1.8Mg_5(OH)_2(CO_3)_4 \cdot 4H_2O + 4KAlSi_3O_8 + 8.8H^+ => 3Mg_3Si_4O_{10}(OH)_2 \cdot H_2O + 4Al^{3+} + 4K^+ + 7.2HCO_3^- + 3.8H_2O$$

2 A reaction between diatom frustules as the main source of Si and hydromagnesite as the source of Mg:

$$3Mg_5(CO_3)_4(OH)_2 \cdot 4H_2O + 20SiO_2 + 7H_2O => 5Mg_3Si_4O_{10}(OH)_2 \cdot H_2O + 12HCO_3^- + 12H^+$$

3 The same reaction as in (2) with aqueous Mg^{2+} from pore water instead of hydromagnesite:

$$3Mg^{2+} + 4SiO_2 + 5H_2O => Mg_3Si_4O_{10}(OH)_2 \cdot H_2O + 6H^+$$

Detrital silicates, which represent 12 to 39 wt.% of the sediment content, could be a source of silica for the formation of Mg-silicates similar to those in Lake Dziani Dzaha. In Dziani Dzaha, the diagenetic Mg-silicates contain significant amounts of Al (3.65 wt.% on average; Milesi *et al.*, 2019). Accordingly, some Al-containing Mg-silicates were observed. However, they were rare and mostly spatially associated with altered detrital silicate phases (Figs 6 and S6). By contrast, diatom frustules appear as a more likely source of SiO_2 involved in the diagenetic formation of Mg-silicates in Lake Alchichica sediments. First, they are abundant enough (around 35 wt.% of the uppermost sediments) to provide all of the Si necessary for the formation of the Mg-silicates detected in the sediments. Second, there is very good correlation between the disappearance of the FTIR bands of amorphous silica and the concomitant appearance of silicates bands below 10 cm (Fig. 5). Last, SEM and TEM analyses showed a massive pseudomorphic replacement of the amorphous silica composing diatoms by Mg-silicates, providing direct images of this diagenetic process (Figs 7 and 8). It can be noted that some Mg-silicate grains do not form as pseudomorphic replacements of diatoms but likely precipitate in the

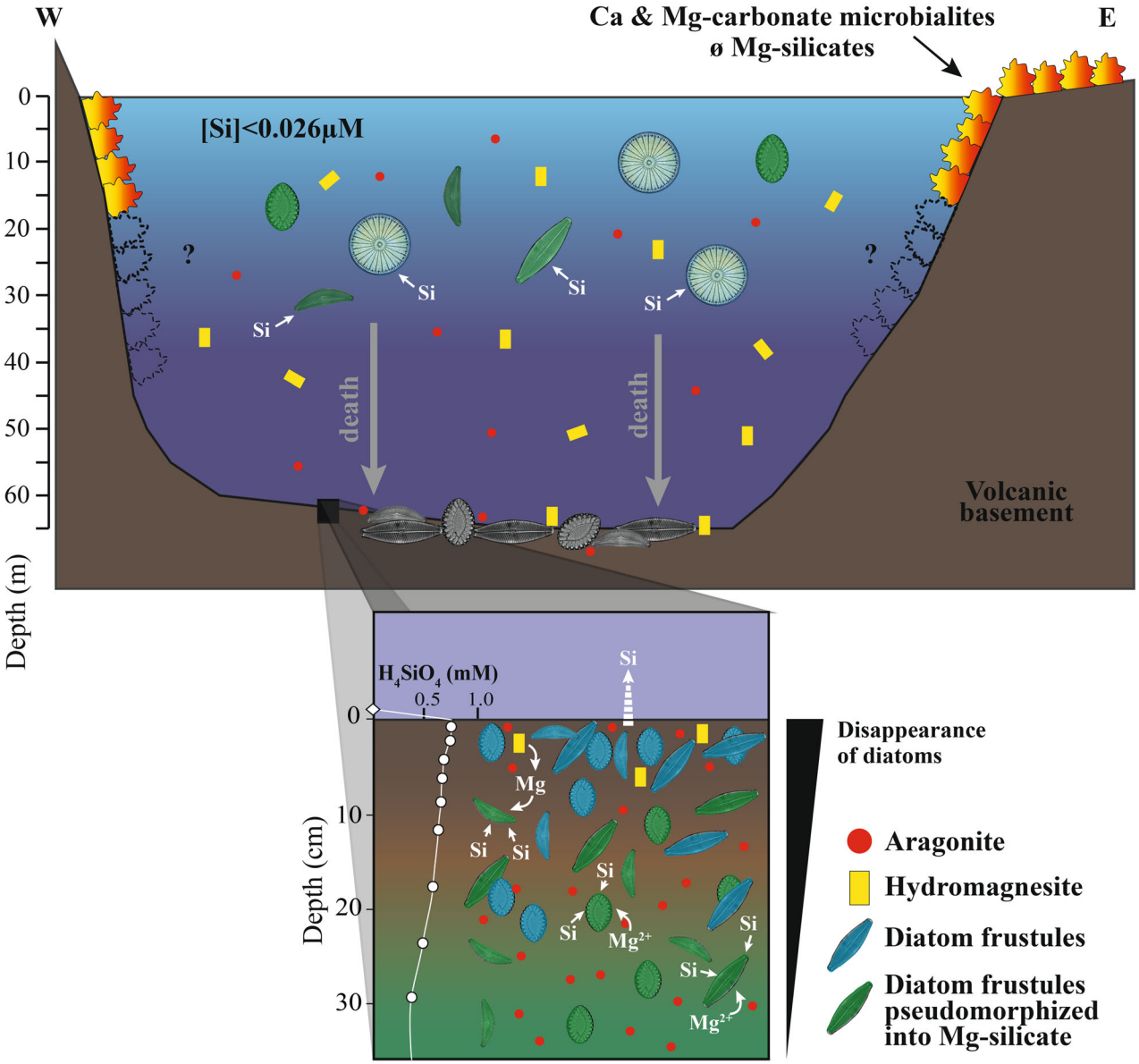

Fig. 11. Summarizing sketch of the mineralogical evolution of the first centimetres of sediments in Lake Alchichica compared to that of the shallow microbialites populating lake waters. In Lake Alchichica, microbialites form at low concentrations of H_4SiO_4 in the lake because the living diatoms are an active SiO_2 sink. They are mainly composed of aragonite (in red) and hydromagnesite (in yellow). In contrast, in the sediments, hydromagnesite rapidly disappears and diatom frustules (in blue) are progressively pseudomorphized into Al-poor Mg-silicates, which become a dominant phase (in green). Therefore, the authigenesis of Mg-silicates in the sediments is mainly controlled by the spontaneous dissolution of diatom frustules which reduces the diffusion rate of H_4SiO_4 from the sediments to the water column.

pore water containing high orthosilicic acid concentrations dissolved from diatoms. Authigenesis of Mg-silicates on diatom frustules was previously observed in the sediments of Bolivian saline lakes (Badaut *et al.*, 1979; Hoffert, 1980; Badaut & Risacher, 1983; Bentz & Peterson, 2020) and marine settings (Michalopoulos & Aller, 2004). The pseudomorphic replacement of the amorphous silica of diatoms by Mg-silicates was also observed occasionally in some microbialites (e.g. Zeyen *et al.*, 2021) but this did not produce the massive amounts

of Mg-silicates as observed in Lake Alchichica sediments.

In cases where diatoms are replaced by Mg-silicates, two sources of Mg can contribute to this process: hydromagnesite and/or dissolved Mg^{2+}. In Lake Alchichica sediments, hydromagnesite disappears below the first 3 cm of sediments, possibly entirely consumed by reaction (2). Using chemical and mineralogical data, the authors calculated that the 20 wt.% of hydromagnesite present in the uppermost sediments (at 0 to 3 cm depth) represent 0.17 mmol of Mg g^{-1} sediment. However, 42 wt.% of Mg-silicates are formed along the core, which represent 0.24 mmol of Mg g^{-1} sediment on average (at 41 to 85 cm; $n = 16$). Therefore, some dissolved Mg^{2+} may also contribute to the formation of Mg-silicates by reaction (3). In addition, between 30 cm and 40 cm depth, hydromagnesite is not totally consumed. Therefore, it is suggested that a lower input of diatoms to the sediments from this depth, at the time they settled down, limited the reaction of Mg-silicates formation, preserving some hydromagnesite. Overall, this suggests that the amount of amorphous silica provided by the diatom frustules (and therefore the ecological dynamics of diatom populations in the lake) is one major control of the extent of Mg-silicates authigenesis in Lake Alchichica sediments.

Geochemical conditions necessary for the authigenesis of Mg-silicates in sediments

While the replacement of amorphous silica by Mg-silicates is massive in Lake Alchichica sediments, and possibly other lakes, it does not obviously occur in all lakes. This work discusses the conditions necessary for this process to take place. For this purpose, the chemical composition of the pore water is helpful. Pore waters in the first 10 cm of the sediments had a constant orthosilicic acid activity (Fig. 3), around 661 ± 24 on average, suggesting a potential control by the solubility of a silica phase that would have a log(Ks) of −3.18 (log(Ks) = log ($a[H_4SiO_4]$); Fig. S7). This value is consistent with what is known for the solubility of diatom silica. Indeed, the solubility constant of diatom frustules is known to be variable and a function of the physicochemical properties of the solid material (for example, degree of condensation and order of the silica framework, water and impurity contents, specific surface area; Willey, 1980; Hurd & Birdwhistell, 1983; Beck *et al.*, 2002; Dixit & Van Cappellen, 2002; Gehlen & Van Raaphorst, 2002; Loucaides *et al.*, 2012a) and of the surrounding solution (for example, temperature, salinity, pressure; Loucaides *et al.*, 2012b). As a result, it likely varies substantially between different diatom species. Overall, it has been shown that diatomaceous silica solubilities exhibit a large variability from 200 to 1600 μM in seawater [log(Ks) between −3.70 and − 2.79; Loucaides *et al.*, 2012a,b, and references therein]. Badaut & Risacher (1983) observed similar solubilities in continental saline lakes around −3. Therefore, the log(Ks) of −3.18 tentatively inferred from the chemical measurements in the pore water of Lake Alchichica is consistent with an equilibrium of pore waters with the amorphous silica phase composing the abundant diatoms of the sediments.

Below 11.5 cm in the sediment depth, the activity of orthosilicic acid is no longer constant, which is consistent with the observed disappearance of silica in the solid by, for example, FTIR. However, the $\log[a(Mg^{2+})/a(H^+)^2]/\log[a(H_4SiO_4)]$ becomes constant (see trend 2 in Fig. 3), i.e. in a $\log[a(Mg^{2+})/a(H^+)^2]$ versus $\log[a(H_4SiO_4)]$ graph, pore waters become aligned along a trend parallel to the solubility line of the 'amorphous sepiolite' defined by Wollast *et al.* (1968) at 25°C (with a log(Ks) of 18.78). The log(Ks) inferred for the Mg-silicate phase observed in Alchichica sediments at 15°C is 19.26 (Fig. S7). This strongly suggests that below 11.5 cm depth, a Mg-silicate phase with this solubility controls the activities of protons, Mg^{2+} and orthosilicic acids in the pore water. This is again in agreement with the fact that such a phase becomes a dominant Si and Mg-bearing phase in the sediments at these depths. This also answers the question of the geochemical conditions necessary for the formation of Mg-silicates in sediments: the ionic product of the solution should be higher or equal to the solubility of a Mg-silicate phase close to that of 'amorphous sepiolite'.

Tosca *et al.* (2011) suggested that a much higher saturation of the solution was needed so that precipitation could spontaneously occur. According to those authors, the different solubility constants obtained by their study versus that by Wollast *et al.* (1968) were related to the source of Si used in their experiments (i.e. respectively sodium metasilicate nonahydrate versus tetraethyl orthosilicate). Here, the observations point to a phase less soluble than that formed in the Tosca *et al.* (2011) experiments.

However, the critical supersaturation line defined by these authors refers to the conditions allowing homogeneous nucleation of Mg-silicates. In Alchichica sediments, the replacement of the diatom frustules by Mg-silicates likely involves heterogeneous nucleation, which is known to occur at lower saturations than homogenous nucleation. Therefore, this may explain why the solubility of the Mg-silicate phase formed in the sediments of Lake Alchichica is lower than that determined by Tosca *et al.* (2011) and closer to that of the 'amorphous sepiolite' defined by Wollast *et al.* (1968). In any case, the authors suggest that the solubility constant determined here should be considered when modelling the formation of Mg-silicates in a natural environment.

Now that the geochemical conditions necessary for the formation of Mg-silicates have been better assessed, some other observations can be understood. First, despite oversaturation relative to the reported solubilities of Mg-silicate phases such as kerolite, stevensite, talc and sepiolite below 30 m depth, the whole water column of Lake Alchichica remains undersaturated with 'amorphous sepiolite'. This explains why no Mg-silicate was observed in the mineral assemblage of the uppermost sediments, suggesting that they do not precipitate from the lake water. Second, pore waters in Lake Dziani Dzaha sediments were undersaturated with 'amorphous sepiolite' at almost all depths, explaining why Al-poor Mg-silicates could not form there and therefore were not observed (Fig. S7). One reason why the saturation in Lake Dziani sediments might be lower than in Lake Alchichica and Bolivian saline lakes sediments (Badaut & Risacher, 1983) may relate to the low abundance of diatoms in the water column of this lake (Gérard *et al.*, 2018). However, Mg-silicates detected in the sediments of Lake Dziani Dzaha were rich in Al (Milesi *et al.*, 2019) in contrast to those observed in Alchichica sediments. Al-rich Mg-silicates have a lower solubility (Milesi *et al.*, 2020), explaining why those phases may form in Lake Dziani Dzaha sediments.

In Lake Dziani Dzaha, the formation of Mg-silicates from detrital silicates by reaction (1) consumes protons and can therefore be driven by a pH decrease. Milesi *et al.* (2019, 2020) proposed that oxidation of organic matter and input of volcanic CO_2 tend to decrease the pH of pore waters, which promotes destabilization of hydromagnesite and ultimately allows Mg supply for the formation of saponite. In Lake Alchichica sediments, the decrease of pH from 9.25 to 8.46 and the DIC increase from 34.1 to 43.2 mM may also reflect oxidation of organic matter and/or input of volcanic CO_2. However, reactions (2) and (3) based on diatom transformation produce protons instead of consuming them. Therefore, these reactions are encouraged by a pH increase, provided that concentrations of Mg and Si are high enough to reach the supersaturation with respect to Mg-silicates precursors, i.e. 'amorphous sepiolite'. Thus, it is suggested here that, in Alchichica sediments, the spontaneous dissolution of the diatom frustules and not organic matter mineralization drives Mg-silicates authigenesis.

Some implications of massive authigenesis of Mg-silicates

Three possible geochemical implications associated with the massive authigenesis of Mg-silicates in Lake Alchichica sediments can be noted.

First, the precipitation of Mg-silicates in Alchichica sediments imposes lower dissolved H_4SiO_4 concentrations in pore waters than if they were in equilibrium with the silica of diatoms (such as in the top 10 cm of sediment, Fig. 3). Therefore, it is suggested that the H_4SiO_4 concentration gradient between the sediments and the water column is also lower, decreasing the diffusion rate of this species from the sediments to the water column. Accordingly, although the H_4SiO_4 concentration increases with lake water depth from below the detection limit to 0.026 mM at 60 m depth and 0.084 mM at the sediment interface, it is much lower than the pore water concentration of 0.76 mM (Table 1). This low Si release rate from the sediments, in addition to a possibly higher abundance of diatoms in the water column, could ultimately favour the low concentrations of H_4SiO_4 observed in Lake Alchichica compared with other lakes in the vicinity (namely Lakes Atexcac and La Preciosa).

Second, the diagenetic formation of Mg-silicates calls for care when interpreting the palaeoenvironmental message carried by the sedimentary record. The presence/absence of Mg-silicates has been suggested to provide information about the palaeochemistry of lakes. However, in Lake Alchichica, the authors observed on the one hand shallow microbialitic deposits without Mg-silicate and on the other hand deep sediments dominated by Mg-silicates. A basin-

wide assessment should therefore be considered whenever possible. In the modern system of Lake Alchichica, it is clear that stromatolites form at low concentrations of H_4SiO_4 in the lake because the living diatoms are an active SiO_2 sink, whereas in the sediments, the dead diatoms are a source of Si that feeds the Mg-silicates precipitation. How likely would it be to find signatures of this process in ancient sediments? Although fossilization of microorganisms by silicates was occasionally observed in modern microbialites (Zeyen *et al.*, 2015), the preservation of diatom morphologies/structures in sediments is not systematic (Michalopoulos & Aller, 2004). In Alchichica, they rather gradually disappear through the massive authigenesis of Mg-silicate around diatoms (Fig. 6). Therefore, the presence/absence of diatoms is not a robust criterion to identify this diagenetic process in the past.

Last, better understanding silicate authigenesis in a variety of environments is key to evaluating the effect of reverse weathering, and especially its involvement in the long-term cycles of C and Si (Mackenzie & Kump, 1995). Reverse weathering refers to the reactions that produce authigenic silicates, which consume soluble cations generated by silicate weathering, but unlike carbonates do not consume carbon (e.g. Isson & Planavsky, 2018; Krissansen-Totton & Catling, 2020). Therefore, it affects not only Si and C cycles but also the climate by retaining CO_2 within the atmosphere–ocean system. While robust evidence for clay authigenesis in modern environments has emerged (Badaut & Risacher, 1983; Michalopoulos & Aller, 1995; Wallmann *et al.*, 2008; Ehlert *et al.*, 2016; Bentz & Peterson, 2020), both laboratory studies (Michalopoulos & Aller, 1995) and analyses of natural marine sediments (Wallmann *et al.*, 2008; Ehlert *et al.*, 2016) suggest that it is almost exclusively restricted to environments characterized by extremely high rates of biogenic opal remineralization (Michalopoulos & Aller, 2004; Ehlert *et al.*, 2016). This type of environment is supposedly rare. Consequently, reverse weathering is generally estimated to constitute only a relatively minor (<10%) component of total dissolved silica export in the modern oceans (e.g. Wallmann *et al.*, 2008). The present study shows a continental system in which Mg-silicate authigenesis by diatom remineralization is major. This allowed us to refine the conditions under which authigenesis occurs. Furthermore, models have tried to quantify reverse weathering over geological times (Isson & Planavsky, 2018; Krissansen-Totton & Catling, 2020). In the Precambrian, before the advent of significant biogenic silica precipitation, ocean silica concentrations were likely elevated (Siever, 1992; Conley *et al.*, 2017), deriving from continental and seafloor weathering (Isson & Planavsky, 2018). Isson & Planavsky (2018) argued that these elevated silica levels may have increased the reverse weathering flux, maintained high levels of CO_2 and warmed the Precambrian climate. Additionally, these authors proposed that reverse weathering is strongly pH dependent, and thus may have buffered ocean pH and stabilized the atmosphere–ocean pCO_2 during the Precambrian. A key parameter in these models is the solubility of authigenic silicates, which has been determined by laboratory experiments and is still debated (Wollast *et al.*, 1968; Tosca *et al.*, 2011). The present work provides a solubility constant deduced from a natural system, lower than that proposed by Tosca *et al.* (2011) and Tosca & Masterson (2014). Therefore, despite there being no observational evidence to date suggesting a greater importance of reverse weathering in the past, its proportion associated with this solubility constant could be higher than predicted by Tosca *et al.* (2011), and thus have a greater impact on pH buffering potential of the oceans and climate regulation. The authors also showed that Mg-silicate authigenesis in Alchichica is strongly driven by diatoms, which appeared late in geological history, likely during the Cretaceous (Girard *et al.*, 2020). Earlier organisms such as sponges, radiolarians and some bacteria (Li *et al.*, 2022) may also have produced silica-rich sediments by biomineralization in the past, which may have fed this reverse weathering process in the same way.

CONCLUSION

Alchichica lacustrine sediments exhibit a particular mineralogical evolution in their first centimetres, which can be explained by early diagenetic reactions (Fig. 11). Below *ca* 3 cm in depth, hydromagnesite rapidly disappears and diatom frustules are progressively pseudomorphized by an Al-poor Mg-silicate phase with a composition corresponding to stevensite. Interestingly, the replacement of amorphous silica by Mg-silicates is massive in Lake Alchichica sediments and contrasts with the absence of

authigenic Mg-silicates in Alchichica shallow microbialites, mainly composed of aragonite and hydromagnesite (Fig. 11). This observation raises questions about the palaeoenvironmental message carried by the sedimentary record, since the presence/absence of Mg-silicates is considered to provide information about the palaeochemistry of lakes. However, in Lake Alchichica, microbialites form at low concentrations of H_4SiO_4 in the lake because the living diatoms are an active SiO_2 sink, whereas in the sediments, the spontaneous dissolution of the diatom frustules drives the Mg-silicates precipitation (Fig. 11). Therefore, an appraisal at the basin scale should be considered whenever possible. Moreover, this study confirms that the preservation of diatom morphologies/structures in sediments is not systematic, and not a robust criterion to identify this process in the past.

In Lake Alchichica sediments, Mg-silicate authigenesis by diatom pseudomorphosis occurs in pore waters saturated with 'amorphous sepiolite' as defined by Wollast *et al.* (1968) (Fig. 3). The solubility constant deduced from this study [log(Ks) = 19.26 at 15°C] is thus lower than that proposed by Tosca *et al.* (2011) and Tosca & Masterson (2014) [log(Ks) = 33.82 at 25°C]. The authors propose that this deduced solubility constant should be considered when modelling the formation of Mg-silicates in a natural environment. The reassessment of this higher solubility constant suggests that reverse weathering may have a greater impact on climate stabilization than previously thought.

ACKNOWLEDGEMENTS

This work was supported by IMPMC (Muséum National d'Histoire Naturelle de Paris, CNRS and Sorbonne University, France), the Adaptation MITI program of the CNRS, the European Research Council under the European Community's Seventh Framework Program (FP7/200-7-2013 Grant Agreement 30711-0-ERC CALCYAN) and Agence Nationale de la Recherche (France; ANR Microbialites, grant number ANR-18-CE02-0013-02). We thank Ludovic Delbes and Benoit Baptiste who managed the XRD platform at IMPMC where analyses were performed. We thank Keevin Beneut and Maxime Guillaumet who managed the FTIR platform at IMPMC where analyses were performed. We thank Imene Esteve, Béatrice Doisneau and Stéphanie Delbrel who managed the SEM platform at IMPMC where analyses were performed. We thank SARM (Nancy, France) for bulk chemical analyses of solids. We thank Laure Cordier for performing ion chromatography analyses at IPGP (France) and Céline Liorzou for performing ICP-AES analyses at Pôle Spectrométrie Océan (Laboratoire Géo-Océan, Brest, France). We thank the anonymous reviewer and Andrea Martín Pérez for their constructive reviews.

CONFLICT OF INTEREST

The authors declare no conflict of interest.

DATA AVAILABILITY STATEMENT

The data that supports the findings of this study are included in this article and available in Supplementary Material.

REFERENCES

Alcocer, J. (2021) Lake Alchichica limnology. In: *The Uniqueness of a Tropical Maar Lake*, p. 491. Springer Nature, Berlin/Heidelberg, Germany.

Alcocer, J. and **Hammer, U.T.** (1998) Saline lake ecosystems of Mexico. *Aquat. Ecosyst. Health Manage.*, **1**, 291–315.

Alcocer, J. and **Oseguera, L.A.** (2019) Lago Alchichica: Una joya de biodiversidad. In: *El cuerpo de agua* (Ed **Facultad de Estudios Superiores Iztacala, Universidad Nacional Autónoma de México**), pp. 63–75. Comisión Nacional para el Conocimiento y Uso de la Biodiversidad, Mexico City, 1a edición. pp.

Alcocer, J., **Lugo, A.**, **Escobar, E.**, **Sánchez, M.D.R.** and **Vilaclara, G.** (2000) Water column stratification and its implications in the tropical warm monomictic Lake Alchichica, Puebla, Mexico. *Int. Vereinigung für theoretische und angewandte Limnologie: Verhandlungen*, **27**, 3166–3169.

Armienta, M.A., **Vilaclara, G.**, **De la Cruz-Reyna, S.**, **Ramos, S.**, **Ceniceros, N.**, **Cruz, O.**, **Aguayo, A.** and **Arcega-Cabrera, F.** (2008) Water chemistry of lakes related to active and inactive Mexican volcanoes. *J. Volcanol. Geotherm. Res.*, **178**, 249–258.

Arp, G., **Reimer, A.** and **Reitner, J.** (2003) Microbialite formation in seawater of increased alkalinity, Satonda crater Lake, Indonesia. *J. Sediment. Res.*, **73**, 105–127.

Arredondo-Figueroa, J.L. (2002) Los axalapascos de la cuenca oriental, Puebla. In: *Lagos y presas de México* (Eds De la Lanza-Espino, G. and García Calderón, J.L.), **8**(1), pp. 81–107. Biotica, compiladores, AGT. México, DF.

Arredondo-Figueroa, J.L., **Borrego-Enríquez, L.E.**, **Castillo-Domínguez, R.M.** and **Valladolid-Laredo, M.A.** (1983) Batimetría y morfometría de los lagos "maars" de la cuenca de Oriental, Puebla, México. *Biótica*, **8**, 37–47.

Assayag, N., **Rivé, K.**, **Ader, M.**, **Jézéquel, D.** and **Agrinier, P.** (2006) Improved method for isotopic and quantitative

analysis of dissolved inorganic carbon in natural water samples. *Rapid Commun. Mass Spectrom.*, **20**, 2243–2251.

Badaut, D. and **Risacher, F.** (1983) Authigenic smectite on diatom frustules in Bolivian saline lakes. *Geochim. Cosmochim. Acta*, **47**, 363–375.

Badaut, D., **Risacher, F.**, **Paquet, H.**, **Eberhart, J.P.** and **Weber, F.** (1979) Néoformation de minéraux argileux à partir de frustules de diatomées: le cas des lacs de l'Altiplano Bolivien. *C. R. Acad. Sci.*, **289**(16), 1191–1193.

Beck, L., **Gehlen, M.**, **Flank, A.M.**, **Van Bennekom, A.J.** and **Van Beusekom, J.E.E.** (2002) The relationship between Al and Si in biogenic silica as determined by PIXE and XAS. *Nucl. Instrum. Methods Phys. Res., Sect. B*, **189**(1–4), 180–184.

Bentz, J.L. and **Peterson, R.C.** (2020) The formation of clay minerals in the mudflats of Bolivian salars. *Clays and Clay Minerals*, **68**(2), 115–134.

Benzerara, K., **Menguy, N.**, **Guyot, F.**, **Vanni, C.** and **Gillet, P.** (2005) TEM study of a silicate-carbonate-microbe interface prepared by focused ion beam milling. *Geochim. Cosmochim. Acta*, **69**, 1413–1422.

Benzerara, K., **Meibom, A.**, **Gautier, Q.**, **Kaźmierczak, J.**, **Stolarski, J.**, **Menguy, N.** and **Brown, G.E.** (2010) Nanotextures of aragonite in stromatolites from the quasi-marine Satonda crater lake, Indonesia. *Geol. Soc. Lond. Spec. Publ.*, **336**, 211–224.

Blanc, P., **Lassin, A.**, **Piantone, P.**, **Azaroual, M.**, **Jacquemet, N.**, **Fabbri, A.** and **Gaucher, E.C.** (2012) Thermoddem: a geochemical database focused on low temperature water/rock interactions and waste materials. *Appl. Geochem.*, **27**, 2107–2116.

Bontognali, T.R., **Vasconcelos, C.**, **Warthmann, R.J.**, **Bernasconi, S.M.**, **Dupraz, C.**, **Strohmenger, C.J.** and **McKenzie, J.A.** (2010) Dolomite formation within microbial mats in the coastal sabkha of Abu Dhabi (United Arab Emirates). *Sedimentology*, **57**, 824–844.

Brindley, G.W., **Bish, D.L.** and **Wan, H.M.** (1977) The nature of kerolite, its relation to talc and stevensite. *Mineral. Mag.*, **41**(320), 443–452.

Bristow, T.F. and **Milliken, R.E.** (2011) Terrestrial perspective on authigenic clay mineral production in ancient martian lakes. *Clays Clay Minerals*, **59**, 339–358.

Bristow, T.F., **Kennedy, M.J.**, **Derkowski, A.**, **Droser, M.L.**, **Jiang, G.** and **Creaser, R.A.** (2009) Mineralogical constraints on the paleoenvironments of the Ediacaran Doushantuo formation. *Proc. Natl. Acad. Sci.*, **106**, 13190–13195.

Burne, R.V., **Moore, L.S.**, **Christy, A.G.**, **Troitzsch, U.**, **King, P.L.**, **Carnerup, A.M.** and **Hamilton, P.J.** (2014) Stevensite in the modern thrombolites of Lake Clifton, Western Australia: a missing link in microbialite mineralization? *Geology*, **42**, 575–578.

Capet, X. (1990). Clay mineralogy of sites 671 and 672, Barbados accretionary complex and Atlantic abyssal plain: Paleoenvironmental and diagenetic implications. In: *Proceedings of the Ocean Drilling Program, scientific results*, pp. 85–96. Ocean Drilling Program.

Chahi, A., **Fritz, B.**, **DuPlay, J.**, **Weber, F.** and **Lucas, J.** (1997) Textural transition and genetic relationship between precursor stevensite and sepiolite in lacustrine sediments (Jbel Rhassoul, Morocco). *Clays Clay Minerals*, **45**, 378–389.

Conley, D.J., **Frings, P.J.**, **Fontorbe, G.**, **Clymans, W.**, **Stadmark, J.**, **Hendry, K.R.**, **Marron, A.O.** and **De La Rocha, C.L.** (2017) Biosilicification drives a decline of dissolved Si in the oceans through geologic time. *Front. Mar. Sci.*, **4**, 397.

Couradeau, E., **Benzerara, K.**, **Moreira, D.**, **Gerard, E.**, **Kaźmierczak, J.**, **Tavera, R.** and **López-García, P.** (2011) Prokaryotic and eukaryotic community structure in field and cultured microbialites from the alkaline Lake Alchichica (Mexico). *PloS One*, **6**, e28767.

Couradeau, E., **Benzerara, K.**, **Gérard, E.**, **Estève, I.**, **Moreira, D.**, **Tavera, R.** and **López-García, P.** (2013) Cyanobacterial calcification in modern microbialites at the submicrometer scale. *Biogeosciences*, **10**, 5255–5266.

Cuadros, J., **Diaz-Hernandez, J.L.**, **Sanchez-Navas, A.**, **Garcia-Casco, A.** and **Yepes, J.** (2016) Chemical and textural controls on the formation of sepiolite, palygorskite and dolomite in volcanic soils. *Geoderma*, **271**, 99–114.

Deocampo, D.M. (2005) Evaporative evolution of surface waters and the role of aqueous CO_2 in magnesium silicate precipitation: Lake Eyasi and Ngorongoro crater, northern Tanzania. *S. Afr. J. Geol.*, **108**, 493–504.

Deocampo, D.M. (2015) Authigenic clay minerals in lacustrine mudstones. *Geol. Soc. Am. Spec. Pap.*, **515**, SPE515-03.

d'Espinose de la Caillerie, J.B., **Kermarec, M.** and **Clause, O.** (1995) ^{29}Si NMR observation of an amorphous magnesium silicate formed during impregnation of silica with Mg(II) in aqueous solution. *J. Phys. Chem.*, **99**, 17273–17281.

Dixit, S. and **Van Cappellen, P.** (2002) Surface chemistry and reactivity of biogenic silica. *Geochim. Cosmochim. Acta*, **66**, 2559–2568.

Ehlert, C., **Doering, K.**, **Wallmann, K.**, **Scholz, F.**, **Sommer, S.**, **Grasse, P.**, **Geilert, S.** and **Frank, M.** (2016) Stable silicon isotope signatures of marine pore waters–biogenic opal dissolution versus authigenic clay mineral formation. *Geochim. Cosmochim. Acta*, **191**, 102–117.

Farmer, V. C. (1974) *The Infrared Spectra of Minerals*. Mineralogical Society, London, UK.

Ferrari, L., **Orozco-Esquivel, T.**, **Manea, V.** and **Manea, M.** (2012) The dynamic history of the trans-Mexican Volcanic Belt and the Mexico subduction zone. *Tectonophysics*, **522**, 122–149.

Fukushi, K. and **Matsumiya, H.** (2018) Control of water chemistry in alkaline lakes: solubility of monohydrocalcite and amorphous magnesium carbonate in $CaCl_2$–$MgCl_2$–Na_2CO_3 solutions. *ACS Earth Space Chem.*, **2**, 735–744.

Galán, E. and **Pozo, M.** (2011) Palygorskite and sepiolite deposits in continental environments. Description, genetic patterns and sedimentary settings. In: *Developments in Clay Science*, Vol. **3**, pp. 125–173. Elsevier, Amsterdam, The Netherlands.

García Martínez, J. (2010) *Efectos climáticos sobre el agua subterránea y el Lago Alchichica, Puebla, México* (Doctoral dissertation, Dissertation, Universidad Nacional Autónoma de México, Mexico).

Gehlen, M. and **Van Raaphorst, W.** (2002) The role of adsorption–desorption surface reactions in controlling interstitial $Si(OH)_4$ concentrations and enhancing $Si(OH)_4$ turn-over in shallow shelf seas. *Cont. Shelf Res.*, **22**, 1529–1547.

Gérard, E., **Ménez, B.**, **Couradeau, E.**, **Moreira, D.**, **Benzerara, K.**, **Tavera, R.** and **López-García, P.** (2013) Specific carbonate–microbe interactions in the modern microbialites of Lake Alchichica (Mexico). *ISME J.*, **7**, 1997–2009.

Gérard, E., **De Goeyse, S.**, **Hugoni, M.**, **Agogué, H.**, **Richard, L.**, **Milesi, V.**, **Guyot, F.**, **Lecourt, L.**, **Borensztajn, S.**,

Joseph, M.-B., **Leclerc, T.**, **Sarazin, G.**, **Jézéquel, D.**, **Leboulanger, C.** and **Ader, M.** (2018) Key role of alphaproteobacteria and cyanobacteria in the formation of stromatolites of Lake Dziani Dzaha (Mayotte, Western Indian Ocean). *Front. Microbiol.*, **9**, 796.

Girard, V., **Saint Martin, S.**, **Buffetaut, E.**, **Saint Martin, J.P.**, **Néraudeau, D.**, **Peyrot, D.**, **Roghi, G.**, **Ragazzi, E.** and **Suteethorn, V.** (2020) Thai amber: insights into early diatom history? *BSGF-Earth Sci. Bull.*, **191**, 191.

Hoffert, M. (1980) Les" Argiles rouges des grands fonds" dans le Pacifique Centre-Est. In: *Authigenese, Transport, Diagenese*, Vol. **61**. Persée-Portail des revues scientifiques en SHS, Strasbourg (France).

Hollingbery, L.A. and **Hull, T.R.** (2012) The thermal decomposition of natural mixtures of huntite and hydromagnesite. *Thermochimica Acta*, **528**, 45–52.

Hurd, D.C. and **Birdwhistell, S.** (1983) On producing a more general model for biogenic silica dissolution. *Am. J. Sci.*, **283**, 1–28.

Iniesto, M., **Moreira, D.**, **Reboul, G.**, **Deschamps, P.**, **Benzerara, K.**, **Bertolino, P.**, **Saghaï, A.**, **Tavera, R.** and **López-García, P.** (2021) Core microbial communities of lacustrine microbialites sampled along an alkalinity gradient. *Environ. Microbiol.*, **23**, 51–68.

Işik Ece, Ö. (1998) Diagenetic transformation of magnesite pebbles and cobbles to sepiolite (meerschaum) in the Miocene Eskisehir lacustrine basin, Turkey. *Clays Clay Minerals*, **46**, 436–445.

Isson, T.T. and **Planavsky, N.J.** (2018) Reverse weathering as a long-term stabilizer of marine pH and planetary climate. *Nature*, **560**, 471–475.

Jones, B.F. and **Galan, E.** (1988) Sepiolite and palygorskite. *Rev. Mineral.*, **19**, 631–674.

Jones, B.F. and **Mumpton, F.A.** (1986) Clay mineral diagenesis in lacustrine sediments. *US Geol. Surv. Bull.*, **1578**, 291–300.

Jones, B.F. and **Spencer, R.J.** (1999) Clay mineral diagenesis at Great SaltLake, Utah, USA. In: *Geochemistry of the Earth's Surface, Proceedings of the 5th International Symposium on Geochemistry of the Earth's Surface* (Ed Armannsson, H.), pp. 293–297. Rotterdam, Balkema.

Jones, B.F. and **Weir, A.H.** (1983) Clay minerals of Lake Abert, an alkaline, saline lake. *Clays and Clay Minerals*, **31**(3), 161–172.

Kangal, O., **Firat, C.** and **Güney, A.** (2005) Flotation properties of unusual carbonates: huntite and hydromagnesite. *Miner. Eng.*, **18**, 631–634.

Kaźmierczak, J., **Kempe, S.**, **Kremer, B.**, **López-García, P.**, **Moreira, D.** and **Tavera, R.** (2011) Hydrochemistry and microbialites of the alkaline crater lake Alchichica, Mexico. *Facies*, **57**, 543–570.

Krissansen-Totton, J. and **Catling, D.C.** (2020) A coupled carbon-silicon cycle model over earth history: reverse weathering as a possible explanation of a warm mid-Proterozoic climate. *Earth Planet. Sci. Lett.*, **537**, 116181.

Léveillé, R.J., **Fyfe, W.S.** and **Longstaffe, F.J.** (2000a) Geomicrobiology of carbonate–silicate microbialites from Hawaiian basaltic sea caves. *Chem. Geol.*, **169**, 339–355.

Léveillé, R.J., **Fyfe, W.S.** and **Longstaffe, F.J.** (2000b) Unusual secondary Ca-Mg-carbonate-kerolite deposits in basaltic caves, Kauai, Hawaii. *J. Geol.*, **108**, 613–621.

Léveillé, R.J., **Longstaffe, F.J.** and **Fyfe, W.S.** (2002) Kerolite in carbonate-rich speleothems and microbial deposits from basaltic caves, Kauai, Hawaii. *Clays Clay Mineral.*, **50**, 514–524.

Li, J., **Liu, P.**, **Menguy, N.**, **Zhang, X.**, **Wang, J.**, **Benzerara, K.**, **Feng, L.**, **Sun, L.**, **Zheng, Y.**, **Meng, F.**, **Gu, L.**, **Leroy, E.**, **Hao, J.**, **Chu, X.** and **Pan, Y.** (2022). Intracellular silicification by early-branching magnetotactic bacteria. *Sci. Adv.*, **8**(19), eabn6045.

Loucaides, S., **Van Cappellen, P.**, **Roubeix, V.**, **Moriceau, B.** and **Ragueneau, O.** (2012a) Controls on the recycling and preservation of biogenic silica from biomineralization to burial. *Silicon*, **4**, 7–22.

Loucaides, S., **Koning, E.** and **Van Cappellen, P.** (2012b) Effect of pressure on silica solubility of diatom frustules in the oceans: results from long-term laboratory and field incubations. *Mar. Chem.*, **136**, 1–6.

Mackenzie, F.T. and **Kump, L.R.** (1995) Reverse weathering, clay mineral formation, and oceanic element cycles. *Science*, **270**, 586.

Melim, L.A. and **Spilde, M.N.** (2018) A new unified model for cave pearls: insights from cave pearls in Carlsbad cavern, New Mexico, USA. *J. Sediment. Res.*, **88**, 344–364.

Michalopoulos, P. and **Aller, R.C.** (1995) Rapid clay mineral formation in Amazon delta sediments: reverse weathering and oceanic elemental cycles. *Science*, **270**, 614–617.

Michalopoulos, P. and **Aller, R.C.** (2004) Early diagenesis of biogenic silica in the Amazon delta: alteration, authigenic clay formation, and storage. *Geochim. Cosmochim. Acta*, **68**, 1061–1085.

Milesi, V.P., **Jézéquel, D.**, **Debure, M.**, **Cadeau, P.**, **Guyot, F.**, **Sarazin, G.**, **Claret, F.**, **Vennin, E.**, **Chaduteau, C.**, **Virgone, A.**, **Gaucher, E.C.** and **Ader, M.** (2019) Formation of magnesium-smectite during lacustrine carbonates early diagenesis: study case of the volcanic crater lake Dziani Dzaha (Mayotte–Indian Ocean). *Sedimentology*, **66**, 983–1001.

Milesi, V.P., **Debure, M.**, **Marty, N.C.**, **Capano, M.**, **Jézéquel, D.**, **Steefel, C.**, **Rouchon, V.**, **Albéric, P.**, **Bard, E.**, **Sarazin, G.**, **Guyot, F.**, **Virgone, A.**, **Gaucher, E.C.** and **Ader, M.** (2020) Early diagenesis of lacustrine carbonates in volcanic settings: the role of magmatic CO2 (Lake Dziani Dzaha, Mayotte, Indian Ocean). *ACS Earth Space Chem.*, **4**, 363–378.

Miller, A.Z., **Pereira, M.F.**, **Calaforra, J.M.**, **Forti, P.**, **Dionísio, A.** and **Saiz-Jimenez, C.** (2014) Siliceous speleothems and associated microbe-mineral interactions from Ana Heva lava tube in Easter Island (Chile). *Geomicrobiol. J.*, **31**, 236–245.

Millot, G. (1970) Superficial geochemistry and the silicate cycle. In: *Geology of Clays*, pp. 355–388. Springer, Berlin, Heidelberg.

Negendank, J.F.W., **Emmermann, R.**, **Krawczyk, R.**, **Mooser, F.**, **Tobschall, H.** and **Werle, D.** (1985) Geological and geochemical investigations on the eastern Transmexican Volcanic Belt. *Geofísica Int.*, **24**, 477–575.

Nied, D., **Enemark-Rasmussen, K.**, **L'Hopital, E.**, **Skibsted, J.** and **Lothenbach, B.** (2016) Properties of magnesium silicate hydrates (MSH). *Cem. Concr. Res.*, **79**, 323–332.

Pace, A., **Bourillot, R.**, **Bouton, A.**, **Vennin, E.**, **Galaup, S.**, **Bundeleva, I.**, **Patrier, P.**, **Dupraz, C.**, **Thomazo, C.**, **Sansjofre, P.**, **Yokoyama, Y.**, **Franceschi, M.**, **Anguy, Y.**, **Pigot, L.**, **Virgone, A.** and **Visscher, P.T.** (2016) Microbial and diagenetic steps leading to the mineralisation of great salt Lake microbialites. *Sci. Rep.*, **6**, 1–12.

Parkhurst, D.L. and **Appelo, C.A.J.** (2013) Description of input and examples for PHREEQC version 3—a computer program for speciation, batch-reaction, one-dimensional

transport, and inverse geochemical calculations. *US Geol. Surv. Techniques Methods*, **6**(A43), 497.

Pozo, M. and **Calvo, J.P.** (2018) An overview of authigenic magnesian clays. *Minerals*, **8**, 520.

Reimer, A., **Landmann, G.** and **Kempe, S.** (2009) Lake Van, eastern Anatolia, hydrochemistry and history. *Aquat. Geochem.*, **15**, 195–222.

Rhouta, B., **Kaddami, H.**, **Elbarqy, J.**, **Amjoud, M.**, **Daoudi, L.**, **Maury, F.**, **Senocq, F.**, **Maazouz, A.** and **Gerard, J.F.** (2008) Elucidating the crystal-chemistry of Jbel Rhassoul stevensite (Morocco) by advanced analytical techniques. *Clay Minerals*, **43**(3), 393–403.

Saghaï, A., **Zivanovic, Y.**, **Moreira, D.**, **Benzerara, K.**, **Bertolino, P.**, **Ragon, M.**, **Tavera, R.**, **López-Archilla, A.I.** and **López-García, P.** (2016) Comparative metagenomics unveils functions and genome features of microbialite-associated communities along a depth gradient. *Environ. Microbiol.*, **18**(12), 4990–5004.

Saghaï, A., **Zivanovic, Y.**, **Zeyen, N.**, **Moreira, D.**, **Benzerara, K.**, **Deschamps, P.**, **Bertolino, P.**, **Rogon, M.**, **Tavera, R.**, **López-Archilla, A.** and **López-García, P.** (2015) Metagenome-based diversity analyses suggest a significant contribution of non-cyanobacterial lineages to carbonate precipitation in modern microbialites. *Front. Microbiol.*, **6**, 797.

Siever, R. (1992) The silica cycle in the Precambrian. *Geochim. Cosmochim. Acta.*, **56**(8), 3265–3272.

Souza-Egipsy, V., **Wierzchos, J.**, **Ascaso, C.** and **Nealson, K.H.** (2005) Mg–silica precipitation in fossilization mechanisms of sand tufa endolithic microbial community, mono Lake (California). *Chem. Geol.*, **217**, 77–87.

Stoessell, R.K. (1988) 25°C and 1 atm dissolution experiments of sepiolite and kerolite. *Geochim. Cosmochim. Acta*, **52**, 365–374.

Tchamabé, B.C., **Carrasco-Núñez, G.**, **Miggins, D.P.** and **Németh, K.** (2020) Late Pleistocene to Holocene activity of Alchichica maar volcano, eastern trans-Mexican volcanic belt. *J. South Am. Earth Sci.*, **97**, 102404.

Tosca, N.J. and **Masterson, A.L.** (2014) Chemical controls on incipient Mg-silicate crystallization at 25 C: implications for early and late diagenesis. *Clay Miner.*, **49**, 165–194.

Tosca, N.J. and **Wright, V.P.** (2018) Diagenetic pathways linked to labile Mg-clays in lacustrine carbonate reservoirs: a model for the origin of secondary porosity in the cretaceous pre-salt Barra Velha formation, offshore Brazil. *Geol. Soc. Lond. Spec. Publ.*, **435**, 33–46.

Tosca, N.J., **Macdonald, F.A.**, **Strauss, J.V.**, **Johnston, D.T.** and **Knoll, A.H.** (2011) Sedimentary talc in Neoproterozoic carbonate successions. *Earth Planet. Sci. Lett.*, **306**, 11–22.

Truesdell, A.H. and **Jones, B.F.** (1974) WATEQ, a computer program for calculating chemical equilibria of natural waters. *J. Res. US Geol. Surv*, **2**, 233–248.

Valdespino-Castillo, P.M., **Hu, P.**, **Merino-Ibarra, M.**, **López-Gómez, L.M.**, **Cerqueda-García, D.**, **Zayas, G.D.**, **Pi-Puig, T.**, **Lestayo, J.A.**, **Holman, H.-Y.** and **Falcón, L.I.** (2018) Exploring biogeochemistry and microbial diversity of extant microbialites in Mexico and Cuba. *Front. Microbiol.*, **9**, 510.

Vilaclara, G., **Chávez, M.**, **Lugo, A.**, **González, H.** and **Gaytán, M.** (1993) Comparative description of crater-lakes basic chemistry in Puebla state, Mexico. *Int. Vereinigung für theoretische und angewandte Limnologie: Verhandlungen*, **25**, 435–440.

Wallmann, K., **Aloisi, G.**, **Haeckel, M.**, **Tishchenko, P.**, **Pavlova, G.**, **Greinert, J.**, **Kutterolf, S.** and **Eisenhauer, A.** (2008) Silicate weathering in anoxic marine sediments. *Geochim. Cosmochim. Acta*, **72**, 2895–2918.

Warren, J.K. (2016) *Evaporites: A geological compendium*. 2nd edn, Springer, Switzerland.

Weaver, C.E. (1989) *Clays, Muds, and Shales. Developments in Sedimentology 44*. Elsevier Science Publisher B.V, The Netherlands.

Willey, J.D. (1980) Effects of aging on silica solubility: a laboratory study. *Geochim. Cosmochim. Acta*, **44**, 573–578.

Wollast, R., **Mackenzie, F.T.** and **Bricker, O.P.** (1968) Experimental precipitation and genesis of sepiolite at earth-surface conditions. *Am. Mineral. J. Earth Planetary Mater.*, **53**, 1645–1662.

Wright, V.P. and **Barnett, A.J.** (2015) An abiotic model for the development of textures in some South Atlantic early cretaceous lacustrine carbonates. *Geol. Soc. Lond. Spec. Publ.*, **418**, 209–219.

Wright, V.P. and **Barnett, A.J.** (2020) The textural evolution and ghost matrices of the cretaceous Barra Velha formation carbonates from the Santos Basin, offshore Brazil. *Facies*, **66**, 1–18.

Zeyen, N., **Benzerara, K.**, **Li, J.**, **Groleau, A.**, **Balan, E.**, **Robert, J.L.**, **Estève, I.**, **Tavera, R.**, **Moreira, D.** and **López-García, P.** (2015) Formation of low-T hydrated silicates in modern microbialites from Mexico and implications for microbial fossilization. *Front. Earth Sci.*, **3**, 64.

Zeyen, N., **Benzerara, K.**, **Menguy, N.**, **Brest, J.**, **Templeton, A.S.**, **Webb, S.M.**, **Gérard, E.**, **Moreira, D.**, **López-García, P.**, **Tavera, R.** and **Morin, G.** (2019) Fe-bearing phases in modern lacustrine microbialites from Mexico. *Geochim. Cosmochim. Acta*, **253**, 201–230.

Zeyen, N., **Benzerara, K.**, **Beyssac, O.**, **Daval, D.**, **Muller, E.**, **Thomazo, C.**, **Tavera, R.**, **López-García, P.**, **Moreira, D.** and **Duprat, E.** (2021) Integrative analysis of the mineralogical and chemical composition of modern microbialites from ten Mexican lakes: what do we learn about their formation? *Geochim. Cosmochim. Acta*, **305**, 148–184.

Manuscript received 14 June 2022; revision accepted 7 December 2022

Supporting Information

Additional information may be found in the online version of this article:

Figure S1. Poorly crystalline phases produce broad diffraction signal on the diffractograms, from which intensity could be estimated.

Figure S2. Example Rietveld fit result (sample AL19_C2a_05) showing the actual data in red and the modelled diffractogram in blue.

Figure S3. Solubility diagram in the: (A) $\log[a(CO_3^{2-})] - \log[a(Ca^{2+})]$; and (B) $\log[a(CO_3^{2-})] - \log[a(Mg^{2+})]$ spaces.

Figure S4. All diffractograms collected on samples from shallowest to deepest.

Figure S5. Fourier transform infrared (FTIR) spectra of the Alchichica sediment cores from the shallowest to the deepest (from top to bottom).

Figure S6. Mg-silicates formed around a detrital feldspar grain.

Figure S7. Solubility diagram in the $\log[a(Mg^{2+})/a(H^{+})^{2}] - \log[a(H_4SiO_4)]$ space determined at 25°C.

Table S1. Sediment composition in wt.% estimated by Rietveld (amorphous free).

Table S2. Stoichiometry of the mineral phases estimated by energy dispersive X-ray spectrometry (EDXS).

Table S3. Method for quantification of mineral phases.

Geochemical Perspectives Letters

The chemical conditions necessary for the formation of microbialites

J. Caumartin[1], K. Benzerara[1*], R. Havas[2], C. Thomazo[2,3], P. Lòpez-García[4], E. Duprat[1]

OPEN ACCESS

https://doi.org/10.7185/geochemlet.2311

Abstract

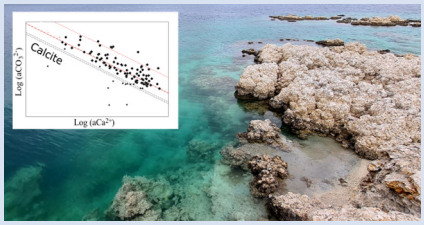

Whether biological and/or physico-chemical variations may have changed the abundance of microbialites over geological times remains debated. This calls for a better appraisal of the conditions necessary for the formation of modern microbialites. Here, we compiled datasets from 140 aqueous environments where modern microbialites have been reported, including their respective physico-chemical parameters. By analysing this database, we find that solutions where microbialites form have a relatively high saturation with calcite, the chemical activities of Ca^{2+} and CO_3^{2-} being controlled by the solubility of amorphous calcium carbonate (ACC) or monohydrocalcite (MHC) in most of these localities. Further statistical analyses of two databases listing ~8000 continental aqueous systems show that only a few of them display saturation with ACC/MHC, appearing as candidates for the detection of overlooked microbialites.

Received 11 July 2022 | Accepted 3 March 2023 | Published 13 April 2023

Introduction

Microbialites are organosedimentary deposits formed by benthic microbial communities that mediate authigenic mineral precipitation (Burne and Moore, 1987). They are found throughout the geological record up to 3.43 billion years ago and are considered as among the oldest traces of life on Earth (Allwood *et al.*, 2007). It has been argued that the diversity of microbialites has varied over geological time with an overall decline at the end of the Proterozoic (*e.g.*, Awramik, 1971). The causes of these fluctuations have fed debates opposing two major models: (i) one involving biotic causes suggests that grazing by Metazoans induced the decline of microbialites (Walter and Heys, 1985), and (ii) a second "abiotic" model proposes that changes in the chemical composition of the ocean were responsible for microbialite decline (Fischer, 1965; Kempe and Kaźmierczak, 1994; Peters *et al.*, 2017).

While this debate is difficult to directly tackle, it emphasises that we still do not understand the conditions necessary for microbialites to form. Modern microbialites have been described in diverse environments (*e.g.*, marine, freshwater, hypersaline) and in the presence of very diverse microbial communities (*e.g.*, Iniesto *et al.*, 2021). Presently, there are many reports in the literature characterising the aqueous geochemistry of single sites where modern microbialites form. However, only a few meta-analyses gathering some of these data provide a broader, statistical overview (*e.g.*, Zeyen *et al.*, 2021). Here, we achieve an unprecedented compilation of datasets from 140 locations where modern microbialites form, spanning freshwater, brackish, saline and hypersaline environments (Table S-1). We analyse the variability of the chemical parameters of microbialite-hosting environments and look for possible invariants. Moreover, in order to assess the rareness/commonness of conditions encountered in microbialite-hosting environments, we compare our database with two databases of continental aqueous systems.

Results

Physico-chemical parameters of microbialite-hosting environments. The compilation was achieved by systematically searching the terms "stromatolite", "thrombolite" or "microbialite" in the literature (see Supplementary Information). The 140 compiled modern microbialite-hosting systems occur on all continents (Fig. S-1) in a diversity of climates and geological contexts. Most of the environments were freshwater, but 34 were marine. The database includes emblematic microbialites, such as those of Shark Bay, Lagoa Vermelha or the Bahamas, that have received much attention as modern analogues of ancient microbialites. Dissolved Ca^{2+} and Mg^{2+} concentrations were measured in a majority (~90 %) of the corresponding aqueous solutions and ranged from 0.001 to 643 mM and 0.001 to 1325 mM, respectively. Concentrations of other major chemical species (Na^+, Cl^-, K^+, SO_4^{2-}) were also generally well documented (~88 % of systems on average). Measurements of the dissolved inorganic carbon (DIC) concentrations ranged between 0.022 and 6236 mM. These measurements were less documented (~76 % of systems) in the database, despite their importance in carbonate-rich environments. In seven lakes, alkalinity values

1. Sorbonne Université, Museum National d'Histoire Naturelle, UMR CNRS 7590, Institut de Minéralogie, de Physique des Matériaux et de Cosmochimie (IMPMC), 75005 Paris, France
2. Université de Bourgogne, Biogéosciences, UMR CNRS EPHE 6282, Dijon, France
3. Institut Universitaire de France, Paris, France
4. Institut Diversité, Ecologie et Evolution du Vivant, UMR 8079, Université Paris-Saclay, France
* Corresponding author (email: karim.benzerara@upmc.fr)

were available and assumed to be equal to DIC (Dickson *et al.*, 1981; Fig. S-2).

Overall, microbialite-forming waters in our database span a high diversity of water chemical types as defined by Boros and Kolpakova (2018), which were: saline (53 % of the occurrences), soda-saline (23 % of the occurrences) and soda (24 % of occurrences) (Fig. S-3). Principal component analyses (PCA) were conducted on 10 chemical variables measured on 545 samples of microbialite-hosting environments in order to find the variables contributing to most of the dataset variability. It showed that most of the variance (~62 %) in the dataset was explained by (i) salinity (logarithms of Na, Cl, K activities) (35.22 %), and (ii) the logarithm of CO_3^{2-} activity anticorrelated with the logarithm of Ca^{2+} activity (26.32 %) (Fig. S-4).

Assessment of the saturation index of waters in which modern microbialites form. The anticorrelation between Ca^{2+} and CO_3^{2-} activities was further analysed by plotting their logarithms against each other. This plot also allows us to assess the saturation index (defined as $SI = \log(IAP/K_s)$, where IAP is the ion activity product and K_s is the solubility constant) of solutions with various $CaCO_3$ phases such as anhydrous crystalline phases and amorphous phases (ACC). Four hundred and sixteen chemical measurements performed on 102 microbialite-forming environments that were available in the database. The mean value was considered for the environments for which several measurements were available (Fig. 1). Conclusions were similar when using the median.

A large majority (89 %) of aqueous environments were highly supersaturated with respect to calcite and aragonite and aligned between the solubility lines of vaterite and an ACC phase (ACC2) as determined by Brečević and Nielsen (1989) (Fig. 1). Diverse ACC phases exist with $\log K_s$ varying between −7.63 and −6.04. Here, many points align close to the solubility lines of MHC and ACC1 phase (another ACC phase as determined by Kellermeier *et al.*, 2014).

A few environments ($n = 5$) appeared significantly undersaturated with calcite. However, three of them harboured microbialites that were siliceous (*e.g.*, Great Obsidian Pool, Mound Spring; Table S-1) or formed by pure trapping and binding of clays (*e.g.*, Lake Untersee, Antarctica; Table S-1). In two others (Kauai caves, Hawaii), microbialites formed on cave walls in freshwater seeping out of basalts and may experience significant chemical variations by evaporation and CO_2 degassing (Léveillé *et al.*, 2007).

Finally, some environments hosting carbonate microbialites were on average supersaturated with anhydrous carbonates but undersaturated with ACC and vaterite ($n = 9$; Figs. 1, S-5). Only one single analysis was available for Ciocaia drill (Romania). However, several ones were available for the other locations. For Pavilion Lake, solution geochemistry varied over time, reaching saturation with ACC at certain periods (Fig. S-5). For Lake Kelly, none of the several available measurements were saturated with ACC but it was reported that microbialites may no longer actively form (Lim *et al.*, 2009). Last, at least four other environments showed spatial chemical heterogeneities. They were undersaturated with ACC on average but supersaturated with ACC at certain locations. For example, Lakes Joyce and Hoare (Antarctica) have chemically stratified waters, and microbialites form at depths where DIC water content rises (Mackey *et al.*, 2018). Pastos Grandes (Bolivia) harbours groundwater outflows chemically evolving by evaporation along their travel away from the source. Microbialites form when water reaches saturation with ACC (Muller *et al.*, 2022). Overall, 98 % of aqueous

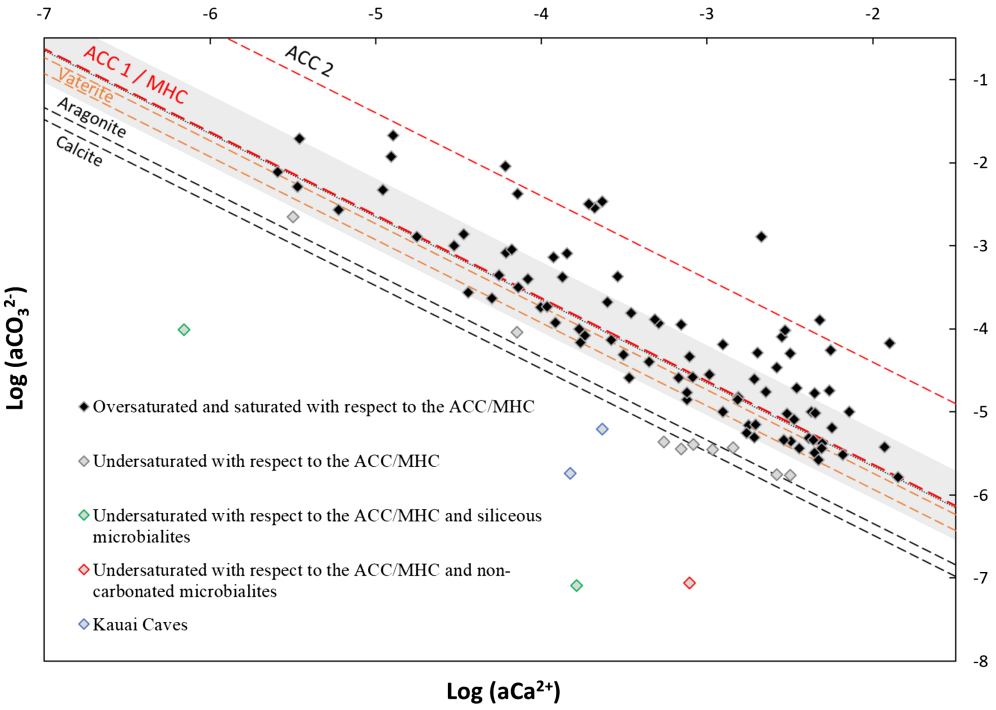

Figure 1 Plot of the log of the activities of CO_3^{2-} *vs.* Ca^{2+} for 102 microbialite-hosting environments. Solubility lines (dashed lines) are reported for calcite ($\log K_s = -8.48$), aragonite ($\log K_s = -8.34$), monohydrocalcite (MHC; $\log K_s = -7.6$), vaterite (De Visscher and Vanderdeelen, 2003), ACC1 as reported by Kellermeier *et al.* (2014; $\log K_s = -7.63$) and ACC2 as reported by Brečević and Nielsen (1989; $\log K_s = -6.39$). Only mean values are provided for each environment by a diamond. Green diamonds correspond to siliceous microbialites; red diamond corresponds to a clayey microbialite. Black diamonds correspond to environments saturated and oversaturated with ACC1 and/or vaterite; grey diamonds correspond to environments undersaturated with vaterite. The grey shaded zone highlights a 95 % confidence interval on the saturation values of microbialite-hosting environments with respect to ACC1/MHC.

environments hosting modern microbialites were saturated with ACC at least part of the time.

Comparison of the chemistry of modern microbialite-hosting aqueous solutions with two global freshwater databases. The chemical compositions of carbonate microbialite-hosting environments were compared with many aqueous environments listed in two general databases, in order to assess how unique the former might be. The Global Lake Ecological Observatory Network (GLEON) database compiles 105,678 samples from 6422 North European lakes with only temperature, pH, DIC and Ca^{2+} concentrations as physico-chemical parameters (Weyhenmeyer *et al.*, 2019; see Supplementary Information). The Environmental Data Initiative (EDI) groups 28,455 samples from 1547 North American lakes with several additional parameters (Supplementary Information). Some of the lakes compiled in the EDI and GLEON databases possibly harbour microbialites but if this is the case, they have not been described in the literature and therefore are not in our microbialites database. The comparison showed that pH, DIC and calcium concentrations in the carbonate microbialite database were significantly higher on average than in lakes from the GLEON and EDI databases (Wilcoxon comparison tests of means; threshold of 0.05 and *p* values of 0, 2.1×10^{-210} and 3.8×10^{-175}, respectively) (Figs. 2a–c, 3 and S-6). A principal component analyses on the physico-chemical parameters from EDI and microbialite-hosting environments databases outlined that ~88 % of the variance of all these aqueous environments is explained by the activity of Cl^- or Ca^{2+} (70.2 % of the variability) and DIC (17.9 %) (Fig. 2d). The EDI lakes spread as

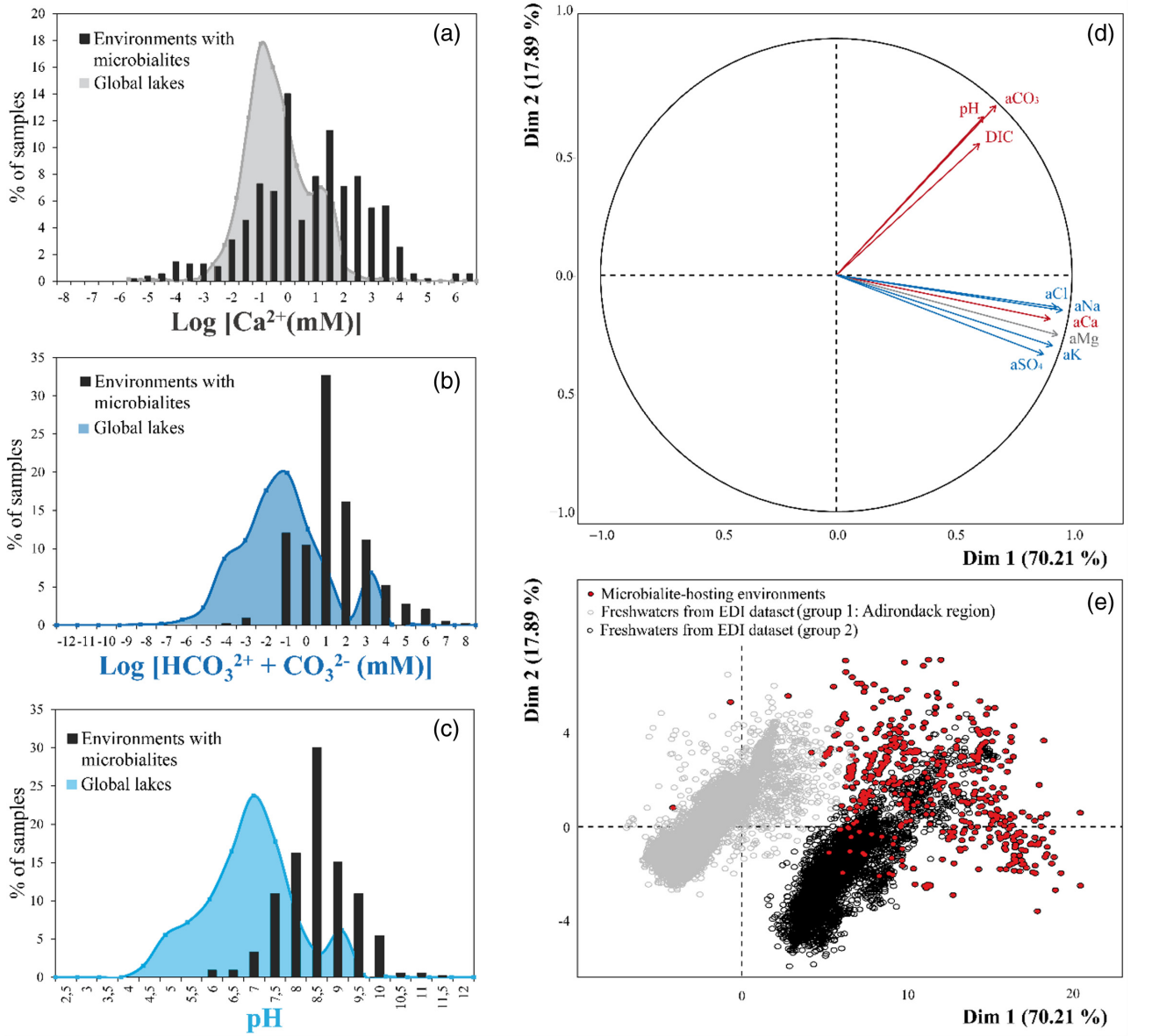

Figure 2 Comparison of the microbialite-hosting environments and lakes in the EDI and GLEON databases. Compared distributions are **(a)** the log [Ca^{2+}(mM)], **(b)** the log [$HCO_3^- + CO_3^{2-}$ (mM)] and **(c)** the pH of the microbialite-hosting environments (black bars) and the EDI and GLEON databases (grey or blue surface). Ca^{2+} activities were calculated using all major ion concentrations in the EDI database, whereas they were approximated to concentrations in the GLEON database. Errors due to this approximation are estimated to be minor (Fig. S-7). **(d)** Correlation circle from the global PCA of the physico-chemical parameters of EDI lakes and microbialite solutions. The logarithms of the activities and DIC were used. The colours correspond to those used to differentiate the principal components on the microbialite-hosting environments PCA (Fig. S-4). **(e)** Plot of all aqueous environments hosting microbialites (red dots) and from the EDI database (black and grey dots) along the two main dimensions of the ACP.

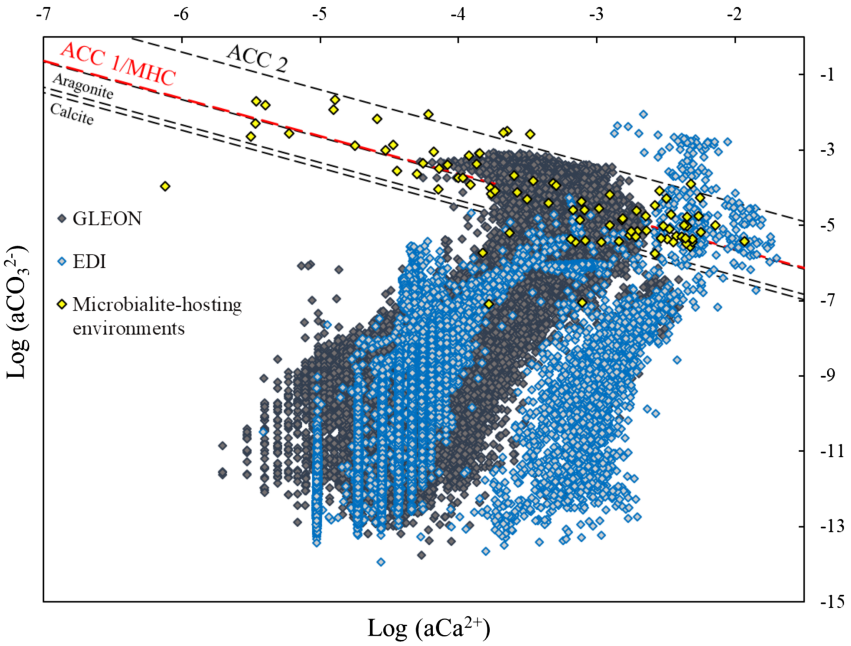

Figure 3 Plot of the activity of CO_3^{2-} *vs.* Ca^{2+} for all lakes from the EDI (blue diamonds), GLEON (grey diamonds) and microbialite-hosting environments (yellow diamonds) datasets. Solubility lines of aragonite, calcite, monohydrocalcite and ACC are the same as in Figure 1.

two groups in the plot of the two PCA dimensions. One group contains Adirondack region lakes (USA), including Mirror Lake, New York, whereas the second group is composed of all other more saline lakes. In this plot, microbialite-forming solutions mostly plot separately and stretch orthogonally to the freshwaters from the EDI database (Fig. 2e). GLEON data were not included in this PCA analysis, because too many parameters were missing.

Finally, by plotting the EDI and GLEON environments in the $CaCO_3$ solubility diagram, less than 5 % of them show saturation with ACC/MHC (Fig. 3).

Discussion

Saturation with vaterite/ACC/MHC as a necessary condition for the formation of microbialites. The need for a relatively high apparent critical saturation of the solutions so that microbialites form is suggested by the analysis of the compiled database. Arp *et al.* (2001) argued that a SI of ~1 relative to calcite was required for biofilm calcification to occur, based on the study of modern non-marine calcifying cyanobacterial biofilms. Such a value approximately corresponds to the solubilities of vaterite, ACC1 or MHC. Moreover, Fukushi *et al.* (2020) observed that several alkaline lakes were saturated with MHC and suggested this phase as a precursor of anhydrous carbonates. Accordingly, many microbialite-hosting environments in our database are alkaline. More recently, the same observation was done by Zeyen *et al.* (2021) in microbialite-hosting lakes in Mexico, who suggested ACC as an alternative precursor. In order to explain these observations, they proposed that ACC may precipitate first, before transforming to the less soluble MHC, then anhydrous carbonate phases, including vaterite. Here, based on a new database of 140 microbialite-bearing systems, encompassing freshwater, saline and hypersaline conditions, we generalise this observation to all environments where microbialites form, suggesting that saturation with ACC1/MHC or with vaterite appears as a necessary condition for the formation of modern microbialites. This model may be further adjusted in the future.

The ACC1 solubility line reported in Figure 1 is a lower bound for ACC. Indeed, the solubility of ACC increases with the Mg content (Mergelsberg *et al.*, 2020). According to Blue and Dove (2015), the partition coefficient K_d of Mg *vs.* Ca in ACC is constant (0.047) for pH below 9.5. Based on this, the Mg/Ca ratio in ACC possibly formed in microbialite-bearing systems ranges between 0.012 and 225, which may correspond to a variation in solubility by ~1 log unit.

Several conditions may allow the achievement of relatively high SI values with $CaCO_3$ as observed in microbialite-hosting environments. Aqueous alkaline environments are fed by fluxes of Ca^{2+} and HCO_3^- ions, *e.g.*, from water-rock interactions, and/or atmospheric inputs (Pulido-Villena *et al.*, 2006). This generally does not directly create high saturation conditions, except when locally, *e.g.*, Ca^{2+}-rich groundwater outflows in high DIC lakes such as in Lake Van (Shapley *et al.*, 2005). In many cases, evaporation is a major driver for concentrating solutions and achieving high saturation with $CaCO_3$ (Pecoraino *et al.*, 2015). This is consistent with the abundance of microbialites in saline environments. The SI values of aqueous solutions are not controlled by the precipitation of crystalline anhydrous $CaCO_3$, which are the least soluble $CaCO_3$ phases. Instead, SI values are higher. Recently, Pietzsch *et al.* (2022), suggested that in some alkaline lakes, orthophosphate concentrations are high and inhibit crystalline anhydrous $CaCO_3$ precipitation, allowing the onset of saturation levels as high as the solubility of ACC. Unfortunately, this cannot be further tested here since dissolved PO_4^{2-} concentrations are only reported in eleven microbialite-forming environments of our database. Similarly, the role of exopolymeric substances (EPS) in locally controlling SI values could be questioned. Whether this inhibition may be a major process in all reported microbialite-hosting environments will require further data acquisition. Once Ca^{2+} and CO_3^{2-} activities reach values high enough so that MHC/ACC solubility is attained, we hypothesise that any further input of Ca^{2+} and/or DIC to the system can contribute to the accumulation of carbonates, partly as microbialites, helping to control their overall abundance in the aqueous system.

Another outcome of the present analyses is that they may help in finding localities where modern microbialites have been potentially overlooked so far, by screening aqueous environments based on their SI with $CaCO_3$ (Fig. 3). Some environments listed in the GLEON and EDI databases are saturated with ACC/MHC. However, we presently do not know if they host microbialites. Two options are possible: (i) all these environments host microbialites, which would imply that saturation with ACC/MHC is a necessary and sufficient condition for microbialite formation; and (ii) some of these environments do not contain microbialites, which means that some other conditions may be necessary in addition to saturation with ACC/MHC to form microbialites.

Presently, it may be speculated that changes in seawater chemistry, possibly at the end of the Proterozoic, from ACC-saturated to ACC-undersaturated seawater, may have caused the decline of microbialite abundances (Fig. S-8). However, to be validated, this speculation will need further constraints on the value of SI_{ACC} in past oceans.

Finally, a control of water chemistry by MHC/ACC precipitation as a necessary condition for the growth of microbialites does not mean that microbial communities or any biological parameter have no impact at all in the formation of microbialites. Instead, it suggests that in order for them to participate in authigenic microbialite formation, at least some specific physico-chemical environmental conditions, *i.e.* saturation with ACC/MHC, must be met.

Acknowledgements

This project received financial support from the CNRS through the MITI interdisciplinary programs and the ANR Microbialites. The authors thank Elodie Muller and Nina Zeyen for their help on setting up of the dataset. JC is funded by a grant from the Interface pour le vivant doctorate programme at Sorbonne Université.

Editor: Satish Myneni

Additional Information

Supplementary Information accompanies this letter at https://www.geochemicalperspectivesletters.org/article2311.

Cite this letter as: Caumartin, J., Benzerara, K., Havas, R., Thomazo, C., Lòpez-García, P., Duprat, E. (2023) The chemical conditions necessary for the formation of microbialites. *Geochem. Persp. Let.* 25, 30–35. https://doi.org/10.7185/geochemlet.2311

References

Allwood, A.C., Walter, M.R., Burch, I.W., Kamber, B.S. (2007) 3.43 billion-year-old stromatolite reef from the Pilbara Craton of Western Australia: Ecosystem-scale insights to early life on Earth. *Precambrian Research* 158, 198–227. https://doi.org/10.1016/j.precamres.2007.04.013

Arp, G., Reimer, A., Reitner, J. (2001) Photosynthesis-Induced Biofilm Calcification and Calcium Concentrations in Phanerozoic Oceans. *Science* 292, 1701–1704. https://doi.org/10.1126/science.1057204

Awramik, S.M. (1971) Precambrian Columnar Stromatolite Diversity: Reflection of Metazoan Appearance. *Science* 174, 825–827. https://doi.org/10.1126/science.174.4011.825

Blue, C.R., Dove, P.M. (2015) Chemical controls on the magnesium content of amorphous calcium carbonate. *Geochimica et Cosmochimica Acta* 148, 23–33. https://doi.org/10.1016/j.gca.2014.08.003

Boros, E., Kolpakova, M. (2018) A review of the defining chemical properties of soda lakes and pans: An assessment on a large geographic scale of Eurasian inland saline surface waters. *PLoS ONE* 13, e0202205. https://doi.org/10.1371/journal.pone.0202205

Brečević, L., Nielsen, A.E. (1989) Solubility of amorphous calcium carbonate. *Journal of Crystal Growth* 98, 504–510. https://doi.org/10.1016/0022-0248(89)90168-1

Burne, R.V., Moore, L.S. (1987) Microbialites: organosedimentary deposits of benthic microbial communities. *PALAIOS* 2, 241–254. https://doi.org/10.2307/3514674

De Visscher, A., Vanderdeelen, J. (2003) Estimation of the Solubility Constant of Calcite, Aragonite, and Vaterite at 25°C Based on Primary Data Using the *Pitzer* Ion Interaction Approach. *Monatshefte für Chemie/Chemical Monthly* 134, 769–775. https://doi.org/10.1007/s00706-002-0587-3

Dickson, A.G. (1981) An exact definition of total alkalinity and a procedure for the estimation of alkalinity and total inorganic carbon from titration data. *Deep Sea Research Part A. Oceanographic Research Papers* 28, 609–623. https://doi.org/10.1016/0198-0149(81)90121-7

Fischer, A.G. (1965) Fossils, early life, and atmospheric history. *Proceedings of the National Academy of Sciences* 53, 1205–1215. https://doi.org/10.1073/pnas.53.6.1205-a

Fukushi, K., Imai, E., Sekine, Y., Kitajima, T., Gankhurel, B., Davaasuren, D., Hasebe, N. (2020) In Situ Formation of Monohydrocalcite in Alkaline Saline Lakes of the Valley of Gobi Lakes: Prediction for Mg, Ca, and Total Dissolved Carbonate Concentrations in Enceladus' Ocean and Alkaline-Carbonate Ocean Worlds. *Minerals* 10, 669. https://doi.org/10.3390/min10080669

Iniesto, M., Moreira, D., Reboul, G., Deschamps, P., Benzerara, K., Bertolino, P., Saghaï, A., Tavera, R., López-García, P. (2021) Core microbial communities of lacustrine microbialites sampled along an alkalinity gradient. *Environmental Microbiology* 23, 51–68. https://doi.org/10.1111/1462-2920.15252

Kellermeier, M., Picker, A., Kempter, A., Cölfen, H., Gebauer, D. (2014) A Straightforward Treatment of Activity in Aqueous $CaCO_3$ Solutions and the Consequences for Nucleation Theory. *Advanced Materials* 26, 752–757. https://doi.org/10.1002/adma.201303643

Kempe, S., Kaźmierczak, J. (1994) The role of alkalinity in the evolution of ocean chemistry, organization of living systems, and biocalcification processes. In: Doumenge, F. (Ed.) *Past and Present Biomineralization Processes. Considerations about the Carbonate Cycle*. IUCN – COE Workshop, 15–16 November 1993, Monaco. Bulletin de l'Institut océanographique, Monaco, numéro special 13, 61–117.

Léveillé, R.J., Longstaffe, F.J., Fyfe, W.S. (2007) An isotopic and geochemical study of carbonate-clay mineralization in basaltic caves: abiotic versus microbial processes. *Geobiology* 5, 235–249. https://doi.org/10.1111/j.1472-4669.2007.00109.x

Lim, D.S.S., Laval, B.E., Slater, G., Antoniades, D., Forrest, A.L., *et al.* (2009) Limnology of Pavilion Lake, B. C., Canada – Characterization of a microbialite forming environment. *Fundamental and Applied Limnology/Archiv für Hydrobiologie* 173, 329–351. https://doi.org/10.1127/1863-9135/2009/0173-0329

Mackey, T.J., Sumner, D.Y., Hawes, I., Leidman, S.Z., Andersen, D.T., Jungblut, A.D. (2018) Stromatolite records of environmental change in perennially ice-covered Lake Joyce, McMurdo Dry Valleys, Antarctica. *Biogeochemistry* 137, 73–92. https://doi.org/10.1007/s10533-017-0402-1

Mergelsberg, S.T., De Yoreo, J.J., Miller, Q.R.S., Michel, F.M., Ulrich, R.N., Dove, P.M. (2020) Metastable solubility and local structure of amorphous calcium carbonate (ACC). *Geochimica et Cosmochimica Acta* 289, 196–206. https://doi.org/10.1016/j.gca.2020.06.030

Muller, E., Ader, M., Aloisi, G., Bougeault, C., Durlet, C., *et al.* (2022) Successive Modes of Carbonate Precipitation in Microbialites along the Hydrothermal Spring of La Salsa in Laguna Pastos Grandes (Bolivian Altiplano). *Geosciences* 12, 88. https://doi.org/10.3390/geosciences12020088

Pecoraino, G., D'Alessandro, W., Inguaggiato, S. (2015) The Other Side of the Coin: Geochemistry of Alkaline Lakes in Volcanic Areas. In: Rouwet, D., Christenson, B., Tassi, F., Vandemeulebrouck, J. (Eds.) *Volcanic Lakes*.